MekIT'17

Ninth national conference on

Computational Mechanics

Trondheim 11-12 May 2017

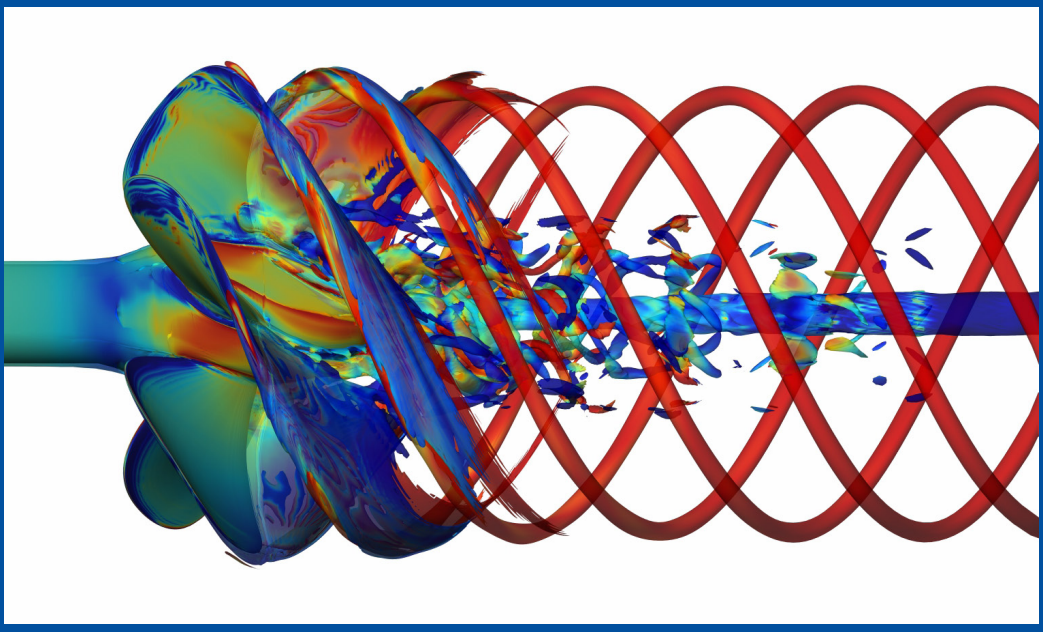

Editors: Bjørn Skallerud and Helge I. Andersson

NTNU
Innovations and Creativity

MekIT'17

Ninth national conference on

Computational Mechanics

Trondheim 11-12 May 2017

Editors: Bjørn Skallerud and Helge I. Andersson

NTNU
Innovations and Creativity

International Center for Numerical Methods in Engineering (CIMNE)
Gran Capitán s/n, 08034 Barcelona, Spain
www.cimne.com

Printed by: Artes Gráficas Torres S.L., Huelva 9, 08940 Cornellà de Llobregat, Spain

Deposito legal: B-16544-2016

ISBN: 978-84-947311-1-2

Preface

The present volume contains 29 of the 37 papers presented at the *9th National Conference on Computational Mechanics - MekIT'17* held at The Norwegian University of Science and Technology (NTNU) in Trondheim (Norway) May 11th and May 12th, 2017.

The series of national conferences on Computational Mechanics dates back to MekIT'01, which was arranged at NTNU in Trondheim early May 2001. The motivation of the first MekIT conference was to bring together those involved in Computational Mechanics in Norway, both in industry and academia, to share their experiences and report on their research in an informal and friendly setting. An arena where those involved with rather different applications of Computational Mechanics, as well as scientists developing new computational methods of more generic nature, could meet was non-existing in Norway at that time.

The conferences have from the very beginning aimed to cover all sub-areas of Computational Mechanics and not only computational solid mechanics and fluid dynamics. In spite of distinctions in approach and methodology the difficulties faced by the researchers are often of similar nature and problems can perhaps be remedied in the same way irrespective of the actual application. It has all the time been our hope that the conference series will demonstrate that computational mechanics is a viable research tool by which both human curiosity and industrial needs can be satisfied by scrutinizing the laws of classical mechanics, provided that adequate numerical methods are implemented in reliable software, and efficient computers are available.

A particular mission has been to offer a stimulating environment in which doctoral students and other young researchers can present results of their own project work, perhaps for the first time, and at the same time get an impression of the multifaceted research which takes place in other research groups and at other institutions in Norway. The biennial conferences have now evolved into a tradition and every odd numbered year, about when the snow melts and the trees turn green in central Norway, a new MekIT-conference takes place.

This year several talks reflected the widespread usage of CFD in marine milieus with applications either in offshore or coastal engineering. This is probably a consequence of the increasing complexity of relevant problems in marine technologies and therefore reflects the need for more realistic mathematical models including both viscous and turbulent effects. Potential flow models, which traditionally have been the preferred modeling choice, do not account for such effects and are therefore unable to provide physical insight in and reliable results for most of the flow problems considered. Besides the complex geometries often encountered in marine CFD, effects of viscosity and turbulence are paramount to compute, for instance, boundary layers, separated flow phenomena, and/or vortical flow. These effects are represented from 1st principles, i.e. without any semi-empirical modeling in direct numerical simulations (DNS). However, the Reynolds number (Re) is so high for many real-world applications that DNS is not feasible. One therefore resort to large-eddy simulations (LES) in which the unresolved flow-scales are modeled, or to the approached based on the Reynolds-averaged Navier-Stokes (RANS) equations for which all scales of the turbulent flow field require modeling. RANS-modeling is formally valid at any Re, but the realism of the RANS-approach relies on the physical realism of the additional modeling of the so-called Reynolds stresses, as well as on an adequate numerical treatment. The national state-of-the-art of marine CFD is demonstrated by the contributions from the NTNU departments of Marine Technology and Civil and Transport Engineering included in these Proceedings.

In addition to the contributed talks, three keynote lectures are delivered by carefully selected scientists, normally recruited from the other Scandinavian countries to give an impression of state-of-the art in Computational Mechanics. This year we were delighted that Professor Ray Ogden (School of Mathematics and Statistics, University of Glasgow), Professor Johan Revstedt (Department of Energy Sciences, Lund University) and Professor Ole Sigmund (Department of Mechanical Engineering, Technical University of Denmark) all shared their vast expertise with us in their fascinating presentations.

The regular contributions have primarily been written by PhD students and other young researchers together with their supervisor(s) or project leader(s) and always in English. The manuscripts were submitted before the start of the conference. Each manuscript has been subjected

to reviewing by at least one member of the Scientific Committee and in most cases also by a peer outside of the Scientific Committee. The authors were thereafter asked to revise their manuscripts in accordance with the comments and suggestions made by the reviewers. The majority of the authors accepted our invitation to prepare a carefully revised version of their manuscript, which now is included in the printed conference proceedings. Following the three papers by the invited lecturers, the 26 contributed papers appear alphabetically according to the family name of the first author and are listed in the Table of Contents. All authors and co-authors of the contributed papers are included in the Author Index.

Earlier proceedings have been published by Tapir Academic Press and Akademika Publishing just prior to the conference. The proceedings were published by CIMNE for the first time in 2015 and not until a couple of months after the conference. This new scheme enables a more thorough reviewing process and hopefully contribute to the quality of this collection of 29 papers.

The conference MekIT'17 was hosted by NTNU's Faculty of Engineering and arranged jointly by Department of Energy and Process Engineering and Department of Structural Engineering. The Editors appreciate the willingness of the authors to stick to the time schedule for paper submission and revision. We are particularly thankful to the members of the Scientific Committee and their peers for reviewing the submitted papers and thereby assure the quality of these Proceedings. The administrative assistance of Ms Ingrid Wiggen is gratefully acknowledged.

September 2017

Helge Andersson
Bjørn Skallerud

Chairmen:

Professor Bjørn Skallerud – Department of Structural Engineering (NTNU)
Professor Helge I. Andersson – Department of Energy and Process Engineering (NTNU)

Scientific Committee:

Helge I. Andersson (NTNU)
Hans Bihs (NTNU)
John Grue (University of Oslo)
Trond Kvamsdal (NTNU/SINTEF)
Mikael Mortensen (University of Oslo)
Muk C Ong (University of Stavanger)
Bjørnar Pettersen (NTNU)
Bjørn Skallerud (NTNU)
Geir Skeie (DNV GL, Oslo)
Magnus Svärd (University of Bergen)

Sponsor: NTNU's Department of Energy and Process Engineering

Front cover graphics:

The Editors would like to express their gratitude to Dr Ville Viitanen (VTT Technical Research Centre of Finland) and Professor Timo Siikonen (Aalto University in Helsinki) for the front cover graphics.

Table of Contents

Hans Petter Langtangen 1

R. W. Ogden and G. A. Holzapfel
On the elasticity and dispersed fibers in soft biological tissues 3

J. Revstedt and J. Lorentzon
Dynamic response and wake structures of cantilevers with square cross-section 7

J. Groen, S. D. Larsen and **O. Sigmund**
Recent developments in large and multiscale topology optimization 21

A. Aggarwal, M. A. Chella, H. Bihs, C. Pakzodi and Ø. A. Arntsen
CFD modelling of irregular and focused waves using wave reconstruction 25

E. Aursand
Modeling planar film boiling of arbitrary inclination with the lubrication approximation 35

J. Berntsen, G. Alendal, H. Avlesen and Ø. Thiem
Numerical investigations of dense water cascading on a slope – the role of the bottom boundary layer 57

H. Bihs, A. Kamath, M. A. Chella and C. Pakozdi
Complex geometry handling for a cartesian grid based solver 71

M. A. Chella, H. Bihs and Ø. A Arntsen
A comparison of wave generation methods simulating exgtreme waves in a numerical wave tank 85

C. Nilsen
Numerical investigation of thermos-viscous instability in immiscible displacement 103

F. H Dadmarzi, V. D. Narasimhamamurthy, H. I. Andersson and B. Pettersen
Influence of computational domain size on wakes behind cross-shaped plates 111

S. Eidnes and T. Ringholm
Energy preserving moving mesh methods applied to the bbm equation 121

P. Fornes, H. Bihs and S. Nordal
Implementation of non-newtonian rheology for granular flow simulation 137

C. J. Friedemann, M. Mortensen and J. Nossen
Multiphase flow simulation in an annulus configuration 151

T. A. Helgedagsrud, Y. Bazilevs, A. Korobenko, K. M. Mathisen and O. A. Øiseth
Using ale-vms to compute wind forces on moving bridge decks 169

H. Liu, V. E. Prot and B. Skallerud
Tissue composition based nonlinear fem simulation of the soft palate using patient specific 3d geometry 191

A. Ilseng, V. Prot, B. Skallerud and B. T. Stokke
Finite element simulations of the swelling of cationic hydrogels 215

J. Z. Lu, A. Kamath and H. Bihs
Simulation of freely-floating bodies in waves using a 6dof algorithm 231

K. M. Mathisen, Y. Bazilevs, B. Haugen, T. A. Helgedagsrud, T. Kvamsdal, K. M. Okstad and S. B. Raknes
A comparative study of beam element formulations for nonlinear analysis: Corotational vs geometrically exact formulations 245

M. Mortensen
Shenfun – automatic the spectral galerkin method 273

M. C. Ong, S. Liu, U. C. Liestyarini and Y. Xing
Three dimensional numerical simulation of flow in blind-tee pipes 299

N. Ahmad, H. Bihs, A. Kamath and Ø. A. Arntsen
A numerical investigation of erosion around offshore pipelines 311

A. Nocente, T. Arslan and E. Ayder
Numerical simulations for the flow inside the pump as a turbine 327

H. Strandenes, F. Jiang, B. Pettersen and H. I. Andersson
Recent developments and new results on the flow around an inclined 6:1 prolate speroid 337

F. Sund
The relative importance of model parameters in transient gas-pipeline flow 351

C. Tian, F. Jiang, B. Pettersen and H. I. Andersson
Numerical investigation of flow around a step cylinder 369

V. M. Vitanen and T. Siikonen
Numerical simulation of cavitating marine propeller flows 385

W. Wang, H. Bihs, A. Kamath and Ø. A. Arntsen
Large scale cfd modelling of wave propagation in Sulafjord for the E39 project 411

W. Yuan, L. Zhao, N. R. Challabotla and H. I. Andersson
Gravity effects on the wall-normal motion of inertial disk-lie particles in turbulent vertical channel flow 425

K. Yang, L. Zhao and H. I. Andersson
Scales of a turbulent Couette-Poiseuille flow with vanishing mean wall shear 441

AUTHOR INDEX 455

Professor Hans Petter Langtangen (03.01.1962-10.10.2016)

It was with great sadness we received the news that Hans Petter passed away last fall. He had struggled with severe illness for more than two years. For everyone that met Hans Petter, he made a lasting impression with his enormous enthusiasm and deep knowledge of computational mechanics and numerical methods. He was always open to new research areas and inter-disciplinary collaboration. Of the many achievements, he has authored ten (!) books. The last two books were written during his time of illness. Many of the books addressed numerical methods and implementation for solution of partial differential equations using C++ (DiffPack) or Python. He was editor-in-chief of SIAM *Journal of Scientific Computing* (2011-2015) and director of Center of excellence (SFF) *Biomedical Computing* from 2007 to 2015.

Hans Petter will always have a special place in the Norwegian computational mechanics community, and he was very central in establishing our National Conference on Computational Mechanics (Mekit). Around year 2000 Helge and Bjørn started throwing ideas about showing current activities in computational mechanics in Norway and finding a meeting place for this. We started thinking about a conference and exchanged ideas with Hans Petter. With many activities on computational mechanics and scientific computing in Oslo (UiO and Simula), it was very important to raise interest there. Hans Petter found the idea of Mekit to be very good, and with his help, we arranged a very successful Mekit'01 in 2001. For the years to come, as member of the scientific board, Hans Petter played a major role in arranging Mekit. This year (Mekit'17) will be special, with a good colleague and friend missing, but we believe that Hans Petter would have been very satisfied with the spirit and scope of this year's conference.

Bjørn Skallerud and Helge I Andersson

9. National Conference on Computational Mechanics
MekIT'17
B. Skallerud and H I Andersson (Eds)

ON THE ELASTICITY OF DISPERSED FIBERS IN SOFT BIOLOGICAL TISSUES

RAY W. OGDEN[1] AND GERHARD A. HOLZAPFEL[2,3]

[1]School of Mathematics and Statistics
University of Glasgow
University Place, Glasgow G12 8SQ, UK
e-mail: raymond.ogden@glasgow.ac.uk

[2]Institute of Biomechanics
Graz University of Technology
Stremayrgasse 16-II, Graz 8010, Austria
e-mail: holzapfel@tugraz.at

[3]Faculty of Engineering Science and Technology
Norwegian University of Science and Technology (NTNU)
7491 Trondheim, Norway

Key words: Fibrous Biological Tissues, Soft Tissue Elasticity, Fiber Dispersion Model, Generalized Structure Tensor, Angular Integration Model

Abstract. In this study the predictions of two models of the elastic properties of fibrous soft biological tissues with dispersed fibers are compared. In particular, it is shown that the predictions of the angular integration model and the model based on a generalized structure tensor are essentially identical, contrary to certain claims in the literature. It is also noted that either model framework is able to accommodate exclusion of the contribution of compressed fibers to the material response.

1 INTRODUCTION

In this extended abstract we compare two models that are used to describe the elastic properties of fiber-reinforced materials with dispersed fibers, with particular reference to soft biological tissues such as artery walls. One model, due to Lanir [1], is based on the method of angular integration (AI), and the other, due to Gasser et al. [2] is based on a generalized structure tensor (GST), so that the associated constitutive frameworks are quite different. It has been shown by Holzapfel and Ogden [3, 4] that the predictions of the two models are virtually identical for a significant range of large deformations, and this has been illustrated for both simple tension and simple shear deformations. This is in sharp contrast to 'results' in the literature which are based on flawed analysis; see, for

example, [5, 6, 7]. Another aspect of the two models is that they are both able to exclude compressed fibers from contributing to the stress response of the materials. Details of the theory and implementation of this for the AI model are provided in [8, 9, 10], while [3] contains a theoretical approach that accommodates exclusion of compressed fibers in the GST model. An alternative approach for the GST model is described in [11].

2 ILLUSTRATIONS

Here we provide two illustrations of the above discussion. First, a comparison of the predictions of the two models for simple shear in the $(1,2)$ plane without exclusion of compressed fibers is shown in Figure 1. The shear stress is denoted $\hat{\sigma}_{12}$ and plotted in dimensionless form $\hat{\sigma}_{12}/\mu$ against the amount of shear γ for a mean fiber angle at an orientation of 60° relative to the 1 direction, where μ is the shear modulus of the isotropic matrix material in which the fibers are embedded. The figure includes plots for three different values of the dispersion parameter κ, namely $\kappa = 0.026, 0.15, 0.26$, which correspond to the values $10, 1.5, 0.1$, respectively, of the concentration parameter in the von Mises distribution that is used to describe the dispersion. The same number (two) of material parameters associated with the fibers is used for each model, and it is clear that the predictions of the two models are essentially identical. Details of the parameter values adopted are contained in [4], from where Figure 1 is adapted, and further illustrations of the comparisons of the predictions of the two models are contained in [3] and [4].

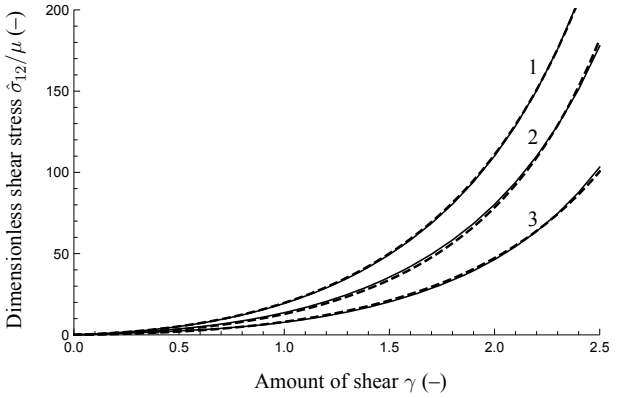

Figure 1: Plots of the dimensionless shear stress $\hat{\sigma}_{12}/\mu$ against the amount of shear γ. Comparison of the GST model (dashed curves) and the AI model (solid curves) predictions for (1) $\kappa = 0.026$, (2) $\kappa = 0.15$, and (3) $\kappa = 0.26$.

The second illustration relates to exclusion of compressed fibers in the GST model based on the discussion in [3]. Again for simple shear, with the representative value $\kappa = 0.277$ of the dispersion parameter (corresponding to concentration parameter 1.0),

Figure 2 shows the shear stress $\hat{\sigma}_{12}$ plotted against the amount of shear γ for four different orientations of the mean fiber angle, denoted $\Theta_{\rm M}$, namely $0°, 45°, 90°, 135°$ relative to the 1 direction. Depending on the mean fiber direction either the excluded fiber model or the all fiber model give the stiffest response. This is in contrast to the case of simple tension with the mean fiber direction in the direction of extension described in [3] for which the excluded fiber model yields the stiffest response for each value of the dispersion parameter.

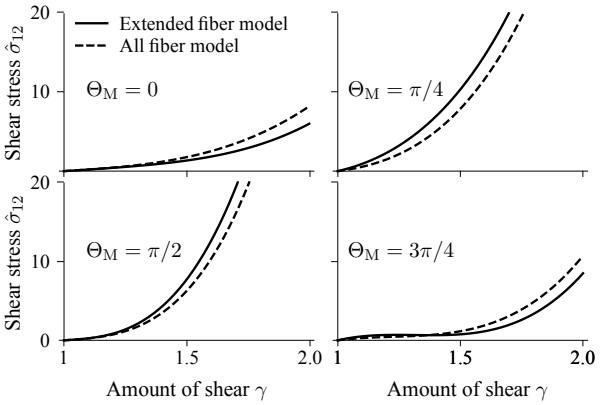

Figure 2: Plots of the shear stress $\hat{\sigma}_{12}$ against the amount of shear γ for the GST model, with all fibers included (dashed curves) and compressed fibers excluded (solid curves) with $\kappa = 0.277$ and four different mean fiber angles $\Theta_{\rm M}$.

3 CONCLUSION

The GST model of the elasticity of fibrous soft tissues, which allows for the dispersion of the fibers, in general predicts quite different material response from models which do not allow for dispersion. It has also been shown that the predictions of the GST and AI dispersion models are essentially indistinguishable when appropriate values of the material and structural parameters are used [3, 4]. Both the GST and AI models are able to exclude the contributions of compressed fibers from the material response, as shown in [8, 9, 10] for the AI model and [3] and [11] for the GST model.

REFERENCES

[1] Lanir, Y. Constitutive equations for fibrous connective tissues. *J. Biomech.* (1983) **16**:1–12.

[2] Gasser, T.C., Ogden, R.W. Ogden and Holzapfel, G.A. Hyperelastic modelling of arterial layers with distributed collagen fibre orientations. *J. R. Soc. Interface* (2006) **3**:15–35.

[3] Holzapfel, G.A. and Ogden, R.W. On fiber dispersion models: exclusion of compressed fibers and spurious model comparisons. *J. Elasticity*, in press. DOI:10.1007/s10659-016-9605-2.

[4] Holzapfel, G.A. and Ogden, R.W. Comparison of two model frameworks for fiber dispersion in the elasticity of soft biological tissues. *Eur. J. Mech. A/Solids*, submitted.

[5] Federico, S. and Herzog, W. Towards an analytical model of soft biological tissues. *J. Biomech.* (2008) **41**:3309–3313.

[6] Cortes, D.H., Lake, S.P., Kadlowec, J.A., Soslowsky, L.J. and Elliot, D.M. Characterizing the mechanical contribution of fiber angular distribution in connective tissue: comparison of two modeling approaches. *Biomech. Model. Mechanobiol.* (2010) **9**:651–658.

[7] Ge, L. A characteristic-based constitutive law for dispersed fibers. *J. Biomech. Eng.* (2016) **138**:071006–1–071006–8.

[8] Holzapfel, G.A. and Ogden, R.W. On the tension–compression switch in soft fibrous solids. *Eur. J. Mech. A/Solids* **49**:561–569.

[9] Li, K., Ogden, R.W. and Holzapfel, G.A. Computational method for excluding fibers under compression in modeling soft fibrous solids. *Eur. J. Mech. A/Solids* (2016) **57**:178–193.

[10] Li, K., Ogden, R.W. and Holzapfel, G.A. An exponential constitutive model excluding fibers under compression: application to extensioninflation of a residually stressed carotid artery. *Math. Mech. Solids*, in press. DOI:10.1177/1081286517712077

[11] Li, K., Ogden, R.W. and Holzapfel, G.A. Modeling of fibrous biological tissues with a general invariant that excludes compressed fibers, submitted.

9. National Conference on Computational Mechanics
MekIT'17
B. Skallerud and H I Andersson (Eds)

DYNAMIC RESPONSE AND WAKE STRUCTURES OF CANTILEVERS WITH SQUARE CROSS-SECTION

JOHAN REVSTEDT[1] AND JOHAN LORENTZON[2]

[1] Department of Energy Sciences
Lund University
221 00 Lund, Sweden
e-mail: johan.revstedt@energy.lth.se - Web page: http://www.fm.energy.lth.se

[2]Department of Theoretical Chemistry
Lund University
221 00 Lund, Sweden
e-mail: johan.lorentzon@teokem.lu.se, Web page: http://www.teokem.lu.se

Key words: FSI, LES, deforming cantilever

Abstract. The dynamic response of cantilevers to a hydrodynamic load has been studied numerically. The Reynolds number of the flow was fixed at 5000 and the variation in reduced velocity was achieved by varying the Young's modulus of the cantilever. Cantilevers with aspect ratios of 5 and 10 were considered for reduced velocities in the range 2 to 30. The simulations were performed using a strongly coupled FSI tool based in the open source projects DEAL.II and OpenFOAM. The results show that as the eigenfrequency of the cantilever coincides with the vortex shedding frequency, the amplitude of the oscillation substantially increases, as expected. However, no desynchronization is observed for higher values of reduced velocity. Instead the amplitude remains fairly constant for the shorter cantilever and continously increase for the longer one.

1 INTRODUCTION

In recent years the combination of flow simulations and structural analysis has become increasingly popular in solving engineering problems that contain hydro- or aerodynamical loading on solid structures. Flow around non-deforming cantilevers of circular cross-section has been studied experimentally by Park and Lee [9] as well as numerically by Afgan et al [1]. Both these studies note the strong three-dimensionality of the wake which is mainly caused by the counter-rotating vortices generated at the free end. This also causes the wake flow to be much more complex than for a cylinder of infinite length. Fujarra et al [6] performed an experimental investigation of vortex-induced vibrations of an elastic cantilever. They found a similar response as for elastically mounted non-deforming

cylinders although the flexible cantilever showed larger amplitudes in the synchronization range. The onset of the initial branch was found at a reduced velocity, $U_R = \frac{U}{f_N D}$, (where U is the bulk velocity upstream of the cylinder, f_N is the eigenfrequency and D is the cylinder diameter) of about 3 and thereafter a rapid increase in amplitude with a maximum amplitude of around $1D$ at $U_R = 6$. Concerning the frequency, the cantilever was reported to oscillate with the shedding frequency of a stiff cantilever up to $U_R \approx 6$ and thereafter with a frequency related to the eigenfrequency of the structure. Similar findings can be seen in the numerical work by Yamamoto et al. [10].

The purpose of this work is to study the deformation of elastic cantilevers due to hydrodynamic forces by coupled fluid-structure interaction simulations. Also, to investigate the effects on the wake structure by the cantilever vibration.

2 METHOD

The equations governing isothermal, incompressible flow of a Newtonian fluid can in non-dimensional form be written as

$$\frac{\partial u_i}{\partial x_i} = 0 \tag{1}$$

$$\frac{\partial u_i}{\partial t} + u_j \frac{\partial u_i}{\partial x_j} = -\frac{\partial p}{\partial x_i} + \frac{1}{Re}\frac{\partial}{\partial x_j}\frac{\partial u_i}{\partial x_j} \tag{2}$$

where u_i is the velocity vector, p is the pressure, t is non-dimensional time and x_i is the non-dimensional spatial coordinate.

The equation of motion for solids takes the following expression,

$$\rho_s \ddot{u}_i + \eta \dot{u}_i - \nabla \cdot \sigma = \rho_s b_i, \tag{3}$$

where u is the displacement with respect to the current configuration x and a reference configuration X, $u = x - X$, ρ_s is the solid density, η is the damping coefficient, σ is the Cauchy stress and b is the body force. The total Lagrangian description is adopted in this study, where the constitutive relations are formulated with respect the reference configuration to which a second Piola-Kirchoff stress tensor S_{ij} can be defined as,

$$S_{ij} = D_{ijkl} E_{kl}, \tag{4}$$

where D_{ijkl} is the Saint Venant-Kirchoff matrix and E_{kl} the finite strain tensor,

$$E_{ij} = \frac{1}{2}\left(\frac{\partial u_i}{\partial X_j} + \frac{\partial u_j}{\partial X_i} + \frac{\partial u_k}{\partial X_i}\frac{\partial u_k}{\partial X_j}\right), \tag{5}$$

where X_j is the material point coordinate in the reference configuration. The relation between second Piola-Kirchoff stress tensor and the Cauchy tensor is as follows,

$$\sigma_{ij} = \frac{1}{J}\frac{\partial x_i}{\partial X_k}\frac{\partial x_j}{\partial X_l} S_{kl}, \tag{6}$$

where $J = det(\frac{\partial x_i}{\partial X_j})$. Using isotropic material assumption, D_{ijkl} can be defined as,

$$D_{ijkl} = \lambda\delta_{ij}\delta_{kl} + \mu(\delta_{ik}\delta_{jl} + \delta_{il}\delta_{jk}), \tag{7}$$

where the Lamé parameters are related to Young's modulus and the Poisson ratio as

$$\lambda = \frac{E\nu}{(1+\nu)(1-2\nu)}, \tag{8}$$

$$\mu = \frac{E}{2(1+\nu)}. \tag{9}$$

The eigenfrequency of the first bending mode is determined from:

$$f_N = \frac{k}{2\pi L^2}\sqrt{\frac{EI}{\rho_s A}}, \tag{10}$$

where L is the beam length and k is a constant dependent on the load case. For the case considered here, i.e. a full moment connection, the value of k is 3.52. The reduced velocity, which can be regarded as a time-scale ratio between the flow and the structural response, is frequently used as a parameter in flow-induced vibration studies. It is defined as

$$U_R = \frac{U_0}{f_N D}. \tag{11}$$

Here the reduced velocity is based on the *in vacuo* eigenfrequency, f_N, and the cross-sectional size of the cantilever, D.

2.1 Solution Method

The solid solver is a standard procedure originated from Bathe et al [3], implemented in DEAL.II framework [2] which provides a tool set for Finite Element Method (FEM). The kinematic description for the solid is the Total Lagrangian using the Finite Strain approximation (Green-Cauchy) with the Piola-Kirchoff Stress tensor [4]. As time marching method an energy conservative settings is applied using the Newmark scheme. The fluid solver applied is the pimpleDyMFoam from OpenFOAM package, a Finite Volume Method package. The discretization schemes are defined by input and chosen for the fluid as follows: TVD scheme blended with upwind scheme (0.1) for divergence term, central difference for gradients with limiter, temporal discretization scheme is backward. The turbulence is modelled by LES using dynamic one-equation eddy approximation [11]. The FSI coupling is implicit stabilized by blending (0.5) over the traction and using IQN-ILS [5] as post correction. To exclude the compression waves and ambient motion, a low-pass blackman filtering is applied, at a cut off 12 Hz on the traction in the AMI interface step in the transfer step from fluid to solid coupling scheme [7]

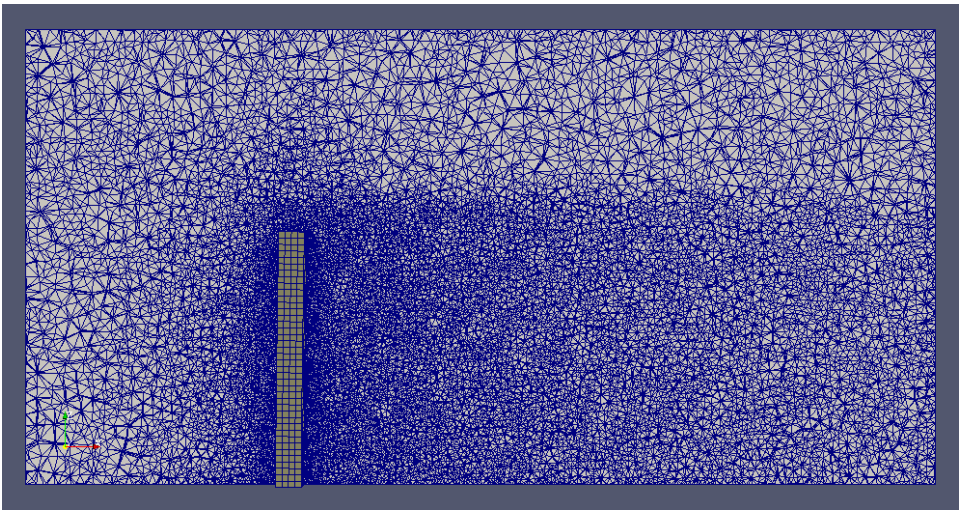

Figure 1: Computational meshes in the solid and fluid

3 COMPUTATIONAL SET-UP

In the flow configuration considered in this study the Reynolds number, based on the bulk velocity and the hydraulic diameter of the cantilever, is kept constant at 5000. Hence, the reduced velocity is varied by varying the Young's modulus. The reduced velocity U_R is varied in the range 2 to 30, i.e. covering both the pre-synchronization range as well as lock-in and the post-synchronization range. Two aspect ratios of the cantilever, 5 and 10, are considered. The density ratio is set to 20. Figure 1 depicts a typical computational domain and mesh. The size of the domain is $36D \times 17D$ in the streamwise and crosswise directions respectively. In the direction along the cantilever the domain extends to $13D$ for the shorter cntilever and to $18D$ for the longer one. In the fluid domain a tetrahedral unstructured mesh is used. The mesh is refined in the vicinity of the cantilever and in the wake. The number of cells is about 675000 for the short cantilever case and about 1250000 for the long cantilever. In the solid domain a hexahedral structured mesh with 4 cells over the cantilever width is used.

The mesh sensitivity was tested for the long cantilever at Re=5000 using a finer mesh with about 2400000 cells. This is denoted as 'Fine' in Figure 2, which depicts the average streamwise velocity and the turbulent kinetic energy at three positions downstream of the cantilever, i.e. x=2D, 4D and 6D, for anon-deforming cantilever. Comparing the average streamwise velocity in Figure 2 one observes only minor differences between the two meshes at all three locations. For the turbulent kinetic energy some differences are visible especially at x=2D at the upper half of the cantilever. The difference is, however,

substantially decreased further downstream. This leads to the reasonable conclusion that to capture the proximal part of the wake accurately one would need to use the finer mesh. Considering a deforming cantilever the wake flow exhibits a similar grid dependence. However, the motion of the cantilever is less affected. For example, is the frequency difference only about 5%, which is an indication of how the added mass is accounted for. In the following the coarser mesh is therefore used since the main purpose of this study is to investigate the response of the cantilever.

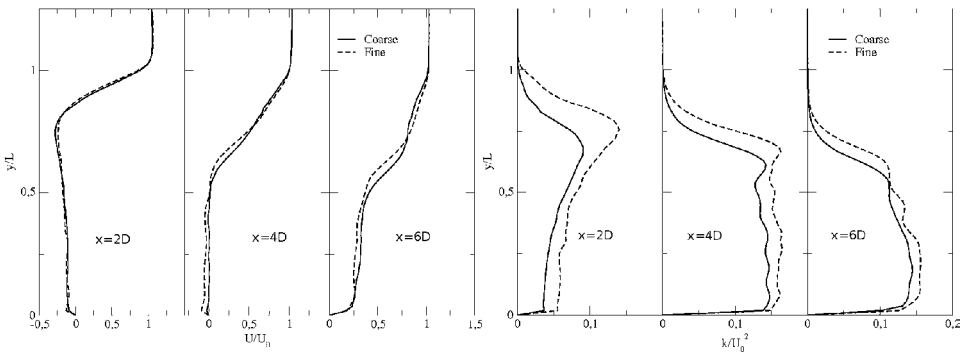

Figure 2: Mean streamwise velocity (left) and turbulent kinetic energy (right) for the coarse and fine meshes.

4 RESULTS

Earlier studies, e.g. [6], of elastic cantilevers indicate that the response to the flow field is similar to that of elastically mounted non-deforming cylinders. In the latter case one observes a large increase in amplitude as the frequency of the vortex shedding (and hence also the lift force) coincides with the eigenfrequency of the spring mounted cylinder. This phenomenon is usually called lock-in and is characterized by the oscillation frequency of the cylinder being locked to the eigenfrequency of the system. Usually this phenomenon persists at reduced velocities beyond the one where the shedding and eigenfrequencies coincide. As the reduced velocity is increases the motion is eventually desynchronized. Hence, the response is usually divided into three distinct regions: The pre-synchronization range, where the motion is governed by the shedding frequency of the flow and the amplitude increases with increasing reduced velocity. The synchronization range, where the motion is locked to the eigenfrequency and the post synchronization range in which the the motion again is related to the shedding frequency and the amplitude decreases.

In the following all amplitudes and deflections have been normalized with the cross-sectional size of the cantilever,D, and the frequencies are normalized using D and the

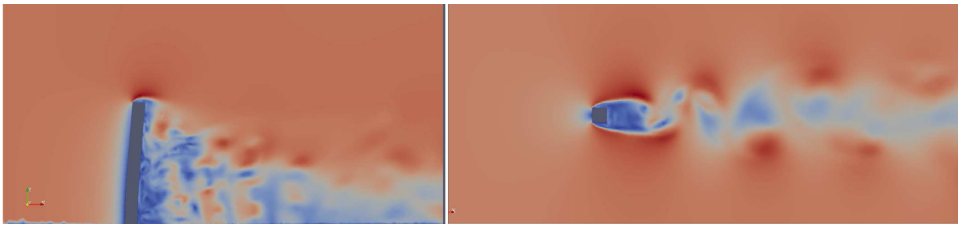

Figure 3: Instantaneous velocity field around a cantilever with $L = 10D$ at $U_R = 20$. Side view through the center(left) and top view at mid-height (right).

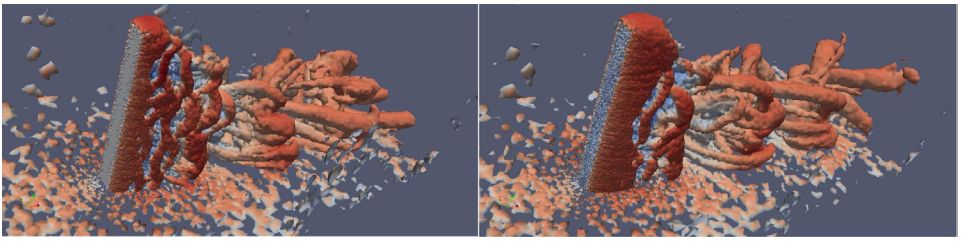

Figure 4: Visualization of the vortex structures in the wake of the cantilever with $L = 10D$ using the Q-criterion. Left: non-deforming. Right: deforming with $U_R = 20$.

inflow velocity U_0, i.e.

$$f^* = \frac{U_0 f}{D} \tag{12}$$

The instantaneous flow around the longer cantilever at $U_R = 20$ is depicted in Figure 3. The flow will of course separate at the upstream corners (as for any square cylinder) and also from the free end of the cantilever. This will create a fairly complex three dimensional vortex shedding downstream of the cantilever. First consider the non-deforming cantilever. Figure 4 depicts a visualization of the vortex structure around the longer cantilever using the q-criterion. At the lower part of the cantilever the vortex shedding resembles that of an infinitely long rod but further away from the wall the shedding from the end surface will have a significant influence on the wake structures. Close to the tip the shedding from the end surface will cause the vortices shed from the sides to move towards the wall similar to what would be the case for any finite length cylinder. However, at about 5D the initial shedding structures will break down and vortices will instead be oriented parallel to the wall. Now comparing this to a strongly deforming cantilever at $U_R = 20$ some differences can be noticed. Firstly, the separation seems to be stabilized in the sense that vortices are shed further downstream. Secondly, the vortices become parallel to the wall somewhat faster, hence the part with "normal" shedding is much shorter.

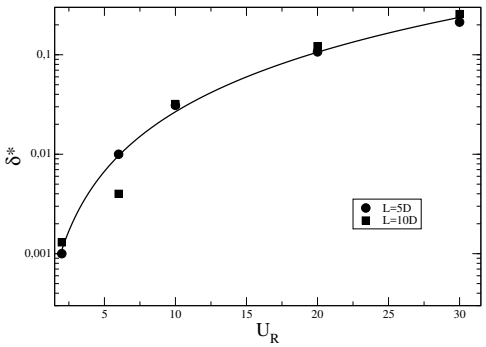

Figure 5: Normalized averaged tip deflection, δ^*, as a function of reduced velocity, U_R, for both cantilever lengths. The solid line is a curve fit to the results for the $L = 5D$ case.

As the cantilever is subjected to a flow it will deform due to the hydrodynamic loading. The pressure difference between the upstream stagnation and the downstream wake will cause the cantilever to bend in the streamwise direction. The deflection should of course increase proportional to U_R^2 for obvious reasons. This is confirmed in Figure 5 which shows the average deflection in the streamwise direction of the cantilever tip. One may also note that the deflection is almost independent of cantilever length, which is consistent with and an effect of how the study is set-up.

As was mentioned above the flow separates both from the sides and from the tip of the cantilever. However, opposed to what is observed for a circular cantilever the shedding frequency is the same on the side of the cantilever and on the end surface. The Strouhal number of the shedding is around 0.1 in this case, based on the bulk velocity and the hydraulic diameter of the cantilever. With this in mind, one should expect the synchronization to begin at a reduced velocity of about 10 since the added mass effects can be considered small at the density ratio considered here. Considering the left graph of Figure 6 this is indeed the case. As the reduced velocity is increased the amplitude in the lateral direction increases exponentially until the reduced velocity reaches 10. Thereafter the amplitude is fairly constant all the way to $U_R = 30$, i.e. there is no evidence of the desynchronization observed for elastically mounted cylinders here. Further evidence of this is seen in the right graph of Figure 6, depicting the frequency of motion of the tip normalized with the eigenfrequency. Below $U_R = 10$ the motion is governed by the the shedding frequency. From $U_R = 10$ the frequency instead coincides with the eigenfrequency of the cantilever's first bending mode. The slight deviation from unity is due do the effect of added mass, which slightly lowers the eigenfrequency as is discussed above.

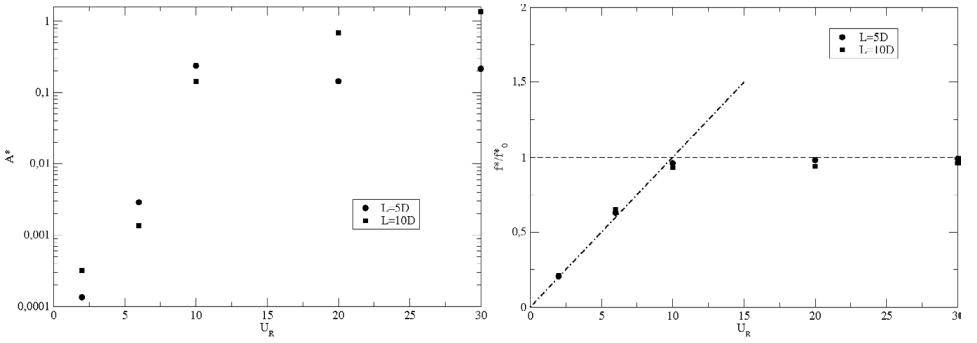

Figure 6: Normalized amplitude (left) and frequency relative to the eigenfrequency (right) as a function of reduced velocity for both cantilever lengths. The dashed line represents the *in vacuo* eigenfrequency and the dot-dashed line is the vortex shedding frequency.

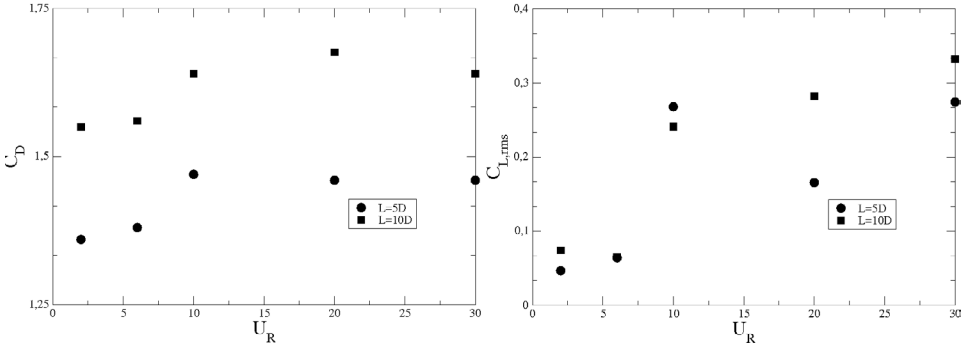

Figure 7: Drag (left) and lift (right) coefficients for both cantilevers as a function of reduced velocity.

The average drag coefficient and rms of the lift coefficient, are depicted in Figure 7. Concerning the drag one can observe a slight increase with increasing reduced velocity up to the onset of resonance, whereafter it remains almost constant up to $U_R = 30$. Both cantilever sizes follow the same trend. It should here be noted that the variations in drag are quite small and the difference to the value for a non-deforming cantilever does not exceed 5%. For the lift the development differs slightly. As for the drag there is a noticeable increase in lift at $U_R = 10$. Beyond that point the development of the lift closely follows the amplitude of the lateral motion, i.e. the lift is increased for the longer cantilever but for the shorter one sees a slight decrease and then a regain.

Turning our attention to how the wake is affected by the cantilever motion, the average streamwise velocity and the turbulent kinetic energy at three positions, at 2D, 4D and 6D downstream of the cantilever are considered. Figure 8 shows this for the longer cantilever

at three values of reduced velocity, 6 10 and 30, i.e. one value from each regime. At the upstream position the wake extends to about 1.1 times the cantilever length for all cases. Considering the non-deforming case the recirculation extends to a height of about 85% of the cantilever length. Following the wake development for the non deforming case one sees a fairly uniform distribution of both U an k up to just above the cantilever half-height and that this position is gradually moved towards the wall as the wake develops. The turbulent kinetic energy has its maximum in the upper part of the cantilever at the closest position, while further downstream the maximum is found in the lower part. The clear distinction in distribution of kinetic energy between $x = 2D$ and $x = 4D$ is noteworthy. It is a clear indication of the change in wake character occurring between these two positions, which was pointed out already in the discussion on Figure 4. Hence, close to the cantilever one observes two distinct wake patterns due to that the shedding from the tip only influences the upper half of the wake. Furthermore, there are two distinctly different wake patterns near and far from the cantilever.

For the deforming cases one observes only minor differences at $U_R = 6$ compared to the non-deforming case, which is to be expected since the amplitude of motion is very small as is seen in Figure 6. Increasing to $U_R = 10$ differences in k can be observed already at $x = 2D$ and at $x = 4D$ the differences in U are also clearly noticeable. At $x = 2D$ the peak in k is much stronger than in the non-deforming case and located closer to the surface. This would indicate that the influence of the tip shedding is stronger in this case but already at $x = 6D$ this effect has totally vanished and the distribution of k is indistinguishable from the lower reduced velocity and non-deforming cases. The mean velocity on the other hand shows that the recirculation is shorter and that the velocity is more evenly distributed over the height. Further increasing the reduced velocity will make these effects even more pronounced as can be seen for the case $U_R = 30$. Now considering the shorter cantilever one would suspect that the tip effects to be more dominating. However, no conclusive evidence of that can be found in this study.

In Figure 9 average velocity and turbulent kinetic energy are depicted at the same reduced velocities and at the same positions as for the longer cantilever case. Overall the differences in U are smaller in this case although the trends are the same, i.e. at the onset of synchronization the recirculation gets shorter and the wake velocity increases. However the general shape of the velocity distribution seems almost unaffected. Also, note the there is a clearly noticeable difference between the non-deforming case and the lowest reduced velocity case, which was not present for the longer cantilever. For the turbulent kinetic energy the trend is similar in as much as the differences are overall smaller close to the cantilever and the distinct peak at $U_R = 10$ is not present here. The turbulent kinetic energy is increased downstream, as for the longer cantilever, but even at $x = 6D$ the distribution differs between the cases although the levels are similar.

In a previous study [8] the wake structures of other cantilever shapes were studied. It is of interest to also consider the shape effect for deforming cantilevers. Here we consider a square cantilever, $L = 5D$, twisted 90 degrees around its axis at $U_R = 10$. Some data

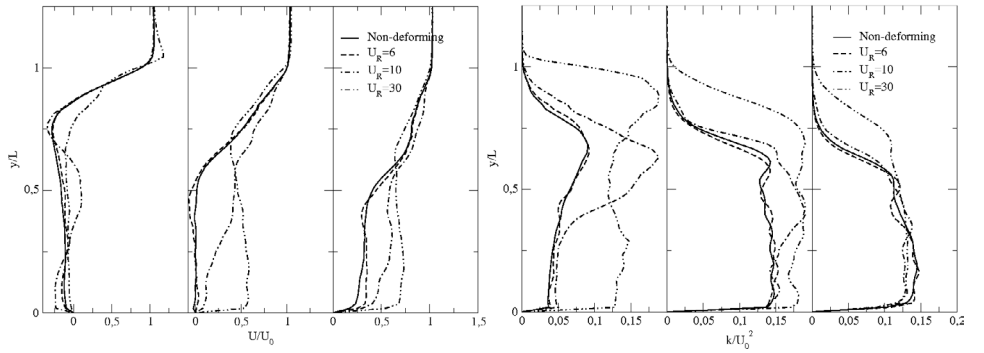

Figure 8: Mean streamwise velocity (left) and turbulent kinetic energy (right) at 2D, 4D and 6D downstream of the cantilever for L/D=10.

for the two cases is summarized in Table 1. Twisting does of course not change the eigenfrequency of the cantilever. Hence, the reduced frequency of the lateral motion is 0.098, i.e. close to the value found for the the straight cantilever. The amplitude, on the other hand, $A^* = 0.073$, is about a factor 4 lower than for the straight case. This is of course due to the differences in shedding behavior, i.e. the twisting will disrupt the shedding of coherent vortices along the whole length of the cantilever thereby to some extent inhibiting the resonance. As a consequence, the rms of the lift coefficient is also lower. Note that since the twisted geometry breaks the symmetry of the flow there will be a non-zero average lift coefficient as well. Looking at the wake flow, depicted in Figure 10, it seems that the average velocity will more closely resemble the straight non-deforming case apart from some instances where it would resemble the straight $U_R = 10$ case. Likewise the turbulent kinetic energy is lower in the twisted case, which is due to the disruption of large coherent structures by the cantilever shape.

Table 1: Comparison of a straight and a twisted cantilever with $L = 5D$ at $U_R = 10$

Case	δ^*	A^*	$\overline{C_D}$	$\sqrt{\overline{C_L^2}}$	f^*
Straight	0.031	0.265	1.47	0.268	0.094
Twisted	0.111	0.073	1.32	0.047	0.098

5 CONCLUSIONS

As an elastic cantilever is immersed in a flow it will deform in the streamwise direction. Since this deformation is dominated by the first bending mode of the cantilever one observes a quadratic dependence of the deflection on the reduced velocity. This also

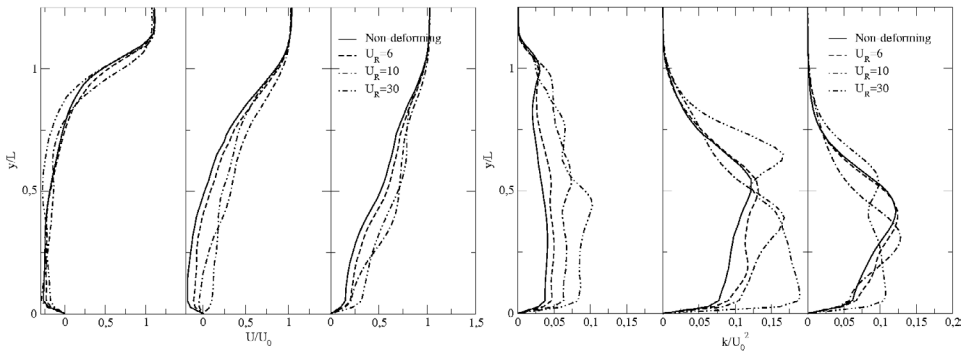

Figure 9: Mean streamwise velocity (left) and turbulent kinetic energy (right) at 2D, 4D and 6D downstream of the cantilever for L/D=5.

leads to that there is no influence of the cantilever length on the streamwise deflection. In the lateral direction on the other hand the situation is somewhat different. At low reduced velocities the cantilever will oscillate with the frequency of the vortex shedding and the amplitude is quite low . However as the shedding frequency coincides with the eigenfrequency of the cantilever the amplitude substantially increases which is a sign of resonance. Further increasing the reduced velocity, i.e. reducing the eigenfrequency, leads to that the cantilever continues to oscillate with a frequency close to the eigenfrequency. The small discrepancy can be attribute to the added mass due to the cylinder motion. Concerning the amplitude, the behaviour differs between the short and long cantilevers. For the shorter one the amplitude is almost constant but for the longer one a continuous increase is observed. Hence, we do not observe the desynchronization obtained in several other studies. The reasons for this might be several. One could be the very low material damping used in this study. In any case further investigation into this phenomenon is needed.

Concerning the influence of the cantilever motion on the wake flow one can conclude that the small amplitudes observed at low reduced velocities does nor affect the wake significantly. In the cases with a large oscillation amplitude the recirculation is shorter and the fluctuations larger in the near wake. It is here interesting to note that already at a distance of $6D$ the effects of the oscillation on the fluctuations has almost disappeared.

6 ACKNOWLEDGEMENT

The simulations were performed on resources provided by the Swedish National Infrastructure for Computing (SNIC) at Lunarc.

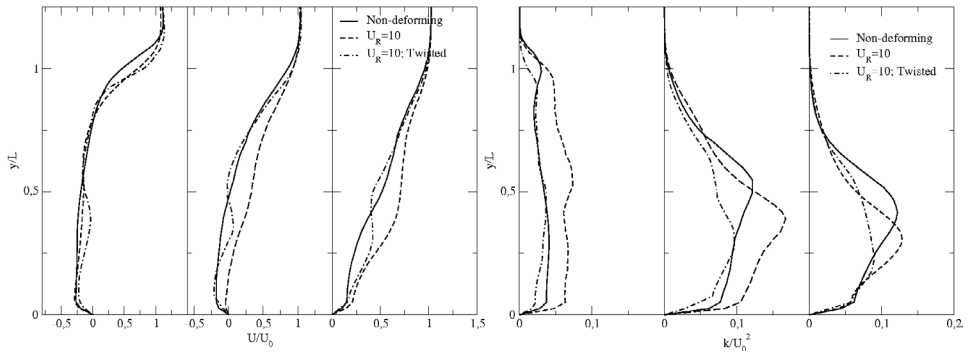

Figure 10: Mean streamwise velocity (left) and turbulent kinetic energy (right) at 2D, 4D and 6D downstream of the cantilever for straight and twisted cantilevers at L/D=5.

REFERENCES

[1] Afgan, I., Moulinec, C., Prosser, R. and Laurence, D. Large eddy simulation of turbulent flow for wall mounted cantilever cylinders of aspect ratio 6 and 10. *int. J. Heat and Fluid Flow*, (2007) textbf28:561–574.

[2] Bangerth, W., Hartmann, R. and Kanschat G. DEAL.II A general-purpose object-oriented finite element library. *ACM Transactions on Mathematical Software (TOMS)* (2007) textbf33:24.

[3] Bathe, K.-J., Ramm, E. and Wilson, E.L. Finite element formulations for large deformation dynamic analysis. *International Journal for Numerical Methods in Engineering* (1975) **9**:353–386.

[4] de Borst, R., Crisfield, M.A., Remmers, J.J.C. and Verhoosel, C.V. *Nonlinear Finite Element Analysis of Solids and Structures* (2012) Wiley Series in Computational Mechanics Wiley (2012).

[5] Degroote, J., Bathe, K.-J. and Vierendeels J. Performance of a new partitioned procedure versus a monolithic procedure in fluid-structure interaction. *Computers and Structures* (2009) **87**:793–801.

[6] Fujarra, A.L.C., Pesce, C.P., Flemming, F. and Williamson, C.H.K. Vortex-induced vibration of a flexible cantilever. *J. Fluids and Structures* (2001) **15**:651–658.

[7] Haelterman, R., Bogaers, A.E.J., Scheufele, K., Uekermann, B. and Mehl, M. Improving the performance of the partitioned qn-ils procedure for fluidstructure interaction problems: Filtering. *Computers & Structures* (2016) **171**:9–17.

[8] Lorentzon, J. and Revstedt, J. A LES study of turbulent flow around twisted and tapered cantilevers. *Proceedings ot the 6th European Confrence on Computational Fluid Dynamics* **V**:5663 – 5676, CIMNE, Barcelona (2014)

[9] Park, C.W. and Lee, S.J. Effects of free-end corner shape on flow structure around a finite cylinder. *J. Fluids and Structures* (2004) **19**:141–158.

[10] Yamamoto, C.T., Meneghini, J.R., Saltara, F., Fregonesi, R.A. and Ferrai Jr, J.A. Numerical simulations of vortex-induced vibration on flexible cylinders. *J. Fluids and Structures* (2004) **19**:467–489.

[11] Yoshizawa, A. and Horiuti, K. A statistically-derived subgrid-scale kinetic energy model for the large-eddy simulation of turbulent flows. *Journal of the Physical Society of Japan* (1985) **54**:2834–2839.

9. National Conference on Computational Mechanics
MekIT'17
B. Skallerud and H I Andersson (Eds)

RECENT DEVELOPMENTS IN LARGE AND MULTISCALE TOPOLOGY OPTIMIZATION

JEROEN GROEN, SIMON D. LARSEN AND OLE SIGMUND

Department of Mechanical Engineering
Technical University of Denmark
2800 Lyngby, Denmark
e-mail: sigmund@mek.dtu.dk, web page: http://www.topopt.dtu.dk/

Key words: Topology Optimization, Multiscale Modelling and Optimization

Abstract. The original approach to topology optimization by Bendsøe and Kikuchi (1988) was based on homogenization and multiscale approaches. However, this technique has largely been replaced by simpler density or level-set approaches. Lately, resolutions for density approaches have reached giga-scale which gives unprecedented levels of details for optimization solutions. However, such resolutions also require extreme computational power. The paper discusses recent activities that revive old homogenization approaches with the aim of achieving giga-resolution at low computational cost.

1 INTRODUCTION

The original homogenization approach to topology optimization introduced by Bendsøe and Kikuchi almost three decades ago[1] paved the way for topology optimization but was largely abandoned in practical use due to computational challenges and complexity of solutions.[2] Instead the approach was substituted by simpler density approaches which later were supplemented by level-set approaches. Presently, density approaches are the main drivers in industrial software solutions and resolutions are approaching giga-scale.[3] The cost of running very high resolution studies are high and may limit applications in really large constructions (e.g. airplanes, bridges and high risers) and certainly prevents interactive design processes as e.g. the TopOpt Apps.[4]

To pave the way for future high-resolution topology optimization studies we revisit the original homogenization approaches and extend them with improved projection and post-processing steps. For the simple 2D studies considered so far, we achieve speed up factors of more than 50 in Matlab implementations. The projection approach takes homogenization results obtained on a very coarse mesh and projects them onto either very fine meshes or simplified frame structures that can be further post-processed or optimized at low computational cost. The former approach has been described in detail[5] and the latter approach is still under development.

2 EXAMPLE

The approach is illustrated in Figure 1. The standard homogenization approach to topology optimization results in two angular fields for optimal laminate directions $\mathbf{e}_i(\mathbf{x})$ as well as lamination parameters a_i. To obtain a smooth angular field description we introduce the scalar fields ϕ_i, which minimize the least squares errors $||\nabla\phi_i(\mathbf{x}) - \mathbf{e}_i(\mathbf{x})||$. For the density projection approach (Figure 1, bottom left), a mapping based on $\cos(P\phi_i(\mathbf{x}))$ and the lamination parameters a_i directly results in a fine scale density distribution which, when cleaned up for small details results in a close to optimal high resolution solution.

The second approach (Figure 1, bottom right) is also based on the ϕ_i fields, however, this time a frame mesh is obtained from direct use of the contour curves of the ϕ_i fields as well as the lamination parameter a_i information. The generated frame ground structure resembles a Michell structure but is rather crude and most be post-optimized for shape and connectivity to reach a satisfactory solution.

3 CONCLUSIONS

The proposed density projection approach saves a factor of 50 compared to a standard high resolution topology optimization approach with little if any decrease in performance. The approach mapping to a frame structure is presently slightly slower but may be sped up based on code improvements and switch to lower level programming languages than Matlab.

This extended abstract has given a small taste of a new projection approach for multi-scale topology optimization. Further details can be found in Groen and Sigmund[5] and a paper soon to be submitted.

REFERENCES

[1] M. P. Bendsøe and N. Kikuchi. Generating optimal topologies in structural design using a homogenization method. *Computer Methods in Applied Mechanics and Engineering*, 71(2):197–224, 1988.

[2] M. P. Bendsøe and O. Sigmund. *Topology Optimization - Theory, Methods and Applications*. Springer Verlag, Berlin Heidelberg, XIV+370 pp., 2003.

[3] N. Aage, E. Andreassen, and B.S. Lazarov. Topology optimization using PETSc: An easy-to-use, fully parallel, open source topology optimization framework. *Structural and Multidisciplinary Optimization*, 51(3):565–572, 2015.

[4] M. Nobel-Jørgensen, N. Aage, A.N Christiansen, T. Igarashi, J.A. Bærentzen, and O. Sigmund. 3d interactive topology optimization on hand-held devices. *Structural and Multidisciplinary Optimization*, 51(6):1385–1391, 2015.

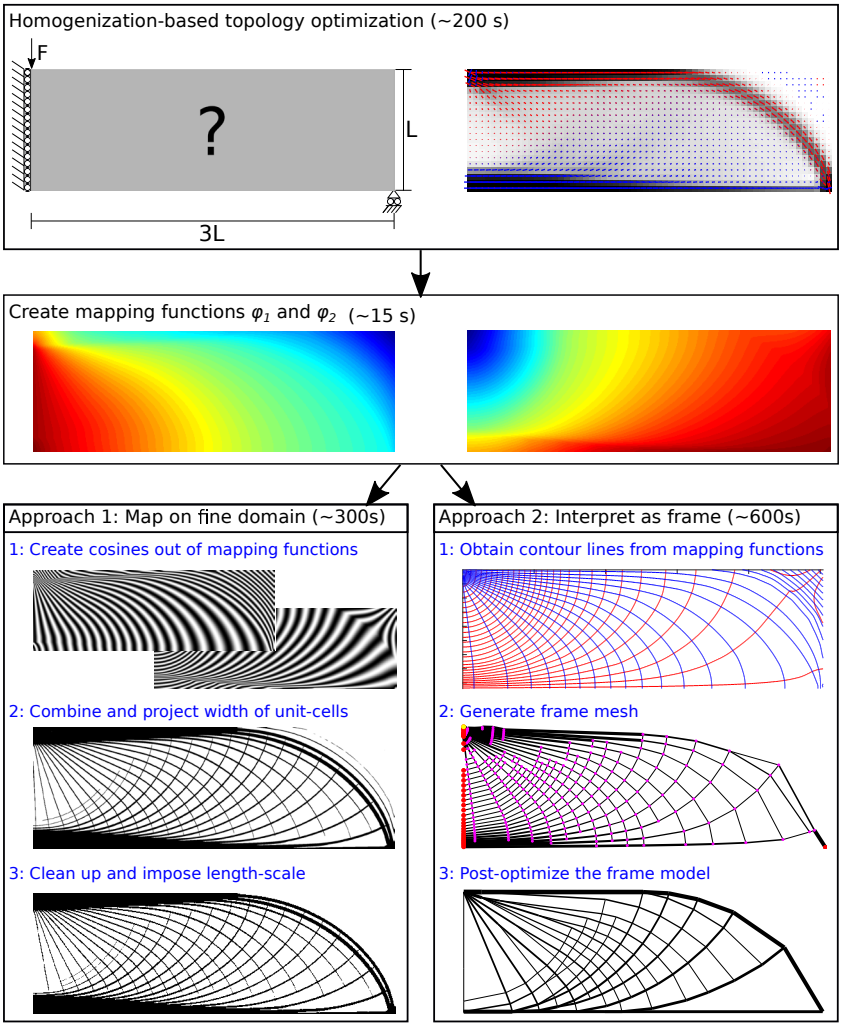

Figure 1: Steps of the projection approach. Top: traditional homogenization based topology optimization for MBB test case. Below: Smoothed mapping functions ϕ_i. Bottom left: pure mapping to fine scale density distribution. Bottom right: mapping to frame structure and subsequent shape optimization.

[5] J.P. Groen and O. Sigmund. Homogenization-based topology optimization for high-resolution manufacturable micro-structures. *Internatinal Journal of Numerical methods in engineering*, 2017. online.

9. National Conference on Computational Mechanics
MekIT'17
B. Skallerud and H I Andersson (Eds)

CFD MODELLING OF IRREGULAR AND FOCUSED WAVES USING WAVE RECONSTRUCTION

ANKIT AGGARWAL*, MAYILVAHANAN ALAGAN CHELLA* , HANS BIHS*, CSABA PÁKZODI†, ØIVIND ASGEIR ARNTSEN*

*Department of Civil and Environmental Engineering
Norwegian University of Science and Technology
Web page: http://www.reef3d.com/
†SINTEF Ocean
Trondheim, Norway

Key words: Computational Fluid Dynamics, wave reconstruction, steep irregular waves

Abstract. The real sea state is composed of the focused and steep irregular waves which makes their study very important in the design of offshore wind turbines. Computational Fluid Dynamics (CFD) can be used as an effective tool to study steep waves. In the present paper, the wave reconstruction method in which the numerical wave free surface elevation is reconstructed by using the Fast Fourier Transformation (FFT) is validated using the open-source CFD based model REEF3D. The validation is performed for the deep water steep irregular waves and the focused waves. The numerical results are compared in time-domain for both cases (focused and irregular waves) with the experiments. The wave peaks and the wave phases are captured well in the numerical model.

1 INTRODUCTION

The study of the wave hydrodynamics is crucial for the design of offshore wind turbines. The real sea state is very complex, multi-directional and highly irregular. It is composed of multi-chromatic irregular waves. When irregular waves coincide at one point in time and space during the nonlinear wave-wave interaction, they can produce focused waves with large wave heights. Therefore, it is important to study both focused and irregular waves while designing the offshore structures.
Many experimental and field investigations have been performed to study the irregular and focused waves. Holthuijsen et al. [1] performed a study for the whitecapping in the open sea and they reported that the probability of a wave group having at least one breaker was higher for longer wave groups. Hajime et al. [2] investigated irregular wave transformation over sloping sea bed and developed a hybrid model to predict the transformations of irregular waves. They used the Pierson-Moskowitz spectrum for the wave

generation. Pákozdi et al. [3] performed laboratory experiments with breaking irregular waves using the Toresthuagen spectrum to measure the global impact loads on the bottom fixed offshore structures. Baldlock et al. [4] performed an experimental study with focused waves and reported that the physical process close to the focusing point is highly nonlinear due to the complex wave-wave interaction. Ning et al. [5] performed some experimental investigations on the evolution of the focused groups and the underlying kinematics.
Numerical modelling can also be used to study the waves. A good validation of the numerical model in time-domain is required to accurately model the breaking and non-breaking waves for real life applications. The potential theory is unable to capture the whole wave breaking process [6]. Computational fluid dynamics (CFD) can simulate the complete wave breaking process without defining any empirical breaking criterion explicitly. Computational Fluid Dynamics (CFD) has been used previously by many researchers to model different types of waves [7][8][9]. The irregular wave train is composed of many regular wave components with different heights, periods and phases. In order to validate the numerical irregular wave surface elevation with the experimental free surface elevation in time domain, the correct phases of the generated numerical irregular waves is to be computed. The wave phases, amplitudes and angular frequencies for the individual waves are computed for the experimental free surface elevation measured close to the wave generation, which are used for the reconstruction of numerical irregular waves. Bredmose et al. [10] and Paulsen et al. [11] investigated irregular and focused waves on monopiles with CFD. They compared the numerical and experimental free surface in time-domain by using the linear reconstruction of waves. Their numerical model showed some disagreements in simulating the peaks and phases in the irregular wave surface. The aim of present paper is to study and validate the free surface reconstruction technique for irregular and focused wave groups. The present study is conducted using the open-source CFD software REEF3D [12]. The numerical results for the irregular waves are compared with the experiments performed by Pákozdi et al. [3] and the numerical results for the focused waves are compared with the experiments performed by Ning et al. [5]

2 NUMERICAL MODEL

The present numerical model is based on the governing equations of fluid dynamics: continuity equation and the Reynolds Averaged Navier-Stokes equations (RANS) with the assumption of an incompressible fluid given as:

$$\frac{\partial u_i}{\partial x_i} = 0 \tag{1}$$

$$\frac{\partial u_i}{\partial t} + u_j \frac{\partial u_i}{\partial x_j} = -\frac{1}{\rho}\frac{\partial p}{\partial x_i} + \frac{\partial}{\partial x_j}\left[(\nu + \nu_t)\left(\frac{\partial u_i}{\partial x_j} + \frac{\partial u_j}{\partial x_i}\right)\right] + g_i \tag{2}$$

where, u is the velocity averaged over time t, ρ is the fluid density, p is the pressure, ν is the kinematic viscosity, ν_t is the eddy viscosity, i and j denote the indices in x and y

direction, respectively and g_i is the acceleration due to gravity.

The numerical model uses a fifth-order finite difference Weighted Essentially Non-Oscillatory (WENO) scheme in multi-space dimensions for the spatial discretization [13]. The third-order TVD Runge Kutta scheme is used for the time discretization [14]. An adaptive time stepping scheme is used in the numerical model [15]. The present study uses the $k-\omega$ model [16] along with the Reynolds Averaged Navier Stokes (RANS) equation. The level set method is used to capture the free surface [17]. The relaxation method [18] for the focused wave case and the Dirichlet method for the irregular wave case, are used in the present study for the wave generation and absorption. Detailed information about the numerical model can be obtained in Bihs et al. [12]. REEF3D has been used in the past for a wide range of marine applications, such as wave-structure interaction [19], breaking wave forces [20], floating body dynamics [21] and sediment transport [22]. For the reconstruction of irregular waves, the Fast Fourier Transformation (FFT) algorithm is used. The wave amplitudes (A_k), angular frequencies (ω_k) and the phase angles (ϵ_k) are computed for the target irregular wave train at the wave generation using FFT. A time series of the free surface elevations can be written as a summation of the Fourier components [23]:

$$\eta(t) = \sum_{k=1}^{N} C_k e^{ik\omega t} \tag{3}$$

where, C_k denotes the Fourier coefficients.

The computed wave amplitudes (A_k), angular frequencies (ω_k) and the phase angles (ϵ_k) are given as an input to the numerical model. The first-order irregular waves are generated by the super-positioning of the linear regular waves components [24][25]. The focused waves are generated by numerically coinciding the irregular waves at one point in time and space [26] .

3 RECONSTRUCTION OF THE FOCUSED WAVES

3.1 Computational setup

The numerical model is tested and validated by comparing the numerically reconstructed and the experimental wave free surface elevation [5]. The experimental wave flume was 69 m long and 3 m wide with a water depth (d) = 0.5 m and the focus point location was 11.4 m away from the wave paddle. The tests were performed for the focused waves with amplitude (A_F) = 0.0313 m and period (T) = 1.2 s. The numerical simulations are performed in a two-dimensional numerical wave tank (NWT) without any structures. A 15 m long and 1 m high NWT with a water depth (d) of 0.5 m is used in the simulations as shown in Fig. 1. Two wave gauges were placed along the NWT at x = 0.0 m (W1) and 7.5 m (W2). The wave amplitudes (A_k), angular frequencies (ω_k) and the phase angles (ϵ_k) are computed for the experimental wave surface elevation

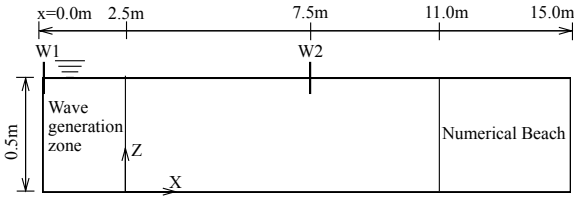

Figure 1: Setup of the numerical wave tank for the generation of focused waves similar to experiments [5].

measured close the wave generation zone (W1), which are given as the input values to the numerical model. The numerical simulations are performed for three different grid sizes (dx) = 0.10 m, 0.05 m and 0.025 m for the grid refinement study. The experimental free surface elevation is reconstructed numerically and the numerical focus point is chose to be at 7.5 m (at W2) from the wave inlet which is far enough to represent the computational efficiency of the numerical model to simulate the focused waves.

3.2 Results

Fig. 2 presents the comparison of the experimental and numerically reconstructed free surface elevation at the focused point (x_F) for this case with different grid sizes (dx) = 0.10 m, 0.05 m and 0.025 m. It is observed that value of the numerical peak for the focused wave is 29 % lower and shifted by 0.25 s in comparison with the experimental values for $dx = 0.10$ m. When a more refined $dx = 0.05$ m is used, some improvements in the numerical results are observed. The difference between the value of numerical and experimental peaks for the focused wave crest is reduced to 9.3 % and is shifted by only 0.09 s. For $dx = 0.025$ m, the peak crest values and the peak crest location for the focused waves are in a good agreement with the experimental results. There is almost no difference between the location of the peak wave crest between the both, and the difference between the value of numerical and experimental peaks for the focused wave crest is reduced to 4 %. Fig. 3 presents the simulated free surface changes with velocity magnitude (m/s) variation for the focused wave at x_F. A scaled up view of the wave free surface elevation is also shown. The increased velocities and higher wave crest can be observed at the focused point due to the superimposition of individual wave components in space and time at x_F.

4 RECONSTRUCTION OF THE IRREGULAR WAVES

4.1 Computational setup

The numerical tests are conducted in a two-dimensional numerical wave tank (NWT) without any structures. The numerical model is validated by comparing the numerical

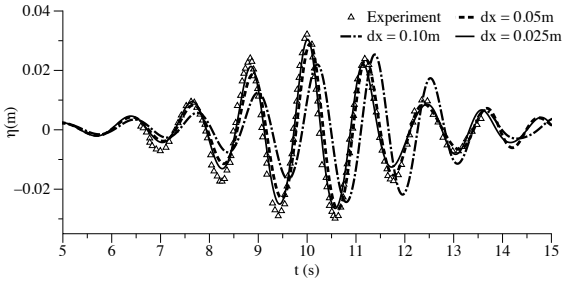

Figure 2: Comparison of the experimental [5] and numerically reconstructed free surface elevation at the focused point (x_F) with different grid sizes (dx) = 0.10 m, 0.05 m and 0.025 m.

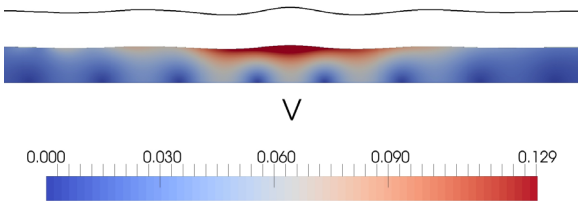

Figure 3: Simulated free surface changes with velocity magnitude (m/s) variation for the focused waves (scaled up view)

results with the experimental data [3]. The wave amplitudes (A_k), angular frequencies (ω_k) and the phase angles (ϵ_k) are computed for the experimental wave surface elevation measured close the wave generation zone (W1), which are given as the input values to the numerical model. The steep irregular waves in experiments were generated using the Torsethaugen spectrum. A 40 m long and 15 m high NWT with a water depth of 10 m is used in the numerical simulations as shown in Fig. 4. The wave gauges in the NWT are placed at x = 1.4 m (W1) and 15.0 m (W2).

4.2 Results

The numerical simulations are performed for the significant wave height (H_s) = 0.345 m and period (T_p) = 2.6 s. Fig. 5 presents the comparison of the numerical and experimental wave free surface elevation (η) over time (t) at two wave gauge locations with three different grid sizes (dx) = 0.10 m, 0.05 m and 0.01 m for the grid refinement study . It is observed that for the wave gauge located next to the wavemaker (W1), some phase

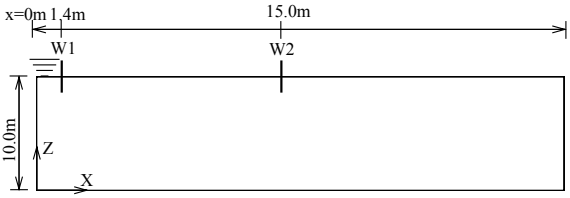

Figure 4: Setup of the numerical wave tank for the generation of steep irregular waves similar to experiments [3].

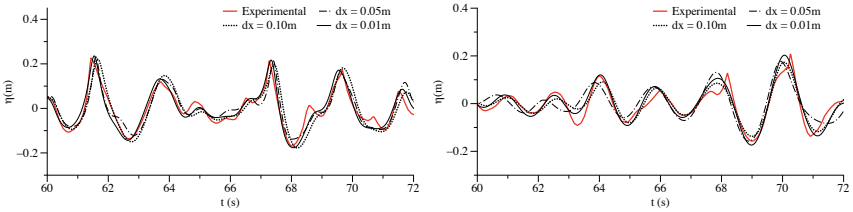

(a) (b)

Figure 5: Comparison of the numerical and experimental [3] wave free surface elevation (m) for the shorter time-series with three different grid sizes at (a) W1 (b) W2

differences are observed between the numerical and experimental results with $dx = 0.10$ m (Fig. 5(a)). These phase differences are slightly reduced for the grid size $dx = 0.05$ m and they are reduced to almost zero for the grid size $dx = 0.01$ m. For the wave gauge located at $x = 1.4$ m (W1), the error between the numerical and the experimental wave crests for all grid sizes for the wave gauge located next to the wave maker (W1) lies between 1 % to 6.6 %. The error for the wave phases between both lies between 1 % to 5 %. For the wave gauge located at $x = 15.0$ m (W2), it is observed that the values of the wave crests are lower than the experimentally measured values and some phase difference is also observed for $dx = 0.10$ m. The results are slightly improved for the finer grid size $dx = 0.05$ m, but still some phase difference can be observed. For the grid size $dx = 0.01$ m, the numerical and experimental wave crests show a error of up to 8 % and the numerical and experimental wave phases show a error of 13 % (Fig. 5(b)). Fig. 6 presents the comparison of the numerical and experimental wave free surface elevation (η) for the longer time-series at two wave gauge locations with $dx = 0.01$ m.

Fig. 7 presents the simulated free surface changes with velocity magnitude (m/s) variation during the propagation of irregular steep waves in the numerical wave tank (NWT) at different time-steps. At $t = 78.34$ s, the steep wave with very a high velocity

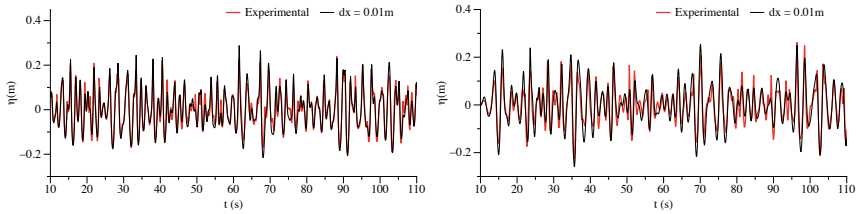

Figure 6: Comparison of the numerical and experimental [3] wave free surface elevation (m) for the longer time-series with grid size (dx)= 0.01 m at (a) W1 (b) W2

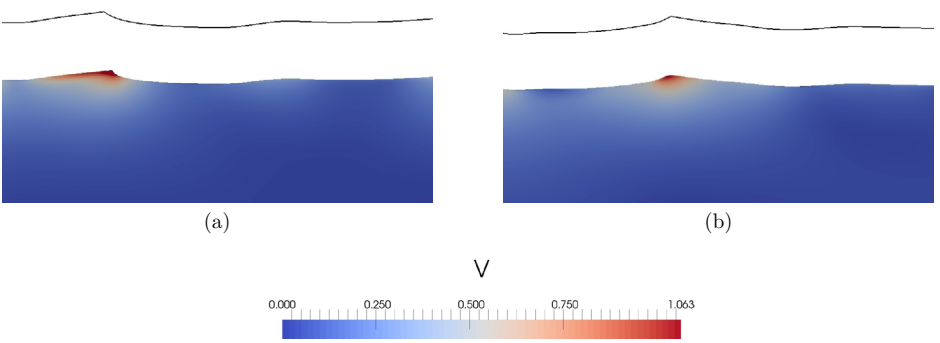

Figure 7: Simulated free surface changes with velocity magnitude (m/s) variation for the irregular waves (Zoomed around the steep wave event)

and large wave crest height is observed (Fig. 7(a)). In the next time step at t = 78. 67 s as shown in Fig. 7(b), after the wave crest reaches it maximum height and attain the maximum crest velocity, the velocities and the wave heights decrease again.

5 CONCLUSIONS

The numerical model REEF3D is used to validate the wave reconstruction method for focused and irregular waves. The waves are reconstructed using the Fast Fourier Transformation (FFT). First, the numerical simulations are performed for the focused waves. The numerical results are compared with the experimentally measured free surface elevation. The wave crest height is correctly reconstructed at the focal point in the numerical model for dx= 0.025 m. Next, a complex case of deep water steep irregular waves is investigated. The free surface elevations computed at two different locations

along the wave tank are compared with the experimental results. The experimental and numerical results at the wave gauge located next to the wave generation (W1) are compared to validate the correct inlet wave. The numerical wave amplitudes and wave phases during the wave propagation along the wave tank are well represented as measured by the wave gauge located at $x = 15.0$ m (W2). However, a further improvement in the numerical results is required in order to simulate the experiments with a better accuracy.

REFERENCES

[1] Holthuijsen, L., and Herbers, T., 1986. "Statistics of breaking waves observed as whitecaps in the open sea". *J. Phys. Oceanogr.,* ***16***, pp. 290–297.

[2] Hajime, M., and Kirby, T. J., 1996. "Hybrid frequency-domain kdv equation for random wave transformation". *Philosophical Transactions: Mathematical, Physical and Engineering Sciences,* ***354(1707)***, pp. 649–676.

[3] Pákozdi, C., Visscher, J., H., Stansberg, C., and Fagertun, J., 2015. "Experimental investigation of global wave impact loads in steep random seas". *Proceedings of ISOPE.*

[4] Baldock, T. E., Swan, C., and Taylor, P. H., 1992. "A laboratory study of nonlinear surface waves on water". *Coastal Engineering.*

[5] Ning, D. Z., Zang, J., Liu, S. X., Eatock Taylor, R., Teng, B., and Taylor, P. H., 2009. "Free-surface evolution and wave kinematics for nonlinear uni-directional focused wave groups". *Ocean Engineering,* ***36***, pp. 1226–1243.

[6] Chen, G., Kharif, C., Zaleski, S., and Li, J., 1999. "Three-dimensional Navier- Stokes simulation of breaking waves". *Phys. Fluids,* ***11***, pp. 121–133.

[7] Jacobsen, N. G., Fuhrman, D., and Fredsøe, J., 2012. "A wave generation toolbox for the open-source cfd library: Openfoam". *International Journal for Numerical Methods in Fluids,* ***70***, pp. 1073–1088.

[8] Alagan Chella, M., Bihs, H., and Myrhaug, D., 2015. "Characteristics and profile asymmetry properties of waves breaking over an impermeable submerged reef". *Coastal engg.,* ***100***, pp. 26–36.

[9] Alagan Chella, M., Bihs, H., Myrhaug, D., and Michael, M., 2016. "Hydrodynamic characteristics and geometric properties of plunging and spilling breakers over impermeable slopes". *Ocean Modelling,* ***103***, pp. 53–72.

[10] Bredmose, H., and Jacobsen, G. N., 2010. "Breaking wave impacts on offshore wind turbine foundations: focused wave groups and CFD". *Proceedings of OMAE, June 6-11.*

[11] Paulsen, T. B., Bredmose, H., and Bingham, B. H., 2014. "An efficient domain decomposition strategy for wave loads on surface piercing circular cylinders". *Coastal Engineering,* ***86***, pp. 57–76.

[12] Bihs, H., Kamath, A., Alagan Chella, M., Aggarwal, A., and Arntsen. A., O., 2016. "A new level set numerical wave tank with improved density interpolation for complex wave hydrodynamics". *Computers and fluids,* ***140***, pp. 191–208.

[13] Jiang, G. S., and Peng, D., 2000. "Weighted ENO schemes for Hamilton Jacobi equations". *SIAM Journal of Scientific Computing,* ***21***, pp. 2126–2143.

[14] Harten, A., Engquist, B., Osher, S., and Chakravarthy, S., 1987. "Uniformly high-order accurate essentially non-oscillatory schemes iii". *Journal of Computational Physics,* ***71***, pp. 231–303.

[15] Griebel, M., Dornseifer, T., and Neunhoeffer, T., 1998. *Numerical Simulations in Fluid Dynamics*. SIAM.

[16] Wilcox, D., 1994. "Turbulence modeling for CFD". *DCW Industries Inc. La Canada, California.*

[17] Osher, S., and Sethian, J. A., 1988. "Fronts propagating with curvature- dependent speed: Algorithms based on hamilton-jacobi formulations". *Journal of Computational Physics,* ***79***, pp. 12–49.

[18] Larsen, J., and Dancy, H., 1983. "Open boundaries in short wave simulations-a new approach". *Coastal Engineering,* ***7***, pp. 285–297.

[19] Kamath, A., Alagan Chella, M., Bihs, H., and Muskulus, M., 2015. "CFD investigations of wave interaction with a pair of large tandem cylinders". *Ocean Eng.,* ***108***, pp. 734–748.

[20] Bihs, H., Kamath, A., Alagan Chella, M., and Arntsen. A., O., 2016. "Breaking-wave interaction with tandem cylinders under different impact scenarios". *Journal of Waterway, Port, Coastal, and Ocean Engineering.*

[21] Bihs, H., and Kamath, A., 2017. "A combined level set/ghost cell immersed boundary representation for simulations of floating bodies.". *International Journal for Numerical Methods in Fluids.*

[22] Afzal, M., Bihs, H., Kamath, A., and Arntsen. A., O., 2015. "Three dimensional numerical modeling of pier scour under current and waves using level set method.". *Journal of Offshore Mechanics and Arctic Engineering-Transactions of The Asme.*

[23] Hoffmann, J. "Matlab und simulink". *Addison Wesley Longman, Inc.*

[24] Aggarwal, A., Alagan Chella, M., Kamath, A., Bihs, H., and Arntsen. A., O., 2016. "Irregular wave forces on a large vertical circular cylinder". *Energy Procedia,* ***94***, pp. 504–516.

[25] Aggarwal, A., Alagan Chella, M., Kamath, A., Bihs, H., and Arntsen. A., O., 2016. "Numerical simulation of irregular wave forces on a horizontal cylinder". *ASME 2016 35th International Conference on Ocean, Offshore and Arctic Engineering, Volume 2: CFD and VIV.*

[26] Bihs, H., Alagan Chella, M., Kamath, A., and Arntsen. A., O., 2017. "Numerical Investigation of Focused Waves and their Interaction with a Vertical Cylinder using REEF3D". *Journal of Offshore Mechanics and Arctic Engineering.*, p. doi:10.1115/1.4036206.

9. National Conference on Computational Mechanics
MekIT'17
B. Skallerud and H. I. Andersson (Eds)

MODELLING PLANAR FILM BOILING OF ARBITRARY INCLINATION WITH THE LUBRICATION APPROXIMATION

ESKIL AURSAND[1]

[1] Department of Energy and Process Engineering (EPT)
Norwegian University of Science and Technology (NTNU)
N-7491 Trondheim, Norway
e-mail: eskil.aursand@ntnu.no, web page: http://www.ntnu.edu/ept

Key words: Film boiling, thin film flow, lubrication approximation, nonlinear, fourth order diffusion, implicit method

Abstract. A model for inclined planar film boiling using the lubrication approximation is derived. A dimensionless form of this model is presented, and it is shown that for a given plane orientation, the dynamics of the film thickness are governed by two dimensionless parameters: The Bond number and the evaporation number. The resulting scalar thin film equation is parabolic, fourth order, and highly nonlinear. A semi-implicit finite-volume method is derived in order to avoid having to satisfy the time step limitations required by explicit methods for the fourth order diffusion term. It is demonstrated how this model can be used to study transient vapor film growth, and the travelling wave instabilities which may occur under certain conditions.

1 INTRODUCTION

When a liquid comes in contact with an isothermal solid surface that is hotter than the liquid's saturation temperature, a vapor phase will start nucleating at the surface, and the liquid will start to boil. This process has an associated flux of heat being conducted from the solid. The relationship between the surface superheat and the heat flux is called the *boiling curve* [1]. The boiling curve shows the intuitive behavior of increasing heat flux with increasing temperature, up to the *critical heat flux*. This represents the transition from *nucleate boiling* to *film boiling* and is seen as a sudden drop in heat flux with increasing surface temperature.

The drop is due to the formation of a continuous vapor film between the solid and the liquid, which has an insulating effect on the heat transfer. In some practical situations film boiling is desirable, and in some it is not. In either case it is of interest to predict the dynamics of the vapor film, its heat flux, and under which conditions it may become unstable and break down (*vapor film collapse* [1]).

The vapor film is very thin, of the order of 100 µm [1, 2], and thus likely much thinner than the length of the solid surface. This makes thin film flow theory applicable for the analysis of the film dynamics. A common way of approaching thin film flow is by use of the *lubrication approximation* [3, Sec. 8.3]. This is a standard approach, using the large difference in length scales to simplify the Navier–Stokes equations. When combined with the mass-conservation principle, this will reduce the full set of governing equations and boundary conditions to a single highly nonlinear scalar PDE [4].

The dynamics of thin liquid films on solid surfaces, including analysis by the lubrication approximation, has been extensively reviewed in the past by Oron, Davis, and Bankoff [5], Myers [4] and Craster and Matar [6]. Some work has also been performed on lubrication analysis of vapor films (film boiling), such as Panzarella, Davis, and Bankoff [7], Tomar et al. [8] and Kim, Lee, and Kim [9]. However, these are all in the case of horizontal planes, where there is no net flow in one direction, and the models are normally reduced to linearized stability analysis in order to study the Rayleigh–Taylor type instability. Models for film boiling with other orientations, mainly vertical, have also been developed, which only considered steady states [10, 11].

The novelty of this work includes:

- A derivation of a thin film equation for planar film boiling of arbitrary inclination.
- Dimensionless scaling with a single length scale, the typical film thickness, based on an analytical steady state solution. This is in contrast to the usual usage of wall length as a length scale, and this demonstrates dynamic similarity in a new form.
- Showing in detail how a semi-implicit numerical method can be implemented in order to deal with the fourth-order diffusion term, including incorporating appropriate boundary conditions for film boiling.
- Demonstrating the possibility of suddenly developing instabilities a certain distance into an initially stable film, in the form of growing travelling waves, and revealing some of their predictable features.

The equation studied in this work can in general be written as

$$\frac{\partial h}{\partial t} + \frac{\partial}{\partial x}\left[h^3\left(a + b\frac{\partial h}{\partial x} + c\frac{\partial^3 h}{\partial x^3}\right)\right] = \frac{E}{h}, \tag{1}$$

where h, x and t are the dimensionless film thickness, distance and time, respectively. The remaining symbols are constants, to be explained. This is an autonomous fourth-order nonlinear parabolic equation with a source term. Such thin film equations have been studied previously by e.g. Myers [4], though commonly in the context of thin liquid films, not film boiling. Due to the stiffness introduced by the discretization of the high order derivatives, it is almost impossible to solve Eq. (1) stably with explicit numerical methods. In this work, a semi-implicit method is derived, which treats the high order

derivative approximations implicitly, while keeping the resulting equation system linear. While the method is inspired by Moriarty, Schwartz, and Tuck [12], this work includes an additional flux term due to not being restricted to the vertical configuration, and has different requirements for boundary conditions.

When Eq. (1) describes film boiling, the constants a and c are always positive, while b may have either sign. In the case where $b > 0$, we essentially have negative second order diffusion, which is a destabilizing influence, and it is partially counteracted by the stabilizing fourth order diffusion (c-term). This situation arises in the liquid-above-vapor configurations, and is essentially a Rayleigh–Taylor-type instability. However, since the orientation is not completely horizontal ($a > 0$) the buoyancy-driven advection term will give running wave instabilities, as opposed to just stationary rising bubbles. Similar running waves have been observed by e.g. Bui and Dhir [13]. Such instabilities predicted by the present model are investigated in a preliminary fashion in this work.

In this paper, Section 2 shows the derivation of the model from physical principles, including a final dimensionless form. A numerical method is derived and tested in Sections 3 and 4, respectively. Using this model, a few test cases are calculated in Section 5, before overall conclusions are drawn in Section 6.

2 MODEL

An illustration of the problem is shown in Fig. 1. The thin vapor film is surrounded by a flat solid wall on one side side and a liquid on the other side. The liquid is assumed to stay at its saturation temperature. The wall has a higher temperature than the liquid, and thus it conducts heat through the vapor film which in turn causes evaporation at the liquid–vapor interface. Buoyancy then drives vapor flow up along the film. The film coordinate system has its origin at the wall surface, with $\hat{\boldsymbol{x}}$ pointing tangentially along the wall, and $\hat{\boldsymbol{z}}$ pointing perpendicularly into the vapor film. The purpose of the model is to predict the spatiotemporal behavior of the liquid–vapor interface, as described by the film thickness function $\delta(X, \tau)$. The symbols X, Z and τ represent the dimensional space-time coordinates, while x, z and t will later be used in the dimensionless formulation.

In order to derive an approximate model for the vapor film dynamics, we make the following assumptions:

- Thickness of the film is much smaller than its length scale.
- Vapor density is constant.
- Vapor viscosity is constant.
- Surface tension is constant.
- Negligible liquid dynamics: Pressure is equal to hydrostatic pressure.
- Pressure jump across liquid–vapor interface is given by surface tension alone.

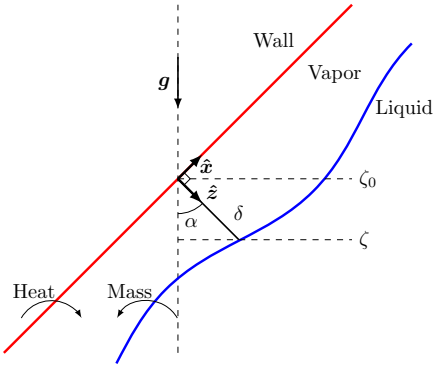

Figure 1: Illustration of the planar film boiling problem. A wall at angle α supplies heat to a boiling liquid, which feeds vapor into the vapor film in between. Buoyancy then drives vapor flow along the wall.

2.1 Lubrication approximation

In the case of thin film flow of an incompressible fluid, we may apply the classical *lubrication approximation* [3, Sec. 8.3]. This method uses the large difference in the film's tangential and perpendicular length scales to neglect several terms in the Navier–Stokes equations. The equations reduce to

$$\frac{\partial p}{\partial X} = \rho_{\mathrm{v}} g_x + \mu_{\mathrm{v}} \frac{\partial^2 u}{\partial Z^2}, \tag{2}$$

and

$$\frac{\partial p}{\partial Z} = \rho_{\mathrm{v}} g_z. \tag{3}$$

Here p is the pressure, u is the x-directed velocity, μ_{v} is the vapor viscosity, ρ_{v} is the vapor density, and g_x, g_z is the gravitational acceleration projected along the x and z-direction, respectively. According to the definition of the inclination angle α in Fig. 1, we have that

$$g_x = -g \sin \alpha, \tag{4}$$
$$g_z = g \cos \alpha, \tag{5}$$

where g is the gravitational acceleration. Under the assumption that $\partial p / \partial X$ is independent of Z, which will be justified in Section 2.2, we find from Eq. (2) that the second derivative of u with respect to Z is constant at a given X, and can be written as

$$\frac{\partial^2 u}{\partial Z^2} = -\frac{1}{\mu_{\mathrm{v}}} D(X), \tag{6}$$

where we have defined the driving force $D(X)$,

$$D(X) \equiv \rho_{\mathrm{v}} g_x - \frac{\partial p}{\partial X}. \tag{7}$$

When using the no-slip boundary condition $u = 0$ at both the wall and the liquid-vapor interface, a choice motivated in appendix A, we see that the solution to Eq. (6) yields the velocity profile,

$$u(X, Z) = \frac{\delta^2}{2\mu_{\mathrm{v}}} D(X) \left[\frac{Z}{\delta} - \left(\frac{Z}{\delta} \right)^2 \right]. \tag{8}$$

This is a parabolic (Poiseuille flow) profile arising from a balance between the driving force and viscous resistance.

2.2 Pressure

In order to go further with Eq. (8), we need to find the driving force, defined in Eq. (7). This requires a model for the pressure in the film. With the boundary condition $p(Z = \delta) = p_{\mathrm{v,i}}$, the solution to Eq. (3) is

$$p = p_{\mathrm{v,i}} - \rho_{\mathrm{v}} g_z \left(\delta - Z \right), \tag{9}$$

where $p_{\mathrm{v,i}}$ is the pressure at the vapor side of the liquid-vapor interface. Since neither $p_{\mathrm{v,i}}$ nor δ are functions of Z, we see that $\partial p / \partial X$ will be independent of Z, as assumed earlier. The pressure jump at the interface is given by the surface tension contribution,

$$p_{\mathrm{l,i}} - p_{\mathrm{v,i}} = \sigma \varkappa, \tag{10}$$

where $p_{\mathrm{l,i}}$ is the interface pressure on the liquid side, σ is the surface tension, and $\varkappa$ is the interface curvature. The sign of the curvature is chosen so that a positive curvature gives a decreased pressure in the vapor film. The liquid pressure at the interface is given by the hydrostatic contribution corresponding to the vertical position of the interface,

$$p_{\mathrm{l,i}} = p_0 - \rho_{\mathrm{l}} g \zeta, \tag{11}$$

where p_0 is a reference pressure, ρ_{l} is the liquid density, and $\zeta = \zeta_0 - \delta \cos(\alpha)$ is the vertical position of the interface. The latter depends on X as

$$\frac{\partial \zeta}{\partial X} = \sin(\alpha) - \cos(\alpha) \frac{\partial \delta}{\partial X}. \tag{12}$$

If we combine Eqs. (9) to (12), we find that

$$\frac{\partial p}{\partial X} = -\rho_{\mathrm{l}} g \sin(\alpha) + \Delta\rho g \cos(\alpha) \frac{\partial \delta}{\partial X} - \sigma \frac{\partial \varkappa}{\partial X}, \tag{13}$$

where $\Delta\rho \equiv \rho_\mathrm{l} - \rho_\mathrm{v}$. The driving force is thus given by

$$D(X) = \Delta\rho g \left[\sin\alpha - \cos\alpha \frac{\partial\delta}{\partial X}\right] + \sigma\frac{\partial\varkappa}{\partial X}. \tag{14}$$

Here it is seen that all gravitational driving forces disappear if the densities become equal, as must be the case.

2.3 Heat transfer

By using the same principles as when reducing the Navier-Stokes equations to Eqs. (2) and (3), and by assuming relatively small normal velocities at the interface compared to the tangential velocities, we can show that the energy equation for incompressible flow in the thin film will reduce to

$$\frac{\partial^2 T}{\partial Z^2} \approx 0, \tag{15}$$

where T is the temperature. This means that there will be a linear temperature profile across the film. If we assume that all the heat conducted into the liquid–vapor interface is spent on evaporation, and that the film is not so thin that the wall will be cooled by the liquid, the vaporization mass flux can be modelled as

$$m_\mathrm{e}(X) = \frac{Q}{\delta(X)}, \tag{16}$$

where Q is a constant given by case conditions and choice of evaporation model. The simplest possible model would be

$$Q = \frac{k_\mathrm{v}\Delta T}{L}, \tag{17}$$

where k_v is the vapor conductivity, ΔT is the difference between wall temperature and liquid saturation temperature, and L is the heat of vaporization.

2.4 Mass conservation

We will now consider vapor mass conservation in a control volume centered at X with a central thickness δ, length ΔX, and depth W. Mass is exchanged by flow along the film, and by evaporation at the liquid–vapor interface. The volume can be found from a Taylor expansion of $\delta(X)$ around its central value,

$$\begin{aligned} V &= W\int_{-\Delta X/2}^{\Delta X/2} \delta(X)\mathrm{d}X \\ &= W\delta\Delta X + \mathcal{O}\left(\delta_{XX}\Delta X^3\right), \end{aligned} \tag{18}$$

where δ_{XX} is a shorthand for $\partial^2\delta/\partial X^2$. The mass flow rate along the film can be found by integrating Eq. (8),

$$\begin{aligned} M &\equiv \int_0^{\delta(X)} \rho_\mathrm{v} u(X,Z) W \mathrm{d}Z, \\ &= W \frac{\rho_\mathrm{v} \delta^3(X)}{12\mu_\mathrm{v}} D(X). \end{aligned} \tag{19}$$

The mass flow rate entering by evaporation can be found by integrating Eq. (16) while Taylor expanding $\delta(X)$ around its central value,

$$\begin{aligned} M_\mathrm{e} &= W \int_{-\Delta X/2}^{\Delta X/2} m_\mathrm{e}(X) \mathrm{d}X, \\ &= W \Delta X \frac{Q}{\delta} + \mathcal{O}\left(\delta_X^2 (\Delta X/\delta)^3\right) + \mathcal{O}\left(\delta_{XX} (\Delta X)^3/\delta^2\right). \end{aligned} \tag{20}$$

We see that the evaporation rate can simply be found from the central film thickness as long as $\Delta X \ll \delta$. The mass conservation principle for the control volume can now be stated as

$$\frac{\partial\left(\rho_\mathrm{v} V\right)}{\partial \tau} + M(X_\mathrm{R}) - M(X_\mathrm{L}) = M_\mathrm{e}(X), \tag{21}$$

where $X_\mathrm{R} = X + \Delta X/2$ and $X_\mathrm{L} = X - \Delta X/2$. By using Eqs. (18) to (20) in the limit of small ΔX, we get

$$\frac{\partial \delta}{\partial \tau} + \frac{1}{12\mu_\mathrm{v}\Delta X}\left[\delta^3(X_\mathrm{R}) D(X_\mathrm{R}) - \delta^3(X_\mathrm{L}) D(X_\mathrm{L})\right] = \frac{Q}{\rho_\mathrm{v}\delta}. \tag{22}$$

The above is the control volume form. If we let $\Delta X \to 0$, we get the PDE,

$$\frac{\partial \delta}{\partial \tau} + \frac{1}{12\mu_\mathrm{v}} \frac{\partial}{\partial X}\left[\delta^3(X) D(X)\right] = \frac{Q}{\rho_\mathrm{v}\delta}. \tag{23}$$

2.5 Dimensionless form

In order to construct a dimensionless form of Eq. (23), we use a typical film thickness δ_0 as a length scale for both dimensions. The film thickness is a model prediction, not a case parameter, so we need to relate it to a given case parameter, such as the length of the solid wall, X_0. In the special case of a vertical wall and negligible surface-tension ($D = \Delta\rho g$), we may find the analytical steady-state solution of Eq. (23) for the initial condition $\delta(0) = 0$, and evaluate this at $X = X_0$. This gives the film-thickness scale

$$\delta_0 = \left(\frac{16\mu_\mathrm{v} Q}{\rho_\mathrm{v}\Delta\rho g} X_0\right)^{1/4}, \tag{24}$$

and a film aspect ratio of

$$\epsilon \equiv \frac{\delta_0}{X_0} = \left(\frac{16 \mu_\text{v} Q}{\rho_\text{v} \Delta\rho g X_0^3} \right)^{1/4}. \tag{25}$$

Based on the length scale, we may define a tangential velocity scale as the average velocity according to Eq. (8) in the special case of vertical wall and negligible surface-tension,

$$u_0 = \frac{\Delta\rho g \delta_0^2}{12 \mu_\text{v}}. \tag{26}$$

The interface normal velocity scale is given by the evaporation rate,

$$w_0 = \frac{Q}{\rho_\text{v} \delta_0}. \tag{27}$$

Using the length scale and tangential velocity scale, we set a time scale as

$$\tau_0 = \frac{\delta_0}{u_0} = \frac{12 \mu_\text{v}}{\Delta\rho g \delta_0}. \tag{28}$$

With the dimensionless film thickness $h = \delta/\delta_0$, the dimensionless space-time coordinates $x = X/\delta_0$ and $t = \tau/\tau_0$, and the dimensionless curvature $\kappa = \varkappa\delta_0$, the PDE becomes

$$\frac{\partial h}{\partial t} + \frac{\partial}{\partial x} \left[h^3 \left(\sin(\alpha) - \cos(\alpha) \frac{\partial h}{\partial x} + \frac{1}{\text{Bo}} \frac{\partial \kappa}{\partial x} \right) \right] = \frac{E}{h}, \tag{29}$$

We see that for a given wall orientation α, the dynamics of the vapor film is governed by two dimensionless groups. These are the Bond number,

$$\text{Bo} = \frac{\Delta\rho g \delta_0^2}{\sigma}, \tag{30}$$

which is the ratio of buoyant forces to surface tension forces, and what we will call the evaporation number,

$$E = \frac{w_0}{u_0} = \frac{12 \mu_\text{v} Q}{\rho_\text{v} \Delta\rho g \delta_0^3} = \frac{3}{4}\epsilon, \tag{31}$$

which is the ratio of normal to tangential velocity scales. Note also how the evaporation number is basically equal to the film aspect ratio.

2.6 Steady-state solution

With negligible surface tension ($\text{Bo} \to \infty$), the steady-state solution h_ss of Eq. (29) for any inclination α is

$$h_\text{ss}(x) = \left(h^4(0) + \frac{\epsilon}{\sin(\alpha)} x \right)^{1/4}, \tag{32}$$

where $h(0)$ is the initial film thickness at $x = 0$. We see that for a vertical plane starting from zero thickness, $h_\text{ss}(1/\epsilon) = 1$, as was intended by the scaling.

2.7 Comments on the model

The dimensionless curvature of the curve $h(x)$ is given by the standard result from differential geometry,

$$\kappa = \frac{\frac{\partial^2 h}{\partial x^2}}{\left(1 + \left(\frac{\partial h}{\partial x}\right)^2\right)^{3/2}} \approx \frac{\partial^2 h}{\partial x^2}, \tag{33}$$

with the final approximation being applicable in the case where $h_x \ll 1$. This approximation will be used in the remainder of this work. Eq. (29) can then be written as,

$$\frac{\partial h}{\partial t} + \frac{\partial}{\partial x}\left[h^3\left(\sin(\alpha) - \cos(\alpha)\frac{\partial h}{\partial x} + \frac{1}{\mathrm{Bo}}\frac{\partial^3 h}{\partial x^3}\right)\right] = \frac{E}{h}. \tag{34}$$

which is an autonomous fourth-order nonlinear parabolic equation.

Besides a different non-dimensionalization, Eq. (34) matches the equation studied by Myers [4] for a liquid film on an inclined plane, when neglecting the Marangoni effect and van der Waals force. The angles are defined differently, but the signs end up the same due to this work having a buoyant vapor film as opposed to a falling liquid film.

In order to represent a real case of film boiling on a submerged heated solid, some boundary conditions need to be set. Physically, the film thickness would have to start from zero somewhere, and this would be at the leading (bottom) edge of the sample. In terms of the model generality, we will apply a set value $h(x = 0) = h_{\mathrm{B}}$ at the inflow boundary of the domain, with the ability to set it to zero. When solving the equation in practice, one must also implement an artificial outflow boundary in order to have a finite domain.

A novel feature of Eq. (34) is that it involves a *fourth order diffusion* term. Such terms are superficially similar to the regular second order diffusion terms, in the way that they will generally serve to smooth out the function. In more precise terms, they have monotonously decreasing "energy". However, they lack a property that all second order diffusion equations have, which is the principle of increasing entropy (maximum principle). This means that new extrema may evolve that were not present in the initial conditions [14].

3 NUMERICAL METHOD

3.1 Finite-volume method

We aim to solve Eq. (34) numerically with a finite-volume method, in order to strictly conserve mass. In the finite-volume formulation, we evolve the cell average or center value of h by estimating a flux function at the cell faces, as illustrated in Fig. 2. The semi-discretized finite-volume form of Eq. (34) is

$$\frac{\mathrm{d}h_i}{\mathrm{d}t} = -\frac{1}{\Delta x}\left[F_{i+1/2} - F_{i-1/2}\right] + \frac{E}{h_i}, \tag{35}$$

and the flux function is evaluated at the cell face,

$$F_{i+1/2} = h_{i+1/2}^3 \left[a + b \left(h_x \right)_{i+1/2} + c \left(h_{xxx} \right)_{i+1/2} \right]. \tag{36}$$

where $a = \sin(\alpha)$, $b = -\cos(\alpha)$, $c = 1/\mathrm{Bo}$. The left face flux $F_{i-1/2}$ is defined equivalently.

We estimate this flux by staggered finite difference operators which operate on the cell center values,

$$F_{i+1/2} \approx \underbrace{\left(\frac{h_{i+1} + h_i}{2} \right)^3}_{H h_{i+1/2}} \left[a + b \underbrace{\left(\frac{h_{i+1} - h_i}{\Delta x} \right)}_{Q_1 h_{i+1/2}} + c \underbrace{\left(\frac{(h_{xx})_{i+1} - (h_{xx})_i}{\Delta x} \right)}_{Q_3 h_{i+1/2}} \right]. \tag{37}$$

If we use the standard centered second order finite difference method to represent the cell centered second derivatives, $(h_{xx})_i$, we get that the Q_3 operator is given by

$$Q_3 h_{i+1/2} = \frac{1}{\Delta x^3} \left(h_{i+2} - 3h_{i+1} + 3h_i - h_{i-1} \right). \tag{38}$$

By using Taylor expansions of $h(x)$ centered at the cell face, it can be verified that $Q_3 h_{i+1/2}$, $Q_1 h_{i+1/2}$ and $H h_{i+1/2}$ are all consistent second order representations of h_{xxx}, h_x, and h^3 at the $(i + 1/2)$ cell face, respectively.

The next question is how to perform the time integration in Eq. (35), i.e. how to evolve from a current time level n to the next $n + 1$. As will be demonstrated in Section 3.2, this is not necessarily straightforward, due to the fourth-order diffusion term.

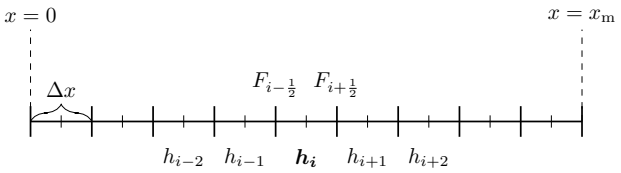

Figure 2: Illustration of the numerical grid. In order to evolve the cell center value h_i in time, we must estimate the flux function on both faces of that cell. This requires the indicated five-point stencil of cell-center values.

3.2 Time step constraints in explicit methods

In order to perform numerical analysis, we derive a simpler linearized version of Eq. (34). This is done by discarding the source term, inserting a solution that is the sum of a uniform steady solution and a small perturbation, $h = \tilde{h} + u$, and discarding higher order

terms in the perturbation. The result is

$$\frac{\partial u}{\partial t} + \tilde{a}\frac{\partial u}{\partial x} + \tilde{b}\frac{\partial^2 u}{\partial x^2} + \tilde{c}\frac{\partial^4 u}{\partial x^4} = 0, \tag{39}$$

where $\tilde{a} = 3a\tilde{h}^2$, $\tilde{b} = b\tilde{h}^3$ and $\tilde{c} = c\tilde{h}^3$. Using standard von Neumann stability analysis with a 2nd order centered finite difference scheme, we can show that the stability condition of an explicit method for the advection term is

$$\Delta t_{\text{adv}} \leq s_{\text{i}} \frac{\Delta x}{\tilde{a}}, \tag{40}$$

where s_{i} is the extent of the time integrator's stability domain along the imaginary axis. However, for the fourth-order diffusion term, a similar analysis yields

$$\Delta t_{\text{4diff}} \leq \frac{s_{\text{r}}}{16} \frac{\Delta x^4}{\tilde{c}}, \tag{41}$$

where s_{r} is the absolute value of the extent of the time integrator's stability domain along the negative real axis. We see that reducing Δx to obtain a converged solution will require an unreasonably small time step, and thus the simple explicit methods will be impractical. A different approach will be presented in Section 3.3.

3.3 A semi-implicit method

A fully implicit method would require solving a non-linear system of equations every time step. In order to avoid this, we implement a semi-implicit method, where all the nonlinear factors (h^3 and $1/h$) are based on values from the current time level, while the derivatives are based on values from the next time step. If we use the explicit/implicit Euler methods, this becomes

$$h_i^{n+1} = h_i^n - \frac{\Delta t}{\Delta x}\left[F_{i+1/2}^{n+1} - F_{i-1/2}^{n+1}\right] + \Delta t \frac{E}{h_i^n}, \tag{42}$$

with the fluxes given by

$$F_{i+1/2}^{n+1} = H h_{i+1/2}^n \left[a + bQ_1 h_{i+1/2}^{n+1} + cQ_3 h_{i+1/2}^{n+1}\right], \tag{43}$$

$$F_{i-1/2}^{n+1} = H h_{i-1/2}^n \left[a + bQ_1 h_{i-1/2}^{n+1} + cQ_3 h_{i-1/2}^{n+1}\right]. \tag{44}$$

Note how the cubic pre-factor is evaluated at time n, not $n+1$. The above yields a linear pentadiagonal system of equations to solve for the cell values at the next time level,

$$\begin{aligned}
&h_{i-2}^{n+1}\left[KH_{i-1/2}^{n}\right] \\
&+h_{i-1}^{n+1}\left[RH_{i-1/2}^{n}-K\left(H_{i+1/2}^{n}+3H_{i-1/2}^{n}\right)\right] \\
&+h_{i}^{n+1}\left[1+(3K-R)\left(H_{i+1/2}^{n}+H_{i-1/2}^{n}\right)\right] \\
&+h_{i+1}^{n+1}\left[RH_{i+1/2}^{n}-K\left(3H_{i+1/2}^{n}+H_{i-1/2}^{n}\right)\right] \\
&+h_{i+2}^{n+1}\left[KH_{i+1/2}^{n}\right] \\
&=h_{i}^{n}+\Delta t\frac{E}{h_{i}^{n}}-C\left(H_{i+1/2}^{n}-H_{i-1/2}^{n}\right),
\end{aligned} \tag{45}$$

where we have used the shorthands

$$C=\frac{a\Delta t}{\Delta x},\quad R=\frac{b\Delta t}{\Delta x^{2}},\quad K=\frac{c\Delta t}{\Delta x^{4}}, \tag{46}$$

$$H_{i+1/2}^{n}=\left(\frac{h_{i+1}^{n}+h_{i}^{n}}{2}\right)^{3},\quad H_{i-1/2}^{n}=\left(\frac{h_{i}^{n}+h_{i-1}^{n}}{2}\right)^{3}. \tag{47}$$

Since the advection term is effectively treated explicitly, the time step should satisfy the CFL condition Eq. (40), with $s_{\mathrm{i}}=1$. Since this is vastly larger than what is required by the fourth order diffusion term, Eq. (41), the semi-implicit treatment is still beneficial. Using Eq. (40) requires the input of a linearized advection speed $\tilde{a}=3\tilde{h}^{2}$. When starting from very thin films, there is a danger of very large time steps. Therefore, $\tilde{h}$ used to determine $\tilde{a}$ in Eq. (40) is set as the largest of the current maximum h and the maximum of the steady state solution according to Eq. (32). Finally, in order to reduce the error and make stability more certain, the time step is reduced by a safety factor of 0.5 relative to the above stability requirement. This is analogous to the CFL-number common in computational fluid dynamics.

3.4 Boundary conditions

In order to study some basic behavior of the PDE, one may set the source term to zero ($E=0$), and apply periodic boundary conditions. In this case, the implementation of boundary conditions with Eq. (45) is trivial. However, if we want to include the effects of evaporation, a periodic domain is impossible without causing boundless film thickness growth. In this case we want to set a given film thickness at the inflow boundary, and implement an artificial outflow boundary. Specifically, we will use the following boundary conditions:

- Left boundary ($x=0$): $h(0)=h_{\mathrm{B}}$ and $h_{xxx}(0)=0$.
- Right boundary ($x=x_{\mathrm{m}}$): $h_{xxx}(x_{\mathrm{m}})=0$ and $h_{xxxx}(x_{\mathrm{m}})=0$.

Due to the five-point stencil of Eq. (45), there are essentially two missing cell values on each side of the domain. These values are solved for by applying numerical version of the above boundary conditions. When we insert these into Eq. (45), it leads to modified equation systems for the two cells on each side closest to the boundaries. The details of this are shown in appendix B.

For orientations where the liquid is above the vapor, i.e. for $\alpha > \pi/2$, this outflow boundary is not necessarily stable. This is because the factor b in Eq. (36) becomes positive, causing physical instabilities related to the Rayleigh–Taylor instability. If the Bond number is large enough, this will cause relatively large waves to impact the outflow boundary, causing instabilities and even a sudden change to inflow conditions.

In order to alleviate this, we implement a *buffer layer* approach. This entails extending the computational domain beyond the domain of interest, and then damping the value of b (which is normally constant) towards zero before approaching the computational boundary. When doing this, the hope is that the solution in the upstream domain of interest is mostly unaffected by the damping procedure, while keeping the computation stable. Specifically, the value of magnitude of b is damped from its physical value to zero by a cosine function in the last half of the buffer layer. A verification of this is presented in Section 4.

4 NUMERICAL TESTS

4.1 Convergence

Convergence of the numerical solution with respect to grid refinement was tested on a case with physical parameters $\mathrm{Bo} = 10$, $E = 0.05$, $\alpha = 3\pi/4$ and $h_{\mathrm{B}} = 0$. The test was run until $t = 1$, starting from a very thin film. The convergence in the domain $x \in [0, 3]$ was checked by comparing the solution at corresponding cell centers at each level of grid refinement to a reference solution. The coarsest grid was at $\Delta x = 0.1$, and Δx was repeatedly reduced by a factor $1/3$ in order to obtain cells with overlapping centers. The reference solution was calculated with a grid spacing of $\Delta x \approx 10^{-4}$. When reducing Δx beyond this, the solutions started showing signs of significant round-off error. This is likely due to K rapidly diverging compared to the other factors in the system, causing the problem to become ill-conditioned.

Recall that the time step Δt is reduced linearly with Δx, according to the rules described in Section 3.3. Since the time-integration methods are the implicit and explicit Euler methods, which are first order in time, we can expect no better than first order convergence. The results are shown in Fig. 3, which indicates slow but sure convergence, approaching first order behavior. Note that this convergence test is imperfect, since the reference solution is subject to numerical error itself. It does, however, confirm convergence to a single solution.

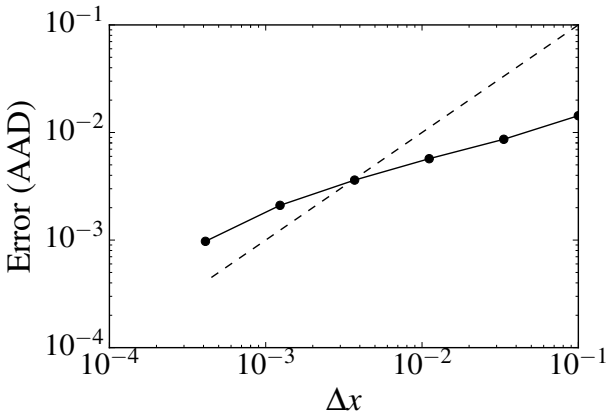

Figure 3: The results from a convergence test, showing the average absolute deviation (AAD error) at different grid spacings, compared to a reference case. The dashed line shows the slope expected of first order convergence.

4.2 Buffer layer

In order to test the validity of the buffer layer outflow boundary, a numerical test was performed. The physical parameters of the test were Bo $= 5$, $E = 0.05$ $\alpha = 3\pi/4$ and $h_{\mathrm{B}} = 0$. Note that in order to promote the troublesome travelling wave instabilities that the buffer layer was designed to handle, α is set larger than $\pi/2$ and Bo is set larger than one.

The case to be tested had a domain of interest $x \in [0, 30]$, and the computational domain was padded with an equally long buffer layer in order to get a stable solution. This solution was then compared to a reference case with the same physical parameters, but with a three times larger computational domain. If the solution in the domain of interest is sufficiently close to the reference case, we can then say that the presence of the buffer layer has not significantly polluted the results. Both cases were run with a grid spacing of $\Delta x = 0.01$, until the time $t = 25$. The results are presented in Fig. 4. It is seen that in the domain of interest, the buffer layer solution is indistinguishable from the reference solution. Such a large buffer layer as long as the domain of interest is used for the remainder of this work, in order to ensure no effect on the domain of interest.

5 NUMERICAL RESULTS

In order to test the model and its numerical implementation, a series of film-establishing cases were run. These cases are run from an initial state of a very thin film until reaching a steady state solution (or lack thereof), while keeping the leftmost face film thickness at $h_{\mathrm{B}} = 0$. Note that since the first cell center is located at $x = \Delta x/2$, no cell will get a

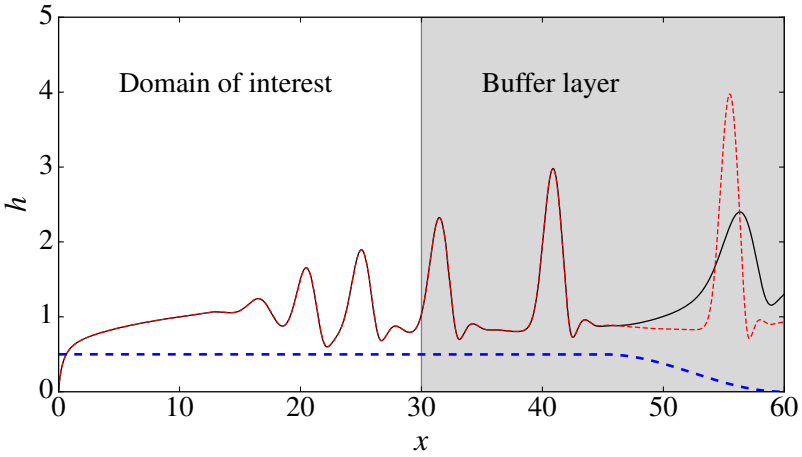

Figure 4: Results from the buffer layer test. The black solid line shows the solution using the buffer layer, and the red dashed line shows the reference solution. The blue dashed line shows the damping of the b-factor, from $b = -\cos(\alpha)$ at $x = 45$ to $b = 0$ at $x = 60$.

diverging E/h source term. Instead, the effect is simply that the left face flux of the first cell will reduce to zero.

The functional form of the initial state was according to Eq. (32), but reduced to represebt a much thinner film than the actual steady state. Specifically, this reduction was made by inserting $10^{-6}\epsilon$ in place of the actual ϵ. This factor was chosen somewhat arbitrarily, but it needed to be small.

Table 1: Overview of numerical test cases.

Case	Bo	E	α
1	1.0	0.05	$\pi/4$
2	1.0	0.05	$3\pi/4$
3	5.0	0.05	$3\pi/4$

An overview of the physical parameters of the test cases is shown in Tab. 1. All cases have an evaporation number of $E = 0.05$, which corresponds to a film aspect ratio of $\epsilon = 1/15$, i.e. the film will reach a thickness of $h \approx 1$ at $x \approx 15$. Cases 1 and 2 have identical parameters besides wall orientation, with liquid-below-vapor and liquid-above-vapor configurations, respectively. Case 3 keeps the orientation of case 2, while increasing the Bond number in order to provoke instabilities and lack of a steady state.

The results for cases 1 and 2 are shown in Fig. 5. It is seen that both these cases reach a steady state, similar to the one predicted by Eq. (32). The fact that they are not identical is expected, as Eq. (32) was derived under the assumption of no surface tension. However, their similarity serves to verify that the numerical results are reasonable. In the simulations, steady state was declared when $|\partial h/\partial t| < 10^{-6}$ in the entire domain, and for these cases it occurred around $t \approx 30$.

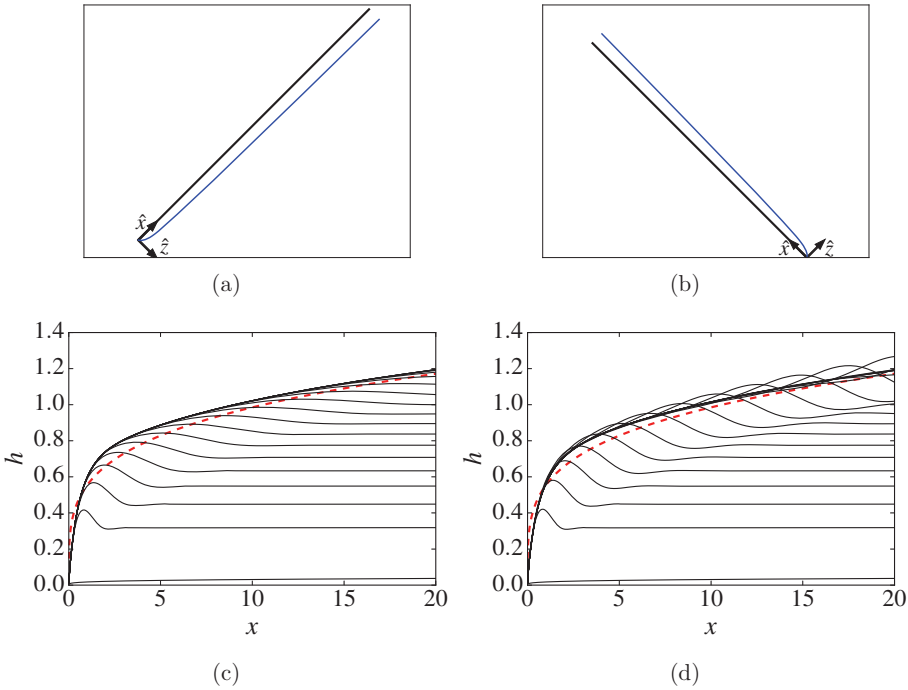

Figure 5: Simulations of an establishing vapor film, from an initial very thin film, to steady state. Both cases have $\mathrm{Bo} = 1$ and $E = 0.05$. The left side case, (a) and (c), has $\alpha = \pi/4$ (Case 1) and the right side case, (b) and (d), has $\alpha = 3\pi/4$ (Case 2). The top shows the final steady state in its real orientation and aspect ratio. The bottom shows the corresponding transient from the initial state. The solid lines are separated by a dimensionless time difference of one. The dashed red line shows the analytical (no surface tension) steady state solution, according to Eq. (32).

Case 3 did not reach a proper steady state, but rather a repeating wave shedding state. The result is shown in Fig. 6. It is seen that the vapor film is stable up to a certain point

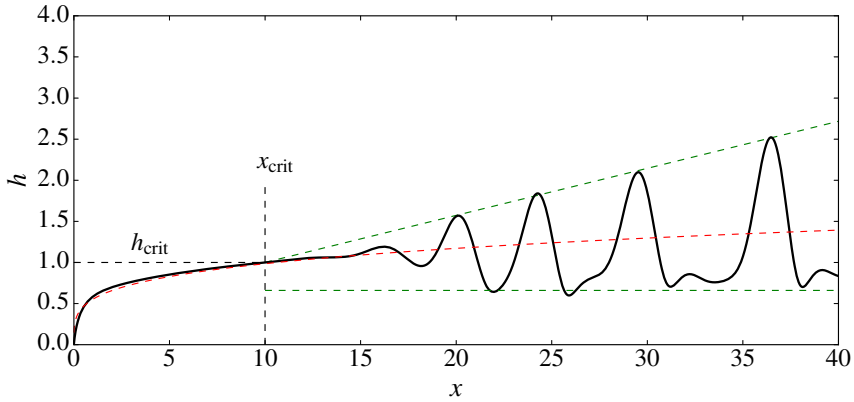

Figure 6: The instabilities occurring with Case 3. The solid black line shows the solution at $t = 30$, while the dashed red line shows the analytical steady state solution according to Eq. (32). The critical point $(x_{\text{crit}}, h_{\text{crit}})$ is the approximate point where the steady film turns unstable, and starts shedding waves. The dashed green lines show the extent of the growing waves. The bottom dashed line is horizontal, and placed at the average wave trough height. The top dashed line is a linear fit of the wave crests, passing through the critical point.

that we may call the *critical point*. Beyond this point, the film turns unstable, and starts shedding travelling waves. These waves have two notable properties:

- A remarkably good linear fit can be made for the line passing through the critical point and the crests of all the developed waves. This means that the ratio of crest speed to crest growth rate is approximately constant. However, the speed and growth rate are not separately constant, since the waves are in fact accelerating, as seen from the increasing crest-to-crest distance (wavelength).
- The wave troughs appear to be capped from below, as opposed to growing deeper. This is likely related to the evaporation effect, injecting more gas if the troughs grow too deep.

The slope of the wave crest linear fit is 0.057, and the wave troughs are capped at approximately $h = 0.7$. At the time shown ($t = 30$), the four developed crests move at speeds 2.3, 2.6, 3.5 and 4.3. This is somewhat close to what can be predicted from the linearized advection speed in Eq. (39), $\tilde{a} = 3\tilde{h}^2$, using the analytical steady state for $\tilde{h}$. However, the linearization over-predicts the wave speeds of the smaller waves, and under-predicts the wave speeds of the larger waves. The rightmost wave has a growth rate of 0.24, which can be divided by its speed 4.3 to show that its crest will follow the mentioned linear fit.

Note that the location of the critical point is sensitive to the Bond number. Exploring this dependence is beyond the scope of this paper.

6 CONCLUSIONS

In this work, a physical model for the interface dynamics of planar film boiling at arbitrary orientation was derived. The resulting thin film equation, similar to other works on thin film liquid flow, was fourth order, highly nonlinear, parabolic, and included a source term. It was then demonstrated how, through the use of a single length scale, a dimensionless version of this equation can be derived, with the Bond number, the evaporation number and the inclination angle as parameters.

A semi-implicit numerical method for solving this equation was derived. This method avoids having to satisfy the intractable time-step limitations required by the fourth order diffusion term, while still limiting the work to solving a linear pentadiagonal system each time step. Specific boundary conditions were derived for the case of a freely growing film starting from a given thickness at the lower end. It was found that a buffer layer approach was useful for approximating a non-reflecting outflow boundary in the cases with incident travelling waves.

A few numerical tests were performed in order to test the model. The tests revealed the potential for running wave instabilities at large Bond numbers in the liquid-above-vapor orientations. In these cases, the vapor film is stable up to a certain critical point, beyond which wave instabilities are shedded. Certain predictable patterns were identified for these growing and accelerating waves.

Future work could be focused on exploring the dependence of the instabilities, especially the critical point, on the dimensionless parameters of the model. This can be done both numerically and with analytical tools such as linear stability analysis. Additional topics could include investigating the effect the instabilities have on the overall heat transfer rate, and the effect of additional model terms sometimes introduced in thin film flow, such as the Marangoni effect and van der Waals forces.

ACKNOWLEDGEMENTS

This work has been carried out as part of a PhD thesis in relation to the research project "Predicting the risk of rapid phase-transition events in LNG spills (Predict-RPT)", financed under the MAROFF program. I acknowledge the Research Council of Norway (244076/O80) and The Gas Technology Centre NTNU-SINTEF (GTS) for support. I would also like to thank my supervisors Bernhard Müller, Morten Hammer, Svend Tollak Munkejord, and Tor Ytrehus for fruitful discussions and feedback.

REFERENCES

[1] V.K. Dhir. "Boiling heat transfer". In: *Annual review of fluid mechanics* 30.1 (1998), pp. 365–401. DOI: 10.1146/annurev.fluid.30.1.365.

[2] H.I. Jouhara and B.P. Axcell. "Forced convection film boiling on spherical and plane geometries". In: *Chemical Engineering Research and Design* 80.3 (2002), pp. 284–289. DOI: 10.1205/026387602753582060.

[3] P.K. Kundu, I.M. Cohen, and D.R. Dowling. *Fluid Mechanics*. 5th. Cambridge: Academic Press, 2007. ISBN: 9780123821003.

[4] T.G. Myers. "Thin films with high surface tension". In: *Siam Review* 40.3 (1998), pp. 441–462. DOI: 10.1137/S003614459529284X.

[5] A. Oron, S. H. Davis, and S. G. Bankoff. "Long-scale evolution of thin liquid films". In: *Reviews of modern physics* 69.3 (1997), p. 931. DOI: 10.1103/RevModPhys.69.931.

[6] R.V. Craster and O.K. Matar. "Dynamics and stability of thin liquid films". In: *Reviews of modern physics* 81.3 (2009), p. 1131. DOI: 10.1103/RevModPhys.81.1131.

[7] C. H. Panzarella, S. H. Davis, and S. G. Bankoff. "Nonlinear dynamics in horizontal film boiling". In: *Journal of Fluid Mechanics* 402 (2000), pp. 163–194. DOI: 10.1017/S0022112099006801.

[8] G. Tomar, G. Biswas, A. Sharma, and S. W. J. Welch. "Multimode analysis of bubble growth in saturated film boiling". In: *Physics of Fluids* 20.9 (2008), p. 092101. DOI: 10.1063/1.2976764.

[9] B. J. Kim, J. H. Lee, and K. D. Kim. "Rayleigh–Taylor instability for thin viscous gas films: Application to critical heat flux and minimum film boiling". In:

International Journal of Heat and Mass Transfer 80 (2015), pp. 150–158. DOI: 10.1016/j.ijheatmasstransfer.2014.08.084.

[10] N.I. Kolev. "Film boiling on vertical plates and spheres". In: *Experimental Thermal and Fluid Science* 18.2 (1998), pp. 97–115. DOI: 10.1016/S0894-1777(98)10021-3.

[11] H. Jouhara and B. P. Axcell. "Film boiling heat transfer and vapour film collapse on spheres, cylinders and plane surfaces". In: *Nuclear Engineering and Design* 239.10 (2009), pp. 1885–1900. DOI: 10.1016/j.nucengdes.2009.04.008.

[12] J.A. Moriarty, L.W. Schwartz, and E.O. Tuck. "Unsteady spreading of thin liquid films with small surface tension". In: *Physics of Fluids A: Fluid Dynamics* 3.5 (1991), pp. 733–742. DOI: 10.1063/1.858006.

[13] T.D. Bui and V.K. Dhir. "Film boiling heat transfer on an isothermal vertical surface". In: *ASME J. Heat Transfer* 107.4 (1985). DOI: 10.1115/1.3247502.

[14] N. Tehseen and P. Broadbridge. "Fourth Order Diffusion Equations with Increasing Entropy". In: *Entropy* 14.7 (2012), pp. 1127–1139. DOI: 10.3390/e14071127.

A VELOCITY BOUNDARY CONDITIONS

At both sides of the vapor film, we assume that the no-slip condition is reasonable, as it usually is when the pressures are not extremely low. At the solid wall side, this trivially reduces to the condition of $u = 0$, since the wall is stationary. At the liquid-vapor interface, it is not that obvious. The no-slip condition still applies, but this is no-slip relative to the liquid, which may itself move.

At the liquid-vapor interface, an additional boundary condition applies, which is the continuity of shear stress. Under the assumptions of the lubrication approximation, this condition may be stated as

$$\mu_{\mathrm{v}} \left.\frac{\partial u}{\partial Z}\right|_{\mathrm{i}} \approx \mu_{\mathrm{l}} \left.\frac{\partial u_{\mathrm{l}}}{\partial Z}\right|_{\mathrm{i}}, \tag{48}$$

where u_{l} is the x-directed liquid velocity, μ_{l} is the liquid viscosity, and the subscript i indicates evaluation at the interface. We now use the parabolic profile in Eq. (8), which admittedly was derived by the assumption being motivated in this section, to estimate the actual shear rate at the interface. This gives

$$\left.\frac{\partial u}{\partial Z}\right|_{\mathrm{i}} \approx -\frac{6}{\delta}\bar{u}, \tag{49}$$

where $\bar{u}$ is the average velocity in the film. If we assume that the liquid velocity profile follows a decreasing quadratic profile reaching zero (and zero derivative) a distance δ_{l} from the interface, such as in [11], we have that

$$\left.\frac{\partial u_{\mathrm{l}}}{\partial Z}\right|_{\mathrm{i}} \approx -\frac{2}{\delta_{\mathrm{l}}}u_{\mathrm{i}}, \tag{50}$$

where u_i is the velocity at the interface. If we insert Eqs. (49) and (50) into Eq. (48), we get that

$$\frac{u_i}{\bar{u}} \approx 3\frac{\mu_\mathrm{v}}{\mu_\mathrm{l}}\frac{\delta_\mathrm{l}}{\delta}. \tag{51}$$

For typical liquid-gas pairs, we have $\mu_\mathrm{v}/\mu_\mathrm{l} \approx 0.01$. This means that if the liquid boundary layer has a somewhat similar thickness to the vapor film, the interface velocity will be negligible compared to the average velocity in the vapor film. This justifies also using the condition $u \approx 0$ at the liquid-vapor interface, which leads to Eq. (8).

B NUMERICAL BOUNDARY CONDITIONS

B.1 Left boundary

The numerical stencil requires two missing cell values to the left of the leftmost cell ($i = 0$). We fill these values based on the following principles:

- Set h_{-1} such that $Hh_{0-1/2}$ becomes a specified boundary value h_B^3.
- Set h_{-2} such that $Q_3 h_{0-1/2} = 0$.

This gives values for the additional cells of

$$h_{-1} = 2h_\mathrm{B} - h_0 \tag{52}$$
$$h_{-2} = h_1 - 6\left(h_0 - h_\mathrm{B}\right). \tag{53}$$

Inserting this into Eq. (45) yields the following equation at the first cell ($i = 0$),

$$\begin{aligned}
&+ h_i^{n+1}\left[1 + 4KH_{i+1/2}^n - R\left(H_{i+1/2}^n + 2h_\mathrm{B}^3\right)\right] \\
&+ h_{i+1}^{n+1}\left[\left(R - 3K\right)H_{i+1/2}^n\right] \\
&+ h_{i+2}^{n+1}\left[KH_{i+1/2}^n\right] \\
&= h_i^n + \Delta t\frac{E}{h_i^n} - C\left(H_{i+1/2}^n - h_\mathrm{B}^3\right) + 2KH_{i+1/2}^n h_\mathrm{B} - 2Rh_\mathrm{B}^4,
\end{aligned} \tag{54}$$

and the following equation for the second cell ($i = 1$),

$$\begin{aligned}
&+ h_{i-1}^{n+1}\left[RH_{i-1/2}^n - K\left(H_{i+1/2}^n + 4H_{i-1/2}^n\right)\right] \\
&+ h_i^{n+1}\left[1 + \left(3K - R\right)\left(H_{i+1/2}^n + H_{i-1/2}^n\right)\right] \\
&+ h_{i+1}^{n+1}\left[RH_{i+1/2}^n - K\left(3H_{i+1/2}^n + H_{i-1/2}^n\right)\right] \\
&+ h_{i+2}^{n+1}\left[KH_{i+1/2}^n\right] \\
&= h_i^n + \Delta t\frac{E}{h_i^n} - C\left(H_{i+1/2}^n - H_{i-1/2}^n\right) - 2KH_{i-1/2}^n h_\mathrm{B}.
\end{aligned} \tag{55}$$

The cubed face value $Hh_{0-1/2}$ is simply set to h_B^3.

B.2 Right (outflow) boundary

The numerical stencil requires two missing cell values to the right of the rightmost cell ($i = m$). We fill these values based on the following principles:

- Set $Q_3 h_{i+1/2} = 0$ for the two rightmost faces.

This has the benefit of keeping the equation system pentadiagonal, which is convenient for computational reasons. This gives values for the additional cells of

$$h_{m+1} = 3h_m - 3h_{m-1} + h_{m-2} \tag{56}$$
$$h_{m+2} = 6h_m - 8h_{m-1} + 3h_{m-2}. \tag{57}$$

Inserting this into Eq. (45) yields the following equation at the last cell ($i = m$),

$$\begin{aligned}
&+ h_{i-2}^{n+1} \left[R H_{i+1/2}^n \right] \\
&+ h_{i-1}^{n+1} \left[R \left(-3H_{i+1/2}^n + H_{i-1/2}^n \right) \right] \\
&+ h_i^{n+1} \left[1 + R \left(2H_{i+1/2}^n - H_{i-1/2}^n \right) \right] \\
&= h_i^n + \Delta t \frac{E}{h_i^n} - C \left(H_{i+1/2}^n - H_{i-1/2}^n \right),
\end{aligned} \tag{58}$$

the following equation for the second to last cell ($i = m - 1$),

$$\begin{aligned}
&+ h_{i-2}^{n+1} \left[K H_{i-1/2}^n \right] \\
&+ h_{i-1}^{n+1} \left[(R - 3K) H_{i-1/2}^n \right] \\
&+ h_i^{n+1} \left[1 + 3K H_{i-1/2}^n - R \left(H_{i+1/2}^n + H_{i-1/2}^n \right) \right] \\
&+ h_{i+1}^{n+1} \left[R H_{i+1/2}^n - K H_{i-1/2}^n \right] \\
&= h_i^n + \Delta t \frac{E}{h_i^n} - C \left(H_{i+1/2}^n - H_{i-1/2}^n \right),
\end{aligned} \tag{59}$$

The cubed face value $H_{m+1/2}$ is set to

$$H_{m+1/2}^n = \left(\frac{h_m + h_{m+1}}{2} \right)^3 = \left(\frac{4h_m - 3h_{m-1} + h_{m-2}}{2} \right)^3. \tag{60}$$

9. National Conference on Computational Mechanics
MekIT'17
B. Skallerud and H I Andersson (Eds)

NUMERICAL INVESTIGATIONS OF DENSE WATER CASCADING ON A SLOPE - THE ROLE OF THE BOTTOM BOUNDARY LAYER

Jarle Berntsen[1], Guttorm Alendal[1], Helge Avlesen[2], and Øyvind Thiem[2]

[1] Department of Mathematics
University of Bergen
Allegaten 41, 5020 Bergen, Norway
e-mail: kontor@math.uib.no, web page: http://www.uib.no/math/

[2] Uni Research Computing
Nygårdsgaten 112-114, 5008 Bergen, Norway
e-mail: computing@uni.no, web page: http://http://uni.no/nb/uni-computing/

Key words: Gravity currents, Rotation, Bottom boundary layer

Abstract. The flow of dense water flowing along a continental slope is addressed. The study is based on a sequence of numerical investigations using the dynamics of overflow mixing and entrainment (DOME) setup. The model used in the present study is a terrain following ocean model facilitating a high resolution near the bottom that may be required to capture the Ekman transports correctly. The focus is on the sensitivity of the plume dynamics to the bottom boundary condition and on the sensitivity to the vertical grid size.

It is found that consistent results with a no-slip bottom boundary conditions and a quadratic drag law are obtained as long as the drag coefficient is computed appropriately. With a quadratic drag law, fewer layers in the vertical are needed, so this is the most cost efficient alternative. However, with a quadratic drag law and a constant value of the drag coefficient the Ekman transports inside the plume will not be captured.

1 INTRODUCTION

The flow of dense water from the marginal seas down the continental slopes and into the deep ocean is very important for the global circulation and such flows have been investigated in many scientific studies based on observations, laboratory investigations, numerical experiments and theory, see for instance [1, 2, 3, 4, 5, 6, 7, 8, 9] and references therein. The rotation of the earth affects the gravity flows, and dense water descending on a slope will lean towards the slope ([10]). In a rotating system, frictional Ekman

transports in the bottom boundary layer will be superimposed on the primary flow of the along slope dense plume ([11, 12, 13]).

The setup from DOME (Dynamics of Overflow Mixing and Entrainment http://www.rsmas.miami.edu/personal/tamay/DOME/dome.html) has been used in many studies of gravity flows along slopes using numerical ocean models, see [14, 15, 16, 17, 18, 19, 20, 21, 22]. In [22], there are two tables that give overviews of parameters used and model choices applied in the DOME tests.

In the numerical DOME studies, three choices of bottom boundary condition have been applied: i) no-slip, ii) quadratic bottom drag with a drag coefficient that is a function of the distance of the bottom most velocity point to the bottom, and iii) quadratic bottom drag with a constant drag coefficient. In addition, a range of vertical grids have been applied, but so far it has not been shown that vertical velocity profiles consistent with Ekman drainage have been reproduced. In the present study, a σ-coordinate ocean model is applied to investigate the sensitivity of the numerical results to vertical resolution and to the bottom boundary condition.

2 MODEL AND RESULTS

2.1 The numerical model and model setup

In this study, a σ-coordinate ocean model named the Bergen Ocean model (BOM) is applied ([23, 24, 25, 26]). A non-hydrostatic version of the BOM has been applied to investigate dense water flows on laboratory scale ([27]). In the present ocean scale studies, non-hydrostatic processes will not be resolved and the hydrostatic version from the [8] study is applied.

A horizontal view of the DOME computational domain is given in Fig. 1. The domain is 1100×700 km, the maximum depth is 3600 m, and a slope with slope steepness 0.01 connects the deep part to the coast where the depth becomes 600 m. From $x = 800$ km, there is a 100 km wide and 600 m deep channel. The dense plume water enters the domain through this embayment. The lateral boundaries to the east and to the west are open, and Neumann boundary conditions are applied to let the flow freely out of or into the computational domain through these boundaries.

The initial ambient stratification, $\rho(z)$, is linear and given by

$$\rho(z) = \rho_b - \frac{N^2 \rho_{ref} z}{g} \tag{1}$$

where $\rho_b = 1022$ kgm^{-3}, $\rho_{ref} = 1021$ kgm^{-3}, the buoyancy frequency $N = 2.3 \times 10^{-3}$ s^{-1}, the gravity $g = 9.81$ ms^{-2}, and z is the vertical distance from the deepest part (3600 m). Through the channel, there is an inflow of dense water, $\rho_{inflow} = \rho_b$, with flux $Q = 5$ Sv ($1\,\mathrm{Sv} = 10^6 \mathrm{m}^3\mathrm{s}^{-1}$). A passive tracer, τ, is introduced as in [17] and τ is initially set to 0 and $\tau = 1$ in the inflowing dense water.

The Coriolis parameter f is 1×10^{-4} s^{-1} and the height above the bottom of the interface of the inflowing water is tilted to achieve an approximate geostrophic balance.

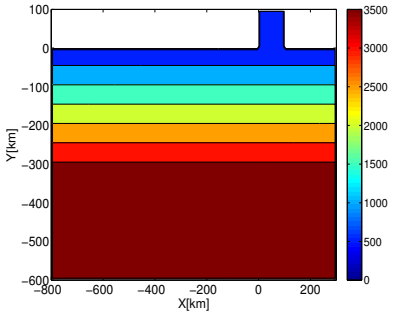

Figure 1: Horizontal view of the DOME computational domain.

The horizontal grid size is 10 km, and in order to investigate the sensitivity of the model outputs to vertical resolution, a sequence of vertical σ-grids, see Fig.2, is produced. For some grids with non-equidistant sigma layer thickness, $\Delta\sigma$, the resolution is finest near the bottom (approximately over the Ekman layer), then there is a layer with intermediate resolution above (covering approximately the body of the plume), and $\Delta\sigma$ is largest in the ambient above. The sigma layer thicknesses are smoothed in the transition zones. In addition, a range of smoothly graded vertical grids is produced using a modified version of the transformation given in [28] with high resolution near the bottom. Let the number of σ-layer interfaces be KB, $\Delta_\epsilon = 1/(KB-1)$, and let the thickness of the bottom most sigma layer be $\Delta\sigma_b$. The algorithm for computing the σ-values at the σ-layer interfaces is

for $K = 1, KB$

$$\epsilon = (K-1)/(KB-1)$$

$$\sigma(KB+1-K) = -1.0 + \epsilon - (\Delta_\epsilon - \Delta\sigma_b)\frac{\sin(\pi\epsilon)}{\sin(\pi\Delta_\epsilon)}$$

end for;

By using this procedure, $\sigma(KB) = -1.0$, $\sigma(KB-1) = -1.0 + \Delta\sigma_b$, $\sigma(1) = 0.0$, and $\sigma(2) \sim -2/(KB-1)$ so that the thickness of the uppermost layer is approximately twice the thickness obtained with an equidistant distribution, see the two plots in Fig.2. For the grids produced with this algorithm, the σ-layer thickness of the bottommost σ-layer is 0.0001 or 0.00002 and the thicknesses increase gradually upwards, see Fig.2b.

The horizontal diffusivity is 10 $\mathrm{m^2 s^{-1}}$ and the horizontal viscosity is 50 $\mathrm{m^2 s^{-1}}$. In addition, there will be numerical diffusivity and numerical viscosity associated with the use of a superbee limiter TVD-scheme for advection, see [29]. The Mellor-Yamada (M-Y) turbulence scheme ([30]) is often used in model studies with terrain following models, and it is also used in the present studies to compute vertical viscosity, ν_v, and vertical diffusivity, κ_v, with minimum values of both set to 2×10^{-5} $\mathrm{m^2 s^{-1}}$.

In order to investigate the sensitivity of the numerical results to the bottom bound-

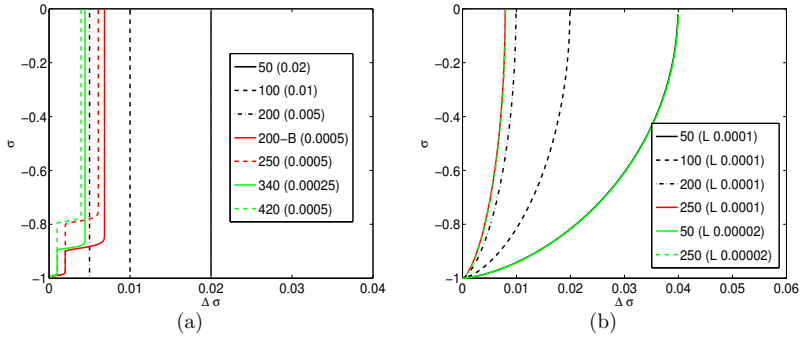

Figure 2: Sigma layer thickness ($\Delta\sigma$) as function of σ for the vertical discretizations considered. The number of sigma layers for each grid is given in the legend. The thicknesses of the bottom most sigma layers ($\Delta\sigma_b$) are also given in the legend. The sigma layer thicknesses for the grids based on the [28] distribution are given to the right and indicated with a L in the legend.

ary condition, the experiments are performed with three choices of bottom boundary condition.

The importance of using a no-slip bottom boundary condition is stressed in [31], and some experiments are performed with the no-slip condition used in the MITgcm, see mitgcm.org and [17],

$$\vec{\tau_b} = \left(2\frac{\nu_v}{\Delta z_b} + C_D|\vec{U_b}|\right)\vec{U_b} \tag{2}$$

where Δz_b is the thickness of the bottom most grid cell, C_D is a drag coefficient, and $\vec{U_b}$ is the velocity vector in the lowermost grid cell, which is a half-cell above the bottom in our staggered C-grid model.

Other experiments are performed with a quadratic drag law

$$\vec{\tau_b} = C_D|\vec{U_b}|\vec{U_b} \tag{3}$$

with C_D given by

$$C_D = \max[0.002, \frac{\kappa^2}{(\ln(z_b/z_0))^2}] \tag{4}$$

where z_b is the distance of the nearest grid point to the bottom. The von Karman constant $\kappa = 0.4$ and the bottom roughness parameter $z_0 = 0.01$ m. The drag coefficient tend to infinity as z_b tend to z_0 and approaches the background level (0.002 in this case) as z_b increases, see Fig. 3. For z_b in the range from 1 m to 75 m, typical for many such studies, C_D is in the range from 0.007 to 0.002.

In Table 1 in [22] there is a list of bottom drag coefficients and $C_D = 0.002$ is a commonly used value. We have also performed some experiments using this constant value rather than C_D computed from Eqn. (4).

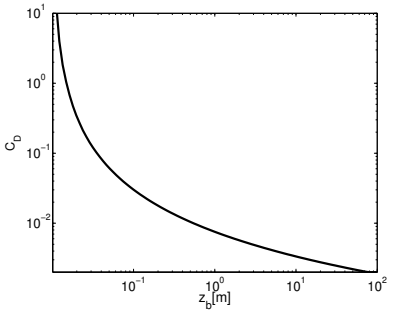

Figure 3: Values of $C_D = \frac{\kappa^2}{(\ln(z_b/z_0))^2}$ as function of z_b (The lower bound in Eqn. (4) is omitted).

The model is time-spilt, and the 3D time step is 180 s and there are 30 2D time steps per 3D step. Each experiment is run for 40 days.

2.2 Model results

Following [22], the *bottom tracer concentration* τ_{bottom} is computed as

$$\tau_{bottom}(x,y) = \frac{\int_{z_{bot}}^{z_{bot}+\Delta z_{plot}} \tau(x,y,z)dz}{\Delta z_{plot}} \tag{5}$$

where $z_{bot}(x,y)$ is the z-coordinate of the bottom, and Δz_{plot} is an averaging depth set to 60 m.

The vertical extent of the plume up to the level where τ becomes less or equal to 0.01, δ_p, is computed from

$$\delta_p(x,y) = \int_{\tau>0.01} dz \tag{6}$$

and called *plume thickness*.

To illustrate the pathway of the dense water plume, the bottom tracer concentrations and the plume thickness after 40 days are given in Fig. 4. These results are produced with a high vertical resolution and a quadratic drag law with C_D computed from Eqn. (4) and the results are in qualitative agreement with corresponding results given in [14, 16, 22] produced with the same horizontal resolution.

Integrated transports in the along slope and cross slope directions for a selection of vertical grids are given in Fig. 5. The results produced with a quadratic drag law are in

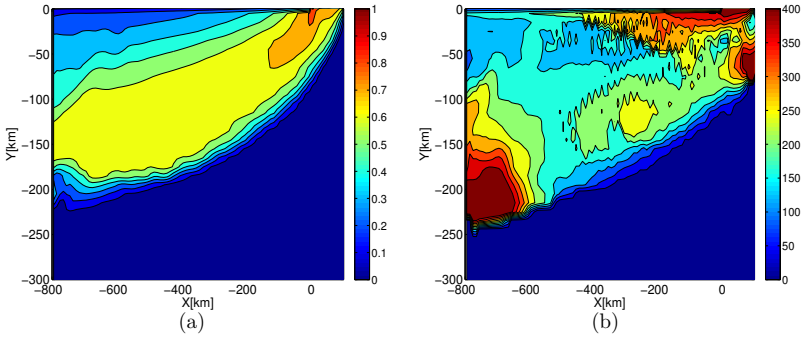

Figure 4: Bottom tracer concentration (to the left) and plume thickness (to the right) after 40 days. The tracer concentration is computed from Eqn. (5) and the plume thickness is computed from Eqn. (6). The results are based on results from the experiment with 250 σ-layers, see left panel of Fig. 2, and C_D computed from Eqn. (4).

general consistent, and even with 50 equidistant σ-layers main features of the plume are captured. Contrary to this, the results produced with a no-slip condition are very sensitive to the vertical grid. With 50 equidistant σ-layers, the plume front basically reaches only half way towards the open boundary after 40 days. The no-slip results become more consistent with the drag law results as the vertical resolution is refined, and it is the thickness of the bottom most cell, $\Delta\sigma_b$, that is the key factor. With a no-slip bottom boundary condition and a [28] σ-layer distribution with $\Delta\sigma_b = 0.00002$, the transports both in x- and y-directions become consistent with corresponding drag law results.

From the vertical profiles of tracer concentration, density, and across slope velocity components given in Fig. 6 it may also be seen that the results produced with a quadratic drag law are far more robust than the no-slip results. The no-slip results produced with a [28] σ-layer distribution and $\Delta\sigma_b = 0.00002$ are, however, consistent with the quadratic drag law results. The down slope maximum speeds are for instance approximately 30 cm s^{-1} in both sets of experiments.

The evidence from this exercise does not support the statements in [31] that a no-slip bottom boundary condition and a high resolution near the bottom are necessary when modeling dense water flow. However, one should bear in mind that this was based results from experiments with a quadratic drag law and a constant coefficient C_D. In [22] the use of constant values of C_D are indicated in their Table 1. Our results suggest that when applying C_D computed from Eqn. (4), which is also the standard procedure in the Princeton Ocean Model (POM) ([32]), the results with quadratic drag law becomes consistent with corresponding no-slip results. In order to investigate the sensitivity of the results to the choice of C_D, some experiments are repeated with $C_D = 0.002$ and the results

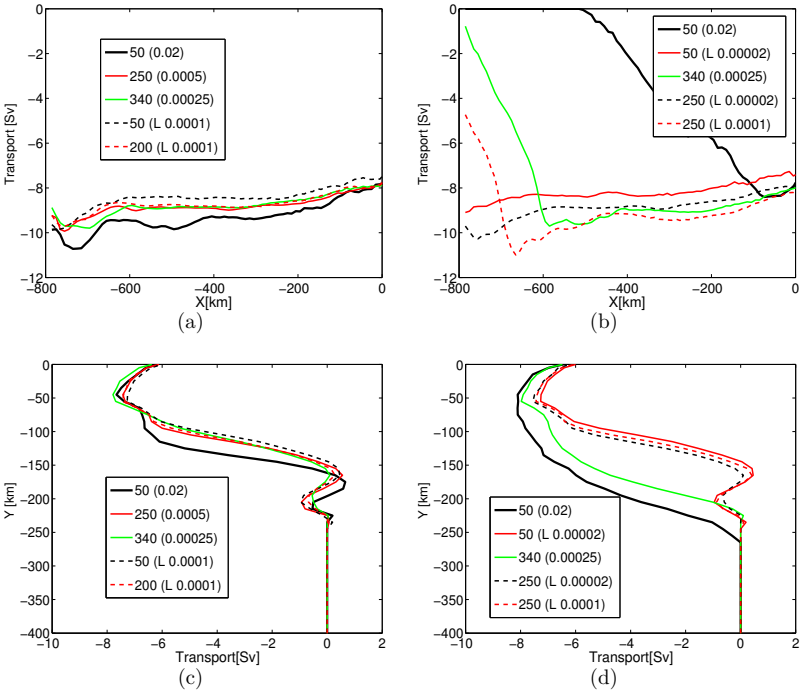

Figure 5: Plume transports after 40 days in the x-direction (top panel) and the y-direction (bottom panel) for a selection of vertical grids. In the legends, the number of σ-layers and the value of $\Delta\sigma_b$ are given, and L is used to indicate that a [28] type σ-layer distribution is used. The results produced with a quadratic drag law are given to the left, and the no-slip results are given to the right.

are compared to results produced with C_D produced from Eqn. (4) in Fig. 7. The along slope transport are relatively robust to the number of vertical layers and to the drag law, see Fig. 7a. However, one may notice that away from the inlet, the transports decrease when increasing the number of σ-layers for the constant C_D case. This tendency becomes more noticable for the across slope transports. When the vertical resolution increases and the bottom most velocity points move into the log-layer, the across slope transports are reduced and the plume becomes more attached to the coast. From Fig. 7c it may be noticed that in the experiment with 250 σ-layers and constant C_D the vertical tracer profile is very different from the corresponding profile obtained with the same vertical resolution and the Eqn. (4) drag law. The vertical profiles of across slope velocities given in Fig. 7d show that the Ekman veering that can be captured with the Eqn. (4) drag law or no-slip bottom boundary condition, will not be captured with a constant C_D drag.

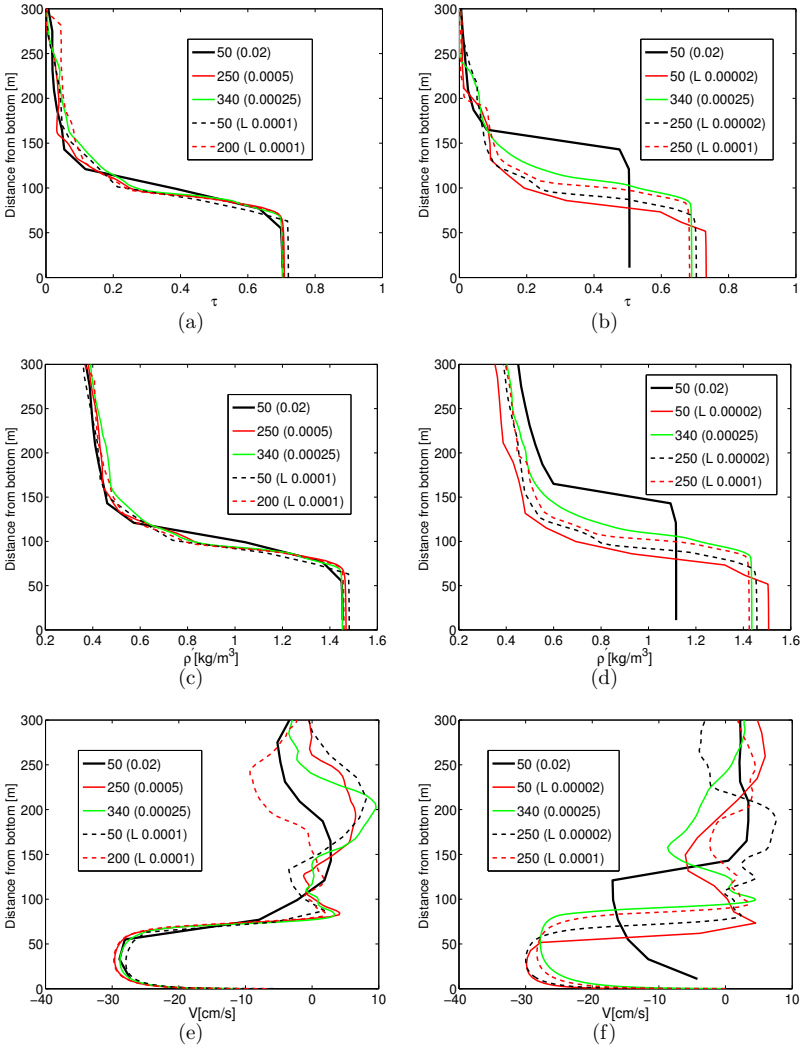

Figure 6: Vertical profiles after 40 days at $(x, y) = (-100\text{km}, -40\text{km})$ of tracer concentration (upper panel), $\rho' = \rho - 1020$ kg m^{-3} (second panel), and across slope velocity components (third panel). The results produced with a quadratic drag law are given to the left, and the no-slip results are given to the right.

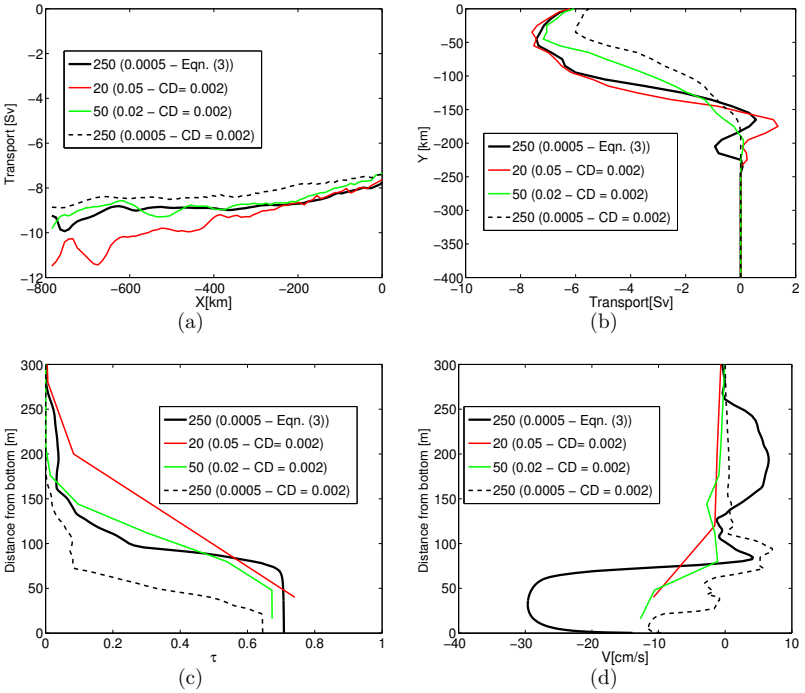

Figure 7: Numerical results after 40 days from the experiments with constant $C_D = 0.002$. The experiments with 20 and 50 σ-layers are performed with equidistant distribution of σ-layers and the experiment with 250 layers is performed with the distribution given in Fig. 2. Corresponding results produced with the Eqn. (4) drag law and 250 layers are also given. Plume transports in the x-direction are given in the upper left panel and transport in the y-direction are given in the upper right panel. Vertical profiles of tracer concentration are given in the lower left panel and vertical profiles of the across slope velocities are given in the lower right panel. The profiles are taken at $(x, y) = (-100\text{km}, -40\text{km})$.

3 DISCUSSION

We have investigated the sensitivity of the DOME results to three different bottom boundary conditions:
i) no-slip,
ii) quadratic drag law with C_D computed from Eqn. (4), and
iii) quadratic drag law with constant C_D.
A range of vertical grids are used to explore the sensitivity to the vertical grid size. The experiments are done with an inflow rate of 5Sv.

It is found that consistent results with bottom boundary conditions i), and ii) may be

obtained given enough resolution. With ii), fewer layers in the vertical are needed, so this is the most cost efficient alternative. With iii), one may balance the number of layers so that overall transports seem reasonable, but the Ekman transports inside the plume will not be captured, so this is not a robust way of representing dense water flows.

The thickness of the Ekman layer is a few tens of meters and the plume thickness is of the order 100 meter. The present results suggest that by using a quadratic drag law with C_D computed from Eqn. (4), and approximately 10 σ-layers over the bottom most 100 m, the near sea bed processes become adequately resolved. By using a transformation such as the one suggested in [28], a distribution of σ-layers that cost efficiently resolves the Ekman transports is obtained.

Many large scale oceanic studies are performed with z-coordinate ocean models using quadratic drag laws with constant drag coefficients and poor resolution of the Ekman layer. The present results suggest that the downward Ekman transports of the densest fluid parcels in dense water plumes will not be captured in such investigations.

REFERENCES

[1] Britter, R. and Linden, P. The motion of the front of a gravity current travelling down an incline. *Journal of Fluid Mechanics* (1980) **99**:531–543.

[2] Borenäs, K. and Lundberg, P. On the deep water flow through the Faroe-Bank Channel. *Journal of Geophysical Research* (1988) **93**:1281–1292.

[3] Simpson, J. *Gravity Currents: In the Environment and the Laboratory*. Cambridge University Press, (1997).

[4] Ivanov, V., Shapiro, G., Huthnance, J., Aleynik, D., and Golovin, P. Cascades of dense water around the world ocean. *Progress in Oceanography* (2004) **60**:47–98.

[5] Davies, P., Wåhlin, A., and Guo, Y. Laboratory and analytical model studies of the Faroe Bank Channel deep-water outflow. *Journal of Physical Oceanography* (2006) **36**:1348–1364.

[6] Ezer, T. Topographic influence on overflow dynamics: Idealized numerical simulations and the Faroe Bank Channel overflow. *Journal of Geophysical Research* (2006) **111**: C02002, doi:10.1029/2005JC3195.

[7] Riemenschneider, U. and Legg, S. Regional simulations of the Faroe Bank Channel overflow in a level model. *Ocean Modelling* (2007) **17**:93–122.

[8] Seim, K., Fer, I., and Berntsen, J. Regional simulations of the Faroe Bank Channel overflow using a σ-coordinate ocean model. *Ocean Modelling* (2010) **35**:31–44.

[9] Cuthbertson, A., Davies, P., Stashchuk, N., and Vlasenko, V. Model studies of dense water overflows in the Faroese Channels. *Ocean Dynamics* (2014) **64**:273–292.

[10] Cenedese, C. and Adduce, C. A New Parameterization for Entrainment in Overflows. *Journal of Physical Oceanography* (2010) **40**:1835–1850.

[11] Johnson, G. and Sanford, T. Secondary Circulation in the Faroe Bank Channel Outflow. *Journal of Physcical Oceanography* (1992) **22**:927–933.

[12] Umlauf, L., Arneborg, L., Hofmeister, R., and Burchard, H. Entrainment in Shallow Rotating Gravity Currents: A Modeling Study. *Journal of Physical Oceanography* (2010) **40**:1819–1834.

[13] Seim, K. and Fer, I. Mixing in the stratified interface of the Faroe Bank Channel overflow: The role of transverse circulation and internal waves. *Journal of Geophysical Research* (2011) **116**: C07022, doi:10.1029/2010JC006805.

[14] Ezer, T. and Mellor, G. A generalized coordinate ocean model and a comparison of the bottom boundary layer dynamics in terrain-following and in z-level grids. *Ocean Modelling* (2004) **6**:379–403.

[15] Özgökmen, T., Fischer, P., Duan, J., and Iliescu, T. Three-Dimensional Turbulent Bottom Density Currents from a High-Order Nonhydrostatic Spectral Element Model. *Journal of Physical Oceanography* (2004) **34**:2006–2026.

[16] Ezer, T. Entrainment, diapycnal mixing and transport in three-dimensional bottom gravity current simulations using the Mellor-Yamada turbulence scheme. *Ocean Modelling* (2005) **9**:151–168.

[17] Legg, S., Hallberg, R., and Girton, J. Comparison of entrainment in overflows simulated by z-ccordinate, isopycnal and non-hydrostatic models. *Ocean Modelling* (2006) **11**:69–97.

[18] Tseng, Y.-H. and Dietrich, D. Entrainment and Transport in Idealized Three-Dimensional Gravity Current Simulation. *Journal of Atmospheric and Oceanic Technology* (2006) **23**:1249–1269.

[19] Legg, S., Jackson, L., and Hallberg, R. Eddy-Resolving Modeling of Overflows. *In Hecht, M. and Hasumi, H., editors, Ocean Modeling in an Eddying Regime* (2008) pages 63–81. AGU-Geophysical Monograph 177.

[20] Wang, Q., Danilov, S., and Schröter, J. Comparison of overflow simulations on different vertical grids using the Finite Element Ocean circulation Model. *Ocean Modelling* (2008) **30**:313–335.

[21] Bates, M., Griffies, S., and England, M. A dynamic, embedded Lagrangian model for ocean climate models, Part II: Idealised overflow tests. *Ocean modelling* (2012) **59-60**:60–76.

[22] Reckinger, S., Petersen, M., and Reckinger, S. A study of overflow simulations using MPAS-Ocean: Vertical grids, resolution, and viscosity. *Ocean Modelling* (2015) **96**:291–313.

[23] Berntsen, J., Xing, J., and Alendal, G. Assessment of non-hydrostatic ocean models using laboratory scale problems. *Continental Shelf Research* (2006) **26**:1433–1447.

[24] Berntsen, J. and Oey, L.-Y. Estimation of the internal pressure gradients in σ-coordinate ocean models: comparison of second, fourth, and sixth order schemes. *Ocean Dynamics* (2010) **60**:317–330.

[25] Berntsen, J. A perfectly balanced method for estimating the internal pressure gradients in σ-coordinate ocean models. *Ocean Modelling* (2011) **38**:85–95.

[26] Berntsen, J., Thiem, Ø., and Avlesen, H. Internal pressure gradient errors in sigma-coordinate ocean models in high resolution fjord studies. *Ocean Modelling* (2015) **92**:42–55.

[27] Berntsen, J., Darelius, E., and Avlesen, H. Gravity currents down canyons: Effects of rotation. *Ocean Dynamics* (2016) **66**:1353–1378.

[28] Lynch, D., Ip, J., Naimie, C., and Werner, F. Convergence studies of tidally-rectified circulation on Georges Bank. *In Lynch, D. and Davies, A., editors, Quantitative Skill Assessment for Coastal Ocean Models.* (1995) American Geophysical Union.

[29] Yang, H. and Przekwas, A. A comparative study of advanced shock-capturing schemes applied to Burgers equation. *Journal of Computational Physics* (1992) **102**:139–159.

[30] Mellor, G. and Yamada, T. Development of a turbulence closure model for geophysical fluid problems. *Reviews of Geophysics and Space Physics* (1982) **20**:851–875.

[31] Wobus, F., Shapiro, G., Maquead, M., and Huthnance, J. *Numerical simulations of dense water cascading on a steep slope. Journal of Marine Research* (2011) **69**:391–415.

[32] Blumberg, A. and Mellor, G. A description of a three-dimensional coastal ocean circulation model. (1987) *In Heaps, N., editor, Three-Dimensional Coastal Ocean Models, Volume 4 of Coastal and Estuarine Series*, pages 1–16. American Geophysical Union.

9. National Conference on Computational Mechanics
MekIT'17
B. Skallerud and H I Andersson (Eds)

COMPLEX GEOMETRY HANDLING FOR A CARTESIAN GRID BASED CFD SOLVER

HANS BIHS[1], ARUN KAMATH[1], MAYILVAHANAN ALAGAN CHELLA[1] and CASABA PAKOZDI [2]

[1]Department of Civil and Transport Engineering
NTNU Trondheim
Høgskoleringen 7A, 7491 Trondheim, Norway
e-mail: hans.bihs@ntnu.no web page: http://www.reef3d.com/

[2]Department of Ocean Engineering
SINTEF Ocean

Key words: CFD, Immersed Boundary, Ray-Casting, Level Set Method, REEF3D

Abstract. Complex geometries can be a challenge for computational fluid dynamics (CFD) solvers that use a Cartesian mesh. In the current paper, an algorithm is described with which complex geometry features can be incorporated in a ghost cell immersed boundary method through a simple and straightforward algorithm. The complex geometries are handled with a trivial triangular surface mesh in the widely used STL format. Grid generation is than achieved with an optimized ray-tracing algorithm, which determines solid and fluid cells, as well as the closest distances from the solid boundaries to the neighboring fluid cells. As the numerical model uses a Cartesian mesh, the presence of irregular solid boundaries is handled by immersing them through ghost cell extrapolation into the fluid domain. The capabilities of the presented method are shown through two real-world examples: wave hydrodynamics around an offshore wind turbine jacket substructure and supercritical flow over the spillways of a hydropower plant.

The numerical model used in this study is REEF3D, an open-source three-dimensional CFD code. It employs the level set method for the representation of the free surface. This approach is capable of handling complex air-water interface topologies. The Reynolds-Averaged Navier-Stokes (RANS) equations are discretized with the fifth-order accurate Weighted Essentially Non-Oscillatory (WENO) scheme in space and with a third-order Runge-Kutta based fractional step scheme in time. For the pressure, the projection method is used on a staggered grid configuration, assuring tight pressure-velocity coupling. The model solves for the pressure Poisson equation using a conjugated gradient solver, which is preconditioned with a geometric multigrid algorithm. Turbulence closure is achieved through the k-ω model. The fully parallelized model uses the domain decomposition approach, making it possible to execute the code on the local supercomputer facilities.

1 INTRODUCTION

For computational fluid dynamics (CFD) solvers, the usage of a Cartesian mesh has many advantages over unstructured body-fitted meshes. The algorithms for the discretization of the governing equations can be implemented in a more straightforward manner, complicated coordinate transformations are not necessary. In addition, the data structures can use a simple structured format. For high-order finite volume or finite differences discretization, large stencils are required. In case of the fifth-order accurate Weighted Essentially Non-Oscillatory (WENO) scheme [14] seven point stencils are needed for each coordinate direction which is handled easier and much faster in the structured Cartesian grid system. The CFD solver presented in the current paper is used mainly for complex free surface flows, which are represented as two-phase flow and modeled with an interface capturing method. At the interface between water and air, a large jump in the matrix coefficients of the Poisson equation occurs due to the density difference. As a consequence, tight pressure-velocity coupling is a priority. The most efficient and robust way of achieving this, is a staggered variable arrangement. With a Cartesian grid, staggering is relatively easy accomplished. For unstructured grids, staggering is quite challenging as coordinate transformations for four different variables have to be performed. As a result, most unstructured grid finite volume CFD codes are implemented as colocated solvers, e.g. OpenFOAM [26]. While unstructured grids can be used to conform to irregularly shaped solid bodies, the mesh quality has a tendency to deteriorate for increasing geometric complexities as well as for moving solid bodies.

The challenge with Cartesian mesh based solvers is the inclusion of complex flow domain boundaries. A lot of attention has been paid to this problem, leading to a range of different immersed boundary methods [20], such as direct forcing [12] or ghost cell immersed boundary methods [24]. Here, a major pre-processing step is assigning solid and fluid cells as well as determining the closest distance from the immersed boundary to the neighboring fluid cells. In [27] a ray-casting algorithm is proposed for inside/outside and closest distance calculation.

In the present manuscript the open-source CFD code REEF3D is employed [8]. The model has been used extensively for complex wave hydrodynamics problems in the field of coastal and ocean engineering [1] [16] [15]. The complex fluid-structure interface is modeled with the ghost cell immersed boundary method [5]. From triangular surface meshes, ray-casting algorithms are used [11] to get inside-outside information in addition to the closest distances to the solid. Compared to [27], a modified and slightly more optimized version of the ray-casting algorithm is implemented. Instead of using two different algorithms for inside/outside and closest distance information, the current implementation calculates both in the same step. In addition, the closest distance field is converted to a signed distance function so that the solid boundary can be represented by a level set function [18]. This streamlines the further data handling inside the CFD solver.

2 NUMERICAL MODEL

In this part, a brief description of the underlying flow solver REEF3D is given, which is used for the examples in the present paper. Further information can be found in [8] [7]. The governing equations of the numerical model are the continuity and the incompressible Reynolds-averaged Navier-Stokes (RANS) equations:

$$\frac{\partial U_i}{\partial x_i} = 0 \tag{1}$$

$$\frac{\partial U_i}{\partial t} + U_j \frac{\partial U_i}{\partial x_j} = -\frac{1}{\rho}\frac{\partial P}{\partial x_i} + \frac{\partial}{\partial x_j}\left[(\nu + \nu_t)\left(\frac{\partial U_i}{\partial x_j} + \frac{\partial U_j}{\partial x_i}\right)\right] + g_i \tag{2}$$

where U is the velocity averaged over time t, ρ is the fluid density, P is the pressure, ν is the kinematic viscosity, ν_t is the eddy viscosity and g the gravity term. The convective terms of the RANS equations are discretized with the fifth-order WENO (weighted essentially non-oscillatory) scheme by Jiang and Shu [14] in the conservative finite-difference framework. The conservative WENO scheme is used to treat the convective terms for the velocities U_i, while the Jacobi-Hamilton version is used for the variables of the free surface and turbulence algorithms. For the time treatment a third-order accurate TVD Runge-Kutta scheme is employed, consisting of three Euler steps [22]:

$$\begin{aligned}
\phi^{(1)} &= \phi^n + \Delta t L\left(\phi^n\right) \\
\phi^{(2)} &= \frac{3}{4}\phi^n + \frac{1}{4}\phi^{(1)} + \frac{1}{4}\Delta t L\left(\phi^{(1)}\right) \\
\phi^{n+1} &= \frac{1}{3}\phi^n + \frac{2}{3}\phi^{(2)} + \frac{2}{3}\Delta t L\left(\phi^{(2)}\right)
\end{aligned} \tag{3}$$

Adaptive time stepping is used in order to control the CFL number.

Chorin's projection method for incompressible flow is used for the treatment of the pressure [10]. During the solution of the RANS-equations at each Euler step of the Runge-Kutta time stepping procedure, the pressure gradient is excluded. Based on the resulting divergence of the flow, a Poisson equation for the pressure is formed with the right hand side containing the continuity defect (Eq. 4). The Poisson equation is solved using high-perfomance solver library HYPRE [9] with fully parallelized BiCGStab [25] preconditioned by a geometry multigrid solver [3]. The gradient of the new pressure field is then used to correct the velocity field, making it divergence free.

$$-\frac{\partial}{\partial x_i}\left(\frac{1}{\rho\left(\phi^n\right)}\frac{\partial P}{\partial x_i}\right) = -\frac{1}{\Delta t}\frac{\partial U_i^*}{\partial x_i} \tag{4}$$

The location of the free water surface is represented implicitly by the zero level set of the smooth signed distance function $\phi(\vec{x}, t)$. The level set function gives the closest

distance to the interface and the two phases are distinguished by the change of the sign. This results in the following properties:

$$\phi(\vec{x},t)\begin{cases} > 0 \; if \; \vec{x} \in phase \; 1 \\ = 0 \; if \; \vec{x} \in \Gamma \\ < 0 \; if \; \vec{x} \in phase \; 2 \end{cases} \tag{5}$$

In addition, the Eikonal equation $|\nabla\phi| = 1$ is valid. When the interface Γ is moved under an externally generated velocity field $\vec{v}$, a convection equation for the level set function is obtained:

$$\frac{\partial\phi}{\partial t} + U_j\frac{\partial\phi}{\partial x_j} = 0 \tag{6}$$

When the interface evolves, the level set function loses its signed distance property. In order to maintain this property and to ensure mass conservation, the level set function is initialized after each time tep. In the present paper a PDE based reinitialization equation is solved [23]:

$$\frac{\partial\phi}{\partial t} + S\left(\phi\right)\left(\left|\frac{\partial\phi}{\partial x_j}\right| - 1\right) = 0 \tag{7}$$

$S\left(\phi\right)$ is the smoothed sign function [19]. With the level set function in place, the material properties of the two phases can be defined for the whole domain. In an area of $1.6\Delta x$ in each direction of the interface, the density ρ and the viscosity ν are smoothed out with a regularized Heaviside function.

3 RAY-CASTING ALGORITHM

For many CFD simulations, complex solid geometries are encountered when meshing the fluid domain. Often, the solid geometries are described with triangular surface meshes, predominantly in the STL (STereo Lithrography) file format. An STL file describes the surface geometry of a three-dimensional body through non-connected triangles and can be either in ASCII or binary format. The current implementation reads ASCII format, as binary STL files can be easily converted with available software such as Paraview [4]. Also, it is expected that the surface mesh is fully intact without any holes or gaps. Different software solutions are available to repair such files. The numerical model REEF3D solves all equations on a staggered Cartesian grid. Non-grid conforming geometries are taken into account through a ghost cell immersed boundary with local-directional extrapolation [5]. In order to go from the triangular surface mesh to an immersed boundary representation on a Cartesian mesh the following information is crucial:

- inside/outside information for all cells
- closest distance from boundary to neighboring fluid cell

The point-in-polygon test [17] is used to determine whether a cell is inside the fluid or inside the solid. When a point is located inside a polygon, any arbitrarily oriented line through this point will intersect with the surrounding polygon. The point-in-polygon test is based on the observation that the number of intersections with the polygon is uneven on either side of the point when it is located inside the polygon (see Fig. 1). When a point lies outside the Polygon, the number of intersections with the polygon is even on either side of the point (see Fig. 2).

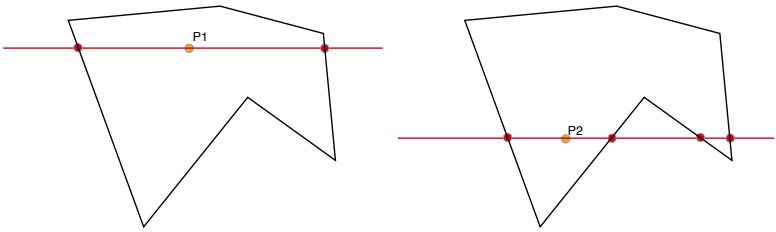

(a) P1 (b) P2

Figure 1: Point in polygon test: P1 and P2 inside the polygon.

In REEF3D the test is implemented as follows: Rays are cast along the x-axis coordinate axis (see Fig. 3). For the given Cartesian mesh those rays or lines coincide with the location of the center of the cells. In the resulting yz-plane, rays are cast only along those cells which are occupied by triangles. The intersection of the line with the triangle is calculated with Algorithm 5.3.4 "Intersecting Line Against Triangle" from [11].

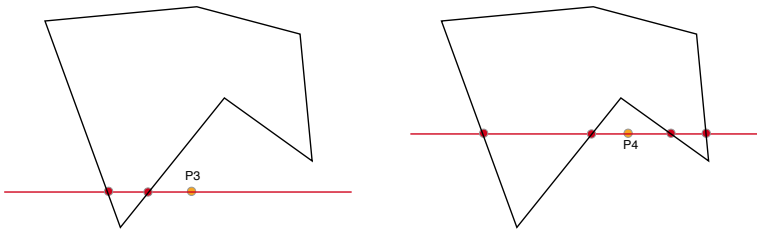

(a) P1 (b) P2

Figure 2: Point in polygon test: P1 and P2 outside the polygon.

For each triangle, intersections of the rays are registered in two different three-dimensional arrays spanning the complete Cartesian mesh. Those arrays register the numbers of "left" and "right" intersections. For an intersection location in cell $i_{intersection}$, for all cells at

the (j, k) position of the ray and i indices smaller than $i_{intersection}$ the "left" array is incremented by one, while the "right' array is incremented along the ray for i indices larger than $i_{intersection}$. After rays have been cast for all triangles, the arrays for "left" and "right" intersections should contain uneven numbers for cells located inside triangular surface mesh and even numbers for those outside. This algorithm is very efficient, as the three-dimensional problem is projected into the 2D space of the yz-plane.

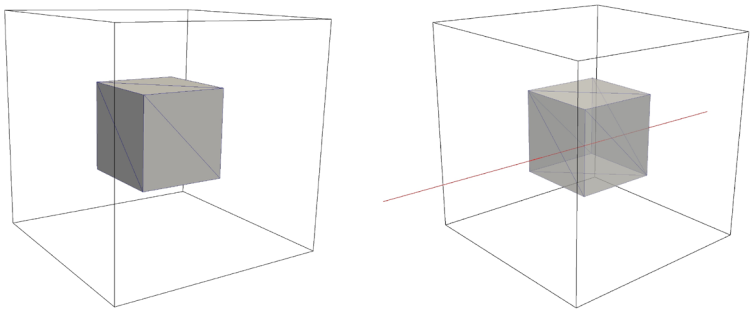

(a) triangular surface mesh (b) Casting of a single ray

Figure 3: Ray-casting for a rectangular box with triangular surface mesh.

The intersection location from the above described algorithm is used to calculate the closest distance from the neighboring cells to the solid boundary. In order to get the closest distances in all three coordinate directions, the ray-casting algorithm is now also performed in y- and z- direction. As a result, the complete algorithm consists of three 2D operations. The ghost cell immersed boundary method used in REEF3D decomposes the ghost cell extrapolation into the three coordinate directions of the mesh [5]. This presents a significant improvement in flexibility and robustness over the original ghost cell immersed boundary method presented by [24], as it resolves sharp corners directly. The closest distance is then converted into a signed distance function. The distance values inside the solid are given a negative sign and in the fluid a positive sign. As an initialisation step before the fluid simulation, the signed distance function is reinitialized with the PDE based scheme by [23] as given in Eq. 7. In contrast to the level set function for the water-air interface, the interface values are not updated. Thus, the signed distance values from the ray-casting are intact also after reinitialization, maintaining the correct closest distance information.

4 EXAMPLES

4.1 Rectangular Box

The first example is a simple rectangular box measuring 0.4 m x 0.4 m x 0.4 m. The box is located in the center of a Cartesian mesh with the lengths 1.0 m x 1.0 m x 1.0 m. The triangular surface mesh (see Fig. 3) has been generated by REEF3D's mesh generation tool DIVEMesh [6]. From this geometric description inside-outside, closest distance and eventually the level set function for the solid box have been generated.

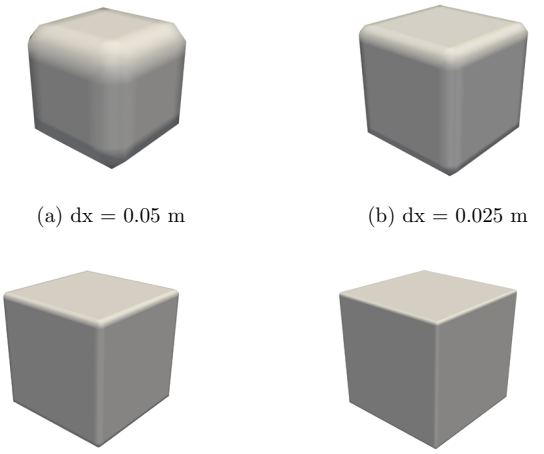

(a) dx = 0.05 m (b) dx = 0.025 m

(c) dx = 0.01 m (d) dx = 0.005 m

Figure 4: Level set representation of the rectangular box for different mesh widths. The zero level set contour is shown. Higher mesh resolutions result in a sharper representation of the edges.

The result for the level set function can be seen in Fig. 4. For dx = 0.05 m, the level set representation of the box has clearly experienced strong smoothing at the edges. With increasingly finer grids, the edge of the level set function becomes shaper. While some smoothing of the level set function appears to be present for all presented mesh widths, it should be kept in mind that the signed distance values closest to the solid surface are unchanged from the ray-casting algorithm for all grid sizes. Fig. 5 shows the merging of two boxes with the lengths 0.4 m x 0.4 m x 0.4 m on the same Cartesian mesh for dx = 0.005 m. The ray casting is performed for each individual box separately, while the inside/outside and closest distance information is carried over from one box to the other. Thus, complicated structures can be build up from using several simple geometric

entities.

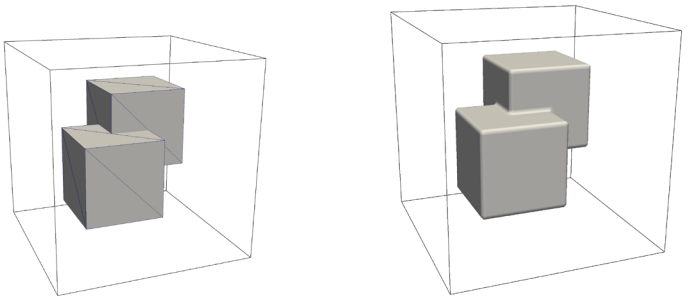

(a) Wedge with mesh and level set function

(b) Signed distance field with the zero level set for the fluid-solid interface

Figure 5: Representation of the solid body with a level set function.

4.2 Offshore Wind Substructure

An example for a complex structure made up of many simple pieces is an offshore wind substructure. The presented geometry is from the WAVESLAM project, a Hydralab IV project jointly headed by the University of Stavanger and NTNU Trondheim [2]. The geometry is a 1:8 scale model which was used for extensive wave impact experiments in the Large Wave Flume (GWK) in Hannover. The jacket is 4 m high and 2.4 m x 2.4 m wide with a tube thickness of 0.14 m. The Cartesian uses a mesh width dx = 0.025m. Again, the triangular surface mesh for the solid structure is generated within DIVEMesh. In Fig. 6, the triangular surface mesh is shown on the left and the level set representation on the right hand side. The level set representation looks very similar to the original geometry, indicating that the details of the complex structure are well captured.. The flow domain is 15 m long, 5 m wide and 4.5 m high, resulting in a mesh with ca. 21 million cells. The waves are generated with a Dirichlet boundary condition at the inlet, where velocities and free surface location are prescribed. At the outlet, wave reflections are avoided with active wave absorption [21].

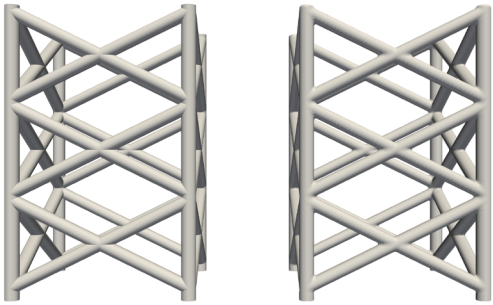

Figure 6: Offshore wind substructure with triangular surface mesh (left) and level set representation (right).

With this setup of the numerical wave tank, the tank domain can be kept relatively short. In fact, the tank is shorter than the generated regular waves, which are of height H = 1.2 m and length L = 20.0m with a still water depth of d = 2.5m. The non-breaking wave impacting the jacket is shown in Fig. 7. It can be seen that the free surface topography at this simulation time instance features a complicated pattern due to the complex flow obstacle that the jacket presents.

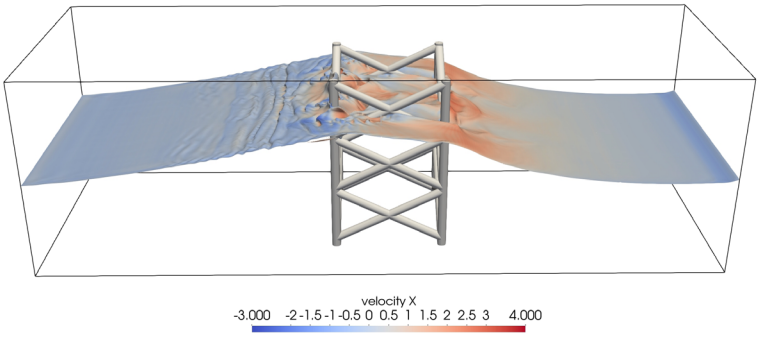

Figure 7: Wave hydrodynamics around offshore wind substructure.

4.3 Hydropower Plant

The Sarpfossen hydropower plant was tested in the hydraulic laboratory at NTNU Trondheim where a 1:45 scale model was built [13]. The capacity of the spillways were

tested for the maximum probable flood. A focus was on the reduced cross section area just upstream of the spillways due to a railroad bridge. The selected discharge for the current simulations is Q = 0.25 m^3/s, corresponding to Q = 3396 m^3/s in full scale. The location of the spillways including the railroad bridge positioned further upstream can be seen in Fig. 8 a) and b).

In contrast to previous cases, here the STL encloses the fluid domain and not the solid. This is easily taken into account by multiplying the solid level set function by -1, effectively reversing the fluid-solid description. Fig. 9 a) shows the simulation results with REEF3D. The solid is represented by the level set function, which captures the details of the complex spillways geometry. The flow domain is 3.8 long in flow direction, 2.4 m wide and 0.8m high. A mesh size of dx = 0.01 m is used for the current CFD calculations, resulting in a total of 7.3 million cells out of which 3.97 million are active fluid cells. The flow solver captures the free surface flow with great detail. Shock waves can be observed around the vertical obstacles in between the spillways. Over the spillways, the flow becomes supercritical which is also indicated through the much increased flow velocity magnitudes.

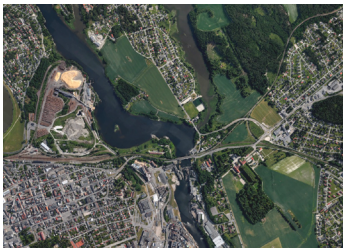

(a) Aerial View, Data: Google 2016

(b) 3D View, Data: Google 2016

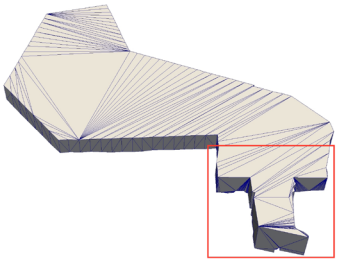

(c) Complete STL file, red box shows simulation domain

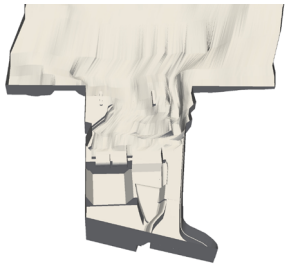

(d) STL file of flow domain with the top boundary removed

Figure 8: Sarpfossen hydropower plant.

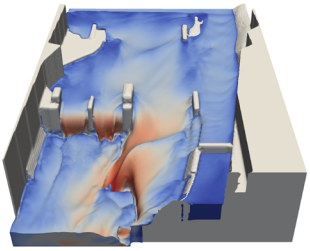

(a) Simulation with REEF3D and solid representation through level set function

(b) Hydraulic laboratory experiment at NTNU Trondheim

Figure 9: Sarpfossen hydropower plant results.

5 CONCLUSIONS

In this paper an innovative method for describing complex solid geometries on a Cartesian mesh with immersed boundaries is presented. The solid body geometries are given through triangular surface meshes. With a ray-casting algorithm, it can be determined from the surface mesh whether cells lie within the fluid or the solid. In addition, the closest distance from the solid to the neighboring fluid cells can be accurately calculated. The distance information is then converted into a level set function, which gives the signed distance from the solid boundary. While the level set function needs to be reinitialized, which could lead to potential smoothing of the function, the interface values are not updated and thus the closest distance values used by the immersed boundary are kept intact. The method was tested for different cases with varying levels of complexity. For the rectangular box, the offshore wind substructure and the hydropower plant, the mesh of the flow domain including the information necessary for the ghost cell immersed boundary were easily generated. The CFD model's capabilities together with the ray-casting algorithm show great potential for ever more complex flow simulations.

ACKNOWLEDGEMENTS

The authors would like to thank Dr. Robert Feurich for providing the geometry of the Sarpfossen hydropower plant.

References

[1] Alagan Chella, M., Bihs, H., Myrhaug, D., and Muskulus, M. (2016). "Hydrodynamic characteristics and geometric properties of plunging and spilling breakers over impermeable slopes." *Ocean Modeling*, 103, 53–72.

[2] Arntsen, Ø. A., Ros, X., and Tørum, A. (2011). "Impact forces on a vertical pile

from plunging breaking waves." *Proceedings of the International Conference Coastal Structures 2011, Yokohama, Japan*, 533–544.

[3] Ashby, S. F. and Flagout, R. D. (1996). "A parallel mulitgrid preconditioned conjugate gradient algorithm for groundwater flow simulations." *Nuclear Science and Engineering*, 124(1), 145–159.

[4] Ayachit, U. (2015). *The ParaView Guide: A Parallel Visualization Application*. Kitware.

[5] Berthelsen, P. A. and Faltinsen, O. M. (2008). "A local directional ghost cell approach for incompressible viscous flow problems with irregular boundaries." *Journal of Computational Physics*, 227, 4354–4397.

[6] Bihs, H. (2017). *DIVEMesh :: User's Guide*. Department of Civil and Environmental Engineering, NTNU Trondheim.

[7] Bihs, H. and Kamath, A. (2017). "Simulation of floating bodies with a combined level set/ghost cell immersed boundary representation." *International Journal for Numerical Methods in Fluids*, 83(12), 905–916.

[8] Bihs, H., Kamath, A., Alagan Chella, M., Aggarwal, A., and Arntsen, Ø. A. (2016). "A new level set numerical wave tank with improved density interpolation for complex wave hydrodynamics." *Computers & Fluids*, 140, 191–208.

[9] Center for Applied Scientific Computing, Lawrence Livermore National Laboratory (2015). *hyper high performance preconditioners - User's Manual*.

[10] Chorin, A. (1968). "Numerical solution of the Navier-Stokes equations." *Mathematics of Computation*, 22, 745–762.

[11] Ericson, C. (2005). *Real-Time Collsion Detection*. Morgen Kaufmann, San Francisco.

[12] Fadlun, E. A., Verzicco, R., Orlandi, P., and Mohd-Yusolf, J. (2000). "Combined immersed-boundary finite-difference methods for three-dimensional complex flow simulations." *Journal of Computational Physics*, 161, 35–60.

[13] Feurich, R. and Olsen, N. R. B. (2012). "Finding free surface of supercritical flows - numerical investigation." *Engineering Applications of Computational Fluid Mechanics*, 6(2), 307–315.

[14] Jiang, G. S. and Shu, C. W. (1996). "Efficient implementation of weighted ENO schemes." *Journal of Computational Physics*, 126, 202–228.

[15] Kamath, A., Alagan Chella, M., Bihs, H., and Arntsen, Ø. A. (2016a). "Breaking wave interaction with a vertical cylinder and the effect of breaker location." *Ocean Engineering*, 128, 105–115.

[16] Kamath, A., Bihs, H., Alagan Chella, M., and Arntsen, Ø. A. (2016b). "Upstream-cylinder and downstream-cylinder influence on the hydrodynamics of a four-cylinder group." *Journal of Waterway, Port, Coastal, and Ocean Engineering*.

[17] O'Rourke, J. (1998). *Computational Geometry in C*. Cambridge University Press.

[18] Osher, S. and Sethian, J. A. (1988). "Fronts propagating with curvature- dependent speed: algorithms based on Hamilton-Jacobi formulations." *Journal of Computational Physics*, 79, 12–49.

[19] Peng, D., Merriman, B., Osher, S., Zhao, H., and Kang, M. (1999). "A PDE-based fast local level set method." *Journal of Computational Physics*, 155, 410–438.

[20] Peskin, C. S. (1972). "Flow patterns around the heart valves." *Journal of Computational Physics*, 10, 252–271.

[21] Schäffer, H. A. and Klopman, G. (2000). "Review of multidirectional active wave absorption methods." *Journal of Waterway, Port, Coastal, and Ocean Engineering*, 126(2), 88–97.

[22] Shu, C. W. and Osher, S. (1988). "Efficient implementation of essentially non-oscillatory shock capturing schemes." *Journal of Computational Physics*, 77, 439–471.

[23] Sussman, M., Smereka, P., and Osher, S. (1994). "A level set approach for computing solutions to incompressible two-phase flow." *Journal of Computational Physics*, 114, 146–159.

[24] Tseng, Y. H. and Ferziger, J. H. (2003). "A ghost-cell immersed boundary method for flow in complex geometry." *Journal of Computational Physics*, 192, 593–623.

[25] van der Vorst, H. (1992). "BiCGStab: A fast and smoothly converging variant of Bi-CG for the solution of nonsymmetric linear systems." *SIAM Journal on Scientific and Statistical Computing*, 13, 631–644.

[26] Weller, H. G., Tabor, G., Jasak, H., and Fureby, C. (1998). "A tensorial approach to computational continuum mechanics using object-oriented techniques." *Computers in Physics*, 12(6), 620–631.

[27] Yang, J. and Stern, F. (2013). "Robust and efficient setup procedure for complex triangulations in immersed boundary simulations." *Journal of Fluids Engineering*, 135, 101107–1–101107–11.

9. National Conference on Computational Mechanics
MekIT'17
B. Skallerud and H I Andersson (Eds)

A COMPARISON OF WAVE GENERATION METHODS FOR SIMULATING EXTREME WAVES IN A NUMERICAL WAVE TANK

MAYILVAHANAN ALAGAN CHELLA [1], HANS BIHS[1] AND ØIVIND ASGEIR ARNTSEN[1]

[1]Department of Civil and Environmental Engineering
Norwegian University of Science and Technology (NTNU)
Trondheim, Norway
e-mail: mayilvahanan.a.chella@ntnu.no

Key words: Extreme waves, focused waves, transient wave packets

Abstract. Extreme wave conditions emanate from the random and instantaneous interaction of waves during storm events. These wave conditions may cause potentially severe damage to ships and offshore oil and gas structures. There are several reported methods for simulating extreme waves. The main purpose of the present study is to simulate extreme waves with two different wave generation methods using the open-source CFD model REEF3D. Two extreme wave generation methods are considered: a focused wave group and an approach based on transient wave packets. The numerical model uses the incompressible Reynolds-Averaged Navier-Stokes (RANS) equations to model the two-phase flow. The free surface is represented with the level set method. A Dirichlet boundary condition is imposed at the inlet of the wave tank. Focused waves are generated by superpositioning of the linear wave components of an irregular sea state at an intended point in space and time. Whereas in the case of the transient wave packets, a large wave is generated at a certain concentration point along the tank by superimposing the wave components of the transient wave train. Further, the temporal and spatial development of extreme waves based on two methods are examined in the numerical wave tank.

1 INTRODUCTION

Over the last few decades, human activities have discharged large amount of carbon dioxide and other greenhouse gases into the atmosphere. The main source of

greenhouse gases is the burning of fossil fuels in order to produce energy and from additional industrial emissions. As a result, an increase in mean global temperature and change in precipitation patterns can be observed. The predicted and observed weather record indicates more frequent storms with higher wind speeds in the future. Resulting extreme wind and wave conditions over the oceans and in coastal areas can cause hazardous events that may lead to severe damage of coastal infrastructure and marine structures. The knowledge concerning the characteristics of extreme waves is essential to determine the design parameters for fixed and floating offshore structures and ships. In particular, the extreme response analysis plays an important role in the design of offshore structures e.g. air-gap and vertical wave impact.

Several numerical studies based on computational fluid dynamics (CFD) have been performed to model non-breaking focused waves over constant depth e.g. Ning et al. [1], Westphalen et al. [2] and Bihs et al. [3]. It is quiet challenging to describe the evolution of a steep focused wave group. Because the focusing mechanism needs to account for the higher-order terms evolve during the wave-wave interactions. This method becomes even more difficult for modeling breaking wave events as the focused wave group breaks early than anticipated location and time. A method based on the transient wave packets is capable of generating large steep waves in a wave tank and this method was proposed by Clauss et al. [4]. This method has been extensively utilized to generate extreme waves in laboratory conditions in order to investigate extreme wave loads on ships and offshore structures [5].

The main purpose of the study is to investigate two different extreme wave generation methods and their time and spatial developments during the focusing and defocusing process. Two methods for simulating extreme waves are namely a dispersed focusing wave group and a method based on transient wave packets. Both methods are widely used to test offshore structures in physical and numerical wave tanks. The time and spatial evolution of the main wave crest are investigated for three different incident waves for each wave type. Further, the free surface changes during the extreme wave propagation are also presented and discussed.

2 NUMERICAL MODEL

In the present study, the open-source hydrodynamic model REEF3D [6] is used to simulate extreme waves in the numerical wave tank. The numerical model has been thoroughly evaluated for simulating breaking waves [7, 8] and their interaction with structures [9, 10] and focused wave interaction with a slender cylinder [3]. The two-phase viscous flow is described by solving the incompressible Reynolds-Averaged

Navier-Stokes (RANS) equations. The governing equations are as follows:

$$\frac{\partial u_i}{\partial x_i} = 0 \tag{1}$$

$$\frac{\partial u_i}{\partial t} + u_j \frac{\partial u_i}{\partial x_j} = -\frac{1}{\rho}\frac{\partial p}{\partial x_i} + \frac{\partial}{\partial x_j}\left[(\nu + \nu_t)\left(\frac{\partial u_i}{\partial x_j} + \frac{\partial u_j}{\partial x_i}\right)\right] + g_i \tag{2}$$

u is the velocity averaged over time t, ρ is the fluid density, p is the pressure, ν is the kinematic viscosity, ν_t is the eddy viscosity, and g is the gravity term. A fifth-order weighted essentially non-oscillatory (WENO) scheme is employed for the discretization of the convective terms in the RANS equations [11]. This higher-order scheme provides good numerical stability and oscillation-free numerical solutions. Hence, an accurate representation of the free surface is highly important to capture the interface deformation. The complex interface deformation is captured using the level set method (LSM) proposed by [12]. The free surface is described by the smooth signed level set function $\phi(\vec{x}, t)$ which is zero at the interface.

2.1 Focused wave generation

The focused wave simulation is performed by superimposing the linear regular wave components present in the irregular wave trains. The linear free surface elevation $\eta^{(1)}$ is defined as:

$$\eta^{(1)} = \sum_{i=1}^{N} A_i cos\theta_i \tag{3}$$

where, A_i is the amplitude of each wave component and θ_i is the phase of each component, which is defined as:

$$\theta_i = k_i x - \omega_i t - \epsilon_i \tag{4}$$

where ω_i is the angular frequency and k_i is the wave number of each component. ϵ_i is the phase angle of each wave component. In the case of a focusing wave group, a focused wave crest is generated by superimposing of the linear wave components of an irregular sea state at an intended point in space (x_f) and time (t_f).

$$\epsilon_i = k_i x_f - \omega_i t_f \tag{5}$$

A focused wave group consists of several wave components and the amplitude of each component can be described as the function of the wave spectrum $S_i(\omega)$ and

the focus amplitude A_f:

$$A_i = A_f \frac{S_i(\omega)\Delta\omega}{\sum_{i=1}^{N} S_i(\omega)\Delta\omega} \tag{6}$$

Here, the contribution of each spectral component to the maximum wave height at the focus point is obtained. The JONSWAP spectrum is employed in the numerical model for the generation of irregular waves. It is described using the significant wave height H_s, the peak angular frequency ω_p and the number of components N.

$$S_i(\omega) = \frac{5}{16} H_s^2 \omega_p^4 \omega_i^{-5} (-\frac{5}{4}) exp((\frac{\omega_i}{\omega_p})^{-4}) \gamma^{exp(\frac{-(\omega-\omega_p)^2}{2\sigma^2 \omega_p{}^2})} A_\gamma \tag{7}$$

The wave spectrum, $S_i(\omega)$ defines the distribution of wave energy over frequency ω.

2.2 Wave packet generation

The propagation of wave packet is first dominated by high frequency wave components followed by low frequency components. A normalized Fourier spectrum defines the transient wave packet which consists of several frequency components:

$$|F| = \frac{27(\omega - \omega_{beg})(\omega - \omega_{end})^2}{4(\omega_{beg} - \omega_{end})^3} \tag{8}$$

Here, ω is the angular frequency and the subscripts beg and end are the start and end of the Fourier spectrum on the x-axis. The scaling factor f and the amplitude of the each wave component are defined as:

$$f = \frac{A_{focus}}{\sum_{i=1}^{N} A'_i} \tag{9}$$

$$A_i = f A'_i \tag{10}$$

For low steep waves, the first-order wave components are sufficient to achieve a intended focus point in space and time. It is important to account for the contribution of higher-order terms to describe the propagation of the focused wave group and the transient wave packets for higher steepness waves. However, the wave packet generation requires a more number of wave components (500 components) than the focused wave generation (20 components). In the present study, the wave components evolve from the non-linear wave-wave interactions are considered up to the second-order and it is implemented in the model based on Ning et al. [1] formulation which

is originally derived from Scäffer et al. [13]. The second-order wave surface elevation and the horizontal and vertical components of particle velocity are defined as follows:

$$\eta = \eta^{(1)} + \eta^{(2)} \tag{11}$$

$$u = u^{(1)} + u^{(2)} \tag{12}$$

$$w = w^{(1)} + w^{(2)} \tag{13}$$

Simu. nos.	Wave type	Cases	Significant wave height, H_s (m)	Peak period , T_p (s)	Focus distance, x_f (m)	Focus time, t_f (s)
1	Focused waves	FW-1	0.05	1.25	7.5	10.0
2		FW-2	0.10	1.25	7.5	10.0
3		FW-3	0.18	1.25	7.5	10.0
4	Wave packets	WP-1	1.10	7.0	20.0	18.0
5		WP-2	1.20	7.0	20.0	18.0
6		WP-3	1.40	7.0	20.0	18.0

Table 1: List of simulation cases

3 Evolution of focused wave group

The numerical set-up consists of a 15m long and 1.0m high wave tank with a water depth of 0.50m which corresponds to the intermediate water depth condition. Three focused wave groups are generated with different significant wave heights (FW-1 to 3) as listed in Table 1. The intended focus time (t_f) and position (x_f) is 10.0s and 7.5m (from the inlet), respectively, for all focused wave cases. At the inlet, a Dirichlet boundary condition is imposed and the relaxation method is employed for the wave absorption at the outlet.

3.1 Time evolution of focused wave group

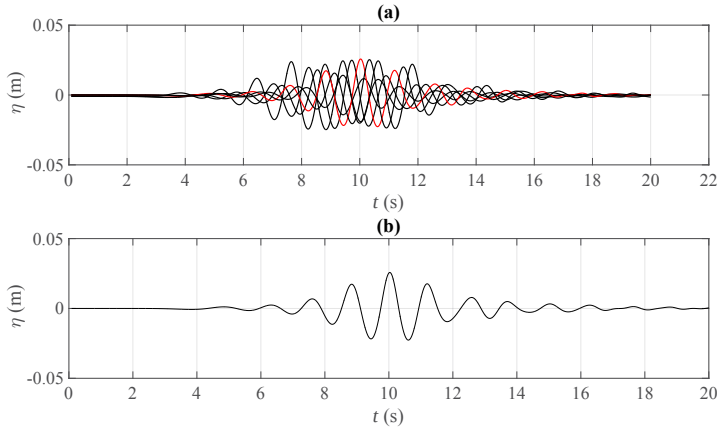

Figure 1: Numerical wave surface elevation of the focused group versus time at (a) different locations for case FW-1 from x from 6.0m to 8.5m at the interval of 0.5m (the red line denotes the wave crest at the focus point) and (b) the focus point, x_f=7.5m (t_f=10.0s).

Figs. 1, 2 and 3 present the computed wave surface elevations (η) of the focused wave group over time for cases FW-1 to 3. In order to examine the time evolution of the focused wave group, the wave surface elevation is computed at 6 different locations along the wave tank (x=6.0m, 6.5m, 7.0m, 7.5m (focus point), 8.0m and 8.5m, x is the distance from the inlet). For low steep waves (FW-1 and 2), the maximum wave height exactly occurs at the intended focus location (x_f) of 7.5 m from the wave inlet and time (t_f) of 10.0s. The amplitude at the focus point (A_f) is 0.026m and 0.052m for case FW-1 and 2, respectively. The height of the wave components immediately ahead of and after the focus point are nearly equal for case FW-1. As the wave spectrum becomes steep, the amplitude of preceding wave component is always higher than the one immediately after the focus point. As can be seen from Fig. 3 that the actual focus point shifts backward in time (t_f=10.5s) when the significant wave height is increased to 0.175. The delay in the focus time is mainly due to the non-linear interaction of steep wave components. For less steep wave cases (FW-1 and 2), the amplitude of the main wave crest gradually increases up to the focus point and then, it decreases gradually downstream. But in the case of steep wave case, the maximum amplitude of the focused group at different wave gauge positions varies significantly, but the variation is gradual for low steep waves.

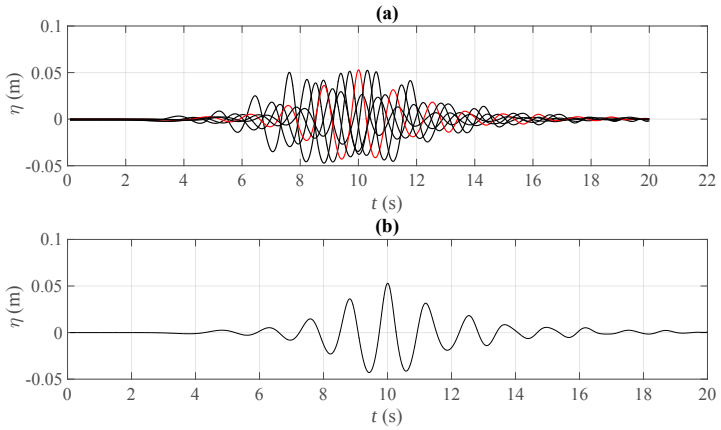

Figure 2: Numerical wave surface elevation of the focused group versus time at (a) different locations for case FW-2 from x from 6.0m to 8.5m at the interval of 0.5m (the red line denotes the wave crest at the focus point) and (b) the focus point, x_f=7.5m (t_f=10.0s).

When the significant wave height increases, the number of steep wave components increase in the focused wave group. Due to the non-linear interactions between the steep wave components give a rise to the higher-order wave components. For all cases, the relationship between the amplitude of the focused wave (A_f) and the significant wave height (H_s) is almost linear which is A_f=0.52H_s. However, the high steep waves influence the focus time significantly.

3.2 Spatial evolution of focused wave group

Figs. 4, 5 and 6 show that the computed wave surface elevations (η) along the wave tank around the focus time (t_f) for cases FW-1 to 3. In general, as the time increases the wave surface elevation increases rapidly while approaching the focus point. Then, the focused wave crest starts to defocus and decreases gradually downstream. For both cases FW-1 and 2, the wave group exactly focuses at x_f=7.5m and t_f=10.0s. Moreover, the computed wave surface elevation of the focused wave group clearly depicts the spatial evolution of the focusing and defocusing process. It also appears that the rate of increase in the amplitude of the main wave crest at each time incident becomes higher for high steep waves.

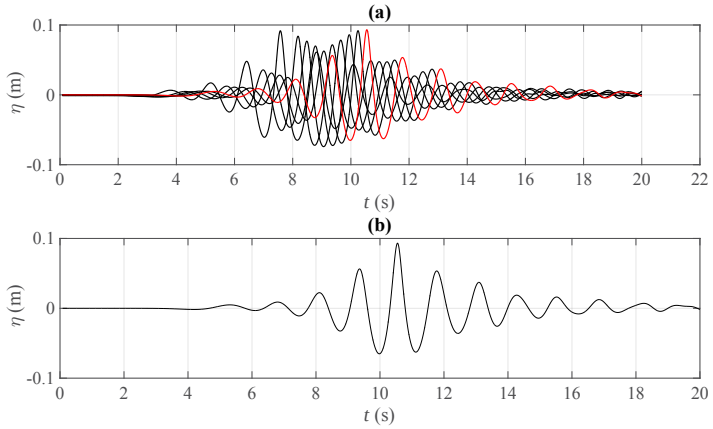

Figure 3: Numerical wave surface elevation of the focused group versus time at (a) different locations for case FW-3 from x from 6.0m to 8.5m at the interval of 0.5m (the red line denotes the wave crest at the focus point) and (b) the focus point, x_f=8.5m (t_f=10.5s).

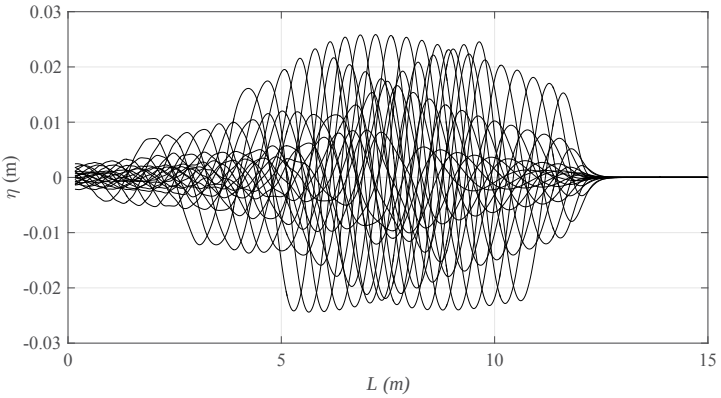

Figure 4: Numerical wave surface elevation of the focused group along the wave tank at different time instants for case FW-1 from t=8.0s to 12.40s at the interval of 0.21s.

As in the case of time evolution, the focus location shifts further downstream (x_f) for the steep wave case (FW-3) as shown in Fig. 6. Since the wave group consists of a large number of steep wave components approaches the focus point, the interaction among the wave components increases resulting in higher-order wave components. It

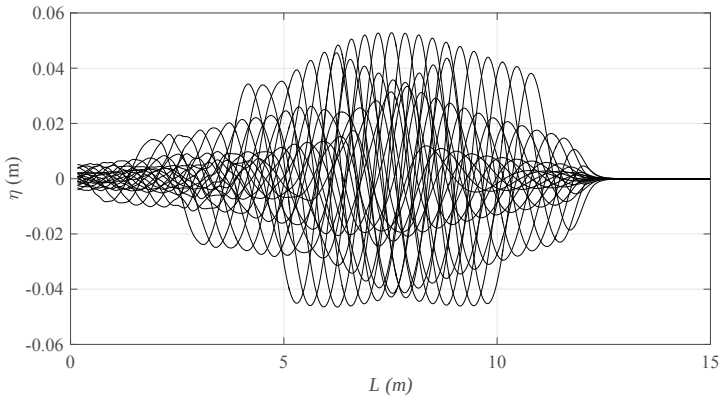

Figure 5: Numerical wave surface elevation of the focused group along the wave tank at different time instants for case FW-2 from t=8.0s to 12.40s at the interval of 0.21s.

means that the interaction between the wave components produces a steep focused wave crest and it becomes unstable. Consequently, the wave group travels further downstream and focuses at x_f=8.5m. The simulated free surface changes along with

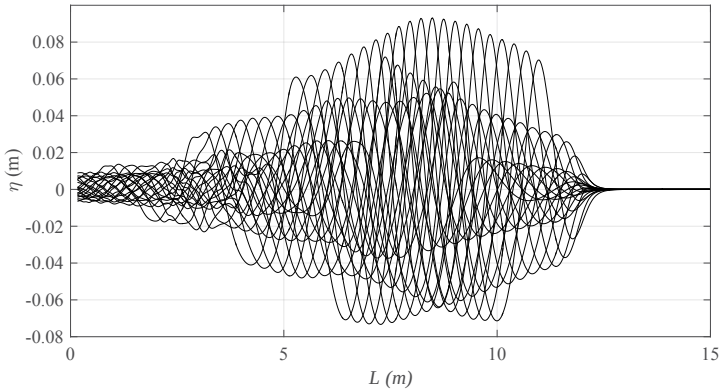

Figure 6: Numerical wave surface elevation of the focused group along the wave tank at different time instants for case FW-3 from t=8.0s to 12.40s at the interval of 0.21s.

the scaled (scale factor=2) contour and velocity magnitude during the focused wave propagation are presented in Fig. 7 for case FW-3 at t=9.5s, 10.0s, 10.25s and 10.50s.

At t=9.5s, the main wave crest in the group approaches the focus point with lower crest velocity (Fig. 7 (a)). As it propagates further downstream, the wave amplitude increases, but the wave components do not focus at the 7.5m as shown in Figs. 7 (b) and (c). Due to the non-linear terms evolved during the wave-wave interaction, the wave group travels further shoreward and focuses at x_f=8.5m (Fig. 7 (d)).

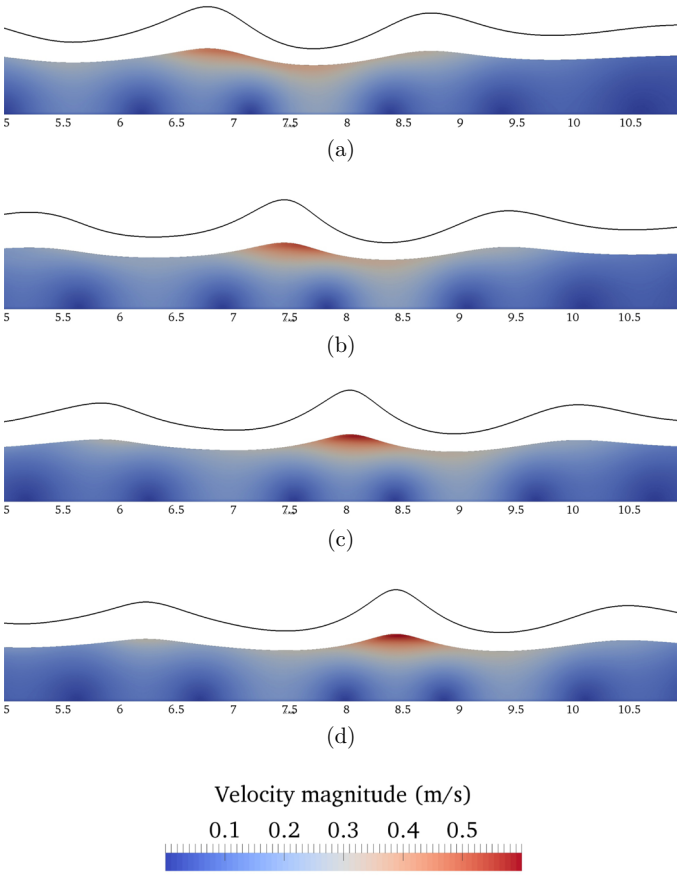

Figure 7: The simulated free surface with the scaled contour line (scale factor=2) for the interface and velocity magnitude (m/s) during the propagation of the focused wave group for case FW-3 at t= (a) 9.5s, (b) 10.0s, (c) 10.25s and (d) 10.50s.

4 Evolution of transient wave packet

The numerical wave tank for simulating transient wave packets is a 25m long and 8.0m high wave tank with a water depth of 4.0m which corresponds to the deep water depth condition. Three cases are simulated with different significant wave heights (cases WP-1 to 3) as listed in Table 1. The location and the time of the concentration point in the wave tank is 20.0m and 18.0s, respectively, for all focused wave packet cases. At the inlet, a Dirichlet boundary condition is imposed and the active absorption method is employed for the wave absorption at the outlet [13].

4.1 Time evolution of transient wave packet

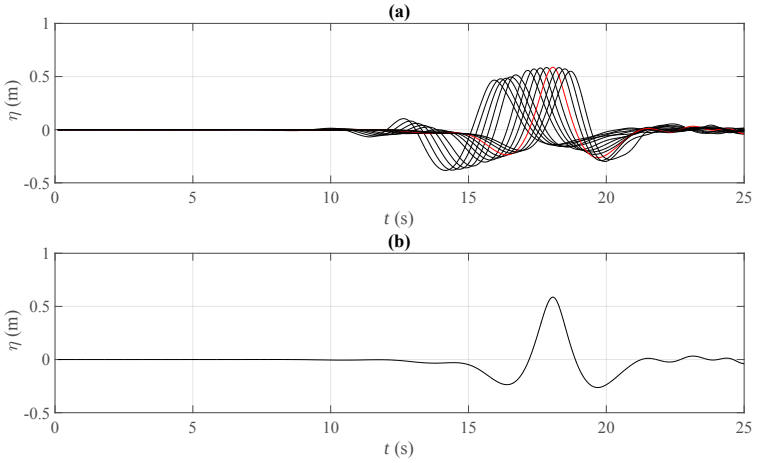

Figure 8: Numerical wave surface elevation of the transient wave packets versus time at (a) different locations from x= 10.0m to 22.0m at the interval of 1.0m for case WP-1 (the red line denotes the wave crest at the concentration point) and (b) the concentration point, x_f=20.0m (t=18.0s).

Figs. 8, 9 and 10 present the development of wave surface elevations of the focused transient wave packets over time for cases WP-1 to 3. The wave surface elevations are computed at different locations from x= 10.0m to 22.0m at the interval of 1.0m for studying the time development of wave surface elevations during the propagation. Unlike the focused wave group, the transient wave packet at the concentration point has a distinct high peak without secondary wave components before and after the main wave crest. With the amplitude Fourier spectrum, first high frequency wave

components followed by the low frequency components are generated in the wave tank. For all cases, the wave packet is focused at t=18.0s and x=20.0m. For all three significant wave heights the transient wave packet concentrates exactly at the intended point in time and space.

At the beginning, the main wave crest of the transient wave group has a deeper

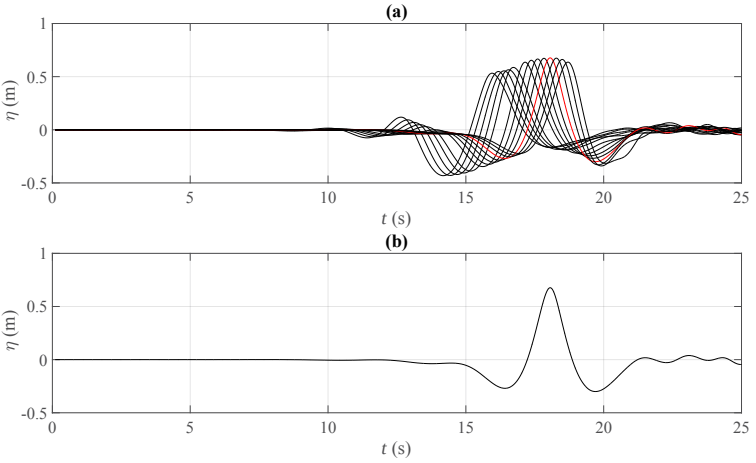

Figure 9: Numerical wave surface elevation of the transient wave packets versus time at (a) different locations from x= 10.0m to 22.0m at the interval of 1.0m for case WP-2 (the red line denotes the wave crest at the concentration point) and (b) the concentration point, x_f=20.0m (t=18.0s).

preceding and a shallower following wave trough and a small upstream wave crest. As the wave group propagates further downstream along the wave tank close to the concentration point, the preceding wave tough becomes shallower, the following wave trough becomes deeper and the upstream wave crest disappears. Thus, the amplitude of the main wave crest increases. In addition, the horizontal asymmetry of the main wave crest decreases as the distance from the focus point decreases. The amplitude at the concentration point is 0.59m ($0.56H_s$), 0.68m ($0.57H_s$) and 0.80m ($0.59H_s$) for case WP-1 to 3. The ratio of the focused amplitude and the significant wave height increases as the incident wave height increases.

4.2 Spatial evolution of transient wave packet

Figs. 11, 12 and 13 show the wave surface elevations of the focused wave packets along the wave tank for case WP-1 to 3 for different time instants from t=16.0s

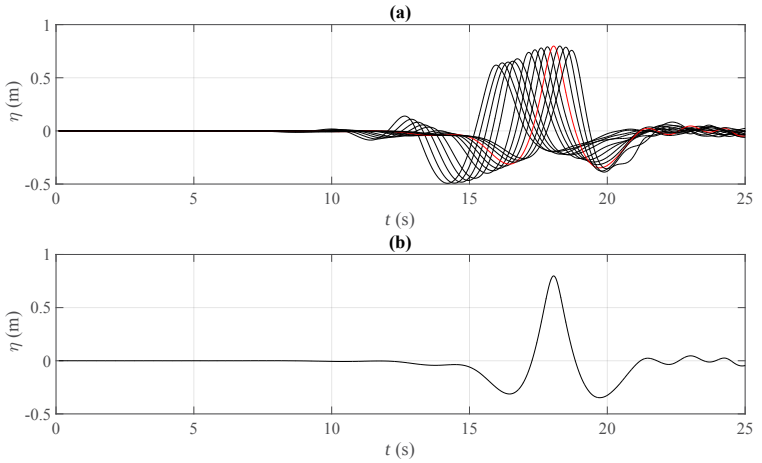

Figure 10: Numerical wave surface elevation of the transient wave packets versus time at (a) different locations from x= 10.0m to 22.0m at the interval of 1.0m for case WP-3 (the red line denotes the wave crest at the concentration point) and (b) the concentration point, x_f=20.0m (t=18.0s).

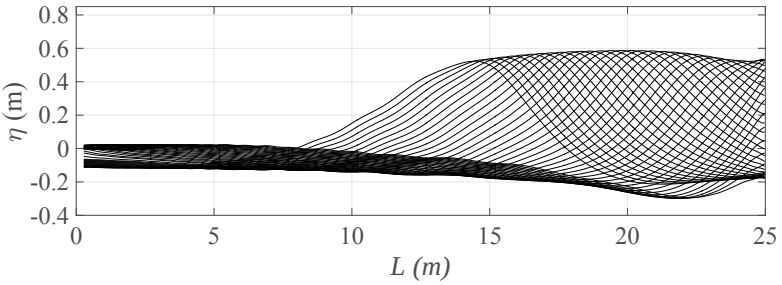

Figure 11: Numerical wave surface elevation of the transient wave packets along the wave tank at different time instants from t=16.0s to 19.0s at the interval of 0.075s for case WP-1.

to 19.0s at the interval of 0.075s. It appears that the development of main wave crest increases slowly and steadily up to the concentration point of x_f=20.0m and decreases slowly. The main wave crest has a relatively deeper wave trough upstream and downstream. Unlike the time development of the main wave crest, the rate of increase and decrease in the amplitude of the main wave crest before and after the

focus point becomes larger for higher significant wave heights. In particular, the transient wave packet has no secondary wave components compared to the focused wave group. When the wave crest approaches the concentration point, the front face of the wave crest gets steeper followed by the rear face and thus, the vertical asymmetry decreases and the horizontal asymmetry increases.

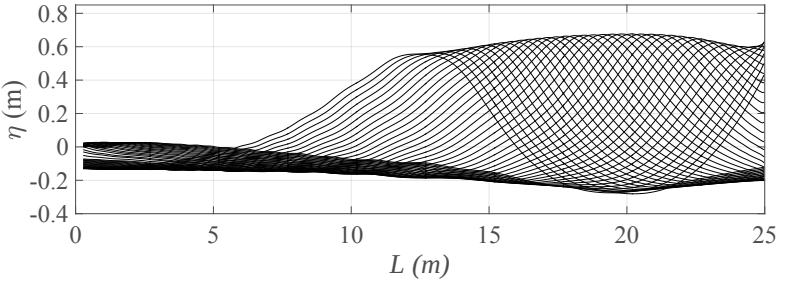

Figure 12: Numerical wave surface elevation of the transient wave packets along the wave tank at different time instants from t=16.0s to 19.0s at the interval of 0.075s for case WP-2.

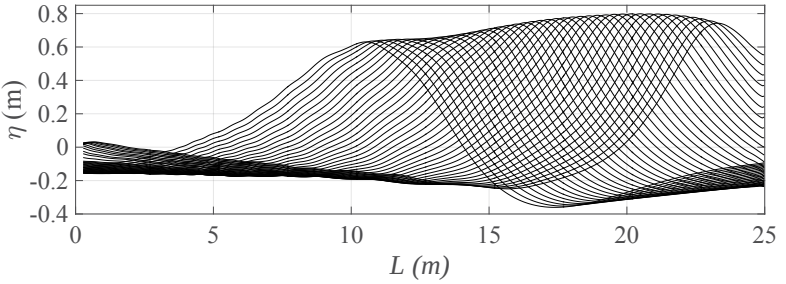

Figure 13: Numerical wave surface elevation of the transient wave packets along the wave tank at different time instants from t=16.0s to 19.0s at the interval of 0.075s for case WP-3.

Fig. 14 shows the simulated free surface with velocity magnitude and the scaled contour line for the interface (scale factor=2) at t=17.0s, 17.5s, 18.0s and 18.5s. Initially, the maximum velocity is noticed under the forward front part of the wave crest than the rear part due its larger vertical asymmetry as shown in Fig. 14. This is also consistent with the previous observation as presented in Fig. 12.

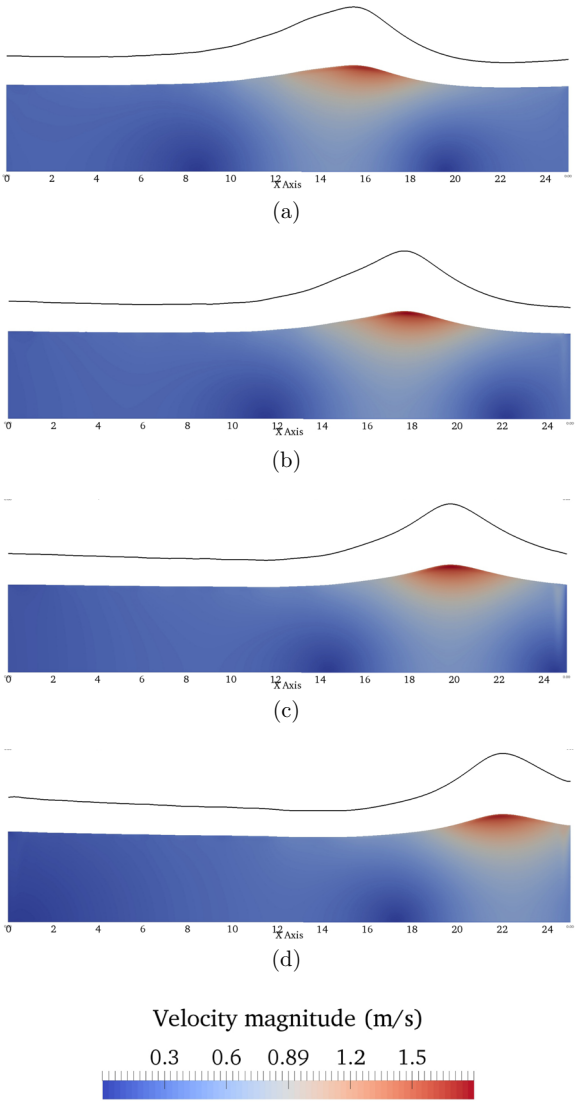

Figure 14: The simulated free surface with the scaled contour (scale factor=2) for the interface and velocity magnitude (m/s) during the propagation of the transient wave packets for case WP-3 at t= (a) 17.0s, (b) 17.50s, (c) 18.0s and (d) 18.50s.

During the propagation, the deformation of the front face of the main wave crest takes place followed by the rear face. At the concentration point (x_f=20.0m), the vertical asymmetry is nearly unity. Then, the amplitude of the main wave crest decreases gradually as the wave group propagates further shoreward (Fig. 14) (d).

5 CONCLUSIONS

This paper has investigated extreme wave generation using two different methods in a numerical wave tank. The numerical simulations are performed with the open-source hydrodynamics model REEF3D. The model uses the incompressible Reynolds-Averaged Navier-Stokes (RANS) equations together with the level set method for free surface. Two wave generation methods for modeling extreme waves are considered in the present study namely a dispersed focusing wave group and a method based on transient wave packets. The focused wave generation is based on superimposing the linear wave components of an irregular wave train at a particular point in space and time. In the case of the transient wave packets, a large single crested wave is generated along the length of the tank at a certain concentration point by superimposing the wave components of the transient wave packets. For high steep waves, the focus time and location shifts downstream for the focused wave group due to the non-linear wave-wave interactions. At the same time, the transient wave packets provide a good representation of large and steep extreme wave crests. Moreover, the evolution of free surface flow features for wave packets and focused waves are represented well in the numerical model.

Acknowledgment

The research work has been funded by the Research Council of Norway through the project "Hydrodynamic Loads on Offshore Wind Turbine Substructures due to Nonlinear Irregular Breaking, High Steep and Extreme Waves" (project number: 246810). The authors gratefully acknowledge the allocation of supercomputing time by NOTUR (NN2620K).

REFERENCES

[1] Ning, D. Z., Zang, J., Liu, S. X., Eatock Taylor, R., Teng, B., and Taylor, P. H., 2009. "Free-surface evolution and wave kinematics for nonlinear uni-directional focused wave groups". *Ocean Engineering,* ***36***, pp. 1226—1243.

[2] Westphalen, J., Greaves, D. M., Williams, C. J. K., Hunt-Raby, A. C., and Zang, J., 2012. "Focused waves and wave-structure interaction in a numerical wave tank". *Ocean Engineering,* ***45***, pp. 9–21.

[3] Bihs, H., Alagan Chella, M., Kamath, A., and Arntsen, Ø. A., 2017. "Numerical investigation of focused waves and their interaction with a vertical cylinder using reef3d". *Journal of Offshore Mechanics and Arctic Engineering.* doi:10.1115/1.4036206.

[4] Clauss, G. F., and Küehnlein, W. L., 1997. "A new tool for sea-keeping tests: Nonlinear transient wave packets". In Proceedings of the 8th International Conference on the Behavior of Offshore Structures BOSS97, pp. 269–285.

[5] Grigoropoulos, G. J., Florios, N. S., and Loukakis, T. A., 1994. "Transient waves for ship and floating structure testing". *Applied ocean research,* ***16***(2), pp. 71–85.

[6] Bihs, H., Kamath, A., Alagan Chella, M., Aggarwal, A., and Arntsen, Ø. A., 2016. "A new level set numerical wave tank with improved density interpolation for complex wave hydrodynamics". *Computers and Fluids,* ***140***, pp. 191–208.

[7] Alagan Chella, M., Bihs, H., Myrhaug, D., and Muskulus, M., 2015a. "Breaking characteristics and geometric properties of spilling breakers over slopes". *Coast. Eng.,* ***95***, pp. 4–19.

[8] Alagan Chella, M., Bihs, H., Myrhaug, D., and Muskulus, M., 2016. "Hydrodynamic characteristics and geometric properties of plunging and spilling breakers over impermeable slopes". *Ocean Modelling,* ***103***, pp. 53–72.

[9] Bihs, H., Kamath, A., Alagan Chella, M., and Arntsen, Ø. A., 2016. "Breaking wave interaction with tandem cylinders under different impact scenarios". *J. Waterw. Port Coast. Ocean Eng.* DOI: 10.1061/(ASCE)WW.1943-5460.0000343.

[10] Alagan Chella, M., Bihs, H., Myrhaug, D., and Muskulus, M., 2017. "Breaking solitary waves and breaking wave forces on a vertically mounted slender cylinder over an impermeable sloping seabed". *Journal of Ocean Engineering and Marine Energy,* ***3***, pp. 1–19.

[11] Jiang, G. S., and Shu, C. W., 1996. "Efficient implementation of weighted ENO schemes". *J. Comput. Phys.,* ***126***, pp. 202–228.

[12] Osher, S., and Sethian, J. A., 1988. "Fronts propagating with curvature-dependent Speed: Algorithms based on Hamilton-Jacobi formulations". *J. Comput. Phys.,* ***79***, pp. 12–49.

[13] Schäffer, H. A., and Klopman, G., 2000. "Review of multidirectional active wave absorption methods". *J. Waterw. Port Coast. Ocean Eng.,* ***126***, pp. 88–97.

9. National Conference on Computational Mechanics
MekIT'17
B. Skallerud and H I Andersson (Eds)

NUMERICAL INVESTIGATION OF THERMO-VISCOUS INSTABILITY IN IMMISCIBLE DISPLACEMENT

Christopher Nilsen

Department of Physics and Technology
University of Bergen, Allégaten 55
N-5007 Bergen, Norway
e-mail: research@christophernilsen.no

Key words: Darcy flow, thermo-viscous instability, Cahn-Hilliard equation, spectral methods

Abstract. We describe a numerical methodology for simulation of immiscible radial displacement in a porous medium or Hele-Shaw cell. A Darcy-Cahn-Hilliard model is used in conjunction with a spectral element numerical approximation. We use a geometry transformation to solve the equations on an unbounded domain, and exponential convergence is accomplished in both the radial and the angular direction.

1 INTRODUCTION

When a fluid is injected into a porous medium saturated with a different fluid, the moving interface between the two fluids can become unstable if the fluid already saturating the medium has the higher viscosity. This classic stability problem was first studied by Hill [1] who did a series of experiments for displacement in a column with packed charcoal. More rigorous stability analyses in linear displacement were performed by Chuoke et al. [2] and Saffman & Taylor [3].

Wilson [4] and Paterson [5] were the first to use linear stability theory to study radial displacement, and they showed the stabilising effect of interfacial tension. Paterson also did radial displacement experiments, and found the theoretical predictions to agree reasonably well with the experimental results. Homsy [6] reviewed the viscous fingering literature for both miscible and immiscible displacement in porous media and Hele-Shaw cells.

When the injecting fluid has a different temperature than the fluid already saturating the porous medium, a second, thermal, front moves behind the fluid front separating the two fluids. The heat shared with the porous matrix causes the thermal front to lag behind the fluid front.

Pritchard [7] studied thermo-viscous instability in radial miscible displacement. The double front system formed when a fluid is injected into a porous medium saturated with

a fluid with different temperature and composition, was studied using linear stability theory. Pritchard found that instabilities on the compositional front tended to dominate due to the solute diffusivity being much lower than the thermal diffusivity.

A similar double front system was studied in a rectilinear geometry by Islam & Azaiez, using linear stability analysis [8] and with numerical simulations [9].

We study the thermo-viscous stability problem that emerges when a diffuse thermal front is interacting with an immiscible fluid or concentration front. Both fronts are potentially unstable. The thermal front is stabilised by diffusion, the fluid front by interfacial tension.

We describe a methodology that can be used to simulate the immiscible thermo-viscous stability problem in a two-dimensional radial geometry, and we document the resulting convergence properties. Since our primary goal is to study the growth of instabilities on the interface, the accuracy of the simulation is of great importance. Small amounts of numerical diffusion could stabilise an otherwise unstable front. For this reason, we use spectral methods, with a Fourier expansion in the angular direction and a polynomial expansion in the radial direction.

The governing equations and the numerical methodology are presented in sections 2 and 3, respectively. Results from convergence tests are shown in section 4, and the findings are summarised in section 5.

2 GOVERNING EQUATIONS

A fluid with viscosity $\hat{\eta}_0$ and temperature $\hat{T}_0$ is injected into a porous medium, or Hele-Shaw cell, saturated with a fluid with viscosity $\hat{\eta}_\infty$ and temperature $\hat{T}_\infty$. The injected fluid spreads radially outwards from the injection point $\hat{r} = 0$, with both thermal and concentration fronts moving as $R \propto \sqrt{t}$.

We use a diffuse-interface approach to describe the immiscible incompressible two-phase flow, with a convective Cahn-Hilliard equation for the concentration. The governing equations for the Darcy-Cahn-Hilliard system [10, 11, 12] are

$$\hat{\nabla} \cdot \hat{\boldsymbol{u}} = 0, \tag{1a}$$

$$\hat{\nabla}\hat{p} = \frac{\hat{\eta}}{\hat{k}}\hat{\boldsymbol{u}} - \hat{\epsilon}\hat{\rho}\hat{\nabla} \cdot ((\hat{\nabla}c)(\hat{\nabla}c)^T), \tag{1b}$$

$$\frac{\partial \hat{T}}{\partial \hat{t}} + \frac{\lambda}{\phi}\hat{\nabla} \cdot (\hat{\boldsymbol{u}}\hat{T}) = \hat{\kappa}_T \hat{\nabla}^2 \hat{T}, \tag{1c}$$

$$\frac{\partial c}{\partial \hat{t}} + \frac{1}{\phi}\hat{\nabla} \cdot (\hat{\boldsymbol{u}}c) = \hat{\kappa}_c \hat{\nabla}^2 \hat{\mu} \tag{1d}$$

and

$$\hat{\mu} = \frac{\partial \hat{f}_0}{\partial c} - \hat{\epsilon}\hat{\nabla}^2 c. \tag{1e}$$

The equations (1a–1e) for velocity $\hat{\boldsymbol{u}}$, temperature $\hat{T}$ and concentration $\hat{c}$ are expressed in a polar coordinate system. The viscosity $\hat{\eta}$ is a function of $\hat{T}$ and $\hat{c}$, while the permeability $\hat{k}$, the density $\hat{\rho}$, the coefficient of capillarity $\hat{\epsilon}$, the effective porosity ϕ, and the diffusion coefficients $\hat{\kappa}_T$ and $\hat{\kappa}_c$ are constants. The thermal lag coefficient [7]

$$\lambda = \frac{\phi_t \hat{\rho}_{\text{fluid}} \hat{C}_{\text{fluid}}}{\phi_t \hat{\rho}_{\text{fluid}} \hat{C}_{\text{fluid}} + (1-\phi_t)\hat{\rho}_{\text{matrix}} \hat{C}_{\text{matrix}}} < 1 \tag{2}$$

quantifies the thermal lag caused by heat being shared with the porous matrix. $\hat{C}$ is the specific heat capacity and ϕ_t is the total porosity. For a Hele-Shaw cell, $\lambda = 1$.

We non-dimensionalize equations (1a) to (1e) and introduce the stream function ψ, defined such that

$$u_r = \frac{1}{r}\frac{\partial \psi}{\partial \theta} \tag{3a}$$

and

$$u_\theta = -\frac{\partial \psi}{\partial r}, \tag{3b}$$

where u_r and u_θ are the radial and angular non-dimensional velocities. In order to resolve the moving fronts more easily, $\xi = r/\sqrt{2t}$ is introduced and the equations are transformed from (r, θ, t) to the variables (ξ, θ, t). The steady fluid or concentration front is located at $\xi = 1$ and the thermal front at $\xi = \lambda$.

The resulting governing equations are

$$\begin{aligned} \nabla^2 \psi - \left(\beta_T \frac{\partial T}{\partial \xi} + \beta_c \frac{\partial c}{\partial \xi}\right)\frac{\partial \psi}{\partial \xi} - \frac{1}{\xi^2}\left(\beta_T \frac{\partial T}{\partial \theta} + \beta_c \frac{\partial c}{\partial \theta}\right)\frac{\partial \psi}{\partial \theta} \\ = \frac{C}{S\eta}\frac{1}{2t\xi}\left(\frac{\partial c}{\partial \theta}\frac{\partial}{\partial \xi}\left(\nabla^2 c\right) - \frac{\partial c}{\partial \xi}\frac{\partial}{\partial \theta}\left(\nabla^2 c\right)\right), \end{aligned} \tag{4a}$$

$$2t\frac{\partial T}{\partial t} - \xi \frac{\partial T}{\partial \xi} + \frac{\lambda}{\xi}\left(\frac{\partial \psi}{\partial \theta}\frac{\partial T}{\partial \xi} - \frac{\partial \psi}{\partial \xi}\frac{\partial T}{\partial \theta}\right) = \frac{1}{P_T}\nabla^2 T, \tag{4b}$$

$$2t\frac{\partial c}{\partial t} - \xi \frac{\partial c}{\partial \xi} + \frac{1}{\xi}\left(\frac{\partial \psi}{\partial \theta}\frac{\partial c}{\partial \xi} - \frac{\partial \psi}{\partial \xi}\frac{\partial c}{\partial \theta}\right) = \frac{1}{P_c}\nabla^2 \mu \tag{4c}$$

and

$$\mu = \frac{\partial f_0}{\partial c} - \frac{C}{2t}\nabla^2 c, \tag{4d}$$

where the Laplacian is defined as

$$\nabla^2 q = \frac{1}{\xi}\frac{\partial}{\partial \xi}\left(\xi \frac{\partial q}{\partial \xi}\right) + \frac{1}{\xi^2}\frac{\partial^2 q}{\partial \theta^2}. \tag{5}$$

For an immiscible interface, the dimensionless Helmholtz free energy function f_0 is convex. We use the function

$$f_0 = c^2(1-c)^2. \tag{6}$$

The non-dimensional viscosity depends on the temperature and concentration as

$$\eta = e^{-\beta_T T - \beta_c c}. \tag{7}$$

If $\beta_{T,c}$ is negative, the viscosity is greater ahead of the front and the front is potentially unstable. The Cahn number C, the source strength S and the Péclet numbers P_T and P_c are all constants.

3 NUMERICAL METHODOLOGY

We use a Galerkin formulation and discretise the weak forms of equations (4a) to (4d). The weak form of each equation is found by multiplying with a test function v and integrating over the domain (omitted for brevity).

The equations are solved with the boundary conditions

$$T = 0, \quad c = 0, \quad \nabla c = \mathbf{0}, \quad \psi = \theta \quad \text{at} \quad \xi = 0 \tag{8a}$$

and

$$T \to 1, \quad c \to 1, \quad \nabla c \to \mathbf{0}, \quad \psi \to \theta \quad \text{as} \quad \xi \to \infty. \tag{8b}$$

The boundary conditions at $\xi \to \infty$ pose a challenge for the discretisation because imposing the same boundary conditions at the end of a large but finite domain, will incur a finite error. This is handled by using a geometry transformation to solve the equations on an infinite domain [13, 14]. We divide the domain into E ring-shaped elements ($\theta \in (-\pi, \pi)$), where the radial coordinate ξ in each domain is expressed as a function of the reference variable $\zeta \in (-1, 1)$. The first $E-1$ elements use linear geometry transformations, while element E uses

$$\xi^E(\zeta) = \frac{1+\zeta}{1-\zeta} L_E + \xi^{E-1}(1), \tag{9}$$

where L_E determines how fast the grid approaches infinity.

The temperature T in element e is approximated, using a Fourier approximation in the θ-direction and a polynomial approximation in the ξ-direction, as

$$T^e(\zeta, \theta) \approx \sum_{m=-M/2+1}^{M/2} \sum_{n=0}^{N} \tilde{T}^e_{mn} \exp(\mathrm{i}m\theta) l_n(\zeta), \tag{10}$$

and similarly for c and ψ. As the test function v, we use

$$v = \exp(-\mathrm{i}j\theta) l_k(\zeta), \tag{11}$$

where l_k is the N-order Lagrangian interpolant through the $N+1$ Gauss Lobatto Legendre nodes.

We use a combination of explicit and implicit stiffly stable schemes [15] to integrate the equations in time. Both explicit and implicit schemes are of third order accuracy and only the biharmonic operator in the concentration equation and the Laplacian in the temperature equation are treated implicitly.

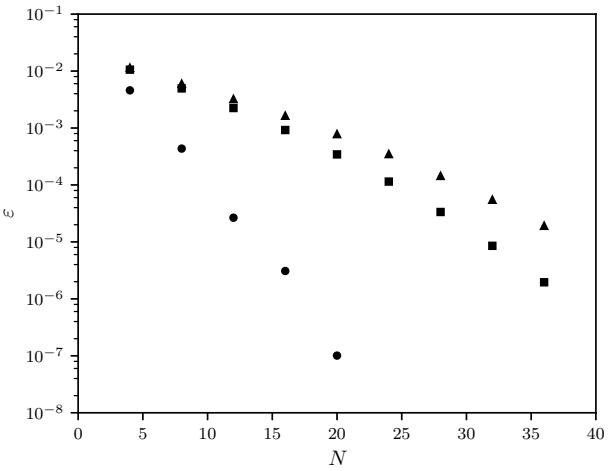

Figure 1: Numerical error ε as a function of polynomial order N for T (circles), c (squares) and ψ (triangles), with $M = 256$

4 RESULTS

In order to test the convergence properties of the numerical methodology, we perform a series of simulations with a wide range of M and N values. For our test simulations, we use $\lambda = 0.9$, $P_T = 20$, $P_c = 10^3$, $C = 10^{-5}$, $S = 1$ and $\beta_T = \beta_c = -\log 10$. With this combination of parameters, both fronts will be unstable. The radial and angular structure of the solution are both sufficiently complex to provide a challenge for the numerical approximation. We use $E = 7$ elements, with the last one stretching to infinity.

The error is estimated by comparing the solution at the final time with a reference simulation using $M = 256$ and $N = 60$, and computing the maximum norm $\varepsilon(T) = ||T_{MN} - T||_\infty$. The reference simulation is initialised from the axisymmetric base solution for T and c at $t = 0.01$, and white noise with amplitude 10^{-8} for ψ. All the other simulations are then initialised from the reference simulation at $t = 0.2$ and simulated until $t = 1$.

Figure 1 shows the approximation error ε for T, c and ψ as a function of the polynomial order N. We observe exponential convergence for T, c and ψ, but with significantly lower error in T than in c and ψ. This is to be expected considering the highly diffusive thermal front. It is clear that the use of an infinite domain has not compromised the exponential convergence we expect from a spectral approximation.

In figure 2 the error ε is plotted as a function of M, showcasing the convergence properties of the Fourier expansion. Again, we observe exponential convergence, with

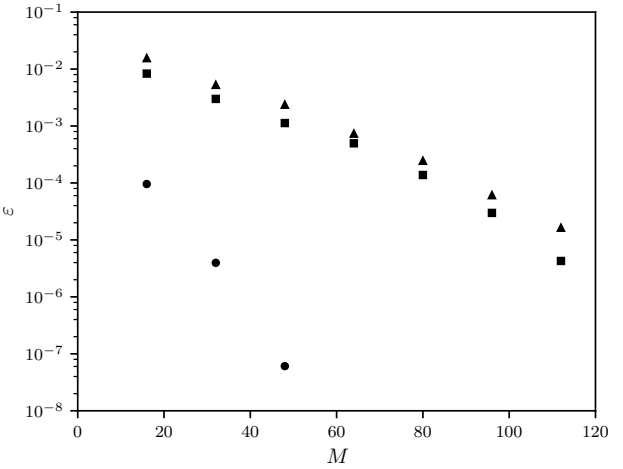

Figure 2: Numerical error ε as a function of Fourier expansion order M for T (circles), c (squares) and ψ (triangles), with $N = 60$

particularly rapid convergence for T.

5 SUMMARY AND CONCLUSIONS

We have described a numerical methodology used to simulate two-dimensional immiscible radial displacement. A diffuse interface Darcy-Cahn-Hilliard system coupled with the energy equation is used to represent the two-dimensional porous-medium or Hele-Shaw flow. The equations are discretised using a spectral element approximation, with a Fourier expansion in the angular direction and a polynomial expansion in the radial direction.

We have seen that the numerical approximation converges exponentially, in both the radial and the angular direction, and this is accomplished on an unbounded domain. The combination of a diffuse interface model with a spectral approximation, gives an efficient and highly accurate solution methodology for immiscible displacement problems.

ACKNOWLEDGMENTS

The project was funded by VISTA, a basic research program in collaboration between The Norwegian Academy of Science and Letters, and Statoil.

REFERENCES

[1] Hill, S. Channeling in packed columns. *Chem. Eng. Sci.* (1952) **1**:247–253.

[2] Chuoke, R. L., van Meurs, P. and van der Poel, C. The instability of slow, immiscible, viscous liquid-liquid displacements in permeable media. *Trans. AIME* (1959) **216**:188–194.

[3] Saffman, P. G. and Taylor, G. The penetration of a fluid into a porous medium or Hele-Shaw cell containing a more viscous liquid. *Proc. Roy. Soc. London* (1958) **245**:312–329.

[4] Wilson, S. D. R. A note on the measurement of dynamic contact angles. *J. Colloid Interface Sci.* (1975) **51**:532–534.

[5] Paterson, L. Radial fingering in a Hele Shaw cell. *J. Fluid Mech.* **113**:513–529.

[6] Homsy, G. M. Viscous fingering in porous media. *Ann. Rev. Fluid Mech.* **19**:271–311.

[7] Pritchard, D. The instability of thermal and fluid fronts during radial injection in a porous medium. *J. Fluid Mech.* (2004) **508**:133-163.

[8] Islam, M. N. and Azaiez, J. Miscible thermo-viscous fingering instability in porous media. Part 1: Linear stability analysis. *Transp. Porous Med.* (2010) **84**:821–844.

[9] Islam, M. N. and Azaiez, J. Miscible thermo-viscous fingering instability in porous media. Part 2: Numerical simulations. *Transp. Porous Med.* (2010) **84**:845–861.

[10] Chen, C.-Y., Huang, Y.-S. and Miranda, J. A. Diffuse-interface approach to rotating Hele-Shaw flows. *Phys. Rev. E* (2011) **84**:046302.

[11] Chen, C.-Y., Huang, Y.-S. and Miranda, J. A. Radial Hele-Shaw flow with suction: Fully nonlinear pattern formation. *Phys. Rev. E* (2014) **89**:053006.

[12] Chen, C.-Y. and Yan, P.-Y. A diffuse interface approach to injection-driven flow of different miscibility in heterogeneous porous media. *Phys. Fluids* (2015) **27**:083101.

[13] Grosch, C. E. and Orszag, S. A. Numerical solution of problems in unbounded regions: Coordinate transforms. *J. Comp. Phys.* (1977) **25**:273–295.

[14] Boyd, J. P. The optimization of convergence for Chebyshev polynomial methods in an unbounded domain. *J. Comp. Phys.* (1982) **45**:43–79.

[15] Karniadakis, G. E., Israeli, M., and Orszag, S. A. High-order splitting methods for the incompressible Navier-Stokes equations. *J. Comp. Phys.* (1991) **97**:414-443.

9. National Conference on Computational Mechanics
MekIT'17
B. Skallerud and H I Andersson (Eds)

INFLUENCE OF COMPUTATIONAL DOMAIN SIZE ON WAKES BEHIND CROSS-SHAPED PLATES

Fatemeh H. Dadmarzi[1], Vagesh D. Narasimhamurthy[2], Helge I. Andersson[3] and Bjørnar Pettersen[1]

[1]Department of Marine Technology, Norwegian University of Science and Technology, NO-7491, Trondheim, Norway

[2] Department of Applied Mechanics, Indian Institute of Technology Madras, Chennai 600036, India

[3] Department of Energy and Process Engineering, Norwegian University of Science and Technology, NO-7491, Trondheim, Norway

Key words: computational domain size, DNS, wake, viscous flows

Abstract. The influence of the computational domain size in a DNS study of the three-dimensional wake behind a cross formed by two intersecting flat plates has been investigated. The Reynolds number based on the uniform inflow velocity U_0 and the plate width d is 1000. The wake flow is characterized by qualitatively different flow regimes; from the three-dimensional wake in the intersection region with suppressed vortex shedding, to quasi two-dimensional shedding flow behind the outer branches.The spanwise base pressure gradient indicates the existence of secondary flows. The effect of the free-slip condition employed at the two vertical sides of the computational domain, as well as along the top and the bottom planes, is demonstrated for two cases. Moreover, the influence of the domain size on the base pressure and mean fluctuating kinetic energy is shown. By extending the plate lengths from $21d$ to $31d$, the adverse effects of the free-slip boundary conditions were eliminated and the cross-configuration mimicked infinitely long crossing plates.

1 INTRODUCTION

The wake behind multiple bluff-body configurations has received many researcher's interest due to its importance in academic and engineering fields. Intersecting configurations, e.g. a perpendicular arrangement of cylinders, have applications in offshore structures, aquaculture etc. The turbulent wake behind two intersecting circular cylinders was studied by Osaka et al.[1], Zdravkovich[2] and Fox and Toy[3] experimentally. For two intersecting flat plates Donoso et al.[4] studied the effect of intersection upon the

vortex shedding from each plate. The wake behind two intersecting plates has been investigated by the present authors ([5, 6]). The wake flow behind intersecting plates/cylinders can be characterized by a complex massive separated flow in the intersection region which changed to quasi-two dimensional vortex streets behind the outer branches. A base pressure gradient drives the flow away from the intersection region towards the outer branches. In addition, secondary flow of second kind as classified by Prandtl is also observed as four pairs of vortices located symmetrically with respect to the geometrical symmetry planes. The aim of present study is to investigate the influence of the computational domain size in simulating such a complex wake flow. In particular, the effect of computational set-up on the base pressure and mean fluctuating kinetic energy is studied.

2 Flow configuration and numerical method

The cross-plate structure consists of two intersecting thin flat plates, placed normal to the inflow. The whole geometry is positioned in a single plane and the Reynolds number Re based on the inflow velocity U_0 and the width of a plate d, is 1000. The mass conservation and Navier-Stokes equations for an incompressible flow of a viscous fluid are given in Eq. (1) and (2):

$$\partial u_j/\partial x_j = 0 \tag{1}$$

$$\partial u_i/\partial t + u_j(\partial u_i/\partial x_j) = -1/\rho(\partial p/\partial x_i) + \nu(\partial^2 u_i/\partial {x_j}^2) \tag{2}$$

Direct Numerical Simulation(DNS) of the flow past the cross-plate configuration has been carried out by the finite-volume code (MGLET)[7]. The code has a second-order central-differencing scheme for spatial discretization and a third-order explicit Runge-Kutta scheme for marching in time. The Poisson equation is solved by an iterative strongly implicit procedure (SIP). The code uses a staggered Cartesian grid and a direct forcing Immersed Boundary Method (IBM)[8] is employed in order to implement the surface of the cross-plate in the computational grid.

Two computational domains have been used in the DNS study. The small domain has 20d length in streamwise direction and 21d length in spanwise and cross-stream directions, with $384 \times 366 \times 366$ number of grid points in each direction[5]. The large domain has also 20d length in streamwise but 31d length in spanwise and cross-stream directions with a grid consisting of $384 \times 474 \times 474$ degrees of freedom[6] (figure 1). All the spatial dimensions are normalized by the plate width d, and all velocities are scaled by the inflow velocity U_0.

The boundary conditions consist of uniform inflow velocity U_0 without any free-stream perturbations at the inlet $x/d = -5$, and free-slip conditions at the vertical side planes of the computational domain as well as along the top and the bottom planes. At the outlet x/d = +15, a Neumann boundary condition is used for the velocity components

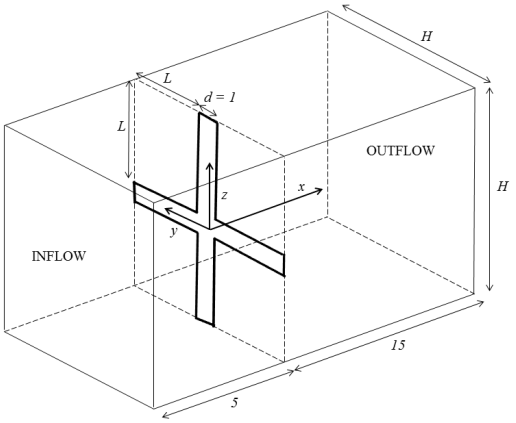

Figure 1: Computational domain (not to scale). The plate width is d = 1. In the small domain $L = 10$ and $H = 21$. In the large domain $L = 15$ and $H = 31$.

and the pressure is set to zero. The time step is chosen to be $\Delta t = 0.001 d/U_0$. This time step satisfies the stability criterion and is comparable with the time step used in earlier DNS studies of wake flows at moderate Reynolds numbers. The ratio of the local grid size $\delta = (\Delta x \Delta y \Delta z)^{1/3}$ to the local Kolmogorov length scale $\eta = (\nu^3/\varepsilon)^{1/4}$ is less than 5 for both computational set-ups. Here, ε is the dissipation rate of turbulent kinetic energy $\varepsilon = \nu\overline{(\partial u_i/\partial x_j)(\partial u_i/\partial x_j)}$. The same grid resolution was used in both cases and the energy spectra shown in Figure 5 in Dadmarzi et al. [6] indicate that the resolution is appropriate for the present purpose.

3 Results and discussion

Figure 2 shows the mean streamline patterns in the horizontal (x, y)-plane through the centerline of the horizontal plate from both the small and the large domain simulations. For the intersecting plates, with the suppression of the vortex shedding at the intersection region, the spanwise pressure gradient along the plates drives the fluid out from the intersection toward the outer branches. As figure 2(a) shows, for the small domain, the outward-driven secondary flow from the intersection is still strong close to the boundaries. The free-slip condition at the surrounding boundaries suppresses the normal velocity component and the blockage effect appeared in a form of a small recirculation bubble just next to the surrounding computational planes (shown by red circles in the figure). Figure 2 shows how effectively the enlargement of the domain size in the spanwise and cross-stream directions reduces the adverse effect of the free-slip boundary condition on

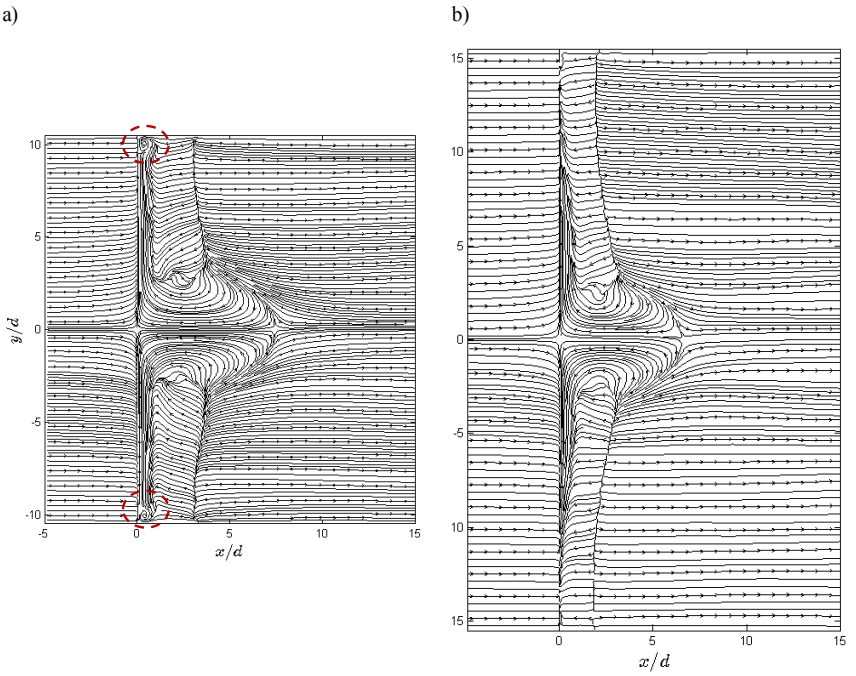

Figure 2: Streamline patterns in the horizontal (x, y)-plane through the centerline of the horizontal plate ($z/d = 0$), (a) for small (with $21d$ length in y and z directions) and (b) large (with $31d$ length in y and z directions) domain simulations.

the flow dynamics close to the vertical (and horizontal) sides. In the small-domain case, a small recirculation bubble appears next to the vertical boundaries (at $y/d = \pm 10$), whereas in the large-domain simulation, in figure 2(b), this effect is not visible. For the large domain simulation, the secondary flow is negligible close to the computational boundaries and at the outer branches the results are similar to a single flat plate as shown by Dadmarzi et al.[6]. Therefore we can say that the large domain results are comparable with flow past a single cross with infinitely long branches. Based on the results shown in figure 2, it is likely to believe that results obtained using an even larger domain, say 20d x 41d x 41d, will only be marginally different from those in figure 2(b).

The spanwise distribution of the base suction coefficient along the center-line of one of the horizontal branches from two simulations[5, 6] compared with the experimental data from Zdravkovich[2], Donoso et al.[4], Fox and Toy[3] are presented in figure 3. As the figure shows, the base suction coefficient in both simulations with the small and the large computational domain follow the trend of the experimental results qualitatively.

In the intersection region ($|y/d| < 2$) with suppressed vortex shedding, the base suction pressure coefficient has its lowest value. By moving away from the intersection region up to $y/d = 3$, $-(\bar{C_P})$ increases and reaches its local maximum. In the intersection region, the base suction pressure is almost the same for the both domains, they differ as we approach the maxima ($y/d \sim 3$). The local peak at $y/d = 3$ obtained from the simulation with the large domain, is higher than the value obtained with the small domain. After passing the peak in the large domain, the base suction pressure approaches the value for a single flat plate close to the boundaries, as shown by Dadmarzi et al.[6] in their figure 8 (b). On the contrary, in the small domain the suction pressure decreases continuously until the side boundary of the domain. The lower value of the base suction pressure might be associated with the presence of the secondary flow along the whole span of the plates.

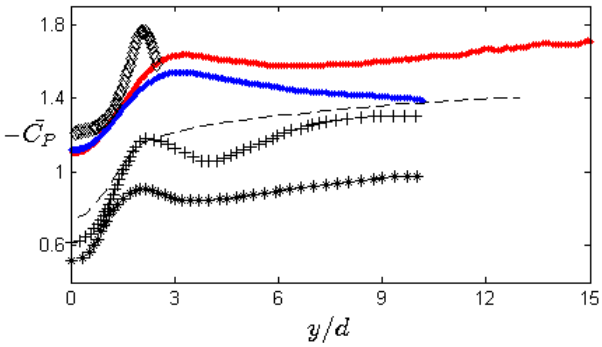

Figure 3: Spanwise base suction coefficient along the center-line of one half of the horizontal plate. The blue line and the red line show DNS results from the small and the large domain simulation, respectively. Experimental data from Zdravkovich[2]: $\diamond$, $Re = 9.4 \times 10^4$, for intersecting circular cylinders; Donoso et al.[4]: –, for intersecting plates; Fox and Toy[3]: *, $Re = 2 \times 10^4$, for intersecting circular cylinders; Fox and Toy[3]: +, $Re = 2 \times 10^4$, for intersecting square cylinders, are also shown.

The time mean streamwise velocity U/U_0 profile along the wake centerline at the intersection and the outer branches for both the small[5] and the large domains[6], is shown in figure 4. The recirculation length at the intersection of the small domain simulation exceeds $7.5d$ with the largest velocity defect of about $0.80U_0$. However, for the large domain, the recirculation length is about $6.5d$ with maximum velocity defect $0.85U_0$. This is consistent with the observed streamline patterns in figure 2. The mean streamwise velocity trend remains the same, i.e. smaller recirculation length and larger velocity defect for the large domain compared to the small domain simulation, along the branches until close to the side boundaries (dashed-dotted lines in figure 4). At the outer branches in the small domain[5], a larger recirculation bubble with slightly lower primary shedding frequency ($0.162U_0/d$) compared to the large domain[6] (i.e. $0.165U_0/d$), is observed.

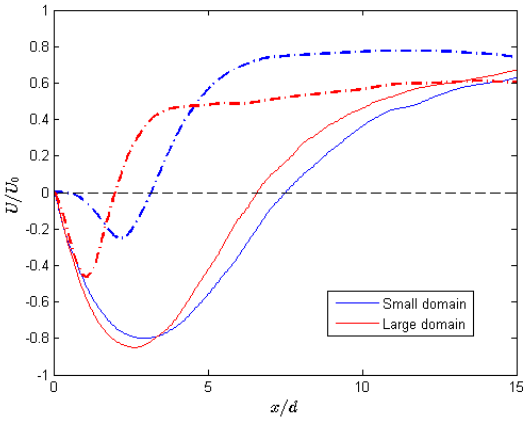

Figure 4: Evolution of the time-mean streamwise velocity with streamwise position. The blue and red solid lines show U/U_0 along the intersection bubble in the small and the large domain simulations respectively. The blue and the red dashed-dotted lines show U/U_0 along the wake centerline at the outer branches, $1.5d$ distance from the side boundaries, in the small and the large domain simulations, respectively.

Figure 5 shows the time-mean spanwise velocity V/U_0 along the wake centerline a short distance from the intersection ($y/d = 2d$) as well as $1.5d$ from the side boundaries in the small and the large domain simulations[5, 6]. As the figure shows, the secondary mean flow is stronger closest to the intersection and then decreases as we approach the boundaries. The spanwise velocity in the intersection region of the large domain simulation has slightly larger values compared to the small domain one. Close to the boundary, the spanwise velocity in the small domain still has a value about 10% of the free-stream velocity U_0 while the corresponding value in the large domain simulation is almost zero.

Figure 6 shows the streamwise variation of variance of the fluctuating velocity components (figure 6(a,c,d)) and the mean fluctuating kinetic energy (figure 6(b)) next to the corner of the intersecting plates, where only incoherent motions contribute to the velocity fluctuations. These data are taken at $y = z = 1.2d$ on the diagonal $z = y$ in the cross-sectional plane. As mentioned by Dadmarzi et al.[6], along the bisector $z = y$ the primary production of $\overline{u^2}$ along the vertical branch becomes equally important as the primary production along the horizontal branch and $\overline{u^2}$ attains its maximum value. It is noteworthy to mention that the peak value in the $\overline{u^2}$ profiles is at the same x-position in both simulations and it is about twice the peak values in the $\overline{v^2}$ and $\overline{w^2}$ profiles. The trend of the variation of the velocity fluctuations and thereby also of the mean fluctuating kinetic energy, is similar for the small and the large domain simulations. However, the values corresponding to the large domain are larger. The spanwise and cross stream ve-

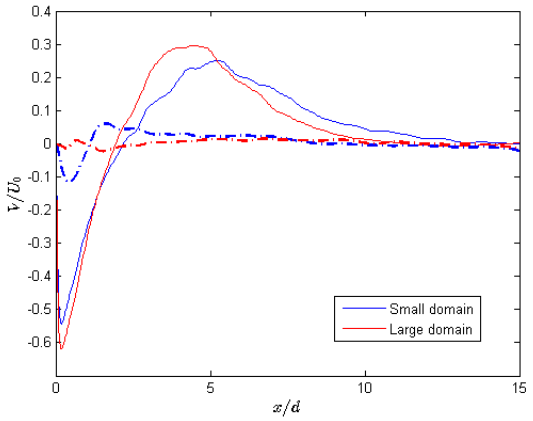

Figure 5: Variation of the time-mean spanwise velocity (V/U_0) with streamwise position. The blue and the red solid lines show V/U_0 along the wake centerline $2d$ from the intersection ($y/d = 2$) in the small and the large domain simulations, respectively. The blue and red dashed-dotted lines show V/U_0 along wake centerline at the outer branches, $1.5d$ from the side boundaries, in the small and the large domain simulations, respectively.

locity fluctuation components are almost identical due to the symmetry of the flow about the intersection. The shift in the x-position of maxima in $\overline{v^2}$ and $\overline{w^2}$ curves in the small domain compared to the large domain might be associated with the prolongation of the recirculation length in the intersection of the small domain, as seen in figure 2.

4 Conclusion

The results of two DNS studies of the wake behind a cross-plate configuration at Re = 1000 with different computational domain sizes were compared. The spanwise base pressure gradient indicated the existence of secondary flows ventilated from the intersection region towards the branches. The effect of the free-slip condition at the sides as well as top and bottom boundaries, with respect to presence of the secondary flow, was demonstrated. The base pressure and mean fluctuating kinetic energy were shown for the two computational set-ups and their differences were discussed. Although a spanwise plate length $21d$ might at first sight seem appropriate, the present comparative study showed that the free-slip boundary conditions had an unexpectedly large influence on the computed wake flow characteristics. However, by extending the plate lengths to $31d$, these adverse effects were eliminated and the cross-configuration mimicked infinitely long crossing plates.

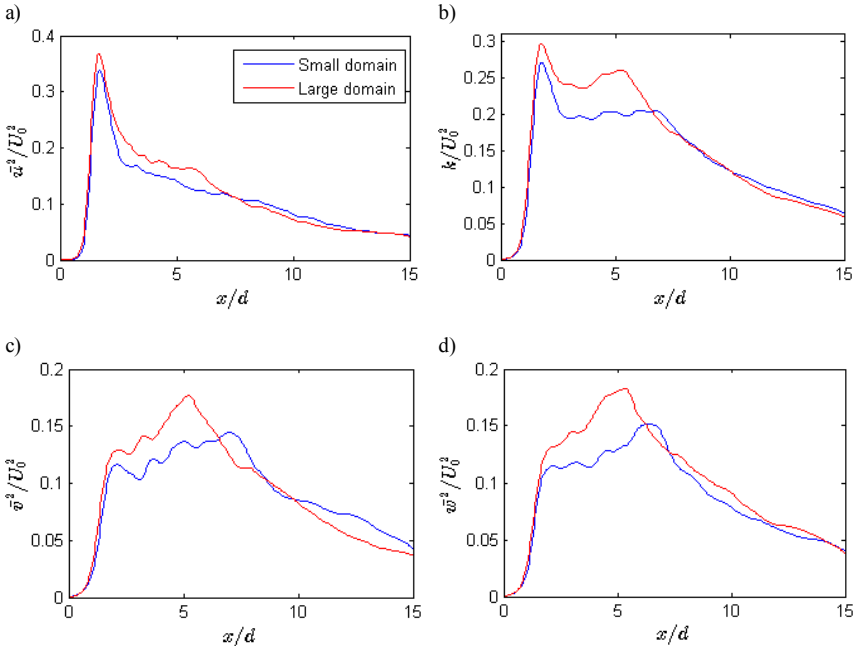

Figure 6: Streamwise variation of (a) $u^2(U_0^2)$, (b) $k(U_0^2)$, (c) $v^2(U_0^2)$ and (d) $w^2(U_0^2)$ close to the intersection corner at $y/d = z/d = 1.2$.

Acknowledgement

This work has received support from The Research Council of Norway (Program for Supercomputing) through a grant of computing time. The first author is the recipient of a research fellowship offered by The Research Council of Norway.

REFERENCES

[1] Osaka, H., Nakamura, I., Yamada, H., Kuwata, Y., and Kageyama, Y.. *The Structure of a Turbulent Wake behind a Cruciform Circular Cylinder: 1st Report, The Mean Velocity Field.*. Bulletin of JSME 26 (213): 356−363 (1983).

[2] Zdravkovich, M. M. *Flow Around Two Intersecting Circular Cylinders*. Journal of Fluids Engineering 107 (4): 507−511 (1985).

[3] Fox, T. A., and N. Toy. *Wind Effects on Structural Intersections*. Journal of Wind Engineering and Industrial Aerodynamics 34 (1): 27−44 (1990).

[4] Donoso, J. A. and Hillier, R. and Yeung, C. K. *The effect of strong three-dimensional disturbance on vortex shedding*. Journal of Wind Engineering and Industrial Aerodynamics 11 (1): 381−392 (1983).

[5] Dadmarzi, F. H. and Narasimhamurthy, V. D. and Andersson, H. I. and Pettersen, B. *Direct numerical simulation of turbulent wake behind two intersecting plates*. Begell house Inc. doi:10.1615/ICHMT.2012.ProcSevIntSympTurbHeatTransfPal.1620 (2012).

[6] Dadmarzi, F. H. and Narasimhamurthy, V. D. and Andersson, H. I. and Pettersen, B. *Turbulent Wake behind Two Intersecting Flat Plates*. International Journal of Heat and Fluid Flow 62, Part B: 482−498 (2016).

[7] Manhart, M. *A Zonal Grid Algorithm for DNS of Turbulent Boundary Layers*. Computers and Fluids 33 (3): 435−461 (2004).

[8] Peller, N., Duc, A.L., Tremblay, F. and Manhart, M. *High-Order Stable Interpolations for Immersed Boundary Methods*. International Journal for Numerical Methods in Fluids 52 (11): 1175−1193(2006).

9. National Conference on Computational Mechanics
MekIT'17
B. Skallerud and H I Andersson (Eds)

ENERGY PRESERVING MOVING MESH METHODS APPLIED TO THE BBM EQUATION

SØLVE EIDNES AND TORBJØRN RINGHOLM

Department of Mathematical Sciences
Norwegian University of Science and Technology
N–7491 Trondheim, Norway
Corresponding author: Sølve Eidnes, e-mail: solve.eidnes@ntnu.no

Key words: Energy preserving methods, Partition of unity method, Adaptive methods, Moving Mesh Method, Benjamin–Bona–Mahony equation

Abstract. Energy preserving numerical methods for a certain class of PDEs are derived, applying the partition of unity method. The methods are extended to also be applicable in combination with moving mesh methods by the rezoning approach. These energy preserving moving mesh methods are then applied to the Benjamin–Bona–Mahony equation, resulting in schemes that exactly preserve an approximation to one of the Hamiltonians of the system. Numerical experiments that demonstrate the advantages of the methods are presented.

1 INTRODUCTION

Numerical solutions of differential equations by standard methods will typically not inherit invariant properties from the original, continuous problem. Since the energy-preserving methods of Courant, Friedrichs and Lewy were introduced in [1], the development of conservative methods has garnered much interest and considerable research, surveyed in [2] up to the early 1990s. In some important cases, conservation properties can be used to ensure numerical stability or existence and uniqueness of the numerical solution. In other cases, the conservation of one or more invariants can be of importance in its own right. In addition, as noted in [3], one may expect that when properties of the continuous dynamical system are inherited by the discrete dynamical system, the numerical solution can be more accurate, especially over large time intervals.

The discrete gradient methods for ordinary differential equations (ODEs), usually attributed to Gonzalez [4], are methods that preserve first integrals exactly. Since the late 1990s, a number of researchers have worked on extending this theory to create a counterpart for partial differential equations (PDEs), see e.g. [5, 6]. Such methods, which are either called discrete variational derivative methods or discrete gradient methods for

PDEs, aim at preserving some discrete approximation of a first integral which is preserved by the continuous system. Up to very recently, the schemes presented have typically been based on a finite difference approach, and exclusively on fixed, uniform grids. Two different discrete variational derivative methods on fixed, non-uniform grids were presented by Yaguchi, Matsuo and Sugihara in [7, 8]. In [9], Miyatake and Matsuo introduce integral preserving methods on adaptive grids for certain classes of PDEs. Eidnes, Owren and Ringholm presented in [10] a general approach to extending the theory of discrete variational derivative methods, or discrete gradient methods for PDEs, to adaptive grids, using either a finite difference approach, or the partition of unity method, which can be seen as a generalization of the finite element method.

In this paper, we present an application of the approach introduced in [10] to the Benjamin–Bona–Mahony (BBM) equation, also called the regularized long wave equation in the literature. Although what we present here is a finite element method, the theory can be easily applied in a finite difference setting. Previously, there have been developed integral preserving methods for this equation [11], as well as adaptive moving mesh methods [12], but the schemes we are to present here are, to our knowledge, the first combining these properties. In fact, in [12] it is noted that combining integral preservation with adaptivity is an interesting topic for further research.

2 THE DISCRETE GRADIENT METHODS FOR PDEs

We give a quick survey of the discrete gradient methods for PDEs, and present an approach to the spatial discretization by the partition of unity method (PUM).

2.1 Problem statement

Consider a PDE of the form

$$u_t = f(\mathbf{x}, u^J), \qquad \mathbf{x} \in \Omega \subseteq \mathbb{R}^d, \quad u \in \mathcal{B} \subseteq L^2, \tag{1}$$

where u^J denotes u itself and its partial derivatives of any order with respect to the spatial variables $x_1, ..., x_d$, and where we assume that $\mathcal{B}$ is sufficiently regular to allow all operations used in the following.

We define a *first integral* of (1) to be a functional $\mathcal{I}[u]$ satisfying

$$\left\langle \frac{\delta \mathcal{I}}{\delta u}[u], f(\mathbf{x}, u^J) \right\rangle_{L^2} = 0, \quad \forall u \in \mathcal{B},$$

recalling that the *variational derivative* $\frac{\delta \mathcal{I}}{\delta u}[u]$ is defined as the function satisfying

$$\left\langle \frac{\delta \mathcal{I}}{\delta u}[u], v \right\rangle_{L^2} = \left. \frac{\mathrm{d}}{\mathrm{d}\epsilon} \right|_{\epsilon=0} \mathcal{I}[u + \epsilon v] \quad \forall v \in \mathcal{B}.$$

This means that $\mathcal{I}[u]$ is preserved over time by (1), since

$$\frac{\mathrm{d}\mathcal{I}}{\mathrm{d}t} = \left\langle \frac{\delta \mathcal{I}}{\delta u}[u], \frac{\partial u}{\partial t} \right\rangle_{L^2} = 0.$$

Furthermore, we may observe that if there exists some operator $S(\mathbf{x}, u^J)$, skew-symmetric with respect to the L^2 inner product, such that

$$f(\mathbf{x}, u^J) = S(\mathbf{x}, u^J)\frac{\delta \mathcal{I}}{\delta u}[u],$$

then $\mathcal{I}[u]$ is a first integral of (1), and we can state (1) on the form

$$u_t = S(\mathbf{x}, u^J)\frac{\delta \mathcal{I}}{\delta u}[u]. \tag{2}$$

The idea behind the discrete variational derivative methods is to derive a discrete version of the PDE on the form (2), by obtaining a so-called discrete variational derivative and approximate $S(\mathbf{x}, u^J)$ by a skew-symmetric matrix, see e.g. [5].

As proven in [10], all discrete variatonal derivative methods can be expressed as discrete gradient methods on a system of ODEs obtained by discretizing (2) in space, to get a system

$$\frac{\mathrm{d}\mathbf{u}}{\mathrm{d}t} = S(\mathbf{u})\nabla I(\mathbf{u}), \tag{3}$$

where $S(\mathbf{u})$ is a skew-symmetric matrix. The discrete gradient methods for such a system of ODEs preserve the first integral $I(\mathbf{u})$ [13]. These numerical methods are given by

$$\frac{\mathbf{u}^{n+1} - \mathbf{u}^n}{\Delta t} = \bar{S}(\mathbf{u}^n, \mathbf{u}^{n+1})\overline{\nabla} I(\mathbf{u}^n, \mathbf{u}^{n+1}),$$

where $\bar{S}(\mathbf{u}^n, \mathbf{u}^{n+1})$ is a consistent skew-symmetric time-discrete approximation to $S(\mathbf{u})$ and $\overline{\nabla} I(\mathbf{v}, \mathbf{u})$ is a discrete gradient of $I(\mathbf{u})$, defined as a function satisfying

$$(\overline{\nabla} I(\mathbf{v}, \mathbf{u}))^T(\mathbf{u} - \mathbf{v}) = I(\mathbf{u}) - I(\mathbf{v}),$$
$$\overline{\nabla} I(\mathbf{u}, \mathbf{u}) = \nabla I(\mathbf{u}).$$

There are many possible choices of discrete gradients. For the numerical experiments in this note, we will use the Average Vector Field (AVF) discrete gradient [6], given by

$$\overline{\nabla} I(\mathbf{v}, \mathbf{u}) = \int_0^1 \nabla I(\xi\mathbf{u} + (1-\xi)\mathbf{v})\mathrm{d}\xi,$$

Note that when discretizing the system (2) in space, we do so by finding a discrete approximation $\mathcal{I}_\mathbf{p}$ to the integral $\mathcal{I}$, and define an energy preserving method to be a method preserving this approximation.

2.2 Partition of unity method on a fixed mesh

The partition of unity method is a generalization of the finite element method (FEM). Stating a weak form of (2), the problem consists of finding $u \in \mathcal{B}$ such that

$$\langle u_t, v\rangle_{L^2} = \left\langle S(\mathbf{x}, u^J)\frac{\delta \mathcal{I}}{\delta u}[u], v \right\rangle_{L^2} = -\left\langle \frac{\delta \mathcal{I}}{\delta u}[u], S(\mathbf{x}, u^J)v \right\rangle_{L^2} \quad \forall v \in \mathcal{B}.$$

We define an approximation to u by

$$u^h(x,t) = \sum_{i=0}^{M} u_i(t)\varphi_i(x),$$

where the test functions $\varphi_i(x)$ span a finite-dimensional subspace $\mathcal{B}^h \subseteq \mathcal{B}$. Referring to [10] for details, we then obtain the Galerkin form of the problem: Find $u_i(t), i = 0, \ldots, M$, such that

$$\sum_{i=0}^{M} \frac{\mathrm{d}u_i}{\mathrm{d}t}\langle \varphi_i, \varphi_j\rangle_{L^2} = -\sum_{i=0}^{M} w_i(\mathbf{u})\left\langle \varphi_i, S(\mathbf{x}, u^{h,J})\varphi_j\right\rangle_{L^2} \quad \forall j \in \{0, ..., M\},$$

where, with $A_{ij} = \langle \varphi_i, \varphi_j\rangle_{L^2}$,

$$\mathbf{w}(\mathbf{u}) = A^{-1}\nabla \mathcal{I}_{\mathbf{p}}(\mathbf{u}).$$

We end up with an ODE for the coefficients u_i:

$$\frac{\mathrm{d}\mathbf{u}}{\mathrm{d}t} = S_{\mathbf{p}}(\mathbf{u})\nabla \mathcal{I}_{\mathbf{p}}(\mathbf{u}). \tag{4}$$

Here, $S_{\mathbf{p}}(\mathbf{u}) = -A^{-1}B(\mathbf{u})A^{-1}$ is a skew-symmetric matrix, with $B(\mathbf{u})$ given by $B(\mathbf{u})_{ji} = \left\langle \varphi_i, S(\mathbf{x}, u^{h,J})\varphi_j\right\rangle_{L^2}$, and the system is thereby of the form (3). Then, the scheme

$$\frac{\mathbf{u}^{n+1} - \mathbf{u}^n}{\Delta t} = S_{\mathbf{p}}(\mathbf{u}^n, \mathbf{u}^{n+1})\overline{\nabla}\mathcal{I}_{\mathbf{p}}(\mathbf{u}^n, \mathbf{u}^{n+1}).$$

will preserve the approximated first integral $\mathcal{I}_{\mathbf{p}}$ in the sense that $\mathcal{I}_{\mathbf{p}}(\mathbf{u}^{n+1}) = \mathcal{I}_{\mathbf{p}}(\mathbf{u}^n)$.

3 ADAPTIVE SCHEMES

The primary motivation for using an adaptive mesh is usually to increase accuracy while keeping computational cost low, by improving discretization locally. Such methods are typically useful for problems with e.g. traveling wave solutions and boundary layers. The different strategies for adaptive meshes can be classified into two main groups [14]: The quasi-Lagrange approach involves coupling the evolution of the mesh with the PDE, and then solving the problems simultaneously; The rezoning approach consists of calculating the function values and mesh points in an intermittent fashion. Our method can be coupled with any adaptive mesh strategy utilizing the latter approach.

3.1 Adaptive discrete gradient methods

Let $\mathbf{p}^n$, $\mathbf{u}^n$, $\mathbf{p}^{n+1}$, and $\mathbf{u}^{n+1}$ denote the discretization parameters and the numerical values obtained at the current time step and next time step, respectively. Note that we now alter the notion of a preserved first integral further, to requiring that $\mathcal{I}_{\mathbf{p}^{n+1}}(\mathbf{u}^{n+1}) = \mathcal{I}_{\mathbf{p}^n}(\mathbf{u}^n)$. The idea behind our approach is to find $\mathbf{p}^{n+1}$ based on $\mathbf{u}^n$ and $\mathbf{p}^n$, transfer $\mathbf{u}^n$ to $\mathbf{p}^{n+1}$ to obtain $\hat{\mathbf{u}}$, and then use $\hat{\mathbf{u}}$ to propagate in time to get $\mathbf{u}^{n+1}$. If the transfer operation between the meshes is preserving, i.e. if $\mathcal{I}_{\mathbf{p}^{n+1}}(\hat{\mathbf{u}}) = \mathcal{I}_{\mathbf{p}^n}(\mathbf{u}^n)$, then the next time step can be taken with the discrete gradient method for static meshes. If, however, non-preserving transfer is used, corrections are needed in order to get a numerical scheme. We introduce in [10] the scheme

$$\mathbf{u}^{n+1} = \hat{\mathbf{u}} - \frac{(\mathcal{I}_{\mathbf{p}^{n+1}}(\hat{\mathbf{u}}) - \mathcal{I}_{\mathbf{p}^n}(\mathbf{u}^n))\mathbf{z}}{\left\langle \overline{\nabla}\mathcal{I}_{\mathbf{p}^{n+1}}(\hat{\mathbf{u}}, \mathbf{u}^{n+1}), \mathbf{z} \right\rangle} + \Delta t S_{\mathbf{p}^{n+1}}(\hat{\mathbf{u}}, \mathbf{u}^{n+1}) \overline{\nabla}\mathcal{I}_{\mathbf{p}^{n+1}}(\hat{\mathbf{u}}, \mathbf{u}^{n+1}), \tag{5}$$

where $\mathbf{z}$ is a vector which should be chosen so as to obtain a minimal correction, and such that $\langle \overline{\nabla}\mathcal{I}_{\mathbf{p}^{n+1}}(\hat{\mathbf{u}}, \mathbf{u}^{n+1}), \mathbf{z} \rangle \neq 0$. In the numerical experiments to follow, we have used $\mathbf{z} = \overline{\nabla}\mathcal{I}_{\mathbf{p}^{n+1}}(\hat{\mathbf{u}}, \mathbf{u}^{n+1})$.

A preserving transfer can by obtained using the method of Lagrange multipliers. Depending on whether r- p- or h-refinement (or a combination) is used between time steps, we expect the shape and/or number of basis functions to change. See e.g. [14] or [15] for examples of how the basis may change through adaptivity. Denote by $\mathcal{B}^h = \text{span}\{\varphi_i\}_{i=0}^{M}$ the trial space from the current time step and by $\hat{\mathcal{B}}^h = \text{span}\{\hat{\varphi}_i\}_{i=0}^{\hat{M}}$ the trial space for the next time step, and note that in general, $M \neq \hat{M}$. We wish to transfer the approximation u^h from $\mathcal{B}^h$ to $\hat{\mathcal{B}}^h$, obtaining an approximation $\hat{u}^h$, while conserving the first integral, i.e. $\mathcal{I}[u^h] = \mathcal{I}[\hat{u}^h]$. This can be formulated as a constrained minimization problem:

$$\min_{\hat{u}^h \in \hat{\mathcal{B}}^h} ||\hat{u}^h - u^h||_{L^2}^2 \quad \text{s.t.} \quad \mathcal{I}[\hat{u}^h] = \mathcal{I}[u^h]. \tag{6}$$

Observe that

$$\begin{aligned} ||\hat{u}^h - u^h||_{L^2}^2 &= \sum_{i=0}^{\hat{M}} \sum_{j=0}^{\hat{M}} \hat{u}_i \hat{u}_j \hat{A}_{ij} - 2 \sum_{i=0}^{\hat{M}} \sum_{j=0}^{M} \hat{u}_i u_j^n C_{ij} + \sum_{i=0}^{M} \sum_{i=0}^{M} u_i^n u_j^n A_{ij} \\ &= \hat{\mathbf{u}}^T \hat{A} \hat{\mathbf{u}} - 2\hat{\mathbf{u}}^T C \mathbf{u}^n + \mathbf{u}^n A \mathbf{u}^n, \end{aligned}$$

where $A_{ij} = \langle \varphi_i, \varphi_j \rangle_{L^2}$, $\hat{A}_{ij} = \langle \hat{\varphi}_i, \hat{\varphi}_j \rangle_{L^2}$ and $C_{ij} = \langle \hat{\varphi}_i, \varphi_j \rangle_{L^2}$. The problem (6) can thus be reformulated as

$$\min_{\hat{\mathbf{u}} \in \mathbb{R}^{\hat{M}+1}} \hat{\mathbf{u}}^T \hat{A} \hat{\mathbf{u}} - 2\hat{\mathbf{u}}^T C \mathbf{u}^n + \mathbf{u}^n A \mathbf{u}^n \quad \text{s.t.} \quad \mathcal{I}_{\mathbf{p}^{n+1}}(\hat{\mathbf{u}}) - \mathcal{I}_{\mathbf{p}^n}(\mathbf{u}^n) = 0.$$

This is a quadratic minimization problem with one nonlinear equality constraint, for which the solution $\hat{\mathbf{u}}$ is the solution of the nonlinear system of equations

$$\begin{aligned} \hat{A}\hat{\mathbf{u}} - C\mathbf{u}^n - \lambda \nabla \mathcal{I}_{\mathbf{p}^{n+1}}(\hat{\mathbf{u}}) &= 0 \\ \mathcal{I}_{\mathbf{p}^{n+1}}(\hat{\mathbf{u}}) - \mathcal{I}_{\mathbf{p}^n}(\mathbf{u}^n) &= 0, \end{aligned}$$

which can be solved numerically using a suitable nonlinear solver.

4 ADAPTIVE ENERGY PRESERVING SCHEMES FOR THE BBM EQUATION

4.1 The BBM equation

The BBM equation was introduced by Peregrine [16], and later studied by Benjamin et al. [17] as a model for small amplitude long waves on the surface of water in a channel. Conservative finite difference schemes for the BBM equation were proposed in [18] and [11], the latter being a discrete gradient method on fixed grids. A moving mesh FEM scheme employing a quasi-Lagrange approach is presented by Lu, Huang and Qiu in [12], which we also refer to for a more extensive list of references to the existing numerical schemes for the BBM equation.

Consider now an initial-boundary value problem of the one-dimensional BBM equation with periodic boundary conditions,

$$u_t - u_{xxt} + u_x + uu_x = 0, \qquad x \in [-L, L], \quad t \in (0, T] \tag{7}$$

$$u(x, 0) = u_0(x), \qquad x \in [-L, L] \tag{8}$$

$$u(-L, t) = u(L, t), \qquad t \in (0, T]. \tag{9}$$

By introducing the new variable $m(x,t) := u(x,t) - u_{xx}(x,t)$, equation (7) can be rewritten on the form (2) as

$$m_t = \mathcal{S}(m)\frac{\delta \mathcal{H}}{\delta m},$$

for two different pairs of an antisymmetric differential operator $\mathcal{S}(m)$ and a Hamiltonian $\mathcal{H}[m]$:

$$\begin{aligned} \mathcal{S}^1(m) &= -(\frac{2}{3}u + 1)\partial_x - \frac{1}{3}u_x, \\ \mathcal{H}^1[m] &= \frac{1}{2}\int (u^2 + u_x^2)\mathrm{d}x, \end{aligned}$$

and

$$\begin{aligned} \mathcal{S}^2(m) &= -\partial_x + \partial_{xxx}, \\ \mathcal{H}^2[m] &= \frac{1}{2}\int (u^2 + \frac{1}{3}u^3)\mathrm{d}x. \end{aligned}$$

4.2 Discrete schemes

We apply the PUM approach to create numerical schemes which preserve an approximation to either $\mathcal{H}^1[m]$ or $\mathcal{H}^2[m]$, splitting $\Omega := [-L, L]$ into M elements $\{[x_i, x_{i+1}]\}_{i=0}^{M-1}$. Defining the matrices A and E by their components

$$A_{ij} = \int_\Omega \varphi_i \varphi_j \mathrm{d}x \quad \text{and} \quad E_{ij} = \int_\Omega \varphi_{i,x} \varphi_{j,x} \mathrm{d}x,$$

we set $\mathbf{m} = (A+E)\mathbf{u}$. Note that the matrices A and E depend on the mesh, and thus will change when adaptivity is used. We will then distinguish between matrices from different time steps by writing e.g. A^n and A^{n+1}.

Approximating u by u^h as in section 2.2, we find

$$\begin{aligned}\mathcal{H}^1_{\mathbf{p}}(\mathbf{m}) = \mathcal{H}^1[m^h] &= \frac{1}{2}\int_\Omega (u^h)^2 + (u^h_x)^2 \mathrm{d}x \\ &= \frac{1}{2}\sum_{i,j} u_i u_j \int_\Omega \varphi_i \varphi_j \mathrm{d}x + \frac{1}{2}\sum_{i,j} u_i u_j \int_\Omega \varphi_{i,x}\varphi_{j,x}\mathrm{d}x \\ &= \frac{1}{2}\mathbf{u}^{\mathrm{T}}(A+E)\mathbf{u}\end{aligned}$$

The integrals can be evaluated exactly and efficiently by considering elementwise which basis functions are supported on the element before applying Gaussian quadrature to obtain exact evaluations of the polynomial integrals. We define the matrix $B_1(\mathbf{u})$ by

$$B_1(\mathbf{u})_{ji} = -\frac{2}{3}\sum_{k=0}^{M-1} u_k \int_\Omega \varphi_i \varphi_{j,x}\varphi_k \mathrm{d}x - \int_\Omega \varphi_i \varphi_{j,x}\mathrm{d}x - \frac{1}{3}\sum_{k=0}^{M-1} u_k \int_\Omega \varphi_i\varphi_j\varphi_{k,x}\mathrm{d}x.$$

An approximation to the gradient of $\mathcal{H}^1$ with respect to m is found by the AVF discrete gradient

$$\begin{aligned}\overline{\nabla}\mathcal{H}^1_{\mathbf{p}}(\mathbf{m}^n, \mathbf{m}^{n+1}) = (A+E)^{-1}\overline{\nabla}\mathcal{H}^1_{\mathbf{p}}(\mathbf{u}^n, \mathbf{u}^{n+1}) &= (A+E)^{-1}\int_0^1 \nabla\mathcal{H}^1_{\mathbf{p}}(\xi\mathbf{u}^n + (1-\xi)\mathbf{u}^{n+1})\mathrm{d}\xi \\ = (A+E)^{-1}\frac{1}{2}(A+E)\left(\mathbf{u}^n + \mathbf{u}^{n+1}\right) &= \frac{1}{2}\left(\mathbf{u}^n + \mathbf{u}^{n+1}\right).\end{aligned}$$

Thus we have the required terms for forming the system (4) and applying the adaptive discrete gradient method to it. Corresponding to (5), we get the scheme

$$\begin{aligned}(A^{n+1}+E^{n+1})\left(\mathbf{u}^{n+1}-\hat{\mathbf{u}}\right) = &\frac{\left(\hat{\mathbf{u}}^{\mathrm{T}}\left(A^{n+1}+E^{n+1}\right)\hat{\mathbf{u}} - \left(\mathbf{u}^n\right)^{\mathrm{T}}\left(A^n+E^n\right)\mathbf{u}^n\right)\left(\hat{\mathbf{u}}+\mathbf{u}^{n+1}\right)}{\left(\hat{\mathbf{u}}+\mathbf{u}^{n+1}\right)^{\mathrm{T}}\left(\hat{\mathbf{u}}+\mathbf{u}^{n+1}\right)} \\ &+ \frac{\Delta t}{2}B_1^{n+1}\left(\frac{\hat{\mathbf{u}}+\mathbf{u}^{n+1}}{2}\right)\left(\hat{\mathbf{u}}+\mathbf{u}^{n+1}\right).\end{aligned}$$

Here we have chosen the skew-symmetric matrix B_1 to be a function of $\hat{\mathbf{u}}$ and $\mathbf{u}^{n+1}$, but could also have chosen e.g. $B_1(\hat{\mathbf{u}})$, resulting in a decreased computational cost at the expense of less precise results. During testing, the basis functions were chosen as piecewise cubic polynomials.

In the same manner we may obtain a scheme that preserves $\mathcal{H}^2\,[m]$. In this case

$$\begin{aligned}\mathcal{H}^2_{\mathbf{p}}(\mathbf{m}) = \mathcal{H}^2[m^h] &= \frac{1}{2}\int_\Omega (u^h)^2 + \frac{1}{3}(u^h)^3 \mathrm{d}x \\ &= \frac{1}{2}\sum_{i,j} u_i u_j \int_\Omega \varphi_i \varphi_j \mathrm{d}x + \frac{1}{6}\sum_{i,j,k} u_i u_j u_k \int_\Omega \varphi_i \varphi_j \varphi_k \mathrm{d}x.\end{aligned}$$

and

$$(B_2)_{ji} = -\int_\Omega \varphi_i \varphi_{j,x} \mathrm{d}x + \int_\Omega \varphi_i \varphi_{j,xxx} \mathrm{d}x.$$

Note that the skew-symmetric matrix B_2 is independent of $\mathbf{u}$.

Defining the tensor D by its elements

$$D_{ijk} = \int_\Omega \varphi_i \varphi_j \varphi_k \mathrm{d}x,$$

we get, with the convention of summation over repeated indices, the AVF discrete gradient with respect to $\mathbf{u}$ given by the elements

$$\left(\overline{\nabla}\mathcal{H}^2_{\mathbf{p}}(\mathbf{u}^n, \mathbf{u}^{n+1})\right)_i = \frac{1}{2}A_{ij}(u^n_j + u^{n+1}_j) + \frac{1}{6}D_{ijk}(u^n_j(u^n_k + \frac{1}{2}u^{n+1}_k) + u^{n+1}_j(\frac{1}{2}u^n_k + u^{n+1}_k)).$$

and again the discrete gradient with respect to $\mathbf{m}$ by

$$\overline{\nabla}\mathcal{H}^2_{\mathbf{p}}(\mathbf{m}^n, \mathbf{m}^{n+1}) = (A+E)^{-1}\overline{\nabla}\mathcal{H}^2_{\mathbf{p}}(\mathbf{u}^n, \mathbf{u}^{n+1}).$$

If we employ integral preserving transfer between the meshes, we get the scheme

$$\mathbf{u}^{n+1} - \hat{\mathbf{u}} = \Delta t(A+E)^{-1}B_2(A+E)^{-1}\overline{\nabla}\mathcal{H}^2_{\mathbf{p}}(\hat{\mathbf{u}}, \mathbf{u}^{n+1}),$$

where we note that $S_{\mathbf{p},2} := (A+E)^{-1}B_2(A+E)^{-1}$ is a skew-symmetric matrix. If non-preserving transfer is used, we need a correction term, as in the $\mathcal{H}^1$ scheme above. The calculation of such a term is straightforward, but we omit it here for reasons of brevity.

To approximate the third derivative in B_2, we need basis functions of at least degree three, and to guarantee skew-symmetry in B_2, these basis functions need to be C^2 on the element boundaries. This is not obtainable with regular nodal FEM basis functions, so we have instead used third order B-spline basis functions as described in [19] during testing.

5 NUMERICAL RESULTS

To demonstrate the performance of our methods, we have tested them on two one-dimensional simple problems: A soliton solution, and the interaction of two waves. We have tested our $\mathcal{H}^1$- and $\mathcal{H}^2$-preserving schemes on uniform and moving meshes, and compared the results to those obtained using the explicit midpoint method. For the transfer operation between meshes, we have used a piecewise cubic interpolation method in the $\mathcal{H}^1$ preserving scheme, and exact transfer in the $\mathcal{H}^2$ preserving scheme.

5.1 Mesh adaptivity

As noted in section 3, our methods can be coupled with any adaptive mesh strategy using the rezoning approach. For our numerical experiments, we have used a simple method for r-adaptivity based on the equidistribution principle: Splitting Ω into M intervals, we require that

$$\int_{x_i}^{x_{i+1}} \omega(x)\mathrm{d}x = \frac{1}{M}\int_{-L}^{L} \omega(x)\mathrm{d}x,$$

where the monitor function ω is a function measuring how densely grid points should lie, based on the value of u. For a general discussion on the choice of an optimal monitor function, see e.g. [20, 21]. For the problems we have studied, a generalized solution arc length monitor function proved to yield good results. This is given by

$$\omega(x) = \sqrt{1 + k^2\left(\frac{\partial u}{\partial x}(x)\right)^2}.$$

For $k = 1$, this is the usual arc length monitor function, in which case the equidistribution principle amounts to requiring that the arc length of u over each interval is equal. In applications, we only have an approximation of u, and hence ω must be approximated as well. We have applied a finite difference approximation and obtained approximately equidistributing grids using de Boor's method as explained in [14, pp. 36-38].

5.2 Soliton solution

With $u_0(x) = 3(c-1)\operatorname{sech}^2\left(\frac{1}{2}\sqrt{1-\frac{1}{c}}x\right)$, the exact solution of (7)–(9) is

$$u(x,t) = 3(c-1)\operatorname{sech}^2\left(\frac{1}{2}\sqrt{1-\frac{1}{c}}l(x,t)\right),$$

with $l(x,t) = \min_{j\in\mathbb{Z}}|x - ct + 2jL|$. This is a soliton solution which travels with a constant speed c in x-direction while maintaining its initial shape.

To evaluate the numerical solutions, we have compared them to the exact solution and calculated errors in shape and phase. The phase error is evaluated as

$$E_n^{\text{phase}} = |ct_n - x^*|,$$

where $x^* = \arg\max_x u_h(x,t_n)$, i.e. the location of the peak of the soliton in the numerical solution. The shape error is given by

$$E_n^{\text{shape}} = \left|\left|u_h(x,t_n) - u\left(x, \frac{x^*}{c}\right)\right|\right|,$$

where the peak of the exact solution is translated to match the peak of the numerical solution, and the difference in the shapes of the solitons is calculated.

The results of the numerical tests can be seen in figures 1–3. Here, M denotes the degrees of freedom used in the spatial approximation and Δt the fixed time step size. DG1 and DG1MM denotes the $\mathcal{H}^1_{\mathbf{p}}$ preserving scheme with fixed, uniform grid and adaptive grid, respectively; similary DG2 and DG2MM denotes the $\mathcal{H}^2_{\mathbf{p}}$ preserving scheme with uniform and adaptive grids.

In Figure 1 we see the relative errors in $\mathcal{H}^1_{\mathbf{p}}$ and $\mathcal{H}^2_{\mathbf{p}}$. The DG1 and DG1MM schemes are compared to schemes using the same 3rd order nodal basis functions, but the trapezoidal rule for time-stepping, denoted by TR and TRMM. Likewise, the DG2 and DG2MM schemes are compared to the IM and IMMM schemes, using B-spline basis functions and the implicit midpoint method for discretization in time. The error in $\mathcal{H}^1_{\mathbf{p}}$ is very small for the DG1 and DG1MM schemes, as expected. Also the error in $\mathcal{H}^2_{\mathbf{p}}$ is very small for the DG2 and DG2MM schemes. The order of the error is not machine precision, but is instead dictated by the precision with which the nonlinear equations in each time step is solved. We can also see that while the TR and IM schemes, with and without moving meshes, have poor conservation properties, the moving mesh DG schemes seem to preserve quite well even the integrals they are not designed to preserve.

In figures 2 and 3 we see the phase and shape errors, of our methods compared to non-moving mesh methods and non-preserving methods, respectively. The advantage of using moving meshes is clear, especially for the $\mathcal{H}^2_{\mathbf{p}}$ preserving schemes. The usefulness on integral preservation is ambiguous in this case. It seems that what we gain in precision in phase, we lose in precision in shape, and vice versa.

5.3 A small wave overtaken by a large one

A typical test problem for the BBM equation is the interaction between two solitary waves. With an initial condition

$$u_0(x) = 3(c_r - 1)\operatorname{sech}^2\left(\frac{1}{2}\sqrt{1 - \frac{1}{c_r}}(x - x_r)\right) + 3(c_s - 1)\operatorname{sech}^2\left(\frac{1}{2}\sqrt{1 - \frac{1}{c_s}}(x - x_s)\right),$$

one wave will eventually be overtaken by the other as long as $c_r \neq c_s$, i.e. if one wave is larger than the other. There is no available analytical solution for this problem. The two waves are not solitons, as the amplitudes will change a bit after the waves have interacted [22].

Solutions obtained by solving the problem with our two energy preserving schemes, giving very similar results, are plotted in Figure 4. Also, to illustrate the mesh adaptivity, we have included a plot of the mesh trajectories in Figure 6. Each line represents the trajectory of one mesh point in time, and we can see that the mesh points cluster nicely around the edges of the waves as they move.

To illustrate the performance of our methods, we have in Figure 5 compared solutions obtained by using the $\mathcal{H}^2_{\mathbf{p}}$-preserving moving mesh method with the solutions obtained

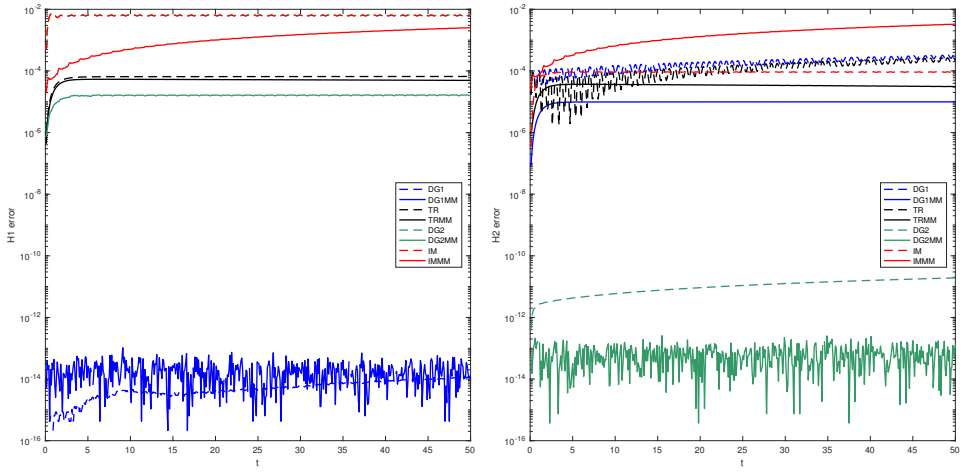

Figure 1: The soliton problem. Relative error in the approximated Hamiltonians $\mathcal{H}^1_{\mathbf{p}}$ (left) and $\mathcal{H}^2_{\mathbf{p}}$ (right) plotted as a function of time $t \in [0, 50]$. $c = 3, L = 200, \Delta t = 0.1$, $M = 200$.

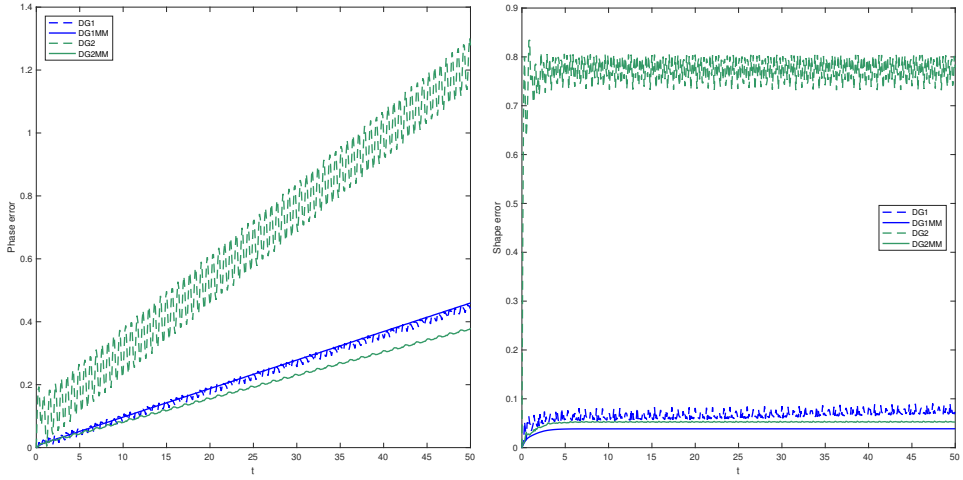

Figure 2: The soliton problem. Phase error (left) and shape error (right) as a function of time. $c = 3, L = 200, \Delta t = 0.1$, $M = 200$.

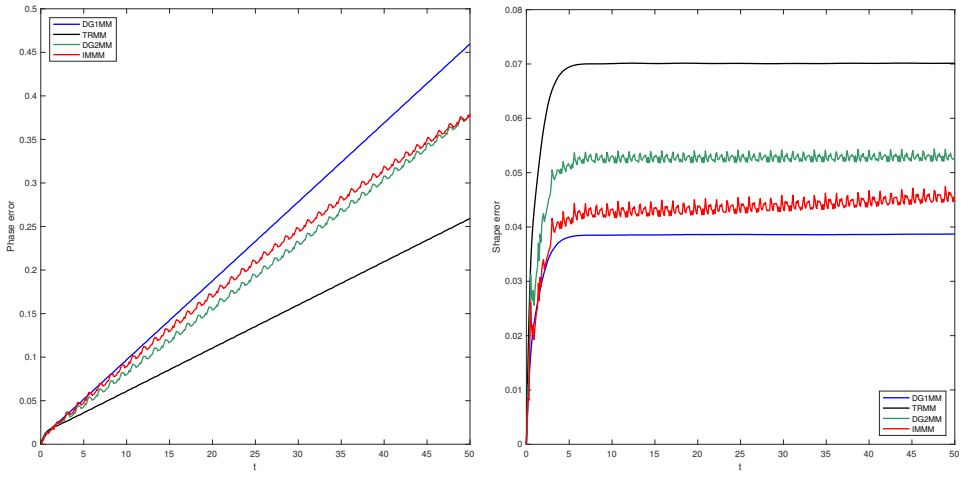

Figure 3: The soliton problem. Phase error (left) and shape error (right) as a function of time. $c = 3, L = 200, \Delta t = 0.1,\ M = 200$.

by using a fourth order Runge–Kutta method on a static mesh, with the same, and quite few, degrees of freedom. The DG2MM solution is visibly closer to the solutions in Figure 4. The non-preserving RK scheme does a worse job of preserving the amplitude and speed of the waves compared to the DG2MM scheme, and we observe unwanted oscillations.

In Figure 7 we have plotted the Hamiltonian errors for this problem. Again we see that the energy preserving schemes preserve both Hamiltonians better than the Runge–Kutta scheme, but we do also observe that the DG1 scheme preserves $\mathcal{H}_{\mathrm{P}}^2$ better than the DG1MM scheme, and vice versa for the DG2 and DG2MM schemes. Note also that an increase in the errors can be observed when the two waves interact, but that this increase is temporary.

6 CONCLUSIONS

In this paper, we have presented energy preserving schemes for a class of PDEs, first on general fixed meshes, and then on adaptive meshes. These schemes are then applied to the BBM equation, for which discrete schemes preserving two of the Hamiltonians of the problem are explicitly given.

Numerical experiments are performed, using the energy preserving moving mesh schemes on two different BBM problems: a soliton solution, and two waves interacting. Plots of the phase and shape errors illustrate how, for the given parameters, the usage of moving meshes gives improved accuracy, while the integral preservation gives comparable results to existing methods, without yielding a categorical improvement. We will remark, how-

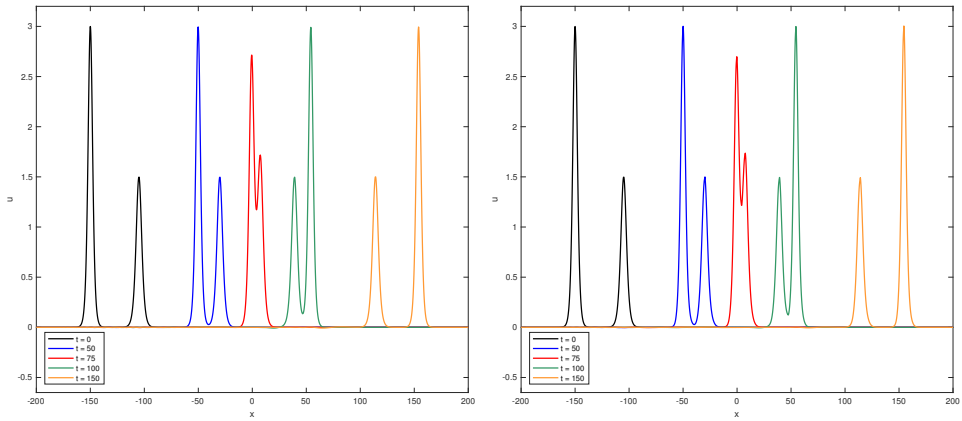

Figure 4: The interacting waves problem. Solutions at $t = \{0, 50, 75, 100, 150\}$ found by DG1MM (left) and DG2MM (right). $x_r = 150, x_s = 105, c_r = 2, c_s = 1.5, L = 200, \Delta t = 0.1$, $M = 1000$.

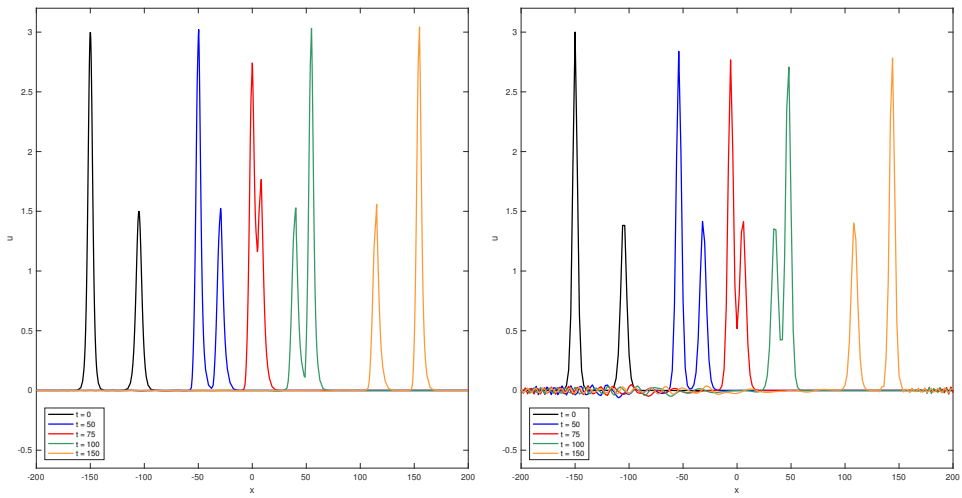

Figure 5: The interacting waves problem. Solutions at $t = \{0, 50, 75, 100, 150\}$ found by DG2MM (left) and RK (right). $x_r = 150, x_s = 105, c_r = 2, c_s = 1.5, L = 200, \Delta t = 0.1$, $M = 200$.

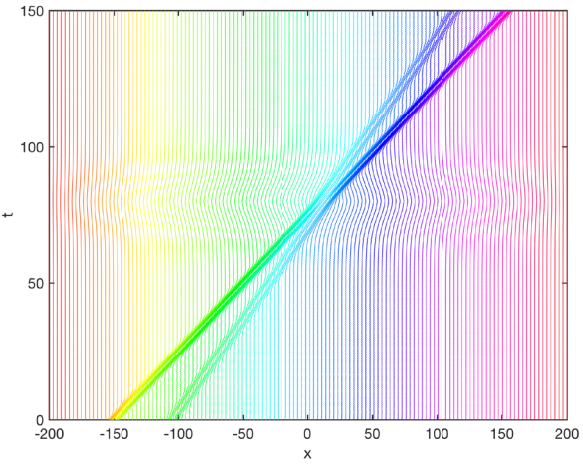

Figure 6: Mesh point trajectories in time. Each line represents one mesh point.

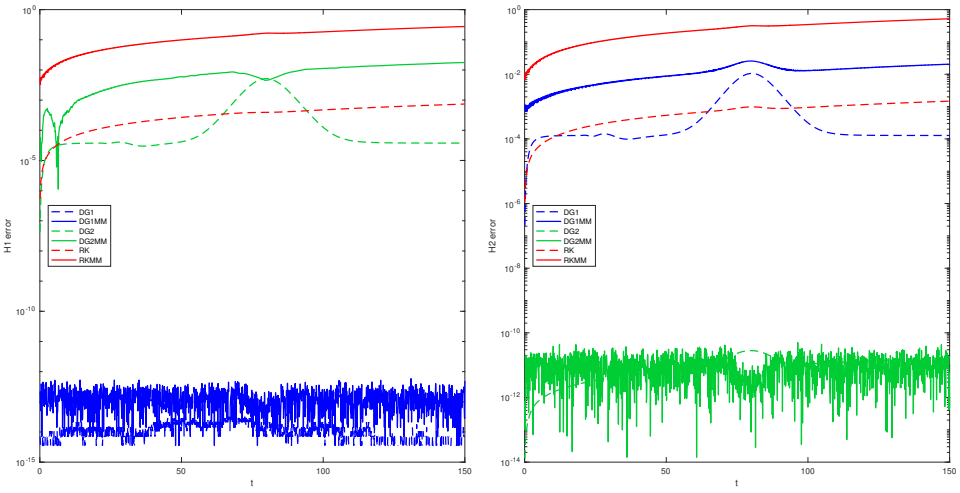

Figure 7: The interacting waves problem. Error in the approximated Hamiltonians $\mathcal{H}^1_{\mathbf{p}}$ (left) and $\mathcal{H}^2_{\mathbf{p}}$ (right) plotted as a function of time $t \in [0, 150]$. $x_r = 150, x_s = 105, c_r = 2, c_s = 1.5, L = 200, \Delta t = 0.1,\ M = 1000$.

ever, that in many cases, the preservation of a quantity such as one of the Hamiltonians in itself may be a desired property of a numerical scheme. For the two wave interaction problem, we do not have an analytical solution to compare to, but plots of the solution indicate that our schemes perform well compared to a Runge–Kutta scheme.

Although the numerical examples presented here are simple one-dimensional problems, the adaptive discrete gradient methods should also be applicable for multi-dimensional problems. This could be an interesting direction for further work, since the advantages of adaptive meshes are typically more evident when increasing the number of dimensions.

REFERENCES

[1] R. Courant, K. Friedrichs, and H. Lewy, "Über die partiellen Differenzengleichungen der mathematischen Physik," *Math. Ann.*, vol. 100, no. 1, pp. 32–74, 1928.

[2] S. Li and L. Vu-Quoc, "Finite difference calculus invariant structure of a class of algorithms for the nonlinear Klein-Gordon equation," *SIAM J. Numer. Anal.*, vol. 32, no. 6, pp. 1839–1875, 1995.

[3] E. Hairer, C. Lubich, and G. Wanner, *Geometric numerical integration*, vol. 31 of *Springer Series in Computational Mathematics*. Springer-Verlag, Berlin, second ed., 2006. Structure-preserving algorithms for ordinary differential equations.

[4] O. Gonzalez, "Time integration and discrete Hamiltonian systems," *J. Nonlinear Sci.*, vol. 6, no. 5, pp. 449–467, 1996.

[5] D. Furihata and T. Matsuo, *Discrete variational derivative method*. Chapman & Hall/CRC Numerical Analysis and Scientific Computing, CRC Press, Boca Raton, FL, 2011. A structure-preserving numerical method for partial differential equations.

[6] E. Celledoni, V. Grimm, R. I. McLachlan, D. I. McLaren, D. O'Neale, B. Owren, and G. R. W. Quispel, "Preserving energy resp. dissipation in numerical PDEs using the "average vector field" method," *J. Comput. Phys.*, vol. 231, no. 20, pp. 6770–6789, 2012.

[7] T. Yaguchi, T. Matsuo, and M. Sugihara, "An extension of the discrete variational method to nonuniform grids," *J. Comput. Phys.*, vol. 229, no. 11, pp. 4382–4423, 2010.

[8] T. Yaguchi, T. Matsuo, and M. Sugihara, "The discrete variational derivative method based on discrete differential forms," *J. Comput. Phys.*, vol. 231, no. 10, pp. 3963–3986, 2012.

[9] Y. Miyatake and T. Matsuo, "A note on the adaptive conservative/dissipative discretization for evolutionary partial differential equations," *J. Comput. Appl. Math.*, vol. 274, pp. 79–87, 2015.

[10] S. Eidnes, B. Owren, and T. Ringholm, "Adaptive energy preserving methods for partial differential equations," *arXiv preprint, arXiv:1507.02484*, 2015.

[11] D. Cohen and X. Raynaud, "Geometric finite difference schemes for the generalized hyperelastic-rod wave equation," *J. Comput. Appl. Math.*, vol. 235, no. 8, pp. 1925–1940, 2011.

[12] C. Lu, W. Huang, and J. Qiu, "An adaptive moving mesh finite element solution of the Regularized Long Wave equation," *ArXiv e-prints*, June 2016.

[13] R. I. McLachlan, G. R. W. Quispel, and N. Robidoux, "Geometric integration using discrete gradients," *R. Soc. Lond. Philos. Trans. Ser. A Math. Phys. Eng. Sci.*, vol. 357, no. 1754, pp. 1021–1045, 1999.

[14] W. Huang and R. Russell, *Adaptive Moving Mesh Methods*, vol. 174 of *Springer Series in Applied Mathematical Sciences*. Springer-Verlag, New York, 2010.

[15] I. Babuška and B. Guo, "The h, p and h-p version of the finite element method; basis theory and applications," *Advances in Engineering Software*, vol. 15, pp. 159–174, 1992.

[16] D. Peregrine, "Calculations of the development of an undular bore," *Journal of Fluid Mechanics*, vol. 25, no. 02, pp. 321–330, 1966.

[17] T. B. Benjamin, J. L. Bona, and J. J. Mahony, "Model equations for long waves in nonlinear dispersive systems," *Philos. Trans. Roy. Soc. London Ser. A*, vol. 272, no. 1220, pp. 47–78, 1972.

[18] T.-C. Wang and L.-M. Zhang, "New conservative schemes for regularized long wave equation," *Numerical Mathematics A Journal of Chinese Universities English Series*, vol. 15, no. 4, pp. 348–356, 2006.

[19] J. A. Cottrell, T. J. Hughes, and Y. Bazilevs, *Isogeometric Analysis*. Wiley, 2009.

[20] C. J. Budd, W. Huang, and R. D. Russell, "Adaptivity with moving grids," *Acta Numer.*, vol. 18, pp. 111–241, 2009.

[21] J. Blom and J. Verwer, "On the use of the arclength and curvature monitor in a moving-grid method which is based on the method of lines," tech. rep., NM-N8902, CWI, Amsterdam, 1989.

[22] W. Craig, P. Guyenne, J. Hammack, D. Henderson, and C. Sulem, "Solitary water wave interactions," *Physics of Fluids*, vol. 18, no. 5, p. 057106, 2006.

9. National Conference on Computational Mechanics
MekIT'17
B. Skallerud and H I Andersson (Eds)

IMPLEMENTATION OF NON-NEWTONIAN RHEOLOGY FOR GRANULAR FLOW SIMULATION

Petter Fornes[1,†], Hans Bihs[1] and Steinar Nordal[1]

[1]Department of Civil and Environmental Engineering
Norwegian University of Science and Technology (NTNU)
Trondheim, Norway
[†]e-mail: petter.fornes@ntnu.no

Key words: CFD, Non-Newtonian Rheology, Granular Flow, Geotechnical, REEF3D

Abstract. Landslides of the debris flow type pose a serious natural hazard. These landslides are often triggered by hydro-meteorological processes during extreme precipitation events. Debris flows usually form a dense flow composed of water and poorly graded soil particles. The propagation of these landslides greatly influences the consequences they have. The run-out of debris flows is usually simulated with depth-averaged models. These are fast to simulate due to the integration over the flow height, which reduces the problem from three to two dimensions. For the design of countermeasures resisting the pressure from the flow, it can be advantageous to use more advanced 3D numerical methods, such as computational fluid dynamics (CFD). The particle phase of debris flows has here been considered as a granular flow, and implemented as a non-Newtonian viscoplastic rheology in the open-source CFD code REEF3D. In the numerical model, the Reynolds-Averaged Navier-Stokes (RANS) equations are discretized with the fifth-order accurate Weighted Essentially Non-Oscillatory (WENO) scheme in space and with a third-order Runge-Kutta based fractional step scheme in time. The level set method used for representing the free surface handles the complex air-granular flow interface topology. The pressure gradient is modelled with Chorin's projection method for incompressible flow. The granular flow rheology includes a Coulomb frictional yield stress, increasing with the normal stress, and a viscous term that is non-linear dependent on the shear rate. The implementation has been validated using results from laboratory dam break experiments with dry sands.

1 INTRODUCTION

Debris flows and debris avalanches are landslide phenomena that can potentially cause large damages and pose a serious natural hazard [1]. A debris flow is a mix of water and poorly graded soil particles, forming a dense flow [2]. This type of landslides is often triggered by hydro-meteorological processes during extreme precipitation events, see Fig.

Figure 1: Debris flow in Hunnedalen, Norway, June 2016. [Photo: NPRA]

1. The expected increase in precipitation due to climate changes may lead to higher frequency of Norwegian debris flow events in the future. This provides the motivation for studying debris flows in the Norwegian SFI project KLIMA2050 [3], which this work is a part of.

The debris flow propagation determines a large portion of the consequences and the risk associated with the landslides. Run-out parameters include the maximum distance reached, flow velocities, thickness and distribution of deposits, as well as the interaction behavior with obstacles in the flow path [4, 5, 6]. To predict the run-out distance and to design countermeasures for reducing the consequences, a solid understanding and description of the debris flow mechanism is necessary. In engineering practice, the propagation of debris flows is usually simulated with depth-averaged models considering the debris flow as a single-phase material. These models are fast to run simulations with due to the integration over the flow height, which reduces the problem from three to two dimensions. Although neglecting variation in the velocity profile over the height reduces the accuracy of the models, they can produce sufficiently good run-out distance results. However, the complete velocity profile may be more important for interactions between the flow and structures.

For the design of countermeasures resisting the pressure from the flow, it may be necessary to use more advanced three dimensional numerical methods. With the recent increases in computer power, it is now feasible to consider methods such as Computational Fluid Dynamics (CFD). The debris flow material can also here be represented as a single-phase material, although a multiphase approach is more appropriate [7]. For the

interstitial fluid phase, consisting of water with fine particles in suspension, a viscoplastic non-Newtonian rheology may be sufficient [8]. The particle phase of debris flows can be assumed to have a non-Newtonian rheology appropriate for granular flows. In this paper, the viscoplastic Herschel-Bulkley rheology is modified to include Coulomb friction for granular flow.

2 NUMERICAL MODEL

2.1 Navier-Stokes equations

The open-source CFD code REEF3D [9] is used in this work. In REEF3D, the three-dimensional Navier-Stokes equations, which govern the behavior of viscous and incompressible fluids, are solved numerically with the finite difference method. For the conservation of mass and momentum, the code considers the continuity and Reynolds Averaged Navier-Stokes (RANS) equations:

$$\frac{\partial u_i}{\partial x_i} = 0 \tag{1}$$

$$\frac{\partial u_i}{\partial t} + u_j \frac{\partial u_i}{\partial x_j} = -\frac{1}{\rho}\frac{\partial p}{\partial x_i} + \frac{\partial}{\partial x_j}\left[(\nu + \nu_t)\left(\frac{\partial u_i}{\partial x_j} + \frac{\partial u_j}{\partial x_i}\right)\right] + g_i \tag{2}$$

where u is the velocity, ρ is the fluid density, p is the pressure, ν is the kinematic viscosity, ν_t is the eddy viscosity and g is the gravitational acceleration. On the left hand side of the RANS equations are the transient and convective velocity terms. On the right hand side are the surface and volume forces, the viscous and pressure terms, and the gravity, respectively. The Reynold stress term capturing the turbulence is modelled separately in REEF3D. However, in this paper laminar flow is considered and the eddy viscosity is set to zero.

The RANS equations are discretized in the numerical model with the fifth-order accurate Weighted Essentially Non-Oscillatory (WENO) scheme in space [10] and with a third-order Runge-Kutta based fractional step scheme in time [11].

2.2 Pressure

The pressure gradient is modelled with Chorin's projection method [12] for incompressible flow. A staggered grid is used to avoid decoupling of velocity and pressure. The momentum equation with the pressure gradient removed is solved for an intermediate velocity field u_i^*. The pressure for the new time step p^{n+1} is determined and used to correct the velocity field. In order to create divergence free flow field, the pressure needs to fulfil the following equation:

$$\frac{\partial}{\partial x_i}\left(\frac{1}{\rho\left(\phi^n\right)}\frac{\partial p^{n+1}}{\partial x_i}\right) = \frac{1}{\Delta t}\frac{\partial u_i^*}{\partial x_i} \tag{3}$$

2.3 Level set method

The level set method proposed by Osher and Sethian [13] is employed for locating the free surface. Air is modelled as a second fluid in this approach. This approach can handle the complex air-debris flow interface topology. To define the interface Γ between the two fluids, the following continuous signed distance function is used:

$$\phi(\vec{x},t)\begin{cases} >0 & \text{if } \vec{x} \in \text{phase 1} \\ =0 & \text{if } \vec{x} \in \Gamma \\ <0 & \text{if } \vec{x} \in \text{phase 2} \end{cases} \tag{4}$$

The level set function $\phi(\vec{x},t)$ is coupled to the velocity field u_j with a convection equation, and the spatial discretization is determined with the Hamilton-Jacobi WENO scheme version [14]:

$$\frac{\partial \phi}{\partial t} + u_j \frac{\partial \phi}{\partial x_j} = 0 \tag{5}$$

3 NON-NEWTONIAN RHEOLOGY

3.1 Herschel-Bulkley rheology

The non-Newtonian Herschel-Bulkley rheology has been implemented in the REEF3D CFD code [15], for the purpose of modelling the interstitial fluid phase of debris flows. The interstitial fluid consists of water with fine particles in suspension, for which the viscoplastic Herschel-Bulkley rheology can be considered appropriate [16, 17, 18].

The Herschel-Bulkley rheology has a non-linear stress relationship with the shear rate $\dot{\gamma}$ and features a yield stress τ_y. In order to have shear deformation of the material, the shear stress acting on it must exceed this yield stress. For shear stresses lower than the yield stress, the shear rate is zero. The Herschel-Bulkley rheology is defined by the following shear stress and shear rate relation:

$$\tau(\dot{\gamma}) = \tau_y + K\dot{\gamma}^n \tag{6}$$

and

$$\dot{\gamma} = \begin{cases} 0 & \text{if } \tau < \tau_y \\ \left(\frac{1}{K}(\tau - \tau_y)\right)^{\frac{1}{n}} & \text{if } \tau \geq \tau_y \end{cases} \tag{7}$$

where τ is the shear stress, $\dot{\gamma}$ is the shear rate, τ_y is the yield stress, K is the consistency parameter, n is the Herschel-Bulkley exponent. If $n > 1$ shear-thickening behavior is defined, and $n < 1$ defines shear-thinning behavior. If $n = 1$ it becomes the Bingham rheology, and if additionally $\tau_y = 0$, it becomes the Newtonian rheology.

The Herschel-Bulkley rheology is implemented in the REEF3D code as a generalized Newtonian fluid, with a non-linear shear rate dependent viscosity. The kinematic viscosity

$\nu(\dot{\gamma})$ is determined as the non-linear shear stress $\tau(\dot{\gamma})$ in Eq. 6 divided by the shear rate $\dot{\gamma}$ (and the density ρ). To prevent numerical issues related to the kinematic viscosity approaching infinity as the shear rate goes to zero, a maximum kinematic viscosity ν_0 is used for low shear rates:

$$\nu(\dot{\gamma}) = \min \begin{cases} \nu_0 \\ \left(\frac{\tau_y}{\dot{\gamma}} + K\dot{\gamma}^{n-1} \right) \frac{1}{\rho} \end{cases} \tag{8}$$

where ν is the kinematic viscosity included in Eq. 2, ν_0 is the maximum kinematic viscosity and ρ is the density. The kinematic viscosity ν is determined locally for each cell in every time step since it varies spatially and temporally, and it is considered as an isotropic property. The scalar shear rate $\dot{\gamma}$ used to calculate the viscosity is determined as the magnitude of the three-dimensional shear rate tensor $\mathbf{D}$:

$$\dot{\gamma} = \|\mathbf{D}\| = \sqrt{\frac{1}{2} \sum_{i=1}^{3} \sum_{j=1}^{3} \dot{\gamma}_{ij} \dot{\gamma}_{ij}} \tag{9}$$

The implementation of the viscosity (Eq. 8) makes the rheology bi-viscous. It results in a material that can not come to rest at a sloped angle when the flow finally slows down. Even though the viscosity is very high for low shear rates, the material will continue to flow slowly until leveling off horizontally. This is unlike depositions of landslides composed by materials with yield strength, which can support an inclined slope surface. Therefore, the flowing material will be considered as having stopped when the magnitude of velocity is several orders of magnitude lower than while propagating.

An alternative implementation to avoid infinite viscosity could be to employ a regularization parameter [19]. If so, an exponential function will be included in the yield stress term in Eq. 6, reducing it to zero for very small shear rates. This will make the shear rate dependendent viscosity function continuous, which may improve the stability. However, it will not prevent the slow deformation after depostion, and has not been considered necessary.

3.2 Granular flow rheology

Granular materials have a frictional resistance to shearing that increases with increased contact pressure between the individual particles, normally given by the Mohr-Coulomb failure criterion (Eq. 10). When granular soils are yielding, the shear stress is proportional to the effective normal stresses, which is the contact pressure between the soil grains. The internal frictional angle φ thus provides a frictional coefficient $\mu = \tan \varphi$ which determines how much shear stress the material can sustain without deforming for a given pressure. This determines for example how steep the slope angle of a pile of dry sand can be naturally.

$$\tau_y = \sigma_n' \cdot \tan \varphi + c \tag{10}$$

where τ_y is the yield shear strength, σ'_n is the effective normal stress, φ is the friction angle and c is the cohesion (low for dry granular soils).

For Eularian description of dry granular flows (or the particle phase of debris flows), modelling the granular material as a single-phase continuum, including Coulomb friction in a visco-plastic rheology can be considered. Johnson [20] proposed a Coulomb-viscous rheology for debris flows, adding the Mohr-Coulomb failure criterion (Eq. 10) as the yield strength to the Bingham rheology (Eq. 6, $n = 1$). Savage and Hutter [21] included Coulomb criterion in a depth-averaged model for dry granular flows. In the $\mu(I)$ rheology for dense granular flow by Jop et al. [22], the frictional coefficient μ is a non-linear function of the intertial number I, which is a number that depends on the shear rate and pressure. Moriguchi et al. [23] used a Coulomb-viscous rheology (Bingham with Coulomb friction for the yield strength) to back-calculate laboratory tests of dry sand dam breaks in a slope. A maximum value for the generalized viscosity was used, like in Eq. 8. Domnik et al. [24] proposed a similar Coulomb-viscoplastic model for a granular material, with a regularizition parameter included as in [25] instead of a biviscous implementation.

Here, the Herschel-Bulkley rheology (Eq. 6) is modified by including the Coulomb friction relation in Eq. 10 as the yield stress. This makes it similar to the Coulomb-viscous rheology in Moriguchi et al. [23], but also including Herschel-Bulkley exponent n makes it possible for a non-linear dependency on the shear rate. In this paper, the flowing material is assumed to be a single-phase dry sand with constant density. The effective normal stress σ'_n in the Mohr-Coulomb criterion can then be equated to the fluid pressure p (which is determined in Eq. 3 with the dry granular density). Thus, the following Coulomb Herschel-Bulkley rheology is considered:

$$\tau(\dot{\gamma}, p) = p \tan \varphi + c + K\dot{\gamma}^n \tag{11}$$

where τ is the shear stress, $\dot{\gamma}$ is the shear rate, p is the fluid pressure, φ is the dynamic friction angle of the granular material, c is cohesion, K is the consistency parameter and n is the Herschel-Bulkley exponent. This rheology is implemented in the REEF3D code like this:

$$\nu(\dot{\gamma}, p) = \min \begin{cases} \nu_0 \\ \left(\max \left[0, \frac{p \tan \varphi + c}{\dot{\gamma}} \right] + K\dot{\gamma}^{n-1} \right) \frac{1}{\rho} \end{cases} \tag{12}$$

where ν, p and $\dot{\gamma}$ are variables, determined locally in each time step, while ν_0, φ, c, ρ, K and n are material constants, given as input parameters at the start of the calculation. A max-criterion is included to ensure that the expression for the yield stress is never lower than zero, which could make the viscosity negative. That is unphysical and would also cause severe convergence problems.

For a dry sand with only compressible air in the pore spaces, the assumption $\sigma'_n = p$ is considered acceptable. For a debris flow however, the presence of interstitial pore water fluid, may complicate the situation. If considering both the water fluid phase and

the granular particle phase, an Eularian multiphase (mixture theory) approach might be suitable [26, 27]. It has been observed that interstitial pore water fluid pressure can build up during deformation, which reduces the contact stress between the particles and consequently reduces the frictional resistance of the flowing mass [28]. When there is water present, the effective normal stress can be determined as the total normal stress (pressure) minus the interstitial pore fluid pressure. The build up of so-called excess pore pressure should be considered in the rheology.

4 EXPERIMENTS

To validate the REEF3D Coulomb frictional yield stress implementation, a laboratory dam break test with dry sand by Moriguchi et al. [23] is considered here. $50kg$ of the material was placed in a box 50x30x30cm. It was released and driven only by gravity down a 180cm long, 30cm wide flume, with slope angles $\theta = 45, 50, 55, 60, 65°$. At the end of the slope, a plate with a pressure sensor measured the impact force.

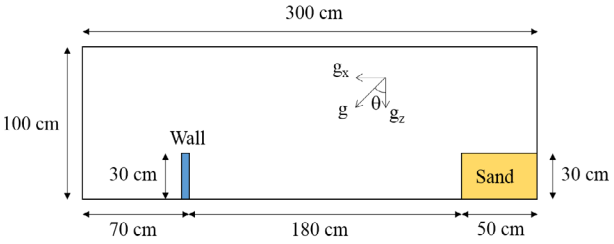

Figure 2: Model experiment dimensions

Simulation of this experiment has been done with a 2D REEF3D model (1 cell out of the plane), see Fig. 2. The calculation domain had dimensions 300x100cm and cell length was 0.25cm. This resulted in a mesh with 480000 cells. A 30cm tall, 5cm wide obstacle was placed 180cm from the 50x30cm starting sand body, representing the pressure plate. The rest of the domain was filled with air, with density $1.205kg/m^3$ and kinematic viscosity $1.41 \cdot 10^{-5}m^2/s$. The experiment simulated here was done with a slope angle θ of 45°. In the numerical model, this was modelled by giving the gravitational acceleration as $g_x = g \cdot \sin\theta$ and $g_z = g \cdot \cos\theta$.

The material properties in the numerical simulation are presenteted in Table 1. These base case values were based on the values used by Moriguchi et al. [23]. A parametric study was done to check the senstivity of the material properties included in Coulomb Herschel-Bulkley rheology; friction angle φ, cohesion c, consistency parameter K and the Herschel-Bulkley exponent n. The parameters were varied individually, values are presented in Table 2. One case was added where the friction angle was set to zero, which

means that the yield strength is equal to the cohesion. This makes it essentially the Herschel-Bulkley or Bingham ($n = 1$) rheology, without the Coulomb friction.

Table 1: Base case material properties

Material property	Unit	Base case
Density ρ	$[kg/m^3]$	1379.0
Maximum kinematic viscosity ν_0	$[m^2/s]$	1000000.0
Friction angle φ	$[^\circ]$	30.0
Cohesion c	$[Pa]$	1.0*
Consistency parameter K	$[Pa \cdot s^n]$	1.0
Herschel-Bulkley exponent n	$[-]$	1.0

*Small value assumed to avoid numerical issues

Table 2: Parametric study of material properties, parameters sets (PS)

Parameter	Unit	PS-BC	PS-φ	PS-c	PS-K	PS-n	PS-τ_y
φ	$[^\circ]$	30.0	45.0	30.0	30.0	30.0	0.0
c	$[Pa]$	1.0	1.0	1000.0	1.0	1.0	1000.0
K	$[Pa \cdot s^n]$	1.0	1.0	1.0	10.0	1.0	1.0
n	$[-]$	1.0	1.0	1.0	1.0	0.35	1.0

5 RESULTS

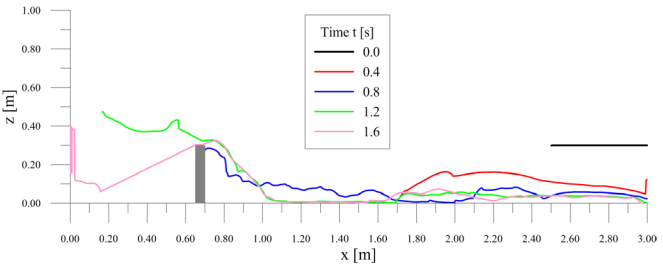

Figure 3: Base case, free surface elevation with time t [s]

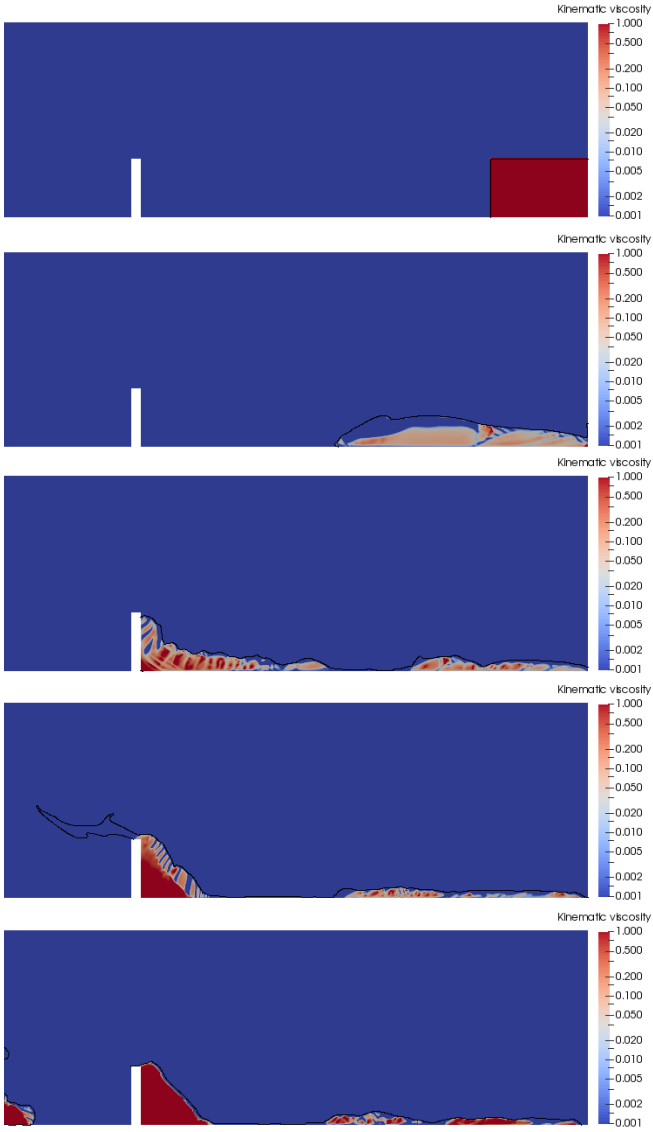

Figure 4: Base case, kinematic viscosity ν at time $t = 0.0, 0.4, 0.8, 1.2, 1.6s$

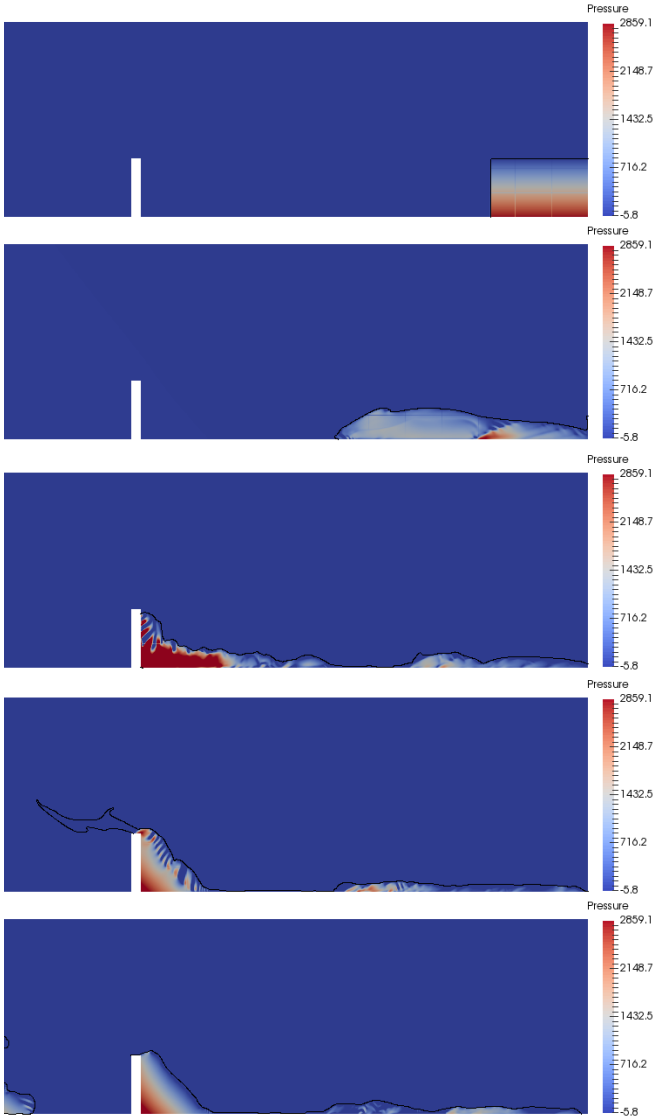

Figure 5: Base case, pressure p at time $t = 0.0, 0.4, 0.8, 1.2, 1.6s$

The results from the numerical simulations of the dam break experiments are presented

here. Fig. 3 shows the evolution of the free surface with time for the base case material properties given in Table 1. After around $0.8s$ the sand starts to flow over the wall, which was not included in the physical experiment. Compared to the experimental results in [23], the main flow behaviors observed in the laboratory was captured in the numerical simulation.

Fig. 4 shows contours of the kinematic viscosity ν, which depends on the local shear rate $\dot{\gamma}$ and the local cell pressure p. The pressure is shown in Fig. 5. Shear bands can be observed where the viscosity is low due to the locally high shear rates. Because of the coupling between pressure and velocity, this affects the pressure contours.

The pressure acting on the wall obstructing the flow is integrated, and the total horizontal forces with time is presented in Fig. 6. The figure also shows the results from the sensitivity study of the different material properties. For both cases with increased cohesion, there are large oscillations after the impact. There seems to be less spikes in the force at impact and more gradual increase when either friction angle or consistency parameter is increased. The final forces reached in all the cases have similar values as in

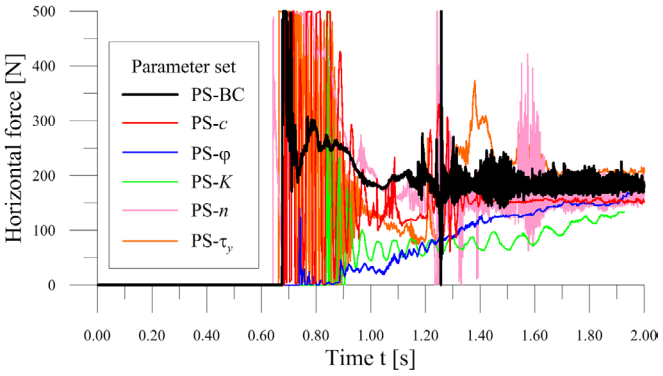

Figure 6: Horizontal forces acting on wall with time (spikes cropped at 500 N)

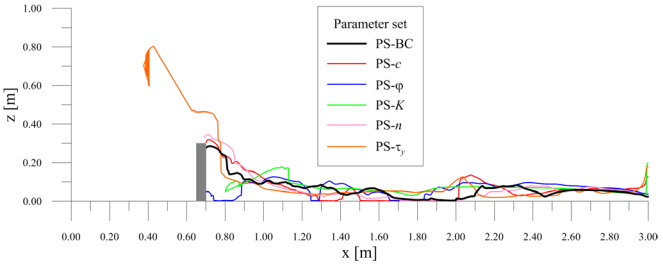

Figure 7: Parametric study, free surface elevation at time $t = 0.8s$

the original experiment, almost $200N$. There, the same extent of oscillations and spikes were not observed, however.

The effect of the individual material properties is also shown in Fig. 7, plotting the free surfaces at time $t = 0.8s$. There is little effect observed of varying the Herschel-Bulkley exponent n from 1.0 to 0.35. The latter value is appropriate for fine grain suspensions [8]. Increasing consistency parameter K increases the viscous shear stress, and increasing the friction angle φ increases the contribution from the Coulomb friction to the yield strength. For both cases, the flow is slowed slightly down, and impacts the wall later. Increasing the cohesion c also increases yield strength, but does not affect the results at $0.8s$ much. Only using increased c, with zero friction angle, makes the flow quite more mobile. Back-calculation has not been done to obtain a parameter set with better match to the experimental results. To improve the match, a higher friction angle and consistency parameter should be considered.

6 CONCLUSIONS

- A non-Newtonian granular flow rheology is implemented in the REEF3D open-source CFD code. Coulomb frictional yield stress is included in the viscoplastic Herschel-Bulkley rheology. It has been validated for laboratory dam break experiments on dry granular sand.

- The yield stress is modelled as a very high viscosity at low shear rates with the generalized Newtonian implementation. This means that even if a flowing material slows down and is practically depositioned, the deformation will never stop until resting with a horizontally levelled surface. This can be considered sufficent as long as the velocity becomes very small. To allow for deposition with a sloped surface the yield stress should be accounted for more realistically, potentially with a coupled elastoplastic and viscoplastic model.

- The implemented rheology can be appropriate for the particle phase of debris flows. However, full debris flow behavior, including the collisions between the larger sized grains, the buildup of excess pore pressure, temporal and spatial rheological changes, cannot realistically be captured with a single-phase continuum material. An Eularian multiphase CFD model may be suitable for this purpose.

REFERENCES

[1] Takahashi, T. *Debris flows: mechanics, predictions and countermeasures* (2007) Taylor & Francis, New York

[2] Iverson, R.M. The physics of debris flows. *Reviews of Geophysics* (1997) 35(3):245-296.

[3] KLIMA2050, *www.klima2050.no*

[4] Crosta, G.B., Cucchiaro, S. and Frattini, P. Validation of semi-empirical relationships for the definition of debris-flow behavior in granular materials. *Debris-Flow Hazards Mitigation: Mechanics, Prediction, and Assessment, Vols 1 and 2* (2003) 821-831.

[5] Rickenmann, D. Runout prediction methods. *Debris-flow hazards and related phenomena* (2005) Springer, 305-324.

[6] Hungr, O. Classification and terminology. *Debris-flow hazards and related phenomena* (2005) Springer, 9-23.

[7] Iverson, R.M. The debris-flow rheology myth. *Debris-Flow Hazards Mitigation: Mechanics, Prediction, and Assessment, Vols 1 and 2:* (2003) 303-314.

[8] Laigle, D. and Coussot, P. Numerical modeling of mudflows *Journal of Hydraulic Engineering-Asce* (1997) 123(7):617-623.

[9] Bihs, H., Kamath, A., Alagan Chella, M., Aggarwal, A. and Arntsen, .A. A new level set numerical wave tank with improved density interpolation for complex wave hydrodynamics. *Computers & Fluids* (2016) 140:191-208.

[10] Jiang, G.S. and Shu, C. W. Efficient implementation of weighted ENO schemes. *Journal of Computational Physics* (1996) 126(1):202-228.

[11] Shu, C.W. and Osher, S. Efficient Implementation of Essentially Non-Oscillatory Shock-Capturing Schemes. *Journal of Computational Physics* (1988) 77(2):439-471

[12] Chorin, A.J. Numerical Solution of Navier-Stokes Equations. *Mathematics of Computation* (1968) 22(104): 745-&.

[13] Osher, S. and Sethian, J.A. Fronts Propagating with Curvature-Dependent Speed - Algorithms Based on Hamilton-Jacobi Formulations. *Journal of Computational Physics* (1988) 79(1):12-49.

[14] Jiang, G.S. and Peng, D.P. Weighted ENO schemes for Hamilton-Jacobi equations. *Siam Journal on Scientific Computing* (2000) 21(6):2126-2143.

[15] Fornes, P., Bihs, H., Thakur, V. and Nordal, S. Implementation of non-Newtonian rheology for debris flow simulation with REEF3D. *Proceedings of the 37th IAHR World Congress*(Submitted)

[16] Coussot, P., Laigle, D., Arattano, M., Deganutti, A. and Marchi, L. Direct determination of rheological characteristics of debris flow. *Journal of Hydraulic Engineering-Asce* (1998) 124(8):865-868.

[17] Kaitna, R. and Rickenmann, D. Flow of different material mixtures in a rotating drum. *Debris-Flow Hazards Mitigation: Mechanics, Prediction, and Assessment. Proceedings of the 4th International DFHM Conference, Chengdu, China, Citeseer.* (2007)

[18] Kaitna, R., Rickenmann, D. and Schatzmann, M. Experimental study on rheologic behaviour of debris flow material. *Acta Geotechnica* (2007) 2(2):71-85.

[19] Saramito, P. and Wachs, A. Progress in numerical simulation of yield stress fluid flows. *Rheologica Acta* (2016) :1-20.

[20] Johnson, A.M. *Physical processes in geology: A method for interpretation of natural phenomena; intrusions in igneous rocks, fractures, and folds, flow of debris and ice* (1970) Freeman, Cooper.

[21] Savage, S.B. and Hutter, K. The motion of a finite mass of granular material down a rough incline. *Journal of Fluid Mechanics* (1989) 199:177-215.

[22] Jop, P., Forterre, Y. and Pouliquen, O. A constitutive law for dense granular flows *Nature* (2006) 441(7094):727-730.

[23] Moriguchi, S., Borja, R.I., Yashima, A. and Sawada, K. Estimating the impact force generated by granular flow on a rigid obstruction. *Acta Geotechnica* (2009) 4(1):57-71.

[24] Domnik, B., Pudasaini, S.P., Katzenbach, R. and Miller, S.A. Coupling of full two-dimensional and depth-averaged models for granular flows *Journal of Non-Newtonian Fluid Mechanics* (2013) 201:56-58.

[25] Papanastasiou, T.C. Flows of Materials with Yield *Journal of Rheology* (1987) 31(5):385-404.

[26] Iverson, R.M. and George, D.L. A depth-averaged debris-flow model that includes the effects of evolving dilatancy. I. Physical basis. *Proceedings of the Royal Society a-Mathematical Physical and Engineering Sciences*(2014) 470(2170).

[27] von Boetticher, A., Turowski, J.M., McArdell, B.W., Rickenmann, D. and Kirchner, J.W. DebrisInterMixing-2.3: a Finite Volume solver for three dimensional debris flow simulations based on a single calibration parameter-Part 1: Model description. *Geoscientific model development discussions* (2016) 8(8).

[28] McArdell, B.W., Bartelt, P. and Kowalski, J. Field observations of basal forces and fluid pore pressure in a debris flow. *Geophysical Research Letters* (2007) 34(7)

9. National Conference on Computational Mechanics
MekIT'17
B. Skallerud and H I Andersson (Eds)

MULTIPHASE FLOW SIMULATIONS IN AN ANNULUS CONFIGURATION

Christopher J. Friedemann[1], Mikael Mortensen[1] and Jan Nossen[2]

[1]Department of Mathematics
University of Oslo
Nils Henrik Abels hus, 0851 Oslo, Norway
e-mail: postmottak@mn.uio.no, web page: http://www.mn.uio.no

[2] Institute for Energy Technology (IFE)
Oil and Gas
Instituttveien 18, 2007 Kjeller, Norway
e-mail:firmapost@ife.no, web page: https://www.ife.no/en

Key words: CFD,Multiphase, OpenFOAM,VOF, Concentric annulus

Abstract. In this present study, four multiphase flow cases were simulated in an annulus pipe configuration using the interFoam solver in OpenFOAM. Three of the cases were conducted using a $k-\omega$ RANS model while the remaining simulation was executed with a one equation LES formulation. The annulus consists of two concentric cylinders where the outer diameter is 0.1 m and the inner diameter is 0.05 m. Pipe geometries of lengths between 2 and 10 m were meshed and applied with periodic boundary conditions across the inlet and outlet. A pressure drop was administered throughout the domain of each case with a magnitude between 110 Pa/m and 1157 Pa/m. Additionally the mesh used in the RANS simulation model was constructed with a symmetric boundary condition along xy-plane to reduce the size of the computational mesh. The internal domain was initialized with liquid volume fractions and superficial velocities based on experimental data provided by IFE. The cases yielded wavy flow with indications of a possible transition to slug flow in cases 3 and 4. All cases displayed waves of varying amplitude and frequency. Comparing to experiments conducted at IFE, the high frequency low amplitude flow regime in case 1 matched well in terms of the velocity field. Cases 3 and 4 with larger waves had prevalent discrepancies between the applied pressure drop and expected phase velocity when contrasted to the experimental Results

1 INTRODUCTION

Multiphase pipe flow is most frequently associated with the oil, gas and power industries. That said, it is applicable to a vast range of other fields including aerospace and

medicine. Generally speaking multiphase flow problems consist of two or more separate fluids present in a system. These fluids behave according to their state, physical conditions and properties of the system such as pressure, surface roughness and fluid velocities. When considering an annulus configuration the hydraulic diameter also plays a vital part. The coupling between the phase interaction and pipe geometry further contribute to the complexity of the problem. The accurate prediction of flow pattern, liquid holdup, phase fraction at arrival and pipeline pressure distribution are of immediate concern to oil companies[1, 6]. These concerns consist of several aspects, including pipeline design and maintenance, flow efficiency, safety and preservation of the environment.

There are several empirical models such as the method developed by Beggs et al.[2] and mechanistic models that can be used to predict pipeline behavior. Mechanistic models include the original pioneering work of Taitel et al. [10] which in turn has lead to more recent efforts, one of which is the methods devised by Petalas [8]. Mechanistic models are more robust compared to the empirical counterpart as they are based on fundamental physics. However they too employ said empirical correlations as well as other estimates which contributes to an underlying uncertainty built into the results. Even so, a good mechanistic model is often reasonable enough when employed correctly that it can be used together with well data or experiments to validate a CFD model.

Empirical models are easy to use and readily available from several sources. Although easy to implement they are still only as good as the data from which they are derived and as such should only ever be used for similar cases. Even in cases that are applicable the simplification of the physics involved contribute to a significant uncertainty [11].

Most ready-made models, including empirical, mechanistic and commercial flow simulators are set up to handle multiphase pipe flow in a conventional configuration. Despite the direct relationship with the drilling and well control industries, very little work has been done to categorize flow within an annulus. In industry annulus flow occurs intentionally in the gas-filled compartment of a gas-lifted well [6], and unintentionally in the drilling industry during a blow-out. Considering how important annulus multiphase flow is in the industry, it comes as a surprise that there is a serious lack of dedicated research to the topic. Perhaps the lack of concern can be attributed to the fact that prior to the Deepwater Horizon Oil spill in 2010 no incident had occurred which warranted extensive research.

After the 2010 oil spill regular multiphase flow models were used to estimate the oil spill based on the frequency of slugs at the site. However questions should be raised about the approach of applying these methods to an annulus. Considering that the encased cylinder drastically alters the behavior of the flow within, it affects the hydraulic diameter, the friction factor, the interfacial area between the fluids and so on. At the time of the Deepwater horizon incident there were but a few published papers which dealt with any form of multiphase flow in an annulus such as the Caetano[3] thesis in 1985 and Ekberg's[4] paper in 1999, this lack of information somewhat explains why the standard models were used, but not why it was accepted.

Taking into account the lack of experimental studies conducted using an annulus, it was as expected that even less research has been conducted using CFD. It is, after all, very difficult to validate a CFD model without any experimental or field data to compare with.

In this paper an initial attempt at performing CFD simulation using the OpenFOAM solver interFoam on a multiphase annulus problem has been carried out. The simulations will eventually be compared with extensive experiments performed at IFE Kjeller where an ongoing campaign is being conducted and scheduled to run through 2018. The data is available as part of this research project and by utilizing simulations together with the experimental work it nurtures an excellent possibility of expanding the current knowledge base of multiphase flow in the annulus configuration.The two turbulence models used are the Smagorinsky sub grid model for the LES simulation and the k-ω RANS model. The k-ω model has previously been implemented in RANS simulations by Shuard[9] while Peters[7] successfully utilized the Smagorinsky model for his LES simulations in his thesis. As this project is in its infancy these models were chosen as a suitable starting point.

1.1 interFoam Solver

The solver used in this paper was the interFoam solver. This solution method accepts a variety of LES and RANS turbulence models, and can easily be manipulated for different setups. What is important to mention is that the "Volume of Fluid" (VOF) method, which interFoam utilizes, solves the continuity and momentum equations as though the fluids were one. This differs from other possible solvers such as multiphaseEulerFoam which calculates the momentum equations for each phase separately. The VOF method models the flow by solving the momentum equation for the two fluids as if they were a homogeneous mixture, thus density and velocity are averaged and the averaged continuity equation becomes

$$\nabla \cdot \bar{u} = 0, \tag{1}$$

where $\bar{u}$ is the averaged velocity of the two phases such that

$$\bar{u} = \alpha_g u_g + \alpha_l u_l. \tag{2}$$

The subscripts l and g, signify liquid and gas, while α is the phase fraction. Applying them to the momentum equation, while using a similar approach to Eq. 2 for other mixture properties such as density and viscosity yields the momentum equation as

$$\frac{D\bar{u}}{Dt} = -\frac{1}{\bar{\rho}}\nabla p + \bar{\nu}_{eff}\nabla \cdot (\nabla \bar{u} + (\nabla \bar{u})^T) + g + \frac{F_s}{\bar{\rho}}. \tag{3}$$

F_s is the surface tension force, g gravity, while the overbar quantities denote averages of the two phase values.

A governing equation is solved for the phase fraction α

$$\frac{D\alpha_l}{Dt} + \nabla \cdot (u_c \alpha_l \alpha_g) = 0. \tag{4}$$

This equation employs interface sharpening in the region where both phases are present by adding an artificial interface velocity u_c, this interface velocity serves only to create a sharper interface between the phases. The magnitude of the velocity depends on the interface sharpening coefficient (C_α), which in case of this work was set between 0.7 and 1. For interface sharpening coefficients of magnitude equal to or less than 1 the interface compression velocity becomes :

$$u_c = C_\alpha |u| \frac{\nabla \alpha_l}{|\nabla \alpha_l|}. \tag{5}$$

2 GEOMETRY, MESH AND BOUNDARY CONDITIONS

The Geometry of the concentric annulus pipe used in these simulations was created in Gmsh. The outer diameter of the pipe is 0.1 m while the inner diameter is 0.05 m. The pipes used are between 2 and 10 m long. While the 10 m pipe consist of approximately 1.5 million cells, the 2 m pipe has 1.55 million cells. The cells are uniformly distributed in the streamwise and circumferential directions while the cells between the two cylinder walls are refined in the near wall regions as seen in Fig.1.

By carefully describing the separation of the grid elements along transfinite lines it was possible to create the entire mesh using only hexahedral elements as seen in Fig. 1. This is advantageous for the VOF method which the interFoam solver uses. Generating the mesh along transfinite lines with hexahedral elements creates uniform cells with little if any skewness. The direct description of the elements makes the Courant Number estimation for simulation purposes straight forward while also simplifying the mapping of the periodic conditions. The mapping is made trivial because the inlet and outlet patches are an exact geometric match.

The model geometry for the RANS simulation cases were further simplified by applying a symmetric boundary condition across the xy-plane. When there is insignificant amounts of crossflow and the RANS turbulence model is used, Shuard[9] determined that the final results from the full and half mesh were the same. Thus the mesh density can be vastly improved while maintaining or reducing the required simulation time. From previous iterations of the simulations presented here it was the observed that the RANS simulations are indeed mirrored about the centerline.

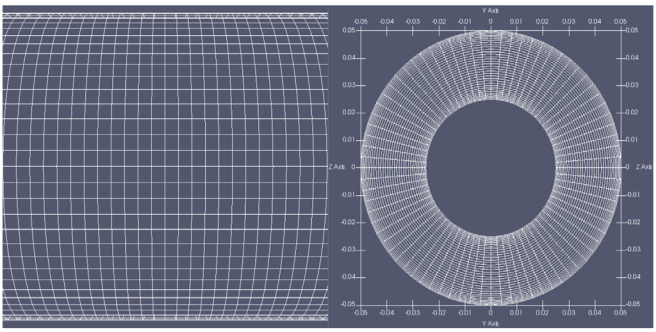

Figure 1: 2 m pipe with 1.55 million cells

After creating the mesh it was converted to the OpenFOAM format. Within the case files of the OpenFOAM framework the boundary conditions and the dynamic solution method was specified.

The initial conditions were chosen by referencing experimental data from IFE, the flow map for multiphase pipe flow by Lee et al.[5] and approximating the superficial phase velocities for the liquid and gas phases in the annulus configuration. The phase velocities, pressure drop, liquid volume fraction and Courant number restrictions for each case are summarized in Table 1. Each case was selected because they are near or at data points provided by IFE and can be compared qualitatively in regards to flow regime and final velocities.

Table 1: Initial conditions

CASE	u_g (m/s)	u_l (m/s)	$\alpha_l(\%)$	$\Delta P(Pa/m)$	CFL_{alpha}	CFL
1	3.24	0.4	22.5	110	0.30	0.40
2	3.23	1.05	38.0	155	0.25	0.40
3	3.24	1.5	43.0	340	0.30	0.40
4	3.0	1.2	38.0	1157	0.30	0.40

In combination with the initial state of the system typical physical properties for oil and gas were chosen to resemble those used in experiments by Nossen et.al[6]. These are summarized in Table 2.

Table 2: Physical properties

Phase	viscosity (m^2/s)	density (kg/m^3)	σ
Oil	$2.0 \cdot 10^{-6}$	800.0	0.0285
Gas	$7.56 \cdot 10^{-7}$	24.0	0.0285

As with many computational fluid dynamic problems there are several possible sets of valid boundary conditions or solution methods in OpenFOAM. For this array of simulations periodic inlet and outlet conditions have been used together with a prescribed pressure drop. The standard boundary conditions are summarized in Table 3. Note that, depending on the type of simulation, some of these parameters may not be used. For example, an LES simulation has no need for the omega values and are thus omitted.

Table 3: Boundary conditions

parameter	inlet	outlet	walls
alpha	Mapped	inletOutlet	zeroGradient
U	Mapped	pressureinletOutletVelocity	noSlip
k	Mapped	inletOutlet	kqRWallFunction
ω	Mapped	inletOutlet	omegaWallFunction
prgh	totalPressure	totalPressure	fixedFluxPressure
ν_T	calculated	calculated	nutkWallFunction

There are several ways of estimating k and ω, for this work a method based on the turbulent intensity and hydraulic diameter was used. The turbulent intensity can be determined by

$$I = 0.16 Re_{d_h}^{-\frac{1}{8}}, \tag{6}$$

where the reynolds number based on the hydraulic diameter is

$$Re_{d_h} = \frac{\bar{u} \cdot d_h}{\bar{\nu}}. \tag{7}$$

The aforementioned averaging procedure based on the phase fraction as seen in Eq. 2 was used to solve for the velocity and viscosity components, while the hydraulic diameter of a concentric pipe is defined as

$$d_h = d_{outer} - d_{inner}. \tag{8}$$

Using Eq. 6-8 the turbulent kinetic energy is solved for by

$$k = \frac{3}{2}(\bar{u}I)^2, \tag{9}$$

after which one can use k to solve for the specific dissipation ω

$$\omega = \frac{C_\mu^{-\frac{1}{4}} k^{\frac{1}{2}}}{l}. \tag{10}$$

Here $C_\mu = 0.09$, and l is the turbulent length scale. For the sake of consistency the turbulent length has been determined as a function of the hydraulic diameter and is solved for as $l = 0.007 d_h$.

3 Results

3.1 Case 1 RANS simulation

Case 1 was carried out both as a large eddy simulation (LES) and as a k-ω RANS. Several different meshes was used to study the effect of the mesh density on the flow pattern. The two turbulence models resulted in similar flow patterns and therefore only the RANS model will be discussed. An LES simulation will be presented in Case 2. Case 1, which utilized an initial gas velocity (u_g) of 3.24 m/s and liquid velocity (u_l) of 0.87 m/s was run with the interior domain consisting of 77 % gas and 23 % oil at their relative velocities. The interface Courant Number was restricted to 0.3 while the cells with purely one phase in them were restricted to 0.5. The Courant number was used to limit the time step, with the largest allowed time step being 0.005 s. Using these initial conditions and a pressure drop of 110 Pa/m the smooth laminar flow at startup develops into frequent low amplitude waves.

3.1.1 10 m pipe with coarse mesh

Case 1 was first run in a 10 m pipe using a mesh of 672,000 cells using periodic boundary conditions between inlet and outlet as well as symmetry conditions across the centerline (y-axis) while using an interface compression of 1. The mesh information is reiterated in Table 4.

Table 4: Mesh and pipe Information

Cell dir.	Length (m)	cell size (m)	#.faces
Streamwise	10.0	$6.67{\cdot}110^{-3}$	1500
Outer Dia.	0.1	$5.24{\cdot}110^{-3}$	30
Inner Dia	0.05	$2.62{\cdot}110^{-3}$	30
Annulus	eccentricity=0	$6.72{\cdot}110^{-4}$ to $2.1{\cdot}110^{-3}$	19

The cells in the streamwise direction are spaced 6.67 mm apart evenly throughout the domain. The cells closest to the walls are 0.67 mm thick while the interior region cells are 2.1 mm thick, the near wall region uses a linear progression to merge from the near wall interior region where the cell thickness is constant.

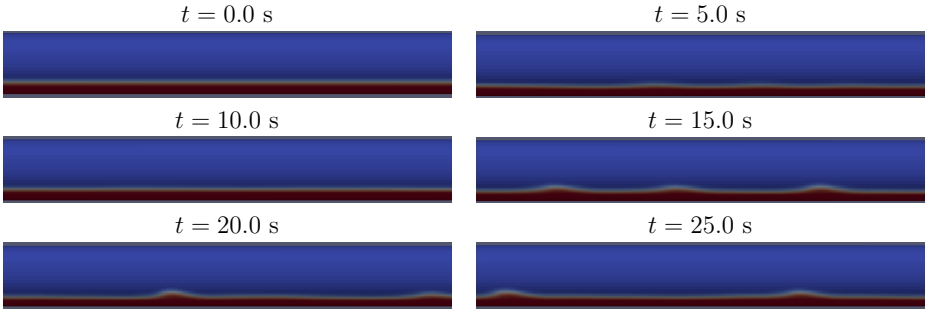

Figure 2: Snapshots of phase field with 5 s time steps.

In previous iterations of these flow simulations a startup slug was formed due to poor initial conditions. In the 5 s timestep image if you carefully inspect the central region, there is a small visible buildup of liquid. Because the initial conditions are close to the final result this liquid accumulation does not form the aforementioned slug and significantly reduces the required simulation time. The wave frequency is approximately 4 Hz which resembles that observed during the experiments at IFE. Concerning the wave amplitude it appears that the experimental wave formations have a noticeably larger amplitude than the simulated case. A typical set of waves seen in experiment for this case is shown in Fig.3.

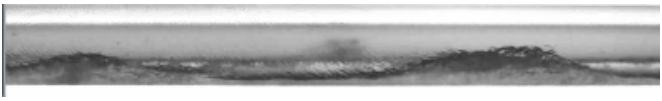

Figure 3: IFE experiment [6]

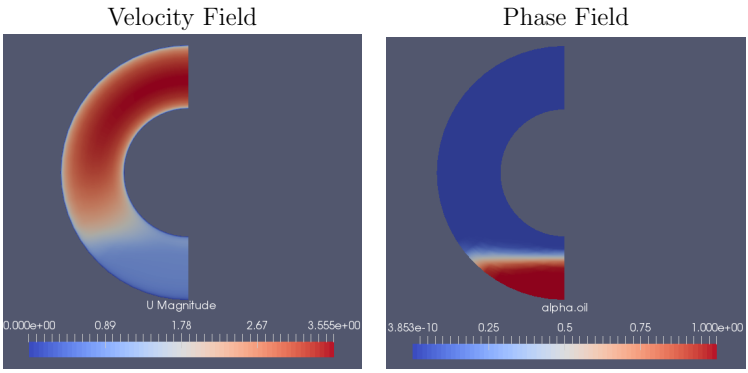

Figure 4: Velocity field and phase fraction distribution at x=5.0 m t=40 s

As seen in Fig.4 the fully developed mean velocity for the gas phase is around 3.0 m/s while the liquid phase is very near the original 0.87 m/s used to initialize the problem. These values match within 10 % of the original magnitudes and indicate that the pressure drop from the experimental results is applicable to this flow regime for pressure driven flow simulations.

3.1.2 3 m pipe with 840 k cells

The second mesh studied in case 1 is significantly refined when compared to the previous iteration and contains 840 k cells distributed along the 3 m pipe. Similarly to the former mesh the pipe is split along the centerline and applied with symmetric boundary conditions to mirror the behavior across the yx-plane.

Table 5: Mesh and pipe Information

Cell dir.	Length (m)	cell size (m)	#.faces
Streamwise	3.0	$3.33{\cdot}10^{-3}$	900
Outer Dia.	0.1	$5.1{\cdot}10^{-3}$	32
Inner Dia	0.05	$2.55{\cdot}10^{-3}$	32
Annulus	eccentricity=0	$5.37{\cdot}10^{-4}$ to $1.0{\cdot}10^{-3}$	32

The cells along the x-axis (streamwise) of the pipe are a constant 3.33 mm long, while their thickness varies from 0.537 mm close to the wall to 1.0 mm in the central interior region. Along the outer diameter the cells stretch 5.1 mm while along the inner diameter

they are half of that. Compared to the original mesh most of the refinement occurs in the streamwise direction where the number of faces per meter was doubled and in the annulus where the number of faces was increased by 68 %.

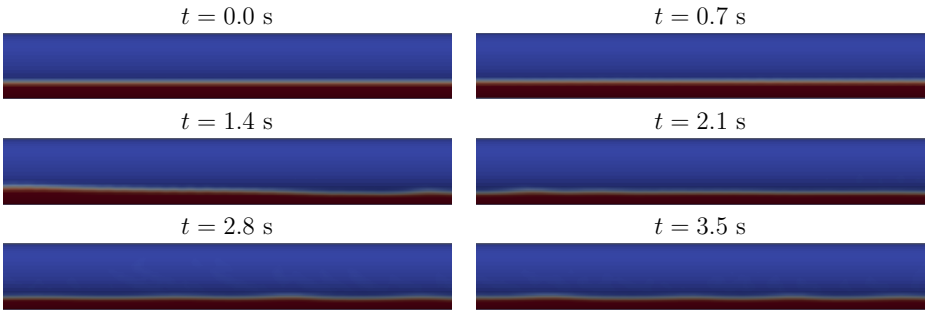

Figure 5: Snapshots of phase field with 0.7 s time steps

In comparison to the coarse mesh flow regime shown in Fig. 2, the refined pipe flow acts consistent with the coarse mesh behavior. By 2.8 and 3.5 s there are visible oscillations of the surface, these oscillations were seen as a precursor to the formation of larger waves in the coarse mesh where they first occurred at around 10 s. The coarse mesh is a significantly longer pipe which may have an impact on the initial development of the flow when using periodic boundary conditions since the laminar smooth section will stretch further from startup and could explain why oscillations are seen earlier during this sub case.

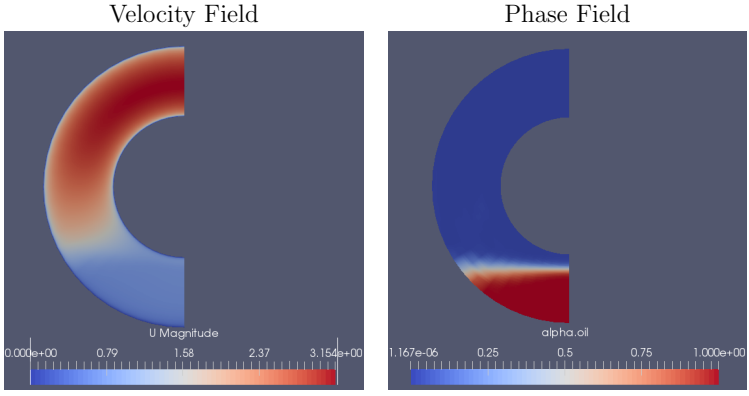

Figure 6: Velocity field and phase fraction distribution at x=1.5 m t=3.5 s

When comparing Fig.6 to Fig.4 it is important to remember that the flow in Fig. 4 is already fully developed wave flow. Fig.6 shows a flow pattern which is still developing, although if the two meshes were to be compared at similar stages the relationship between the two velocity fields remain the same. In the fine mesh both phases are slowed down 11 % when compared to the coarse mesh. The only major difference between the two simulations is that the pipe is shorter with a significantly refined mesh. Further simulation time is required to determine if this decreased velocity experienced will alter the resultant flow regime.

3.2 Case 2 - 2 m Pipe with 1550 k cells

The second case was carried out as a one equation LES simulation, using the Smagorinsky sub grid model. The pipe which is 2 m long and fully concentric consists of 1.55 million cells. The interior domain was initially filled with 38% liquid and 62% gas. At start up the superficial liquid velocity was 0.4 m/s, while the gas phase was travelling at a superficial velocity of 2.0 m/s. A pressure drop of 310 Pa was imposed between the inlet and the outlet of the pipe. As with the remainder of the simulations periodic conditions were used to map the phase distribution and velocity field from the outlet back to the inlet effectively creating an infinite pipe.

Table 6: Mesh and pipe Information

Cell dir.	Length (m)	cell size (m)	#.faces
Streamwise	2.0	$3.63{\cdot}10^{-3}$	550
Outer Dia.	0.1	$3.98{\cdot}10^{-3}$	80
Inner Dia	0.05	$1.99{\cdot}10^{-3}$	80
Annulus	eccentricity=0	$3.79{\cdot}10^{-4}$ to $8.82{\cdot}10^{-4}$	38

Although further work is needed to determine if the LES simulation solution is converged with respect to mesh size, the mesh described in Fig.6 is the finest used in any of the cases presented in this paper. In the streamwise direction the cells are placed 3.63 mm apart, along the inner diameter the cells are 1.99 mm apart while along the outer diameter they are exactly twice as long. Within the annulus the cells thickness increase by linear progression from 0.379 mm nearest either wall to 0.882 mm in the central region where the width of each cell is held constant.

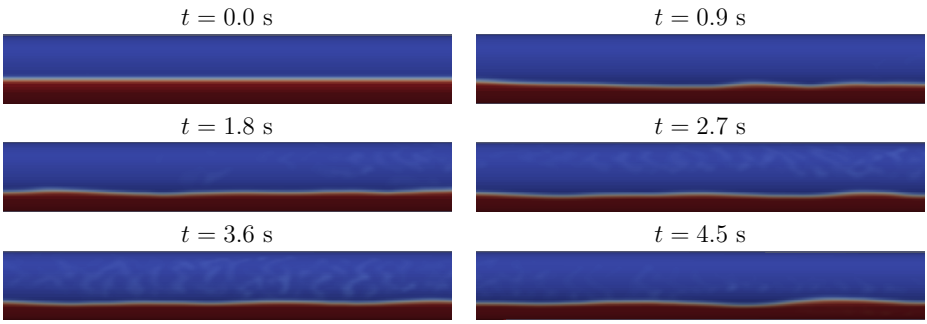

Figure 7: Snapshots of phase field with 0.9 s time steps

Within the 2m domain of this pipe the flow quickly transitions from smooth stratified flow to wavy flow with distinct waves being visible by 2.7 s. There appears to be some mist like structures throughout the domain especially noticeable at the 3.6 s mark. The turbulent eddies that form in the LES simulation lift and carry these liquid droplets through the domain. As seen in the 4.5 s and 2.7 s image there is less of the mist present, with time it will be possible to determine whether these structures persist throughout the simulation or if it is a passing occurrence related to initialization.

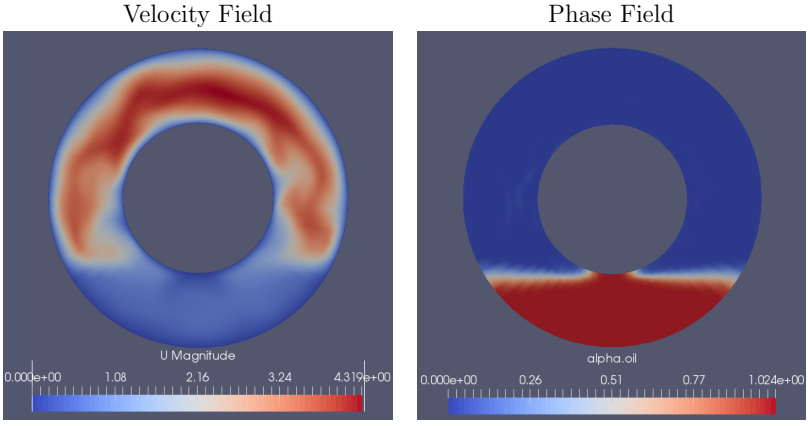

Figure 8: Velocity field and phase fraction distribution $x = 1.5$ m and $t = 4.5$ s

The velocity field distribution and local holdup profile presented in Fig.8 indicate that superficial gas and liquid velocities have deviated in regards to their initial values. At the

given location the liquid holdup is 27%, which yields superficial gas and liquid velocities of 2.36 and 0.29 m/s respectively. When compared to experimental data these flow velocities should generate wavy flow, Fig.3.2 reflects this expected behavior. There are visible patches in the velocity field distribution, these eddy regions seem to closely match the areas where there are liquid droplets in the phase field. Turbulent eddies have been known to lift liquid particles from the surface and transport them through the gas phase which could explain this apparent behavior.

3.3 Case 3 - 4 m pipe with 784k cells

Case 3 was simulated in a 4 m pipe with 784 k mesh elements.A symmetric boundary condition was applied along the centerline creating a mirrored boundary about the y-axis. Information about the mesh is summarized in figure 7. The interior was filled with liquid fraction $\alpha_l = 0.43$ and the pressure drop through the domain was set as 1360 Pa. The internal conditions were initialized such such that the superficial gas and liquid velocities was set to 1.85 and 0.65 m/s respectfully. The interface compression coefficient was 0.9.

Table 7: Mesh and pipe Information

Cell dir.	Length (m)	cell size (m)	#.faces
Streamwise	4.0	$4.0\text{x}10^{-3}$	1000
Outer Dia.	0.1	$5.61{\cdot}10^{-3}$	30
Inner Dia	0.05	$2.80{\cdot}10^{-3}$	30
Annulus	eccentricity=0	$5.3{\cdot}10^{-4}$ to $1.0{\cdot}10^{-3}$	30

The mesh size within the annulus is refined in the near wall region. Using a linear progression the cells adjacent the wall are $0.53\text{x}10^{-4}$ m thick while the largest cell in the refinement region is $0.95\text{x}10^{-4}$ m, these cells border the constant thickness region of the interior where the cells are 1.0 mm wide. The refinement region covers 0.005 m from either wall and thus occupies 40% of the interior space.

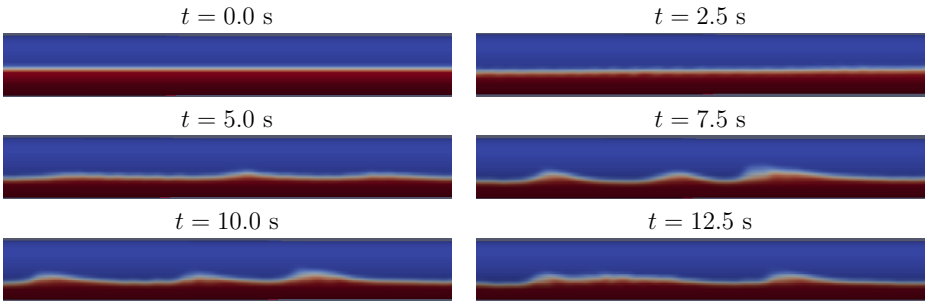

Figure 9: Snapshots of phase field with 2.5 s time steps

The flow quickly develops from smooth stratified to wavy flow. As seen above there appears to be two sets of waves distinguished by their amplitude. The large amplitude waves are seen at t = 7.5 and 10.0 s while the more frequent low amplitude waves are visible at t=5.0, 10.0 and 12.5 s. In both the snapshots at 5.0 and 7.5 s the low amplitude waves are located in between large amplitude waves. When you inspect the 7.5 second image it is noticeable that two of the waves are about to merge and create a larger wave whilst in the 12.5 s snapshot two waves have already come together to generate a significantly longer wave although of low amplitude. Several of these mergers can cause the formation of a large slug. With further simulation time it will be possible to determine if these waves merging lead to the transition from wavy flow to slug flow.

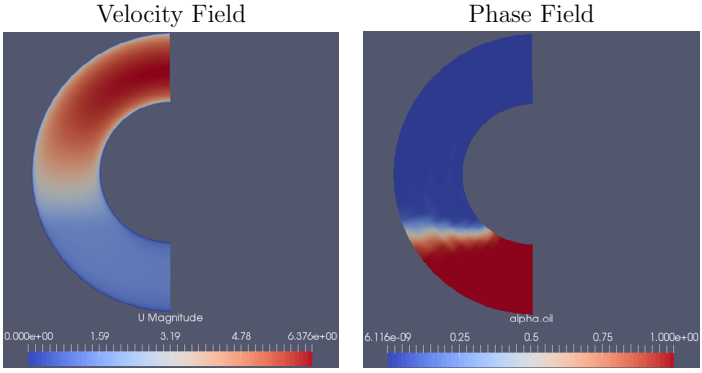

Figure 10: Velocity field and phase fraction distribution at x=2 m, t=12.5 s

The velocity profile snapshot indicates that the flow is accelerated from the initial conditions. The superficial gas velocity is approximately 2.73 m/s while the liquid superficial

velocity is 0.8127 m/s, this equates to an increase of around 45 and 25 % respectively when compared to the initialized field. If the flow pattern transitions to slug flow most likely the velocity distribution will drastically change and will have to be reevaluated. Further simulation time and studies are needed to determine if the discrepancy is caused by mesh dependency or if it will be resolved by the transition to slug flow.

3.4 CASE 4 - 4 m pipe with 1000 k cells

Using the k-ω RANS model and a 4 m pipe split down the y-plane with a total of 1 million cells case 4 was expected to yield slug flow. The computational domain was initially filled with liquid and gas volume fractions of 0.38 and 0.62 respectively. A pressure drop of 4628 Pa between inlet and outlet was applied while the velocity field was initialized for the two phases as $u_g = 3.0$ m/s and $u_l = 1.2$ m/s

Table 8: Mesh and pipe Information

Cell dir.	Length (m)	cell size (m)	#.faces
Streamwise	4.0	$3.64{\cdot}10^{-3}$	1100
Outer Dia.	0.1	$5.07{\cdot}10^{-3}$	32
Inner Dia	0.05	$2.53{\cdot}10^{-3}$	32
Annulus	eccentricity=0	$5.34{\cdot}10^{-4}$ to $9.38{\cdot}10^{-4}$	33

As shown above the mesh within the annulus varies, the finest elements are placed near the walls while the central interior region is coarser. The cell closest to the wall is 0.534 mm thick while the widest cell is 0.938 mm. The cells in the streamwise direction are a constant 3.64 mm, while the cells along the outer diameter are 5.07 mm and the inner diameter 2.53 mm.

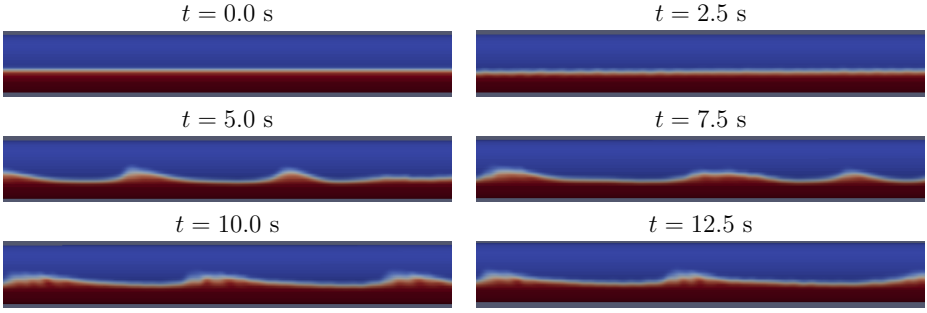

Figure 11: Snapshots of phase field with 2.5 s time steps

As with case 1 and 3 the flow quickly develops from the laminar smooth startup regime to wavy flow. Similarly to case 3 there are indications that waves are combining to produce an increased local liquid holdup, the right hand side of $t = 7.5$ s shows one such case of two waves having merged together. A closer look on the wave interaction beforehand is shown in figure 12.

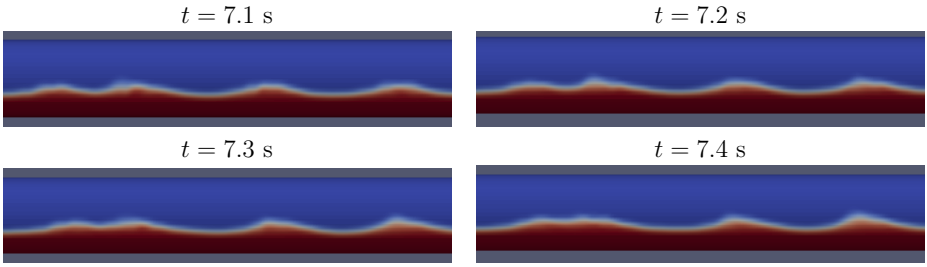

Figure 12: Merging wave

The wave merging seen above takes place just prior to the snapshot at 7.5 s in Fig. 11. The two waves combine to form a local accumulation of liquid. If several of these wave mergers occur it may eventually lead to a situation where the liquid holdup is increased enough to completely fill the cross section of the pipe. A phenomena commonly known as slugging.

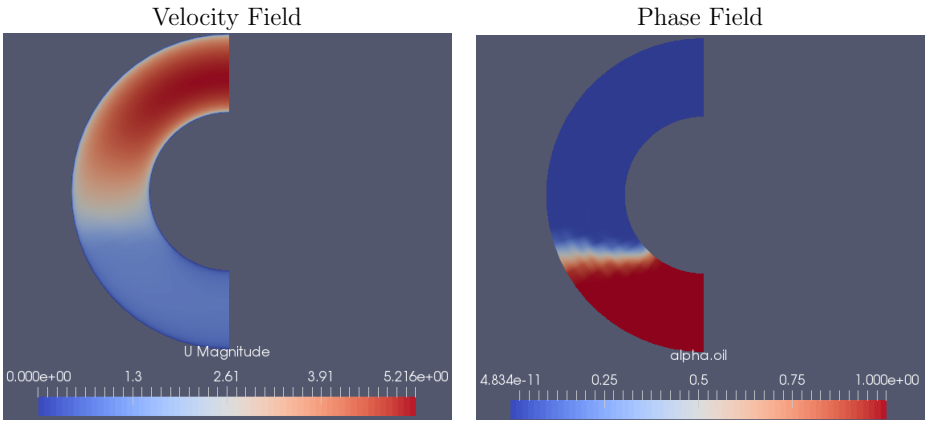

Figure 13: Velocity field and phase fraction distribution at x=1.85 m, t=7.5 s

The cross sectional view shown above was taken directly between two wave peaks, compared to the initial velocity both the liquid and gas phases have experienced a roughly 30% increase to their relative velocities. Similarly to the other cases further work is needed to determine if this discrepancy from experiment is caused by mesh dependencies, experimental setup or other causes.

4 CONCLUSIONS

The four cases studied in this paper yielded wavy flow with indications that transition to slug flow was possible in at least two cases (3,4). Cases 1,3 and 4 were run using a $k-\omega$ RANS formulation while case 2 was simulated using a one equation LES model. All the simulations were carried out using periodic boundary conditions thus mapping the inlet and outlet together. The RANS simulations had a symmetric boundary condition applied about the centerline y-axis reducing the computational domain when compared to the LES simulation. All cases were simulated using the interFoam solver in OpenFOAM and with an applied interface compression coefficient between 0.7 and 1.0

Case 1 resulted in the formation of low amplitude wave flow with liquid holdup up close to the projected result based on experimental data provided by Nossen et.al[6]. Compared to experiment the waves were smaller in amplitude but of similar frequency. Cases 3 and 4 yielded both small and large amplitude waves, in these two cases smaller waves were observed merging together. The waves merging lead to the formation of larger waves and an increase in the local liquid holdup. This behavior is a known precursor to slug flow and with further simulation time it will be possible to determine if these cases will undergo a transition from wavy flow to slug formation.

Early indications point toward a discrepancy with regards to flow pattern and the applied pressure drop across the pipe in comparison to experiment. While the low amplitude high frequency waves reproduce experimental data quite well (Case 1). Cases such as 3 and 4 result in a 30-40% velocity increase in both phases while not yet transitioning to slug flow as the experiments did. It is possible that the increase in the velocity field is exactly because the flow is yet to transition and further work is needed to determine the cause of this disparity. Whether it is simply because it has not transitioned yet or if the discrepancy is caused by the mesh density or other tuning parameters are issues to be investigated in the near future. Analyzing case 1 early results indicate that the mesh density is having an effect on the velocity field and further studies are needed to determine mesh convergence with regards to the final results.

5 ACKNOWLEDGEMENTS

The participants would like to thank the Research Council of Norway, who is funding the project through the PETROMAKS2 program.

REFERENCES

[1] Ali, S. F. and Yeung, H. *Experimental Investigation and Numerical Simulation of Two-Phase Flow in a Large-Diameter Horizontal Flow Line Vertical Riser*. Petroleum Science and Technology (2010) **28** 11

[2] Beggs, D. H. and Brill, J. P. *A study of Two-Phase Flow in Inclined Pipes*. Journal of Petroleum Technology (1973) **25** 05

[3] Caetano, E. F., Shoham, O. and Brill, J. P. *Upward vertical two-phase flow through an annulus* Thesis. The University of Tulsa (1985)

[4] Ekberg, N. P et al *Gas-liquid two-phase flow in narrow horizontal annuli*. Nuclear Engineering and Design (1999) **192** 01:59-80.

[5] Lee, A. H., Sun, J. Y. and Jepson, W.p *Study of Flow Regime Transitions of Oil-Water-Gas Mixtures in Horizontal Pipelines*. Proceedings of the Third (1993) International Offshore and Polar Engineering Conference

[6] Nossen, J. *An experimental study of two-phase flow in horizontal and inclined annuli*. to be published in Introduction to Multiphase 2017 - 'The Cannes Conference'

[7] Peeters, P. T. *CFD of Multiphase Pipe Flow: A Comparison of Solvers* TU Delft Thesis,2016

[8] Petalas, N. and Aziz, K. *A Mechanistic Model for Multiphase Flow in Pipes*. Journal of Canadian Petroleum Technology (2000) **39** 06

[9] Shuard, A. M., Mahmud, H. B. and King, A.j. *Comparison of Two-Phase Pipe Flow in OpenFOAM with a Mechanistic Model* IOP Conference Series: Materials Science and Engineering

[10] Taitel, Y. and Dukler, A. E. *A model for predicting flow regime transitions in horizontal and near horizontal gas-liquid flow*. AIChe Journal (1976) **22** 01

[11] Zhang, H., Wang, Q., Sarica,C. and Brill, J. P. *Unified Model for Gas-Liquid Pipe Flow via Slug Dynamics -Part 1: Model Development* ASME. J. Energy Resour. Technol (2003) **125** 4:266-273

9. National Conference on Computational Mechanics
MekIT'17
B. Skallerud and H I Andersson (Eds)

USING ALE-VMS TO COMPUTE WIND FORCES ON MOVING BRIDGE DECKS

TORE A. HELGEDAGSRUD[1], YURI BAZILEVS[2], ARTEM KOROBENKO[3], KJELL M. MATHISEN[1] AND OLE A. ØISETH[1]

[1]Department of Structural Engineering
Norwegian University of Science and Technology (NTNU)
Richard Birkelands v 1a, NO-7491 Trondheim, Norway
e-mail: tore.a.helgedagsrud@ntnu.no

[2]Department of Structural Engineering
University of California, San Diego, USA

[3]Department of Mechanical & Manufacturing Engineering
University of Calgary, Canada

Key words: Computational Fluid Dynamics, Moving Domain, Bridge Engineering, Aerodynamic Forces

Abstract. A framework for simulating the forced-vibration wind tunnel experiment using stabilized ALE-VMS techniques has been developed. With a user-defined motion of the bridge deck the problem reduces to a flow computation on a moving domain with time-dependent essential boundary conditions. This leads to a coupled problem between the fluid and the fluid mesh, which can be solved very effectively in a block-iterative fashion. An important advantage with the forced-vibration method from a computational point of view is that no steady state response needs to develop. The motion-dependent forces are thus obtained at a low computational cost. Numerical results show good agreement with the experiments.

1 INTRODUCTION

The Norwegian Public Roads Administration (NPRA) launched in 2014 their ambitions to complete the E39 Coastal Highway Route as a continuous and ferry free route within the next 20 years[49]. This implies eight extreme fjord crossings for which the current technology literally falls short. Several concepts are under investigation, such as submerged floating tunnels, tension legged platform (TLP) bridges, pontoon bridges, long span suspension bridges and hybrids. Common for all is that with increasing span width, dynamic effects becomes a major issue and often the main concern in design.

On slender bridges, with inevitably low eigenfrequencies, subjected to wind loading, self-excited vibration phenomena such as galloping and flutter are of particular interest, since these

may cause devastating effects leading to structural collapse like the infamous Tacoma Narrows bridge failure. Such effects are largely dependent on the shape of the cross section, on which most of todays calculations are based on extensive use of wind tunnel. A moderate use of wind tunnel tests together with an increased use of numerical simulations can increase the accuracy and efficiency of response calculations and make it possible to validate on a full scale. Such numerical simulations may represent a technological advance in future long-span bridge design.

Efficient and accurate modelling of Computational Fluid Dynamics (CFD) and Fluid-Structure Interaction (FSI) problems have seen a huge development in the recent decades. The core technology is the residual-based variational multiscale (RBVMS) formulation of the Navier Stokes equations for incompressible flows (see e.g. [2, 9, 19, 20, 21, 41, 46, 47]) in the Arbitrary Lagrangian-Eulerian (ALE) formulation [22]. The ALE formulation is an interface-tracking technique to describe the fluid in a time dependent domain. This may also be achieved with the Deforming Spatial Domain/Stabilized Space Time (DSD/SST) method [38, 43, 44, 45, 48]. These methods have been applied to some of the most challenging moving interface problems in the recent years. Both methods rely on Streamline-Upwind/Petrov-Galerkin and Pressure-Stabilizing/Petrov-Galerkin (SUPG/PSPG) stabilization [9, 38, 40] and stabilization of the incompressibility constraint[46].

The moving domain extension of RBVMS is referred to as the ALE-VMS formulation[2, 36], and has successfully been applied to simulation of turbulent flows and FSI in e.g. [3, 4, 18, 27, 37]. An important feature of the ALE-VMS method is the weakly enforced essential boundary conditions (BCs), introduced in [5]. Weak enforcement of the no-slip conditions improve the accuracy significantly[1, 7, 17] when the boundary layer mesh is relatively coarse, which in practice is always the case. In the limit of infinitely small elements, the weak enforcement gives strongly enforced BCs. The simulations in this work are based on the ALE-VMS formulation with weak BCs.

With this computational framework, we perform numerical simulations of the forced-vibration wind tunnel experiment of the Hardanger Bridge sectional model, carried out at the Norwegian University of Science and Technology (NTNU). In the forced-vibration experiment[15, 30] the bridge section model is subjected to a prescribed motion, from which we read the motion-dependent forces. This method is an alternative to the free-vibration method[32], where the bridge section model is suspended on springs. The motion-dependent forces are analogous to aerodynamic stiffness and damping, and are thus essential in the study of dynamic response.

The Hardanger Bridge is chosen for several reasons. Most importantly, we have access to extensive wind tunnel experiments. Moreover, it represents a new generation of suspension bridges, with highly optimized aerodynamic design. A fully coupled free-vibration Fluid-Object Interaction (FOI) simulation of the same bridge was carried out in [37].

We consider a sufficiently wide slice of the bridge deck, which is treated as a rigid object. As there in a forced-vibration context is no need to evaluate the linear and angular momentum, this type of problem consists of two blocks which can be solved in a block-iterative fashion: 1) use essential boundary conditions to set the current position of the object and solve the fluid mesh problem, and 2) solve the fluid problem. In the fluid mesh problem, the boundary layer

elements, which constitute approximately half of the mesh degrees-of-freedom, are treated as rigid. This results in a relatively inexpensive solution of the fluid mesh problem, keeping mesh distortion to a minimum.

The governing equations are presented in Sec. 2 and the discrete problem in Sec. 3. In Sec. 4 a brief description of wind forces in the context of bridge engineering is presented. Numerical results are presented in Sec. 5, and concluding remarks are given in Sec. 6.

2 GOVERNING EQUATIONS FOR FLUID MECHANICS IN MOVING DOMAINS

In this section the weak form of the Navier-Stokes equations for incompressible flows are presented in the ALE framework. A detailed derivation is given in [8].

Let $\hat{\Omega} \in \mathbb{R}^{n_{sd}}$, $n_{sd} = 2, 3$, represent the reference fluid mechanics domain with coordinates $\hat{\mathbf{x}}$ and boundary $\hat{\Gamma}$. The time dependent fluid domain Ω_t with coordinates $\mathbf{x}$ and boundary Γ_t is given as:

$$\Omega_t = \left\{ \mathbf{x} \,|\, \mathbf{x} = \boldsymbol{\phi}\left(\hat{\mathbf{x}}, t\right) \, \forall \hat{\mathbf{x}} \in \hat{\Omega}, t \in (0, T) \right\}, \tag{1}$$

where the ALE-mapping is obtained through the time-dependent displacements of the fluid domain, $\hat{\mathbf{y}}\left(\hat{\mathbf{x}}, t\right)$:

$$\boldsymbol{\phi}\left(\hat{\mathbf{x}}, t\right) = \hat{\mathbf{x}} + \hat{\mathbf{y}}\left(\hat{\mathbf{x}}, t\right). \tag{2}$$

See Fig. 1. Let $\mathcal{S}_u$ and $\mathcal{S}_p$ represent sets of infinite-dimensional trial functions for the fluid velocity $\mathbf{u}$ and pressure p, respectively. These function sets are formally written:

$$\mathcal{S}_u = \left\{ \mathbf{u} | \mathbf{u}\left(\cdot, t\right) \in \left(H^1\left(\Omega_t\right)\right)^{n_{sd}}, u_i = g_i \text{ on } \left(\Gamma_t\right)_{gi} \right\}, \tag{3}$$

$$\mathcal{S}_p = \left\{ p | p\left(\cdot\right) \in L^2\left(\Omega_t\right), \int_{\Omega_t} p d\Omega = 0 \text{ if } \Gamma_t = \left(\Gamma_t\right)_g \right\}. \tag{4}$$

Here $L^2\left(\Omega_t\right)$ denotes the space of scalar-valued functions that are square-integrable on Ω_t, and $\left(H^1\left(\Omega_t\right)\right)^{n_{sd}}$ the space of vector-valued functions with square-integrable derivatives on Ω_t. The functions in $\mathcal{S}_u$ satisfy the essential boundary conditions $u_i = g_i$ on $\left(\Gamma_t\right)_{gi}$ for the fluid mechanics problem. In the case of essential boundary conditions on all boundaries, we require that the average pressure on Ω_t is zero.

With the trial functions we define the test functions $\mathcal{V}_u$ and $\mathcal{V}_p$ as:

$$\mathcal{V}_u = \left\{ \mathbf{w} | \mathbf{w}\left(\cdot\right) \in \left(H^1\left(\Omega_t\right)\right)^{n_{sd}}, w_i = 0 \text{ on } \left(\Gamma_t\right)_{gi} \right\}, \tag{5}$$

$$\mathcal{V}_p = \mathcal{S}_p. \tag{6}$$

Note that the test functions only differ in the definition of the boundary conditions, for which the test functions for linear momentum balance, $\mathcal{V}_u$, vanish on the part of the boundary where the fluid velocity is prescribed.

The variational formulation of the fluid mechanics problem can then be stated in terms of the semi-linear and linear forms B and F, respectively, as follows. Find $\mathbf{u} \in \mathcal{S}_u$ and $p \in \mathcal{S}_p$ such

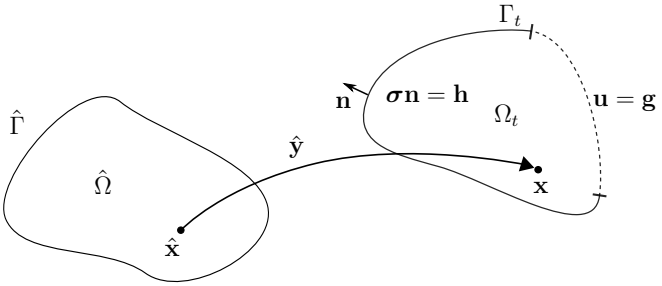

Figure 1: Fluid domain and its boundary in the current configuration.

that $\forall \mathbf{w} \in \mathcal{V}_u$ and $q \in \mathcal{V}_p$:

$$B\left(\{\mathbf{w}, q\}, \{\mathbf{u}, p\}; \hat{\mathbf{u}}\right) - F\left(\{\mathbf{w}, q\}\right) = 0, \tag{7}$$

where

$$\begin{aligned} B\left(\{\mathbf{w}, q\}, \{\mathbf{u}, p\}; \hat{\mathbf{u}}\right) = &\int_{\Omega_t} \mathbf{w}\rho \left(\left.\frac{\partial \mathbf{u}}{\partial t}\right|_{\hat{x}} + (\mathbf{u} - \hat{\mathbf{u}}) \cdot \boldsymbol{\nabla}\mathbf{u} \right) \mathrm{d}\Omega \\ &+ \int_{\Omega_t} \boldsymbol{\varepsilon}(\mathbf{w}) : \boldsymbol{\sigma}(\mathbf{u}, p)\, \mathrm{d}\Omega + \int_{\Omega_t} q \boldsymbol{\nabla} \cdot \mathbf{u}\, \mathrm{d}\Omega, \end{aligned} \tag{8}$$

and

$$F\left(\{\mathbf{w}, q\}\right) = \int_{\Omega_t} \mathbf{w}\rho\mathbf{f}\, \mathrm{d}\Omega + \int_{(\Gamma_t)_h} \mathbf{w} \cdot \mathbf{h}\, \mathrm{d}\Gamma. \tag{9}$$

Here, ρ is the density, $\mathbf{f}$ the body forces, $\mathbf{h}$ is prescribed surface tractions on $(\Gamma)_h$ and $\hat{\mathbf{u}} = \left.\frac{\partial \hat{\mathbf{y}}}{\partial t}\right|_{\hat{x}}$ is the fluid domain velocity. $\left.\right|_{\hat{x}}$ denotes that the time derivative is taken with respect to the reference coordinates of the fluid domain. The Cauchy stress tensor $\boldsymbol{\sigma}$ is defined as:

$$\boldsymbol{\sigma}(\mathbf{u}, p) = -p\mathbf{I} + 2\mu\boldsymbol{\varepsilon}(\mathbf{u}), \tag{10}$$

where $\mathbf{I}$ is the identity tensor, μ the dynamic viscosity and $\boldsymbol{\varepsilon}(\mathbf{w})$ the symmetric strain-rate tensor given by:

$$\boldsymbol{\varepsilon}(\mathbf{w}) = \frac{1}{2}\left(\boldsymbol{\nabla}\mathbf{w} + \boldsymbol{\nabla}\mathbf{w}^T\right). \tag{11}$$

3 ALE-VMS FORMULATION WITH WEAKLY-ENFORCED BCs

This section presents the residual-based variational multiscale (RBVMS) version of the Navier-Stokes equations for incompressible flows in the ALE setting. RBVMS was originally developed for nonmoving domains and successfully applied to turbulent flows (see e.g. [1, 6, 19, 23]). The moving-domain extension of RBVMS, the ALE-VMS formulation [36], was introduced in [2]. With weak enforcement of essential boundary conditions, the no-slip

condition is imposed in a penalty-like fashion allowing for some slip on the interface. This method, which is purely based on numerical stability considerations behaves similarly to a wall model and represents a significant improvement in accuracy for coarse boundary-layer resolution [1, 5, 7, 17].

For the discrete problem we now partition the time-dependent fluid domain into n_{el} finite element subdomains Ω_t^e. Further, we decompose the fluid-object interface Γ_t^b into n_{eb} surface elements. The finite-dimensional functional spaces for trial functions are denoted $\mathcal{S}_u^h$ and $\mathcal{S}_p^h$ and the corresponding test functions $\mathcal{V}_u^h$ and $\mathcal{V}_p^h$ for the velocity and pressure, respectively. We also introduce trial and test functions for the fluid mesh displacement $\hat{\mathbf{y}}$. Superscript h indicate that its attribute is finite-dimensional.

$$\mathcal{S}_m^h = \left\{ \hat{\mathbf{y}}^h | \hat{\mathbf{y}}^h \left(\cdot, t\right) \in \left(H^1\left(\Omega_t\right)\right)^{n_{sd}},\ \hat{y}_i^h = g_i \text{ on } \left(\Gamma_t\right)_{g_i} \right\}, \tag{12}$$

$$\mathcal{V}_m^h = \left\{ \mathbf{w}_m^h | \mathbf{w}_m^h \left(\cdot\right) \in \left(H^1\left(\Omega_t\right)\right)^{n_{sd}},\ w_{mi}^h = 0 \text{ on } \left(\Gamma_t\right)_{g_i} \right\}, \tag{13}$$

$$\tag{14}$$

The ALE-VMS formulation augmented with weak BCs is then given: Find $\mathbf{u}^h \in \mathcal{S}_u^h$, $p^h \in \mathcal{S}_p^h$ and $\hat{\mathbf{y}}^h \in \mathcal{S}_m^h$, such that $\forall \mathbf{w}^h \in \mathcal{V}_u^h$, $q^h \in \mathcal{V}_p^h$ and $\mathbf{w}_m^h \in \mathcal{V}_m^h$:

$$\begin{aligned} &B^{VMS}\left(\left\{\mathbf{w}^h, q^h\right\}, \left\{\mathbf{u}^h, p^h\right\}; \hat{\mathbf{u}}^h\right) + B^{WBC}\left(\left\{\mathbf{w}^h, q^h\right\}, \left\{\mathbf{u}^h, p^h\right\}; \hat{\mathbf{u}}^h\right) \\ &\quad - F^{VMS}\left(\left\{\mathbf{w}^h, q^h\right\}\right) + B^{MSH}\left(\left\{\mathbf{w}_m^h\right\}, \left\{\hat{\mathbf{y}}^h(t) - \hat{\mathbf{y}}^h(\tilde{t})\right\}\right) = 0, \end{aligned} \tag{15}$$

where

$$\begin{aligned} &B^{VMS}\left(\left\{\mathbf{w}^h, q^h\right\}, \left\{\mathbf{u}^h, p^h\right\}; \hat{\mathbf{u}}^h\right) = \\ &\quad \int_{\Omega_t} \mathbf{w}^h \cdot \rho \left(\left.\frac{\partial \mathbf{u}^h}{\partial t}\right|_{\hat{x}} + \left(\mathbf{u}^h - \hat{\mathbf{u}}^h\right) \cdot \boldsymbol{\nabla} \mathbf{u}^h \right) \mathrm{d}\Omega \\ &\quad + \int_{\Omega_t} \boldsymbol{\varepsilon}(\mathbf{w}^h) : \boldsymbol{\sigma}(\mathbf{u}^h, p^h) \,\mathrm{d}\Omega + \int_{\Omega_t} q^h \boldsymbol{\nabla} \cdot \mathbf{u}^h \,\mathrm{d}\Omega \\ &\quad + \sum_{e=1}^{n_{el}} \int_{\Omega_t^e} \tau_{\mathrm{SUPS}} \left(\left(\mathbf{u}^h - \hat{\mathbf{u}}^h\right) \cdot \boldsymbol{\nabla} \mathbf{w}^h + \frac{\boldsymbol{\nabla} q^h}{\rho} \right) \cdot \mathbf{r}_M\left(\mathbf{u}^h, p^h\right) \,\mathrm{d}\Omega \\ &\quad + \sum_{e=1}^{n_{el}} \int_{\Omega_t^e} \rho \nu_{\mathrm{LSIC}} \boldsymbol{\nabla} \cdot \mathbf{w}^h \mathrm{r}_C(\mathbf{u}^h) \,\mathrm{d}\Omega \\ &\quad - \sum_{e=1}^{n_{el}} \int_{\Omega_t^e} \tau_{\mathrm{SUPS}} \mathbf{w}^h \cdot \left(\mathbf{r}_M\left(\mathbf{u}^h, p^h\right) \cdot \boldsymbol{\nabla} \mathbf{u}^h\right) \,\mathrm{d}\Omega \\ &\quad - \sum_{e=1}^{n_{el}} \int_{\Omega_t^e} \frac{\boldsymbol{\nabla} \mathbf{w}^h}{\rho} : \left(\tau_{\mathrm{SUPS}} \mathbf{r}_M\left(\mathbf{u}^h, p^h\right)\right) \otimes \left(\tau_{\mathrm{SUPS}} \mathbf{r}_M\left(\mathbf{u}^h, p^h\right)\right) \,\mathrm{d}\Omega, \end{aligned} \tag{16}$$

$$F^{VMS}\left(\left\{\mathbf{w}^h, q^h\right\}\right) = \int_{\Omega_t} \mathbf{w}^h \rho \,\mathbf{f}^h \,\mathrm{d}\Omega + \int_{(\Gamma_t)_h} \mathbf{w}^h \cdot \mathbf{h}^h \,\mathrm{d}\Gamma, \tag{17}$$

$$
\begin{aligned}
B^{WBC}\left(\left\{\mathbf{w}^h, q^h\right\}, \left\{\mathbf{u}^h, p^h\right\}; \hat{\mathbf{u}}^h\right) = \\
&- \sum_{b=1}^{n_{eb}} \int_{\Gamma^b \cap (\Gamma_t)_g} \mathbf{w}^h \cdot \boldsymbol{\sigma}\left(\mathbf{u}^h, p^h\right) \mathbf{n} \, \mathrm{d}\Gamma \\
&- \sum_{b=1}^{n_{eb}} \int_{\Gamma^b \cap (\Gamma_t)_g} \left(2\mu\boldsymbol{\varepsilon}\left(\mathbf{w}^h\right)\mathbf{n} + q^h\mathbf{n}\right) \cdot \left(\mathbf{u}^h - \mathbf{g}^h\right) \, \mathrm{d}\Gamma \\
&- \sum_{b=1}^{n_{eb}} \int_{\Gamma^b \cap (\Gamma_t)_g^-} \mathbf{w}^h \cdot \rho\left(\left(\mathbf{u}^h - \hat{\mathbf{u}}^h\right) \cdot \mathbf{n}\right)\left(\mathbf{u}^h - \mathbf{g}^h\right) \, \mathrm{d}\Gamma \\
&+ \sum_{b=1}^{n_{eb}} \int_{\Gamma^b \cap (\Gamma_t)_g} \tau_{\mathrm{TAN}}^B \left(\mathbf{w}^h - \left(\mathbf{w}^h \cdot \mathbf{n}\right)\mathbf{n}\right) \cdot \left(\left(\mathbf{u}^h - \mathbf{g}^h\right) - \left(\left(\mathbf{u}^h - \mathbf{g}^h\right) \cdot \mathbf{n}\right)\mathbf{n}\right) \, \mathrm{d}\Gamma \\
&+ \sum_{b=1}^{n_{eb}} \int_{\Gamma^b \cap (\Gamma_t)_g} \tau_{\mathrm{NOR}}^B \left(\mathbf{w}^h \cdot \mathbf{n}\right)\left(\left(\mathbf{u}^h - \mathbf{g}^h\right) \cdot \mathbf{n}\right) \, \mathrm{d}\Gamma. \qquad (18)
\end{aligned}
$$

and

$$
B^{MSH}\left(\left\{\mathbf{w}_m^h\right\}, \left\{\hat{\mathbf{y}}^h(t) - \hat{\mathbf{y}}^h(\tilde{t})\right\}\right) = \int_{\Omega_{\tilde{t}}} \boldsymbol{\varepsilon}(\mathbf{w}_m^h) : \mathbf{D}\,\boldsymbol{\varepsilon}\left(\hat{\mathbf{y}}^h(t) - \hat{\mathbf{y}}^h(\tilde{t})\right) \, \mathrm{d}\Omega. \qquad (19)
$$

In Eqs. 16 – 18 $\mathbf{n}$ is the outward normal vector, τ_{SUPS}, ν_{LSIC}, τ_{TAN} and τ_{NOR} are stabilization parameters which depend on discretization and time stepping (see e.g. [6, 9, 38, 46, 47]). $(\Gamma_t)_g^-$ is defined as the inflow part of $(\Gamma_t)_g$:

$$
\Gamma_g^- = \left\{\mathbf{x} | \left(\mathbf{u}^h - \hat{\mathbf{u}}^h\right) \cdot \mathbf{n} < 0, \forall \mathbf{x} \subset (\Gamma_t)_g\right\}. \qquad (20)
$$

$\mathbf{r}_M$ and r_C are residuals of the linear-momentum balance and continuity, respectively, given by

$$
\mathbf{r}_M = \rho\left(\left.\frac{\partial \mathbf{u}^h}{\partial t}\right|_{\hat{x}} + \left(\mathbf{u}^h - \hat{\mathbf{u}}^h\right) \cdot \boldsymbol{\nabla}\mathbf{u}^h - \mathbf{f}^h\right) - \boldsymbol{\nabla} \cdot \boldsymbol{\sigma}\left(\mathbf{u}^h, p^h\right), \qquad (21)
$$

$$
\mathrm{r}_C = \boldsymbol{\nabla} \cdot \mathbf{u}^h. \qquad (22)
$$

The fluid mesh part of the problem, Eq. 19, is the result of a linear-elastic solid with zero inertia and no external forcing and is governed by the fluid mesh strain rates (Eq. 11) and the elasticity tensor $\mathbf{D}$ evaluated in the fluid-domain configuration at time $\tilde{t} < t$. See [3] for a detailed description. For the fluid mesh material we use Jabobian-based stiffening [26, 42, 44], a non-physical material law whose only purpose is to preclude high mesh distortion at a low computational cost.

In a forced-vibration setting, the mesh velocity $\hat{\mathbf{u}}^h$ is prescribed on all surfaces, including the fluid-object interface, which completes the fluid mesh problem.

We let $\mathbf{U} = [\mathbf{u}_B]$, $\dot{\mathbf{U}} = [\dot{\mathbf{u}}_B]$ and $\mathbf{P} = [p_B]$ denote the vectors of nodal velocity, acceleration and pressure for the fluid problem, respectively, and $\ddot{\hat{\mathbf{Y}}} = \left[\ddot{\hat{\mathbf{y}}}_B\right]$, $\dot{\hat{\mathbf{Y}}} = \left[\dot{\hat{\mathbf{y}}}_B\right]$ and $\hat{\mathbf{Y}} = [\hat{\mathbf{y}}_B]$ denote the vectors of nodal fluid mesh acceleration, velocity and displacements, respectively.

With this definition, the semi-discrete form of Eq. 15 becomes: find $\mathbf{U}$, $\dot{\mathbf{U}}$, $\mathbf{P}$, $\ddot{\hat{\mathbf{Y}}}$, $\dot{\hat{\mathbf{Y}}}$ and $\hat{\mathbf{Y}}$ such that:

$$\mathbf{N}_M\left(\dot{\mathbf{U}}, \mathbf{U}, \mathbf{P}, \ddot{\hat{\mathbf{Y}}}, \dot{\hat{\mathbf{Y}}}, \hat{\mathbf{Y}}\right) = \mathbf{0}, \tag{23}$$

$$\mathbf{N}_C\left(\dot{\mathbf{U}}, \mathbf{U}, \mathbf{P}, \ddot{\hat{\mathbf{Y}}}, \dot{\hat{\mathbf{Y}}}, \hat{\mathbf{Y}}\right) = \mathbf{0}, \tag{24}$$

$$\mathbf{N}_{msh}\left(\dot{\mathbf{U}}, \mathbf{U}, \mathbf{P}, \ddot{\hat{\mathbf{Y}}}, \dot{\hat{\mathbf{Y}}}, \hat{\mathbf{Y}}\right) = \mathbf{0}, \tag{25}$$

where $\mathbf{N}_M$, $\mathbf{N}_C$ and $\mathbf{N}_{msh}$ are the discrete residual vectors for fluid linear-momentum balance and continuity and fluid mesh linear-momentum, respectively. The nonlinear equation system at Eqs. 23 – 25 is solved using a predictor-multicorrector Newton-Raphson method with generalized-α time integration, which is a second order accurate, unconditionally stable algorithm for both first and second order systems, with control over high-frequency dissipation [3, 13, 25].

4 AERODYNAMIC FORCES ON BRIDGES AND THE FORCED-VIBRATION EXPERIMENT

This section gives a brief introduction to the aerodynamic forces in the context of bridge engineering. The motion-induced forces have been emphasized, since these are the main focus in this work. Further, the forced-vibration wind tunnel experiment is introduced, and an algorithm for numerical simulation of such problems is given.

4.1 Motion induced wind forces and forced-vibration wind tunnel experiments

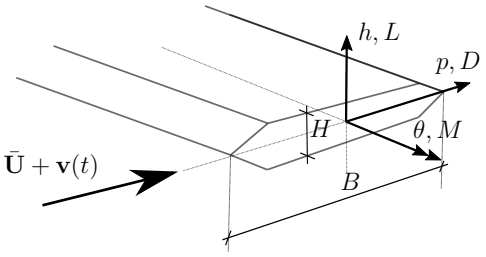

Figure 2: Aerodynamic forces on bridge section.

Aerodynamic forces on bridge decks for strong winds are commonly computed from quasi-steady theory [29] and the strip method [39]. With this approach the wind speed is split into a stationary part $\bar{\mathbf{U}} = [U, 0]^T$ and a fluctuating part with zero mean $\mathbf{v}(t) = [u(t), w(t)]^T$.

The lateral, vertical and rotational degrees of freedom with respect to the deck centroid are denoted $p(t)$, $h(t)$, and $\theta(t)$, respectively, with corresponding aerodynamic forces $\mathbf{Q}(t) = [D(t), L(t), M(t)]^T$. See Fig. 2.

The quasi-steady forces are given as:

$$\mathbf{Q}(t) = \mathbf{Q}_s + \mathbf{Q}_{se}(t) + \mathbf{Q}_b(t), \tag{26}$$

where $\mathbf{Q}_s$ is the static force vector due to mean wind:

$$\mathbf{Q}_s = \begin{bmatrix} D_s \\ L_s \\ M_s \end{bmatrix} = \frac{1}{2}\rho U^2 \begin{bmatrix} HC_D(\theta) \\ BC_L(\theta) \\ B^2 C_M(\theta) \end{bmatrix}, \tag{27}$$

where B and H are the width and height of the cross section, respectively. C_M, C_L and C_M are the shape-dependent drag, lift and pitching moment coefficients, respectively. The self-excited forces, $\mathbf{Q}_{se}(t)$[12, 24, 33, 35], are introduced by structural motions, and the buffeting forces $\mathbf{Q}_b(t)$[10, 11, 14, 31] are induced by horizontal and vertical wind fluctuations. As the turbulence intensity in the wind tunnel is very low the buffeting forces are neglected. Thus, the self-excited forces are simply obtained by subtracting the mean forces (Eq. 26). In the simulations we define zero turbulence by using smooth inflow boundary conditions.

As an alternative to the free vibration wind tunnel experiment[32], the forced-vibration experiment[16] has proven to be an efficient method to obtain the self-excited forces and flutter characteristics of bridge sections[15, 30]. Here the sectional model is subjected to a prescribed motion history for which the forces are measured. The aerodynamic forces, $\mathbf{Q}(t)$, are obtained as the difference between in-wind and still air measurements. The wind tunnel experiments performed in this work are carried out at the Fluid Mechanics Laboratory, Department of Energy and Process Engineering, NTNU. A description of the rig can be found in [34]. The experiments are typically performed for vibration frequencies up to 2.5 Hz and wind speeds ranging from 3 to 12 m/s.

4.2 Numerical simulation of the forced-vibration experiment

To simulate the forced-vibration experiment, a 2D rigid body motion of the bridge deck is implemented as follows. Let $\mathbf{X}$ and $\mathbf{x}$ be the reference and current coordinates of a set of rigidly connected points, respectively. Further, let $\mathbf{X}_c$ and $\mathbf{x}_c$ denote the center of rotation in the various configurations. Any 2D rigid body motion can then be uniquely defined by the rotation θ and displacements $\mathbf{d}_c = \mathbf{x}_c - \mathbf{X}_c = [p,\, h]^T$ of the center of rotation, corresponding to the three wind tunnel degrees of freedom (Fig. 2).

The current position, $\mathbf{x}(t)$, is then given:

$$\mathbf{x}(t) = \mathbf{R}\left(\theta(t)\right)\left(\mathbf{X} - \mathbf{X}_c\right) + \mathbf{x}_c(t), \tag{28}$$

where $\mathbf{R}\left(\theta\right)$ is the rotation tensor.

For a prescribed motion, Eq. 28 is used to govern the time-dependent fluid mesh boundary conditions. These are applied to the bridge deck and its boundary layer elements and the interior surface enclosing the wake (see Sec. 5.1). In contrast to FSI/ FOI computations, where tractions

from the fluid mechanics block is used to move the structure and fluid mesh, we have here chosen to solve the fluid mesh problem first and implemented the following algorithm.

Algorithm 1: CFD analysis around rigid objects with prescribed motion.

```
Partition for parallel computation, initialize;
Loop over time steps;
for t = 1 to T do
    Predict solution vectors U, P, and Ŷ̇;
    Multicorrector stage;
    for iter = 1 to itermax do
        Solve fluid mesh problem (iter = 1);
            Set fluid mesh boundary conditions:
            Ŷ_t = R(θ)(X − X_c) + x_c at object surface and boundary layers, and
            Ŷ_t = R(θ/2)(X − X_c) + x_c at wake surface;
            Build LHS matrix and RHS vector;
            Precondition and solve to obtain Ŷ_t, Ŷ̇_t Ŷ̈_t;
        Solve fluid mechanics problem;
            Build LHS matrix and RHS vector of the ALE-VMS equations;
            Precondition and solve to obtain U_t, U̇_t and P_t;
    end
end
```

A detailed description to each step can be found in [8].

5 NUMERICAL RESULTS

In this section results from the numerical simulations of the Hardanger Bridge sectional model are presented and compared with experimental data. The vertical and pitching motions are analyzed.

5.1 Analysis setup

The flow domain is taken as a 500 mm wide slice of the wind tunnel with the inflow and outflow surface 1200 mm and 2800 mm from the bridge deck centroid, respectively. The domain height is 1815 mm and the deck centroid is placed 930 mm above the floor, which correspond to the physical dimensions of the wind tunnel.

For the fluid mechanics boundary conditions, smooth flow of $U = 4$ m/s is prescribed on the inflow surface. The walls, including the transverse boundaries, are constrained with no penetration, and on the bridge deck weakly enforced no-slip boundary condition is employed. The outflow surface is traction-free.

An interior surface enclosing the deck and its wake (see Fig. 3) is defined in order to perform local mesh refinement around the deck and in the wake region, and to employ mesh moving boundary conditions. This surface is constrained to follow the vertical and horizontal motions

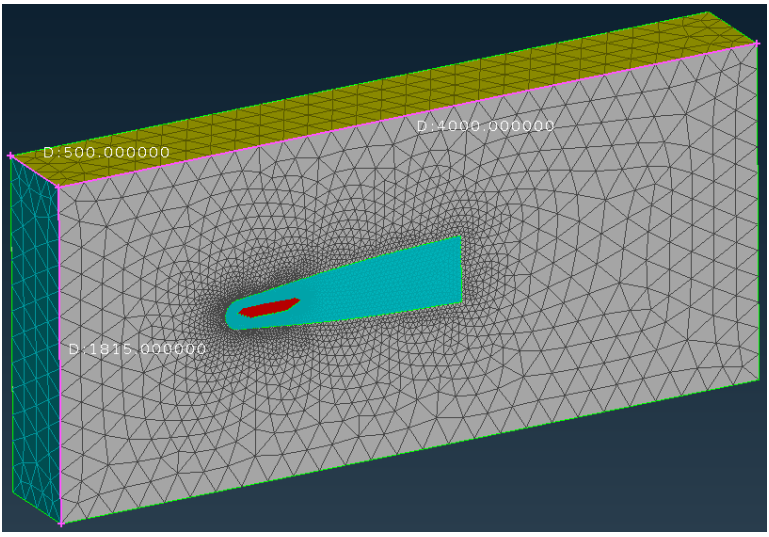

Figure 3: The analysis domain represents a 500 mm wide slice of the wind tunnel.

of the bridge deck and rotate with half the magnitude. With this definition mesh resolution in the turbulent region is maintained, even for relatively large rotations.

At the bridge deck surface 10 layers of prismatic elements with thickness 0.25 mm are generated. These boundary layers constitute approximately half of the nodes in the computational model, see Fig. 4b. In the fluid mesh problem these are treated rigidly, which besides keeping the mesh distortion at a minimum also reduce the fluid mesh problem significantly. Other volumes are meshed with linear tetrahedra, giving approximately $4 \cdot 10^6$ elements in total. The bridge deck grid, on which the aerodynamic forces are evaluated, is unstructured with local refinement near all features, see Fig. 5.

5.2 Forced-vibration, vertical mode

In this test, the bridge deck is excited in a vertical harmonic motion with amplitude 15 mm, same as in the wind tunnel, and a frequency of 1.1 Hz. From a fully developed turbulent flow field 5 cycles are run. The current flow velocity, time stepping and discretization yield a Courant number of approximately 2.4 throughout the analysis. Fig. 6 shows the total unfiltered forces from the analysis, and Fig. 7 shows velocity streamline plots at points ”a” and ”b” (ref. Fig. 6). To obtain the self-excited forces, we subtract the mean forces, $D = 0.335$ N/m, $L = 0.685$ N/m and $M = 0.0476$ Nm/m, and remove the vortex shedding fluctuations by applying a cascaded buttersworth filter[28] with cutoff frequency of 3 Hz. The filtered and unfiltered self-excited forces are shown in Fig. 8.

To compare with the experimental values, we choose a random time window from the wind

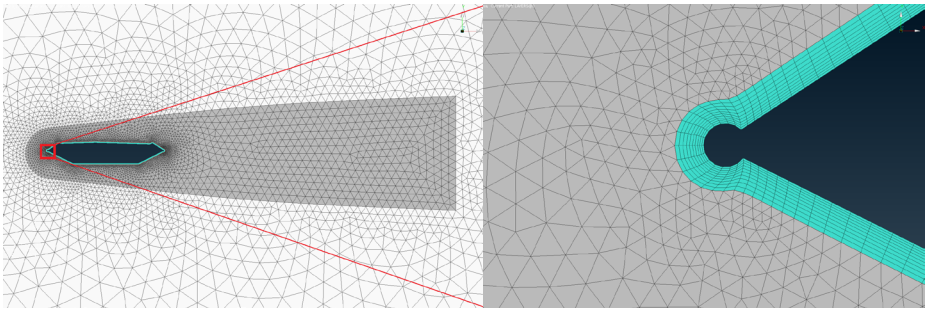

(a) Wake. **(b)** Boundary layer elements.

Figure 4: Closeup of the aerodynamic mesh near the bridge deck.

tunnel and compute the self-excited forces in a similar manner, using the same digital filter. Since the mean wind velocity is slightly different, the self-excited forces is now represented in terms of the dimensionless load coefficients, $C_{D,se}$, $C_{L,se}$ and $C_{M,se}$ (ref. Eq. 27), normalized with $\rho = 1.225\text{kg/m}^3$, $B = 0.366$ m, and $H = 0.0666$ m. The results are shown in Fig. 9. While the self-excited lift and pitching moment are in very good agreement with the experiments, both with respect to phase and magnitude of the loads, the self-excited drag does not match. One should however note that the self-excited drag force is very small for heaving modes and difficult to measure experimentally. The resulting signal thus contains a lot of noise. This is not an issue in the simulations, and a periodic drag in the same phase as the lift and pitching moment is revealed.

5.3 Forced-vibration, torsional mode

Next we study the torsional mode of the bridge deck. In the experiments and simulation the deck is excited in a harmonic motion with amplitude 2° and a frequency of 1.1 Hz. The wind velocity is approximately $U = 4$ m/s. 5 cycles are run, and the total unfiltered forces are shown in Fig. 10. Note how the drag is almost constant for such small rotations. Fig. 11 shows velocity streamline plots one nose up and one nose down instance (points ”c” and ”d” in Fig. 10). Note the alternating turbulent flow on the top and bottom of the deck.

In the same way as for the vertical mode, the forces are filtered and detrended, and a comparison of the self-excited forces for the simulation and the wind tunnel experiment is shown in Fig. 12. Again, lift and pitching moment is accurately represented. For the motion-dependent drag, we can see a common content of a double frequency signal, but the drag is also here vanishingly small and difficult to capture in the experiments, at least in the time domain.

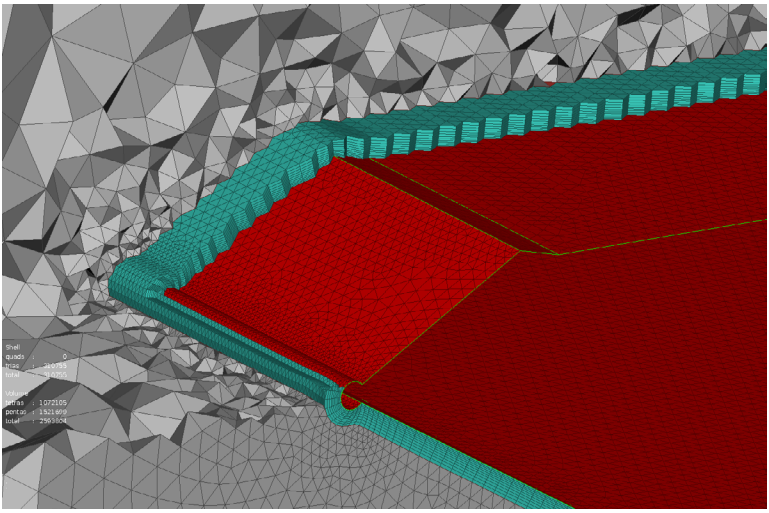

Figure 5: 3D view of mesh resolution near the bridge deck.

6 CONCLUSIONS

A framework for numerical simulation of forced-vibration wind tunnel experiments has successfully been developed using ALE-VMS techniques. Numerical studies of the Hardanger Bridge section model was carried out for harmonic excitation of one vertical and one torsional mode, and the results are in very good agreement with the wind tunnel experiments.

Such flow computations lead to a one-way coupled problem between the fluid and the fluid mesh. We have prescribed the motions to not only the bridge deck surface but also to the boundary layer elements, which constitute a large proportion of the fluid mesh degrees-of-freedom. This moves the mesh distortion away from the area of interest and reduces the fluid mesh problem significantly. In fact, there is only a small increase in computational cost compared to CFD analysis itself.

In bridge engineering, self-excited forces are used to govern the flutter characteristics. This requires the dependency of wind velocity and vibration frequency on the self-excited forces and several experiments must be performed. This can be very effectively done using the computational framework presented herein, as the numerical results reveal that three, or even two cycles, are sufficient to provide an accurate representation of self-excited lift and pitching moment. In the present experiments the self-excited drag is so small that no clear repeating pattern is recognized. For the simulations however, we see harmonic components also in the drag, suggesting that we for such small forces may actually produce more reliable and realistic results than the experiments.

This work shows that the ability of the ALE-VMS method to effectively perform bluff body

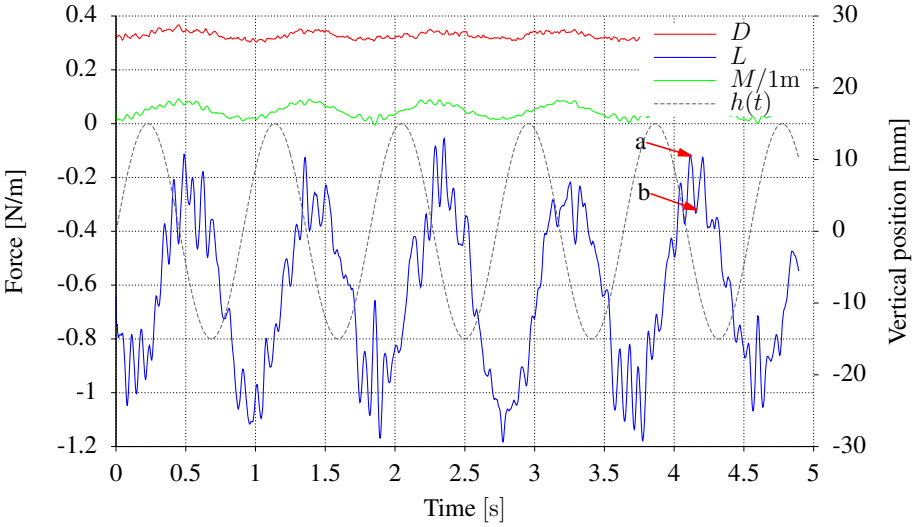

Figure 6: Total forces, vertical mode, $h = 15$ mm, $U = 4$ m/s, $f = 1.1$ Hz.

aerodynamic computations in moving domains with high accuracy may support the design process for a new generation of long-span suspension bridges. It can also be helpful to verify scalability of wind tunnel experiments.

7 ACKNOWLEDGMENT

This work was carried out with financial support from the Norwegian Public Roads Administration. The authors greatly acknowledge this support.

Further, we would like to acknowledge Bartosz Siedziako and Henrik Skyvulstad, Dept. of Structural Engineering, NTNU, for providing the wind tunnel results used in this work and Prof. Ming-Chen Hsu, Mechanical Engineering, Iowa State University, for computer-specific support.

The simulations were performed on resources provided by UNINETT Sigma2 - the National Infrastructure for High Performance Computing and Data Storage in Norway.

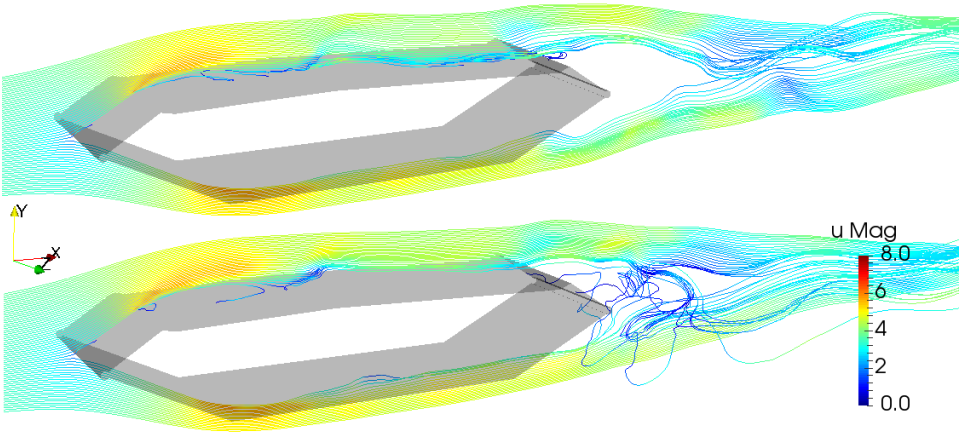

Figure 7: Velocity streamlines near maximum and minimum vortex fluctuations at $t = 4.125$ s (top) and $t = 4.175$ s (bottom), corresponding to point a and b in Fig. 6, respectively.

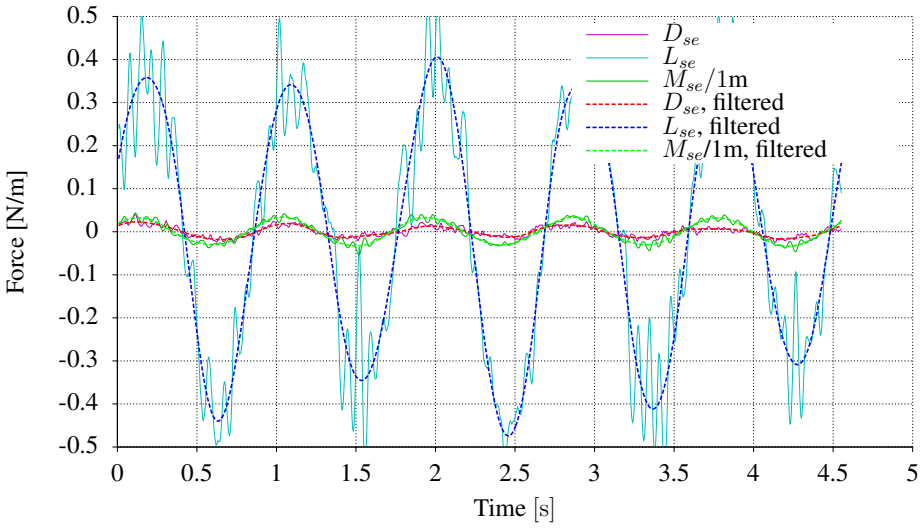

Figure 8: Raw and filtered self-excited forces, vertical mode, $h = 15$ mm, $U = 4$ m/s, $f = 1.1$ Hz.

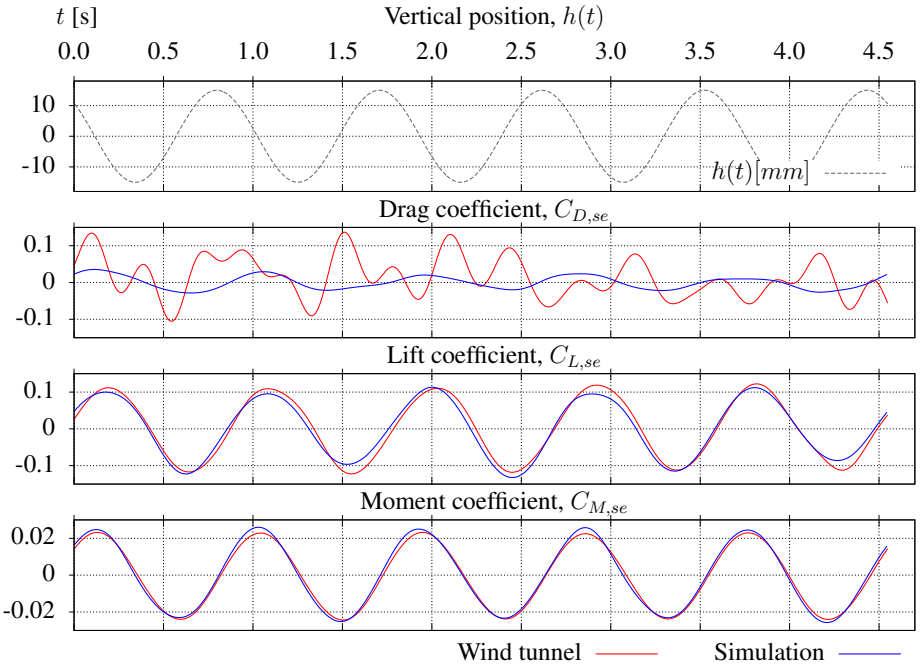

Figure 9: Load coefficients for self-excited aerodynamic forces, vertical mode, $h = 15$ mm, $U = 4$ m/s, $f = 1.1$ Hz.

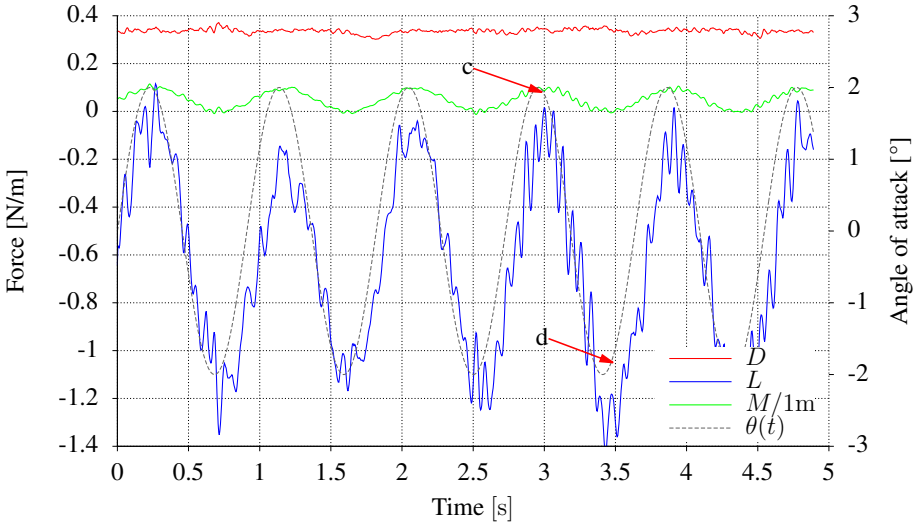

Figure 10: Total forces, pitching mode, $\theta = 2°$, $u = 4$ m/s, $f = 1.1$ Hz.

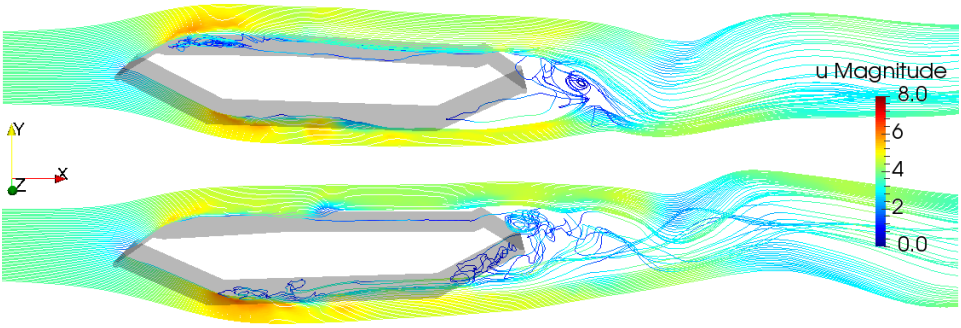

Figure 11: Velocity streamlines near maximum and minimum vortex fluctuations at $t = 2.984$ s (top) and $t = 3.484$ s (bottom), corresponding to point c and d in Fig. 10, respectively.

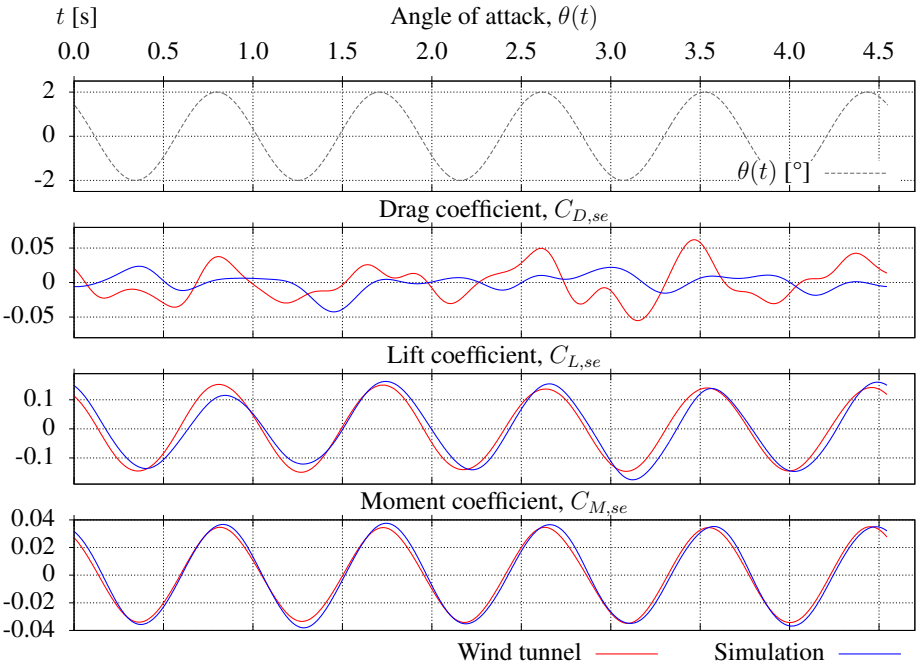

Figure 12: Load coefficients for self-excited aerodynamic forces, torsional mode, $\theta = 2°$, $U = 4$ m/s, $f = 1.1$ Hz.

REFERENCES

[1] Bazilevs, Y. and Akkerman, I. Large eddy simulation of turbulent Taylor-Couette flow using isogeometric analysis and the residual-based variational multiscale method. *Journal of Computational Physics* (2010) **229**:3402–3414.

[2] Bazilevs, Y., Calo, V.M., Cottrell, J.A., Hughes, T.J.R., Reali, A. and Scovazzi, G. Variational multiscale residual-based turbulence modeling for large eddy simulation of incompressible flows. *Computer Methods in Applied Mechanics and Engineering* (2007) **197**:173–201.

[3] Bazilevs, Y., Calo, V.M., Hughes, T.J.R. and Zhang, Y. Isogeometric fluid-structure interaction: Theory, algorithms, and computations. *Computational Mechanics* (2008) **43**:3–37.

[4] Bazilevs, Y., Gohean, J.R., Hughes, T.J.R., Moser, R.D. and Zhang, Y. Patient-specific isogeometric fluid-structure interaction analysis of thoracic aortic blood flow due to implantation of the Jarvik 2000 left ventricular assist device. *Computer Methods in Applied Mechanics and Engineering* (2009) **198**:3534–3550.

[5] Bazilevs, Y. and Hughes, T.J.R. Weak imposition of Dirichlet boundary conditions in fluid mechanics. *Computers and Fluids* (2007) **36**:12–26.

[6] Bazilevs, Y., Michler, C., Calo, V.M. and Hughes, T.J.R. Weak Dirichlet boundary conditions for wall-bounded turbulent flows. *Computer Methods in Applied Mechanics and Engineering* (2007) **196**:4853–4862.

[7] Bazilevs, Y., Michler, C., Calo, V.M. and Hughes, T.J.R. Isogeometric variational multiscale modeling of wall-bounded turbulent flows with weakly enforced boundary conditions on unstretched meshes. *Computer Methods in Applied Mechanics and Engineering* (2010) **199**:780–790.

[8] Bazilevs, Y., Takizawa, K. and Tezduyar, T.E. *Computational Fluid-Structure Interaction: Methods and Applications*. John Wiley & Sons, Ltd, Vol. I (2013).

[9] Brooks, A.N. and Hughes, T.J.R. Streamline upwind/Petrov-Galerkin formulations for convection dominated flows with particular emphasis on the incompressible Navier-Stokes equations. *Computer Methods in Applied Mechanics and Engineering* (1982) **32**:199–259.

[10] Chen, X. and Kareem, A. Advances in Modeling of Aerodynamic Forces on Bridge Decks. *Journal of Engineering Mechanics* (2002) **128**:1193–1205.

[11] Chen, X., Matsumoto, M. and Kareem, A. Time Domain Flutter and Buffeting Response Analysis of Bridges. *Journal of Engineering Mechanics* (2000) **126**:7–16.

[12] Chen, Z.Q., Yu, X.D., Yang, G. and Spencer, B.F. Wind-Induced Self-Excited Loads on Bridges. *Journal of Structural Engineering* (2005) **131**:1783–1793.

[13] Chung, J. and Hulbert, G.M. A Time Integration Algorithm for Structural Dynamics With Improved Numerical Dissipation: The Generalized-α Method. *Journal of Applied Mechanics* (1993) **60**:371–375.

[14] Davenport, A.G. Buffeting of a suspension bridge by stormy winds. *J. Struct. Div.* (1962) **88**:233–268.

[15] Haan, F.L., Kareem, A. and Szewczyk, A.A. The effects of turbulence on the pressure distribution around a rectangular prism. *Journal of Wind Engineering and Industrial Aerodynamics* (1998) **77**:381–392.

[16] Halfman, R.L. Experimental Aerodynamic Derivatives of a Sinusoidally Oscillating Airfoil in Two-Dimensional Flow. *Technical report*, Massachusetts Inst. of Tech.; Cambridge. (1952).

[17] Hsu, M.C., Akkerman, I. and Bazilevs, Y. Wind turbine aerodynamics using ALE–VMS: validation and the role of weakly enforced boundary conditions. *Computational Mechanics* (2012) **50**:499–511.

[18] Hsu, M.C., Bazilevs, Y., Takizawa, K. and Tezduyar, T.E. ALE-VMS and ST-VMS methods for computer modeling of wind-turbine rotor aerodynamics and fluid-structure interaction. *Mathematical Models and Methods in Applied Sciences* (2014) **22**:1–62.

[19] Hughes, T.J.R. Multiscale phenomena: Green's functions, the Dirichlet-to-Neumann formulation, subgrid scale models, bubbles and the origins of stabilized methods. *Computer Methods in Applied Mechanics and Engineering* (1995) **127**:387–401.

[20] Hughes, T.J.R., Feijóo, G.R., Mazzei, L. and Quincy, J.B. The variational multiscale method—a paradigm for computational mechanics. *Computer Methods in Applied Mechanics and Engineering* (1998) **166**:3–24.

[21] Hughes, T.J.R., Franca, L.P. and Balestra, M. A new finite element formulation for computational fluid dynamics: V. Circumventing the babuška-brezzi condition: a stable Petrov-Galerkin formulation of the stokes problem accommodating equal-order interpolations. *Computer Methods in Applied Mechanics and Engineering* (1986) **59**:85–99.

[22] Hughes, T.J.R., Liu, W.K. and Zimmermann, T.K. Lagrangian-Eulerian finite element formulation for incompressible viscous flows. *Computer Methods in Applied Mechanics and Engineering* (1981) **29**:329–349.

[23] Hughes, T.J.R., Oberai, A.A. and Mazzei, L. Large eddy simulation of turbulent channel flows by the variational multiscale method. *Physics of Fluids* (2001) **13**:1784–1799.

[24] Jain, A., Jones, N.P. and Scanlan, R.H. Coupled Flutter and Buffeting Analysis of Long-Span Bridges. *Journal of Structural Engineering* (1996) **122**:716–725.

[25] Jansen, K.E., Whiting, C.H. and Hulbert, G.M. A generalized-α method for integrating the filtered Navier-Stokes equations with a stabilized finite element method. *Comput. Methods Appl. Mech. Engrg.* (2000) **190**:305–319.

[26] Johnson, A.A. and Tezduyar, T.E. Mesh update strategies in parallel finite element computations of flow problems with moving boundaries and interfaces. *Computer Methods in Applied Mechanics and Engineering* (1994) **119**:73–94.

[27] Korobenko, A., Hsu, M.C., Akkerman, I., Tippmann, J. and Bazilevs, Y. Structural Mechanics Modeling and Fsi Simulation of Wind Turbines. *Mathematical Models and Methods in Applied Sciences* (2013) **23**:249–272.

[28] Matthaei, G.L., Young, L. and Jones, E.M.T. *Microwave filters, impedance-matching networks, and coupling structures*. McGraw-Hill, Vol. I (1964).

[29] Parkinson, G. and Brooks, N. On the aeroelastic instability of bluff cylinders. *Journal of applied mechanics* (1961) **47**:557–566.

[30] Sarkar, R.R., Jones, N.P. and Scanlan, R.H. Identification of aeroelastic parameters of flexible bridges. *ASCE J. Eng. Mech.* (1994) **120**:1718–1742.

[31] Scanlan, R.H. Problematics in Formulation of Wind Force Models for Bridge Decks. *Journal of Engineering Mechanics* (1993) **119**:1353–1375.

[32] Scanlan, R.H. and Sabzevari, A. Experimental Aerodynamic Coefficients in the Analytical Study of Suspension Bridge Flutter. *Journal of Mechanical Engineering Science* (1969) **11**:234–242.

[33] Scanlan, R.H. and Tomko, J. Airfoil and bridge deck flutter derivatives. *Journal of the Engineering Mechanics Division* (1971) **97**:1717–1737.

[34] Siedziako, B., Øiseth, O. and Rönnquist, A. A new setup for section model tests of bridge decks. *Proceedings of 12th UK Conference on Wind Engineering* (2016) :11–14.

[35] Singh, L., Jones, N.P., Scanlan, R.H. and Lorendeaux, O. Identification of lateral flutter derivatives of bridge decks. *Journal of Wind Engineering and Industrial Aerodynamics* (1996) **60**:81–89.

[36] Takizawa, K., Bazilevs, Y. and Tezduyar, T.E. Space-Time and ALE-VMS Techniques for Patient-Specific Cardiovascular Fluid-Structure Interaction Modeling. *Archives of Computational Methods in Engineering* (2012) **19**:171–225.

[37] Takizawa, K., Bazilevs, Y., Tezduyar, T.E., Hsu, M.C., Øiseth, O., Mathisen, K.M., Kostov, N. and McIntyre, S. Engineering Analysis and Design with ALE-VMS and Space-Time Methods. *Archives of Computational Methods in Engineering* (2014) **21**:481–508.

[38] Takizawa, K. and Tezduyar, T.E. Multiscale space–time fluid–structure interaction techniques. *Computational Mechanics* (2011) **48**:247–267.

[39] Tamura, Y. and Kareem, A. *Advanced structural wind engineering*. Springer Japan, Vol. I (2013).

[40] Tezduyar, T.E. Stabilized Finite Element Formulations for Incompressible Flow Computations. *Advances in Applied Mechanis* (1992) **28**:1–44.

[41] Tezduyar, T.E. Computation of moving boundaries and interfaces and stabilization parameters. *International Journal for Numerical Methods in Fluids* (2003) **43**:555–575.

[42] Tezduyar, T.E., Aliabadi, S., Behr, M., Johnson, A. and Mittal, S. Parallel finite-element computation of 3D flows. *Computer* (1993) **26**:27–36.

[43] Tezduyar, T.E., Behr, M. and Liou, J. A new strategy for finite element computations involving moving boundaries and interfaces—The deforming-spatial-domain/space-time procedure: I. The concept and the preliminary numerical tests. *Computer Methods in Applied Mechanics and Engineering* (1992) **94**:339–351.

[44] Tezduyar, T.E., Behr, M., Mittal, S. and Johnson, A.A. Computation of unsteady incompressiblke flows and massively parallel implementations. *New Methods in Transient Analysis* (1992) **246**:7–24.

[45] Tezduyar, T.E., Behr, M., Mittal, S. and Liou, J. A new strategy for finite element computations involving moving boundaries and interfaces—The deforming-spatial-domain/space-time procedure: II. Computation of free-surface flows, two-liquid flows, and flows with drifting cylinders. *Computer Methods in Applied Mechanics and Engineering* (1992) **94**:353–371.

[46] Tezduyar, T.E. and Osawa, Y. Finite element stabilization parameters computed from element matrices and vectors. *Computer Methods in Applied Mechanics and Engineering* (2000) **190**:411–430.

[47] Tezduyar, T.E. and Park, Y.J. Discontinuity-capturing finite element formulations for nonlinear convection-diffusion-reaction equations. *Computer Methods in Applied Mechanics and Engineering* (1986) **59**:307–325.

[48] Tezduyar, T.E. and Sathe, S. Modeling of fluid-structure interactions with the space-time finite elements: solution techniques. *International Journal for Numerical Methods in Fluids* (2007) **54**:855–900.

[49] Vegdirektoratet. Statusrapport Ferjefri E39. *Technical report* (2015).

Tissue composition based nonlinear FEM simulation of the soft palate using patient specific 3D anatomy

Hongliang Liu[1]; Victorien Emile Prot[1]; Bjørn Helge Skallerud[1]

([1]Biomechanics Division, Department of Structural Engineering, The Norwegian University of Science and Technology, NTNU, NO-7491 Trondheim, Norway)
e-mail: hongliang.liu@ntnu.no

Abstract

Obstructive sleep apnea syndrome affects a large part of the population. In the current study, modeling and simulation of the response of the soft palate in the upper airway is addressed. A 3D patient specific finite element model is developed based on CT images. The quantitative histology study of (Ettema and Kuehn, Journal of Speech, Language, and Hearing Research: 37 1994) is used as a basis for soft tissue organization and modeling. The tissue is simplified to consist of three types, each with their specific constitutive models and corresponding parameters: muscle and connective tissue (three cases including the Holzapfel type anisotropic model and Neo-Hookean model), adipose tissue (accounting for fiber dispersion according to Holzapfel model), and glandular tissue (Neo-Hookean model). The influence of different boundary conditions is also investigated, comparing response obtained with a cantilever plate model and a plate constrained on three sides (corresponding to the actual anatomy). Comparison of homogenous and layered tissue response predictions is provided. Finally, using the patient specific 3D model, the influence of gravity is examined. The results show that anatomically representative boundary conditions should be accounted for, and that a detailed layered material model may make the simulation more physiological.

Keywords: Soft palate; Biomechanics; Anisotropy; Nonhomogeneous; 3D modeling; Tissue composition

1 Introduction

The soft palate is a complex soft tissue structure located at the back of the mouth that prevents food and fluids from entering the nasal cavity during swallowing and guides the airflow through either the mouth or the nose during breathing. In addition, the anatomy and the biomechanical behavior of the soft palate play a key role in understanding Obstructive Sleeping Apnea (OSA) (Balsevičius et al. 2015; Cho et al. 2013). During the upper airway obstruction process with mouth closed, the soft palate comes into contact with the posterior pharynx wall due to the pressure drop and this will close the upper airway and bring corresponding sleeping problems to the patients. Therefore, detailed mechanical modeling of the soft palate in the upper airway (see Fig. 1) may improve our understanding of OSA.

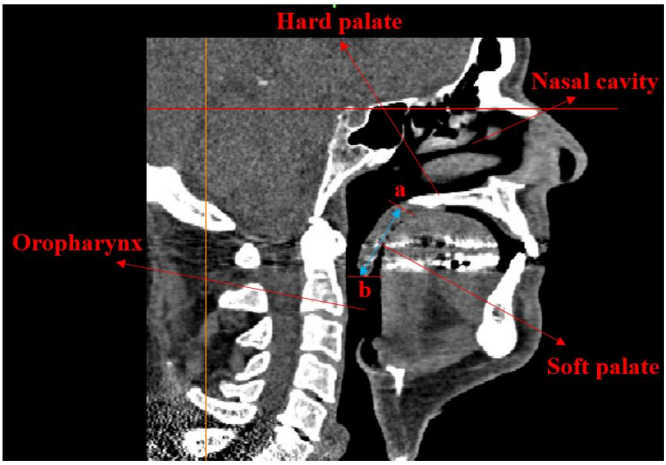

Fig. 1 CT image of the upper airway. The markers 'a' and 'b' denote the side between the soft palate and the hard palate and the bottom edge of the soft palate tip, respectively.

Upper airway models have been used to investigate the air flow features including the pressure distribution and velocity variation using computational fluid dynamics (CFD) simulations (Wang and Elghobashi 2014; Zhao et al. 2013a) or fluid-solid interaction (FSI) simulations (Pirnar et al. 2015; Zhao et al. 2013b). Additionally, the soft palate's response to the airway's pressure field has been investigated. Berry et al. (1999) presented an approximate 2D cantilever model of the soft palate and the collapse shape of the soft palate was obtained. Malhotra et al. (2002) employed a 2D planar model to investigate the closing pressure of the soft palate. In their finite element (FE) model, based on clinical results, a fitted Young's modulus value of soft palate was obtained. Huang et al. (2007) further developed a partial three dimensional upper airway model including the soft palate in which the midsagittal profile of the soft palate was used. Sun et al. (2007) presented the movement of soft palate during breathing with a simplified 3D soft palate geometry model. All the above research works for the soft palate are based on 2D and simplified 3D models. Therefore, it motivates to create a more accurate anatomic and physiologic model of the soft palate to study pharyngeal collapse, which is one of the key physiological factors for OSA.

Material and geometrical nonlinearities, non-uniform and time varying pressure distribution have to be taken into account in numerical analysis of the global response of the soft palate. FSI procedures using detailed 3D geometries of the upper airway may be successful to obtain a physiological air pressure field. However, this is computationally expensive. Wang et al. (2012) developed anatomically accurate FSI models of the upper airway and soft palate. The deformations of the soft palate obtained in their study were somewhat small and the soft palate was modeled as a homogeneous linear elastic material.

Previous numerical studies of the soft palate have focused on 2D and 3D models with linear elastic homogeneous materials. Linear elasticity may be sufficient under particular conditions (Pirnar et al. 2015; Wang et al. 2012). However, in order to investigate pharyngeal collapse

due to the soft palate, analyses of large deformations need to be addressed and thus material nonlinearities accounted for. Additionally, Ettema and Kuehn (1994) showed that the structure of soft palate resembles a composite material. Hence, the material properties of its different constituents need to be considered.

Muscle activation has an influence on the biomechanical behavior of the soft palate and the neuromuscular response of the soft palate to the airway narrowing was observed by Mortimore et al. (1995). However, during sleep, the OSA patients' neuromuscular response is much smaller than that of normal people (Patil et al. 2007). This neuromuscular compensation defectiveness during sleep for the obstructive sleep apnea patients is further validated by the study of McGinley et al. (2008). A comparison study between the OSA patients group and control normal group showed that the neuromuscular response is smaller in the patient group than for the normal group. Therefore, it may be sufficient to consider only the passive condition for numerical modeling of OSA.

Medical imaging technologies, such as computed tomography (CT) or magnetic resonance (MR) are valuable tools in order to reconstruct the soft palate geometries. These techniques have been used to create upper airway models (Mihaescu et al. 2008; Mylavarapu et al. 2009; Sera et al. 2015; Sung et al. 2006), but soft palate models reconstructed from medical images are scarce (see (Wang et al. 2012)). Therefore, in this study, we present a nonlinear FE model of the soft palate reconstructed from CT images and taking into account material nonlinearities (i.e. hyperelasticity and anisotropy) and heterogeneities. This model is used to investigate the global response of the soft plate of a specific patient suffering from OSA. Our goals are: to provide a guide on how to assign different material properties to the different constituents of the soft palate, to investigate the importance of boundary conditions and anisotropy in such models and to quantify the influence of gravity on the global response of the soft palate. The predicted OSA closing pressures are compared to measured clinical patient data from the literature.

The paper is organized as follows. First, the histology of the soft palate is described, providing a guide to assign material models to different tissues and also pointing out the simplification when one assumes a homogeneous material. Then, simplified 3D and anatomical 3D shape models are presented with corresponding finite element meshes and alternative constitutive models to be employed in the simulations. In addition, the influence of different boundary conditions are provided here. Results from simplified 3D simulations and patient specific 3D simulations (with different boundary conditions and material models) are then provided, followed by a discussion and concluding remarks.

2 Materials and methods

2.1 Histology

The histology study of the soft palate shows that a typical adult soft palate consists of several major tissue layers including: the oral aspect adipose tissue, two middle muscle layers, a super

anterior veli palatini tendon layer and an inferior glandular tissue layer (Kuehn and Kahane 1990). A further quantitative histology study of the human adult soft palate presented the tissue composition (Ettema and Kuehn 1994). According to their study, the main composition of the soft palate includes the adipose tissue, the glandular tissue, the muscle tissue and the connective tissue. Therefore, we can divide the soft palate into three layers (Fig. 2): the adipose tissue top layer, the muscle and connective tissue middle layer and the glandular tissue dominant bottom layer. Other material constituents, contributing with much lower percentages to the soft palate tissue, were lumped into the glandular tissue layer and given the same material properties as for the glandular tissue.

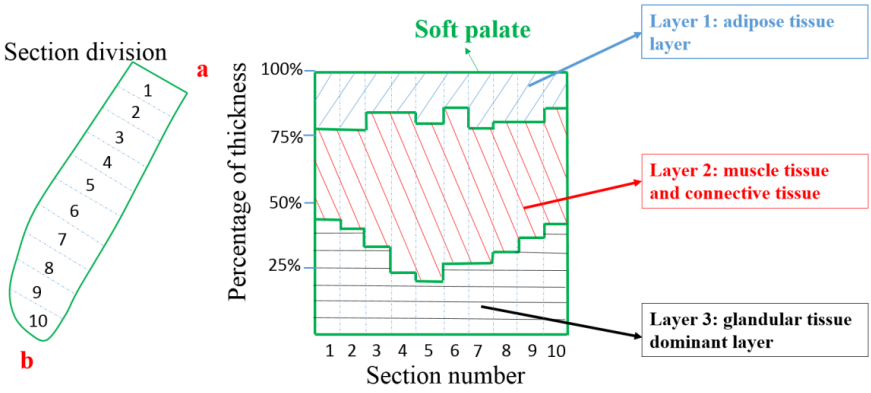

Fig. 2 Tissue composition layers division based on the quantitative histology study of the human adult soft palate (adapted from Figure 10 in the reference paper (Ettema and Kuehn 1994)). In this reference figure, the percentage composition of each tissue ingredient of soft palate is displayed clearly by dividing the soft palate into 10 sections from the anterior side to the posterior side.

To the authors' knowledge, a detailed tissue composition based 3D nonlinear finite element method (FEM) simulation of the soft palate has not been presented yet. In this study, according to the quantitative histology study for tissue composition, the soft palate is divided into three tissue layers and we will assign a specific material model to each layer. The detailed description will be presented in Section 2.5.

2.2 Simplified 3D geometry

A simplified geometry of the soft palate was obtained based on the CT images of a 68-year-old male patient and his apnea-hypopnea index (AHI) was found to be 22.8. This academic use of the CT images was approved by the Norwegian Regional Committee for Medical Research Ethics (REK) and was registered in Clinicaltrials.gov. (NCT01282125). During CT scan, the patient's body position was calibrated by a medical doctor trying to keep the airway axis normal to the CT scan plane. As shown in Fig. 3, the length, width and the inclination angle were measured manually using the commercial software Mimics. From these measurements, a

simplified geometry was generated by extruding the sagittal midsection profile of the soft palate, see Fig. 4.

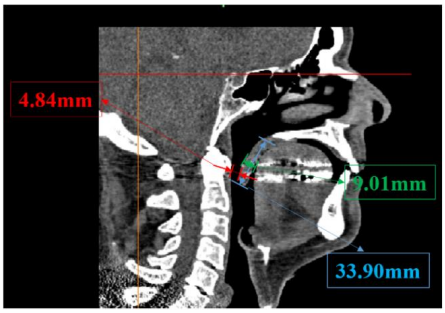

(a) Dimensions of the soft palate

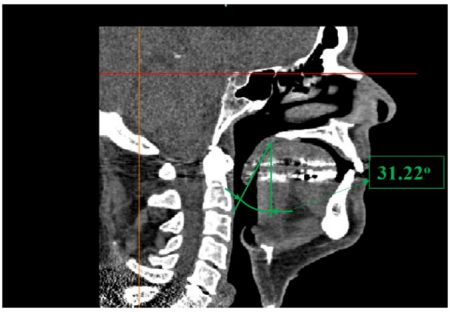

(b) Inclination angle of the soft palate

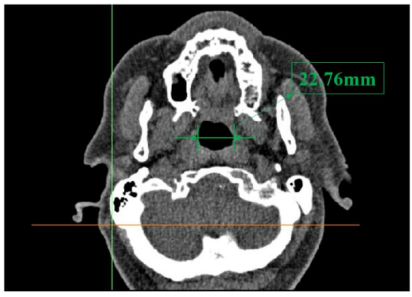

(c) Width of the air way

Fig. 3 Soft palate's CT images from a male patient. The length and the thickness of the soft palate were measured on the medical images using the commercial software Mimics. In addition, the inclination angle and the width were measured to be 31.22° degree and 22.76mm, respectively.

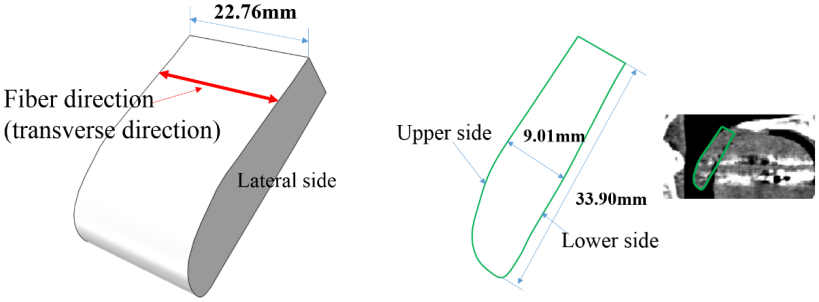

Fig. 4 Simplified 3D geometry of soft palate (left) and the sagittal midsection profile (right).

2.3 3D patient specific geometry

In this section, we present the 3D patient specific finite element model (Fig. 5) obtained from corresponding computed tomography (CT) images of the patient.

First the DICOM file (CT images file) was imported into the commercial software Mimics for visualization. Through some basic operations like segmentation and mask editing, the soft palate was then isolated with some parts of the pharynx wall. The meshing capabilities of Mimics can be used to generate a finite element mesh. In our case, this leads to an irregular mesh and some numerical difficulties in the finite element analyses. In order to obtain a smoother geometry, we exported planar polylines representing the airway for 44 parallel slices every 0.7 mm in the commercial software Mimics. The polylines were imported into ABAQUS\CAE and the final geometry was generated and meshed through some smooth editing operations.

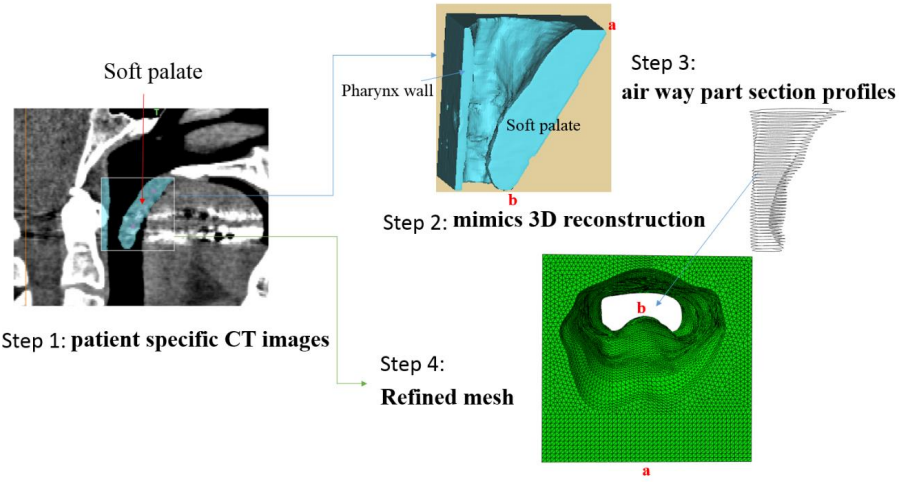

Fig. 5 3D geometry reconstruction of the soft palate with respect to the specific patient's CT images. The markers 'a' and 'b' denote the side between the soft palate and the hard palate and the bottom edge of the soft palate tip, respectively.

The 3D model includes the airway in the soft palate region and a part of the pharynx wall to account for the airway's obstruction when the soft palate inclines backward toward the pharynx wall. On the other hand, the geometric boundary between the soft palate and tongue was detected manually according to the CT images. Note that the tongue's influence on the soft palate's biomechanical behavior is neglected in this study.

2.4 Homogeneous tissue assumption material models

We assigned homogenous material properties to our simplified model. In addition, we tested two material constitutive models: an isotropic hyperelastic material model for comparison with different boundary conditions and a transversely isotropic material model to investigate the influence of anisotropy on the global response.

For the isotropic case, we used a Neo-Hookean material model defined by the following strain-energy function:

$$\psi(\bar{I}_1, J) = \psi_{\text{isochoric}} + \psi_{\text{volumetric}} = \underbrace{c(\bar{I}_1 - 3)}_{\text{isochoric}} + \underbrace{\frac{1}{D_1}(J-1)^2}_{\text{volumetric}} \tag{1}$$

Here, J is the determinant of the deformation gradient, $\bar{I}_1 = J^{-2/3} I_1, I_1 = \text{tr}(\boldsymbol{C})$, $\boldsymbol{C}$ is the right Cauchy-Green tensor. c and D_1 are material parameters derived from the Young's modulus E and Poisson ratio υ provided in (Berry et al. 1999) with the following relations:

$$c = \frac{E}{4(1+\upsilon)}, \quad D_1 = \frac{6(1-2\upsilon)}{E} \tag{2}$$

For the transversely isotropic case, we used the following Holzapfel type strain energy function:

$$\psi(\bar{I}_1, \bar{I}_4) = \underbrace{c(\bar{I}_1 - 3)}_{\text{isochoric-isotropic}} + \underbrace{\frac{k_1}{2k_2}[e^{k_2(\bar{I}_4 - 1)^2} - 1]}_{\text{isochoric-anisotropic}} \tag{3}$$

Here, $\bar{I}_4 = \boldsymbol{a}_0 \cdot \bar{\boldsymbol{C}} \boldsymbol{a}_0 = \bar{\boldsymbol{C}} : \boldsymbol{a}_0 \otimes \boldsymbol{a}_0$ with $\boldsymbol{a}_0$ a unit vector defining the fiber orientation in the undeformed configuration. k_1, k_2 are material parameters.

2.5 Histology based nonhomogeneous material models

In order to treat the soft palate as a nonhomogeneous composite material, based on the quantitative histology study of the human adult soft palate in section 2.1, we divided the patient specific 3D geometry model (Fig. 5) into three layers. The different components (i.e. adipose, muscle+connective and glandular tissues) material properties were assigned to specific layers of the soft palate model. In order to simplify the calculation, the soft palate model was divided into two parts: the anterior and the posterior parts, each with three tissue layers (Fig. 6). The discrete stepwise tissue distribution in Fig. 2 was smoothed. The connective tissue was lumped with the muscle tissue and the anisotropy was taken into consideration.

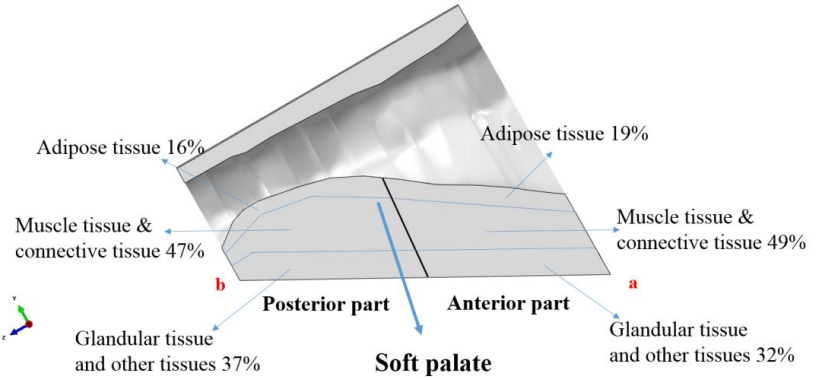

Fig. 6 Schematic of tissue layers based on the quantitative histology study of the human soft palate in the midsection view. The percentage composition of each tissue ingredient was calculated according to Fig. 2 based on the corresponding quantitative histology study (Ettema and Kuehn 1994).

Muscle and connective tissue

In this study, the passive condition of the muscle tissue is considered to investigate the global response of the soft palate for the OSA patient. The same material property was set to the muscle tissue and the connective tissue. According to the histology study of the soft palate (Kuehn and Kahane 1990), there are two middle layers mainly consisting of transverse muscle tissue of the levator veli palatini and one longitudinal musculus uvulae fiber layer. Since the longitudinal musculus uvulae mainly controls the motion of uvula in active condition and its percentage composition is smaller than that of the middle transverse levator veli palatini, in this study, we consider only the fiber families in the transverse direction.

Unfortunately, the local mechanical data for soft palate muscle tissue is still not presented in the literature. However, mechanical test data of muscle tissue in other parts of the human body is available. The test data of the passive human thigh muscle and brachialis muscle are presented in (Affagard et al. 2015) and (Gennisson et al. 2010). Trabelsi et al. (2010) presented a test of the upper airway trachea muscle. In their experiments, two fiber families were present and the one in the longitudinal direction contributes to movements of the trachea during swallowing. This is similar to the levator veli palatini that contracts and elevates the soft palate during swallowing (Matsuo and Palmer 2008). In detail, the muscle types and the fitted constitutive models for the above three kinds of human muscle tissues are summarized in Table 1. The original data of brachialis muscle provided in the reference paper is the shear modulus. Here, we fitted it to the Neo-Hookean model with an assumed Poisson's ratio of 0.49.

Table 1 Human muscle tissue locations and the corresponding constitutive material models previously reported in the literature

Positions	Constitutive models	Reference papers	Model parameters
Thigh muscle tissue	Neo-Hookean model (Eq. (1))	(Affagard et al. 2015)	c=0.0116MPa, D_1=11.9MPa^{-1}
Brachialis muscle tissue	Neo-Hookean model (Eq. (1))	(Gennisson et al. 2010)	c=0.0074MPa, D_1=2.72MPa^{-1}
Trachea muscle tissue	Holzapfel type model (Eq. (3))	(Trabelsi et al. 2010)	c=0.000877MPa, k_1=0.000154MPa, k_2=34.157

Based on the obtained parameters of the above fitted constitutive models, uniaxial stretch and stress relationships can be calculated as shown in Fig. 7. The results show different mechanical behaviors for the three human muscle tissues, and the trachea smooth muscle is softer than the skeletal muscles. Therefore, we employ three cases of the muscle tissue to investigate the global response of the soft palate: case 1, case 2 and case 3 correspond to the thigh muscle tissue material property, brachialis muscle tissue material property and trachea muscle tissue material property, respectively. Note that the incompressibility and the anisotropy were considered in case 3 with the Holzapfel type model (Eq. (3)) and the fiber orientation was set to be in the transverse direction.

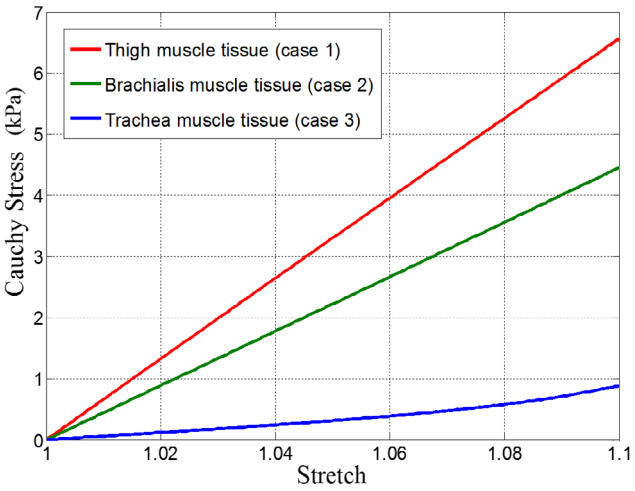

Fig.7 Uniaxial stretch-stress relationships of the human muscle tissues reported in Table 1.

Adipose tissue

The adipose tissue's main constituent is lipid filled cells called adipocytes. Mechanical data on adipose tissue of the human soft palate are not available. However, data on the mechanical behavior of adipose tissue in other parts of the human body have been reported (Affagard et al. 2015; Samani and Plewes 2004; Sommer et al. 2013). The types and corresponding constitutive models are summarized in Table 2.

Table 2 Human adipose tissue locations and the corresponding constitutive material models previously reported in the literature

Positions	Constitutive models	Reference papers	Model parameters
Abdominal adipose tissue	Holzapfel model (Eq. (4))	(Sommer et al. 2013)	c=0.0003MPa, k_1=0.0008MPa, k_2=47.3, κ=0.09
Thigh adipose tissue	Neo-Hookean model (Eq. (1))	(Affagard et al. 2015)	c=0.00064MPa, D_1=29.4MPa^{-1}
Female breast adipose tissue	Polynomial model $(\psi(\bar{I}_1,\bar{I}_2)=\sum_{i+j=1}^{2} c_{ij}(\bar{I}_1-3)^i(\bar{I}_2-3)^j)$	(Samani and Plewes 2004)	c_{10}=0.00031MPa, c_{01}=0.0003MPa, c_{11}=0.00225MPa, c_{20}=0.0038MPa, c_{02}=0.00472MPa

Based on the obtained parameters of the above fitted constitutive models, uniaxial stretch and stress relationships can be calculated as shown in Fig. 8. The stretch level in the 3D patient specific soft palate model was estimated to be close to 1.05. As can be seen in Fig. 8, when the stretch is smaller than 1.05, the difference between these three kinds of adipose tissues is small. Moreover, we performed a comparison of global response using the above constitutive material models. The results indicated that the difference in closing pressure between the simulations using the stiffest material property (the abdominal adipose tissue) and the softest material property (the thigh adipose tissue) is smaller than 10%.

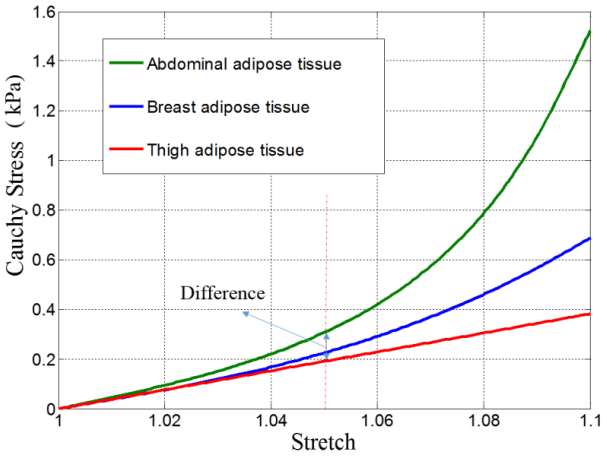

Fig. 8 Uniaxial stretch-stress relationships of the human adipose tissues reported in Table 2

Therefore, we choose one adipose tissue data set to simulate the soft palate. The study of Sommer et al. (2013) is comprehensive and based on a thorough analysis of abdominal adipose tissue. We used the following strain energy function proposed in their study in the analyses of our soft palate model.

$$\psi(\bar{I}_1,\bar{I}_4)=\frac{c}{2}(\bar{I}_1-3)+\frac{k_1}{k_2}(\exp\{k_2[\kappa\bar{I}_1+(1-3\kappa)\bar{I}_4-1]^2\}-1) \tag{4}$$

Here, κ is an anisotropy degree parameter and is used to account for fiber dispersion (Gasser et al. 2006). The corresponding material parameters are shown in Table 2. The mean fiber dispersion direction for the adipose tissue was set to be parallel to the transverse direction. In addition, as the test assumed incompressible material, the adipose tissue was modeled as an incompressible material in our study.

Glandular tissue

We assumed the glandular tissue to be isotropic and the Neo-Hookean model described in Eq. (1) was chosen to define its material property. Material properties for in vivo human breast glandular tissue can be found in (Li et al. 2015) and (Jiang et al. 2015). In addition, Cheng et al. (2011) presented in vivo magnetic resonance elastography measurements of the human soft palate and the shear modulus of the human soft palate was found to be 0.00253MPa. The corresponding Young's modulus and material parameters c and D_1 can be obtained assuming a Poisson ratio of 0.49 (Zhu et al. 2012). As Table 3 shows, the difference of the Young's modulus between the human breast glandular tissue and the soft palate is small. This motivates us to use the data of the whole soft palate to define the material properties of the glandular tissue dominant layer.

Table 3 The in vivo material properties of the human breast glandular tissue and soft palate previously reported in the literature

	Young's modulus (MPa)	Poisson's ratio	c (MPa)	D_1 (MPa^{-1})
Human soft palate (Cheng et al. 2011)	0.007539	0.49(Zhu et al. 2012)	0.001265	15.917
Breast glandular tissue (Li et al. 2015)	0.006593	0.49	0.001106	18.201
Breast glandular tissue (Jiang et al. 2015)	0.006	0.5	0.001	-

In addition, in the 3D patient specific geometry model, part of the pharynx wall is included. Because of its influence on the global response of the soft palate is very slight, we assume its material property to be same as that of the soft palate presented in Table 3.

2.6 Boundary conditions

The simplified 3D model of the soft palate was created to test the different boundary conditions. Two types of boundary conditions were tested. First, according to the previous 2D model of the soft palate proposed by Berry et al. (1999), only the nodes connected to the hard palate were constrained in all directions. This corresponds to a cantilever model. However, according to the anatomy of the soft palate, the lateral sides are connected to the surrounding soft tissue. This means that a cantilever model may not be physiological. Therefore, we tested a second set of boundary conditions where the lateral sides (see Fig. 4) were also constrained. We call it full boundary conditions.

Finally, we applied a uniform pressure field corresponding to the pressure difference between the lower and upper sides of the soft palate (Fig. 4). This pressure drop is called the negative pressure in this study:

$$P_{\text{negative}} = P_{\text{upper}} - P_{\text{lower}} \tag{5}$$

When the negative pressure develops, the soft palate will have a posterior oblique deformation. If the negative pressure is large enough, the soft palate will stick to the pharynx wall and OSA occurs. We call this critical negative pressure the closing pressure. The specific value for the closing pressure will vary from different patients. According to Han et al. (2002), the closing pressures of OSA patients were estimated to be -4~-8 cm H_2O. In addition, the average closing pressure in normal adults was found to be -13 cm H_2O (Schwartz et al. 1988).

The negative pressure was applied on the upper surface for the simplified model and on the internal surface of the soft tissue in contact with the airflow for the 3D patient specific geometry model.

2.7 Finite element mesh

The simplified FE model was meshed with eight noded hybrid solid elements (C3D8H ABAQUS type) and the 3D patient specific FE model with four noded hybrid tetrahedral elements (C3D4H ABAQUS type). Mesh convergence studies were performed on both models. A -5 cm H_2O negative pressure was applied in both the simplified model and the 3D patient specific model. The Neo-Hookean model with the data of the soft palate (Table 3) was assigned to the simplified model and the layered material model with the thigh muscle tissue's data was used for the 3D patient specific model.

The displacement magnitude of a point in the mid-section of the soft palate was chosen as a critical parameter and compared for different mesh densities (Fig. 9). For the simplified model, four mesh densities were tested with 10.660, 30.818, 54.280 and 77.688 elements, corresponding to Mesh 1, Mesh 2, Mesh 3, and Mesh 4, respectively. The difference for the critical parameter between Mesh 3 and Mesh 4 was 0.17%. For the patient specific model, four mesh densities were also tested with 131.403, 313.258, 463.856 and 560.221 elements, corresponding to Mesh 1, Mesh 2, Mesh 3, and Mesh 4, respectively. The difference for the critical parameter between Mesh 3 and Mesh 4 was 0.4%.

Therefore, considering the simulation accuracy and computational time efficiency, we used a mesh composed of 54.280 elements and a mesh composed of 463.856 elements for the simplified model and the patient specific model, respectively, in the remaining of this paper.

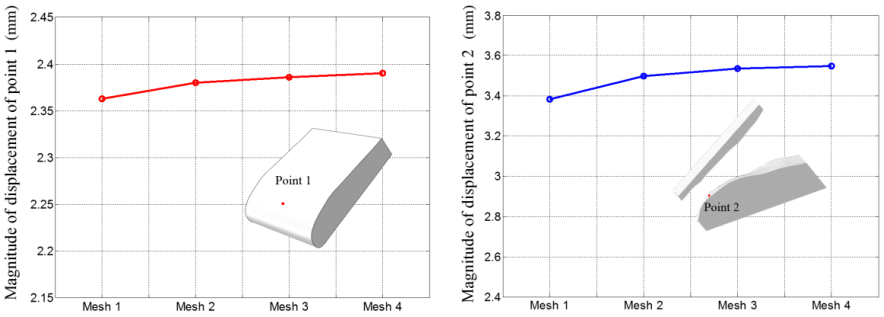

(a) Simplified model (b) 3D patient specific model

Fig. 9 Mesh size convergence analyses for the simplified model (a) and 3D patient specific geometry model (b).

3 Results

3.1 Simplified 3D models, homogeneous material, and effect of boundary conditions

First, we compare the global response of the simplified 3D model subjected to the negative pressure using the two types of boundary conditions presented in Section 2.6. In this comparison, the soft palate is modeled as a homogeneous material using the Neo-Hookean strain energy function (Eq. (1)) and the material parameters presented in Table 3. The loading negative pressure was set to be -0.5 cm H_2O (much less negative than the physiological closing pressure). Using the cantilever boundary conditions, the displacement of the tip's posterior surface was found to be 20.55mm (Fig. 10), which is much larger than the CT measured value 4.84 mm (Fig. 3(a)). On the other hand, when the lateral sides of the soft palate are also constrained, the displacement was found to be 0.26mm. Therefore, the cantilever model overestimates the displacement of the soft palate.

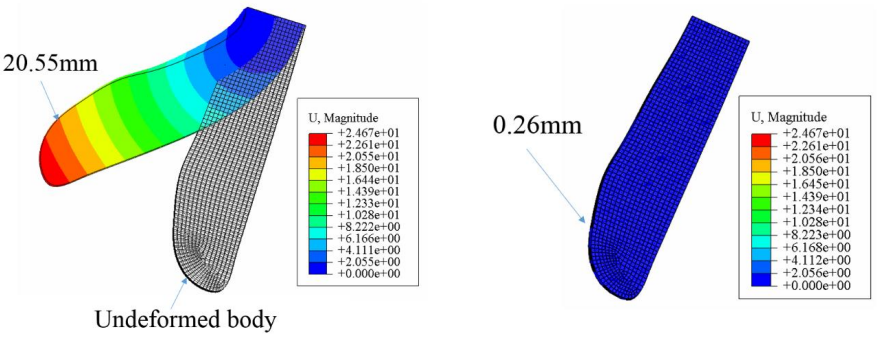

(a) Cantilever boundary conditions (b) full boundary conditions

Fig. 10 Displacement magnitudes for different boundary conditions with the simplified soft palate model.

Second, we compare the global response of the simplified model when the soft palate is modeled as a homogeneous material using a Neo-Hookean material model (Eq. (1)) and a hyperelastic transversely isotropic material model (Eq. (3)). As the fiber stiffness contributes mainly when the deformations are large, in this comparison, we set the negative pressure value to be -5 cm H_2O. Moreover, the fiber direction was defined parallel to the transverse direction (Fig. 4) according to the histology study of soft palate (Kuehn and Kahane 1990). The mentioned parameters of the transversely isotropic model for case 3 of the muscle tissue in Section 2.5 was used: c=0.000877MPa, k_1=0.000154MPa, k_2=34.157. For the Neo-Hookean isotropic model, the parameter c was set with the same value (c=0.000877MPa) and the Poisson ratio was set to be 0.49. In this comparison, the full boundary conditions were used.

According to our calculation results (Fig. 11), the displacement of the soft palate is smaller when anisotropy is taken into account, i.e. 3.18mm versus 3.57mm. Therefore, it is reasonable to consider the anisotropic property in the large deformation calculation of soft palate.

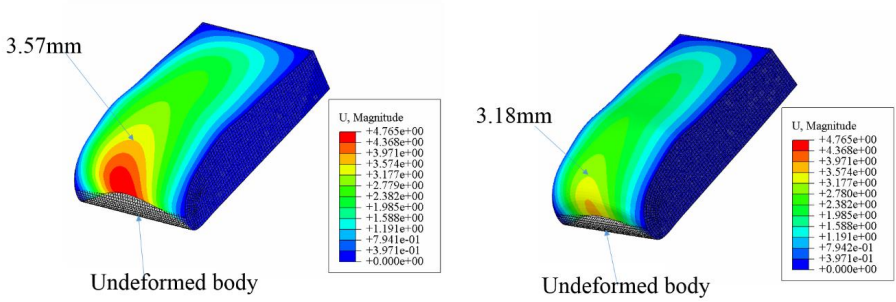

(a) Isotropic constitutive model (b) anisotropic constitutive model

Fig. 11 Displacement magnitudes for the simplified soft palate model using isotropic and anisotropic constitutive models.

3.2 Finite element analyses of the patient specific model with layered tissue properties of the soft palate

Based on the simulation results obtained from the simplified model, we chose to constrain the lateral sides of the soft palate. In addition, the pharynx wall was also constrained considering it is attached to the cervical vertebra. Therefore, the boundary conditions of our patient specific 3D model were confirmed as Fig. 12. The material models were assigned based on different tissue layers. Note that we tested three cases for the muscle tissue layer's material property.

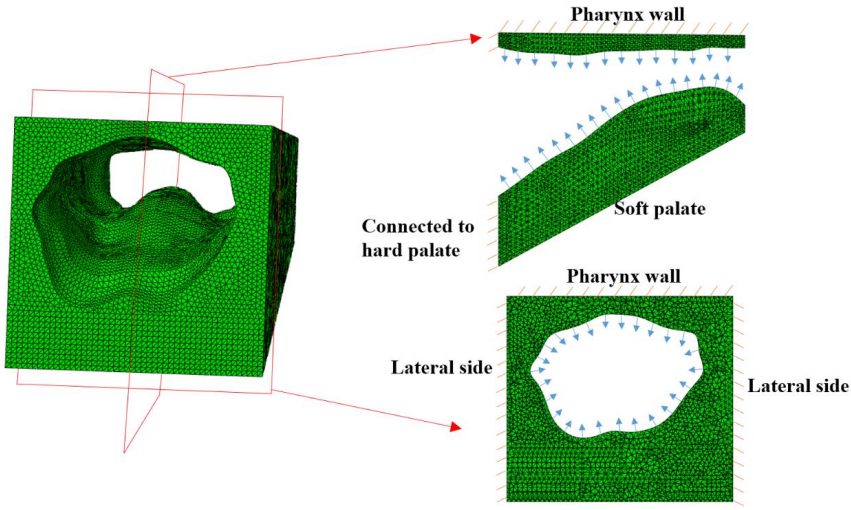

Fig. 12 Boundary conditions for the 3D patient specific model: the external side of the pharynx wall, the lateral sides and the side connected to the hard palate are constrained in all directions. The negative pressure is set on the tissue-airway contact surface.

The collapse of the soft palate in the upper airway can be observed directly in the 3D patient specific geometry as shown in Fig. 13. Additionally, we used the norm of the displacement of point A to present the inclination displacement of the posterior surface of the soft palate tip, see Fig. 14 (note that the point A is different from the point 2 in Fig. 9(b)). As can be seen from Fig. 15, the norm of the displacement of Point A exhibits a nonlinear behavior. Fig. 15 also shows that the soft palate closing pressure in case 1 is -7.9 cm H_2O, -6.7 cm H_2O in case 2 and -4.4 cm H_2O in case 3. This means that case 1 with the stiffest thigh muscle material property has a -3.52 cm H_2O (79.8%) lower closing pressure than the softest case 3 with the trachea muscle tissue's property. Therefore, the closing pressures obtained in the above cases are less negative than the normal adults' closing pressure -13 cm H_2O (Schwartz et al. 1988) and correspond to the clinical research for the OSA patients (Han et al. 2002). Here, the closing pressure is the pressure at which the soft palate posterior surface and the pharynx wall are in contact.

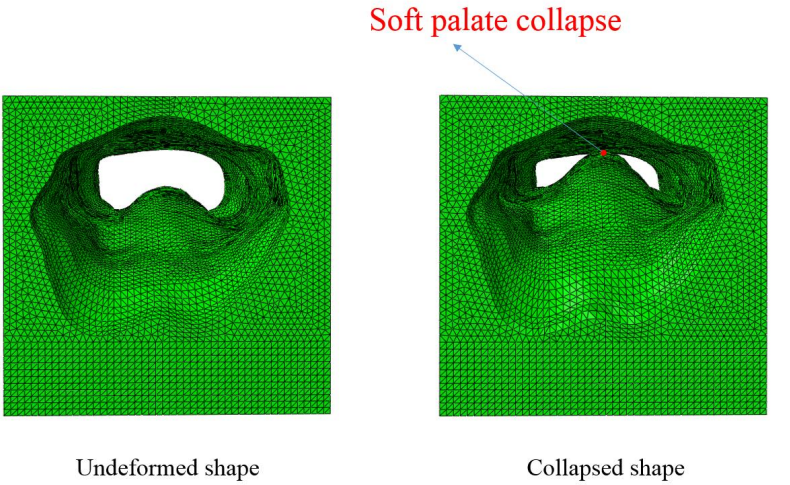

Fig. 13 Collapsed deformation of the 3D patient specific geometry tissue composition based soft palate model (view from the nasopharynx cavity).

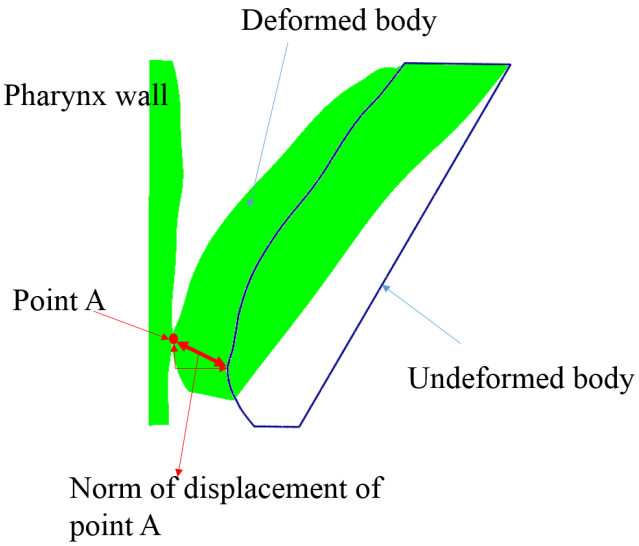

Fig. 14 Definition of point A and of the norm of its displacement in the 3D patient specific geometry model in the sagittal midsection plane. Point A is defined to be the first point of the soft palate posterior surface to be in contact with the pharynx wall in the sagittal midsection plane. The displacement of point A is used to represent the inclination displacement of soft palate tip's posterior surface.

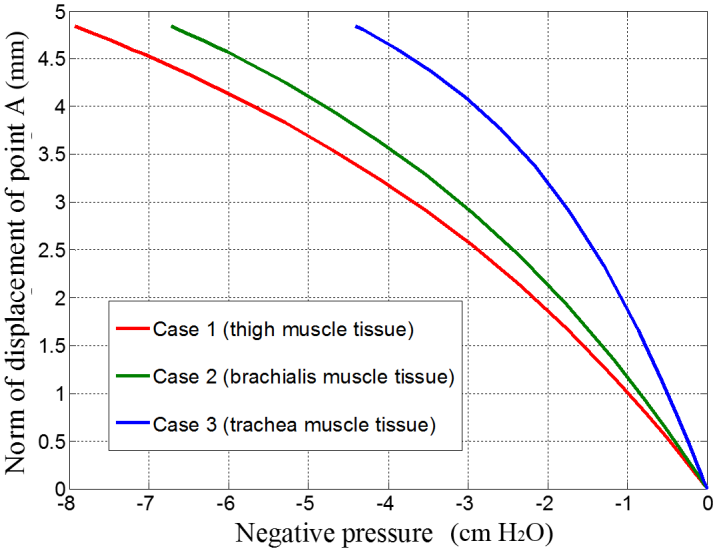

Fig. 15 Negative pressure versus the norm of the displacement of Point A for the 3D patient specific tissue composition based model including three cases for the muscle tissue properties.

3.3 Comparison between the reference 2D model from Malhotra et al. and our 3D patient specific model using an isotropic homogeneous constitutive model

In this section, we compare our 3D patient specific model with the 2D model presented by Malhotra et al. (2002). In their study, a 2D model of the soft palate for normal adult was created using a linear constitutive model with a Young's modulus of 0.006MPa to estimate the soft palate's deformations for different negative pressures in the passive condition. Moreover, the Young's modulus was obtained by fitting the FEM calculation results to clinical data.

In this comparison, the material of our 3D patient specific model is first modeled with a Hookean model using a Young's modulus of 0.006MPa and a Poisson's ratio 0.49. Second, using the same Young's modulus and Poisson ratio, we also model the material with the Neo-Hookean model from Eq. (1) and the corresponding material parameters c and D_1 derived from Eq. (2).

According to Malhotra et al., the closing pressure of their 2D model with the Hookean linear elastic material for a male adult is -5 cm H_2O. On the other hand, in our study, for the 3D model, the closing pressure value is -4.39mm H_2O (Fig. 16), which is 12.2% less negative than that of their 2D model. This is reasonable, as the patient suffers OSA. Meanwhile, as can be seen from Fig. 16, we observe very similar results concerning the norm of displacement of Point A (see Fig. 14) when using a Hookean elastic material or a Neo-Hookean hyperelastic material with our 3D patient specific model. In addition, the relation between the norm of the displacement of Point A and pressure (Fig. 16) seems to be almost linear in these cases.

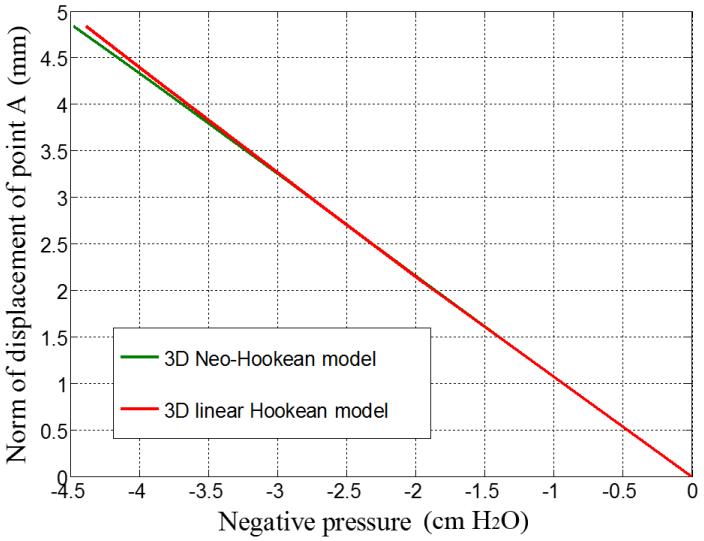

Fig. 16 Negative pressure versus the norm of the displacement of Point A for the 3D patient specific shape model with the isotropic elastic Hookean model and Neo-Hookean hyperelastic model.

3.4 Influence of gravity

To the best of our knowledge, the gravity's influence on soft palate's biomechanical behavior has not been addressed yet. Based on the 3D patient specific geometry tissue composition model, we investigated the gravity's influence on the global response of the soft palate. Two common body positions were investigated: the lying down and the seated positions (Fig. 17). The tissue's density was set to be 1110kg/m^3 (van der Velden et al. 2016)(CES-Edupack. 2011). Since the CT images were recorded with a supine position for the patient, we have considered the lying down position gravity in the above simulation process. Then, we tested the other case that corresponds to the seated position. An inverse lying down direction gravity coupling with the seated direction gravity were applied to the model in an initial load step followed by a second load step where the negative pressure was ramped. This leads to an initial negative displacement of point A compared to the lying down case for zero pressure in Fig. 18. As our simulation results show, the gravity brings different global responses of the soft palate for the tested two body positions. Additionally, for the seated position, a more negative closing pressure is obtained compared with the lying down position. Here, in order to investigate the influence of the gravity on the OSA patient, we used the softest muscle tissue property with the data of the trachea muscle tissue.

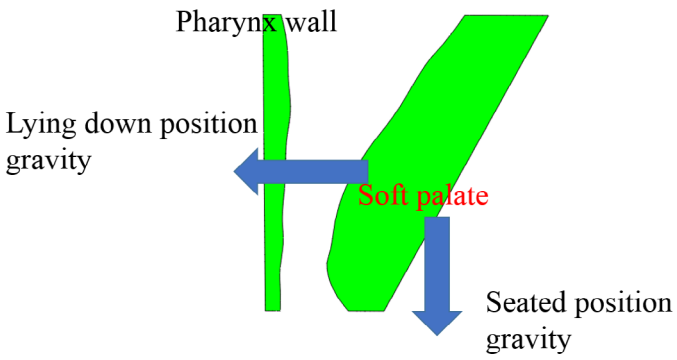

Fig. 17 Gravity's directions applied to the soft palate in the sagittal midsection view corresponding to two positions.

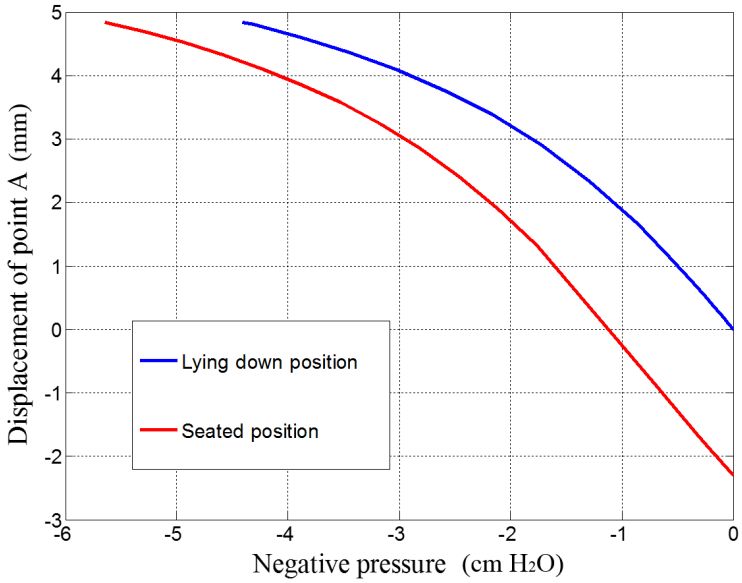

Fig. 18 Negative pressure versus the displacement of Point A for the gravity's influence including two human body positions. The negative displacement means the soft palate has an anterior oblique deformation.

4 Discussion

In the present work, we employ a 3D refined mesh FE model of the human soft palate with a patient specific geometry and inhomogeneous material properties. The geometry is obtained from CT images, taken from one male patient, processed with the commercial software Mimics. The material properties are assigned according to histology provided by Ettema and Kuehn (1994). Herein, three material layers are considered: the muscle and connective tissue layer, the adipose tissue layer and the glandular tissue dominant layer. The anisotropy of the muscle and connective tissue layer is taken into account (case 3). Comparing the tissue composition based inhomogeneous calculation results (Fig. 15) with the isotropic homogeneous calculation results (Fig. 16), nonlinear behavior occurs in the tissue composition based model.

In addition, we use a simplified 3D model to investigate the influence of the boundary conditions on the global response of the soft palate. Our results show that when the soft palate is modeled as a cantilever plate, the displacement of the soft palate tip is overestimated (Fig. 10). Therefore, we conclude the influence of the soft tissues surrounding the lateral sides of the soft palate must be accounted for in the FE analysis. Moreover, our simplified model shows that the anisotropy arising from the muscle and connective tissue may have an influence on the global response of the soft palate.

In this study, as the corresponding experimental data of the soft palate is not available, we used data retrieved from other parts of the human body to define the material properties of the muscle tissue and adipose tissue. Considering the stretch levels obtained in the soft palate at closing pressure, the difference between the three adipose models is small. For the three muscle models, the difference is larger. However, the closing pressures obtained for this specific OSA patient agree with the clinical research for all muscle model cases employed. In future studies local material experimental tests of the soft palate's muscle tissue and adipose tissue will contribute to acquiring more accurate calculation results. Additionally, we only considered the passive properties of the materials, i.e. muscle activation is not accounted for. We make this assumption based on the following: the presence of neuromuscular compensation defectiveness during sleep for the patient (McGinley et al. 2008). Nevertheless, the influence arising from the muscle activation should be investigated in future work.

The histology study of the soft palate (Kuehn and Kahane 1990) shows that two muscle fiber layers are imbedded in the soft palate tissue and are mainly distributed in the transverse direction. In our simulation process, the fiber orientation was set in the transverse direction to investigate the influence of the fiber stiffness on the soft palate's biomechanical behavior. In the real case, the fiber may not be strictly distributed in the transverse direction. This needs to be further investigated. In addition, for simplicity, we assumed the muscle tissue and connective tissue have the same material property. More experimental mechanical tests on the different ingredients of the soft palate are needed in order to refine our model.

We defined the pressure drop between the lower surface and upper surface of the soft palate (Fig. 4) as the negative pressure (Eq. (5)). In order to simplify the calculation, we applied the negative pressure as a uniformly distributed load. However, this is not the case in reality. Therefore, fluid-structure interaction analysis may be employed in order to predict a more realistic pressure distribution for the large deformation problems. This will be a task in further studies of the soft palate's biomechanical response. Moreover, in our study, we neglected the influence of the tongue on the deformation of the soft palate. According to the results in (Kirkness et al. 2005), a surface tension should be considered for the upper airway tissues. Hence, how this surface tension from the tongue influences the deformation of the soft palate remains to be investigated in further work.

The gravity's influence on two human body positions is estimated. The lying down position seems to increase the motion of the soft palate towards the pharynx wall and the seated position may prevent the soft palate from collapsing. Therefore, considering the gravity influence on the soft palate's global response, we can conclude that the lying down position will make the obstructive situation in the patient's upper airway worse.

Finally, note that the specific patient CT images were obtained from the patient with his mouth closed. With mouth open, the midsection profile and the position of soft palate with respect to the pharynx wall may be different. Hence, the mouth open case needs to be investigated in the future research of the soft palate.

5 Conclusion

Based on our 3D simplified model and 3D patient specific geometry model with inhomogeneous material properties of the soft palate, we have the following concluding remarks:

1. A cantilever model, where only the soft palate section attached to the hard palate is constrained, overestimates the global deformation of the soft palate subjected to negative pressure and the influence of the lateral tissues needs to be accounted for.
2. As can be seen from Figs. 15 and 16, when the soft palate undergoes large deformations, the material nonlinearities affect the mechanical behavior.
3. According to clinical research of normal adults (Schwartz et al. 1988), the closing pressure of this specific patient is less negative than that of the normal people (-13 cm H_2O), corresponding to the patient's OSA diagnosis.
4. The influence of gravity seems important with respect to the soft palate deformations.

ACKNOWLEDGEMENTS

The project has been funded in part from a grant from the Research council of Norway and a grant from NTNU, Norway. The CT images of the specific patient is provided by Mads H. S. Moxness form the department of Otolaryngology, Aleris Hospital and NTNU and Professor Ståle Nordgård from the department of Otolaryngology/Head and Neck Surgery, St. Olavs Hospital and NTNU.

Conflict of interest: The authors declare that they have no conflict of interest.

References

Affagard J-S, Feissel P, Bensamoun SF (2015) Identification of hyperelastic properties of passive thigh muscle under compression with an inverse method from a displacement field measurement. Journal of biomechanics 48:4081-4086 doi:http://dx.doi.org/10.1016/j.jbiomech.2015.10.007

Balsevičius T, Uloza V, Sakalauskas R, Miliauskas S, Jarutienė I (2015) Efficacy of radiofrequency treatment of the soft palate for patients with mild to moderate obstructive sleep apnea hypopnea syndrome: treatment protocol with nine lesions to the soft palate. Sleep and Breathing 19:1003-1009 doi:10.1007/s11325-014-1004-y

Berry DA, Moon JB, Kuehn DP (1999) A Finite Element Model of the Soft Palate. The Cleft Palate-Craniofacial Journal 36:217-223 doi:10.1597/1545-1569(1999)036<0217:AFEMOT>2.3.CO;2

Cheng S, Gandevia SC, Green M, Sinkus R, Bilston LE (2011) Viscoelastic properties of the tongue and soft palate using MR elastography. Journal of biomechanics 44:450-454 doi:http://dx.doi.org/10.1016/j.jbiomech.2010.09.027

Cho JH, Kim JK, Lee HY, Yoon JH (2013) Surgical anatomy of human soft palate. The Laryngoscope 123:2900-2904 doi:10.1002/lary.24067

Ettema SL, Kuehn DP (1994) A Quantitative Histologic Study of the Normal Human Adult Soft Palate. Journal of Speech, Language, and Hearing Research 37:303-313 doi:10.1044/jshr.3702.303
Gasser TC, Ogden RW, Holzapfel GA (2006) Hyperelastic modelling of arterial layers with distributed collagen fibre orientations. Journal of The Royal Society Interface 3:15
Gennisson J-L, Deffieux T, Macé E, Montaldo G, Fink M, Tanter M (2010) Viscoelastic and Anisotropic Mechanical Properties of in vivo Muscle Tissue Assessed by Supersonic Shear Imaging. Ultrasound in Medicine & Biology 36:789-801 doi:http://dx.doi.org/10.1016/j.ultrasmedbio.2010.02.013
Han D, Ye J, Wang J, Yang Q, Lin Y, Wang J (2002) Determining the Site of Airway Obstruction in Obstructive Sleep Apnea With Airway Pressure Measurements During Sleep. The Laryngoscope 112:2081-2085 doi:10.1097/00005537-200211000-00032
Huang Y, White DP, Malhotra A (2007) Use of Computational Modeling to Predict Responses to Upper Airway Surgery in Obstructive Sleep Apnea. The Laryngoscope 117:648-653 doi:10.1097/MLG.0b013e318030ca55
Jiang Y, Li G-Y, Qian L-X, Hu X-D, Liu D, Liang S, Cao Y (2015) Characterization of the nonlinear elastic properties of soft tissues using the supersonic shear imaging (SSI) technique: Inverse method, ex vivo and in vivo experiments. Medical Image Analysis 20:97-111 doi:http://dx.doi.org/10.1016/j.media.2014.10.010
Kirkness JP, Christenson HK, Wheatley JR, Amis TC (2005) Application of the 'pull-off' force method for measurement of surface tension of upper airway mucosal lining liquid. Physiological Measurement 26:677
Kuehn DP, Kahane JC (1990) Histologic Study of the Normal Human Adult Soft Palate. The Cleft Palate-Craniofacial Journal 27:26-35 doi:10.1597/1545-1569(1990)027<0026:HSOTNH>2.3.CO;2
Li X, Wang J-N, Fan Z-Y, Kang S, Liu Y-J, Zhang Y-X, Wang X-M (2015) Determination of the Elasticity of Breast Tissue during the Menstrual Cycle Using Real-Time Shear Wave Elastography. Ultrasound in Medicine & Biology 41:3140-3147 doi:http://dx.doi.org/10.1016/j.ultrasmedbio.2015.07.013
Malhotra A et al. (2002) The Male Predisposition to Pharyngeal Collapse. American Journal of Respiratory and Critical Care Medicine 166:1388-1395 doi:10.1164/rccm.2112072
Matsuo K, Palmer JB (2008) Anatomy and Physiology of Feeding and Swallowing: Normal and Abnormal. Physical Medicine and Rehabilitation Clinics of North America 19:691-707 doi:http://dx.doi.org/10.1016/j.pmr.2008.06.001
McGinley BM, Schwartz AR, Schneider H, Kirkness JP, Smith PL, Patil SP (2008) Upper airway neuromuscular compensation during sleep is defective in obstructive sleep apnea. Journal of Applied Physiology 105:197-205 doi:10.1152/japplphysiol.01214.2007
Mihaescu M, Murugappan S, Kalra M, Khosla S, Gutmark E (2008) Large Eddy Simulation and Reynolds-Averaged Navier-Stokes modeling of flow in a realistic pharyngeal airway model: an investigation of obstructive sleep apnea. Journal of biomechanics 41:2279-2288 doi:10.1016/j.jbiomech.2008.04.013
Mortimore IL, Mathur R, Douglas NJ (1995) Effect of posture, route of respiration, and negative pressure on palatal muscle activity in humans. Journal of Applied Physiology 79:448-454
Mylavarapu G, Murugappan S, Mihaescu M, Kalra M, Khosla S, Gutmark E (2009) Validation of computational fluid dynamics methodology used for human upper airway flow simulations. Journal of biomechanics 42:1553-1559 doi:http://dx.doi.org/10.1016/j.jbiomech.2009.03.035
Patil SP, Schneider H, Marx JJ, Gladmon E, Schwartz AR, Smith PL (2007) Neuromechanical control of upper airway patency during sleep. Journal of Applied Physiology 102:547-556 doi:10.1152/japplphysiol.00282.2006
Pirnar J, Dolenc-Grošelj L, Fajdiga I, Žun I (2015) Computational fluid-structure interaction simulation of airflow in the human upper airway. Journal of biomechanics 48:3685-3691 doi:http://dx.doi.org/10.1016/j.jbiomech.2015.08.017

Samani A, Plewes D (2004) A method to measure the hyperelastic parameters of ex vivo breast tissue samples. Physics in Medicine and Biology 49:4395

Schwartz AR, Smith PL, Wise RA, Gold AR, Permutt S (1988) Induction of upper airway occlusion in sleeping individuals with subatmospheric nasal pressure. Journal of Applied Physiology 64:535-542

Sera T, Uesugi K, Yagi N, Yokota H (2015) Numerical simulation of airflow and microparticle deposition in a synchrotron micro-CT-based pulmonary acinus model. Computer Methods in Biomechanics and Biomedical Engineering 18:1427-1435 doi:10.1080/10255842.2014.915030

Sommer G et al. (2013) Multiaxial mechanical properties and constitutive modeling of human adipose tissue: A basis for preoperative simulations in plastic and reconstructive surgery. Acta Biomaterialia 9:9036-9048 doi:http://dx.doi.org/10.1016/j.actbio.2013.06.011

Sun X, Yu C, Wang Y, Liu Y (2007) Numerical simulation of soft palate movement and airflow in human upper airway by fluid-structure interaction method. Acta Mechanica Sinica 23:359-367 doi:10.1007/s10409-007-0083-4

Sung S-J, Jeong S-J, Yu Y-S, Hwang C-J, Pae E-K (2006) Customized Three-dimensional Computational Fluid Dynamics Simulation of the Upper Airway of Obstructive Sleep Apnea. The Angle Orthodontist 76:791-799 doi:doi:10.1043/0003-3219(2006)076[0791:CTCFDS]2.0.CO;2

Trabelsi O, del Palomar AP, Lopez-Villalobos JL, Ginel A, Doblare M (2010) Experimental characterization and constitutive modeling of the mechanical behavior of the human trachea. Med Eng Phys 32:76-82 doi:10.1016/j.medengphy.2009.10.010

van der Velden WCP, van Zuijlen AH, de Jong AT, Lynch CT, Hoeve LJ, Bijl H (2016) Acoustic simulation of a patient's obstructed airway. Computer Methods in Biomechanics and Biomedical Engineering 19:144-158 doi:10.1080/10255842.2014.996877

Wang Y, Elghobashi S (2014) On locating the obstruction in the upper airway via numerical simulation. Respiratory Physiology & Neurobiology 193:1-10 doi:http://dx.doi.org/10.1016/j.resp.2013.12.009

Wang Y et al. (2012) Fluid–structure interaction modeling of upper airways before and after nasal surgery for obstructive sleep apnea. International Journal for Numerical Methods in Biomedical Engineering 28:528-546 doi:10.1002/cnm.1486

Zhao M, Barber T, Cistulli P, Sutherland K, Rosengarten G (2013a) Computational fluid dynamics for the assessment of upper airway response to oral appliance treatment in obstructive sleep apnea. Journal of biomechanics 46:142-150 doi:http://dx.doi.org/10.1016/j.jbiomech.2012.10.033

Zhao M, Barber T, Cistulli PA, Sutherland K, Rosengarten G (2013b) Simulation of upper airway occlusion without and with mandibular advancement in obstructive sleep apnea using fluid-structure interaction. Journal of biomechanics 46:2586-2592 doi:http://dx.doi.org/10.1016/j.jbiomech.2013.08.010

Zhu JH, Lee HP, Lim KM, Lee SJ, Teo LSL, Wang DY (2012) Passive movement of human soft palate during respiration: A simulation of 3D fluid/structure interaction. Journal of biomechanics 45:1992-2000 doi:http://dx.doi.org/10.1016/j.jbiomech.2012.04.027

CES-Edupack. 2011. Material database software. Cambridge, UK: Granta Design Limited.

9. National Conference on Computational Mechanics
MekIT'17
B. Skallerud and H. I. Andersson (Eds)

FINITE ELEMENT SIMULATIONS OF THE SWELLING OF CATIONIC HYDROGELS

ARNE ILSENG[1], VICTORIEN PROT[1], BJØRN SKALLERUD[1] AND BJØRN T. STOKKE[2]

[1] Biomechanics, Department of Structural Engineering, NTNU, Norwegian University of Science and Technology, 7491 Trondheim, Norway

[2] Biophysics and Medical Technology, Department of Physics, NTNU, Norwegian University of Science and Technology, 7491 Trondheim, Norway

Key words: Hydrogels, FEM, Transient swelling

Abstract. A constitutive model for the kinetic swelling of cationic hydrogels is outlined and implemented as a user subroutine for the commercial finite element software Abaqus. Experimental data previously presented in the literature on the swelling of acrylamide-based hydrogels with different fractions of cationic monomers are used as a benchmark to optimize the material parameters of the model. A good quantitative fit between the experimental data and the calculated model response is demonstrated for the equilibrium swelling behaviour. In addition, the model is shown to capture the experimentally observed swelling kinetics in a semi-quantitative manner.

1 INTRODUCTION

Hydrogels are polymer networks swollen in an aqueous solution. Such gels commonly appear in nature (e.g. human cartilage), are widely used in commercial products (e.g. disposable diapers and contact lenses), and have a tremendous potential for applications like smart valves [2], tissue engineering [5], drug delivery systems [4, 13], and biological sensors [16]. For many of these applications, the capability of hydrogels to swell or shrink as a response to stimuli (e.g. changes in temperature, mechanical forces, pH, salinity level, electric field, specific molecules recognized by included capture moieties) is exploited. To improve our understanding of the process of hydrogel swelling and capability to predict the response of a hydrogel to a change in its environment, modelling and simulation of hydrogel swelling are of interest.

In recent years, a significant effort has been put into developing constitutive models for finite element simulations that account for the specific features of hydrogel swelling. These efforts have contributed to improved hyperelastic models that describe the equilibrium swelling behaviour of hydrogels [14, 15, 12, 7], and more complex time-dependent

models that also describe the transient nature of swelling [11, 19, 17, 6, 3]. However, most of the work dealing with the modelling of hydrogel swelling present in the literature perform purely qualitative evaluations of the models capability of capturing important features of the swelling process. Consequently, there is a lack of studies that aims at establishing representative material parameters and doing quantitative comparisons between experimental measurements and simulation results. The focus of this contribution is therefore to use reported quantitative data on the swelling of cationic gels [16] to obtain material parameters representative for the tested hydrogels and to compare the numerical and experimental results.

The present study is organized as follows: In the following section, some important features of the experimental set-up used by Tierney et al. [16] are presented. In Section 3 a constitutive model for the transient behaviour of cationic hydrogels is outlined. Thereafter, in Section 4, the finite element model used to represent the experimental set-up is presented, and Section 5 discusses the fitting of the material parameters used in the model. Section 6 presents the results from both equilibrium and transient analyses and compare them with the benchmark experimental data. In the final section, some concluding remarks are given.

2 EXPERIMENTAL DATA

In a previous study by Tierney et al. [16], quantitative experimental data for the swelling of acrylamide-based hydrogels with different fractions of cationic monomers (DMAPAA) were presented. The level of DMAPAA was varied between two and seven mole percent relative to the acrylamide content. An illustration of the experimental set-up that was applied is shown in Figure 1. Using an optical fibre, a light signal was sent into a hemi-ellipsoidal gel fixed at the tip of the fibre. The reflected waves were then used to measure the optical length from the optical fibre - hydrogel interface to the hydrogel - external solution interface utilizing interferometry. To determine the actual swelling of the gel, the physical change in gel length must be calculated from the measured change in optical length. The relation between the measured optical length L_{opt} and the physical length L_{phys} of the gel can be found from the relation [16]

$$L_{phys} = \frac{L_{opt}}{n_{gel}} \tag{1}$$

where n_{gel} represents the refractive index of the gel. In the following, the data on optical length change presented by Tierney et al. [16] is converted to changes in physical gel length by using a value of 1.34 for n_{gel}.

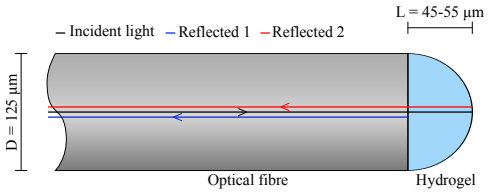

Figure 1: Illustration of the experimental set-up used to measure gel swelling

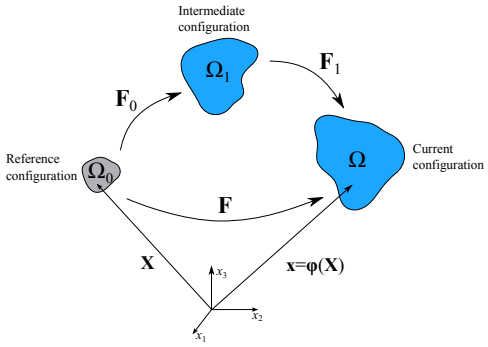

Figure 2: Illustration of the split in reference, intermediate, and current configuration

3 CONSTITUTIVE FORMULATION

3.1 Kinematics

Let Ω_0 and Ω be the reference (dry state) and current configurations, respectively. The deformation map $\boldsymbol{\varphi}(\mathbf{X}) : \Omega_0 \rightarrow \mathbf{R}^3$ transforms a material point $\mathbf{X} \in \Omega_0$ into the related current position $\mathbf{x} = \boldsymbol{\varphi}(\mathbf{X}) \in \Omega$. Therefore, the deformation gradient $\mathbf{F}$ is defined as $\mathbf{F} = \partial\boldsymbol{\varphi}(\mathbf{X})/\partial\mathbf{X} = \partial\mathbf{x}/\partial\mathbf{X}$, with the volume ratio $J = \det\mathbf{F} > 0$. For further use, we introduce an intermediate configuration Ω_1, the deformation gradient of the intermediate configuration Ω_1 relative to the dry configuration Ω_0 named $\mathbf{F}_0$, and the deformation gradient of the current configuration Ω relative to the intermediate configuration Ω_1 named $\mathbf{F}_1$, as illustrated in Figure 2. This leads to the following relations

$$\mathbf{F} = \mathbf{F}_1\mathbf{F}_0, \quad J_0 = \det\mathbf{F}_0, \quad J_1 = \det\mathbf{F}_1, \quad J = J_0J_1 \tag{2}$$

In the present study, all finite element simulations starts in the intermediate configuration Ω_1 where the gel is assumed stress free and in a state of homogeneous swelling such that $\mathbf{F}_0 = \lambda_0\mathbf{1}$ where $J_0 = \lambda_0^3$. The value of λ_0 is found by numerically solving $\boldsymbol{\sigma} = \mathbf{0}$ (where $\boldsymbol{\sigma}$ is the Cauchy stress tensor) for the given material parameters of the hydrogel and the composition of the external solution in which the gel is equilibrated.

The right Cauchy Green deformation tensor $\mathbf{C}$ is defined as

$$\mathbf{C} = \mathbf{F}^T\mathbf{F} \tag{3}$$

3.2 Cationic gel behaviour

To model the behaviour of cationic gels it is first necessary to establish some relations regarding the chemical potential of the diffusible species and the different ways to express their concentrations. The chemical potential for the different mobile species (H^+,+,− see Figure 3), indicated by the subscript, is given by [14, 11]

$$\mu_+ = k_B T \ln\left(\frac{\bar{c}_+}{c_+^{ref}}\right) \tag{4}$$

$$\mu_- = k_B T \ln\left(\frac{\bar{c}_-}{c_-^{ref}}\right) \tag{5}$$

$$\mu_{H^+} = k_B T \ln\left(\frac{\bar{c}_{H^+}}{c_{H^+}^{ref}}\right) \tag{6}$$

where k_B is the Boltzmann constant, T the absolute temperature, $\bar{c}_\alpha$ and c_α^{ref} are the concentration in the external solution and the reference concentration of given species α, respectively. The chemical potential μ_S of the solvent at the equilibrium state is found as

$$\mu_S = -k_B T v_S \sum_{\alpha \neq S} \bar{c}_\alpha \tag{7}$$

with v_S the volume per solvent molecule. Note that here $v = v_S$, where v is the volume per monomer (see Eq.(15)) [14]. The relation between the nominal concentration $C_\alpha(\mathbf{X})$ in Ω_0 and the true concentration $c_\alpha(\mathbf{x})$ in Ω (see Figure 2) of given species α inside the network is

$$C_\alpha = J c_\alpha \tag{8}$$

while the relation between the volumetric concentration c_α and molar concentration $[\alpha]$ can be written

$$c_\alpha = N_A[\alpha] \tag{9}$$

where N_A is Avogadro's number. We assume the individual polymer and solvent molecules to be incompressible and the volume fraction of the mobile ions to be sufficiently low to neglect their contributions to the volume of the gel. Consequently, the volume ratio J reads:

$$J = 1 + v_s C_s \tag{10}$$

Note that for the dry network $J = 1$. For $v_S C_S \gg 1$ Eq.(10) reduces to

$$J \simeq v_S C_S \tag{11}$$

In a cationic polymer network the actual charge density is governed by the equilibrium

$$A + H_2O \rightleftharpoons AH^+ + OH^- \tag{12}$$

which can be rewritten as

$$AH^+ \rightleftharpoons A + H^+ \tag{13}$$

yielding positively charged monomer groups upon association. The relation in Eq.(13) can be expressed through K_a as

$$K_a = \frac{[H^+][A]}{[AH^+]} \tag{14}$$

The conservation of ionizable groups in the cationic network yields

$$C_A(\mathbf{X}) + C_{AH^+}(\mathbf{X}) = \frac{f}{v} \tag{15}$$

where f is the fraction of monomers with ionizable groups and v is the volume per monomer. In addition, it is required that electroneutrality is maintained inside and outside the the gel. In the external solution, this condition is expressed as

$$\bar{c}_{H^+} + \bar{c}_+ = \bar{c}_- \tag{16}$$

and inside the cationic network as

$$C_{H^+}(\mathbf{X}) + C_+(\mathbf{X}) + C_{AH^+}(\mathbf{X}) = C_-(\mathbf{X}) \tag{17}$$

3.3 Material model

In order to describe the mechanical behaviour of the cationic gels studied by Tierney et al. [16], we use a free energy function U consisting of four parts

$$U = U_{str} + U_{mix} + U_{ion} + U_{as} \tag{18}$$

U_{str} represents the free energy of stretching per volume of the polymer chains and is given as [9, 11, 12]

$$U_{str} = \frac{1}{2} N k_B T \left(I_1 - 3 - 2\ln(J)\right), \quad \text{with } I_1 = \mathrm{tr}\mathbf{C} \tag{19}$$

where N is the network crosslink density. U_{mix} represents the free energy of mixing of the polymer and the solvent [18, 9]

$$U_{mix} = \frac{k_B T}{v_s}\left(v_s C_s \ln\left(\frac{v_s C_s}{1 + v_s C_s}\right) + \chi\left(\frac{v_s C_s}{1 + v_s C_s}\right)\right) \tag{20}$$

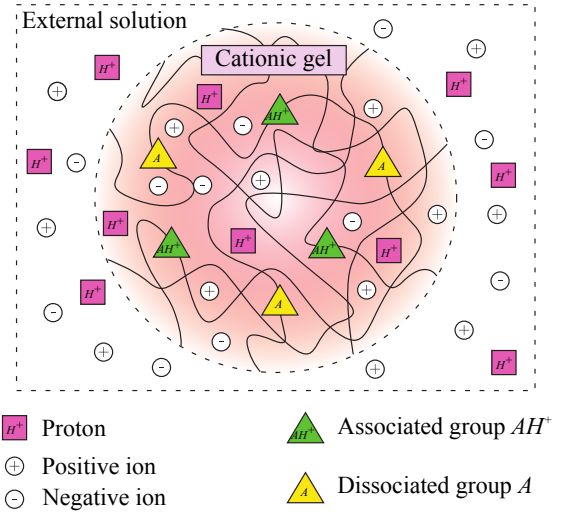

Figure 3: Illustration of a cationic gel in an external solution

which by using Eq.(10) becomes

$$U_{mix} = \frac{k_B T}{v_s}\left((J-1)\ln\left(1-\frac{1}{\mathrm{J}}\right)+\chi\left(1-\frac{1}{\mathrm{J}}\right)\right) \tag{21}$$

where χ is the Flory-Huggins parameter. The free energy of mixing of the mobile ions U_{ion} is given by Hong et al. [10]

$$U_{ion} = k_B T \sum_{\alpha \neq s} C_\alpha \left(\ln \frac{C_\alpha}{v_s C_s c_\alpha^{ref}} - 1\right) \tag{22}$$

which using Eq.(11) can be written as

$$U_{ion} = k_B T \sum_{\alpha \neq s} C_\alpha \left(\ln \frac{C_\alpha}{J c_\alpha^{ref}} - 1\right) \tag{23}$$

The free energy of association U_{as} can be expressed as

$$U_{as} = k_B T \left(C_{AH^+} \ln\left(\frac{C_{AH^+}}{C_{AH^+}+C_A}\right) + C_A \ln\left(\frac{C_A}{C_{AH^+}+C_A}\right)\right) + \gamma C_{AH^+} \tag{24}$$

with γ the molar heat of association. Finally, the free energy of the gel is a function of $\mathbf{C}$, C_{H^+}, C_+, C_-

$$U = U(\mathbf{C}, C_{H^+}, C_+, C_-) \tag{25}$$

Following Marcombe et al. [14] and using Eq.(25), the conditions for ionic equilibrium give the following relations

$$c_+ = \bar{c}_+ \frac{c_{H^+}}{\bar{c}_{H^+}}, \tag{26}$$

$$c_- = \bar{c}_- \frac{\bar{c}_{H^+}}{c_{H^+}}, \tag{27}$$

$$\text{and} \quad c^{ref}_{H^+} e^{\frac{\gamma}{k_B T}} = \frac{c_{H^+}(\frac{f}{vJ} - (c_- - c_{H^+} - c_+))}{c_- - c_{H^+} - c_+} \tag{28}$$

Eqs.(26) and (27) are known as the Donnan equations. Using Eqs.(8), (9), (14), (15), and (17) the right hand side of Eq.(28) can be identified as $N_A K_a$

$$N_A K_a = \frac{c_{H^+}(\frac{f}{vJ} - (c_- - c_{H^+} - c_+))}{c_- - c_{H^+} - c_+} \tag{29}$$

Clearly, $N_A K_a = c^{ref}_{H^+} e^{\frac{\gamma}{k_B T}}$ and an expression for the molar heat of association γ can be identified as

$$\gamma = k_B T \ln \frac{N_A K_a}{c^{ref}_{H^+}} \tag{30}$$

Eqs.(26), (27), and (29) lead to a system of equations that can be solved for c_{H^+}, c_+ and c_- when the concentrations $\bar{c}_{H^+}$, $\bar{c}_+$ and $\bar{c}_-$ in the external solution are known. Subsequently, C_{AH^+} and C_A can be determined using Eqs.(17) and (15) and relation (8).

In order to implement the constitutive material model into the commercial finite element code Abaqus [1] via the user subroutine UMAT, we use a Legendre transformation of the free energy density function U (see [14, 10])

$$\hat{U}(\mathbf{C}, \bar{c}_{H^+}, \bar{c}_+, \bar{c}_-) = U(\mathbf{C}, C_{H^+}, C_+, C_-) - C_-(\mu_- + \mu_+) - C_+(\mu_+ - \mu_-) - \mu_S C_S \tag{31}$$

which can be used to solve the equilibrium with prescribed concentrations $\bar{c}_{H^+}$, $\bar{c}_+$ and $\bar{c}_-$ in the external solution.

The second Piola-Kirchhoff stress tenor $\mathbf{S}$ and the Cauchy stress tenor $\boldsymbol{\sigma}$ are derived from the potential function $\hat{U}$ using

$$\mathbf{S} = 2\frac{\partial \hat{U}}{\partial \mathbf{C}}, \quad \boldsymbol{\sigma} = \frac{1}{J}\mathbf{F}^{\mathrm{T}}\mathbf{S}\mathbf{F} \tag{32}$$

3.4 Kinetic behaviour

The material model presented in Section 3.3 may be used to model the equilibrium swelling of a cationic hydrogel immersed in an external solution with given $\bar{c}_{H^+}$, $\bar{c}_{H^+}$ and $\bar{c}_-$ levels assuming that the solvent molecules have a chemical potential μ_S given by relation (7). However, in order to simulate the transient swelling process of hydrogels, the migration of solvent molecules into the hydrogel network must be accounted for. In

this work, we assume that the diffusion coefficient of the solvent molecules D is isotropic and independent of the deformation gradient $\mathbf{F}$ and the concentration C_S [11]. The flux vector $\mathbf{j}(\mathbf{X}, t)$ is the number of molecules per unit time crossing per unit area the current state Ω and is expressed as [8]

$$j_k = -\frac{c_S D}{k_B T}\frac{\partial \mu_S}{\partial x_k}, \quad \text{with } c_S = \frac{C_S}{J} \tag{33}$$

The governing equation of diffusion is obtained by assuming the conservation of the solvent molecules and reads [17]

$$\int_V \frac{1}{J}\frac{\partial C_S}{\partial t} dV + \int_S j_k dS = 0 \tag{34}$$

Following the methodology of Tho et al. [17], we assume that C_S is only a function of μ_S, $\bar{I}_1$ and $\mathrm{tr}\boldsymbol{\sigma}$, and can consequently rewrite the time derivative of C_S by use of the chain rule

$$\frac{\partial C_S}{\partial t} = \frac{\partial C_S}{\partial \mu_S}\frac{\partial \mu_S}{\partial t} + \frac{\partial C_S}{\partial \bar{I}_1}\frac{\partial \bar{I}_1}{\partial t} + \frac{\partial C_S}{\partial \mathrm{tr}\boldsymbol{\sigma}}\frac{\partial \mathrm{tr}\boldsymbol{\sigma}}{\partial t} \tag{35}$$

Combining Eq.(34) and (35) we find that

$$\int_V \frac{1}{J}\frac{\partial C_S}{\partial \mu_s}\frac{\partial \mu_s}{\partial t} dV + \int_S j_k dS = -\int_V \frac{1}{J}\left(\frac{\partial C_S}{\partial \bar{I}_1}\frac{\partial \bar{I}_1}{\partial t} + \frac{\partial C_S}{\partial \mathrm{tr}\boldsymbol{\sigma}}\frac{\partial \mathrm{tr}\boldsymbol{\sigma}}{\partial t}\right) dV \tag{36}$$

In order to implement Eq.(36) in Abaqus [1], an analogy with heat transfer is utilized so that the built-in coupled temperature-displacement elements can be adopted. The right-hand term of Eq.(36) is implemented as an internal heat source via the user subroutine HETVAL, and μ_S, $v\frac{\partial C_S}{\partial \mu_s}$, $\frac{1}{J}$, and vc_sD are identified as the temperature, the specific heat, the mass density and the conductivity, respectively. The deformation gradient $\mathbf{F}$ and the chemical potential μ_S are solved for by Abaqus, D is a prescribed variable, while the rest of the values are calculated as internal variables. A further discussion on the similarities between heat transfer and diffusion of solvent molecules in hydrogels are provided by Toh et al. [17].

4 FINITE ELEMENT MODEL

A finite element model of the hemi-ellipsoidal gel used in the study by Tierney et al. [16] (see Figure 1) was defined in the commercial finite element software Abaqus [1]. The axisymmetric properties of the problem were utilized to build a highly efficient axisymmetric model meshing only a quarter of an ellipse. An illustration of the axisymmetric model and the mesh used is shown in Figure 4. The bonding to the tip of the optical fibre was included by defining a rigid constraint to the nodes at the bottom edge of the gel. The radius of the gel was set to D/2=62.5 µm, while the initial length of the gel L was set according to the initial length measured for each gel in the experiments of

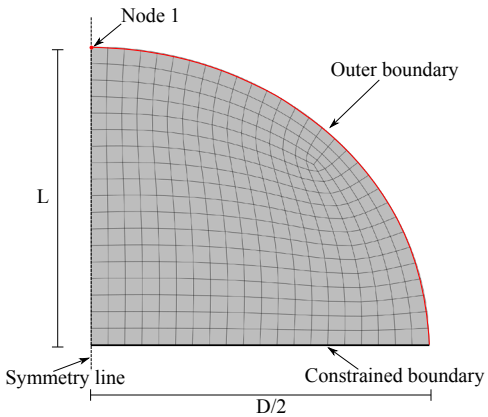

Figure 4: Illustration of axisymmetric finite element model

equilibrium swelling due to changing salinity levels in Tierney et al. [16]. Approximately 300 quadratic axisymmetric coupled temperature-displacement elements with reduced integration (CAX8RT in Abaqus) were used to mesh the ellipse, with the temperature part of the elements representing the chemical potential in the gel. For the equilibrium simulations the chemical potential was changed homogeneously in the whole model, while a stepwise change in the chemical potential was applied to the outer boundary of the gel in the kinetics simulations. The length change obtained in the model was calculated by extracting the position of Node 1 throughout the simulations.

5 MATERIAL PARAMETERS

The constitutive model outlined in Section 3 was implemented in Fortran as a user subroutine for the commercial finite element software Abaqus [1]. Material parameters for hydrogels with different molfractions of DMAPAA were found by comparing simulation results to experimental data on equilibrium swelling for salinity levels between 0.01 and 0.3 M. The value of Nv, where $1/Nv$ represents the number of monomers per polymer chain, was set to 0.035 for all DMAPAA levels, as it gave a reasonable fit between experimental data and simulation results. Assuming a volume per molecule of $v = 10^{-28}$ m^3 [11], this value of Nv leads to a stiffness of the dry gel network, Nk_BT, of approximately 1.4 MPa at room temperature (293 K). For all DMAPAA levels, a pKa value of 8.6 was assumed [16] and the model parameter K_a in Eq. (14) could be found through $K_a = 10^{-pKa}$. The model parameter representing the fraction of ionizable groups f was set according to the level of DMAPAA in each gel.

The Flory-Huggins parameter χ is in this study suggested to have a linear dependence on the salt concentration $c0$ through: $\chi(c0) = \chi_a c0 + \chi_b$. The value of χ_b was fixed to 0.4 for all gels while the value of χ_a was optimized for each DMAPAA level by minimizing

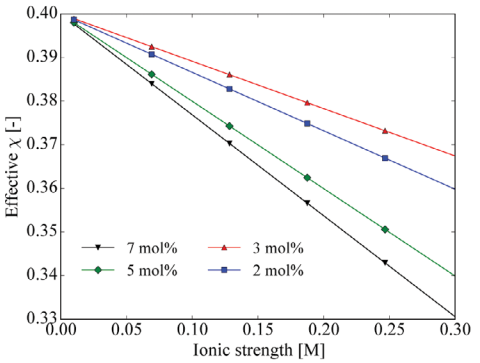

Figure 5: Effective value of χ as a function of ionic strength optimized for hydrogels with DMAPAA levels between 2 and 7 mol%

the function

$$S = \frac{1}{n}\sum_{i=1}^{n}\left(\frac{L_i^{FEM} - L_i^{exp}}{L_i^{exp}}\right)^2 \tag{37}$$

where L_i^{FEM} is the physical length obtained in the FEM simulation for every data point i in the experimental data set and L_i^{exp} is the physical length obtained in the experiments at every data point i. The Nelder-Mead minimization method in the scipy.optimize package for Python was used to obtain the values of χ_a presented in Table 1. Figure 5 illustrates how the effective value of the Flory-Huggins parameter $\chi(c0)$ is reduced with increasing salt concentration for the different levels of DMAPAA. Generally, a lower effective χ value is obtained at a given salinity level as the DMAPAA level is increased. However, the 3 mol% gel do not follow this pattern, as its effective χ value is greater than that of the 2 mol% gel.

Table 1: Optimized values for χ_a

DMAPAA	χ_a [M^{-1}]
2 mol%	−0.134
3 mol%	−0.109
5 mol%	−0.200
7 mol%	−0.231

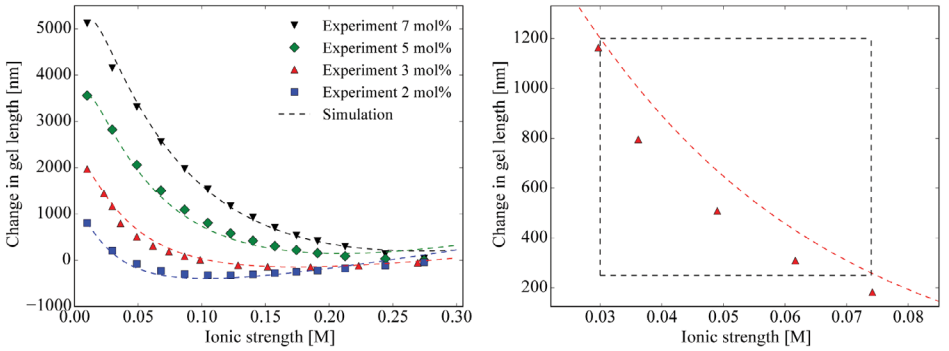

(a) (b)

Figure 6: (a) Comparison between experimental data [16] and simulation results using optimized material parameters for all gels, and (b) zoomed in comparison for the 3 mol% DMAPAA material with the dashed box indicating the region for experiments on swelling kinetics

6 RESULTS

6.1 Equilibrium swelling

Quantitative data on the equilibrium swelling during a change in salinity from 0.01 M to 0.3 M for hydrogels with DMAPAA content between 2 and 7 mol% were presented by Tierney et al. [16]. To model such equilibrium swelling, the salinity level of the gel in the finite element model is set be homogeneous and to change from 0.01 to 0.3 M during the simulation. A comparison between the experimental data of Tierney et al. [16] and the simulation results is presented in Figure 6a. Clearly, using the outlined material model with the optimized model parameters (see Section 5) yields a very good fit between the experimental data and the model response for all levels of DMAPAA during the complete change of salinity level. However, the trend of a clearly increasing gel length at high salinity levels for both the 2 mol% and 5 mol% gels indicates that the validity of the obtained parameters is limited to the tested range of salinity.

6.2 Kinetics

High quality quantitative data on the kinetics of hydrogel swelling is scarce in the literature, however, Tierney et al. [16] presented swelling data vs time for a 3 mol% gel exposed to a change in salinity between 0.03 M and 0.074 M. Using the material parameters for equilibrium swelling obtained in Section 5, the kinetics of swelling with changing salinity level was simulated. To model the kinetics of hydrogel swelling, the salinity level at the outer boundary of the hemi-ellipsoidal gel was increased stepwise

during time and the modelled diffusion behaviour ensures a time-dependent swelling.

A comparison between experimental data and simulation results is shown in Figure 7. It can be seen that the model is unable to represent the correct level of equilibrium swelling for each step change of salinity, however, the total accumulated swelling as the salinity level reach 0.074 M is well captured. This fact can be fully explained from the fit of the equilibrium response for the 3 mol% material presented in Figure 6b where it can be seen that the finite element model predicts a too stiff response for the equilibrium swelling in the salinity range where the experiments on swelling kinetics are performed. Therefore, if experimental data on the kinetics of swelling were available for a combination of DMAPAA level and salinity range where a better reproduction of the equilibrium swelling response is obtained, an improved match between the experimental and numerical results for the equilibrium swelling levels would be expected.

Figure 7 present results from the model using a diffusion parameter D between $2{\cdot}10^{-3}$ and $10{\cdot}10^{-3}$ mm^2/s. As expected, an increase in the value of the diffusion parameter yields a faster convergence towards the predicted equilibrium state. As the equilibrium behaviour is not captured with the present material parameters, it is hard to find a precise optimized value for the diffusion parameter, however, it can be seen from the comparison with the experimental results that a diffusion parameter of approximately $6{\cdot}10^{-3}$ mm^2/s (represented by the solid line) seems to yield a good representation of the experimental swelling kinetics.

7 CONCLUDING REMARKS

A constitutive model for the swelling of cationic gels is presented and the results from finite element simulations of gel swelling are compared with quantitative experimental data. A linear relation between the Flory-Huggins parameter and the salinity concentration is suggested. Material parameters were found that could give a quantitative description of the materials for equilibrium swelling. This shows that the model is capable of describing the dominating features of the swelling process of cationic hydrogels.

In addition, a framework for capturing the kinetics of gel swelling building on the mathematical similarities between solvent diffusion and heat transfer was presented. This transient model was shown to yield reasonable results when compared to the benchmark experimental data.

For further work, the capabilities of the model to describe the equilibrium swelling behaviour of hydrogels due to changes in pH as well as salinity level should be explored. In addition, by obtaining more experimental data on the transient swelling behaviour of the gels, a further validation of the kinetic part of the model can be performed and a more precise diffusion parameter can be defined for the hydrogels at question.

8 ACKNOWLEDGEMENTS

This work was supported by the Norwegian Research Council (Project no 240299/F20).

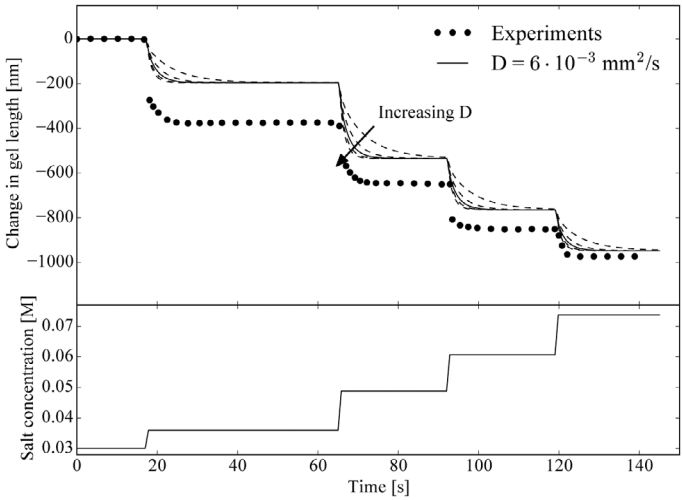

Figure 7: Comparison between experimental data [16] and simulation results for swelling kinetics of a gel with 3 % DMAPAA with varying salt concentration. In the five simulation results shown the diffusion parameter is changed between $2{\cdot}10^{-3}$ and $10{\cdot}10^{-3}$ mm^2/s in intervals of $2{\cdot}10^{-3}$ mm^2/s.

REFERENCES

[1] Abaqus. *6.13-1.* Dassault Systèmes, 2013.

[2] Beebe, D. J., Moore, J. S., Bauer, J. M., Yu, Q., Liu, R. H., Devadoss, C., and Jo, B.-H. Functional hydrogel structures for autonomous flow control inside microfluidic channels. *Nature 404*, 6778 (2000), 588–590.

[3] Bouklas, N., Landis, C. M., and Huang, R. A nonlinear, transient finite element method for coupled solvent diffusion and large deformation of hydrogels. *Journal of the Mechanics and Physics of Solids 79* (2015), 21–43.

[4] Bysell, H., and Malmsten, M. Visualizing the interaction between poly-L-lysine and poly(acrylic acid) microgels using microscopy techniques: Effect of electrostatics and peptide size. *Langmuir 22*, 12 (2006), 5476–5484.

[5] Chan, G., and Mooney, D. J. New materials for tissue engineering: towards greater control over the biological response. *Trends in Biotechnology 26*, 7 (2008), 382–392.

[6] Chester, S. A., and Anand, L. A thermo-mechanically coupled theory for fluid permeation in elastomeric materials: Application to thermally responsive gels. *Journal of the Mechanics and Physics of Solids 59*, 10 (2011), 1978–2006.

[7] Drozdov, A. D., and Christiansen, J. D. The Effects of pH and Ionic Strength of Swelling of Cationic Gels. *International Journal of Applied Mechanics 08*, 05 (2016), 1650059.

[8] Feynman, R. P., Leighton, R. B., and Sands, M. L. *The Feynman lectures on physics*. Addison-Wesley Pub. Co., Reading, Mass., 1963.

[9] Flory, P. J. *Principles of polymer chemistry*. Cornell University Press, 1953.

[10] Hong, W., Zhao, X., and Suo, Z. Large deformation and electrochemistry of polyelectrolyte gels. *Journal of the Mechanics and Physics of Solids 58*, 4 (2010), 558–577.

[11] Hong, W., Zhao, X., Zhou, J., and Suo, Z. A theory of coupled diffusion and large deformation in polymeric gels. *Journal of the Mechanics and Physics of Solids 56*, 5 (2008), 1779–1793.

[12] Kang, M. K., and Huang, R. A Variational Approach and Finite Element Implementation for Swelling of Polymeric Hydrogels Under Geometric Constraints. *Journal of Applied Mechanics 77*, 6 (2010), 61004.

[13] Li, J., and Mooney, D. J. Designing hydrogels for controlled drug delivery. *Nature Reviews Materials 1* (oct 2016), 16071.

[14] Marcombe, R., Cai, S., Hong, W., Zhao, X., Lapusta, Y., and Suo, Z. A theory of constrained swelling of a pH-sensitive hydrogel. *Soft Matter 6*, 4 (2010), 784–793.

[15] Prot, V., Sveinsson, H. M., Gawel, K., Gao, M., Skallerud, B., and Stokke, B. T. Swelling of a hemi-ellipsoidal ionic hydrogel for determination of material properties of deposited thin polymer films: an inverse finite element approach. *Soft Matter 9*, 24 (2013), 5815–5827.

[16] Tierney, S., Hjelme, D. R., and Stokke, B. T. Determination of Swelling of Responsive Gels with Nanometer Resolution. Fiber-Optic Based Platform for Hydrogels as Signal Transducers. *Analytical Chemistry 80*, 13 (2008), 5086–5093.

[17] Toh, W., Liu, Z., Ng, T. Y., and Hong, W. Inhomogeneous Large Deformation Kinetics of Polymeric Gels. *International Journal of Applied Mechanics 05*, 01 (2013), 1350001.

[18] Treloar, L. R. G. *The physics of rubber elasticity.* Oxford university press, 1975.

[19] Zhang, J., Zhao, X., Suo, Z., and Jiang, H. A finite element method for transient analysis of concurrent large deformation and mass transport in gels. *Journal of Applied Physics 105*, 9 (2009), 093522.

9. National Conference on Computational Mechanics
MekIT'17
B. Skallerud and H I Andersson (Eds)

SIMULATION OF FREELY-FLOATING BODIES IN WAVES USING A 6DOF ALGORITHM

JIAYI ZHENG LU[1], ARUN KAMATH[2] AND HANS BIHS[3]

[1]Department of Civil and Environmental Engineering
NTNU Trondheim
Høgskoleringen 7A, 7034 Trondheim, Norway
e-mail: jiayi.zhenglu@gmail.com

[2] Department of Civil and Environmental Engineering
NTNU Trondheim
Høgskoleringen 7A, 7034 Trondheim, Norway
e-mail: arun.kamath@ntnu.no

[3] Department of Civil and Environmental Engineering
NTNU Trondheim
Høgskoleringen 7A, 7034 Trondheim, Norway
e-mail: hans.bihs@ntnu.no

Key words: Floating bodies, 6DOF, REEF3D, CFD

Abstract. Interactions between floating bodies and waves are found in several engineering applications like oil platforms or floating breakwaters. Floating bodies are strongly influenced by the free surface and the fluid structure interaction. The modelling of floating bodies in waves needs to consider rigid body dynamics, turbulent and viscous flow around the floating body among others. To resolve these problems, the flow variables need to be solved with high accuracy and detail. A CFD model which solves the Reynold-Averaged Navier-Stokes Equations is suitable for the analysis of floating bodies in waves. In this paper, the open-source CFD model REEF3D with a 6 degrees of freedom algorithm is used to simulate the interaction of a floating barge in waves. The translational and rotational motion of the barge in different directions and around different axes are calculated in two dimensions. The numerical results are compared to experimental data for validation of the model. Three-dimensional simulations with different geometries are carried out and the motion of the barge analysed.

1 INTRODUCTION

Fluid-structure interaction (FSI) is an extensively studied field in engineering. In marine engineering there are floating, moored structures like wave energy conversion devices, oil

platforms or wind turbines. In civil engineering, nearby the coast, there are also floating structures like piers or breakwaters. Breakwaters are needed for coast and harbour defence against the action of the sea. The climate change, is creating a need for new solutions to control the increase of sea water level and wave height during storms. Here, floating breakwaters are a viable option compared to the traditional ways, especially, for areas with a great water depth. For the design of the structures, new models or tools that are able to calculate displacements, motions and forces on the structure with a higher accuracy are needed.

Analytical methods were used to resolve these problems in the past but they don't take into account parameters like fluid viscosity or non-linear effects. Thus, these are limited tools to solve problems of this nature. Since the last decades, numerical simulation with Computational Fluid Dynamics (CFD) software is been used. Floating structures present several challenges caused by the non-linearity of the free surface and the complexity of the problems to solve like turbulence, wave breaking or motion of the body. Navier-Stokes (NS) or Reynolds-averaged Navier-Stokes equations (RANS) are used by several models using the finite difference method or the finite volume method with techniques like Level set function and Volume of fluid to obtain the free surface. The free surface can be computed as a single-flow [1] neglecting the effect of the air or a two-phase flow including the effect of it. First studies used a single-phase flow, the Arbitrary Lagrangian-Eulerian (ALE) Method [2], where the mesh moves with the boundary and interface all the time. However, this method it's not satisfactory for problems where the free surface is not smooth and continuous or has large deformations. Another approach on the ALE method is the Immersed Boundary (IB), introduced by Peskin [3]. On a fixed Cartesian mesh the flow equations are solved and the effect of the boundary is computed with an imaginary force field. With the level set function, the interface between water and air, in the case, becomes the zero-contour of the level set function.

The 6DOF (six degrees of freedom) are composed by 3 displacements and 3 rotations. Displacements are surge, sway and heave in X, Y and Z direction, respectively. Rotations are roll, pitch and yaw around X, Y and Z axis respectively. In this paper a free floating body will be simulated. Firstly, validation of the code is realised with three motions in two dimensions: surge, heave and pitch. Three different cases in three dimensions are simulated as further analysis. All the cases are simulated with REEF3D [4], an open source CFD code developed at the Department of Civil and Transport Engineering at Norwegian University of Science and Technology (NTNU), Norway. The software has been used in several applications being validated in [5], wave forces and free surface analysis around horizontal cylinders in tandem[6], waves forces and wave elevation around vertical cylinders [7]. Firstly, the methodology including governing equations of the model is explained. Secondly, the experiment configuration, validation and simulations. Lastly, conclusions of the paper.

2 NUMERICAL MODEL

2.1 Governing equations

Continuity and incompressible Reynolds-Averaged Navier-Stokes (RANS) equations are the governing equations of the numerical model:

$$\frac{\partial u_i}{\partial x_i} = 0 \tag{1}$$

$$\frac{\partial u_i}{\partial t} + u_j \frac{\partial u_i}{\partial x_j} = -\frac{1}{\rho} + \frac{\partial p}{\partial x_i} + \frac{\partial}{\partial x_j}\left[\nu\left(\frac{\partial u_i}{\partial x_j} + \frac{\partial u_j}{\partial x_i}\right) - \overline{u_i u_j}\right] + g_i \tag{2}$$

where u is the velocity over time t, x is the spatial geometrical scale, ρ is water density, ν is kinematic viscosity, p is pressure, $\overline{u_i u_j}$ represents the Reynold stresses and g is gravity. The spatial domain is discretize with a Cartesian grid for the easiness when defining the geometry and the numerical algorithms. The spatial domain is a numerical wave tank (NWT) which is divided in three zones. In the first zone with a wavelength length, the waves are generated. The second zone is the wave tank where the problem is solved. In the last zone which is two wavelengths long, the waves are dissipated. A relaxation method for the wave generation and numerical beach is used for the generation and dissipation of waves [8]. For the time domain, the explicit third-order Total Variation Diminishing (TVD) Runge-Kutta scheme is used. The equations of the third-order Runge-Kutta scheme for the generic variable ϕ are based on [9].

2.2 Level set function

The free surface is obtained with the level set method as a two-phase system. the zero-contour of the level set function is set between fluids where the zero level set of a signed distance function, $\phi(\vec{x}, t)$ [10], is used to represent the interface between air and water. The two interfaces are distinguished by the change of sign. This results in:

$$\phi(\vec{x}, t) \begin{cases} > \ 0 \ if \ \vec{x} \ \epsilon \ phase \ 1 \\ = \ 0 \ if \ \vec{x} \ \epsilon \ \Gamma \\ < \ 0 \ if \ \vec{x} \ \epsilon \ phase \ 2 \end{cases} \tag{3}$$

The level set function is coupled to the flow field with a pure convection equation:

$$\frac{\partial \phi}{\partial t} + u_j \frac{\partial \phi}{\partial x_j} = 0 \tag{4}$$

When the level set function evolves, the level set function can loose its signed distance property. A solution is to reinitialize the level set function after every time-step. The reinitialization is based on the solution of a partial differential equation [11]:

$$\frac{\partial \phi}{\partial t} + S(\phi)\left(\left|\frac{\partial \phi}{\partial x_j}\right| - 1\right) = 0 \tag{5}$$

The PDEs in Eqs. 4 and 5 are solved with the fifth-order accurate Hamilton-Jacobi version of the WENO scheme [12] for the spatial discretization and the third-order TVD Runge-Kutta scheme [9] for the discretization in time.

2.3 6DOF algorithm

The FSI calculation for the floating body is carried out in the following way. A triangular surface mesh without connectivity is created to define the geometry of the body in STereoLitography (STL) format. A ray-tracing algorithm, calculating the shortest distance to the closest triangle for the grid point, is used to determine the intersections of the surface mesh with the underlying Cartesian grid. The level set method is used to define the boundaries. The standard reinitialize algorithm is used to obtain signed distance properties for the level set function in the vicinity of the solid body. The forces on the surface Ω are determined for each direction i separately with the pressure p and the viscous stress tensor τ:

$$F_{i,e} = \int_{\Omega} (-\mathbf{n}_i p + \mathbf{n_i} \cdot \tau) d\Omega \tag{6}$$

The distance of the centre of gravity from the origin of the body grid can be determined with:

$$\mathbf{r_{cg}} = \frac{1}{m} \int_{V} \mathbf{r} \rho_a dV \tag{7}$$

where $\mathbf{r}$ is the distance from each surface cell to the origin of the body-fitted coordinate system. Assuming that the origin of the body-fitted coordinate system is at the centre of gravity of the floating body, $\mathbf{r}$ is the distance of each surface cell to the centre of gravity. The moment can be calculated with the following equation:

$$L_{i,e} = \int_{\Omega} \mathbf{r} \times (\mathbf{n_i} p + \mathbf{n_i} \cdot \tau) d\Omega \tag{8}$$

The calculation of the discrete surface area is done with a Dirac delta function:

$$d\Omega = \int \delta(\phi)|\nabla\phi|dx \tag{9}$$

The location and orientation of the floating body are given by the position vector and the Euler angles:

$$\boldsymbol{\eta} = (\boldsymbol{\eta_1}, \boldsymbol{\eta_2}) = (x_{cg}, y_{cg}, z_{cg}, \phi, \theta, \psi) \tag{10}$$

The calculation of the moments of inertia can be simplified with two different coordinate systems, one inertial for the fluid and another non-inertial for the floating body. Forces and moments can be calculated in the inertial coordinate system and when the origin of the non-inertial coordinate system coincides with the centre of gravity, the moments of inertia are calculated with a diagonal matrix:

$$\mathbf{I} = \begin{bmatrix} I_x & 0 & 0 \\ 0 & I_y & 0 \\ 0 & 0 & I_z \end{bmatrix} = \begin{bmatrix} mr_x^2 & 0 & 0 \\ 0 & mr_y^2 & 0 \\ 0 & 0 & mr_z^2 \end{bmatrix} \tag{11}$$

where r_x, r_y and r_z are the distance between the point and the centre of gravity in each direction x, y, z.
After, the forces and moments can be expressed in the non-inertial coordinate system with a transformation matrix $\mathbf{J_1^{-1}}$ with three rotations around each axis:

$$\mathbf{a}_{fb} = \begin{bmatrix} c\psi\ c\theta & s\psi\ c\theta & -s\theta \\ -s\psi\ c\phi\ + s\phi\ s\theta\ c\psi & c\psi\ c\phi\ + s\phi\ s\theta\ s\psi & s\phi\ c\theta \\ s\theta s\psi + c\phi\ s\theta\ c\psi & -s\phi\ c\psi\ + c\phi\ s\theta\ s\psi & c\theta\ s\phi \end{bmatrix} \mathbf{a_e} = \mathbf{J_1^{-1}} \mathbf{a_e} \tag{12}$$

where *sin* has been denoted as *s* and *cos* as *c*.
$\mathbf{a}_{fb}$ is the vector in the reference frame of the floating body and $\mathbf{a_e}$ is the vector in the reference frame of the inertial system.

The dynamic rigid body equations can be solved with the forces X, Y, Z; momentums K, M, N and moments of inertia:

$$\begin{aligned} F_i &= \mathbf{J_1^{-1}} F_{i,e} = [X, Y, Z] \\ L_i &= \mathbf{J_1^{-1}} L_{i,e} = [K, M, N] \end{aligned} \tag{13}$$

with:

$$\begin{aligned}
[m(\dot{u} - \nu r + \omega q)] &= X \\
[m(\dot{\nu} - \omega r + \nu q)] &= Y \\
[m(\dot{\omega} - \nu r + \omega q)] &= Z \\
[m(\dot{\omega} - \nu r + \omega q)] &= Z \\
[I_x(\dot{p} + (I_z - I_y)qr] &= K \\
[I_y(\dot{q} + (I_x - I_z)rp] &= M \\
[I_z(\dot{r} + (I_y - I_x)pq] &= N
\end{aligned} \tag{14}$$

where u, v, w the linear velocities and p, q, r the angular velocities obtained before. Then $\dot{u}, \dot{v}, \dot{w}, \dot{p}, \dot{q}$ and $\dot{r}$ can be calculated in an explicit manner.
Linear and angular velocities $\dot{\varphi}$, position or orientation vector φ of the floating body can be calculated with a second-order Adams-Bashforth scheme for the new time-step:

$$\begin{aligned}
\dot{\varphi}^{n+1} &= \dot{\varphi}^{t} + \frac{\Delta t}{2}\left(3\ddot{\varphi}^{n+1} - \ddot{\varphi}^{n}\right) \\
\varphi^{n+1} &= \varphi n + \frac{\Delta t}{2}\left(3\dot{\varphi}^{n+1} - \dot{\varphi}^{n}\right)
\end{aligned} \tag{15}$$

The floating body dynamics are solved in a explicit way. The dynamic rigid body equations are solved in the floating body reference frame. Translations and orientations are also calculated. The transformation is done with the following matrix J_2, where *sin* has been denoted as s, *cos* as c and *tan* as t:

$$\dot{\boldsymbol{\eta}}_{\mathbf{2}} = \begin{bmatrix} 1 & s\phi\ t\theta & c\phi\ t\theta \\ 0 & c\phi & -s\phi \\ 0 & s\phi/c\theta & c\phi/c\theta \end{bmatrix} \boldsymbol{\nu}_{\mathbf{2}} = \mathbf{J}_{\mathbf{2}}\boldsymbol{\nu}_{\mathbf{2}} \tag{16}$$

The boundary conditions for the velocities on the solid-fluid interface result from the motion of the solid body in respect to its centre of gravity:

$$u_i = \dot{\boldsymbol{\eta}}_{\mathbf{1}} + \dot{\boldsymbol{\eta}}_{\mathbf{2}} \times \mathbf{r} \tag{17}$$

Pressure oscillations near the solid body occurs because of solid cells turns into fluid cells and vice versa. The field extension method [13][14][15] is implemented and adapted to the ghost cell immersed boundary method [4]. For non-moving boundaries, a zero-gradient boundary condition is used for the pressure. The following boundary condition for the gradient of the pressure is used to maintain a physical pressure gradient near the floating body:

$$\frac{\partial p}{\partial x_i} = -\frac{1}{\rho}\frac{Du_i}{Dt} \tag{18}$$

To obtain u_i, eq. 17 is differentiated with respect to time and used for the ghost cell values for the pressure:

$$\frac{Du_i}{Dt} = \frac{\partial}{\partial t}(\dot{\boldsymbol{\eta}}_{\mathbf{1}} + \dot{\boldsymbol{\eta}}_{\mathbf{2}} \times \mathbf{r}) \tag{19}$$

To avoid problems caused when a cell becomes a fluid cell and have non-physical values for velocities and pressure, velocities from eq. 17 are used and the pressure is found through interpolation from the fluid.

3 VALIDATION

3.1 Freely floating body in two-dimension simulation

A floating rigid body is simulated in two dimensions under the effect of waves. The body has three degrees of freedom in the simulation: surge, heave and pitch. The floating body consists of a rectangular barge with a length of l=0.30 m and a height of h=0.20 m following Ren[16]. The breadth of the barge is equal to the total width of the tank. The water depth is d=0.4 m. The density is ρ=500 kg/m^3. The initial position is defined by the centroid of the barge at x=7.0 m, z=0.4 m. Results obtained are compared with the experiment. The simulation is carried out in a tank which is 20 m long and a height of 0.8m. The barge is positioned at 7 m from the start of the tank in order to diminish the effect of wave reflection. Waves are 2nd order Stokes type, with wave period T=1.2 s, wave height H=0.04 m and wavelength L=1.93625 m. Different grids are used in the case: 0.01 m and 0.005 m with a total cells of 2000x150 and 4000x300, respectively. The total computational time is 12 s with a time-step size of 0.05 s.
In Fig. 1a the wave elevation is presented with a good correspondence with experiment data. Experiment data matches the simulations after t/T=6.4. The heave results presented in Fig. 1b show a good agreement between both grid sizes and experiment results. The numerical model result are accurate in relation to the height reached by the barge except the second and third crest waves. The troughs of the numerical model result are slightly smaller than the experiment with the exception of the last wave. In Fig. 1c, the rotation of the box around global axis Y is presented. There is a deviation from the coarser grid of 0.01 m to the finer grid of 0.005 m. Results from simulation matches experiment data really well, especially for the 0.005 m grid. In Fig. 1d, the surge motion is shown. Both grid sizes present a negative part in the start of the simulation meaning that the box is coming nearer the start of the tank. The surge presents an oscillatory movement due to the non-linear 2nd order Stokes wave theory used. After the initial negative part, all grids start to move towards the end of the tank. Results with grid size 0.005 m match experiment data really well except the first and second troughs. The grid size of 0.01 m present a shorter movement. The ratio of movement of both grid sizes agrees with the experiment.

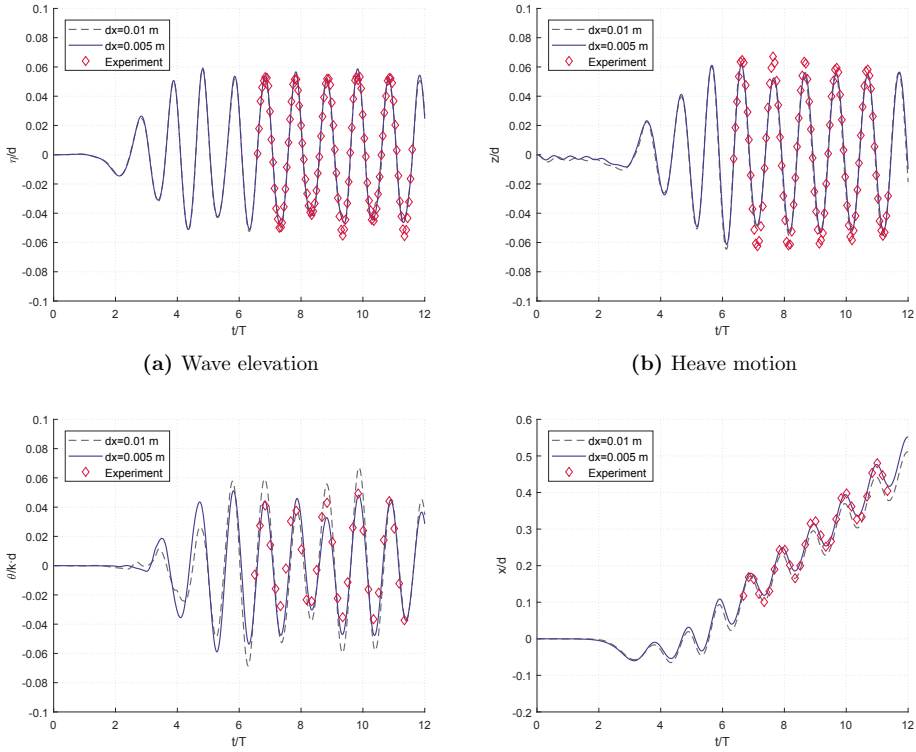

(a) Wave elevation

(b) Heave motion

(c) Pitch motion

(d) Surge motion

Figure 1: Wave elevation, heave, pitch and surge motion and experiment data.

3.2 Freely floating body in three-dimension simulation

In this section, a three-dimension simulation of the barge with the same wave conditions as the case presented in section 3.1 is carried out. The length of the NWT is 20.0 m and the height 0.8 m. The width of the tank varies defining three cases shown in Table 1.

	Case A	Case B	Case C
Tank width (m)	0.2	0.3	0.5
Centre of gravity Y axis (m)	0.1	0.15	0.25

Table 1: Tank width and position of the barge in Y axis

The breadth of the barge is b=0.1 m for all the cases. The length and height remain from section 3.1 as l=0.30 m and h=0.20 m, respectively. The position of the barge is defined by its centroid at x=7.0 m and z=0.4 m. The Y-coordinate of the barge is set in the middle of the tank for all cases, shown in Table 1. The density ρ=500.0 kg/m^3 and water level height d=0.4 m are kept as the two-dimension case 3.1. The wave conditions are the same as the two dimension case. The grid used is 0.01 m for all cases. Total cells are 2000x20x80, 2000x30x80 and 2000x50x80 for case A, B and C, respectively. The grid of 0.01 m is chosen among others for the accuracy-computational time result, seen in the results in section 3.1. Turbulence and water flow in the space between the barge and the tank walls will affect the free floating motion. Results between the cases will be compared.

In Fig. 2a, the wave elevation is presented. The wave height match among cases confirming that all cases have the same wave conditions. A slight difference is observable in case A in the last two troughs. In Fig. 2b the heave motion of the barge is presented. All cases have a little heave motion in the start of the simulation between t/T=0 and t/T=2. It shall be noted that the starting heave is also presented in Fig. 1b with a smaller magnitude. Heave motion is similar between all the cases. Case A shows in general smaller crest than other cases. Case C has a change in the slope around t/T=10 when the body is moving down. Heave motion is similar for the cases so the space between the barge and the tank walls doesn't affect largely this motion. Pitch motion is shown in Fig. 2c. Case A starts with a negative rotation compared to the other two. In this case, the pitch starts irregularly until t/T=5 when it follows the motion of the other cases. This difference is due to the smaller tank width in case A than the others. The flow passing in the gap affects the rotation of the barge. Case B and C have a similar motion in the start of the simulation. However, case B has a smaller pitch motion. It is noticeable that in cases A and C with the smallest and biggest tank width, the pitch motion almost concurs after t/T=6. In Fig. 2d, surge is presented. All cases start with a negative surge motion where the barge is coming closer to the wave generation zone because of the drift. This is notable for case B where the positive surge doesn't start until t/T=5. After, it starts

moving with a slope analogous to case A and C. Surge of case A and C are similar with a movement along X axis.

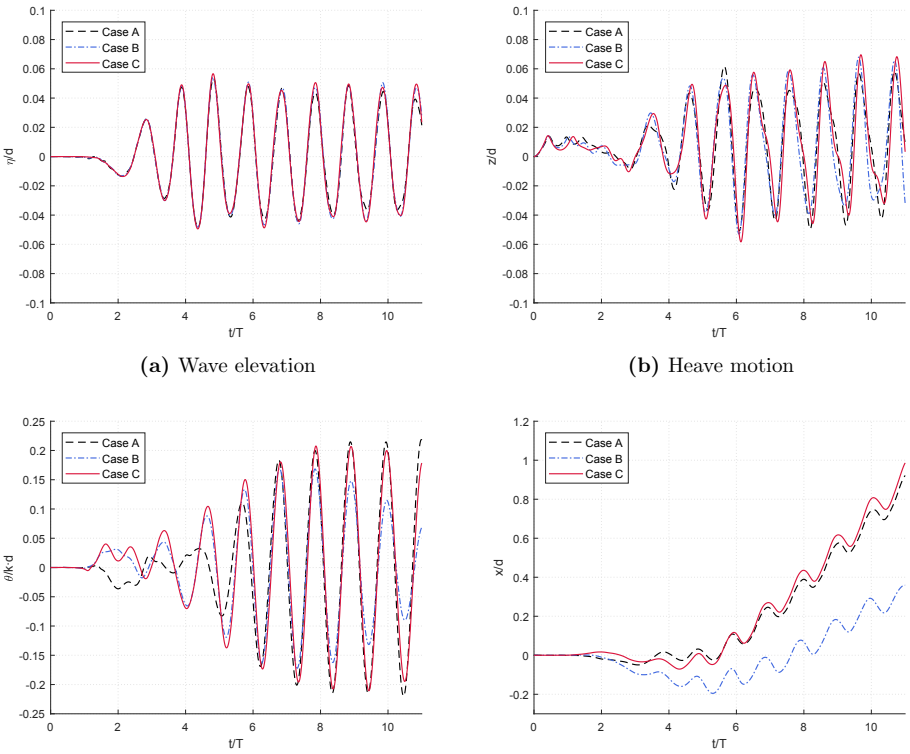

(a) Wave elevation

(b) Heave motion

(c) Pitch motion

(d) Surge motion

Figure 2: Comparison of wave elevation, heave, pitch and surge motion with grid size dx=0.01 m for different tank widths.

In Fig. 3 the motion the box is presented with a time-step of t/T=2 starting at t/T=4 with the first wave. In the Fig. each line presents a case and each row the same time-step. All the Figs. are taken from the same position. This allow to check the motions of the barge over time for a case and compare among cases. Besides the horizontal X velocity is shown along with the free surface. In Figs. 3c, 3f and 3i, it is noticeable the difference in surge motion between case B and case A and C.

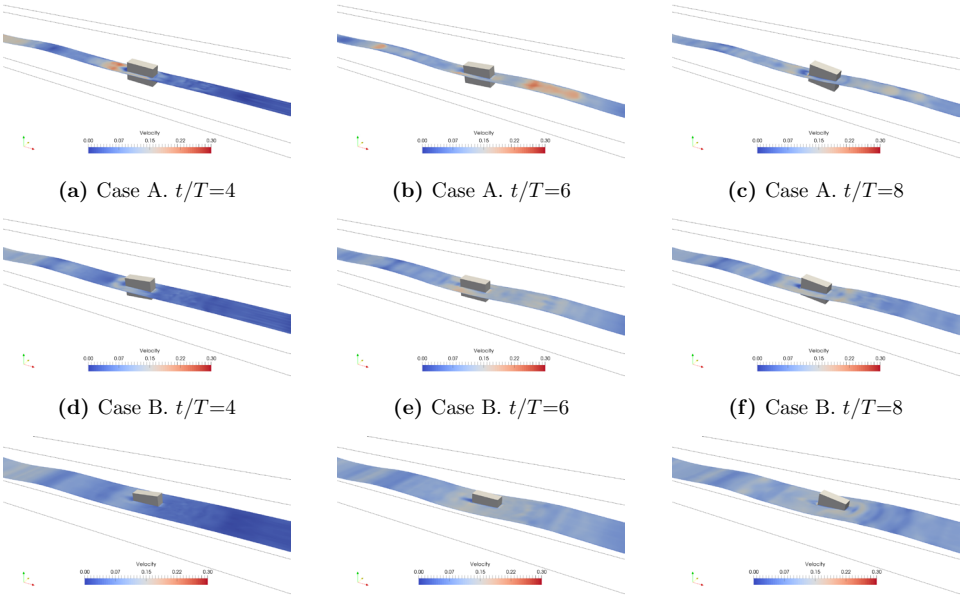

(a) Case A. t/T=4 **(b)** Case A. t/T=6 **(c)** Case A. t/T=8

(d) Case B. t/T=4 **(e)** Case B. t/T=6 **(f)** Case B. t/T=8

(g) Case C. t/T=4 **(h)** Case C. t/T=6 **(i)** Case C. t/T=8

Figure 3: Free surface, motion of the barge and velocity at t/T=4, 6, 8 for cases A, B and C.

4 CONCLUSIONS

The 6DOF algorithm implemented in REEF3D has been analysed, validated and tested for a free floating rectangular barge. A two dimension case has been studied with two grid sizes. It has been noted that a grid size of 0.01 m presents good results in comparison to the finer grid of 0.005 m, so three dimension simulations have been performed with the 0.01 m grid size. Results for the two dimension case match very well the experimental data for the different motions validating the 6DOF algorithm for two dimensions modelling. Further analysis in three dimension have been performed with the same experiment set up. The breadth of the barge has been changed as well as the width of the tank setting three different cases. The motion of the barge affected by the flow and turbulence in the gap between the tank walls and the barge have been studied.

REFERENCES

[1] S Tanaka and K Kashiyama. ALE finite element method for FSI problems with free surface using mesh re-generation method based on background mesh. *International*

Journal Of Computational Fluid Dynamics, 20(3-4):229–236, 2006.

[2] N. Takashi. ALE finite element computations of fluid-structure interaction problems. *Computer Methods in Applied Mechanics and Engineering*, 112(1-4):291–308, 1994.

[3] Charles S. Peskin. The immersed boundary method. *Acta Numerica 2002*, pages 479–517, 2002.

[4] H. Bihs and A. Kamath. Simulation of floating bodies with a combined level set/ghost cell immersed boundary representation. *International Journal for Numerical Methods in Fluids*, 83(12):905–916, 2017.

[5] Hans Bihs, Arun Kamath, Mayilvahanan Alagan Chella, Ankit Aggarwal, and Øivind A. Arntsen. A new level set numerical wave tank with improved density interpolation for complex wave hydrodynamics. *Computers & Fluids*, 140:191–208, 2016.

[6] Muk Chen Ong, Arun Kamath, Hans Bihs, and Mohammad Saud Afzal. Numerical simulation of free-surface waves past two semi-submerged horizontal circular cylinders in tandem. *Marine Structures*, 52:1–14, 2017.

[7] Arun Kamath, Mayilvahanan Alagan Chella, Hans Bihs, and Øivind A. Arntsen. Evaluating wave forces on groups of three and nine cylinders using a 3D numerical wave tank. *Engineering Applications of Computational Fluid Mechanics*, 9(1):343–354, 2015.

[8] Jesper Larsen and Henry Dancy. Open boundaries in short wave simulations–A new approach. *Coastal Engineering*, 7:285–297, 1983.

[9] S. Shu, C. W. and Osher. Efficient implementation of essentially non-oscillatory shock capturing schemes. *Journal of Computational Physics*, 77:439–471, 1988.

[10] J. A. Osher, S. and Sethian. Fronts propagating with curvature- dependent speed: algorithms based on Hamilton-Jacobi formulations. *Journal of Computational Physics*, 79:12–49, 1988.

[11] M. Peng, D. and Merriman, B. and Osher, S. and Zhao, H. and Kang. A PDE-Based Fast Local Level Set Method. *Journal of Computational Physics*, 155(2):410–438, 1999.

[12] G. S. Jiang and D. Peng. Weighted ENO schemes for Hamilton-Jacobi equations. *SIAM Journal on Scientific Computing*, 21:2126–2143, 2000.

[13] J. Yang and E. Balaras. An embedded-boundary formulation for large-eddy simulation of turbulent flows interacting with moving boundaries. *Journal of Computational Physics*, 215:12–40, 2006.

[14] J. Yang and F. Stern. Sharp interface immersed-boundary/level-set method for wave-body interactions. *Journal of Computational Physics*, 228(17):6590–6616, 2009.

[15] H. S. Udaykumar, R. Mittal, P. Rampunggoon, and A. Khanna. A sharp interface cartesian grid method for simulating flows with complex moving boundaries. *Journal of Computational Physics*, 174:345–380, 2001.

[16] Bing Ren, Ming He, Ping Dong, and Hongjie Wen. Nonlinear simulations of wave-induced motions of a freely floating body using WCSPH method. *Applied Ocean Research*, 50:1–12, 2015.

9. National Conference on Computational Mechanics
MekIT'17
B. Skallerud and H I Andersson (Eds)

A COMPARATIVE STUDY OF BEAM ELEMENT FORMULATIONS FOR NONLINEAR ANALYSIS: COROTATIONAL VS GEOMETRICALLY EXACT FORMULATIONS

KJELL M. MATHISEN[1], YURI BAZILEVS[2], BJØRN HAUGEN[3], TORE A. HELGEDAGSRUD[1], TROND KVAMSDAL[4,5], KNUT M. OKSTAD[5] AND SIV B. RAKNES[1]

[1]Department of Structural Engineering
Norwegian University of Science and Technology (NTNU), Trondheim, Norway
e-mail: Kjell.Mathisen@ntnu.no

[2]Department of Structural Engineering, University of California, San Diego, USA

[3]Department of Mechanical and Industrial Engineering, NTNU, Trondheim, Norway

[4]Department of Mathematical Sciences, NTNU, Trondheim, Norway

[5]Department of Mathematics and Cybernetics, SINTEF Digital, Trondheim, Norway

Key words: Nonlinear finite element analysis, Beam structures, Euler-Bernoulli beams, Timoshenko beams, Geometrically exact beam theory, Corotational elements

Abstract. In this work the geometrically exact three-dimensional beam theory has been used as basis for development of a family of isoparametric higher order large deformation curved beam elements. Geometrically exact three-dimensional beam theory has no restrictions with respect to the magnitude of displacements, rotations and deformations. While reduced integration may be used to alleviate transverse shear and membrane locking in linear and quadratic C^0-continuous Lagrange elements, this does not automatically extend to higher order elements. In this study we demonstrate that uniform reduced numerical quadrature rules may be used to obtain locking-free isoparametric large deformation geometrically exact curved beam elements of arbitrary order. A set of carefully selected numerical examples serves to illustrate and assess the performance of the various geometrically exact elements and compare them with one of the most popular finite element formulations for solving nonlinear beam problems based on the corotational formulation.

1 INTRODUCTION

The finite element (FE) method has been widely used in nonlinear analysis of three-dimensional (3D) curved beam-like structural systems subjected to large displacements and large strains for several decades. Numerous approaches have been proposed, but the vast majority of them have been limited to considering the beam element reference geometry being a straight line. In this work we aim to extend the *geometrically exact* (GE) beam model (see Simo [27] and Simo and Vu-Quoc [28, 29]) based on Reissner's 3D beam theory [24], to model arbitrary shaped curved beam geometry. Several authors, e.g., Stolarski and Belytschko [30] and Ibrahimbegović [16], have observed that increasing the accuracy of the approximated curved beam geometry entails a significant increase in accuracy. The curved 3D GE beam formulation presented herein is able to accommodate large displacements, finite rotations and finite strains. In contrast to the corotational (CR)-type of beam elements (see, e.g., Battini and Pacoste [3, 4], Crisfield [9], Felippa and Haugen [11], and Mathisen and Bergan [20]), it can be easily extended to higher-order beam elements. Saje [26] extended the GE beam model to higher-order two-dimensional (2D) curved beams and Ibrahimbegović [16] to 3D curved beams. However, the latter work was restricted to quadratic hierarchical displacement interpolation. To our knowledge the current work represent the first attempt to extend the GE beam model to an arbitrary order of interpolation. Also our extension of the linearly interpolated straight beam formulation proposed by Simo and Vu-Quoc [28] follows more closely the CR approach since we derive the energy-conjugate strains from a polar decomposition of the deformation tensor rather than defining stress resultants and couples *a priori* and achieving energy-conjugate strain measures through the variational formulation which was employed in the original work.

In this context, our aim is to develop a family of GE 3D beam elements free of locking for the analysis of geometrically nonlinear finite deformation curved beam-like structural systems. In order to do that, we propose an extension of the GE beam model presented in [27, 28, 29], to higher-order Lagrangian-based discretization of both the geometry, displacement, and the rotational fields. To alleviate locking, we have proposed and validated quadrature rules based on uniform reduced integration of the translational and rotational part of the beam model for arbitrary order of interpolation.

This paper is outlined as follows. In Section 2, the GE beam model due to Simo [27] and Simo and Vu-Quoc [28, 29] is presented. Section 3 highlights locking effects in beams together with a presentation of the various enhancements used to alleviate locking. In Section 4, the various proposed GE elements are tested and compared with several 2-noded beam elements based on the CR formulation proposed by Battini and Pacoste [3, 4] on a selection of beam problems. Finally, in Section 5 we summarize and draw conclusions.

2 A GEOMETRICALLY EXACT BEAM MODEL

In this section we consider the continuum basis for a GE beam theory that is optimally suited for computational solution by the FE method. GE beam theory is sometimes referred to as the Reissner's beam theory [24], but strictly speaking, the latter is only exact for a planar beam [23]. The theory presented herein is based on the pioneering work of Simo [27] and Simo and Vu-Quoc [28, 29], that in [29] introduced the still-used terminology GE beam model to indicate that Reissner's theory was recast in a form which is valid for finite rotations. The GE beam model has later been revisited and further developed by numerous authors over more than two decades, e.g., Cardona and Géradin [7] and Ibrahimbegović [16], in which the latter extended the theory to handle curved reference geometry. Beam models of this type have been coined *geometrically exact* because they account, without approximation, for the total deformation and strains.

2.1 Beam geometry in 3D space

The beam is viewed as a 3D body, whose material placement can be described by the line of centroids $\mathcal{B}_0 \subset \mathbb{R}^3$, that has attached at each point a planar non-deformable cross section A_0 in the reference configuration. A local curvilinear coordinate system is chosen to parameterize this line through an arc-length coordinate S along $\mathcal{B}_0$ in the reference configuration. Let $\{\boldsymbol{i}_i(S,t)\}_{i=1,2,3}$ represent a local Cartesian moving frame whose origin is fixed at the centroid at all times, $\boldsymbol{i}_1(S,t)$ remains perpendicular to A and $\{\boldsymbol{i}_\alpha(S,t)\}_{\alpha=2,3}$ span the cross section of the beam in the current configuration. Henceforth, we use the summation convention with Latin indices ranging from 1 to 3 and with Greek indices ranging from 2 to 3. In the reference configuration the orthonormal basis vectors are denoted $\boldsymbol{i}_i^0(S) = \boldsymbol{i}_i(S,0)$ and the associated set of cross section coordinates x_α^0 (see Fig. 1). Let $\boldsymbol{X}(S)$ and $\boldsymbol{x}(S,t)$ define the position of $\mathcal{B}_0$ and $\mathcal{B}$ in the 3D space in the reference and current configuration, respectively:

$$\boldsymbol{x}(S,t) = \boldsymbol{X}(S) + \boldsymbol{u}(S,t), \tag{1}$$

where $\boldsymbol{u}(S,t)$ denote the displacement of $\mathcal{B}_0$ at any time t. We assume that the length of the line of centroids $\mathcal{B}_0$ and $\mathcal{B}$ is L_0 and L, respectively.

Without loss of generality, we assume that; (1) the beam has uniform cross sections, i.e., cross-sectional properties remain constant along the entire length of the beam, (2) the beam reference configuration is stress- and strain-free, and (3) the cross sections are initially normal to $\mathcal{B}_0$, hence:

$$\boldsymbol{i}_1^0(S) = \frac{d\boldsymbol{X}(S)}{dS} = \boldsymbol{X}'(S), \tag{2}$$

where prime denotes the derivative with respect to the arc-length coordinate S.

In accordance with standard hypothesis for beams, we further assume that:

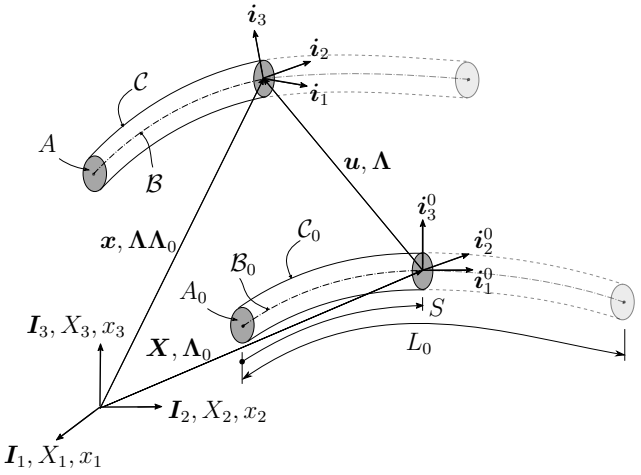

Figure 1: Definition of the various frames and configurations for the GE beam model.

(i) The cross sections remain plane and undeformed in the current configuration, i.e., warping effects are not accounted for.

(ii) The cross sections that initially are normal to $\mathcal{B}_0$ do not necessarily remain normal to the deformed line of centroids $\mathcal{B}$ in the current configuration, i.e., transverse shear deformations are accounted for; hence $\boldsymbol{i}_1(S,t)$ remain normal to A but not necessarily tangent to $\mathcal{B}$.

The orientation of the moving local Cartesian frame $\boldsymbol{i}_i(S,t)$ along $S \in [0,L]$, and through time $t \in [0,T]$ is governed by the orthogonal two-point tensor $\boldsymbol{\Lambda}(S,t)$ such that

$$\boldsymbol{i}_i(S,t) = \boldsymbol{\Lambda}(S,t)\boldsymbol{i}_i^0(S) \Rightarrow \boldsymbol{\Lambda}(S,t) = \boldsymbol{i}_i \otimes \boldsymbol{i}_i^0; \| \boldsymbol{i}_i \| = \| \boldsymbol{i}_i^0 \| = 1 \Rightarrow \boldsymbol{\Lambda}^T\boldsymbol{\Lambda} = \boldsymbol{\Lambda}\boldsymbol{\Lambda}^T = \boldsymbol{I}, \quad (3)$$

where $\boldsymbol{I}$ denote the identity tensor. Defining the reference and current configurations with respect to a global Cartesian frame $\boldsymbol{I}_i$, the above transformation reads:

$$\boldsymbol{i}_i(S,t) = \boldsymbol{\Lambda}(S,t)\boldsymbol{\Lambda}_0(S)\boldsymbol{I}_i \Rightarrow \boldsymbol{\Lambda}_0(S) = \boldsymbol{i}_i^0 \otimes \boldsymbol{I}_i, \quad (4)$$

where $\boldsymbol{\Lambda}_0(S)$ defines the orientation of the local Cartesian frame $\boldsymbol{i}_i^0(S)$ in the reference configuration. The current configuration $\mathcal{C}$ of the 3D beam at any time t will then be uniquely determined by the current position and the rotation of the centroid of the cross section, i.e., the origin of the moving frame:

$$\mathcal{C} = \{\boldsymbol{\varphi} = (\boldsymbol{x}, \boldsymbol{\Lambda}) : [0,L] \times [0,T] \longrightarrow \mathbb{R}^3 \times SO(3)\}, \quad (5)$$

where $SO(3)$ represents the special orthogonal (Lie) group, i.e., the group of all rotations about the origin of $\mathbb{R}^3$ under the operation of composition. As a consequence, the 3D kinematic description of the beam is reduced to a 1D kinematic description with the arc-length coordinate S as the only parameter. With these definitions, the 3D beam geometry in the current configuration may be defined as

$$\boldsymbol{x}^{3\mathrm{D}}(S, x_\alpha^0, t) = \boldsymbol{x}(S,t) + \boldsymbol{p}(S, x_\alpha^0, t), \tag{6}$$

where

$$\boldsymbol{p}(S, x_\alpha^0, t) = \boldsymbol{\Lambda}(S,t)\boldsymbol{p}_0(S, x_\alpha^0) = \boldsymbol{\Lambda}(S,t) x_\alpha^0 \boldsymbol{i}_\alpha^0(S). \tag{7}$$

$\boldsymbol{p}$ and $\boldsymbol{p}_0$ denote the cross section position vector along $\mathcal{B}$, i.e., the position of a point P relative to the centroid within a cross section, in the current and reference configuration, respectively. Herein, we only consider quasi-static analysis of beam problems. However, the kinematic description presented in this section is identical for static and dynamic problems. For that reason, "time" and "pseudo-time" as well as "time step", "incremental step" and "load step" are used as equivalents throughout this work.

2.2 Parameterization of finite 3D rotations

The principal difficulty by representing 3D finite rotations by an orthogonal tensor $\boldsymbol{\Lambda}$ is due to the fact that $SO(3)$ is not a linear (vector) space, but rather a manifold, hence consistent linearization and update procedures are no longer straightforward. In the context of time-independent (static) analysis, Ibrahimbegović [17] overcame this problem by reparameterizing the configuration space of the beam by making use of the so-called rotation vector $\boldsymbol{\theta}$, defined by

$$\boldsymbol{\theta} = \theta \boldsymbol{e}, \tag{8}$$

where $\boldsymbol{e}$ is a unit vector defining the axis of rotation and $\theta = \sqrt{\theta_1^2 + \theta_2^2 + \theta_3^2}$ is the magnitude of the rotation vector. The relation between $\boldsymbol{\Lambda}$ and $\boldsymbol{\theta}$ is governed by the Rodriguez formula which represents a closed form solution of the exponential mapping

$$\boldsymbol{\Lambda} = \exp[\widetilde{\boldsymbol{\theta}}] = \boldsymbol{I} + \frac{\sin\theta}{\theta}\widetilde{\boldsymbol{\theta}} + \frac{1-\cos\theta}{\theta^2}\widetilde{\boldsymbol{\theta}}\widetilde{\boldsymbol{\theta}}, \tag{9}$$

where $\widetilde{\boldsymbol{\theta}}$ denote the skew-symmetric tensor for which $\boldsymbol{\theta}$ is the axial vector, i.e.:

$$\boldsymbol{\theta} = [\theta_1, \theta_2, \theta_3] \Rightarrow \widetilde{\boldsymbol{\theta}} = \mathrm{skew}[\boldsymbol{\theta}] = \begin{bmatrix} 0 & -\theta_3 & \theta_2 \\ \theta_3 & 0 & -\theta_1 \\ -\theta_2 & \theta_1 & 0 \end{bmatrix}. \tag{10}$$

With such a parameterization, the configuration space $\mathcal{C}$ becomes a linear space:

$$\mathcal{C} = \{\boldsymbol{\varphi} = (\boldsymbol{x}, \boldsymbol{\Lambda}) : [0, L] \times [0, T] \longrightarrow \mathbb{R}^3 \times \mathbb{R}^3\}. \tag{11}$$

The admissible variation $\delta\boldsymbol{\Lambda}$ of the orthogonal tensor of finite rotations can be constructed by making use of the exponential mapping

$$\delta\boldsymbol{\Lambda} = \widetilde{\delta\boldsymbol{w}}\boldsymbol{\Lambda} = \boldsymbol{\Lambda}\widetilde{\delta\boldsymbol{\psi}}. \tag{12}$$

Physically, $\widetilde{\delta\boldsymbol{w}}$ and $\widetilde{\delta\boldsymbol{\psi}}$ represent infinitesimal spatial and material rotations superposed onto the existing rotation $\boldsymbol{\Lambda}$. The spatial spin variables, $\delta\boldsymbol{w}$, are also related to the variation of the rotational vector through (see [17])

$$\delta\boldsymbol{w} = \boldsymbol{T}_s(\boldsymbol{\theta})\,\delta\boldsymbol{\theta}, \tag{13}$$

where

$$\boldsymbol{T}_s(\boldsymbol{\theta}) = \boldsymbol{I} + \frac{1-\cos\theta}{\theta^2}\widetilde{\boldsymbol{\theta}} + \frac{\theta-\sin\theta}{\theta^3}\widetilde{\boldsymbol{\theta}}\widetilde{\boldsymbol{\theta}}. \tag{14}$$

If the rotational vector is used as parameterization, the rotations become additive and are updated at each iteration. However, the relation in Eq. (13) cease to be bijection for $\theta = 2n\pi$. Consequently, with the parameterization using the rotational vector, the angle of rotation is limited to 2π. In large deformation analysis, and especially in dynamic large deformation analysis, angles of rotation can become much larger than 2π. In order to overcome this limitation, Cardona and Géradin [7] and Ibrahimbegović *et al.* [17] proposed to apply Eq. (13) only within an increment and introduced the concept of incremental rotation vector, based on the following update procedure:

(i) At the beginning at the time step $(n+1)$, i.e., for iteration $i = 0$, the incremental rotation vector is set to zero:

$$\boldsymbol{\theta}^0_{n+1} = \boldsymbol{0}. \tag{15}$$

(ii) At the i^{th} iteration the incremental rotation vector is updated additively

$$\boldsymbol{\theta}^i_{n+1} = \boldsymbol{\theta}^{i-1}_{n+1} + \Delta\boldsymbol{\theta}, \tag{16}$$

where $\Delta\boldsymbol{\theta}$ represents the iterative change of the incremental rotation vector.

(iii) The corresponding orthogonal tensor $\boldsymbol{\Lambda}$ is updated using exponential mapping

$$\boldsymbol{\Lambda}^i_{n+1} = \exp[\widetilde{\boldsymbol{\theta}^i_{n+1}}]\boldsymbol{\Lambda}_n. \tag{17}$$

Hence, additive updates still apply within each time step and the amplitude of the rotations are thus just limited within each time step. Alternatively, if the spatial spin variables are used to parameterize the finite rotations, the update is performed according to

$$\boldsymbol{\Lambda}^i_{n+1} = \exp[\widetilde{\Delta\boldsymbol{w}}]\boldsymbol{\Lambda}^{i-1}_{n+1}, \tag{18}$$

where $\Delta\boldsymbol{w}$ denote the corresponding iterative change of the spatial spin variables.

2.3 Strain measures

In contrast to previous works [7, 16, 17, 23, 24, 27, 28, 29], where energy-conjugate strain measures were based on stress resultants defined *a priori*, Auricchio *et al.* [1] derived a GE beam model in which proper strain measures at any point of the beam in $\mathcal{C}$ were obtained by a polar decomposition of the deformation gradient $\boldsymbol{F}$. With the definition of the 3D geometry in $\mathcal{C}$, see Eq. (6), the deformation gradient may be expressed as

$$\boldsymbol{F} = \frac{\partial \boldsymbol{x}^{3\mathrm{D}}}{\partial x_i^0} \otimes \boldsymbol{i}_i^0 = \left(\boldsymbol{x}' + \boldsymbol{\Lambda}' x_\alpha^0 \boldsymbol{i}_\alpha^0\right) \otimes \boldsymbol{i}_1^0 + \boldsymbol{i}_\alpha \otimes \boldsymbol{i}_\alpha^0. \tag{19}$$

Utilizing Eq. (12), the derivative of the rotation tensor $\boldsymbol{\Lambda}$ with respect to S may be expressed as

$$\boldsymbol{\Lambda}' = \widetilde{\boldsymbol{\kappa}}\boldsymbol{\Lambda} \Leftrightarrow \widetilde{\boldsymbol{\kappa}} = \boldsymbol{\Lambda}'\boldsymbol{\Lambda}^T, \tag{20}$$

where $\widetilde{\boldsymbol{\kappa}} = \widetilde{\boldsymbol{\kappa}}(S)$ is a skew-symmetric tensor represented by the axial vector $\boldsymbol{\kappa}$ denoting the spatial rotational (torsional and bending) strains, i.e., the spatial curvature. Furthermore, adding and subtracting the tensor $\boldsymbol{i}_1 \otimes \boldsymbol{i}_1^0$ to the right-hand-side and recognizing that $\boldsymbol{i}_i \otimes \boldsymbol{i}_i^0 = \boldsymbol{\Lambda}$, we may rewrite Eq. (19) and make a material polar decomposition of $\boldsymbol{F}$

$$\boldsymbol{F} = \boldsymbol{\Lambda}\left\{\boldsymbol{I} + \left[\boldsymbol{\Lambda}^T\left(\boldsymbol{x}' - \boldsymbol{i}_1\right) + \boldsymbol{\Lambda}^T\widetilde{\boldsymbol{\kappa}} x_\alpha^0 \boldsymbol{i}_\alpha^0\right] \otimes \boldsymbol{i}_1^0\right\} = \boldsymbol{\Lambda}\boldsymbol{U}. \tag{21}$$

In Eq. (21), $\boldsymbol{U}$ defines the right (current local) stretch tensor from which we may derive the Biot strain measure $\boldsymbol{B}$ (often referred to as the Jaumann strains), that are objective corotated engineering strains independent of rigid body displacements

$$\boldsymbol{B} = \boldsymbol{\Lambda}^T\boldsymbol{F} - \boldsymbol{I} = \boldsymbol{U} - \boldsymbol{I} = \boldsymbol{\varepsilon} \otimes \boldsymbol{i}_1 \quad \text{with} \quad \boldsymbol{\varepsilon} = \boldsymbol{\Lambda}^T\left(\boldsymbol{\gamma} + \widetilde{\boldsymbol{\kappa}}\boldsymbol{p}\right) = \boldsymbol{\Gamma} + \widetilde{\boldsymbol{K}}\boldsymbol{p}_0, \tag{22}$$

where $\boldsymbol{\varepsilon}$ represents a generalized convected strain measure, $\boldsymbol{\gamma}$ the translational (axial and transverse shear) spatial strains and $\boldsymbol{\kappa}$ the rotational (torsional and bending) spatial curvature strain vector. The corresponding convected material strains are represented by upper case letters $\boldsymbol{\Gamma}$ and $\boldsymbol{K}$. The relationship between the material and spatial forms may then be expressed as

$$\begin{aligned} \boldsymbol{\Gamma} &= \boldsymbol{\Lambda}^T\boldsymbol{\gamma} \quad \text{with} \quad \boldsymbol{\gamma} = \boldsymbol{x}' - \boldsymbol{i}_1, \\ \boldsymbol{K} &= \boldsymbol{\Lambda}^T\boldsymbol{\kappa} \quad \text{with} \quad \boldsymbol{\kappa} = \boldsymbol{T}_s(\boldsymbol{\theta})\boldsymbol{\theta}'. \end{aligned} \tag{23}$$

A physical interpretation of the spatial strain measures is that the components of $\boldsymbol{\gamma}$ represent the true axial and transverse shear strain measures with respect to the current moving frame $\boldsymbol{i}_i(S,t)$, e.g., γ_1 represents the elongation of an infinitesimal fiber in the direction normal to the cross section while γ_2 and γ_3 are the corresponding transverse shear strains. Similarly, the three components of $\boldsymbol{\kappa}$, represents the true torsional (κ_1) and bending strain measures (κ_2 and κ_3) with respect to the moving frame.

2.4 Stress resultants, constitutive equations and balance laws

Work conjugate with the strain measures in Eq. (23), we define material and spatial stress resultants and couples, $\boldsymbol{N}, \boldsymbol{M}$ and $\boldsymbol{n}, \boldsymbol{m}$, where the latter are obtained by a push-forward of the convected resultants and couples:

$$\boldsymbol{n} = \boldsymbol{\Lambda N} \quad \text{and} \quad \boldsymbol{m} = \boldsymbol{\Lambda M}. \tag{24}$$

The first component of the force resultants $\boldsymbol{n}, \boldsymbol{N}$ denotes the axial force in the direction of $\boldsymbol{i}_1, \boldsymbol{i}_1^0$, while component 2 and 3 denote the transverse shear forces in the directions of $\boldsymbol{i}_\alpha, \boldsymbol{i}_\alpha^0$, respectively. Similarly, the first component of the stress couples $\boldsymbol{m}, \boldsymbol{M}$ denotes the torsional moment about the axis of $\boldsymbol{i}_1, \boldsymbol{i}_1^0$, while component 2 and 3 denote the bending moments about the axes of $\boldsymbol{i}_\alpha, \boldsymbol{i}_\alpha^0$, respectively. For a hyperelastic material the convected resultants may be obtained from a strain energy function $\Psi(\boldsymbol{\Gamma}, K)$ through the relations

$$\boldsymbol{N} = \frac{\partial \Psi(\boldsymbol{\Gamma}, K)}{\partial \boldsymbol{\Gamma}} \quad \text{and} \quad \boldsymbol{M} = \frac{\partial \Psi(\boldsymbol{\Gamma}, K)}{\partial \boldsymbol{K}}. \tag{25}$$

In our study we assume that we have a linear isotropic relation between stresses and strains. This results in a St. Venant–Kirchhoff-type constitutive relation that may be expressed in terms of E and G, denoting the Young's and the shear modulus, respectively. The corresponding resultant constitutive laws reads

$$\boldsymbol{N} = \begin{bmatrix} N^1 \\ N^2 \\ N^3 \end{bmatrix} = \begin{bmatrix} EA_0 & 0 & 0 \\ 0 & G\bar{A}_{02} & 0 \\ 0 & 0 & G\bar{A}_{03} \end{bmatrix} \begin{bmatrix} \Gamma_1 \\ \Gamma_2 \\ \Gamma_3 \end{bmatrix} = \boldsymbol{C}_N \boldsymbol{\Gamma} \text{ with } \begin{matrix} N^i = \boldsymbol{N} \cdot \boldsymbol{i}_i^0 \\ \Gamma_i = \boldsymbol{\Gamma} \cdot \boldsymbol{i}_i^0 \end{matrix}, \tag{26}$$

and

$$\boldsymbol{M} = \begin{bmatrix} M^1 \\ M^2 \\ M^3 \end{bmatrix} = \begin{bmatrix} GI_T & 0 & 0 \\ 0 & EI_{33} & -EI_{32} \\ 0 & -EI_{23} & EI_{22} \end{bmatrix} \begin{bmatrix} K_1 \\ K_2 \\ K_3 \end{bmatrix} = \boldsymbol{C}_M \boldsymbol{K} \text{ with } \begin{matrix} M^i = \boldsymbol{M} \cdot \boldsymbol{i}_i^0 \\ K_i = \boldsymbol{K} \cdot \boldsymbol{i}_i^0 \end{matrix}, \tag{27}$$

where $G\bar{A}_{0\alpha}$ denotes the reduced cross section shear area in the direction of $\boldsymbol{i}_\alpha^0$, I_T the torsional stiffness and $I_{\alpha\beta} = \int_{A_0} x_\alpha^0 x_\beta^0 dA$ the cross section second moment of area.

The corresponding relation between the spatial stress resultants and couples and the energy conjugate strains $\boldsymbol{\gamma}$ and $\boldsymbol{\kappa}$, is obtained by combining Eqs. (23), (24), (26) and (27)

$$\boldsymbol{n} = \boldsymbol{\Lambda C}_N \boldsymbol{\Lambda}^T \boldsymbol{\gamma} \quad \text{and} \quad \boldsymbol{m} = \boldsymbol{\Lambda C}_M \boldsymbol{\Lambda}^T \boldsymbol{\kappa}. \tag{28}$$

As shown by Reissner [23, 24], Simo [27] and Simo and Vu-Quoc [28, 29], the beam balance equations can be obtained without any simplifying hypothesis regarding geometry, and size of displacements and rotations, hence, this theory is referred to as GE. If we consider $\bar{\boldsymbol{n}}$ and $\bar{\boldsymbol{m}}$ to be the externally applied force and moment per unit length the

time-independent linear and angular momentum balance (strong form) equations for the GE beam model reads:

$$\boldsymbol{n}' + \bar{\boldsymbol{n}} = \boldsymbol{0} \quad \text{and} \quad \boldsymbol{m}' + \boldsymbol{x}' \times \boldsymbol{n} + \bar{\boldsymbol{m}} = \boldsymbol{0}. \tag{29}$$

A unique strong form solution must satisfy the balance equations stated in Eq. (29) supplemented with the boundary conditions:

$$\begin{aligned} \boldsymbol{x} &= \bar{\boldsymbol{x}} \quad \text{on} \quad \mathcal{B}_x^{\varphi} \quad \text{and} \quad \boldsymbol{\Lambda} = \bar{\boldsymbol{\Lambda}} \quad \text{on} \quad \mathcal{B}_{\Lambda}^{\varphi}, \\ \boldsymbol{n} &= \bar{\boldsymbol{n}} \quad \text{on} \quad \mathcal{B}_n^{\sigma} \quad \text{and} \quad \boldsymbol{m} = \bar{\boldsymbol{m}} \quad \text{on} \quad \mathcal{B}_m^{\sigma}, \end{aligned} \tag{30}$$

where $\mathcal{B}_x^{\varphi}$, $\mathcal{B}_{\Lambda}^{\varphi}$, $\mathcal{B}_n^{\sigma}$ and $\mathcal{B}_m^{\sigma}$ denote the part of the beam where displacements, rotations, stress resultants and couples are prescribed, respectively.

2.5 Variational equations

The variational or weak form of the static equilibrium equations states that the solution to the beam problem (29) with the associated boundary conditions (30) is the motion $\boldsymbol{\varphi} = (\boldsymbol{x}, \boldsymbol{\Lambda}) \in \mathcal{S}$ that satisfies the principle of virtual work, which states that

$$\delta W = \delta W^{\text{int}} + \delta W^{\text{ext}}, \tag{31}$$

for all admissible virtual variations $\delta\boldsymbol{\varphi} = (\delta\boldsymbol{x}, \delta\boldsymbol{w})$. The internal virtual work carried out by the spatial stress resultants and couples over the associated admissible variations in the current configuration is given by (for more details see, e.g., Cardona and Géradin [7] or Helgedagsrud *et al.* [12]):

$$\delta W^{\text{int}} = \delta W^{\text{int}}(\boldsymbol{\varphi}, \delta\boldsymbol{\varphi}) = \int_L \{(\delta\boldsymbol{x}' + \boldsymbol{x}' \times \delta\boldsymbol{w}) \cdot \boldsymbol{n} + \delta\boldsymbol{w}' \cdot \boldsymbol{m}\} d\ell. \tag{32}$$

The external virtual work due to the distributed externally applied force and moment per unit length may be expressed as:

$$\delta W^{\text{ext}} = \delta W^{\text{ext}}(\delta\boldsymbol{\varphi}) = -\int_L \{\delta\boldsymbol{x} \cdot \bar{\boldsymbol{n}} + \delta\boldsymbol{w} \cdot \bar{\boldsymbol{m}}\} d\ell. \tag{33}$$

Combining the internal and external virtual work terms, we obtain the following spatial form of the variational formulation of the GE beam model: Find $\boldsymbol{\varphi} = (\boldsymbol{x}, \boldsymbol{\Lambda}) \in \mathcal{S}$, such that $\forall \delta\boldsymbol{\varphi} = (\delta\boldsymbol{x}, \delta\boldsymbol{w}) \in \mathcal{V}$:

$$\int_L \{(\delta\boldsymbol{x}' + \boldsymbol{x}' \times \delta\boldsymbol{w}) \cdot \boldsymbol{n} + \delta\boldsymbol{w}' \cdot \boldsymbol{m}\} d\ell = \int_L \{\delta\boldsymbol{x} \cdot \bar{\boldsymbol{n}} + \delta\boldsymbol{w} \cdot \bar{\boldsymbol{m}}\} d\ell. \tag{34}$$

In the formulation, $\mathcal{S}$ and $\mathcal{V}$ are suitably defined trial and test function spaces for the GE beam problem. Strictly speaking, the space of kinematically admissible variations for

the GE beam model is the tangent space at $\boldsymbol{\varphi}$ to the abstract configuration manifold $\mathcal{C}$, which is denoted $\mathcal{T}_{\varphi}\mathcal{C}$. Hence, in general $\delta\boldsymbol{\varphi}$ must be a member of the tangent space $\mathcal{T}_{\varphi}\mathcal{C}$. However, as pointed out in Section 2.2, when $\delta\boldsymbol{w}$ is an infinitesimal rotation superposed on the finite rotation $\boldsymbol{\Lambda}$ and the update is performed as an exponential map, the space of admissible variations is defined as:

$$\mathcal{V} = \{\delta\boldsymbol{\varphi} = (\delta\boldsymbol{x}, \delta\boldsymbol{w}) : [0, L]\times[0, T] \in \mathbb{R}^3\times\mathbb{R}^3 | \delta\boldsymbol{x} = \boldsymbol{0} \text{ on } \mathcal{B}_x^{\varphi} \text{ and } \delta\boldsymbol{w} = \boldsymbol{0} \text{ on } \mathcal{B}_{\Lambda}^{\varphi}\}. \quad (35)$$

2.6 Linearized variational equations

The virtual work equations for the finite deformation GE beam model are in general highly nonlinear. For this reason the problem is reduced to a set of nonlinear algebraic equations, whose solution is obtained utilizing an incremental-iterative Newton–Raphson approach. In order to obtain the consistent tangent of Newton's method, i.e., the tangent granting quadratic convergence rate, a consistent linearization of the associated variational equations must be performed. The incremental virtual work results in two contributions to the tangent stiffness, the material and geometrical part. With the expressions for the incremental and linearized virtual spatial strain measures at hand the material part is obtained by keeping the geometry constant varying the material resultants

$$\int_L \{(\delta\boldsymbol{x}' + \boldsymbol{x}'\times\delta\boldsymbol{w})\cdot\boldsymbol{\Lambda}\boldsymbol{C}_N\boldsymbol{\Lambda}^T(\Delta\boldsymbol{x}' + \boldsymbol{x}'\times\Delta\boldsymbol{w}) + (\delta\boldsymbol{w}')\cdot\boldsymbol{\Lambda}\boldsymbol{C}_M\boldsymbol{\Lambda}^T\Delta\boldsymbol{w}'\}d\ell, \quad (36)$$

whereas the geometric part is obtained keeping the material properties constant while varying the geometry

$$\int_L \{[(\delta\boldsymbol{x}' + \boldsymbol{x}'\times\delta\boldsymbol{w})\times\Delta\boldsymbol{w} - \delta\boldsymbol{w}\times\Delta\boldsymbol{x}']\cdot\boldsymbol{n} + (\delta\boldsymbol{w}'\times\Delta\boldsymbol{w})\cdot\boldsymbol{m}\}d\ell. \quad (37)$$

2.7 Discrete formulation

In this work we assume that standard Lagrangian basis functions are used to discretize both the geometry in the reference and the current configuration, $\boldsymbol{X}$ and $\boldsymbol{x}$, and the virtual and incremental displacement and rotational fields, $\delta\boldsymbol{\varphi} = (\delta\boldsymbol{x}, \delta\boldsymbol{w})$ and $\Delta\boldsymbol{\varphi} = (\Delta\boldsymbol{x}, \Delta\boldsymbol{w})$, of each individual element of the centroidal line $\mathcal{B}_0$:

$$\begin{aligned} &\boldsymbol{X}^h = \sum_{A=1}^{n_n} R_A\boldsymbol{X}_A, \quad \boldsymbol{x}^h = \sum_{A=1}^{n_n} R_A\boldsymbol{x}_A, \quad \delta\boldsymbol{x}^h = \sum_{A=1}^{n_n} R_A\delta\boldsymbol{x}_A, \\ &\delta\boldsymbol{w}^h = \sum_{A=1}^{n_n} R_A\delta\boldsymbol{w}_A, \quad \Delta\boldsymbol{x}^h = \sum_{A=1}^{n_n} R_A\Delta\boldsymbol{x}_A \text{ and } \Delta\boldsymbol{w}^h = \sum_{A=1}^{n_n} R_A\Delta\boldsymbol{w}_A, \end{aligned} \quad (38)$$

where n_n is the number of nodes associated with the element, R_A is the standard Lagrangian basis function accompanying node A, whereas $\boldsymbol{X}_A$, $\boldsymbol{x}_A$, $\delta\boldsymbol{x}_A$, $\delta\boldsymbol{w}_A$, $\Delta\boldsymbol{x}_A$ and $\Delta\boldsymbol{w}_A$ are the corresponding reference and current coordinate, virtual and incremental displacement and rotation parameter, respectively.

The Galerkin formulation of Eq. (34) is obtained by restricting the trial and test function sets to their finite dimensional counterpart comprised of Lagrange suitable basis functions as: Find $\boldsymbol{\varphi}^h = (\boldsymbol{x}^h, \boldsymbol{\Lambda}^h) \in \mathcal{S}^h$, such that $\forall \delta\boldsymbol{\varphi}^h = (\delta\boldsymbol{x}^h, \delta\boldsymbol{w}^h) \in \mathcal{V}^h$:

$$\int_L \{[\delta(\boldsymbol{x}^h)' + (\boldsymbol{x}^h)' \times \delta\boldsymbol{w}^h] \cdot \boldsymbol{n}^h + \delta(\boldsymbol{w}^h)' \cdot \boldsymbol{m}^h\} d\ell = \int_L \{\delta\boldsymbol{x}^h \cdot \bar{\boldsymbol{n}} + \delta\boldsymbol{w}^h \cdot \bar{\boldsymbol{m}}\} d\ell, \tag{39}$$

where $\boldsymbol{n}^h$ and $\boldsymbol{m}^h$, are the current spatial stress resultants and couples derived from the discretized solution $\boldsymbol{\varphi}^h = (\boldsymbol{x}^h, \boldsymbol{\Lambda}^h)$. The matrix counterpart of the discrete form of the variational equations may be written on compact form as:

$$\sum_{A=1}^{n_n} \delta\mathbf{d}_A (\mathbf{F}_A^{\text{int}} - \mathbf{F}_A^{\text{ext}}) = \mathbf{0}, \tag{40}$$

where $\mathbf{d}_A = [\boldsymbol{x}_A, \boldsymbol{w}_A]^T$ denotes the vectors of nodal displacement and rotation unknowns, and $\mathbf{F}_A^{\text{int}}$ and $\mathbf{F}_A^{\text{ext}}$ the vectors of internal and external nodal forces related to node A, respectively:

$$\mathbf{F}_A^{\text{int}} = \int_L \mathbf{B}_A^T \mathbf{r} d\ell \quad \text{with} \quad \mathbf{B}_A = \begin{bmatrix} R_A' \mathbf{I}_3 & \mathbf{0} \\ R_A \widetilde{\boldsymbol{x}}' & R_A' \mathbf{I}_3 \end{bmatrix} \quad \text{and} \quad \mathbf{r} = \begin{Bmatrix} \boldsymbol{n}^h \\ \boldsymbol{m}^h \end{Bmatrix}, \tag{41}$$

and

$$\mathbf{F}_A^{\text{ext}} = \int_L R_A \mathbf{I}_6 \bar{\mathbf{r}} d\ell \quad \text{with} \quad \bar{\mathbf{r}} = \begin{Bmatrix} \bar{\boldsymbol{n}} \\ \bar{\boldsymbol{m}} \end{Bmatrix}, \tag{42}$$

where $\mathbf{I}_k = \lceil 1, 1, \ldots, 1 \rfloor$ is a diagonal unit matrix of dimension k, and $\widetilde{\boldsymbol{x}}'$ is a skew-symmetric matrix whose axial vector is $\boldsymbol{x}'$.

Similarly, the incremental solution, $\Delta\boldsymbol{\varphi}^h = (\Delta\boldsymbol{x}^h, \Delta\boldsymbol{w}^h) \in \mathcal{V}^h$, of the Galerkin formulation associated with the linearized form of Eqs. (36) and (37) is found from its associated discrete approximation that on matrix form can be written:

$$\sum_{A=1}^{n_n} \sum_{B=1}^{n_n} \delta\mathbf{d}_A \{(\mathbf{F}_A^{\text{int}} - \mathbf{F}_A^{\text{ext}}) + (\mathbf{K}_{AB}^{\text{m}} - \mathbf{K}_{AB}^{\text{g}}) \Delta\mathbf{d}_B\} = \mathbf{0}. \tag{43}$$

The material and geometric stiffness matrices, $\mathbf{K}_{AB}^{\text{m}}$ and $\mathbf{K}_{AB}^{\text{g}}$, are obtained by substituting the discrete approximation counterparts of the virtual and incremental displacements from Eq.(38) into Eqs. (36) and (37):

$$\mathbf{K}_{AB}^{\text{m}} = \int_L \mathbf{B}_A^T \mathbf{C} \mathbf{B}_B d\ell \quad \text{with} \quad \mathbf{C} = \begin{bmatrix} \boldsymbol{C}_N & \mathbf{0} \\ \mathbf{0} & \boldsymbol{C}_M \end{bmatrix}, \tag{44}$$

and with some manipulations (see, e.g., Simo and Vu-Quoc [28, 29])

$$\mathbf{K}^{\mathrm{g}}_{AB} = \int_L \mathbf{G}_A^T \mathbf{H} \mathbf{G}_B d\ell \quad \text{with} \quad \mathbf{G}_A = \begin{bmatrix} R'_A \mathbf{I}_3 & \mathbf{0} \\ \mathbf{0} & R'_A \mathbf{I}_3 \\ \mathbf{0} & R_A \mathbf{I}_3 \end{bmatrix}$$
$$\text{and} \quad \mathbf{H} = \begin{bmatrix} \mathbf{0} & \mathbf{0} & -\widetilde{\boldsymbol{n}}^h \\ \mathbf{0} & \mathbf{0} & -\widetilde{\boldsymbol{m}}^h \\ \widetilde{\boldsymbol{n}}^h & \mathbf{0} & (\boldsymbol{n}^h \otimes \boldsymbol{x}' - \boldsymbol{x}' \boldsymbol{n}^h \mathbf{I}_3) \end{bmatrix}. \tag{45}$$

We recall again that in the expression for $\mathbf{H}$, $\widetilde{\boldsymbol{n}}^h$ and $\widetilde{\boldsymbol{m}}^h$ are the skew-symmetric matrices whose axial vectors are $\boldsymbol{n}^h$ and $\boldsymbol{m}^h$, respectively.

It is noted that the final form of the tangent stiffness $\mathbf{K}^{\mathrm{t}} = \mathbf{K}^{\mathrm{m}} + \mathbf{K}^{\mathrm{g}}$, in general, is nonsymmetric. Since symmetry of the material part follows from the symmetry of the constitutive matrix $\mathbf{C}$, the lack of symmetry stems from the geometric part. As pointed out by Simo and Vu-Quoc [28, 29], for conservative loading at an equilibrium state the tangent stiffness is symmetric. However, in general, at non-equilibrated configurations, the tangent stiffness is nonsymmetric. The reason for that is that the configuration space, $\mathcal{T}_\varphi \mathcal{C}$, is a manifold. Our numerical studies has revealed that replacing the nonsymmetric geometric stiffness by its symmetric counterpart will not jeopardize the quadratic convergence rate expected in the Newton iterations.

Parameterizing the finite rotations with the incremental rotation vector, $\boldsymbol{\theta}$ (see Section 2.2), rather than the spatial spin tensor, $\boldsymbol{w}$, yields similar expressions for the tangent stiffness matrices and the out of balance force vector, and may be found in Ibrahimbegović *et al.* [17].

3 LOCKING EFFECTS IN BEAMS

It is well-known that purely displacement-based isoparametric, especially low-order, elements are often affected by spurious strains and stresses which lead to an overestimation of the stiffness. As a consequence, the primary variables like displacements will be underestimated. In the context of curved beam elements, this implies that both spurious transverse shear and axial (membrane) strains may develop in bending dominated problems, consequently the element will have no ability to capture the state of (transverse) shear-free or inextensional bending. The corresponding locking phenomena denoted transverse shear and membrane locking, in general reduces the accuracy and slows down the convergence as the ratio between thickness to length (for straight members) or thickness to radius of curvature (for curved beams) approaches zero. From the definition of the translational spatial strains (23) for the GE elements we observe that $\boldsymbol{\gamma}^h$ is obtained by subtracting the normal to the cross section $\boldsymbol{i}_1^h$ from the arc-length derivative of the discrete line of centroids $\mathcal{B}^h$ in the current configuration. In the following, we investigate whether $\boldsymbol{\gamma}^h$, i.e., the axial and the transverse shear strains vanish when the element is subjected to a state of pure bending. Without loss of generality we consider an initially

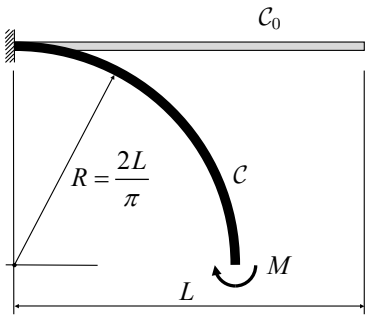

Figure 2: Initial and deformed configuration of a cantilever subjected to a concentrated end moment.

2D straight beam of length L with a rectangular cross section ($A = bh$, with $b = 1$ and $h = 10^{-\rho}$) clamped at one end and subjected to a concentrated moment M at the free end (see Fig. 2). We assume that $L = 1$, $\rho = 3$, $E = 24 \times 10^9$ and $M = \pi EI/2L = \pi$, for which the closed form solution is represented by a quarter of a circle. Fig. 3 shows the resulting distribution of axial and transverse shear strains obtained when the cantilever is discretized with a single GE element of order $p = 1, 2, 3$ and 4, respectively. We observe that all elements sample the exact solution ($\boldsymbol{\gamma} = \mathbf{0}$) at the Gauss points ($n_g = p$) corresponding to uniform reduced integration (URI). We also observe that the amplitudes of the spurious membrane and shear strains reduces dramatically as the order of the interpolant is increased. The ability of the curved Lagrange C^0 isoparametric beam elements to alleviate spurious transverse shear and axial strains with URI was first explored and reported by Stolarski and Belytschko [30] for quadratic and cubic interpolated elements.

In order to evaluate an elements propensity of locking, Hughes [13] introduced an heuristic approach, the so-called *constraint count* method. This method relies on the constraint ratio, r, which is defined as the ratio of the total number of equilibrium equations (n_{eq}) to the total number of constraint equations (n_c):

$$r = \frac{n_{eq}}{n_c}. \tag{46}$$

In order to investigate whether an element is prone to locking, the constraint ratio, r, of the continuous problem is compared with the constraint ratio, r^h, of the discretized problem in the limit of infinite number of elements, $n_e \to \infty$:

$$r^h = \lim_{n_e \to \infty} \frac{n_u^e}{n_c^e}. \tag{47}$$

Here n_u^e denotes the number of unknowns added to the system by adding one more element to a uniform mesh of an infinite number of elements, while n_c^e is the corresponding number of constraints added by this element. Thus, n_c^e is related to the number of quadrature points, n_g, where the constraints are to be evaluated.

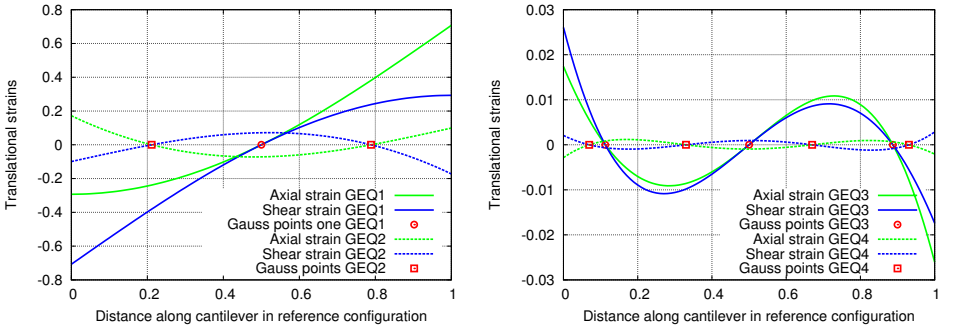

a) b)

Figure 3: Discrete translational strain fields obtained when the cantilever beam subjected to a concentrated end moment is discretized with one single GE element of order $p = 1, 2, 3$ and 4, respectively: a) Solutions for $p = 1$ and 2, denoted GEQ1 and GEQ2, respectively, and b) solutions for $p = 3$ and 4, denoted GEQ3 and GEQ4, respectively.

For an element with $r^h < r$, and especially with $r^h < 1$ (which implies that there are more constraints added than unknowns), the propensity of locking is high. In contrast when $r^h > r$, this indicate that there are too few constraints to approximate the constraint accurately. Consequently, the optimal element satisfy the criterion $r^h = r$.

As pointed out in [30], when investigating the locking behavior of curved C^0 beams for higher-order elements there exists an interrelationship between transverse shear and membrane locking. Thus, transverse shear and membrane locking must be considered simultaneously. Again, for simplicity, we consider a 2D GE element, for which we have three unknowns per node and two constraints per Gauss point. The optimal constraint ratio for the 2D continuous problem is

$$r_{\text{2D}} = \frac{3}{2}. \tag{48}$$

For the discrete problem the discrete constraint ratio reads:

$$r^h_{\text{2D}} = \frac{3p}{2n_g}. \tag{49}$$

Thus, applying URI with $n_g = p$ yields an optimal constraint ratio for the GE elements. Applying URI to the GE elements implies that the rank of the global tangent stiffness is equal to the total number of unknowns, and thus guarantee rank-sufficiency and elements without any zero-energy modes which need to be stabilized.

Even though URI works well independent of the slenderness ratio for elements of polynomial order two and higher, it is well known that the numerical solution gets progressively stiffer for lower order Timoshenko beam (TB) elements compared to the exact one as the

slenderness increases. In order to get an element that is free of locking MacNeal [18, 19] proposed the *residual bending flexibility* (RBF) approach, a device in which the transverse shear stiffness is enhanced by using a substitute reduced shear modulus such that the element reproduces nodally exact solutions independent of the slenderness ratio for a tip loaded straight cantilever beam in the linear regime. In [21], Prathap has shown why the RBF correction yields a correct rate of convergence for linearly interpolated TB elements.

4 NUMERICAL RESULTS

The purpose of the numerical tests is to study the accuracy, performance, robustness and convergence of the GE elements and compare them with 2-noded Euler-Bernoulli (EB) and TB elements based on the CR formulation for the various elements presented in Tab. 1.

All CR elements are based on the formulation proposed by Battini and Pacoste [3, 4]. The EB elements use linear interpolation of the axial displacement and axial rotation about the local beam axis while bending deformations are based on Hermitian cubic shape functions. While the CEBL element is based on classical linear beam theory with only linear terms in the strain expressions, the CEBN element is based on a second order approximation of the Green-Lagrange strains enhanced with a shallow arch definition of the local axial strains to avoid membrane locking. The CEBLS and CEBNS elements are the corresponding EB elements based on the modified Hermitian shape functions accounting for transverse shear deformations. The CR TB elements CTBN and CTBNr are using standard linear interpolation of local displacements and rotations. Except for

Formulation	**Beam theory**	n_n	p	**Strain measure**	**Transverse shear**	**Element name**
Corotational	Euler-Bernoulli	2	1/3	Engineering	No	CEBL
					Yes	CEBLS
				Green-Lagrange	No	CEBN
					Yes	CEBNS
	Timoshenko	2	1	Engineering[1]	Yes	CTBN
						CTBNr[2]
Geometrically exact	Reissner (Timoshenko)	2	1	Biot (Jaumann)	Yes	GEQ1
						GEQ1r[2]
		3	2			GEQ2
		4	3			GEQ3
		5	4			GEQ4
		9	8			GEQ8

Table 1: Various element types compared. [1]Element account for the nonlinear Wagner term in the strain expression. [2]Element has been enhanced with RBF.

the nonlinear Wagner term [31], the strain expression is purely linear for both elements. They utilizes URI to avoid locking and the CTBNr element is further enhanced with RBF to converge to the EB element solution as the slenderness increases.

For each of the various formulations and discretizations considered, the relative error in tip displacement e_u and tip rotation e_θ are chosen as measures of accuracy

$$e_u = \frac{|u^{ref} - u^h|}{|u^{ref}|} \quad \text{and} \quad e_\theta = \frac{|\theta^{ref} - \theta^h|}{|\theta^{ref}|}. \tag{50}$$

The relative error is computed from Eq. (50), where u^{ref} and θ^{ref} are reference solutions obtained with a very fine mesh of eight order GE beam elements.

Since the EB beam elements based on the modified Hermitian shape functions accounting for transverse shear deformations converge to the standard Hermitian interpolated element as the slenderness increases, the comparison between the various TB element formulations are made with the corresponding EB elements accounting for transverse shear deformations. The results obtained for both the linear and the nonlinear EB beam elements accounting for transverse shear almost coincide with those based on the Navier hypothesis for all example problems studied in this paper.

While a few more Newton iterations are needed in the initial than in the final steps for most problems studied, quadratic convergence is obtained in approximately 5 iterations for each step for all discretizations and formulations with a rather tight energy convergence criterion $\varepsilon_E = 10^{-9}$. This also demonstrate that the linearization of the various formulations are consistent. It should also be mentioned that the accuracy and convergence (in the Newton iterations) is independent of the parameterization of the finite rotations.

4.1 Cantilever beam subjected to tip loading

The first example, depicted in Fig. 4, is a straight cantilever beam clamped at one end and subjected to two conservative point loads initially acting in the direction of the local cross-sectional axes at the free end. This example is selected to assess the accuracy and robustness of the various beam formulations under combined bending, shear and torsion when the initial configuration is a straight line. The slenderness ratio for this problem is $\rho_y = L/b = 20$ and $\rho_z = L/h = 40$ for bending in the $xy-$ and $xz-$plane, respectively. The two tip loads are applied over 10 equally sized load increments for all discretizations of the various beam formulations.

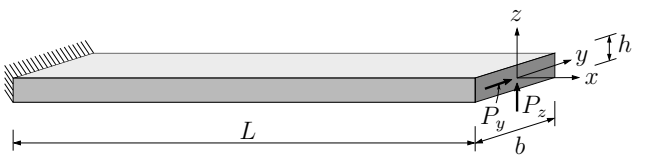

$E = 2.1 \times 10^{11}$
$\nu = 0.3$
$L = 10$
$b = 0.5$
$h = 0.25$
$P_y = 2 \times 10^7$
$P_z = 1 \times 10^7$

Figure 4: Tip loaded cantilever beam: Geometry, loading, boundary conditions and material data.

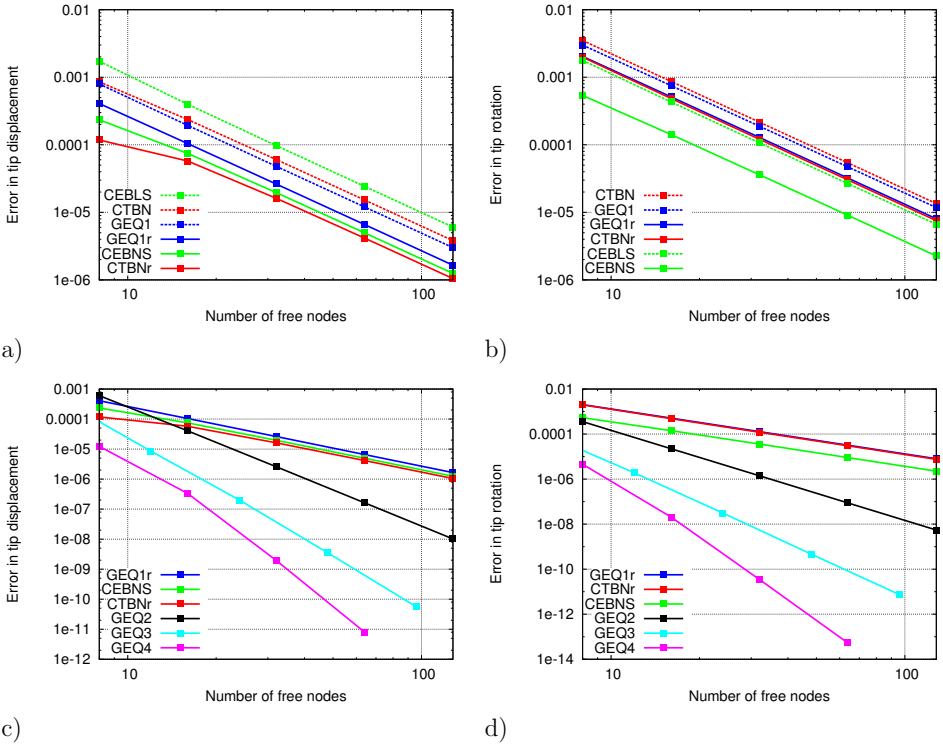

Figure 5: Tip loaded cantilever beam: Relative error in tip displacement and rotation for the various formulations for medium to fine meshes (8–128 free nodes): a) Displacement and b) rotation for all CR- and linear GE-elements, c) displacement and d) rotation for the best CR- and GE-elements of order $p = 1, 2, 3$ and 4.

Fig. 5 shows convergence plots for medium to fine meshes with 8 to 128 free nodes. Firstly, in Figs. 5a and 5b we compare the various EB and linearly interpolated TB elements. It is seen that by adding RBF the error is reduced by a factor of 2 for both the CR and the GE TB elements. We also observe from these figures that for all discretizations with TB elements the accuracy obtained with the CR and the GE formulations are close for the tip displacement and almost coincide for the tip rotation. When comparing the EB and the linearly interpolated TB elements, while the error in tip rotation is almost one order lower for the nonlinear EB element, the accuracy of the tip displacement is of the same order as the linearly interpolated TB elements. We also observe that both the error in tip displacement and rotation is reduced one order when comparing the linear and nonlinear EB elements. Finally, independent of formulation, the convergence order

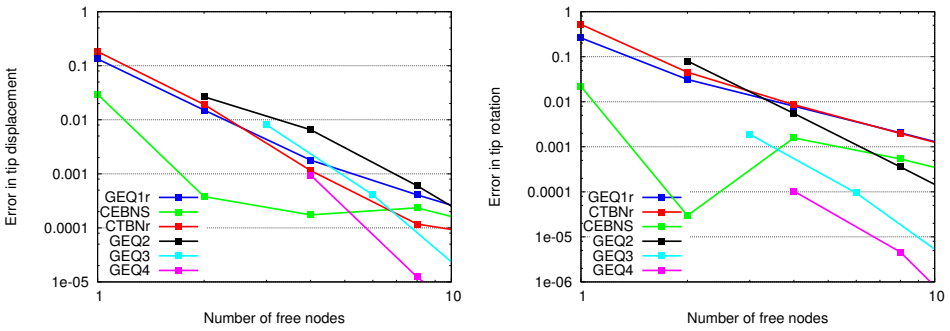

a) b)

Figure 6: Tip loaded cantilever beam: Relative error in tip displacement and rotation for the various formulations for coarse meshes (1–8 free nodes): a) Displacement and b) rotation for the best CR- and GE-elements of order $p = 1, 2, 3$ and 4.

of all 2-noded elements coincide. Next, in Figs. 5c and 5d we compare the best 2-noded elements, i.e. the nonlinear EB and the linearly interpolated TB elements with RBF, with the GE elements of order $p = 2, 3$ and 4. First, we observe as expected that the rate of convergence increases monotonically with polynomial order for both the tip displacement and rotation. We also observe that there is a shift in accuracy of approximately one order when polynomial order is increased.

Fig. 6 shows convergence plots for coarse meshes with 1 to 8 free nodes. We observe that the nonlinear EB element is superior to all other elements for very coarse meshes with 2 to 4 free nodes. However, as the mesh is refined the accuracy of the GE elements of order $p = 2, 3, 4$ is superior to all 2-noded elements.

4.2 Three leg right angle tip loaded space beam

The second example, depicted in Fig. 7, consists of three straight beams, connected at right angles in the reference configuration, such that the beam axis of the three legs are parallel to the $x-$, $y-$ and $z-$axis, respectively. The structure is clamped at one end and subjected to two conservative point loads $P_x = P_z = P$, initially acting in the direction of the negative $x-$ and $z-$axes at the free end. This example was proposed in [25] and has later been revisited in [10], and serves to benchmark nonlinear beam formulations under combined bending, shear and torsion for non-smooth, three-dimensional geometries. The slenderness ratio for this problem is $\rho_y = \rho_z = 10$. The two tip loads are applied over 20 equally sized load increments for all discretizations of the various beam formulations.

In Fig. 8, the displacement and rotation of the tip is plotted versus the load P when each of the three legs are discretized with a uniform mesh of 8 CTBNr and 1024 GEQ8 elements, respectively. We observe that we are not able to distinguish between the results

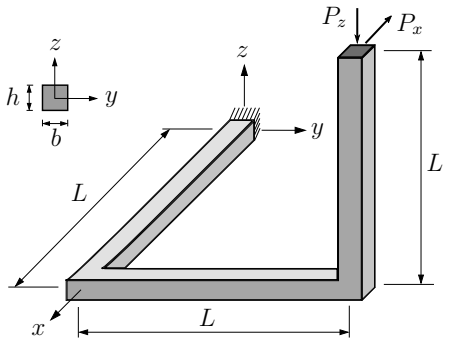

$E = 10^6$
$\nu = 0$
$L = 1$
$b = h = 0.1$
$P_x = P_z = P = 10$

Figure 7: Three leg right angle tip loaded space beam: Geometry, loading, boundary conditions and material data.

obtained with the coarser mesh with 8 CTBNr elements and the reference mesh with 1024 GEQ8 elements.

Analogous to the first example, a convergence plot is given in Fig. 9 to compare the accuracy of the various formulations for meshes with 2 to 32 free nodes per leg. From Figs. 9a and 9b, we observe that the linearly interpolated TB elements enhanced with RBF outperforms the standard formulation. We also observe that the results obtained with the linear EB element CEBLS is indistinguishable from the CR linearly interpolated TB element with added RBF (CTBNr) for all discretizations for both the tip displacement and tip rotation. From the same figures we also observe that independent of formulation

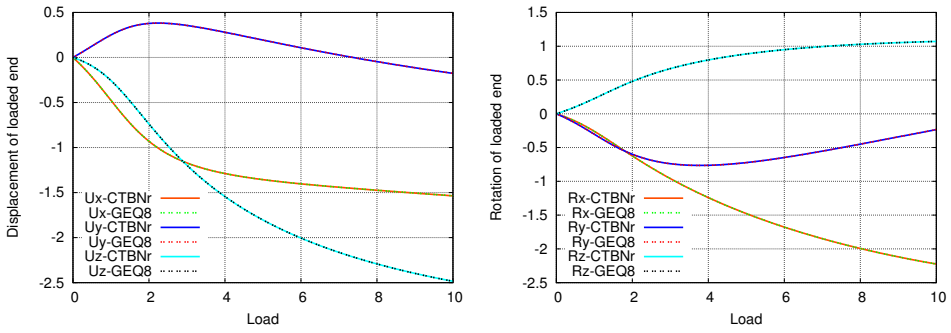

a) b)

Figure 8: Three leg right angle tip loaded space beam: Tip displacement and rotation versus applied load P: a) Displacement and b) rotation for a uniform mesh of 8 CTBNr and 1024 GEQ8 elements per leg, respectively.

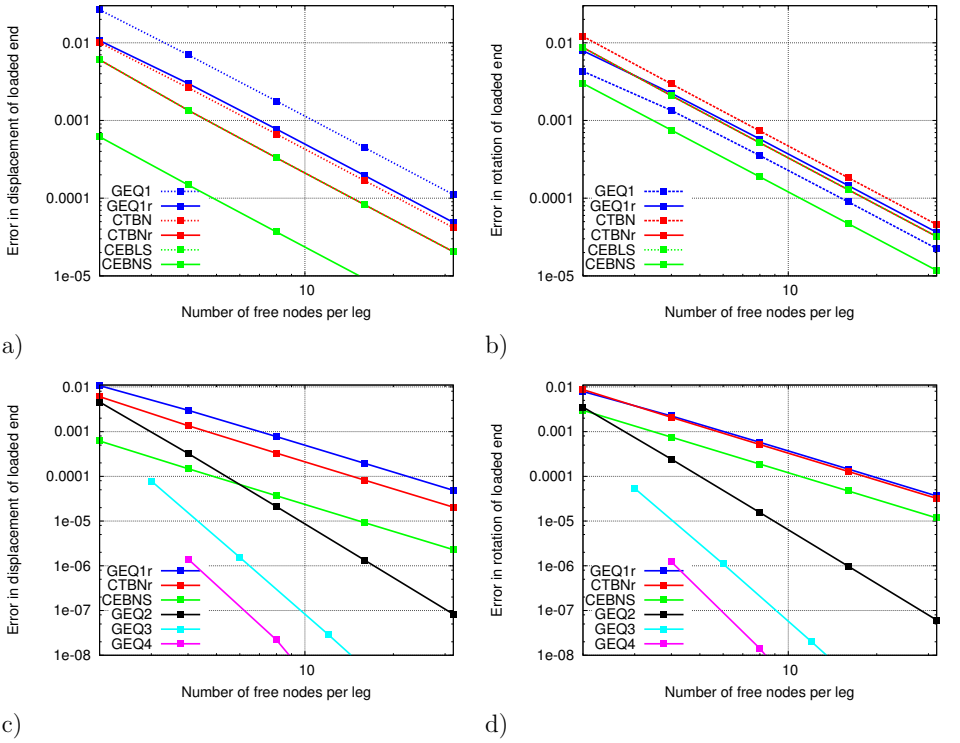

Figure 9: Three leg right angle tip loaded space beam: Relative error in tip displacement and rotation for the various formulations for meshes with 2–32 free nodes per leg: a) Displacement and b) rotation for CR- and linear GE-elements, c) displacement and d) rotation for the best CR- and GE-elements of order $p = 1, 2, 3$ and 4.

the tip displacement for the nonlinear EB element CEBNS is one order more accurate compared with the best linearly interpolated TB elements.

When comparing the best 2-noded elements with GE elements of higher order ($p = 2, 3$ and 4), we observe analogous to the previous example that the rate of convergence for all 2-noded elements coincide while for the higher order GE elements it increases with polynomial order. Also for the GE elements the accuracy is shifted approximately one order as the polynomial order is increased. Again, except for very coarse meshes all higher order GE elements outperform all the 2-noded elements both in terms of accuracy and convergence rate.

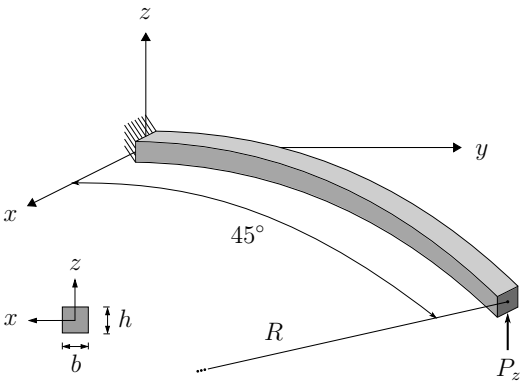

$E = 10^7$
$\nu = 0$
$R = 100$
$b = h = 1$
$P_z = P = 600$

Figure 10: Tip loaded 45° circular cantilever beam: Geometry, loading, boundary conditions and material data.

4.3 Tip loaded 45° circular cantilever beam

In the next example, depicted in Fig. 10, we consider a beam that is curved in its stress-free reference configuration. In particular, 1/8 of a circle with radius R forms the line of centroids that is located in the $xy-$plane in the reference configuration. The curved beam is clamped at one end and subjected to a conservative point load acting in the direction of the $z-$axis in the free end. This problem is a well-established benchmark problem for nonlinear analysis of spatial beams. It was first proposed in [2] and has later been used by a number of authors [5, 6, 7, 9, 10, 15, 25, 28].

Step	Iter	CEBNS	CTBNr	GEQ1r	GEQ2	GEQ3	GEQ4
1	0	4.695×10^{2}	4.695×10^{2}	4.695×10^{2}	4.698×10^{2}	4.698×10^{2}	4.698×10^{2}
	1	8.246×10^{4}	8.239×10^{4}	8.246×10^{4}	8.378×10^{4}	8.379×10^{4}	8.379×10^{4}
	2	1.048×10^{0}	3.918×10^{-1}	2.028×10^{2}	3.188×10^{-1}	3.182×10^{-1}	3.182×10^{-1}
	3	1.131×10^{-3}	9.872×10^{-4}	5.292×10^{-1}	9.649×10^{-4}	9.644×10^{-4}	9.645×10^{-4}
	4	1.441×10^{-8}	1.173×10^{-11}	6.471×10^{-2}	1.646×10^{-7}	1.642×10^{-7}	1.643×10^{-7}
	5	8.382×10^{-17}	3.646×10^{-22}	3.492×10^{-5}	1.192×10^{-14}	1.187×10^{-14}	1.189×10^{-14}
	6			4.949×10^{-10}			
	7			3.572×10^{-21}			
12	0	7.585×10^{1}	7.599×10^{1}	7.597×10^{1}	7.585×10^{1}	7.586×10^{1}	7.586×10^{1}
	1	2.932×10^{2}	2.946×10^{2}	2.946×10^{2}	2.983×10^{2}	2.983×10^{2}	2.983×10^{2}
	2	1.693×10^{-1}	1.695×10^{-1}	1.700×10^{-1}	1.710×10^{-1}	1.710×10^{-1}	1.710×10^{-1}
	3	1.840×10^{-3}	1.847×10^{-3}	1.853×10^{-3}	1.886×10^{-3}	1.886×10^{-3}	1.886×10^{-3}
	4	3.729×10^{-11}	3.343×10^{-11}	2.459×10^{-11}	2.554×10^{-11}	2.554×10^{-11}	2.554×10^{-11}
	5	1.818×10^{-22}	2.053×10^{-22}	5.954×10^{-22}	4.082×10^{-22}	6.091×10^{-22}	8.916×10^{-22}

Table 2: Tip loaded 45° circular cantilever beam: Convergence rates, in the Newton iterations, for the first and final step.

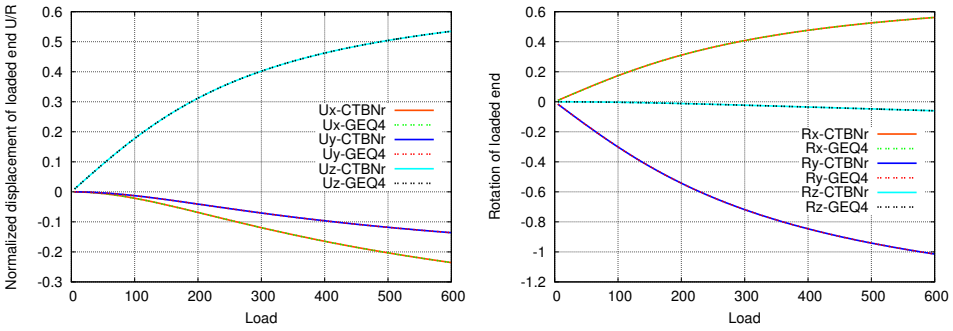

a) b)

Figure 11: Tip loaded 45° circular cantilever beam: Tip displacement and rotation versus applied load P: a) Displacement and b) rotation for a uniform mesh of 8 CTBNr and 1024 GEQ8 elements, respectively.

The tip load is applied over 12 equally sized load increments for all discretizations of the various beam formulations. Tab. 2 shows the convergence rates in terms of energy for the first and last step for the various elements. As shown in Tab. 2, except for the linear interpolated GE element that needs 7 iterations in the initial step, quadratic convergence in the Newton iterations is obtained in 5 iterations for each step for all discretizations and formulations with a rather tight convergence criterion in energy of $\varepsilon_E = 10^{-8}$. All formulations converge to the following displacement and rotation of the loaded end, $u = 59.9984$ and $\theta = 1.16093$. In order to keep the number of unknowns equal for all elements, a uniform mesh of twelve 2-noded elements, six quadratic, four cubic and three quartic elements is used.

In Fig. 11, the normalized displacement and rotation of the tip is plotted versus the load P when the beam is discretized with a uniform mesh of 8 CTBNr and 1024 GEQ4 elements, respectively. As in the previous example, we observe that we are not able to distinguish between the results obtained with the coarser mesh with 8 CTBNr elements and the reference mesh with 1024 GEQ4 elements.

Fig. 12 shows convergence plots for meshes with 2 to 16 free nodes. From Figs. 12b, we observe that independent of formulation the tip rotation for the nonlinear EB element CEBNS is almost one order more accurate compared with the best linearly interpolated TB elements. However, in contrast, from Figs. 12a, we observe that the tip displacement of the CEBNS is less accurate compared with the best linearly interpolated TB elements.

When comparing the best 2-noded elements with GE elements of higher order ($p = 2, 3$ and 4), we observe analogous to the previous example that the rate of convergence for all 2-noded elements coincide while for the higher order GE elements it increases with polynomial order. Also for the GE elements the accuracy is shifted approximately one

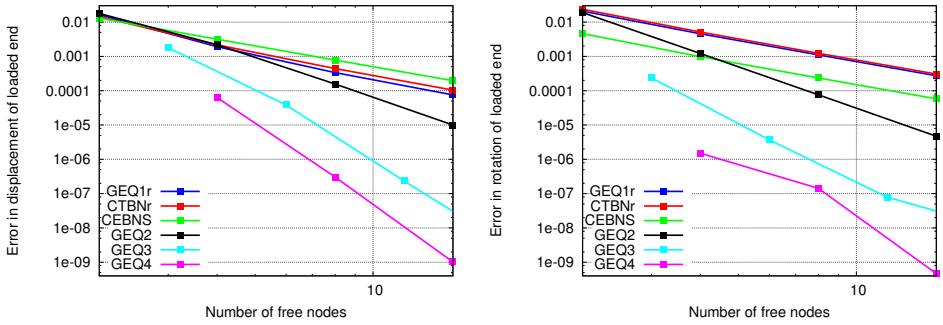

a) b)

Figure 12: Tip loaded 45° circular cantilever beam: Relative error in tip displacement and rotation for the various formulations for meshes with 2–16 free nodes: a) Displacement and b) rotation for the best CR- and GE-elements of order $p = 1, 2, 3$ and 4.

order as the polynomial order is increased. Again, except for the coarsest mesh with 2 free nodes all higher order GE elements outperform all the 2-noded elements both in terms of accuracy and convergence rate. In order to get equal accuracy in tip displacement we need two cubic (36 DOFs), five quadratic (60 DOFS) and 15 linear (90 DOFS) GE elements, 20 TB (120 DOFS) and as much as 30 EB (180 DOFS) CR elements to match the accuracy obtained with one single quartic GE element (24 DOFS). Similarly, as much as three cubic, 11 quadratic, 200 linear GE elements, 200 TB and 100 EB CR elements, is needed to obtain similar accuracy in tip displacement as one quartic GE element. Thus, the accuracy obtained for each DOF invested is much higher for the higher order GE elements compared to all 2-noded elements.

4.4 Tip loaded 90° circular arch

Fig. 13 shows geometry, boundary conditions, loading and material properties for a planar 90° circular arch subjected to a tip shear load P. This problem has also been studied by several other researchers, e.g. Bauer *et al.* [5], however they studied the problem in the linear regime for which there exist a closed form solution, as shown in [5].

Even though the slenderness for this problem, defined as: $R/h = 1000$, is high, the comparison between the various TB element formulations are made with the corresponding EB elements accounting for transverse shear deformations. The tip load is applied over 10 equally sized load increments for all discretizations of the various beam formulations. All formulations converge to the following displacement and rotation of the loaded end, $u = 0.90777806$ and $\theta = 0.99420425$. In Fig. 13, the red curve depicts the final converged configuration.

Fig. 14 shows convergence plots for meshes with 6 to 96 free nodes. When comparing

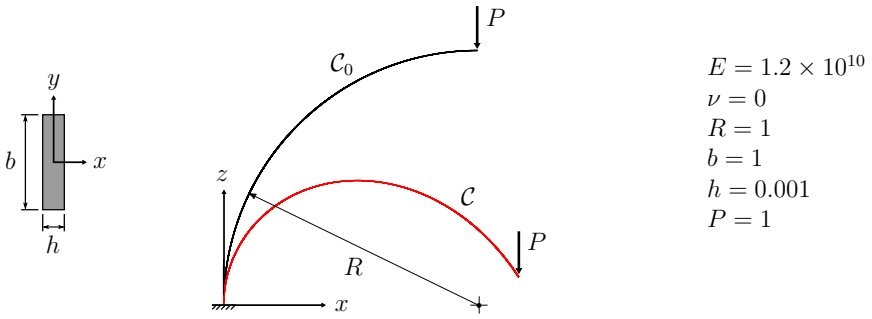

Figure 13: Tip loaded 90° circular cantilever beam: Geometry, loading, boundary conditions and material data.

the best 2-noded elements with GE elements of higher order ($p = 2, 3$ and 4), we observe analogous to the previous example that the rate of convergence for all 2-noded elements coincide while except for the cubic element that exhibit the same convergence as the quadratic element for the higher order GE elements it increases with polynomial order. Furthermore the accuracy is shifted approximately half an order as the number of nodes per element is increased. We also observe that the accuracy and the convergence rate of all discretizations of the CR and the GE 2-noded TB elements, as well as the corotated EB beam with engineering strain are indistinguishable, while the corotated EB beam with Green-Lagrange strain is more accurate both for the tip displacement and the tip rotation. As pointed out in Section 3, both the 2-noded linearly interpolated TB elements based on the GE and the CR formulation denoted GEQ1r and CTBNr have been enhanced with

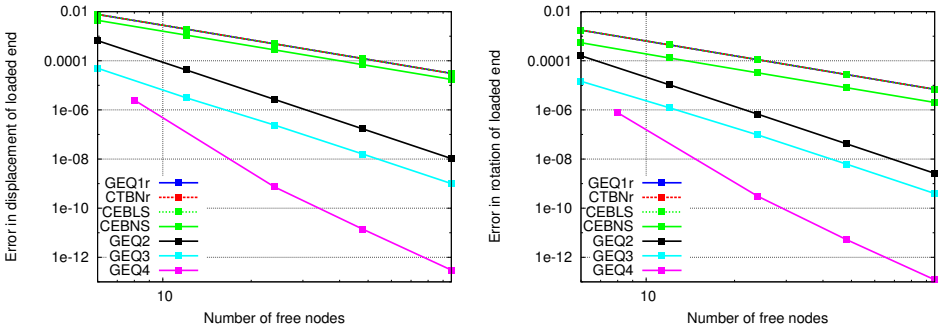

a) b)

Figure 14: Tip loaded 90° circular cantilever beam: Relative error in tip displacement and rotation for the various formulations for meshes with 6–96 free nodes: a) Displacement and b) rotation for the best CR- and GE-elements of order $p = 1, 2, 3$ and 4.

RBF to overcome transverse shear locking as the slenderness increases. The results shown in Fig. 14 demonstrate that the RBF enhancement works very well also in the nonlinear regime for curved geometries in the case of a tip loaded cantilever beam.

5 SUMMARY AND CONCLUDING REMARKS

In this study, we have extended the geometrically exact (GE) beam formulation to an arbitrary order interpolation and compared it with 2-noded Euler-Bernoulli (EB) and Timoshenko beam (TB) elements based on the corotational (CR) formulation, two of the most popular approaches for discretizing nonlinear beams within the context of nonlinear finite element analysis with large displacements and large rotations but small to moderate strains. While these two families of methods have evolved during the last decades and each of them exist with several different enhancements, we have extended the original implementation of the GE formulation as presented in Simo [27] and Simo and Vu-Quoc [28, 29], and the CR formulation proposed by Battini and Pacoste [3, 4]. Both formulations may be extended to non-linear material models (inelastic or plastic), interfacing with other types of structural elements and extended to nonlinear dynamic analysis.

The higher order GE beam elements are the formulation of choice when performance and accuracy are crucial. Despite their complexity, both theoretical and numerical, our study reveals that for the same CPU cost, the elements provide significantly more accurate results than any of the 2-noded CR elements. It turns out that the CPU cost involved in the computation of the higher order GE elements is not significantly higher due to increased number of integration points and DOFS per element. As shown in Helgedagsrud *et al.* [12], the per-degree-of-freedom accuracy of GE beam elements may be even further improved by replacing the Lagrangian FE functions with isogeometric analysis (IGA) based on non-uniform rational B-splines (NURBS) [8, 14, 22].

In spite that we have used a symmetrized tangent stiffness for all GE elements and nonsymmetric tangent stiffness for all CR elements, they all exhibit a quadratic rate of convergence in the Newton iterations. Our numerical study also demonstrates that the accuracy, the number of Newton iterations, and the computational cost is independent of the parameterization of the finite rotations for both formulations.

Another observation is that it is highly recommended to enhance the linearly interpolated 2-noded TB elements with residual bending flexibility whether it is based on the GE or the CR formulation. Furthermore, we cannot claim the superiority of one approach over the other when we restrict our study to 2-noded TB elements. However, among the 2-noded elements, the nonlinear 2-noded cubic interpolated EB element based on the CR approach enhanced with the shallow arch terms exhibit superior accuracy. Modifying the Hermitian shape functions to account for transverse shear deformations, this element allows for a significant reduction of elements used to discretize the structure compared to all other 2-noded elements studied.

6 ACKNOWLEDGEMENT

The first author would like to also acknowledge the support and helpful comments from Professor in Structural Mechanics Jean-Marc Battini at Department of Civil and Architectural Engineering at the Royal Institute of Technology (KTH) in Stockholm, Sweden.

REFERENCES

[1] Auricchio, F., Carotenuto, P. and Reali, A. On the geometrically exact beam model: A consistent, effective and simple derivation from three-dimensional finite-elasticity. *Int. J. Solids. Struct.* (2008) **45**:4766–4781.

[2] Bathe, K.J. and Belourchi, S. Large displacement analysis of three-dimensional beam structures. *Int. J. Numer. Meth. Engrg.* (1979) **14**:961–986.

[3] Battini, J.-M. and Pacoste, C. Co-rotational beam elements with warping effects in instability problems. *Comput. Meth. Appl. Mech. Engrg.* (2002) **191**:1755–1789.

[4] Battini, J.-M. and Pacoste, C. Plastic instability of beam structures using co-rotational elements. *Comput. Meth. Appl. Mech. Engrg.* (2002) **191**:5811–5831.

[5] Bauer, A.M., Breitenberger, M., Philipp, B., Wüchner, R. and Bletzinger, K.-U. Nonlinear isogeometric spatial Bernoulli beam. *Comput. Meth. Appl. Mech. Engrg.* (2016) **303**:101–127.

[6] Betsch, P. and Steinmann, P. Frame-indifferent beam finite elements based upon the geometrically exact beam theory. *Comput. Meth. Appl. Mech. Engrg.* (2002) **54**:1775–1788.

[7] Cardona, A. and Géradin, M. A beam finite element non-linear theory with finite rotations. *Int. J. Numer. Meth. Engrg.* (1988) **26**:2403–2438.

[8] Cottrell, J.A., Hughes, T.J..R. and Bazilevs Y. *Isogeometric Analysis: Toward Integration of CAD and FEA*. John Wiley & Sons, Chichester, England, (2009).

[9] Crisfield, M. A consistent corotational formulation for non-linear, three-dimensional beam elements. *Comput. Meth. Appl. Mech. Engrg.* (1990) **81**:131–150.

[10] Eugster, S.R., Hesch, C., Betsch, P. and Glocker, Ch. Director-based beam finite elements relying on the geometrically exact beam theory formulated in skew coordinates. *Int. J. Numer. Meth. Engrg.* (2014) **97**:111–129.

[11] Felippa, C.A. and Haugen, B. A unified formulation of small-strain corotational finite elements: I. Theory *Comput. Meth. Appl. Mech. Engrg.* (2005) **194**:2285–2335.

[12] Helgedagsrud, T.A., Raknes, S.B. and Mathisen, K.M. On locking-free methods for isogeometric large deformation analysis of geometrically exact three-dimensional beams. *Proc. 8. Nat. Conf. Comput. Mech. (MekIT'15)*, Skallerud, B., and Andersson, H.I. (Eds.), CIMNE, Barcelona, Spain (2015) pp. 167–201.

[13] Hughes, T.J.R. *The Finite Element Method*. Prentice–Hall, Englewood Cliffs, NJ, USA, (1987).

[14] Hughes, T.J.R., Cottrell, J.A. and Bazilevs, Y. Isogeometric Analysis: CAD, Finite Elements, NURBS, Exact Geometry and Mesh Refinement. *Comput. Meth. Appl. Mech. Engrg.* (2005) **194**:4135–4195.

[15] Ibrahimbegović, A. and Frey, F. Finite element analysis of linear and nonlinear planar deformations of elastic initially curved elements. *Int. J. Numer. Meth. Engrg.* (1992) **36**:3239–3258.

[16] Ibrahimbegović, A. On finite element implementation of geometrically nonlinear Reissner's beam theory: Three-dimensional curved beam elements. *Comput. Meth. Appl. Mech. Engrg.* (1995) **122**:11–26.

[17] Ibrahimbegović, A., Frey, F. and Kožar, I. Computational aspects of vector-like parameterization of three-dimensional finite rotations. *Int. J. Numer. Meth. Engrg.* (1995) **38**:3653–3673.

[18] MacNeal, R.H. A simple quadrilateral plate element. *Comput. Struct.* (1978) **8**:175–183.

[19] MacNeal, R.H. *Finite Elements: Their Design and Performance*. Marcel Dekker, New York, USA, (1994).

[20] Mathisen, K.M. and Bergan, P.G. Large displacement analysis of submerged multibody systems. *Engrg. Comput.* (1992) **9**:609–634.

[21] Prathap, G. The variationally correct rate of convergence for a two-noded beam element, or why residual bending flexibility corrections is an extravariational trick. *Commun. Numer. Meth. Engrg.* (1995) **11**:403–407.

[22] Raknes, S.B., Deng, X., Bazilevs, Y., Benson, D.J., Mathisen, K.M. and Kvamsdal, T. Isogeometric rotation-free bending-stabilized cables: Statics, dynamics, bending strips and coupling with shells. *Comput. Meth. Appl. Mech. Engrg.* (2013) **263**:127–143.

[23] Reissner, E. On one-dimensional finite-strain beam theory: The plane problem. *J. Appl. Math. Phys.* (1972) **32**:795–804.

[24] Reissner, E. On finite deformations of space curved beams. *J. Appl. Math. Phys.* (1981) **32**:734–744.

[25] Romero, I. A comparison of finite elements for nonlinear beams: The absolute nodal coordinate and geometrically exact formulations. *Multibody System Dynamics* (2008) **20**:51–68.

[26] Saje, M. Finite element formulation of finite planar deformation of curved elastic beams. *Comput. Struct.* (1991) **39**:327–337.

[27] Simo, J.C. A finite strain beam formulation. The three-dimensional dynamic problem. Part I. *Comput. Meth. Appl. Mech. Engrg.* (1985) **49**:55–70.

[28] Simo, J.C. and Vu-Quoc, L. A three-dimensional finite strain rod model. Part II: Computational aspects. *Comput. Meth. Appl. Mech. Engrg.* (1986) **58**:79–116.

[29] Simo, J.C. Vu-Quoc, L. A geometrically-exact rod model incorporating shear and torsion-warping deformation. *Int. J. Solids. Struct.* (1991) **27**:371–393.

[30] Stolarski, H. and Belytschko, T. Shear and membrane locking in curved C^0 elements. *Comput. Meth. Appl. Mech. Engrg.* (1983) **41**:279–296.

[31] Wagner, H. *Verdrehung und Knickung von offenen Profilen (Torsion and buckling of open sections)*. 25th Anniversary Publication, Technische Hochschule, Danzig (2nd ed.), NACA translation, Technical memo No. 807, Washington DC, USA, (1936).

9. National Conference on Computational Mechanics
MekIT'15
B. Skallerud and H I Andersson (Eds)

SHENFUN - AUTOMATING THE SPECTRAL GALERKIN METHOD

M. Mortensen[1]

[1]University of Oslo
Department of Mathematics
Division of Mechanics
e-mail: mikaem@math.uio.no

Key words: Computational Methods, Spectral, Galerkin, Chebyshev, Legendre

Abstract. With the `shenfun` Python module (github.com/spectralDNS/shenfun) an effort is made towards automating the implementation of the spectral Galerkin method for simple tensor product domains, consisting of (currently) one non-periodic and any number of periodic directions. The user interface to `shenfun` is intentionally made very similar to FEniCS (fenicsproject.org). Partial Differential Equations are represented through weak variational forms and solved using efficient direct solvers where available. MPI decomposition is achieved through the `mpi4py-fft` module (bitbucket.org/mpi4py/mpi4py-fft), and all developed solvers may, with no additional effort, be run on supercomputers using thousands of processors. Complete solvers are shown for the linear Poisson and biharmonic problems, as well as the nonlinear and time-dependent Ginzburg-Landau equation.

1 Introduction

The spectral Galerkin method, see, e.g., Shen [12] or Kopriva [5], combines spectral basis functions with the Galerkin method and allows for highly accurate solutions on simple, tensor product domains. Due to its accuracy and efficiency, the method is often favoured in studies of sensitive fundamental physical phenomena, where numerical errors needs to be avoided.

In this paper we will describe the `shenfun` Python module. The purpose of `shenfun` is to simplify the implementation of the spectral Galerkin method, to make it easily accessible to researchers, and to make it easier to solve advanced PDEs on supercomputers, with MPI, in simple tensor product domains. The package can solve equations for tensor product spaces consisting of any number of periodic directions, but, at the moment of writing, only one non-periodic direction. This configuration may sound trivial, but it occurs surprisingly often in physics, for example in plane shear flows like the channel or pipe. And these simple configurations are used heavily to enhance our understanding of

fundamental physical processes, like turbulence, or transition to turbulence, turbulent mixing, and turbulent combustion.

The `shenfun` package is heavily influenced by the FEniCS project [7], that has made it trivial to solve PDEs in arbitrary complex domains with the finite element method (FEM). FEM also makes use of the Galerin method to set up variational forms. However, where FEM uses basis functions with only local support, the spectral Galerkin method uses basis functions with global support. The local support is one of the many nice features of the FEM, which makes it particularly attractive for unstructured and complex geometries. Spectral methods, on the other hand, are less flexible, but represent the gems of numerical methods, and, whenever possible, when the domain is simple and the solution is smooth, delivers the most accurate approximations.

There are many tools available for working with spectral methods. For MATLAB there is the elegant chebfun package [13], with an extensive list of application for, e.g., PDEs, ODEs or eigenvalue problems. However, being implemented in MATLAB, there is no feasible extension to DNS and supercomputers through MPI. Numpy and Scipy have modules for orthogonal polynomials (Jacobi, Chebyshev, Legendre, Hermite), and for Fourier transforms, which are both utilized by `shenfun`. The orthogonal module makes it easier to work with Chebyshev and Legendre polynomials, as it delivers, for example, quadrature points and weights for different quadrature rules (e.g., Chebyshev-Gauss, Legendre-Gauss).

To the author's knowledge, all research codes developed for studying turbulent flows through Direct Numerical Simulations (DNS) on supercomputers have been written in low-level languages like Fortran, C or C++, see, e.g., [2, 4, 6], or [1] for a list of high performance channel flow solvers. The codes are highly tuned and tailored to a specific target, and, being low-level, the codes are not easily accessible to a non-expert programmer. Mortensen and Langtangen [8] describe how a DNS solver can be written in Python in 100 lines of script-like code, and also show that the code, when optimized in the background using Cython, runs as fast as an identical C++ implementation on thousands of processors with MPI. Shenfun takes it one step further and aims at providing a generic toolbox for creating high performance, parallel solvers of any PDE, in a very high-level language. And without compromising much on computational efficiency. The key to developing such a high-level code in Python is efficient use of Numpy [10], with broadcasting and vectorization, and MPI for Python [9], that wraps almost the entire MPI library, and that can transfer Numpy arrays between thousands of processors at the same speed as a low-level C or Fortran code. Similarly, we utilize the pyFFTW module [11], that wraps most of the FFTW library [3] and makes the FFT as fast when called from Python as it is when used in low-level codes.

This paper is organised as follows: in Section 2 the spectral Galerkin method is introduced. In Section 3 the basics of the `shenfun` package is described and implementations are shown for simple 1D Poisson and biharmonic problems. In Section 4 we move to higher dimensions and tensor product spaces before we, in Sections 5 and 6 end with

some extended functionality and an implementation for the time dependent nonlinear Ginzburg-Landau equation in 2D.

2 Spectral Galerkin Method

The spectral Galerkin method can most easily be described by considering a simple PDE, like the Poisson equation, in a 1D domain Ω

$$-u''(x) = f(x), \quad x \in \Omega, \tag{1}$$

with appropriate boundary conditions (Dirichlet, Neumann or periodic). To solve this equation, we can define a test function $v(x)$ that satisfies the boundary conditions, and that comes with an accompanying weight function $w(x)$. Assuming also that we work with complex valued functions, a weighted continuous inner product of the two functions u and v can be defined as

$$(u, v)_w = \int_\Omega u(x)\overline{v}(x)w(x)dx, \tag{2}$$

where $\overline{v}$ is the complex conjugate of v. The weighted inner product can now be used to create variational forms. If we multiply Eq. (1) with $\overline{v}w$ and integrate over the domain we obtain the variational form of the PDE

$$(-u'', v)_w = (f, v)_w. \tag{3}$$

The variational form can be solved numerically if u and v are approximated using a finite number (N) of test functions $\{v_l(x)\}_{l=0}^{N-1}$, and a solution

$$u(x) = \sum_{l=0}^{N-1} \hat{u}_l v_l(x), \tag{4}$$

where $\hat{\boldsymbol{u}} = \{\hat{u}_l\}_{l=0}^{N-1}$ are the expansion coefficients, that are also recognised as the unknowns in the modal spectral Galerkin method.

If v is chosen from a Fourier or Legendre basis, then the weight function used in the inner product is simply constant, and we may integrate (3) further using integration by parts. However, for a Chebyshev basis the weight function will be $1/\sqrt{1-x^2}$ and integration by parts is thus usually avoided. The weighted continuous inner product may, depending on the function that is to be integrated, be difficult or costly to evaluate. As such, we will in this work use the weighted *discrete* inner product instead, where the integral is approximated using quadrature

$$(u, v)_w^N = \sum_{j=0}^{N-1} u(x_j)\overline{v}(x_j)w_j \approx \int_\Omega u(x)\overline{v}(x)w(x)dx. \tag{5}$$

Here $\{w_j\}_{j=0}^{N-1}$ represents the quadrature weights and $\{x_j\}_{j=0}^{N-1}$ are the quadrature points for the integration.

The test functions v will be chosen based in part on boundary conditions. However, regardless of which space the test functions are chosen from, the procedure for solving a PDE with the spectral Galerkin method is always the same:

- Choose a basis satisfying boundary conditions.
- Derive variational forms from PDEs using weighted inner products.
- Assemble and solve linear systems of equations for expansion coefficients.

In other words it is very much like a finite element method. The major difference is that the basis functions are global, i.e., they all span the entire domain, whereas in FEM the test functions only have local support.

3 Shenfun

`shenfun` is a Python module package containing tools for working with the spectral Galerkin method. Shenfun implements classes for several bases with different boundary conditions, and within each class there are methods for transforms between spectral and real space, inner products, and for computing matrices arising from bilinear forms in the spectral Galerkin method. The Python module is organized as shown in Figure 1.

The `shenfun` language is very simple and closely follows that of FEniCS. A simple form implementation provides operators `div, grad, curl` and `Dx`, that act on three different types of basis functions, the `TestFunction`, `TrialFunction` and `Function`. Their usage is very similar to that from FEniCS, but not as general, nor flexible, since we are only conserned with simple tensor product grids and smooth solutions. The usage of these operators and basis functions will become clear in the following subchapters, where we will also describe the `inner` and `project` functions, with functionality as suggested by their names.

3.1 Classes for basis functions

The following bases are defined in submodules

- shenfun.chebyshev.bases
  - Basis - Regular Chebyshev
  - ShenDirichletBasis - Dirichlet boundary conditions
  - ShenNeumannBasis - Neumann boundary conditions (homogeneous)
  - ShenBiharmonicBasis - Homogeneous Dirichlet and Neumann boundary conditions
- shenfun.legendre.bases

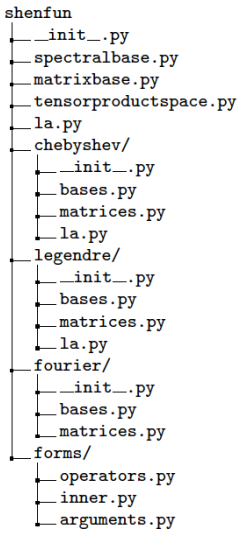

Figure 1: Directory tree of `shenfun` Python module.

  - Basis - Regular Legendre
  - ShenDirichletBasis - Dirichlet boundary conditions
  - ShenNeumannBasis - Neumann boundary conditions (homogeneous)
  - ShenBiharmonicBasis - Homogeneous Dirichlet and Neumann boundary conditions

- shenfun.fourier.bases
  - R2CBasis - Real to complex Fourier transforms
  - C2CBasis - Complex to complex transforms

All bases have methods for transforms and inner products on single- or multidimensional Numpy data arrays. The following code shows how to create a Fourier basis and subsequently perform a forward and an inverse discrete Fourier transform on a random array. The `uc` array is only used to test that the transform cycle returns the original data.

```
>>> from shenfun import *
>>> import numpy as np
>>> N = 16
>>> FFT = fourier.bases.R2CBasis(N, plan=True)
>>> u = np.random.random(N)
>>> uc = u.copy()
>>> u_hat = FFT.forward(u)
>>> u = FFT.backward(u_hat)
>>> assert np.allclose(u, uc)
```

3.2 Classes for matrices

Matrices that arise with the spectral Galerkin method using Fourier or Shen's modified basis functions (see, e.g., Eqs (23), (24)), are typically sparse and diagonal in structure. The sparse structure allows for a very compact storage, and **shenfun** has its own Matrix-class that is subclassing a Python dictionary, where keys are diagonal offsets, and values are the values along the diagonal. Some of the more important methods of the `SparseMatrix` class are shown below:

```
class SparseMatrix(dict):
    def __init__(self, d, shape):
        dict.__init__(self, d)
        self.shape = shape

    def diags(self, format='dia'):
        """Return Scipy sparse matrix"""

    def matvec(self, u, x, format='dia', axis=0):
        """Return Matrix vector product self*u in x"""

    def solve(self, b, u=None, axis=0):
        """Return solution u to self*u = b"""
```

For example, we may declare a tridiagonal matrix of shape N x N as

```
>>> N = 4
>>> d = {-1: 1, 0: -2, 1: 1}
>>> A = SparseMatrix(d, (N, N))
```

or similarly as

```
>>> d = {-1: np.ones(N-1), 0: -2*np.ones(N)}
>>> d[1] = d[-1]  # Symmetric, reuse np.ones array
>>> A = SparseMatrix(d, (N, N))
>>> A
{-1: array([ 1.,  1.,  1.]),
  0: array([-2., -2., -2., -2.]),
  1: array([ 1.,  1.,  1.])}
```

The matrix is a subclassed dictionary. If you want a regular *Scipy* sparse matrix instead, with all of its associated methods (solve, matrix-vector, etc.), then it is just a matter of

```
>>> A.diags()
<4x4 sparse matrix of type '<class 'numpy.float64'>'
    with 10 stored elements (3 diagonals) in DIAgonal format>
>>> A.diags().toarray()
array([[-2.,  1.,  0.,  0.],
       [ 1., -2.,  1.,  0.],
       [ 0.,  1., -2.,  1.],
       [ 0.,  0.,  1., -2.]])
```

3.3 Variational forms in 1D

Weak variational forms are created using test and trial functions, as shown in Section 2. Test and trial functions can be created for any basis in `shenfun`, as shown below for a Chebyshev Dirichlet basis with 8 quadrature points

```
>>> from shenfun.chebyshev.bases import ShenDirichletBasis
>>> from shenfun import inner, TestFunction, TrialFunction
>>> N = 8
>>> SD = ShenDirichletBasis(N, plan=True)
>>> u = TrialFunction(SD)
>>> v = TestFunction(SD)
```

A matrix that is the result of a bilinear form has its own subclass of `SparseMatrix`, called a `SpectralMatrix`. A `SpectralMatrix` is created using `inner` products on test and trial functions, for example the mass matrix:

```
>>> mass = inner(u, v)
>>> mass
{-2: array([-1.57079633]),
  0: array([ 4.71238898,  3.1415
             3.14159265, 3.14159265]),
  2: array([-1.57079633])}
```

This `mass` matrix will be the same as Eq. (2.5) of [12], and it will be an instance of the `SpectralMatrix` class. You may notice that `mass` takes advantage of the fact that two diagonals are constant and consequently only stores one single value.

The `inner` method may be used to compute any linear or bilinear form. For example the stiffness matrix `K`

```
>>> K = inner(v, div(grad(u)))
```

Square matrices have implemented a solve method that is using fast $\mathcal{O}(N)$ direct LU decomposition or similar, if available, and falls back on using Scipy's solver in CSR format if no better method is found implemented. For example, to solve the linear system `Ku=b`

```
>>> fj = np.random.random(N)
>>> b = inner(v, fj)
>>> u = np.zeros_like(b)
>>> u = K.solve(b, u)
```

All methods are designed to work along any dimension of a multidimensional array. Very little differs in the users interface. Consider, for example, the previous example on a three-dimensional cube

```
>>> fj = np.random.random((N, N, N))
>>> b = inner(v, fj)
>>> u = np.zeros_like(b)
>>> u = K.solve(b, u)
```

where `K` is exactly the same as before, from the 1D example. The matrix solve is applied along the first dimension since this is the default behaviour.

The bases also have methods for transforming between spectral and real space. For example, one may project a random vector to the `SD` space using

```
>>> fj = np.random.random(N)
>>> fk = np.zeros_like(fj)
>>> fk = SD.forward(fj, fk) # Gets expansion coefficients
```

and back to real physical space again

```
>>> fj = SD.backward(fk, fj)
```

Note that `fj` now will be different than the original `fj` since it now has homogeneous boundary conditions. However, if we transfer back and forth one more time, starting from `fj` which is in the Dirichlet function space, then we come back to the same array:

```
>>> fj_copy = fj.copy()
>>> fk = SD.forward(fj, fk)
>>> fj = SD.backward(fk, fj)
>>> assert np.allclose(fj, fj_copy) # Is True
```

3.4 Poisson equation implemented in 1D

We have now shown the usage of `shenfun` for single, one-dimensional spaces. It does not become really interesting before we start looking into tensor product grids in higher dimensions, but before we go there we revisit the spectral Galerkin method for a 1D Poisson problem, and show how the implementation of this problem can be performed using `shenfun`.

Periodic boundary conditions. If the solution to Eq. (1) is periodic with periodic length 2π, then we use $\Omega \in [0, 2\pi]$ and it will be natural to choose the test functions from the space consisting of the Fourier basis functions, i.e., $v_l(x) = e^{ilx}$. The mesh $\boldsymbol{x} = \{x_j\}_{j=0}^{N-1}$ will be uniformly spaced

$$\boldsymbol{x} = \frac{2\pi j}{N} \quad j = 0, 1, \ldots, N-1, \tag{6}$$

and we look for solutions of the form

$$u(x_j) = \sum_{l=-N/2}^{N/2-1} \hat{u}_l e^{ilx_j} \quad j = 0, 1, \ldots N-1. \tag{7}$$

Note that for Fourier basis functions it is customary (used by both MATLAB and Numpy) to use the wavenumbermesh

$$\boldsymbol{l} = -N/2, -N/2+1, \ldots, N/2-1, \tag{8}$$

where we have assumed that N is even. Also note that Eq. (7) naively would be computed in $\mathcal{O}(N^2)$ operations, but that it can be computed much faster $\mathcal{O}(N \log N)$ using the discrete inverse Fourier transform

$$\boldsymbol{u} = \mathcal{F}^{-1}(\hat{\boldsymbol{u}}), \tag{9}$$

where we use compact notation $\boldsymbol{u} = \{u(x_j)\}_{j=0}^{N-1}$.

To solve Eq. (1) with the discrete spectral Galerkin method, we create the basis $V^p = \text{span}\{e^{ilx}, \text{ for } l \in \boldsymbol{l}\}$ and attempt to find $u \in V^p$ such that

$$(-u'', v)_w^N = (f, v)_w^N, \quad \forall\, v \in V^p. \tag{10}$$

Inserting for Eq. (7) and using e^{imx} as test function we obtain

$$-(\sum_{l \in \boldsymbol{l}} \hat{u}_l (e^{ilx})'', e^{imx})_w^N = (f(x), e^{imx})_w^N \quad \forall\, m \in \boldsymbol{l} \tag{11}$$

$$\sum_{l \in \boldsymbol{l}} l^2 (e^{ilx}, e^{imx})_w^N \hat{u}_l = (f(x), e^{imx})_w^N \quad \forall\, m \in \boldsymbol{l}. \tag{12}$$

Note that the discrete inner product (5) is used, and we also need to interpolate the function $f(x)$ onto the grid $\boldsymbol{x}$. For Fourier it becomes very simple since the weight functions are constant $w_j = 2\pi/N$ and we have for the left hand side simply a diagonal matrix

$$(e^{ilx}, e^{imx})^N = 2\pi\delta_{ml} \quad \text{for } l, m \in \boldsymbol{l} \times \boldsymbol{l}, \tag{13}$$

where δ_{ml} is the kronecker delta function. For the right hand side we have

$$(f(x), e^{imx})^N = \frac{2\pi}{N}\sum_{j=0}^{N-1} f(x_j)e^{-imx_j} \quad \text{for } m \in \boldsymbol{l}, \tag{14}$$

$$= 2\pi\mathcal{F}_m(f(\boldsymbol{x})), \tag{15}$$

$$= 2\pi\hat{f}_m, \tag{16}$$

where $\mathcal{F}$ represents the discrete Fourier transform that is defined as

$$\hat{u}_l = \frac{1}{N}\sum_{j=0}^{N-1} u(x_j)e^{-ilx_j}, \quad \text{for } l \in \boldsymbol{l}, \tag{17}$$

or simply

$$\hat{\boldsymbol{u}} = \mathcal{F}(\boldsymbol{u}). \tag{18}$$

Putting it all together we can set up the assembled linear system of equations for $\hat{u}_l$ in (12)

$$\sum_{l\in\boldsymbol{l}} 2\pi l^2\delta_{ml}\hat{u}_l = 2\pi\hat{f}_m \quad \forall\, m \in \boldsymbol{l}, \tag{19}$$

which is trivially solved since it only involves a diagonal matrix (δ_{ml}), and we obtain

$$\hat{u}_l = \frac{1}{l^2}\hat{f}_l \quad \forall\, l \in \boldsymbol{l} \setminus \{0\}. \tag{20}$$

So, even though we carefully followed the spectral Galerkin method, we have ended up with the same result that would have been obtained with a Fourier collocation method, where one simply takes the Fourier transform of the Poisson equation and differentiate analytically.

With `shenfun` the periodic 1D Poisson equation can be trivially computed either with the collocation approach or the spectral Galerkin method. The procedure for the spectral Galerkin method will be shown first, before the entire problem is solved. All `shenfun` demos in this paper will contain a similar preample section where some necessary Python classes, modules and functions are imported. We import Numpy since `shenfun` arrays are Numpy arrays, and we import from Sympy to construct some exact solution used to verify the code. Note also the similarity to FEniCS with the import of methods and classes `inner, div, grad, TestFunction, TrialFunction`. The Fourier spectral Galerkin method in

turn requires that the `FourierBasis` is imported as well. The following code solves the Poisson equation in 1D with shenfun:

```
from sympy import Symbol, cos
import numpy as np
from shenfun import inner, div, grad, TestFunction, TrialFunction
from shenfun.fourier.bases import FourierBasis

# Use Sympy to compute a rhs, given an analytical solution
x = Symbol("x")
ue = cos(4*x)
fe = ue.diff(x, 2)

# Create Fourier basis with N basis functions
N = 32
ST = FourierBasis(N, np.float, plan=True)
u = TrialFunction(ST)
v = TestFunction(ST)
X = ST.mesh(N)

# Get f and exact solution on quad points
fj = np.array([fe.subs(x, j) for j in X], dtype=np.float)
uj = np.array([ue.subs(x, i) for i in X], dtype=np.float)

# Assemble right and left hand sides
f_hat = inner(v, fj)
A = inner(v, div(grad(u)))

# Solve Poisson equation
u_hat = A.solve(f_hat)

# Transfer solution back to real space
uq = ST.backward(u_hat)
assert np.allclose(uj, uq)
```

Naturally, this simple problem could be solved easier with a Fourier collocation instead, and a simple pure 1D Fourier problem does not illuminate the true advantages of `shenfun`, that only will become evident when we look at higher dimensional problems with tensor product spaces. To solve with collocation, we could simply do

```
# Transform right hand side
f_hat = ST.forward(fj)

# Wavenumers
k = ST.wavenumbers(N)
k[0] = 1

# Solve Poisson equation (solution in f_hat)
f_hat /= k**2
```

Note that `ST` methods `forward/backward` correspond to forward and inverse discrete Fourier transforms. Furthermore, since the input data `fj` is of type float (not complex), the transforms make use of the symmetry of the Fourier transform of real data, that $\hat{u}_k = \overline{\hat{u}}_{N-k}$, and that $\boldsymbol{k} = 0, 1, \ldots, N/2$ (index set computed as `k = ST.wavenumbers(N)`).

Dirichlet boundary conditions. If the Poisson equation is subject to Dirichlet boundary conditions on the edge of the domain $\Omega \in [-1, 1]$, then a natural choice is to use Chebyshev or Legendre polynomials. Two test functions that strongly fixes the boundary condition $u(\pm 1) = 0$ are

$$v_l(x) = T_l(x) - T_{l+2}(x), \tag{21}$$

where $T_l(x)$ is the l'th order Chebyshev polynomial of the first kind, or

$$v_l(x) = L_l(x) - L_{l+2}(x), \tag{22}$$

where $L_l(x)$ is the l'th order Legendre polynomial. The test functions give rise to functionspaces

$$V^C = \text{span}\{T_l - T_{l+2}, l \in \boldsymbol{l}^D\}, \tag{23}$$
$$V^L = \text{span}\{L_l - L_{l+2}, l \in \boldsymbol{l}^D\}, \tag{24}$$

where

$$\boldsymbol{l}^D = 0, 1, \ldots, N-3. \tag{25}$$

The computational mesh and associated weights will be decided by the chosen quadrature rule. Here we will go for Gauss quadrature, which leads to the following points and weights for the Chebyshev basis

$$x_j^C = \cos\left(\frac{2j+1}{2N}\pi\right) \qquad j = 0, 1, \ldots, N-1, \tag{26}$$
$$w_j^C = \frac{\pi}{N}, \tag{27}$$

and

$$x_j^L = \text{ zeros of } L_N(x) \qquad j = 0, 1, \ldots, N-1, \tag{28}$$

$$w_j^L = \frac{2}{(1-x_j^2)[L_N'(x_j)]^2} \qquad j = 0, 1, \ldots, N-1, \tag{29}$$

for the Legendre basis.

We now follow the same procedure as in Section 3.4 and solve Eq. (1) with the spectral Galerkin method. Consider first the Chebyshev basis and find $u \in V^C$, such that

$$(-u'', v)_w^N = (f, v)_w^N, \quad \forall\, v \in V^C. \tag{30}$$

We insert for $v = v_m$ and $u = \sum_{l \in \boldsymbol{l}^D} \hat{u}_l v_l$ and obtain

$$-(\sum_{l \in \boldsymbol{l}^D} \hat{u}_l v_l'', v_m)_w^N = (f, v_m)_w^N \qquad m \in \boldsymbol{l}^D, \tag{31}$$

$$-(v_l'', v_m)_w^N \hat{u}_l = (f, v_m)_w^N \qquad m \in \boldsymbol{l}^D, \tag{32}$$

where summation on repeated indices is implied. In Eq. (32) $A_{ml} = (v_l'', v_m)_w^N$ are the components of a sparse stiffness matrix, and we will use matrix notation $\boldsymbol{A} = \{A_{ml}\}_{m,l \in \boldsymbol{l}^D \times \boldsymbol{l}^D}$ to simplify. The right hand side can similarily be assembled to a vector with components $\tilde{f}_m = (f, v_m)_w^N$ such that $\tilde{\boldsymbol{f}} = \{\tilde{f}_m\}_{m \in \boldsymbol{l}^D}$. Note that a tilde is used since this is not a complete transform. We can now solve for the unknown $\hat{\boldsymbol{u}} = \{\hat{u}_l\}_{l \in \boldsymbol{l}^D}$ vector

$$-\boldsymbol{A}\hat{\boldsymbol{u}} = \tilde{\boldsymbol{f}}, \tag{33}$$

$$\hat{\boldsymbol{u}} = -\boldsymbol{A}^{-1}\tilde{\boldsymbol{f}}. \tag{34}$$

Note that the matrix $\boldsymbol{A}$ is a special kind of upper triangular matrix, and that the solution can be obtained very efficiently in approximately $4N$ arithmetic operations.

To get the solution back and forth between real and spectral space we require a transformation pair similar to the Fourier transforms. We do this by projection. Start with

$$u(\boldsymbol{x}) = \sum_{l \in \boldsymbol{l}^D} \hat{u}_l v_l(\boldsymbol{x}) \tag{35}$$

and take the inner product with v_m

$$(u, v_m)_w^N = (\sum_{l \in \boldsymbol{l}^D} \hat{u}_l v_l, v_m)_w^N. \tag{36}$$

Introducing now the mass matrix $B_{ml} = (v_l, v_m)_w^N$ and the *Shen* forward inner product $\mathcal{S}_m(u) = (u, v_m)_w^N$, Eq. (36) is rewritten as

$$\mathcal{S}_m(u) = B_{ml}\hat{u}_l, \tag{37}$$

$$\hat{\boldsymbol{u}} = \boldsymbol{B}^{-1}\mathcal{S}(\boldsymbol{u}), \tag{38}$$

$$\hat{\boldsymbol{u}} = \mathcal{T}(\boldsymbol{u}), \tag{39}$$

where $\mathcal{T}(\boldsymbol{u})$ represents a forward transform of $\boldsymbol{u}$. Note that $\mathcal{S}$ is introduced since the inner product $(u, v_m)_w^N$ may, just like the inner product with the Fourier basis, be computed fast, with $\mathcal{O}(N \log N)$ operations. And to this end, we need to make use of a discrete cosine transform (DCT), instead of the Fourier transform. The details are left out from this paper, though.

A simple Poisson problem with analytical solution $\sin(\pi x)(1-x^2)$ is implemented below, where we also verify that the correct solution is obtained.

```
from shenfun.chebyshev.bases import ShenDirichletBasis

# Use sympy to compute a rhs, given an analytical solution
ue = sin(np.pi*x)*(1-x**2)
fe = ue.diff(x, 2)

# Lambdify for faster evaluation
ul = lambdify(x, ue, 'numpy')
fl = lambdify(x, fe, 'numpy')

N = 32
SD = ShenDirichletBasis(N, plan=True)
X = SD.mesh(N)
u = TrialFunction(SD)
v = TestFunction(SD)
fj = fl(X)

# Compute right hand side of Poisson equation
f_hat = inner(v, fj)

# Get left hand side of Poisson equation and solve
A = inner(v, div(grad(u)))
f_hat = A.solve(f_hat)
uj = SD.backward(f_hat)

# Compare with analytical solution
ue = ul(X)
assert np.allclose(uj, ue)
```

Note that the inner product `f_hat = inner(v, fj)` is computed under the hood using the fast DCT. The inverse transform `uj = SD.backward(f_hat)` is also computed using a fast DCT, and we use the notation

$$\begin{aligned} u(x_j) &= \sum_{l \in \boldsymbol{l}^D} \hat{u}_l v_l(x_j) \quad j = 0, 1, \ldots, N-1, \\ \boldsymbol{u} &= \mathcal{S}^{-1}(\hat{\boldsymbol{u}}). \end{aligned} \tag{40}$$

To implement the same problem with the Legendre basis (22), all that is needed to change is the first line in the Poisson solver to `from shenfun.legendre.bases import ShenDirichletBasis`. Everything else is exactly the same. However, a fast inner product, like in (40), is only implemented for the Chebyshev basis, since there are no known $\mathcal{O}(N \log N)$ algorithms for the Legendre basis, and the Legendre basis thus uses straight forward $\mathcal{O}(N^2)$ algorithms for its transforms.

4 Tensor product spaces

Now that we know how to solve problems in one dimension, it is time to move on to more challenging tasks. Consider again the Poisson equation, but now in possibly more than one dimension

$$-\nabla^2 u(\boldsymbol{x}) = f(\boldsymbol{x}) \quad \text{for } \boldsymbol{x} \in \Omega. \tag{41}$$

Lets first consider 2 dimensions, with Dirichlet boundary conditions in the first direction and with periodicity in the second. Let Ω be the domain $[-1, 1] \times [0, 2\pi]$, and $W(x, y) = V^C(x) \times V^p(y)$ be the tensor product function space. We can solve this problem for some suitable function $f(\boldsymbol{x})$ in `shenfun` by constructing a few more classes than were required in 1D

```
from shenfun import Function, TensorProductSpace
from mpi4py import MPI
```

Now the `TensorProductSpace` class is used to construct W, whereas `Function` is a subclass of `numpy.ndarray` used to hold solution arrays. The MPI communicator, on the other hand, is used for distributing the tensor product grids on a given number of processes

```
comm = MPI.COMM_WORLD
N = (32, 33)

K0 = ShenDirichletBasis(N[0])
K1 = FourierBasis(N[1], dtype=np.float)
W = TensorProductSpace(comm, (K0, K1))

# Alternatively, switch order for periodic in first direction instead
# W = TensorProductSpace(comm, (K1, K0), axes=(1, 0))
```

Under the hood, within the `TensorProductSpace` class, the mesh is distributed, both in real, physical space, and in spectral space. In the real space the mesh is distributed along the first index, whereas in spectral space the wavenumbermesh is distributed along the second dimension. This is the default behaviour of `TensorProductSpace`. However, the distribution may also be configured specifically by the user, e.g., as shown in the commented out text, where the Dirichlet basis is found along the second axis. In this case the order of the axes to transform over has been flipped, such that in

spectral space the data is distributed along the first dimension and aligned in the second. This is required for solving the linear algebra system that arises for the Dirichlet basis. The arrays created using `Function` are distributed, and no further attention to MPI is required. However, note that arrays may have different type and shape in real space and in spectral space. For this reason `Function` has a keyword argument `forward_output`, that is used as `w_hat = Function(W, forward_output=True)` to create an array consistent with the output of `W.forward` (solution in spectral space), and `w = Function(W, forward_output=False)` to create an array consistent with the input (solution in real space). Furthermore, we can use `uh = np.zeros_like(w_hat)` and `w_hat = Function(W, buffer=uh)` to wrap a `Function` instance around a regular Numpy array `uh`. Note that `uh` and `w_hat` now will share the same data, and modifying one will naturally modify also the other.

The solution of a complete Poisson problem in 2D is shown below. Very similar code is required to solve the Poisson problem with the Legendre basis. The main difference is that for Legendre it is natural to integrate the weak form by parts and use `matrices = inner(grad(v), grad(u))`

```
from shenfun.chebyshev.la import Helmholtz as Solver

# Create a solution that satisfies boundary conditions
x, y = symbols("x,y")
ue = (cos(4*y) + sin(2*x))*(1-x**2)
fe = ue.diff(x, 2) + ue.diff(y, 2)

# Lambdify for faster evaluation
ul = lambdify((x, y), ue, 'numpy')
fl = lambdify((x, y), fe, 'numpy')

X = T.local_mesh(True)
u = TrialFunction(T)
v = TestFunction(T)

# Get f on quad points
fj = fl(X[0], X[1])

# Compute right hand side of Poisson equation
f_hat = inner(v, fj)

# Get left hand side of Poisson equation
matrices = inner(v, div(grad(u)))

# Create Helmholtz linear algebra solver
H = Solver(**matrices)
```

```
# Solve and transform to real space
u_hat = Function(T)           # Solution spectral space
u_hat = H(u_hat, f_hat)       # Solve
u = T.backward(u_hat)
```

The test functions and function spaces require a bit more attention. Test functions for space $W(x,y) = V^C(x) \times V^p(y)$ are given as

$$\phi_{\mathsf{k}}(x,y) = v_l(x)e^{imy}, \tag{42}$$

which introduces the sans serif tensor product wavenumber mesh $\mathsf{k} = \boldsymbol{l}^D \times \boldsymbol{l}$

$$\mathsf{k} = \{(l,m) | l \in \boldsymbol{l}^D \text{ and } m \in \boldsymbol{l}\}. \tag{43}$$

Similarly there is a tensor product grid $\mathsf{x} = \boldsymbol{x} \times \boldsymbol{y}$, where $\boldsymbol{y} = \{y_k\}_{k=0}^{M-1} = 2\pi k/M$

$$\mathsf{x} = \{(x_j, y_k) | j = 0, 1, \ldots, N-1 \text{ and } k = 0, 1, \ldots, M-1\}. \tag{44}$$

Note that for computing on the tensor product grids using Numpy arrays with vectorization, the mesh and wavenumber components need to be represented as 2D arrays. As such we create

$$\mathsf{x} = (\boldsymbol{x}, \boldsymbol{y}) = \left(\{x_i\}_{i=0}^{N-1} \times I^M, I^N \times \{y_j\}_{j=0}^{M-1}\right), \tag{45}$$

where I^N is an N-length vector of ones. Similarly

$$\mathsf{k} = (\boldsymbol{l}, \boldsymbol{m}) = \left(\{l\}_{l=0}^{N-1} \times I^M, I^N \times \{m\}_{m=0}^{M/2}\right). \tag{46}$$

Such tensor product grids can be very efficiently stored with Numpy arrays, using no more space than the two vectors used to create them. The key to this efficiency is broadcasting. We store k as a list of two numpy arrays, $\boldsymbol{l}$ and $\boldsymbol{m}$, corresponding to the two 1D wavenumber meshes $\{l\}_{l=0}^{N-1}$ and $\{m\}_{m=0}^{M/2}$. However, $\boldsymbol{l}$ and $\boldsymbol{m}$ are now stored as 2D arrays of shape $(N,1)$ and $(1, M/2+1)$, respectively. And broadcasting takes care of the additional dimension, such that the two arrays work just like if they were stored as $(N, M/2+1)$ arrays. We can look up $\boldsymbol{l}(l,m)$, just like a regular $(N, M/2+1)$ array, but the storage required is still only one single vector. The same goes for x, which is stored as a list of two arrays $\boldsymbol{x}$, $\boldsymbol{y}$ of shape $(N,1)$ and $(1,M)$ respectively. This extends straightforward to even higher dimensions.

Assembling a weak form like $(v, \nabla^2 u)_w^N$ leads to two non-diagonal matrices, both the stiffness and mass matrix, since it expands like

$$(v, \nabla^2 u)_w^N = \left(v, \frac{\partial^2 u}{\partial x^2} + \frac{\partial^2 u}{\partial y^2}\right)_w^N. \tag{47}$$

Inserting for test function $v = \phi_{\mathsf{k}} (= \phi_{l,m} = v_l(x)e^{imy})$ and trial function $u = \sum_{(q,r)\in\mathsf{k}} \hat{u}_{q,r}\phi_{q,r}$, we obtain

$$(v, \nabla^2 u)_w^N = \left(\phi_{l,m}, \frac{\partial^2}{\partial x^2} \sum_{(q,r)\in\mathsf{k}} \hat{u}_{q,r}\phi_{q,r} + \frac{\partial^2}{\partial y^2} \sum_{(q,r)\in\mathsf{k}} \hat{u}_{q,r}\phi_{q,r} \right)_w^N, \tag{48}$$

$$= 2\pi \left(\sum_{(q,r)\in\mathsf{k}} A_{lq}\delta_{rm}\hat{u}_{q,r} - \sum_{(q,r)\in\mathsf{k}} r^2 B_{lq}\delta_{rm}\hat{u}_{q,r} \right), \tag{49}$$

$$= 2\pi \left(\sum_{q\in\boldsymbol{l}^D} A_{lq}\hat{u}_{q,m} - m^2 \sum_{q\in\boldsymbol{l}^D} B_{lq}\hat{u}_{q,m} \right) \quad \forall (l,m) \in \boldsymbol{l}^D \times \boldsymbol{l}. \tag{50}$$

As can be seen from Eq.(50), the linear system of equations is set up to act along the Dirichlet direction, whereas for the periodic direction the matrices are diagonal and no additional work is required. The system of equations correspond to a series of 1D Helmholtz problems, that need to be solved once for each $m \in \boldsymbol{l}$. This is what goes on under the hood with the Helmholtz solver imported through `from shenfun.chebyshev.la import Helmholtz as Solver`.

The right hand side of the Poisson problem is computed as

$$(v, f)_w^N = 2\pi \underbrace{\sum_j \underbrace{\frac{1}{N} \sum_k f(x_j, y_k) e^{imy_k}}_{\mathcal{F}_m} v_l(x_j) w_j}_{\mathcal{S}_l} \quad \forall (l,m) \in \boldsymbol{l}^D \times \boldsymbol{l},$$

$$= 2\pi \mathcal{S}(f) = 2\pi \mathcal{S}_l(\mathcal{F}_m(f)). \tag{51}$$

The `TensorProductSpace` class can take any number of Fourier bases. A 3 dimensional tensor product space can be created as

```
N = (32, 33, 34)
K0 = ShenDirichletBasis(N[0])
K1 = C2CBasis(N[1])
K2 = R2CBasis(N[2])
W = TensorProductSpace(comm, (K0, K1, K2))
```

Here the default behaviour of `TensorProductSpace` is to distribute the first 2 indices in real space using two subcommunicators, with a decomposition often referred to as *pencil* decomposition. In spectral space the last two indices will be distributed. For example, using 4 CPUs, a subprocessor mesh of size 2×2 will be created, and 2 subprocessors share the first index and the other two share the second index. If the program is run with 3 processors, then only the first index will be distributed and the subprocessormesh will be 3×1. It is also possible to configure `TensorProductSpace` to run with 4 CPUs and a 4×1 subprocessormesh, or 40,000 CPUs with a 200×200 processormesh. The latter

requires that the mesh is big enough, though, but otherwise it is just a matter of acquiring computing power. The biggest simulations tested thus far used 64,000 CPUs.

Solving a biharmonic problem is just as easy as the Poisson problem. Consider the fourth order biharmonic PDE in 3-dimensional space

$$\nabla^4 u(\boldsymbol{x}) = f(\boldsymbol{x}), \quad \boldsymbol{x} \in \Omega \tag{52}$$

$$u(x = \pm 1, y, z) = \frac{\partial u}{\partial x}(x = \pm 1, y, z) = 0 \tag{53}$$

$$u(x, y + 2\pi, z) = u(x, y, z), \tag{54}$$

$$u(x, y, z + 2\pi) = u(x, y, z). \tag{55}$$

that is periodic in $y-$ and $z-$directions and with clamped boundary conditions at $x = \pm 1$. The problem may be solved using either one of these two bases:

$$V^C = \text{span}\{T_l - \frac{2(l+2)}{l+3} T_{l+2} + \frac{l+1}{l+3} T_{l+4}, l \in \boldsymbol{l}^B\}, \tag{56}$$

$$V^L = \text{span}\{L_l - \frac{2(2l+5)}{2l+7} L_{l+2} + \frac{2l+3}{2l+7}, l \in \boldsymbol{l}^B\}, \tag{57}$$

where $\boldsymbol{l}^B = 0, 1, \ldots, N-5$. A tensor product space may be constructed as $W(x, y, z) = V^C(x) \times V^p(y) \times V^p(z)$, and the variational problem

$$(v, \nabla^4 u)_w^N = (v, f)_w^N, \tag{58}$$

where u and v are trial and test functions in W, may be implemented in `shenfun` as shown below

```
from shenfun.chebyshev.bases import ShenBiharmonicBasis
from shenfun.chebyshev.la import Biharmonic as Solver

N = (32, 33, 34)
K0 = ShenBiharmonicBasis(N[0])
K1 = C2CBasis(N[1])
K2 = R2CBasis(N[2])
W = TensorProductSpace(comm, (K0, K1, K2))
u = TrialFunction(W)
v = TestFunction(W)
matrices = inner(v, div(grad(div(grad(u)))))
f_hat = inner(v, fj)  # Some right hand side
# or for Legendre:
# matrices = inner(div(grad(v)), div(grad(u)))
B = Solver(**matrices)

# Solve and transform to real space
```

```
u_hat = Function(T)           # Solution spectral space
u_hat = B(u_hat, f_hat)       # Solve
u = T.backward(u_hat)
```

5 Other functionality of `shenfun`

In addition to the `div` and `grad` operators, there is `Dx` for a partial derivative

```
from shenfun import Dx
v = TestFunction(W)
du = Dx(v, 0, 1)
```

where the first argument is the basis function, the second (integer) is the axis to take the derivative over, and the third (integer) is the number of derivatives, e.g.,

$$\frac{\partial^2 v}{\partial y^2} = \text{Dx(v, 1, 2)}.$$

The operator can be nested. To compute $\frac{\partial^2 u}{\partial x \partial y}$ one may do

```
v = TestFunction(W)
du = Dx(Dx(v, 0, 1), 1, 1)
```

The operators work on `TestFunctions, TrialFunctions` or `Functions`, where only the last actually contain any data, because a `Function` is used to store the solution. Once a solution has been found, one may also manipulate it further using `project` in combination with operators on `Functions`. For example, to compute $\partial u/\partial x$ of the solution to the biharmonic problem, one can do

```
u = T.backward(u_hat)  # The original solution on space T
K0 = Basis(N[0])
W0 = TensorProductSpace(comm, (K0, K1, K2))
du_hat = project(Dx(u, 0, 1), W0, uh_hat=u_hat)
du = Function(W0)
du = W0.backward(du_hat, du)
```

Note that we are here using a regular Chebyshev space instead of the biharmonic, to avoid enforcing erroneous boundary conditions on the solution. We could in this case also, with advantage, have chosen a Dirichlet space, since the derivative of the biharmonic problem is known to be zero on the edges of the domain (at $x = \pm 1$).

All problems considered thus far have been scalar valued. With `shenfun` there is also some functionality for working with vector equations. To this end, there is a class called `VectorTensorProductSpace`, and there is an additional operator, `curl`, that can only be used on vectors:

```
from shenfun import VectorTensorProductSpace, curl
T = TensorProductSpace(comm, (K0, K1, K2))
Tk = VectorTensorProductSpace([T, T, T])
v = TestFunction(Tk)
u_ = Function(Tk, False)
u_[:] = np.random.random(u_.shape)
u_hat = Tk.forward(u_)
w_hat = inner(v, curl(u_), uh_hat=u_hat)
```

Vector equations have very similar form as scalar equations, but at the moment of writing the different equation components cannot be implicitly coupled.

6 Ginzburg-Landau equation

We end this paper with the implementation of the complex Ginzburg-Landau equation, which is a nonlinear time dependent reaction-diffusion problem. The equation to solve is

$$\frac{\partial u}{\partial t} = \nabla^2 u + u - (1 + 1.5i)u|u|^2, \tag{59}$$

for the doubly periodic domain $\Omega = [-50, 50] \times [-50, 50]$ and $t \in [0, T]$. The initial condition is chosen as one of the following

$$u^0(\boldsymbol{x}, 0) = (ix + y) \exp -0.03(x^2 + y^2), \tag{60}$$
$$u^1(\boldsymbol{x}, 0) = (x + y) \exp -0.03(x^2 + y^2). \tag{61}$$

This problem is solved with the spectral Galerkin method using Fourier bases in both directions, and a tensor product space $W(x, y) = V^p(x) \times V^p(y)$, where V^p is defined as in Section 3.4, but here mapping the computational domain $[-50, 50]$ to $[0, 2\pi]$. Considering only the spatial discretization, the variational problem becomes: find $u(x, y)$ in W, such that

$$\frac{\partial}{\partial t}(v, u)^N = (v, \nabla^2 u)^N + (v, u - (1 + 1.5i)u|u|^2)^N \quad \text{for all} \quad v \in W, \tag{62}$$

and we integrate the equations forward in time using an explicit, fourth order Runge-Kutta method, that only requires as input a function that returns the right hand side of (62). Note that all matrices involved with the Fourier method are diagonal, so there is no need for linear algebra solvers, and the left hand side inner product equals $(2\pi)^2 \hat{\boldsymbol{u}}$.

The initial condition is created using `Sympy`

```
from sympy import symbols, exp, lambdify
x, y = symbols("x,y")
#ue = (1j*x + y)*exp(-0.03*(x**2+y**2))
ue = (x + y)*exp(-0.03*(x**2+y**2))
ul = lambdify((x, y), ue, 'numpy')
```

We create a regular tensor product space, choosing the `fourier.bases.C2CBasis` for both directions if the initial condition is complex (60), whereas we may choose `R2CBasis` if the initial condition is real (61). Since we are solving a nonlinear equation, the additional issue of aliasing should be considered. Aliasing errors may be handled with different methods, but here we will use the so-called 3/2-rule, that requires padded transforms. We create a tensor product space `Tp` for padded transforms, using the `padding_factor=3/2` keyword below. Furthermore, some solution arrays, test and trial functions are also declared.

```
# Size of discretization
N = (201, 201)

# Create tensor product space
K0 = C2CBasis(N[0], domain=(-50., 50.))
K1 = C2CBasis(N[1], domain=(-50., 50.))
T = TensorProductSpace(comm, (K0, K1))

Kp0 = C2CBasis(N[0], domain=(-50., 50.), padding_factor=1.5)
Kp1 = C2CBasis(N[1], domain=(-50., 50.), padding_factor=1.5)
Tp = TensorProductSpace(comm, (Kp0, Kp1))

u = TrialFunction(T)
v = TestFunction(T)
X = T.local_mesh(True)
U = Function(T, False)          # Solution
U_hat = Function(T)             # Solution spectral space
Up = Function(Tp, False)        # Padded solution for nonlinear term
dU_hat = Function(T)            # right hand side
#initialize
U[:] = ul(*X)
U_hat = T.forward(U, U_hat)
```

Note that `Tp` can be used exactly like `T`, but that a backward transform creates an output that is 3/2 as large in each direction. So a $(100, 100)$ mesh results in a $(150, 150)$ output from a backwards transform. This transform is performed by creating a 3/2 times larger padded array in spectral space $\hat{u}^p_{\mathsf{k}^p}$, where $\mathsf{k}^p = \boldsymbol{l}^p \times \boldsymbol{l}^p$ and

$$\boldsymbol{l}^p = -3N/4, -3N/4+1, \ldots, 3N/4-1. \tag{63}$$

We then set $\hat{u}^p_{\mathsf{k}} = \hat{u}_{\mathsf{k}}$ for $\mathsf{k} \in \boldsymbol{l} \times \boldsymbol{l}$, and for the remaining high frequencies $\hat{u}^p_{\mathsf{k}}$ is set to 0.

We will solve the equation with a fourth order Runge-Kutta integrator. To this end we need to declare some work arrays to hold intermediate solutions, and a function for the right hand side of Eq. (62)

```
U_hat0 = Function(T)
U_hat1 = Function(T)
w0 = Function(T)
a = [1./6., 1./3., 1./3., 1./6.]          # Runge-Kutta parameter
b = [0.5, 0.5, 1.]                        # Runge-Kutta parameter
def compute_rhs(rhs, u_hat, U, Up, T, Tp, w0):
    rhs.fill(0)
    U = T.backward(u_hat, U)
    rhs = inner(v, div(grad(U)), output_array=rhs, uh_hat=u_hat)
    rhs += inner(v, U, output_array=w0, uh_hat=u_hat)
    rhs /= (2*np.pi)**2  # (2pi)**2 represents scaling with inner(u, v)
    Up = Tp.backward(u_hat, Up)
    rhs -= Tp.forward((1+1.5j)*Up*abs(Up)**2, w0)
    return rhs
```

Note the close similarity with (62) and the usage of the padded transform for the nonlinear term. Finally, the Runge-Kutta method is implemented as

```
t = 0.0
dt = 0.025
end_time = 96.0
tstep = 0
while t < end_time-1e-8:
    t += dt
    tstep += 1
    U_hat1[:] = U_hat0[:] = U_hat
    for rk in range(4):
        dU_hat = compute_rhs(dU_hat, U_hat, U, Up, T, Tp, w0)
        if rk < 3:
            U_hat[:] = U_hat0 + b[rk]*dt*dU_hat
        U_hat1 += a[rk]*dt*dU_hat
    U_hat[:] = U_hat1
```

The code that is described here will run in parallel for up to a maximum of $\min(N[0], N[1])$ processors. But, being a 2D problem, a single processor is sufficient to solve the problem in reasonable time. The real part of $u(\boldsymbol{x}, t)$ is shown in Figure 2 for times $t = 16$ and $t = 96$, where the solution is initialized from (60). The results starting from the real initial condition in (61) is shown for the same times in Figure 3. There are apparently good agreements with figures published from using `chebfun` on *www.chebfun.org/examples/pde/GinzburgLandau.html*. In particular, the figures in 2 are identical by the eye norm. One interesting feature, though, is seen in the right plot of Figure 3, where the results can be seen to have preserved symmetry, as they should. This symmetry is lost with chebfun, as commented in the referenced webpage. An asymmetric solution is also obtained with `shenfun` if no de-aliasing is applied. However, the simulations

are very sensitive to roundoff, and it has also been observed that a de-aliased solution using `shenfun` may loose symmetry simply if a different FFT algorithm is chosen on runtime by FFTW.

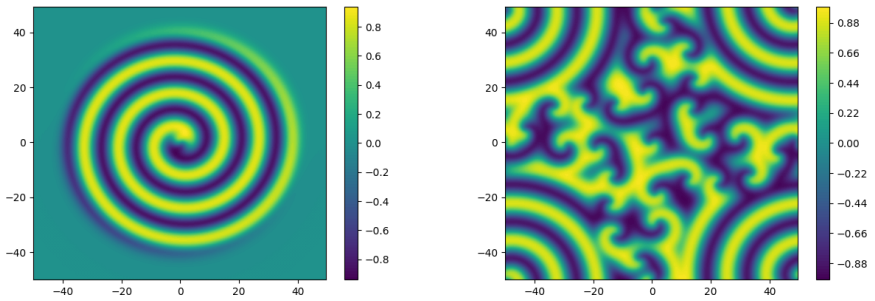

Figure 2: Ginzburg-Landau solution (real) at times 16 and 96, from complex initial condition.

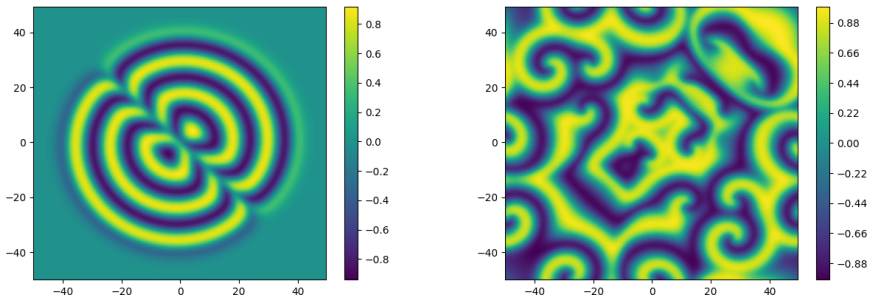

Figure 3: Ginzburg-Landau solution (real) at times 16 and 96 from real initial condition.

7 Conclusions

In this paper, the Python module `shenfun` has been described. Within this module there are tools that greatly simplify the implementation of the spectral Galerkin method for tensor product grids, and parallel solvers may be written with ease and comfort. `Shenfun` provides a FEniCS like interface to the spectral Galerkin method, where equations are cast on a weak form, and where the required script-like coding remains very similar to the mathematics. We have verified and shown implementations for simple Poisson or biharmonic problems, as well as the nonlinear complex Ginzburg-Landau equation. On a final note, it should be mentioned that these tools have also been used to implement various Navier Stokes solvers within the `spectralDNS` project (github.com/spectralDNS), that has run on the Shaheen II supercomputer at KAUST, on meshes of size up to 2048^3.

8 Acknowledgements

This research is a part of the 4DSpace Strategic Research Initiative at the University of Oslo.

References

[1] G. Alfonsi, S. A. Ciliberti, M. Mancini, and L. Primavera. Direct numerical simulation of turbulent channel flow on high-performance GPU computing system. *Computation*, 4:13, 2016.

[2] S. de Bruyn Kops. Classical scaling and intermittency in strongly stratified boussinesq turbulence. *J. Fluid Mechanics*, 775:436–463, 2015.

[3] M. Frigo and S. G. Johnson. The Design and Implementation of FFTW3. *Proceedings of the IEEE*, 93(2):216–231, Feb 2005.

[4] S. Hoyas and J. Jiménez. Scaling of the Velocity Fluctuations in Turbulent Channels Up to $Re_\tau = 2003$. *Physics of Fluids*, 18(1), 2006.

[5] D. A. Kopriva. *Implementing Spectral Methods for Partial Differential Equations*. Springer, 2009.

[6] M. Lee and R. D. Moser. Direct Numerical Simulation of Turbulent Channel Flow Up to $Re_\tau \approx 5200$. *J. Fluid Mechanics*, 774:395–415, 7 2015.

[7] A. Logg, K.-A. Mardal, G. N. Wells, et al. *Automated Solution of Differential Equations by the Finite Element Method*. Springer, 2012.

[8] M. Mortensen and H. P. Langtangen. High performance Python for direct numerical simulations of turbulent flows. *Computer Physics Communications*, 203:53–65, 2016.

[9] MPI for Python. Https://bitbucket.org/mpi4py/mpi4py/, 2017.

[10] NumPy. Http://www.numpy.org, 2017.

[11] pyFFTW. https://pypi.python.org/pypi/pyFFTW, 2017.

[12] J. Shen. Efficient spectral-galerkin method ii. direct solvers of second- and fourth-order equations using chebyshev polynomials. *SIAM Journal on Scientific Computing*, 16(1):74–87, 1995.

[13] L. N. Trefethen. *Approximation Theory and Approximation Practice*. SIAM, 2013.

9. National Conference on Computational Mechanics
MekIT'17
B. Skallerud and H I Andersson (Eds)

THREE DIMENSIONAL NUMERICAL SIMULATION OF FLOW IN BLIND-TEE PIPES

MUK CHEN ONG[1], SHENGNAN LIU[1], UTARI CENDHY LIESTYARINI[1], YIHAN XING[2]

[1]Department of Mechanical and Structural Engineering and Materials Science
University of Stavanger,
Stavanger, Norway. Email: muk.c.ong@uis.no

[2]Emerson Automation Solutions, Roxar
Stavanger, Norway

Key words: Pipe flow, Blind-tee pipe, Three dimensional, CFD.

Abstract. Blind-tee pipes are often encountered in the process piping of the refinery plants. The objective of the present study is to investigate numerically whether the increment of blind-tee length will improve the mixing of the fluids inside the pipe. Three dimensional (3D) computational fluid dynamic (CFD) laminar-flow simulations have been performed to study the internal flow physics inside pipes with blind-tee lengths varying from 1*D* to 5*D*. Here *D* is the diameter of the pipe. The investigated Reynolds number is 1000. First, 3D flow simulations in a straight pipe with 10*D* are performed, and the numerical results are compared with the analytical solution. The computed velocity profile in the straight pipe case is then used as the inlet velocity profile for the simulations of flow in the blind-tee pipes. Numerical results, such as streamlines and pressure contours, are computed and discussed. Flow circulations in the blind tee section are studied and show that good fluid mixing in the pipe (no stagnant fluid) is observed when the blind tee length is less than 2*D*. Stagnant flow circulation is observed towards the end of the blind-tee section when the blind tee length is more than 2*D*.

1 INTRODUCTION

The process piping in the refinery plant does not always have straight pipe geometry. The configuration of these pipelines are usually zigzag or snake-like. The pipe fittings or joints such as elbow pipe, blind-tee pipe, T-pipe, Y-pipe are commonly seen. One of the reasons why the pipelines are layered in these configurations is due to the limited space.

At the connections or joint parts of the pipelines, fluid flow will behave differently from the flow of fluid in a straight pipe. The physical flow inside these joints needs to be studied in order to ensure an appropriate flow engineering design. First, it should be investigated whether there will be any deposits inside the pipe joints which may affect the flow in the pipe. Second, it should be checked whether the flow (especially multiphase flow) is well mixed during and after

crossing the pipe fittings, so that the relevant sensors (such as particle-concentration sensors) can perform the measurement successfully.

According to the open literature, many experimental, analytical and numerical studies have been performed to investigate the flow inside straight pipes, curved pipes, 90^o tee-junction pipes and T-junction pipes, see e.g. Hornbeck [1], Friedmann et al. [2], Shirayama and Kuwahar [3], Costa et al. [4], Vasava [5], Cade et al. [6] and Beneš et al. [7]. To the authors' knowledge, the flow physics in blind-tee pipes have not yet been investigated in details. A typical blind-tee pipe is shown in Figure 1.

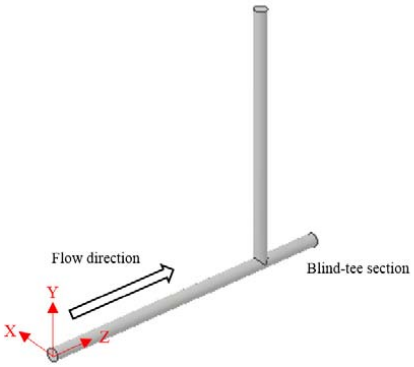

Figure 1. A typical blind-tee pipe.

In the present study, the objective is to investigate the flow physics in the blind-tee pipes with the blind-tee section lengths varying from 0 to 5D using three-dimensional (3D) computational fluid dynamics (CFD) simulations. Here D is the pipe diameter. The fluid mixing condition in the blind-tee section will be studied. Through the present study, a critical length of blind-tee section should be determined in order to avoid fluid deposition in the blind-tee section. The investigated Reynolds number (Re = $U_{z,average}D/\nu$) is 1000, which is in laminar flow regime. Here $U_{z,average}$ is the average inlet flow velocity and ν is the kinematic viscosity of the fluid. Since there is no available data for the flow in the blind-tee pipes, 3D flow in a straight pipe has been simulated and the numerical results are then verified against the analytical solutions given in Cengel and Cimbala (2014). Subsequently, the pipe flow with the verified incoming velocity profile will be set at the inlet of the blind-tee pipes with various blind-tee section lengths. The effect of the blind-tee section length on the pipe flow characteristics in the blind-tee sections will be investigated by studying the flow pattern and the pressure distribution along the pipes.

2 MATHEMATICAL FORMULATION

2.1 Flow model

The equations to be solved are incompressible Navier-Stokes equations. The open source CFD code OpenFOAM is used here. OpenFOAM is mainly applied for solving problems in

continuum mechanics. It is developed based on the tensorial approach and object oriented techniques (Weller et al. [8]). The pimpleFOAM solver is employed in the present study. According to OpenFOAM [9], the pimpleFOAM is a large time-step transient solver which is suitable for incompressible Newtonian flow. This solver uses the merged PISO-SIMPLE algorithm which is known as PIMPLE algorithm. The spatial schemes for gradient, Laplacian and divergence are Gauss linear, Gauss linear corrected and Gauss linear schemes, respectively. All these schemes are in second order. The first-order Euler scheme is used for the time integration. Further details of these schemes are given in OpenFOAM [9].

2.2 Computational domain and boundary conditions

The computational domains and boundary conditions for the straight pipe and the blind-tee pipes are shown in Figure 2.

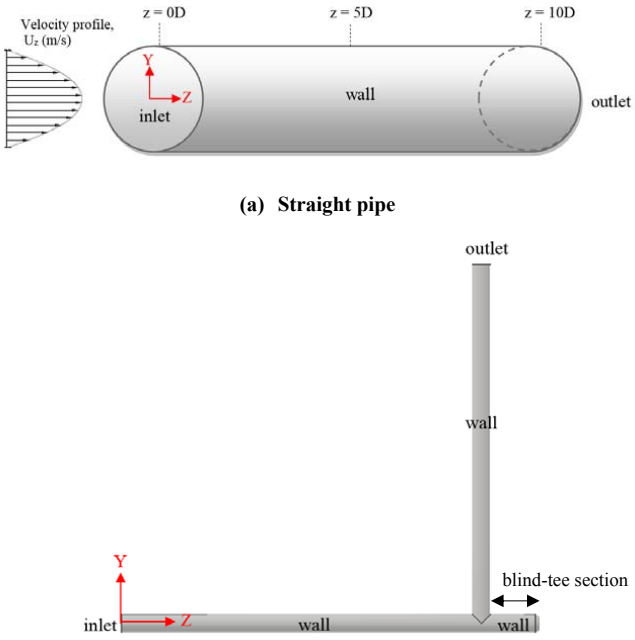

(a) Straight pipe

(b) Blind-tee pipe

Figure 2. Computational domains and boundary conditions for the straight pipe and the blind-tee pipes.

a) Inlet

A developed velocity profile with the initial average velocity equal to 1 m/s is computed analytically based on the classical formula given in Cengel and Cimbala [10] (i.e. $U_{z,average} = 1$ m/s). The equation of the velocity profile is $U_z\,(r) = 2U_{z,average}\ (1 - r^2/R^2)$, where R is the radius

of the pipe and r is the radial distance from the centre of the pipe. The computed velocity profile is set at the inlet in order to save the simulation time and avoid using a very large computational domain. The pressure boundary condition at the inlet is set as zero normal gradient.

b) Wall

On the internal walls of the pipe, a non-slip boundary condition is prescribed and the pressure boundary condition is set as zero normal gradient.

c) Outlet

At the outlet, the velocity boundary condition is set as zero normal gradient and the pressure boundary condition is set to be zero.

3 RESULTS AND DISCUSSION

3.1 Straight pipe

Three-dimensional CFD simulations have been performed to compute the flow in a straight pipe with D = 1m and the pipe length (L) = 10D at Re = 1000, where $U_{z,average}$ = 1 m/s and ν = 0.001 m^2/s. A grid convergence study is carried out with Mesh 1 = 36000 elements, Mesh 2 = 55120 elements and Mesh 3= 71928 elements, as well as Maximum Courant number = 0.125. Figure 3 show the present predicted U_z velocity profiles of Mesh 1, Mesh 2 and Mesh 3 with respect to r = -0.5D to 0.5D at the location z = 5D. The computed analytical solution of the velocity profile has been used as the inlet velocity profile. The corresponding analytical solution of the velocity profile is also included in the figure for comparison. It appears that Mesh 1 with 36000 elements give sufficient numerical accuracy, and the predicted velocity profile is in good agreement with the analytical solution.

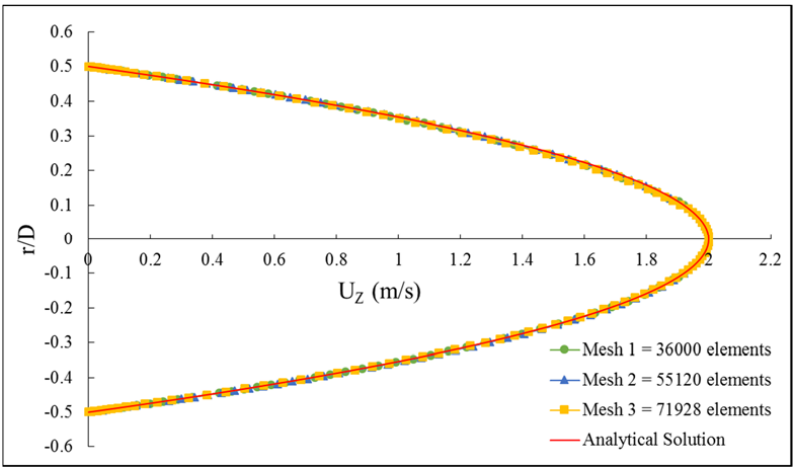

Figure 3. Cross-sectional velocity profiles for the grid convergence study of the straight pipe case.

A time-step convergence study has been performed for Mesh 1 (36000 elements) with three different Maximum Courant numbers, i.e. 0.125, 0.2, 0.3. Figure 4 shows the results of the time-step convergence study. It appears that the simulation with the maximum Courant number = 0.3 is found to be sufficiently accurate as compared to the analytical solution.

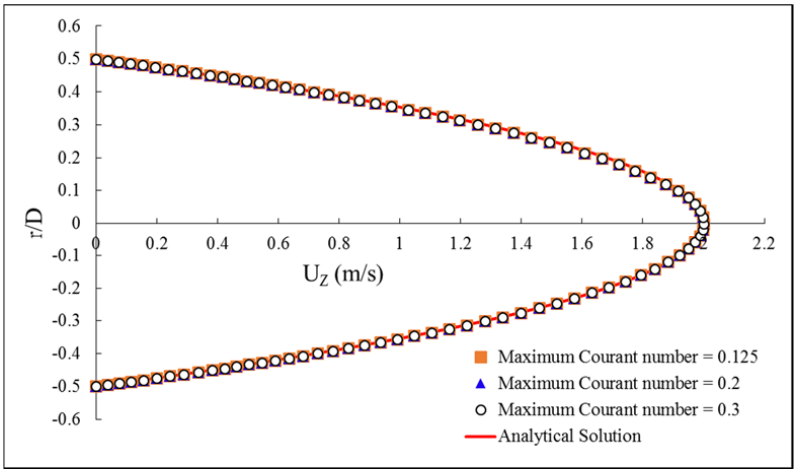

Figure 4. Cross-sectional velocity profiles for the time-step convergence study of the straight pipe case.

Overall, it appears that the mesh with 36000 elements (Mesh 1) with the maximum Courant number = 0.3 gives sufficient numerical accuracy and the predicted velocity profile is in good agreement with that of the analytical solution.

3.2 Blind-tee pipes

The flow prediction for the straight pipe case discussed in Section 3.1 showing an approach to achieve a fully developed laminar pipe flow can be utilized for simulating flow physics in the blind-tee pipes. The fully developed velocity profile at Re = 1000 which is obtained from the straight pipe case is set as the velocity profile at the inlet of the blind-tee pipes. 3D CFD simulations of flow in blind-tee pipes with 5 different blind-tee lengths (BTL=1D, 2D, 3D, 4D, 5D) are performed in the present study. The main objective is to investigate numerically how the increment of blind-tee length affects the fluid mixing inside the blind-tee pipes.

Grid resolution tests have been performed for all the cases. Here the case with BTL = 4D is chosen to show the comparison of the cross-sectional velocity profiles at Location A (y, z) = (0, 5D) and Location B (y, z) = (0, 15D) obtained from the simulations with 184350 mesh elements and 269862 mesh elements, respectively, with a maximum Courant number = 0.3. Figure 5 shows the locations where the cross-sectional velocity profiles are extracted for comparison.

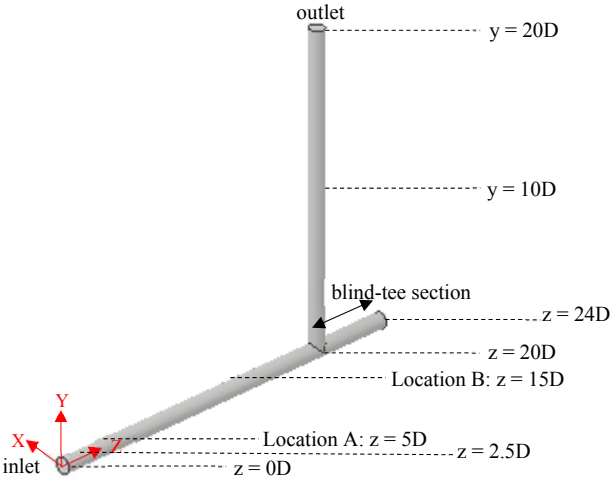

Figure 5. Locations where the cross-sectional velocity profile is extracted for the case with BTL = 4*D*.

Figure 6 shows the comparison of the instantaneous cross-sectional velocity profiles at Locations A and B (shown in Figure 5) for the simulations with 184350 mesh elements and 269862 mesh elements. It is clearly seen that the cross-sectional velocity profiles for the simulations with 184350 mesh elements and 269862 mesh elements are close to each other. Therefore, the mesh with 184350 elements is considered to have sufficient grid resolution.

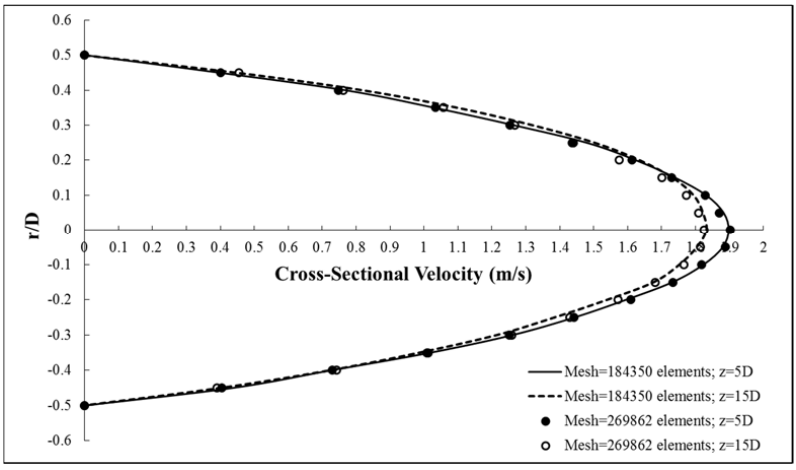

Figure 6. Instantaneous cross-sectional velocity profiles for the grid resolution test of the blind-tee pipe with BTL = 4*D*.

Figure 7 shows the comparison of the instantaneous cross-sectional velocity profiles at the selected locations (i.e., $z = 2.5D$, $z = 5D$, $z = 15D$ and $y = 10D$ shown in Figure 5) together with the velocity profile at the inlet (the analytical solution). It is clearly seen that the maximum velocity decreases when the fluid flows towards the blind-tee section. Flow circulation and vortices are generated due to the existence of the blind-tee section and the pipe bend (see Figure 8(d) for the flow visualization). Therefore, the instantaneous cross-sectional velocity profile at $y = 10D$ does not have a parabolic shape which is different from the velocity profiles at $z = 2.5D$, $z = 5D$ and $z = 15D$.

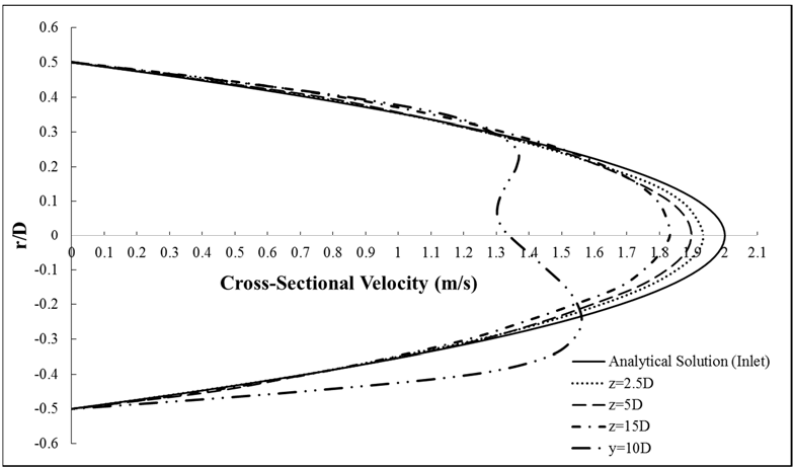

Figure 7. Instantaneous cross-sectional velocity profiles at locations $z = 2.5D$, $z = 5D$, $z = 15D$ and $y = 10D$ for the blind-tee pipe with BTL = 4*D*.

Three dimensional laminar flow simulations in blind-tee pipes with BTL=1*D* to 5*D* have been carried out at Re = 1000. The instantaneous streamlines of the in the blind-tee pipes with BTL = 1*D* to 5*D* are shown in Figure 8(a) to (e). The streamlines are colored by the U_z contour ranges from -0.8 m/s to 2m/s.

By plotting the streamlines of the fluid flow inside the investigated pipes, the behavior of how the fluid is flowing can be observed clearly. It can be seen that the streamlines coming from the inlet, show straight lines. When they reach the blind-tee section, some fluid flows towards the outlet and some fluid flows towards the blind-tee section. Since the end of the blind-tee section is blanked-off, the fluid is trapped in this part. As the result, when the fluid flow hits the blanked-off side, it flows back and creates flow circulation.

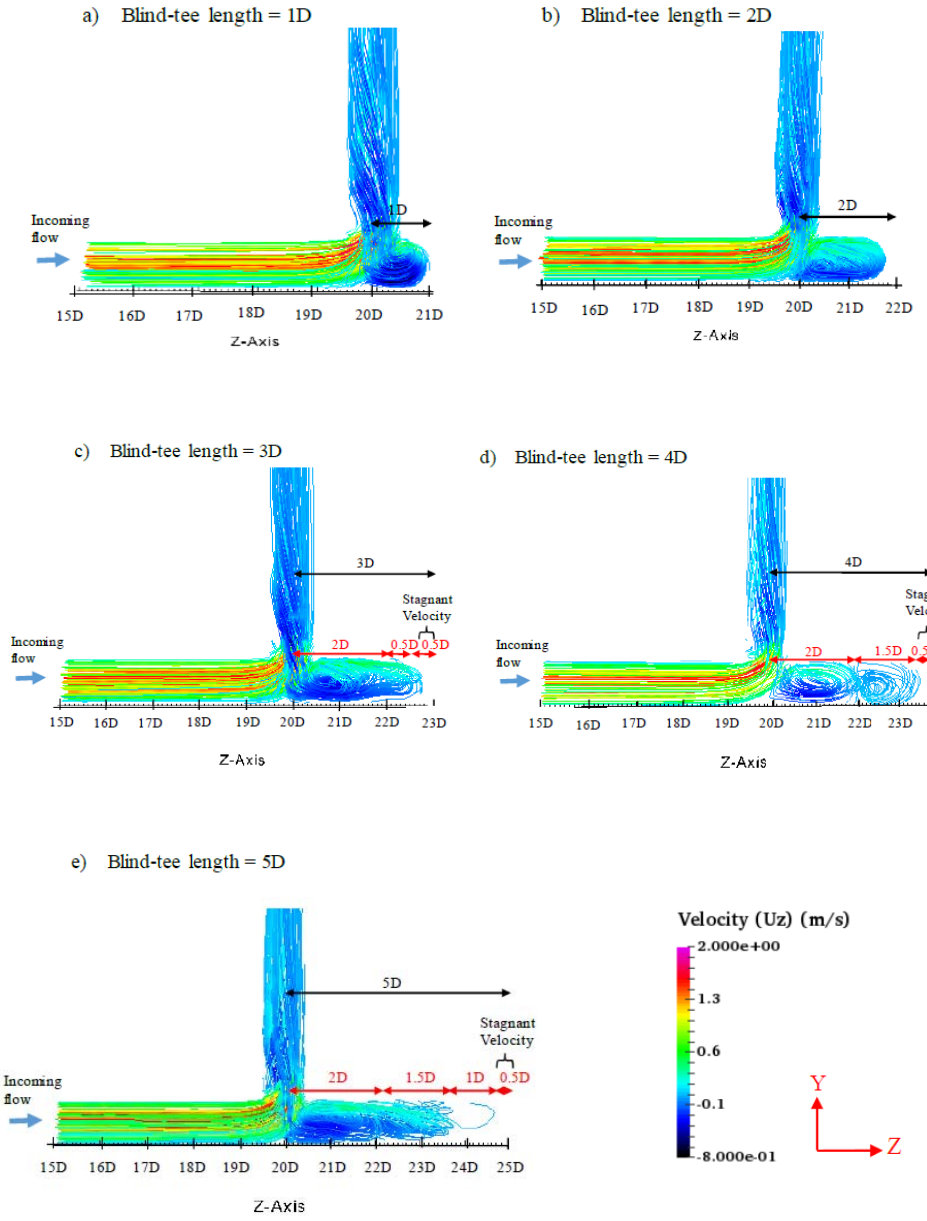

Figure 8. Instantaneous streamline plots for the blind-tee pipes with BTL = 1*D* to 5*D*. The typical values of U_z at $y = 5D$ range from -0.016 m/s to 0.197 m/s.

The flow circulation inside the blind-tee sections shows different sizes according to the length of the blind-tee section. For the blind-tee pipe with BTL = 1*D*, the flow circulation size is 1*D*. For the blind-tee pipe with BTL = 2*D*, the flow circulation size is 2*D*. When BTL is larger than 2*D*, a second flow circulation in the blind-tee section begins to appear. For the blind-tee pipe with BTL = 3*D*, the size of the first flow circulation is 2*D*. The second flow circulation with a size of 0.5*D* is formed even though it appears to have a vague shape, see Figure 8(c). For the blind-tee pipe with BTL = 4*D*, it can be clearly seen that the two flow circulations occur. The first flow circulation size inside this particular blind-tee pipe is 2*D*. The second flow circulation has a size of 1.5*D*. The second flow circulation can be taken as a stagnant flow circulation, since the fluid exchange between this flow circulation and the flow in the main pipe is observed to be limited. Figure 8(e) shows that three flow circulations are created inside the blind-tee pipe with BTL = 5*D*. The size of the first two flow circulations are 2D and 1.5D, respectively. The third flow circulation starts to develop. However, the strength of the third flow circulation is obviously weak. It seems that the fluid there becomes almost fully stagnant.

Generally, it can be concluded that the flow which is trapped inside the blind-tee section with BTL < 2*D* forms one flow circulation, while for BTL > 2*D*, more than two flow circulations are formed. It appears that the maximum capability of the first flow to create circulation inside the blind-tee section is only limited to the size of 2*D*. The size of the next flow circulation is 1.5*D* which is smaller than that of the first flow circulation. It means that the flow becomes weaker when it travels towards the end of the blind-tee section; and this is physically sound.

Figures 9(a) – 9(e) show the pressure contour in the five investigated blind-tee pipes. It can be clearly seen that the pressure in the blind-tee section increases as the length of the blind-tee section increases. It means that more stagnant fluid exists for the blind-tee pipes with longer blind-tee section. This observation is consistent with the flow characteristics observed in the streamlines plots Figure 8(a) - 8(e).

By summarizing the aforementioned findings for *Re* = 1000 in the present study, the blind-tee section can improve the mixing of the multiphase fluid, provided that the length of the blind-tee section should be less than 2*D*. For BTL > 2*D*, stagnant flow circulation is observed and this will cause fluid deposition (i.e. bad fluid-mixing condition).

4 CONCLUSION

Laminar flows in blind-tee pipes with the blind-tee section length varying from 1*D* to 5*D* at *Re* = 1000 have been investigated using three-dimensional CFD simulations. The main objective is to study the effect of the blind-tee section length on the fluid mixing condition in the blind-tee pipes. The flow physics are discussed by investigating the streamlines and the pressure contour in the blind-tee pipes.

It is found that when the length of the blind-tee section is less than 2*D*, the fluid in the blind-tee section has a good mixing condition. When the length of the blind-tee section is larger than 2*D*, at least two flow circulations are formed in the blind-tee section. The second flow circulation has limited fluid exchange with the flow in the main pipe. The size of the second flow circulation is smaller than the size of the first flow circulation. For the blind-tee pipes

with the blind-tee length larger than 4*D*, stagnant flow is observed towards the end of the blind-tee section; and this will generally cause the fluid deposition.

Experimental data are required before a conclusion regarding the validity of this numerical approach can be given. In the meantime, this method should be useful as an engineering tool for understanding the flow physics in blind-tee pipes.

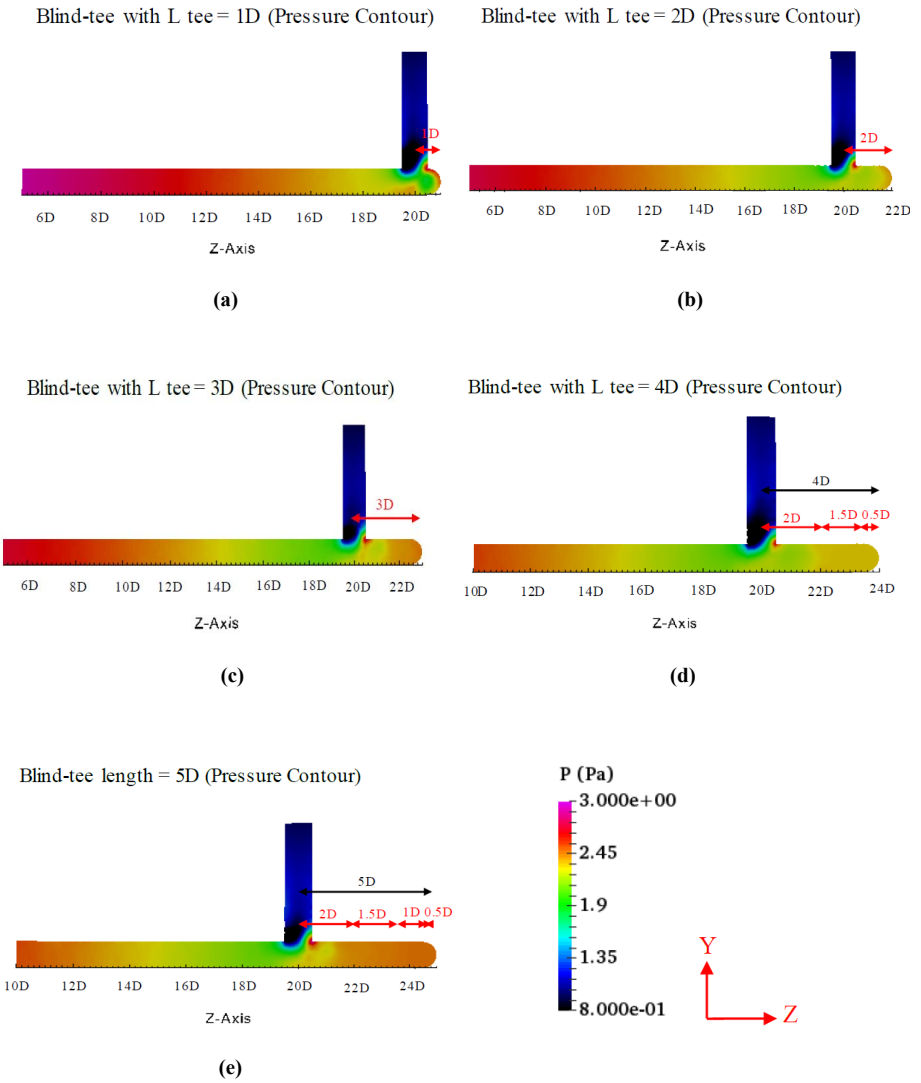

Figure 9. Pressure contours for the blind-tee pipes with BTL = 1*D* to 5*D*.

ACKNOWLEDGEMENT

The authors would like to thank Mr. Zhong Li for his technical assistance. This study was supported in part with computational resources provided by the Norwegian Metacenter for Computational Science (NOTUR), under Project No: NN9372K.

REFERENCES

[1] Hornbeck, R. Laminar flow in the entrance region of a pipe. *Applied Scientific Research*. (1964):224-232.

[2] Friedmann, M., Gillis, J. and Liron, N. Laminar flow in a pipe at low and moderate Reynolds numbers. *Applied Scientific Research*. (1968) **19(1):**426-438.

[3] Shirayama, S. and Kuwahara, K. Computational study of flow in a curved pipe with circular cross section. *KSME Journal*. (1987) **1**:52-59.

[4] Costa, N.P., Maia, R., Proença, M.F. and Pinho, F.T. Edge effects on the flow characteristics in a 90 deg Tee junction. *Journal of Fluids Engineering*. (2006) **128**:1204-1217.

[5] Vasava, P.R. *Fluid Flow in T-Junction of Pipes*. Master Thesis, Lappeenranta University of Technology (2007).

[6] Cade, M., Lima, W., Farias Neto, S. and Lima, A. Natural gas laminar flow in elliptic cylindrical pipes: a numerical study. *Brazilian Journal of Petroleum and Gas*. (2010) **4**:19-33.

[7] Beneš, L, Louda, P., Kozel, K.,Keslerová, R. and Štigler, J. Numerical simulations of flow through channels with T-junction. *Applied Mathematics and Computation*. (2013) **219(13)**:7225-7235.

[8] Weller, H.G., Tabor,G., Jasak,H. and Fureby,C. A tensorial approach to computational continuum mechanics using object-oriented techniques. *Computers in Physics*. (1998) **12**:620-631.

[9] OpenFOAM. *OpenFOAM: Standard Solvers.* http://www.openfoam.org/features/standard-solvers.php (2011) [Accessed 2 May 2016].

[10] Cengel, Y. and Cimbala, J. *Fluid Mechanics*. 3rd Edition, Mc Graw Hill Education, Singapore. (2014).

9. National Conference on Computational Mechanics
MekIT'17
B. Skallerud and H I Andersson (Eds)

A NUMERICAL INVESTIGATION OF EROSION AROUND OFFSHORE PIPELINES

Nadeem Ahmad[1], Hans Bihs[1], Arun Kamath[1], Øivind A. Arntsen[1]

[1]Department of Civil and Environmental Engineering
Norwegian University of Science and Technology
Trondheim 7491, Norway
e-mail: nadeem.ahmad@ntnu.no

Key words: Pipeline, sea bed materials, Tunnel and lee-wake erosion, Keulegan-Carpenter number, Wave hydrodynamics, REEF3D.

Abstract. In this paper, a numerical investigation is carried out to model sea bed erosion around offshore pipelines deployed at the shoreline. The open-source CFD model REEF3D is used for the numerical modeling. The model solves the Reynolds-averaged Navier-Stokes equations to calculate the flow hydrodynamics. Turbulence around the pipeline under the wave action is calculated using the $k-\omega$ model. The convective terms of the governing equations are discretized using the fifth-order finite difference WENO scheme. The free surface is captured with the level set method. The morphological evolution of the erosion process is calculated based on the simulated hydrodynamics. A fully coupled hydrodynamics-sediment model is used in the present study. For a more realistic capturing of the sea bed deformation, the modified critical bed shear stress on a sloping bed together with a sand slide algorithm is implemented in the model. The sea bed elevations are captured based on the Exner formula. The numerical model is validated against the experimental data for pipeline erosion under the influence of waves. A good agreement between experimental data and simulated results is observed. The numerical model is then utilised to simulate the erosion around offshore pipelines placed on different sea bed materials namely silt, coarse sand and very coarse sand. The temporal variation of the maximum erosion beneath the pipeline, erosion extent and the magnitude for different sea bed materials are presented and discussed. It is found that the silt sea bed offers more sea bed stability compared to the very coarse sand sea bed. Furthermore, the effect of the Keulegan-Carpenter (KC) number on the maximum erosion beneath the pipeline is also investigated. It is observed that the maximum erosion beneath the pipeline increases with KC number.

1 INTRODUCTION

The oil and gas from the offshore production facilities are generally transported through subsea pipelines. The stability of these subsea pipelines is threatened due to the loss of sea bed support. Since the pipelines on the shoreline in shallow water are exposed to continuous wave action, the sea bed material is eroded, forming a bowl-shaped depression beneath the pipelines. When the extent of the scour becomes long enough along the pipeline, the pipe sags, resulting in lateral instability and leakages in the pipeline. Hence, a detailed study is necessary to investigate pipeline erosion for different types of sea bed materials such as silt, coarse sand and very coarse sand as well as for different wave conditions.

In current literature, there are several experimental studies, analytical and numerical models to investigate sea bed erosion around pipelines e.g. [1] [2] [3] [4] [5]. These studies discuss the steady state and oscillatory flow hydrodynamics around pipelines using different turbulence models e.g. k-ϵ, standard k-ω and Wilcox high-Reynolds-number k-ω turbulence model. Finally, the maximum erosion and the temporal development of pipeline erosion process under waves and current action are analysed. Recently, Fuhrman et al. (2014) [6] developed a 2D numerical model for local scour around pipelines under wave action. The flow field is solved using the $k-\omega$ turbulence model. A fully coupled modeling approach is applied to simulate scour for different KC numbers. The simulated results agree well with the experimental observations. Additionally, the wave-induced backfilling process is also studied. The limitation of the model is that it overlooks the discussion about nonlinear wave generation and free surface calculation. Liu et al. (2016) [7] developed a 2D dimensional numerical model to predict local scour around pipelines. Instead of being simplified to oscillatory flow, the wave motion is modeled using a fully nonlinear wave model. The numerical investigations suggested the necessity of utilising the free surface wave model rather than the simplified oscillatory flow model to study local scour around pipelines. The study focuses more on erosion on sloping sea beds rather than the different parameters affecting pipeline erosion such as the effect of the sea bed material, the temporal evolution of the erosion process and the wave conditions.

The objective of the present paper is to develop a numerical model that is capable of predicting the temporal evolution of erosion below a pipeline for different sea bed materials. The model calculates the wave hydrodynamics along with the $k-\omega$ model for turbulence. The wave generation and absorption are carried out using the active wave generation and absorption method. The free surface is obtained with the level set method. The simulated flow field is linked with sediment transport algorithms where the updated morphology is captured with the Exner formulation. A sand slide model is employed to update the bed profile. The simulated scour profile is verified against experimental observations carried out by Sumer and Fredsøe (1990) [2]. Finally, the study discusses the results for pipeline erosion for different sea bed materials and wave conditions.

2 NUMERICAL MODEL

2.1 Hydrodynamic Model

The open-source CFD model REEF3D [8] [9] is used for the numerical modeling of the wave hydrodynamics and the erosion process. It solves the incompressible Reynolds-Averaged Navier-Stokes (RANS) equations, along with the continuity equation to calculate the velocity field in the numerical wave tank. The continuity and momentum equations are shown below:

$$\frac{\partial u_i}{\partial x_i} = 0 \tag{1}$$

$$\frac{\partial u_i}{\partial t} + u_j \frac{\partial u_i}{\partial x_j} = -\frac{1}{\rho}\frac{\partial p}{\partial x_i} + \frac{\partial}{\partial x_j}\left[(\nu + \nu_t)\left(\frac{\partial u_i}{\partial x_j} + \frac{\partial u_j}{\partial x_i}\right)\right] + g_i \tag{2}$$

where u_i is the velocity averaged over time t, p is the pressure, ρ is the density of water, ν is the kinematic viscosity of the water, ν_t is the eddy viscosity, g is the gravitational acceleration. The k-ω model [10] is used to calculate eddy viscosity by solving the two variables namely, the turbulent kinetic energy (k) and the specific turbulent dissipation (ω). Detailed description of the hydrodynamic and turbulence model can be found in [8].

2.2 Numerical schemes and solver

The model approximates spatial derivatives using advanced finite difference methods on a Cartesian grid, where the convective terms of the momentum equations are discretized with the fifth-order accurate Weighted Essential Non-Oscillatory (WENO) scheme developed by Jiang and Shu (1996) [11]. The convective terms of the turbulence model and the level set function are discretized with the Hamilton-Jacobi formulation of the WENO scheme proposed by Jiang and Shu (2000) [12]. A TVD third-order Runga-Kutta time scheme [13] is used for time stepping of the governing equations. The hydrodynamic time step for the transient flow field is calculated with adaptive time stepping [14]. The pressure is solved using the projection method proposed by Chorin (1996) [15]. The preconditioned conjugate gradient (PCG) solver from the high-performance solver package HYPRE [16] with a semi-coarsening multi-grid solver PFMG, is implemented to solve the Poison equation. An immersed boundary method with a local directional ghost cell approach [17] is used to define boundary conditions for complex geometry.

2.3 Morphological model

The simulated flow field from the hydrodynamic model is used to calculate the sediment transport process using the morphological model in REEF3D [18] [19] [20] [21]. The morphological model is implemented as follows. The bed stress on the sea bed is calculated using the hydraulically rough wall function. Hence, the shear velocity near the sea bed boundary layer is determined using the velocity from the nearest cell by considering a

logarithmic velocity profile near the sea bed. The bed shear stress (τ) is defined as follows:

$$\frac{u}{u^*} = \frac{1}{\kappa}\, ln\left(\frac{30z}{k_s}\right) \quad and \quad \tau = \rho u^{*2} \tag{3}$$

where u is the velocity, u^* is the shear velocity, $\kappa = 0.4$ is the von Karman constant, z is the vertical height above the sea bed to the nearest cell center, k_s is the Nikuradse's equivalent sand roughness, d_{50} is the median grain size. The bedload calculations are made with the bedload formulation proposed by van Rijn (1984) [22]. The particle mobility is calculated by subtracting the modified critical bed stresses [Eqs.6] from the actual bed stresses [Eqs.3]

$$\frac{q_{b,i}}{d_{50}^{1.5}\sqrt{\frac{(\rho_s-\rho_w)g}{\rho_w}}} = 0.053\frac{\left(\frac{\tau-\tau_{c,i}}{\tau_{c,i}}\right)^{2.1}}{\left(\left(\frac{\rho_s/(\rho_w-1)g}{\nu^2}\right)^{1/3}\right)^{0.3}} \tag{4}$$

where, $q_{b,i}$ is the bedload transport, $\tau_{c,i}$ is the critical bed shear stress, ρ_s is the sediment density, ρ_w the water density, g is the gravity, d_{50} is the median particle diameter, ν is the kinematic viscosity of water.

The critical bed shear stress calculated using the Shields diagram approach might lead to underestimation of the sediment transport because it does not account for the effects of the sloping bed. This problem is handled with the modified critical shear formulation on sloping beds proposed by Dey (2003) [23]. The effect of the sloping bed is accounted for by considering the longitudinal bed slope θ, the transverse bed slope α, the angle of repose φ and the drag and lift forces. The expression for the bed shear stress reduction factor r is defined as follows:

$$\begin{aligned} r = \frac{1}{\left(1-\eta\tan\varphi\right)\tan\varphi}\Big\{&-\left(\sin\theta+\eta\tan^2\varphi\sqrt{\cos^2\theta-\sin^2\alpha}\right) \\ &+\left[\left(\sin\theta+\eta\tan^2\varphi\sqrt{\cos^2\theta-\sin^2\alpha}\,\right)^2\right. \\ &\left.+\left(1-\eta^2\tan^2\varphi\right)\left(\cos^2\theta\tan^2\varphi-\sin^2\alpha\tan^2\varphi-\sin^2\theta-\sin^2\alpha\right)\right]^{0.5}\Big\} \end{aligned} \tag{5}$$

where η is the ratio of the drag force to the inertia force. Finally, the modified critical bed stress (τ_c) is calculated by multiplying the reduction factor r with the bed shear stresses τ_0 calculated from Eq. 3 as follows:

$$\tau_c = r \cdot \tau_0 \tag{6}$$

The change in bed elevations is calculated with the Exner formula. The method is based on the conservation of the sediment mass where the horizontal spatial variation in the bedload is conserved with the spatial change in the vertical z-direction. The morphological evolution occurs as a nonlinear propagation of the bed level deformations in the direction

of the sediment transport. The formulation for the transient change in bed level is given as follows:

$$\frac{\partial z_b}{\partial t} + \frac{1}{(1-n)} \left[\frac{\partial q_{bi,x}}{\partial x} \right] + E - D = 0 \tag{7}$$

where z is the bed-level, $q_{bi,x}$ is the bedload in the x direction, n is the sediment porosity, D is the deposition rate, expressed as volume of sediment grain settling and E is the entrainment rate, sediment grains settling from the suspension.

3 NUMERICAL SETUP

The computational setup is practically the same as the one employed by Sumer and Fredsøe (1990) [2]. The water depth is 0.4 m and the maximum velocities are $u_m = 0.23$ m/s. The sea bed material consists of coarse sand with $d_{50} = 0.58$ mm. The Shields parameter for the sea bed material is $\theta_c = 0.11$. The coarse sand sea bed is assumed to be hydraulically rough. The roughness height k_s is maintained at $3d_{50}$, which is a widely accepted value for the Nikuradse roughness (k_s) on a flat sea bed. The wave amplitude a = 0.06 m and wave length $\lambda = 5$ m, are calculated based on the maximum velocities u_m = 0.23 m/s and wave period $T = 1.43$ s. Accordingly, the KC number is calculated to be KC = $u_m T/D = 7$. Here D is the diameter of the pipeline.

The numerical test for the sea bed erosion around the pipelines are conducted in a 2D numerical wave tank. It is 2.54 m long and 1 m high including a 0.3 m sea bed with a water depth of $d = 0.4$ m . The length of the NWT is assumed to be half of the wave length i.e. $l = \lambda/2$. A pipeline of diameter $D = 0.05$ m is fixed on the sea bed. The 5th-order Stokes waves are chosen based on incident wave characteristics. The active wave generation and absorption method [24] is used for the wave generation in the numerical wave tank by prescribing the wave elevation η and the wave velocities at the inlet. The reflected waves from the end of the domain are managed using negative of corrected velocity u_c, which is described as follows:

$$u_c = \sqrt{\frac{g}{d}}.\eta_r \tag{8}$$

where η_r is reflected wave amplitude which is defined as:

$$\eta_r = \eta_m - h \tag{9}$$

where η_m is measured free surface elevation, h is the still water level in the tank. The free surface is captured using the level set method [25]. It uses a continuous signed distance function $\phi(x,t)$ to define the interface between two immiscible fluids, which is defined as follows:

$$\phi(\vec{x},t) \begin{cases} > 0 & if\ \vec{x}\ is\ in\ phase\ 1 \\ = 0 & if\ \vec{x}\ is\ at\ the\ interface \\ < 0 & if\ \vec{x}\ is\ in\ phase\ 2 \end{cases} \tag{10}$$

Here ϕ (x,t) is calculated using convection equations with externally generated velocity field u_j from RANS equations.

$$\frac{\partial \phi}{\partial t} + u_j \frac{\partial \phi}{\partial x_j} = 0 \tag{11}$$

4 GRID CONVERGENCE STUDY

The numerical tests are conducted in a 2D numerical wave tank (NWT). The purpose of the tests is to determine the minimum grid size required to maintain wave quality. The length of the NWT is equal to half of the wavelength i.e. L = 2.5 m. The active wave absorption (AWA) is used for the wave generation in the NWT. One probe is fixed at the center location of the tank where the pipeline is suppose to be fixed. Different grid sizes dx = 0.04 m, 0.03 m, 0.02 m, and 0.01 m are tested. Results discuss the wave accuracy of the wave by one-to-one comparisons between wave theory and numerically simulated results. It is found that wave accuracy increases with finer grid size and the solution is assumed to be converged at dx = 0.01 m.

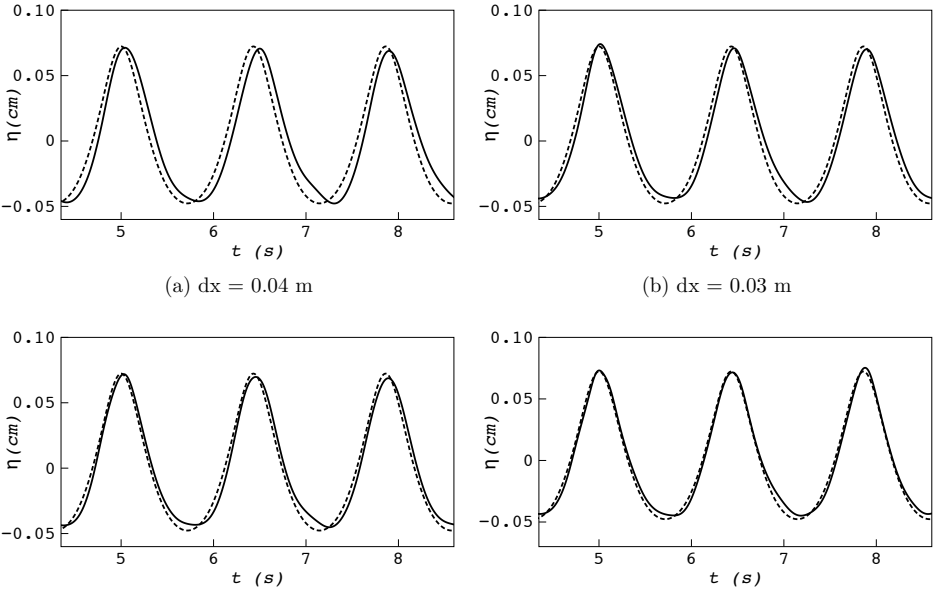

(a) dx = 0.04 m (b) dx = 0.03 m

(c) dx = 0.02 m (d) dx = 0.01 m

Figure 1: Comparison between simulated and theoratical free surafce elevation for the grid convergence study. Black solid line: simulated; dotted line: theoretical

5 RESULTS

5.1 Sea bed erosion around the pipeline

The first set of the numerical analysis investigates the erosion process beneath the pipeline. The simulation is run as a fully coupled model until equilibrium erosion is achieved. The results are captured at three different time intervals t = 0.2, 5 and 55 minutes. Numerical results suggest that pipeline erosion evolves through three stages. The first stage is the onset stage. In this stage, the pipeline is assumed to be fully buried in the sea bed material and there is no gap for flow beneath the pipeline. The erosion is caused by the pressure difference between the upstream and downstream sides of the pipeline. Once a small gap is created by the onset erosion, the second stage of the pipeline erosion is initiated. At this stage, a strong water jet is formed in the gap between the pipeline and the sea bed. It increases the bed shear stress beneath the pipeline and results in quick erosion. This process is called tunnel erosion. This process is quick and develops maximum erosion within the first 5-10 waves incident on the pipeline. The final stage of the erosion is lee-wake erosion. It is initiated by the lee-wake at the upstream and downstream sides of the pipeline. The intensity and extent of the lee-wake erosion depends on the wave characteristics and the sea bed material beneath the pipeline. It might trigger additional erosion beneath the pipeline with the lee-wake erosion intruding into the tunnel eroded sea bed.

Fig. 2(a) shows a well-developed profile of tunnel erosion. The maximum erosion below the pipeline takes place within $t = 0.2$ minute. The upstream and downstream sides of the pipeline are found to be completely safe from lee-wake erosion. A good match between the simulated results and the experimental observation [2] is seen which indicates the robustness of the model in capturing tunnel erosion. Tunnel erosion is considered to be the most crucial stage because the maximum erosion beneath the pipeline takes place during this process. The prediction is also equally important from an engineering point of view. If intensive erosion takes place at an early stage of the erosion process, the design of protective measures cannot be avoided. Fig. 2(b-c) shows the lee-wake erosion at t = 5 and 55 minutes respectively. Results indicate that the erosion on the downstream side of the region is generated by the lee-wake vortices. The maximum erosion beneath the pipeline agrees with the experimental data but the erosion at the downstream side of the pipeline is slightly underestimated. The reason for the underestimation of the erosion might be the nature of the wake vortex at the upstream and downstream sides of the pipeline, which changes continuously with the development of the scour hole beneath the pipeline.

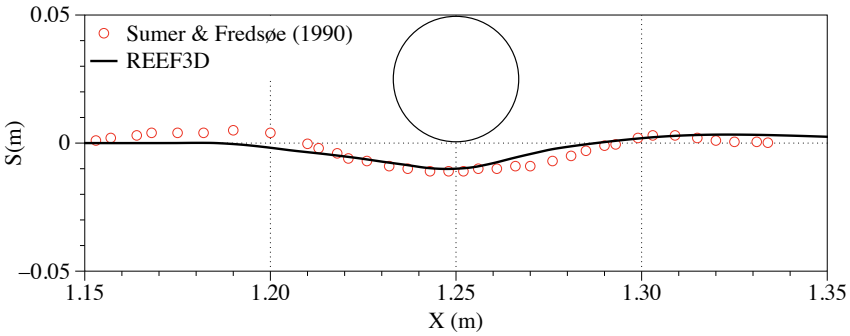

(a) t = 0.2 min

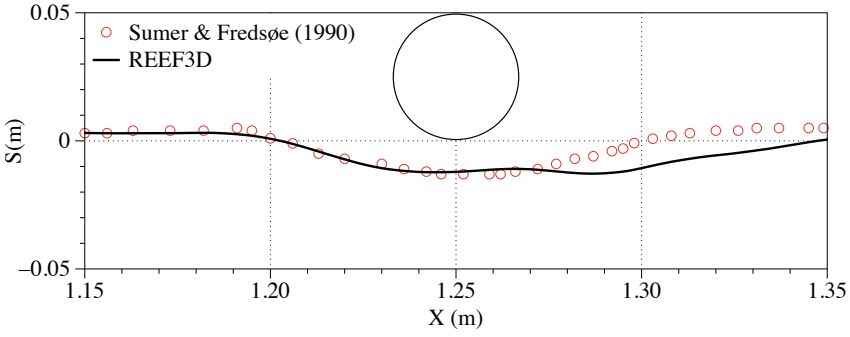

(b) t = 5 min

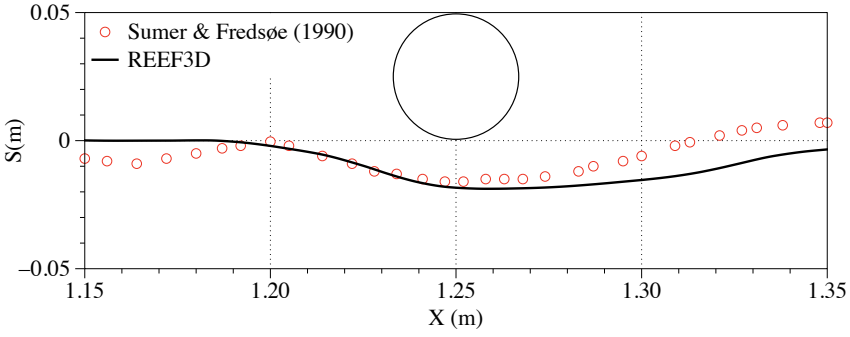

(c) t = 55 min

Figure 2: Time development of the pipeline erosion profiles on coarse sand sea bed, $\theta_c = 0.11$, $d_{50} = 0.58$ mm, KC = 7. Black solid line: simulated results; Red circles: Experiment by Sumer and Fredsøe (1990)[2]

5.2 Effect of sea bed material on erosion around pipeline

Three numerical tests are carried out to investigate the effect of the sea bed material on pipeline erosion. The sea bed materials selected for the tests are silt (d_{50} = 0.06 mm, θ_c = 0.17), coarse sand (d_{50} = 0.58 mm, θ_c = 0.11) and very coarse sand (d_{50} = 1 mm, θ_c = 0.035). Shields parameter for each test is calculated from the experimental observations [2] and the Shields diagram based on the median particle diameter. The input wave condition is same for all tests i.e. a = 0.06 m, T = 1.43 s and KC = 7. The fully coupled simulation is run until the equilibrium erosion state is achieved. Finally, the eroded profile around the pipeline and the temporal evolution of the maximum erosion are evaluated. Fig. 3(a) shows the eroded profile of the silt sea bed. It is seen that a small amount of erosion S_{max} = 5 mm takes place beneath the pipeline which indicates weak tunnel erosion. The result demonstrates the high shear strength of the sea bed against the low bed shear stress generated by the flow jet below the pipeline. There is no lee-wake erosion at the upstream and downstream sides of the pipeline which indicates ineffective lee-wake vortices against the high shear strength of the sea bed. Fig. 3(b) shows the eroded sea bed profile of the coarse sand sea bed. A maximum erosion of S_{max} = 20 mm takes place beneath the pipeline. However, the far upstream and downstream sides of the pipeline are moderately affected by the erosion. This signifies a strong tunnel erosion regime over the lee-wake erosion. Fig. 3(c) shows the eroded profile of the very coarse sand sea bed. The maximum erosion beneath the pipeline is 30 mm and the downstream side of the pipeline is adversely affected by the lee-wake erosion. The maximum erosion at downstream is almost S_{max} = 80 mm which indicates a strong influence of the lee-wake vortices on the very coarse sand sea bed material.

Table 1: Test conditions and results comparison

Parameters	Test1	Test 2	Test 3
Cylinder diameter D (mm)	50	50	50
Wave time period T (s)	4	4	4
Maximum bed orbital velocity U_m (m/s)	0.23	0.23	0.23
Wavelength λ (m)	5	5	5
Amplitude a (m)	0.06	0.06	0.06
KC number	7	7	7
Median grain size d_{50} (mm)	0.06	0.58	1
Critical Shields parameter θ_c	0.17	0.11	0.035
Simulated maximum scour depth S_{max} (mm)	5	20	80

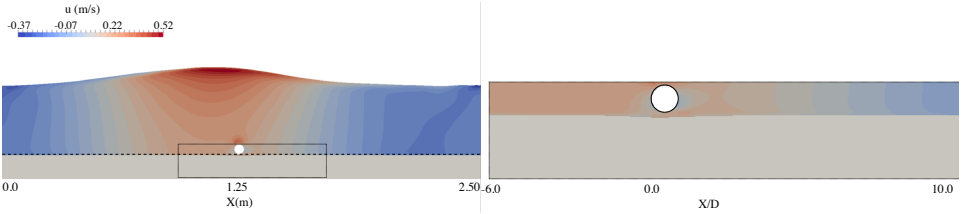

(a) Silt sea bed, $d_{50} = 0.06$ mm, $\theta_c = 0.17$ (b) Zoom in view of scour under the pipeline

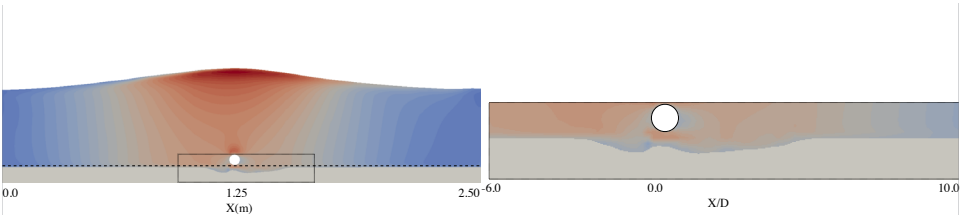

(c) Coarse sand sea bed, $d_{50} = 0.58$ mm, $\theta_c = 0.11$ (d) Zoom in view of scour under the pipeline

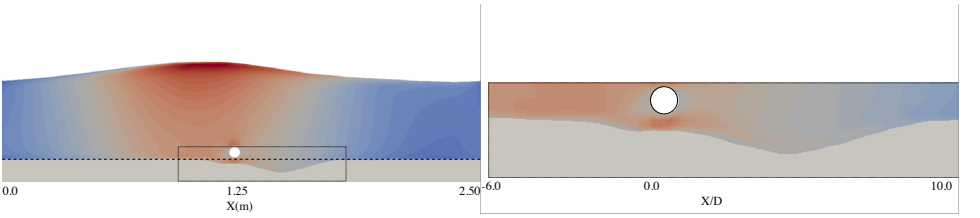

(e) Very coarse sand sea bed, $d_{50} = 1$ mm, $\theta_c = 0.035$ (f) Zoom in view of scour under the pipeline

Figure 3: Simulated free surface and the maximum erosion on different sea bed materials below the pipeline during the wave peak action. Black dotted line represents the initial sea bed level.

Fig. 4 represents the temporal development of the maximum erosion around the pipeline and non-dimensional scour depth S/D with θ_c. The fluctuation in the temporal evolution of the process represents erosion and refilling of the scour hole with back and forth action of the waves. Fig. 4(a) depicts the temporal evolution of the erosion process for the silt sea bed ($\theta_c = 0.17$). It is clearly seen that the maximum erosion takes place within the first $t = 20$ s. The wave propagation over the pipeline after $t = 20$ s, contributes to small fluctuations in erosion, while the resulting maximum erosion beneath the pipeline remains unaffected. Fig. 4(b) shows the temporal evolution of the maximum erosion for the coarse sand sea bed ($\theta_c = 0.11$). It is understood that a decrease in the shear strength of the sea bed results in higher erosion. Almost 20 mm of erosion takes

place within the first $t = 5$ s of wave action. It indicates an increase in tunnel erosion with a decrease in the sea bed strength. The small non-uniformity in the erosion pattern after $t = 5$ s, indicates interference of lee-wake erosion with tunnel erosion. Fig. 4(c) shows the temporal evolution of the pipeline erosion for very coarse sand sea bed. Almost 30 mm erosion takes place within $t = 5$ s which indicates a higher action of tunnel erosion on a very coarse sand sea bed. Furthermore, after t = 5 s, the temporal evolution of the process is non-uniform which indicates the presence of a strong lee-wake erosion at the upstream and downstream sides of the pipeline.

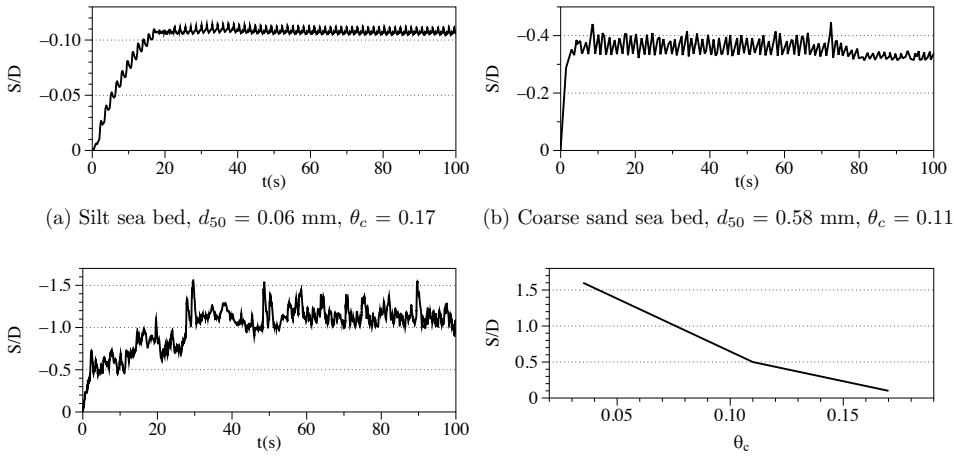

(a) Silt sea bed, $d_{50} = 0.06$ mm, $\theta_c = 0.17$

(b) Coarse sand sea bed, $d_{50} = 0.58$ mm, $\theta_c = 0.11$

(c) Very coarse sand sea bed, d_{50}=1 mm, $\theta_c = 0.035$

(d) S/D plotted against θ_c

Figure 4: Time development of the maximum erosion around the pipeline

Fig. 4(d) represents the variation of the non-dimensional scour depth S/D with critical Shields parameter (θ_c). Here S is the maximum scour depth and D is the pipeline diameter. It is interesting to note that the erosion pattern and magnitude increases with decreasing critical Shields parameter. The very coarse sand sea bed is more adversely affected by erosion compared to the silt sea bed.

5.3 Effect of KC number on erosion around pipeline

The numerical model is further tested for the calculation of the maximum erosion below the pipelines for different wave conditions by changing the KC number. Fig. 5 depicts the variation of the maximum scour depth S/D with the KC number. It is found that the maximum scour depth increases with increasing KC number. The present numerical results are also found to be consistent with the empirical formula based on experimental

observations by Sumer and Fredsøe (2002) [26], where, S/D = 0.1(KC)$^{0.5}$.

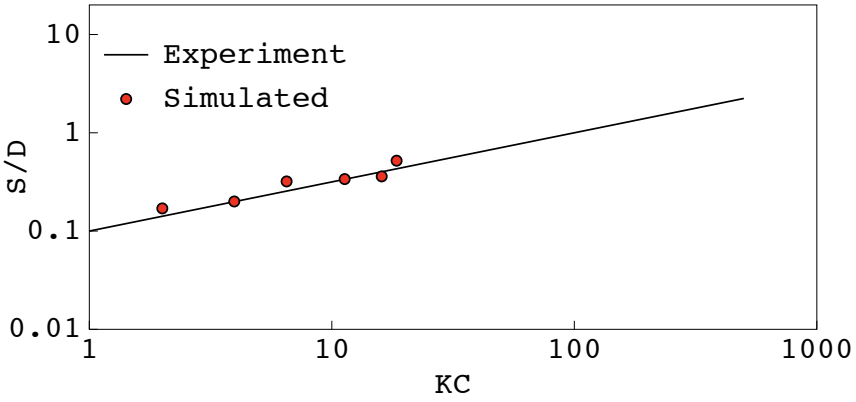

Figure 5: Maximum erosion beneath the pipeline plotted against KC. Coarse sand sea bed, $d_{50} = 0.58$ mm, $\theta_c = 0.11$

6 CONCLUSIONS

The open-source CFD model REEF3D has been developed to predict the erosion process around pipelines for different sea bed materials. A fully coupled modeling approach is implemented to investigate pipeline erosion. The bed deformation is calculated using the Exner formulation. A sand slide model is introduced to smooth out the morphological irregularities of scour profiles. The simulated results are verified against experimental data. Based on the numerical results, the following conclusions can be reached.

- The results for the erosion beneath the pipeline indicate that the model predicts the hydrodynamics and sediment transport with acceptable accuracy in a fully coupled manner. Also, the results for different sea bed materials indicate the possibilities for modeling the real field case studies including cohesive and active sediment in permafrost regions.

- For the silt sea bed, maximum erosion takes place under the pipeline only. While the upstream and downstream sides of the pipeline are found to be safe.

- Results suggest that tunnel erosion is a quick process which takes place within the first 5-20 s of the whole process.

- For the coarse sand sea bed, both tunnel erosion and lee-wake erosion are involved and the maximum erosion is governed by the tunnel erosion.

- For the very coarse sand sea bed, the maximum erosion is highly influenced by the lee-wake erosion.
- The maximum erosion increases with a decrease in the critical Shields parameter θ_c.
- Maximum erosion beneath the pipeline increases with the KC number.

7 ACKNOWLEDGEMENT

This research work is supported by funding received from the Polish-Norwegian Research Programme operated by the National Centre for Research and Development under the Norwegian Financial Mechanism 2009-2014 under the Project No. POL-NOR/200336/95/2014

REFERENCES

[1] Sumer, B., Jensen, H., Mao, Y. and Fredsøe, J. Effect of lee-wake on scour below pipelines in current. *Journal of Waterway, Port, Coastal, and Ocean Engineering* 1998. **114**(5):599–614.

[2] Sumer, B. and Fredsøe, J. Scour below pipelines in waves. *Journal of Waterway, Port, Coastal, and Ocean Engineering* 1990. **116**(3):307–323.

[3] Brørs, B. Numerical modeling of flow and scour at pipelines. *Journal of Hydraulic Engineering* 1999. **125**(5):511–523.

[4] Myrhaug, D., Ong, M.C., Fien, H., Gjengedal, C. and Leira, B.J. Scour below pipelines and around vertical piles due to second-order random waves plus a current. *Ocean Engineering* 2009. **36**(8):605 – 616.

[5] Liang, D. and Cheng, L. Numerical modeling of flow and scour below a pipeline in currents: Part I. flow simulation. *Coastal Engineering* 2005. **52**(1):25 – 42.

[6] Fuhrman, D.R., Baykal, C., Sumer, B.M., Jacobsen, N.G. and Fredsøe, J. Numerical simulation of wave-induced scour and backfilling processes beneath submarine pipelines. *Coastal Engineering* 2014. **94**:10 – 22.

[7] Liu, M.M., Lu, L., Teng, B., Zhao, M. and Tang, G. Numerical modeling of local scour and forces for submarine pipeline under surface waves. *Coastal Engineering* 2016. **116**:275 – 288.

[8] Bihs, H., Kamath, A., Alagan Chella, M., Aggarwal, A. and Arntsen, Ø.A. A new level set numerical wave tank with improved density interpolation for complex wave hydrodynamics. *Computers & Fluids* 2016. **140**:191–208.

[9] Bihs, H. and Kamath, A. A combined level set/ghost cell immersed boundary representation for floating body simulations. *International Journal for Numerical Methods in Fluids* 2017. **83**(12):905–916.

[10] Wilcox, D.C. *Turbulence modeling for CFD.* DCW Industries Inc., La Canada, California., 1994.

[11] Jiang, G.S. and Shu, C.W. Efficient implementation of weighted ENO schemes. *Journal of Computational Physics* 1996. **126**:202–228.

[12] Jiang, G.S. and Peng, D. Weighted ENO schemes for Hamilton-Jacobi equations. *SIAM Journal on Scientific Computing* 2000. **21**:2126–2143.

[13] Shu, C.W. and Osher, S. Efficient implementation of essentially non-oscillatory shock capturing schemes. *Journal of Computational Physics* 1988. **77**:439–471.

[14] Griebel, M., Dornseifer, T. and Neunhoeffer, T. *Numerical simulation in fluid dynamics: a practical introduction.* SIAM, 1998.

[15] Chorin, A. Numerical solution of the Navier-Stokes equations. *Mathematics of Computation* 1968. **22**:745–762.

[16] Falgout, R.D., Jones, J.E. and Yang, U.M. *Numerical Solution of Partial Differential Equations on Parallel Computers.* Springer Berlin Heidelberg, 2006. pp. 267–294.

[17] Berthelsen, P.A. and Faltinsen, O.M. A local directional ghost cell approach for incompressible viscous flow problems with irregular boundaries. *Journal of Computational Physics* 2008. **227**:4354–4397.

[18] Afzal, M.S., Bihs, H., Kamath, A. and Arntsen, Ø.A. Three-dimensional numerical modeling of pier scour under current and waves using level-set method. *Journal of Offshore Mechanics and Arctic Engineering* 2015. **137**(3):032001.

[19] Ahmad, N., Afzal, S., Bihs, H. and Arntsen, Ø.A. Three-dimensional numerical modeling of local scour around a non-slender cylinder under varying wave conditions. In: *36th IAHR World Congress, June 2015, The Netherlands.*

[20] Ahmad, N., Bihs, H., Kamath, A. and Arntsen, Ø.A. CFD modeling of local scour around a pair of tandem cylinders under wave conditions. In: *Proceedings - International Conference on Port and Ocean Engineering under Arctic Conditions, June 2015, Norway.*

[21] Ahmad, N., Bihs, H., Kamath, A. and Arntsen, Ø.A. Three-dimensional CFD modeling of wave scour around side-by-side and triangular arrangement of piles with REEF3D. *Procedia Engineering* 2015. **116**:683 – 690.

[22] van Rijn, L.C. Sediment transport, part I: Bed load transport. *Journal of Hydraulic Engineering* 1984. **110**(10):1431–1456.

[23] Dey, S. Threshold of sediment motion on combined transverse and longitudinal sloping beds. *Journal of Hydraulic Research* 2003. **41**(4):405–415.

[24] Schäffer, H.A. and Klopman, G. Review of multidirectional active wave absorption methods. *Journal of Waterway, Port, Coastal, and Ocean Engineering* 2000. **126**(2):88–97.

[25] Osher, S. and Sethian, J.A. Fronts propagating with curvature-dependent speed: algorithms based on Hamilton-Jacobi formulations. *Journal of Computational Physics* 1988. **79**:12–49.

[26] Sumer, B.M., Roulund, A., Fredsøe, J. and Michelsen, J. Three-dimensional numerical modeling of flow and scour around a pile. In: *Proc.,* 1*st International Conference on scour of foundations*. pp. 795–809.

9. National Conference on Computational Mechanics
MekIT'17
B. Skallerud and H I Andersson (Eds)

NUMERICAL SIMULATIONS FOR THE FLOW INSIDE THE PUMP AS TURBINE

ALESSANDRO NOCENTE[1], TUFAN ARSLAN[2] and ERKAN AYDER[3]

[1]Norwegian University of Science and Technology (NTNU)
Trodheim, Norway
e-mail: alessandro.nocente@n tnu.no/

[2]Norwegian University of Science and Technology (NTNU)
Trodheim, Norway
e-mail: tufan.arslan@ntnu.no/

[3]Istanbul Technical University (ITU)
Istanbul, Turkey
e-mail: aydere@itu.edu.tr /

Key words: Computational Method, CFD, Fluent, CFD, rotating machinery, pump, turbine, PAT

Abstract. In small hydroelectric plants, where the power production is small and the efficiency has not significant role, the use of pumps in inverse operation (pumps as turbine - PAT) can be an inexpensive solution for electricity production. The use of a pump instead of a turbine to transform the hydraulic power into mechanical power can be advantageous in particular circumstances. In fact, the cost of a pump can be much lower than the cost of a turbine. The object of this study is to evaluate the performance of a pump in turbine mode using CFD methods. Performance characteristics of a single stage centrifugal pump with spiral casing are calculated by using appropriate boundary conditions and the results were validated with experimental data. After this comparison, the performance of the pump in turbine mode was calculated using numerical methods. Results shows that head and flow rate at the best efficiency point are higher than the pump mode.

1 INTRODUCTION

Thanks to the recent developments in the field of electric motors and turbomachinery, today it is possible for pumped-storage hydroelectric plants to work with only one hydraulic/electric group instead of a two-groups system, i.e. pump/electric motor and turbine/generator. Both the electric and the hydraulic machines can, in fact, work in direct and inverse operation. This represents an investment cost much lower than the conventional solution. This solutions does not

decrease the overall efficiency which, especially for for small-sized hydro-plants. Small-sized installation became very interesting as an inexpensive method to recover energy in situation such as small rivers, or to replace the lamination valves in industrial processes [1]. A pump working in reverse operation is normally indicated as Pump as Turbine (PAT) [2], [3], [4].

The selection of the pump for the installation is the most challenging part of the plant design. In fact, the manufacturer provide all the information regarding the direct operation, but no data are given for PAT mode. Many scholars tried to obtain empirical equations to calculate the head and flow rate of the PAT in turbine mode starting from the given characteristics of the pump. The results are only approximations of the turbine hydraulic characteristics and give no information about the flow conditions in the machine [5]. For both modes, the hydraulic efficiency of the machine is the most important parameter in the design process and the working scenario of the plant must be considered carefully. That is rather easy to handle for pumps which will work on turbine mode and can be done by simply redesigning the impeller.

In this work, performance charts of a norm type single-staged end suction centrifugal pump designed with characteristics of Hm = 80 m, Q = 400 kg/s, P = 300 kW and n= 80% at best efficiency point is calculated with CFD methods for both pump and turbine mode and the curves are compared to test data for the pump mode.

2 COMPUTATIONAL DOMAIN

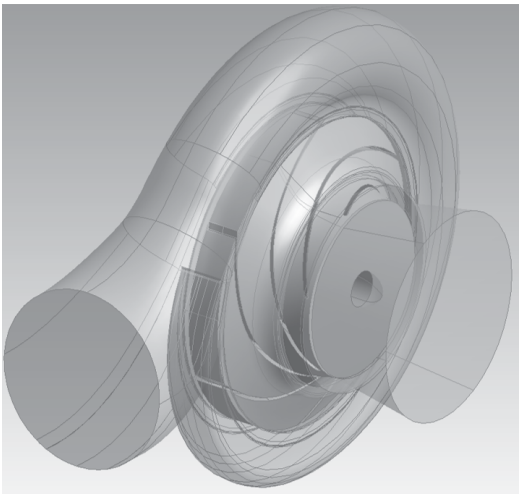

Figure 1: CAD representation of the numerical domain

Simulations were performed on the pump model provided by the company Turbosan [6]. The 3D model of the computational domain is shown in Fig. 1. Figure 2 illustrates the exploded view of the CAD model. The figure shows that the computational domain is formed by three volumes: the inlet pipe, the impeller and the volute fluid.

The computational model consists of tetrahedral, hexahedral and pyramidal type cells. A check done after the simulation shows in fact that the y^+ is in the range $30 < y^+ < 300$ for every time step. This allows to use proper wall modelling in calculation of the turbulence, as it will be further explained in the next section.

The effect of the design change (number of blades, blade angles, blade profile etc.) of the impeller on the performance will be investigated later. In Figure 3 the mesh is shown for three particular zones, represented by the squares on Fig. 1. Figure 3 a) shows the

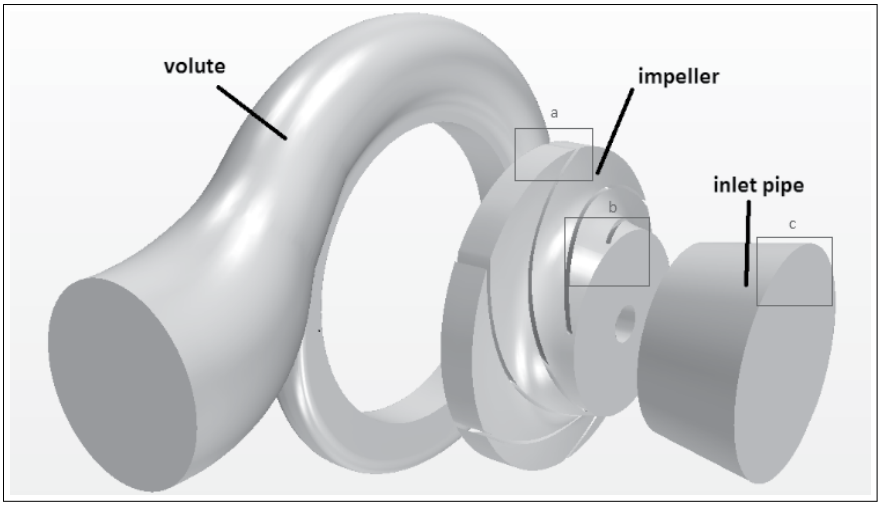

Figure 2: Exploded view of CAD model of the hydraulic machine

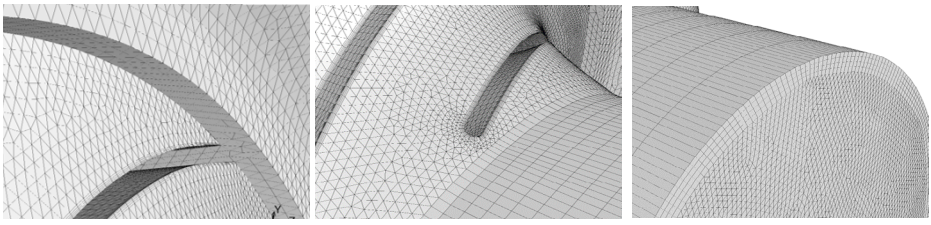

a) b) c)

Figure 3: Particulars of the computational mesh (5 million cells): a) interface between the rotor and the volute casing; b) interface between the rotor and the inlet pipe; c) inlet pipe

rotor and the volute casing mesh, including one of the rotor blades and the rotor-stator interface. The interface between the inlet pipe and the rotor is shown in Fig. 3 b) including the structural layer around the leading edge and the surface of the rotor blade. The mesh configuration of the inlet pipe and its structural layer on the external surface is shown in Fig. 3 c).

2.1 Boundary Conditions

No-slip wall condition has been specified for all the wall boundaries such as pipes, hubs, shrouds, blades plus the upper and lower wall of both the impeller and the volute. At the pipe inlet the mass flow is imposed for the pump mode. Atmospheric pressure is imposed at the diffuser outlet in order to calculate the head. Turbulent intensity is considered moderate and

it is imposed at 5 % at the inlet. For the turbine mode, inlet and outlet boundary conditions is swapped, mass flow is imposed to volute outlet and atmospheric pressure (zero gauge) is defined for the pipe inlet.

3 MATHEMATICAL MODELLING

The commercial software ANSYS Fluent was used for the calculation. The code uses a Finite Volume Method to solve steady and unsteady 3D Navier-Stokes equations. The turbulence is simulated by a realizable k-ε model with adequate wall modelling in most of the turbine mode and pump mode simulations. However, to show the effects of turbulence modelling, variants of k-ε model, k-ω model and Reynolds Stress Model (RSM) were used and the result were showed comparatively. The turbulence is simulated by five different Reynolds Averaged Navier-Stokes (RANS) models: Standard, Realizable, RNG k-ε and SST k-ω and RSM models. The pressure-velocity coupling is handled using SIMPLE scheme. Turbulent kinetic energy (k), turbulent dissipation ratio (ε), specific dissipation rate (ω) and Reynolds stresses are discretised with a second order upwind scheme as well as the momentum equation. The CFD calculations were repeated for several flow rates ranging between 200 and $600\ kg/s$ at $1500\ rpm$.

4 RESULTS

The performance characteristics (variations of pump and turbine head and efficiency with flow rate) are plotted in Fig. 4. The comparison between the machine hydraulic performance while working in pump and turbine mode shows similarities to the observations reported in the literature [7]. The effect of the computational mesh resolution is studied and the simulations performed at 4 different level of mesh sizes: 3, 5, 10 and 27 million cells. The performance of the pump at design conditions ($400\ kg/s$ and $1500\ rpm$) is shown for four different meshes in Table 1. It can be seen that the deviation of the integral quantities are low and the numerical error coming from spatial discretization does not affect the performance characteristics significantly. It is concluded that 5 million cells is fine enough to solve such problem.

Mesh	Head [m]	Hydraulic Power [kW]	Efficiency [%]
3M	75.4	296	82
5M	76	298	82
10M	75.9	298	82
27M	76.1	299	83

Table 1: Performance characteristics of the hydraulic machine, pump mode (at 1500 rpm and 400 kg/s) for four different mesh sizes. (Realizable k-εmodel)

This part of the work focuses the turbulence modelling. In both operation modes (pump

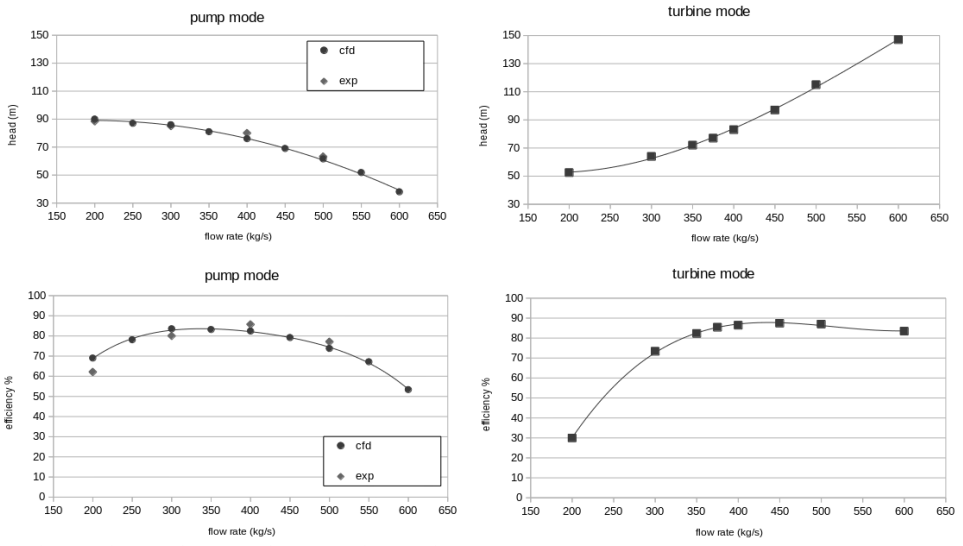

Figure 4: Performance characteristics of the hydraulic machine, pump mode (upper), turbine mode (lower). Only CFD results are presented for turbine mode (5M cells mesh).

mode and turbine mode) the turbulence models used for the simulations are 5: standard k-ε, RNG k-ε, realizable k-ε, SST k-ω and the Reynolds Stress Model (RSM).

The flow conditions has been simulated in steady state at the design point (400 kg/s and 1500 rpm) each time using a different model. The results have been analysed and the integral quantities (head, power and efficiency) evaluated. The results for the different turbulence models are reported in Table 2 for the pump mode and in Table 3 for the turbine mode.

The contours of the static pressure head on the mid-plane of the pump is shown for five turbulence models: Fig.5 for the pump mode and Fig. 6 for the turbine mode. The pressure head values shown in water column (metres) are negative because the pressure is defined as zero at the outlet for the pump mode.

Model	Head [m]	Hydraulic Power [kW]	Efficiency [%]
SST k-ω	75.5	296	81
realizable k-ϵ	76	298	82
standard k-ϵ	75.5	296	81
RNG k-ϵ	76.3	299	82
RSM	74.5	292	81

Table 2: Performance characteristics of the hydraulic machine, pump mode (at 1500 rpm and 400 kg/s) for five different turbulence models (5M cells mesh)

Model	Head [m]	Hydraulic Power [kW]	Efficiency [%]
SST k-ω	82	322	86
realizable k-ϵ	83	326	86
standard k-ϵ	83	324	85
RNG k-ϵ	83	324	86
RSM	82	321	86

Table 3: Performance characteristics of the hydraulic machine, turbine mode (at 1500 rpm and 400 kg/s) for five different turbulence model (5M cells mesh)

5 CONCLUSIONS AND FUTURE WORK

In this work, performance characteristics of a single stage centrifugal pump with spiral casing is calculated for both pump and turbine mode and the results were validated with experimental data. The results from simulations in pump mode show that CFD is a reliable tool to predict the reverse performance of the pump systems when they are working in turbine mode. This represents a great advantage for engineers for the selection of the pumps in the design phase of small hydro power plants which will use PAT.

Results shows that head and flow rate at the best efficiency point are higher than the pump mode. The results of the integral quantities for the design point volume flow compared to the data obtained from the manufacturer showed that in the influence of the turbulence model is negligible. This statement was confirmed by an analysis of the velocity and pressure field in the diffuser channel by another work has been done in the literature [8]. According to these considerations, a realizable k-ε model has been chosen for it robustness and for its wide use in industry for internal flow problems. The calculations were performed by the supercomputer VILJE [9]. Scalability of the parallel calculations using multiple nodes would be worthy future work. The effect of the design change (number of blades, blade angles, blade profile etc.) of the impeller on the performance will be investigated later.

ACKNOWLEDGEMENTS

The authors thank NTNU via NOTUR (The Norwegian Metacenter for computational Science) for supporting the computing time. The authors also thank to Turbosan company for their collaboration and support

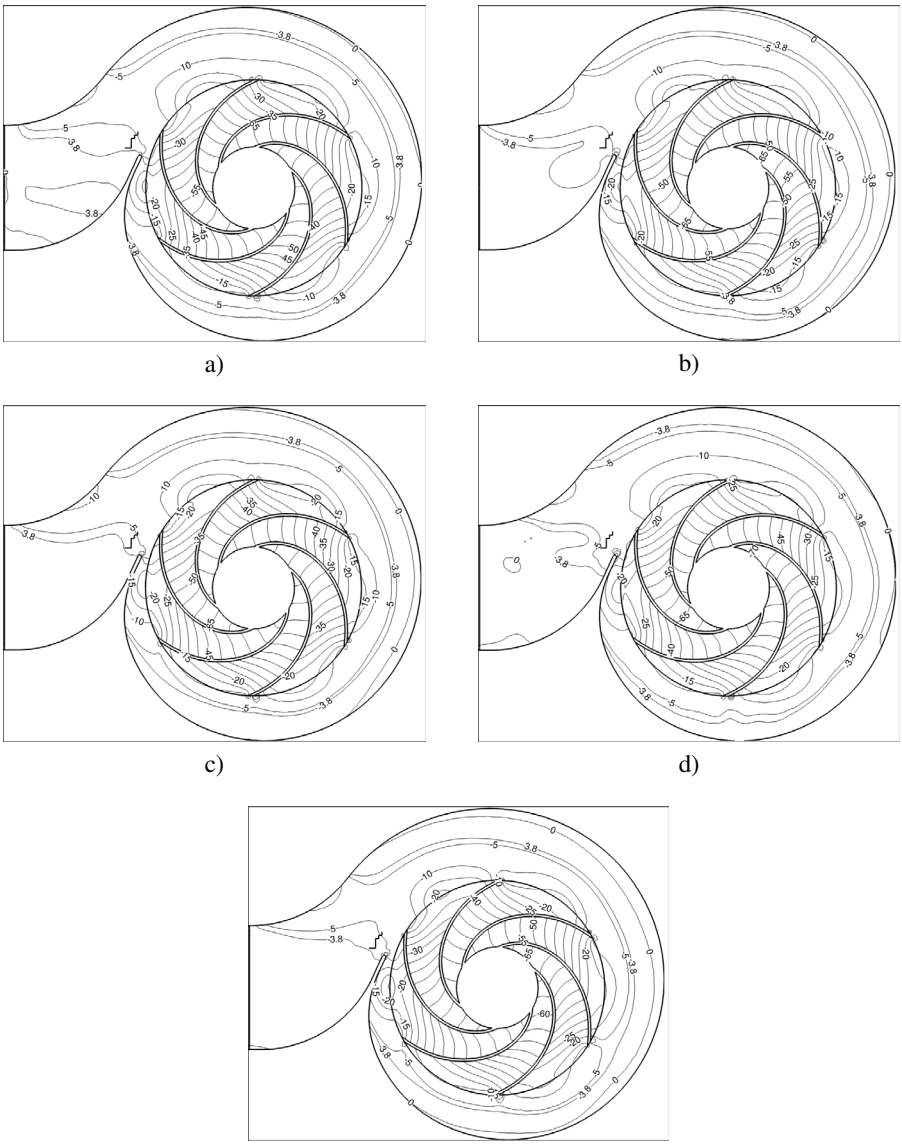

Figure 5: Static pressure head distribution in water column (metres) for each different turbulence model at n=1500 rpm in pump mode (5M cells mesh) a) SST k-ω, b) realizable k-ε, c)standard k-ε, d) RNG k-ε, e) RSM

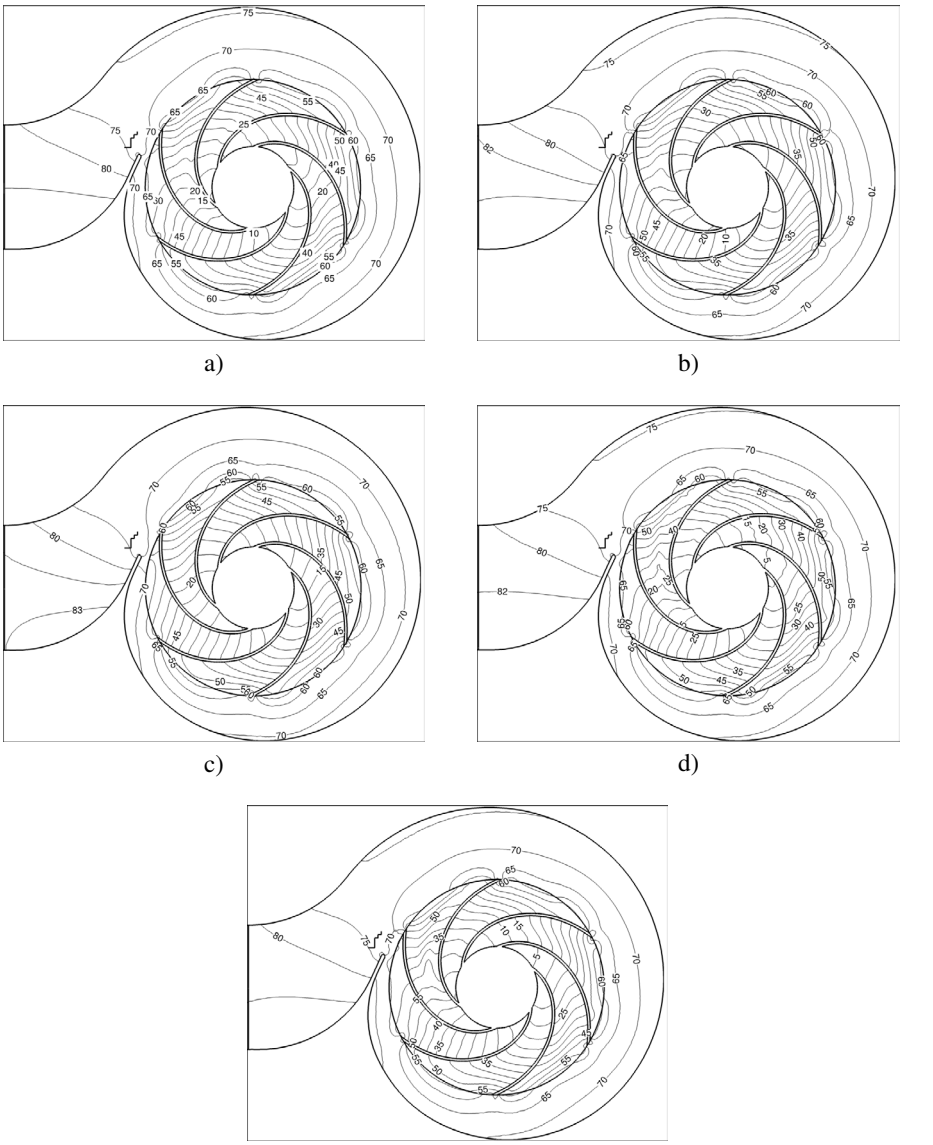

Figure 6: Static pressure head distribution in water column (metres) for each different turbulence model at n=1500 rpm in turbine mode (5M cells mesh): a) SST k-ω, b) realizable k-ε, c)standard k-ε, d) RNG k-ε, e) RSM

NOMENCLATURE

ϵ	Turbulence dissipation rate $[m^2/s^3]$
η	Efficiency $[rpm]$
ω	Specific turbulence dissipation rate $[1/s]$
BEP	Best Efficiency Point
H	pump Head $[m]$
k	Turbulence kinetic energy $[m^2/s^2]$
n	Rotational speed $[rpm]$
PAT	Pump as Turbine
Q	Flow rate $[m^3/h]$
$RANS$	Reynolds Averaged Navier-Stokes equations
RNG	Re-Normalization Group
RSM	Reynolds Stress Model
SST	Shear Stress Transport
T	Torque $[Nm]$
y^+	Dimensionless wall distance

REFERENCES

[1] H. Ramos and A. Borga, "Pumps as turbines: an unconventional solution to energy production," *Urban Water*, vol. 1, no. 3, pp. 261–263, 1999.

[2] P. Garey, "Using pumps as hydro-turbines," *Hydro Review*, pp. 52–61, 1990.

[3] S. V. Jain and R. N. Patel, "Investigations on pump running in turbine mode: a review of the state-of-the-art," *Renewable and Sustainable Energy Reviews*, vol. 30, pp. 841–868, 2014.

[4] H. Nautiyal, A. Kumar, *et al.*, "Reverse running pumps analytical, experimental and computational study: a review," *Renewable and Sustainable Energy Reviews*, vol. 14, no. 7, pp. 2059–2067, 2010.

[5] S.-S. Yang, S. Derakhshan, and F.-Y. Kong, "Theoretical, numerical and experimental prediction of pump as turbine performance," *Renewable Energy*, vol. 48, pp. 507–513, 2012.

[6] Turbosan. http://turbosan.com.

[7] R. S. Stelzer and R. N. Walters, "Estimating reversible pump-turbine characteristics," tech. rep., Bureau of Reclamation, Denver, CO (USA). Engineering and Research Center, 1977.

[8] A. Nocente, T. Arslan, and T. K. Nielsen, “Numerical simulation of flow inside centrifugal pump by two different solvers,” in *Proceedings of MekIT 2015 Conference* (B. Skallerud and H. I. Andersson, eds.), pp. 333–342, 2015.

[9] Vilje. https://www.hpc.ntnu.no/display/hpc/Vilje.

9. National Conference on Computational Mechanics
MekIT'17
B. Skallerud and H I Andersson (Eds)

RECENT DEVELOPMENTS AND NEW RESULTS ON THE FLOW AROUND AN INCLINED 6:1 PROLATE SPHEROID

HÅKON STRANDENES[1,3], FENGJIAN JIANG[1], BJØRNAR PETTERSEN[1] AND HELGE I. ANDERSSON[2]

[1]Department of Marine Technology
[2]Department of Energy and Process Engineering

Norwegian University of Science and Technology
Trondheim, Norway

[3] Corresponding author: hakon.strandenes@ntnu.no

Key words: CFD, flow, inclined, spheroid

Abstract. In the light of new computational resources and improved simulation tools we present new simulations of the flow around an inclined 6:1 prolate spheroid. We present the development of the flow from the symmetric and laminar case at Reynolds number 800 to the fully turbulent and highly asymmetric case at Reynolds number 3000.

Already at Reynolds number 1000 we find strong transient behaviour in the flow that has not previously been reported. We attribute this finding to the improved grid resolution in this case. At Reynolds number 3000 the new computational setup we use in the present study shows a very long initial development phase with a symmetric wake configuration previously never reported before.

NOMENCLATURE

C_{Fx}	Drag coefficient	U_∞	Inlet (freestream) velocity
C_{Fy}	Lift coefficient	u, v, w	Velocity components
C_{Fz}	Side force coefficient	x, y, z	Cartesian coordinates
D	Minor axis diameter	λ_2	Vortex identification criterion by [1]
d	Volume-equivalent sphere diameter	ν	Kinematic viscosity of fluid
F	Force on spheroid	ρ	Fluid density
Re_D	Reynolds number $Re = DU_\infty/\nu$	ω_x	Vorticity $\omega_x = \partial w/\partial y - \partial v/\partial z$

1 BACKGROUND

Jiang et al. [2, 3, 4, 5] studied the wake behind a 6:1 prolate spheroid at 45 degree inclination at various Reynolds numbers by means of DNS. Depending on the actual physical size, the spheroid can serve as a model for various objects ranging from microfibers to underwater drones and submarines. This configuration gives rise to a wide range of interesting flow features, such as 3-D flow separation and wake asymmetry which makes it an interesting case for high-resolution flow simulations.

When the Re_D is lower than 1000, perfectly steady and symmetric wake consisting of a counter-rotating vortex pair that develops from the vortex sheets separated from the two sides of the spheroid is reported [3].

At $Re_D = 1000$, they observed steady and symmetric wake close to the spheroid, whereas a clear asymmetry developed in the intermediate region. However, the wake was in general steady. Based on the zero side force and the slight quasi-periodic oscillations in the far wake, they concluded that, at $Re_D = 1000$, the wake behind this particular geometry is still fully laminar and just on the verge of becoming unsteady [3]. This statement was further supported by a later study where the wake at $Re_D = 800$, 1000, and 1200 were carefully compared [2]. The comparison showed the scenario of how the wake gradually lost its symmetry and turns unsteady within a small Reynolds number range.

In [4] and [5], the Reynolds number were increased from $Re_D = 1200$ to $Re_D = 3000$. A strong transitional wake was found. At $Re_D = 3000$, both the instantaneous wake and the time-averaged wake turned out to be very asymmetric, which means the wake curved towards one side. The time-averaged asymmetric wake also contributes to a distinct side force, which was almost 75% of the drag force. The counter-rotating vortex pair clearly observed at lower Reynolds numbers was almost no longer present in the instantaneous wake, but one concentrated vortex tube, which proved to be a helical vortex, managed to persist itself as a main coherent structure in the wake. In [5], the authors did detailed analysis on this coherent structure and observed several interesting phenomena, such as the vortex decomposition in the generation stage, a new helical symmetry alteration scenario in the developing stage, and self-similarity in the far wake.

It is worth to mention that in 2014, for the $Re_D = 1000$ case, the authors used 512 processors on the HPC cluster *Vilje* to run a mesh of less than 0.2 billion Cartesian grid cells. It took 2.2 seconds to march the simulation one time step onward [3]. While in 2015, for the $Re_D = 3000$ case, the authors used 1792 processors on the same system to run a mesh consisting of 0.75 billion Cartesian grid cells, and it took about 3.1 seconds to march the simulation one step forward. Almost 1 million CPU hours were consumed for the $Re_D = 3000$ case in [5].

2 CURRENT WORK

In the recent years, there have been a huge effort in improving our simulation tools and methods to be able to simulate higher Reynolds numbers and resolve more complicated

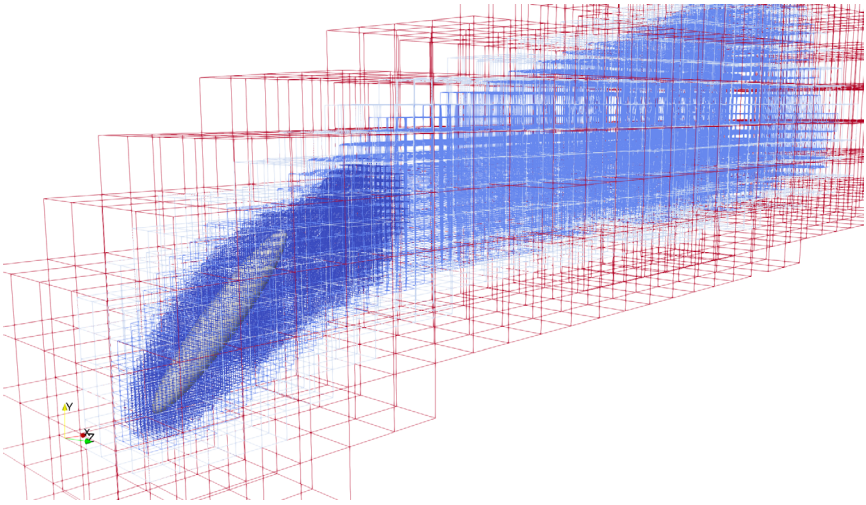

Figure 1: Illustration of the grid configuration used in the present paper. Each cube contain $40 \times 40 \times 40$ grid cells. The coarsest grids are not shown to avoid cluttering the figure.

physics. The performance has improved tremendously, for large cases the improvements can be up to a factor of ten or more.

Recently we got access to the computer system *Fram*, provided by *Uninett Sigma2*. This allowed us to look at the previously published cases with new tools to verify the results and explore potential new physics in flow regions far behind the spheroid, which has never been studied before. Some of these results are presented here.

2.1 NUMERICAL METHODS AND SIMULATION CODE

The code MGLET [6] has been used to perform all simulations presented in the references and this paper. MGLET uses a staggered Cartesian grid and introduces the solid geometry through an immersed boundary method [7]. The grid can be locally refined with a zonal approach, in which Cartesian grid boxes are stacked together in an unstructured manner. For each level of grid refinement, each parent grid cell is split into eight equal (3-D) child cells [8]. One important difference between MGLET and other CFD codes with local refinement possibilities, is that within MGLET we never remove cells that are refined. This means that a particular physical location can be present in many different grid cells at once, one per refinement level. The advantage of this approach is two-fold: first we refine the grid around our geometry and flow features. Secondly we keep a grid hierarchy that we use in the solver for the pressure equation (of Poisson-type), easily creating an efficient multigrid solver.

Previously, using many grid levels in this way was very costly due to inefficient commu-

nication and load balancing issues in MGLET. Due to this, using one large Cartesian grid and only using cell stretching was the only way of clustering grid cells around regions of interest in the flow. This was not very efficient because a lot of cells were wasted outside of the region of interest.

The new way of creating computational grids, illustrated in figure 1, gives us the possibility of only refining the flow regions of interest without sacrificing either grid quality (as the aspect ratio is always 1:1:1 everywhere in the domain) or wasting any cells.

3 THE FLOW AROUND AN INCLINED SPHEROID

In the next paragraphs we will give a brief overview of the development of the flow around an inclined 6:1 prolate spheroid as the Reynolds number increase from 800 to 3000. In this *Re*-range the wake topology changes from a steady symmetric wake to a turbulent and asymmetric wake configuration.

The simulations are all conducted on the same computational grid, which is shown in figure 1. The origin of the coordinate system in this figure is in the center of the spheroid. The grid consists of 29471 individual Cartesian grid boxes of size 40^3 grid cells, distributed over 5 different grid refinement levels. This gives a total of 1.89 billion individual grid cells. No grid convergence study has been performed, instead we keep the grid slightly finer than the grid used in [4]. The minimum grid resolution is $0.005D$, which is kept in a region surrounding the entire spheroid and up to a position $x/D = 10$ in the wake region. Behind $x/D = 10$ the grid is coarsened with a factor of two, which mean that the grid resolution behind this position is $0.010D$. In comparison, at the location $x/D = 23$, the grid used in [4] with stretching has a spacing of $0.084D$ in the streamwise direction.

In the present work we have focused on exploring a broad range of Reynolds numbers, and how the wake develops gradually from laminar to turbulent. Despite the fact that the highest Reynolds number currently does not exceed earlier studies, we manage to take advantage of the development of the simulation tool and could use much finer mesh in the far wake. This has not only given us the possibility to verify the improvements of the code, but also offered us new insight on how the far wake develops. It also serves as a motivation for even higher Reynolds number simulations.

The force coefficients presented in this work is normalized as

$$C_F = \frac{F}{\frac{1}{2}\rho U_\infty^2 \frac{\pi d^2}{4}} \tag{1}$$

where d is the diameter of a sphere with the same volume as the 6:1 prolate spheroid discussed here ($d = 1.817D$).

3.1 Reynolds number 800

The flow at Reynolds number 800 is perfectly symmetric, laminar and steady. Figure 2 shows the wake vortices illustrated by λ_2 [1], and figure 3 shows the streamwise vorticity

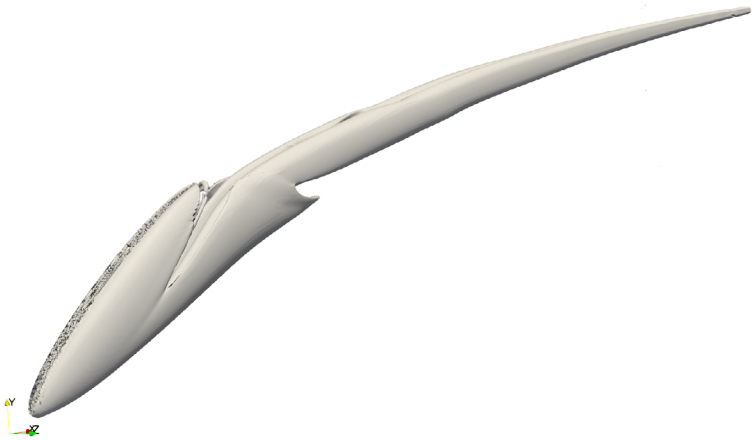

Figure 2: Isosurface of $\lambda_2 = -1.0$ for Reynolds number 800.

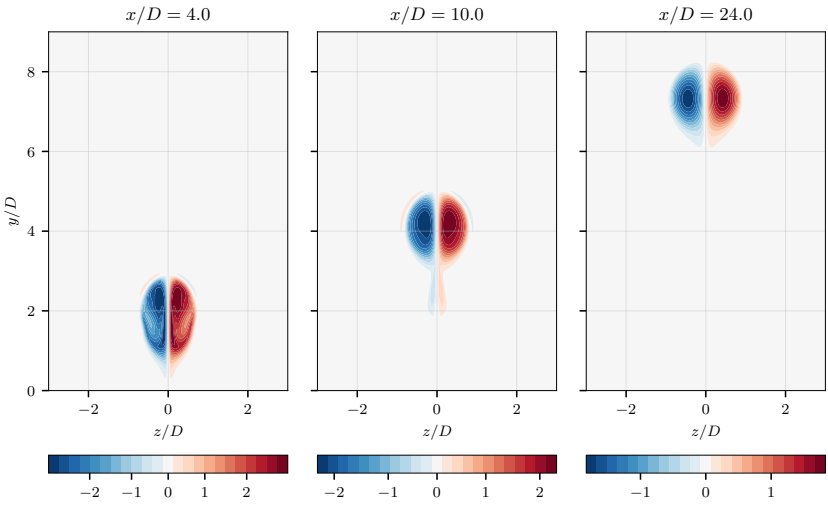

Figure 3: Time-averaged streamwise vortcity ω_x for the Reynolds number 800 case for three different cross-sections in the wake.

in the wake. From close examination of the time evolution of the velocity in the three planes in figure 3 (not shown here), we cannot find any signs of transient behaviour after the initial evolution from an non-physical initial condition to a resolved wake.

In summary, we cannot find any new flow features in this case compared to what was shown earler in [2] with a coarser grid.

3.2 Reynolds number 1000

In [3] the wake at Reynolds number 1000 was reported to be laminar, but with a significant asymmetry. Although the wake structures were reported to be 'steady', some fluctuations were found in the velocities in the far wake ($x/D = 20$), while the near wake remained completely stationary. The magnitude of the oscillations at $x/D = 20$ was approximately $0.002U_\infty$.

In the present simulations, we also find an asymmetry in the wake. However, we find significant and strong transient behaviour in the velocity signal too. In our simulations we see oscillations in streamwise velocity at $x/D = 24$ of magnitude $0.1U_\infty$. Although the sampling plane is not at the same streamwise location as in [3], the wake topology in the far wake, seen in figure 4, is also clearly different from the one in [3].

It is also worth mentioning, that although the wake in the present case is asymmetric, there is no sideways force on the spheroid at all.

3.3 Reynolds number 1200

At Reynold number 1200 the wake is entering a transitional state. The instabilities are larger, and the point of transition from a steady and laminar vortex tube to a more chaotic wake happens just behind $x/D = 10$. As seen in figure 6 the wake is regular and repetitive, with a certain vortex pattern that almost repeats itself downstream.

Except from the fact that the wake region now is significantly better resolved, no major new phenomena have been observed in this case.

3.4 Reynolds number 1500

At Reynolds number 1500 the instabilities have moved almost all the way up onto the spheroid surface as seen in figure 7. Even in the sampling plane at $x/D = 4.0$ there is now signs of asymmetry and instabilities. One interesting observation is that the asymmetry in the average vorticity at $x/D = 24$ is less evident compared to the Reynolds number 1000 case.

In this case the side force is now becoming non-zero, although with a very small magnitude (about 1 % of the drag force).

3.5 Reynolds number 2000

At Reynolds number 2000, as shown in figure 9 and 10 the most significant feature discovered is that the sideways force is now for the first time strongly non-zero, about 20%

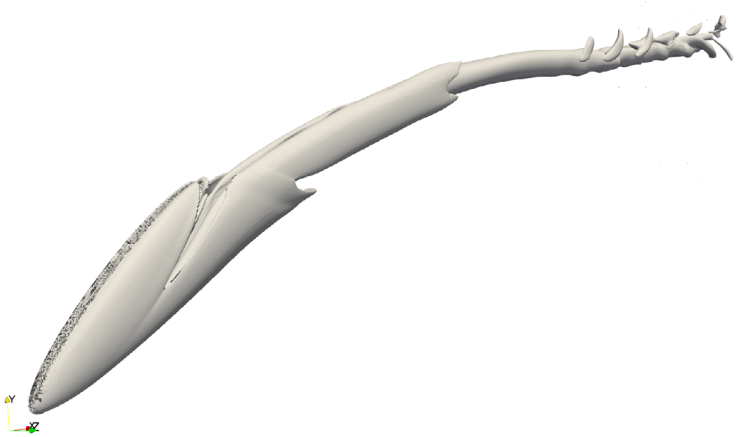

Figure 4: Isosurface of $\lambda_2 = -1.0$ for Reynolds number 1000.

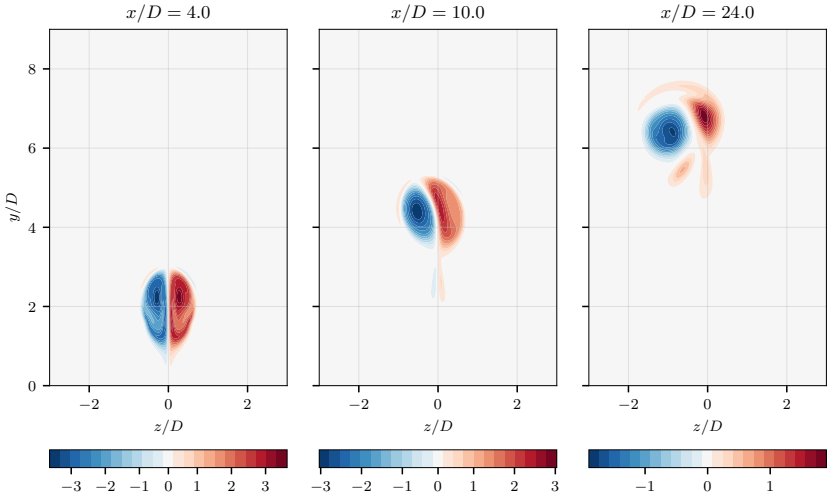

Figure 5: Time-averaged streamwise vortcity ω_x for the Reynolds number 1000 case for three different cross-sections in the wake.

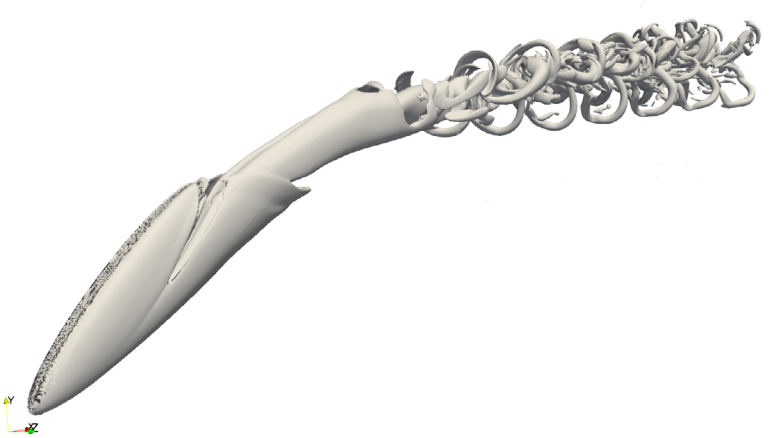

Figure 6: Isosurface of $\lambda_2 = -1.0$ for Reynolds number 1200.

of the value of the drag force. The history of the force coefficients are shown in figure 10. An interesting phenomena is that the sideways force seems to be reaching the non-zero average value very slowly, it has a long period of more than 150 tU_∞/D where the drag coefficient is zero. The drag- and lift-forces are exhibiting some intermittent high-frequent oscillations, while the sideways force is oscillating with very low frequencies after the initial development into a non-zero state.

The wake is now very transitional, and perhaps even entering a turbulent regime in the far wake. The regular, repetitive patterns in the wake topology we have seen up to Reynolds number 1500 are much less visible, and the wake is more dominated by smaller and more irregular vortex filaments.

3.6 Reynolds number 3000

The Reynolds number 3000 case, as illustrated in figure 11, is so far the most interesting. The flow has been described extensively in [4] and [5]. The wake is clearly more turbulent (while the very near wake is still transitional), and is extremely asymmetric compared with the lower Reyholds numbers. In fact, the wake is so asymmetric that the main part of the vortex core falls outside of our original sampling plane in figure 12. The vortex core in the sampling plane at $x/D = 4$ has grown extremely strong, with a maximum ω_x that is two to three times stronger than in the other cases we have shown here.

The sideways force, shown in figure 13, has grown significantly. The sideways force is now almost as strong as the drag force, which in itself is surprising.

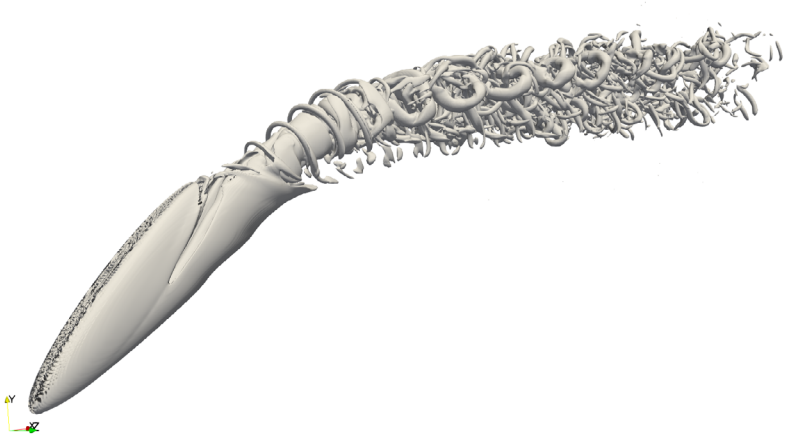

Figure 7: Isosurface of $\lambda_2 = -1.0$ for Reynolds number 1500.

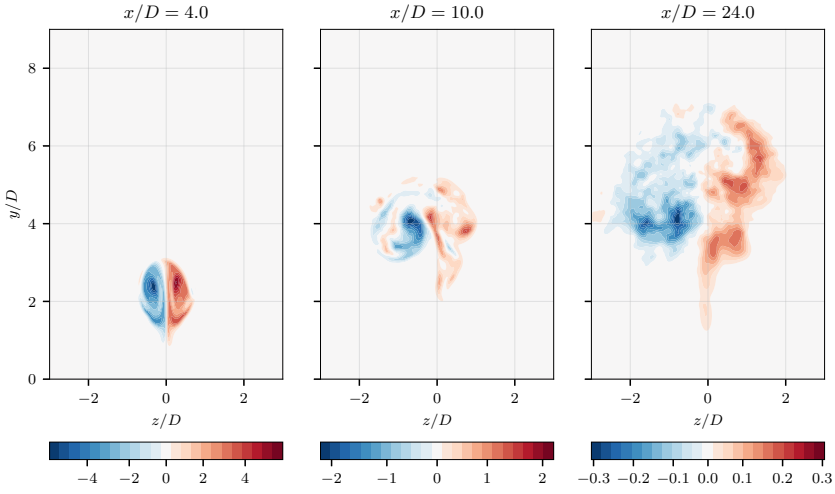

Figure 8: Time-averaged streamwise vortcity ω_x for the Reynolds number 1500 case for three different cross-sections in the wake.

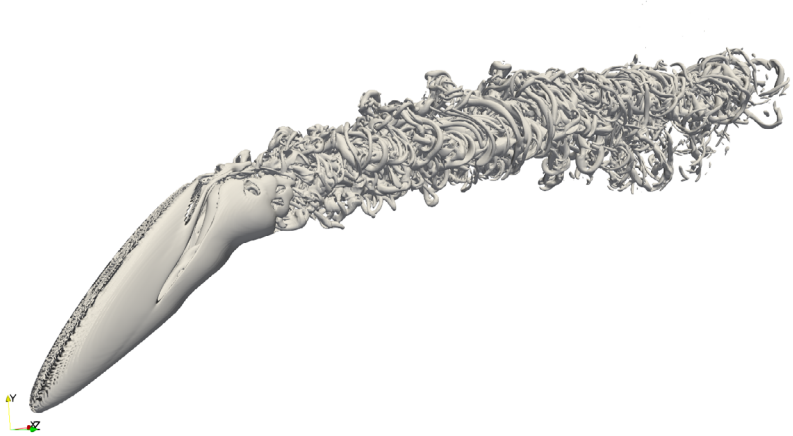

Figure 9: Isosurface of $\lambda_2 = -1.0$ for Reynolds number 2000.

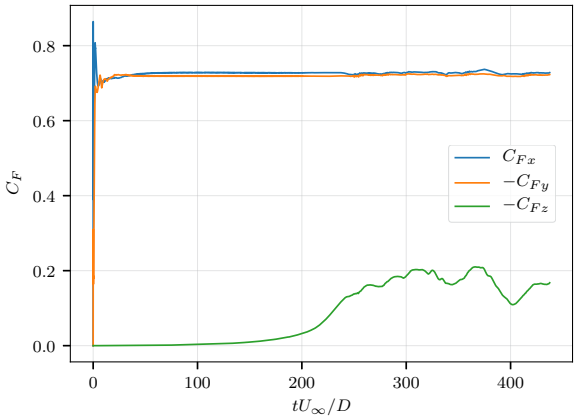

Figure 10: History of the drag, lift and crossflow force coefficient for the Reynolds number 2000 case

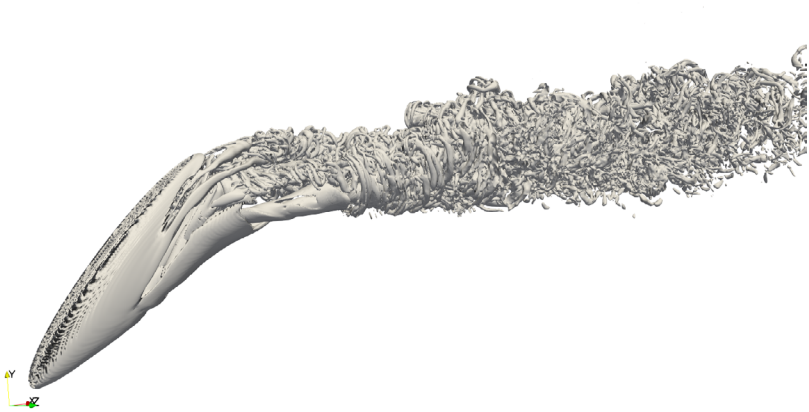

Figure 11: Isosurface of $\lambda_2 = -1.0$ for Reynolds number 3000.

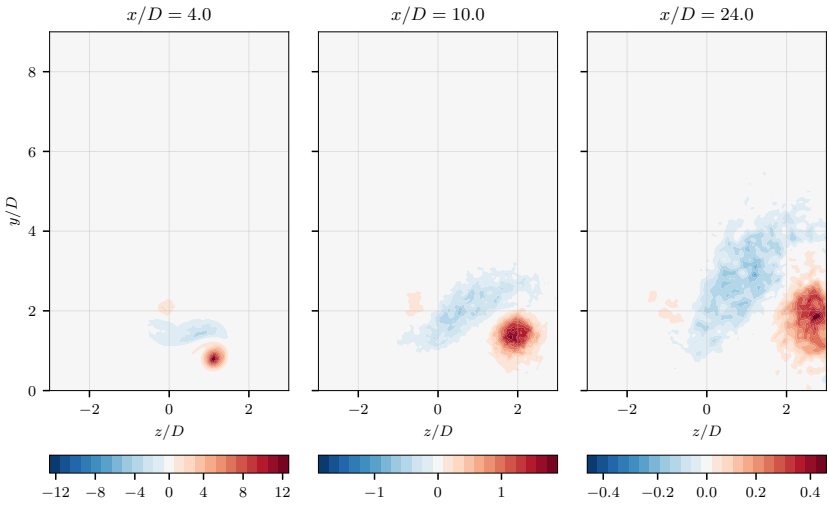

Figure 12: Time-averaged streamwise vortcity ω_x for the Reynolds number 3000 case for three different cross-sections in the wake.

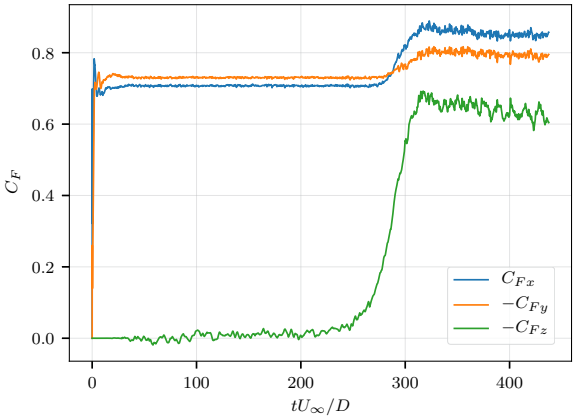

Figure 13: History of the drag, lift and crossflow force coefficient for the Reynolds number 3000 case.

In contrast to the works in [4] and [5], we are now able to study the entire wake, up to a distance of $30D$ behind the spheroid due to the improved code and grid generator. Another interesting aspect that is clearly visible in figure 13 is that it takes a significant amount of time to develop the asymmetry. The net sideways force is about zero for more than 200 tU_∞/D before the flow suddenly become asymmetric. In the previous works [4] and [5] this change happened more or less instantly when starting the simulation. The reason(s) for this could be either that the refined computational grid leads to lower numerical errors or that the pressure solver that we use in the present work produces less asymmetric residual patterns. At the current stage we are not yet sure about the exact cause, but this will be subject to further investigations.

For the simulation results shown here, we used 2560 processors on the *Fram* HPC cluster (which is a *Lenovo NeXtScale nx360* system with 1006 compute-nodes each equipped with dual *Intel E5-2683v4* CPU's), and in average, the time used to march one timestep was 1.68 seconds. In other words, it took 4300 CPU-seconds to advance the simulation one timestep. In the previous work [4], the number of CPU-seconds used to advance one timestep was 5550. When taking into account that the current grid consist of 1.89 billion grid cells, and the previous grid consist of only 0.75 billion grid cells, the advances in computational effort are impressive.

4 CONCLUDING REMARKS AND FURTHER WORK

The ultimate goal of this work is obviously to increase the Reynolds number even further, beyond 3000. We have described a flow that goes from a steady and laminar flow to a highly asymmetric transitional flow. An important question is how the asymmetry

will behave when further increasing the Reynolds number.

A peculiar remark is that in all works on this flow case, the asymmetry develops towards the same side. This is strange, as one should expect that the cases would develop asymmetries to 'random' sides. This is probably due to asymmetries in the numerical methods, which we will need to look further into.

ACKNOWLEDGEMENTS

This work would not have been possible without the support from the computational resources on the computers *Vilje* and *Fram* provided by UNINETT Sigma2.

REFERENCES

[1] J. Jeong and F. Hussain. 'On the identification of a vortex'. *Journal of Fluid Mechanics* 285 (1995), pp. 69–94. DOI: doi.org/10.1017/S0022112095000462.

[2] F. Jiang, J. P. Gallardo and H. I. Andersson. 'Transition and loss of symmetry in the wake behind an inclined prolate spheroid'. In: *8th National Conference on Computational Mechanics MekIT'15*. Ed. by B. Skallerud and H. I. Andersson. International Center for Numerical Methods in Engineering (CIMNE), Barcelona, Spain, 2015, pp. 219–232.

[3] F. Jiang, J. P. Gallardo and H. I. Andersson. 'The laminar wake behind a 6:1 prolate spheroid at 45° incidence angle'. *Physics of Fluids* 26 (11) (2014), p. 113602.

[4] F. Jiang, J. P. Gallardo, H. I. Andersson and Z. Zhang. 'The transitional wake behind an inclined prolate spheroid'. *Physics of Fluids* 27 (9) (2015), p. 093602.

[5] F. Jiang, H. I. Andersson, J. P. Gallardo and V. L. Okulov. 'On the peculiar structure of a helical wake vortex behind an inclined prolate spheroid'. *Journal of Fluid Mechanics* 801 (2016), pp. 1–12.

[6] M. Manhart, F. Tremblay and R. Friedrich. 'MGLET: a parallel code for efficient DNS and LES of complex geometries'. In: *Parallel Computational Fluid Dynamics - Trends and Applications*. Ed. by C. B. Jenssen et al. Elsevier Science B.V., 2001, pp. 449–456.

[7] N. Peller, A. L. Duc, F. Tremblay and M. Manhart. 'High-order stable interpolations for immersed boundary methods'. *International Journal for Numerical Methods in Fluids* 52 (11) (Apr. 2006), pp. 1175–1193. ISSN: 1097-0363. DOI: 10.1002/fld.1227.

[8] M. Manhart. 'A zonal grid algorithm for DNS of turbulent boundary layers'. *Computers & Fluids* 33 (3) (Mar. 2004), pp. 435–461. ISSN: 0045-7930. DOI: 10.1016/s0045-7930(03)00061-6.

9th National Conference on Computational Mechanics
MekIT'17
B. Skallerud and H I Andersson (Eds)

THE RELATIVE IMPORTANCE OF MODEL PARAMETERS IN TRANSIENT GAS-PIPELINE FLOW

Filip Sund[1,2]

[1]Norwegian University of Science and Technology
Department of Energy and Process Engineering
7491 Trondheim, Norway

[2]Uni Research Polytec
5527 Haugesund, Norway
e-mail: filip.sund@polytec.no

Key words: Computational methods, transient non-isothermal flow, natural gas pipeline, compressible flow, offshore pipeline

Abstract. *A sensitivity study on a numerical transient flow model for compressible gas was performed to determine the most important parameters when simulating long offshore gas pipelines. A simplified pipeline was simulated with synthetic transient boundary conditions, while systematically modifying different model parameters and correlations. It was found that, for the mass flow and pressure, the most important parameters by a large margin, are the friction factor and the compressibility factor. For the temperature, the parameter with the highest impact was found to be the derivative of the compressibility factor with respect to temperature (at constant density), closely followed by the isochoric gas heat capacity and the friction factor.*

1 INTRODUCTION

Natural gas exported from Norway to Europe accounts for around 25 percent of the yearly gas consumption in the European Union. The gas is transported from Norway through pipelines that are up to 1166 km long. To ensure that the pipelines stay within their operating limits, to monitor the pipelines for leaks, and to track changes in gas quality, it is important to know the state of the gas in the pipelines. But measurements of the state of the gas are usually only available at the inlet and outlet, which means that numerical models are necessary to know the state of the gas between the endpoints.

Simulating compressible gas flow is a highly complex issue, so to reduce the problem to a tractable one, several empirical correlations and simplifications like the Colebrook-White equation [1] and the Dittus-Boelter equation [2, 3] are typically used to model different aspects of the system. When doing this, inaccuracies are introduced into the

simulations, the total effect of which can be hard to calculate *a priori*, and which will depend on the state and system being simulated.

The objective of this study is to investigate which parameters and correlations in the gas models that have greatest impact on the modelled results, especially during transient conditions, to know where to apply effort when trying to improve the models. A similar study limited to steady state models was done by Langelandsvik [4], and some work using transient models was by Helgaker [5]. The present work deals with transient one-dimensional non-isothermal models for compressible natural gas mixtures, and a simplified pipeline is modelled using synthetic but representative flow transients as boundary conditions.

This article is structured as follows: The theoretical foundation and underlying equations are presented in section 2, followed by a presentation of the studied pipeline system in section 4. Results are presented and discussed in section 5 while concluding remarks are drawn in section 6.

2 THEORY

The description of the theoretical foundation closely follows the description in [6].

2.1 Conservation laws

The governing equations for compressible, non-isothermal, transient pipeline gas flow are derived by averaging the Reynolds time-averaged conservation laws for viscous flow over the cross-section, resulting in:

the **continuity equation**

$$\frac{\partial \rho}{\partial t} + \frac{\partial (\rho u)}{\partial x} = 0, \tag{1}$$

the **momentum equation** [7]

$$\rho \left(\frac{\partial u}{\partial t} + u \frac{\partial u}{\partial x} \right) + \frac{\partial p}{\partial x} = -\frac{f \rho \left| u \right| u}{2D} - \rho g \sin \theta, \tag{2}$$

and the **energy equation** [8]

$$\rho \left(\frac{\partial e}{\partial t} + u \frac{\partial e}{\partial x} \right) + p \frac{\partial u}{\partial x} = \frac{f \rho u^3}{2D} + \frac{\Omega}{A_h}, \tag{3}$$

where ρ is gas density, e is internal energy, f is the friction factor, Ω is heat transfer through the pipe wall, and A_h is the area through which the heat is transferred.

The two terms containing the friction factor f in eqs. (2) and (3) model respecively viscous shear stress at the wall of the pipe, and viscous dissipation – the transfer of mechanical energy to thermal energy via viscous stresses, and should account for dissipation

at all length scales. The last term in the energy equation model heat transfer to the surroundings, and includes turbulent heat transfer via the standard inner film coefficient. See section 2.2 for more details on this.

Using a real gas equation of state

$$\frac{p}{\rho} = ZRT, \tag{4}$$

where Z is the compressibility factor, and introducing the mass flow rate $\dot{m} = \rho u A$, the governing equations are developed into partial differential equations for mass flow $\dot{m}$, pressure p, and temperature T

$$\frac{\partial p}{\partial t} = \left(\frac{1}{p} - \frac{1}{Z}\frac{\partial Z}{\partial p}\bigg|_T\right)^{-1}\left[\left(\frac{1}{T} + \frac{1}{Z}\frac{\partial Z}{\partial T}\bigg|_p\right)\frac{\partial T}{\partial t} - \frac{ZRT}{pA}\frac{\partial \dot{m}}{\partial x}\right] \tag{5}$$

$$\begin{aligned}\frac{\partial \dot{m}}{\partial t} = {} & \frac{\dot{m}ZRT}{pA}\left[-2\frac{\partial \dot{m}}{\partial x} + \dot{m}\left(\frac{1}{p} - \frac{1}{Z}\frac{\partial Z}{\partial p}\bigg|_T\right)\frac{\partial p}{\partial x} - \dot{m}\left(\frac{1}{T} + \frac{1}{Z}\frac{\partial Z}{\partial T}\bigg|_p\right)\frac{\partial T}{\partial x}\right] \\ & - A\frac{\partial p}{\partial x} - \frac{fZRT\dot{m}\,|\dot{m}|}{2DAp} - \frac{pA}{ZRT}g\sin\theta\end{aligned} \tag{6}$$

$$\begin{aligned}\frac{\partial T}{\partial t} = {} & -\frac{\dot{m}ZRT}{pA}\frac{\partial T}{\partial x} - \frac{\dot{m}\,(ZRT)^2}{pAc_v}T\left(\frac{1}{T} + \frac{1}{Z}\frac{\partial Z}{\partial T}\bigg|_\rho\right) \\ & \cdot\left[\frac{1}{\dot{m}}\frac{\partial \dot{m}}{\partial x} + \left(\frac{1}{T} + \frac{1}{Z}\frac{\partial Z}{\partial T}\bigg|_p\right)\frac{\partial T}{\partial x} - \left(\frac{1}{p} - \frac{1}{Z}\frac{\partial Z}{\partial p}\bigg|_T\right)\frac{\partial p}{\partial x}\right] \\ & + \frac{f}{2c_vD}\left(\frac{ZRT|\dot{m}|}{pA}\right)^3 + \frac{ZRT}{pc_v}\frac{\Omega}{A_h}.\end{aligned} \tag{7}$$

The resulting non-linear partial differential equations are discretized using the cell-centered backward-time centered-space (BTCS) implicit finite difference method [9, 10], and solved using matrix inversion and the Jacobi iterative method [11], as described in further detail in section 3.1.

2.2 Closure relations

2.2.1 Heat transfer

To calculate the heat transfer Ω between the gas and the surroundings, a transient one-dimensional radial model [12] is used. This model includes heat storage in the pipeline wall and surrounding medium, and has been shown to give accurate results for the temperature development in long off-shore pipelines [13–15], given accurate ambient temperatures [16].

When calculating the heat transfer Ω, the inner and outer heat transfer coefficients are used to calculate respectively the heat transfer between the gas and the pipeline wall, and

the heat transfer between the pipeline wall and the ambient. The heat transfer coefficient h can be determined from the Nusselt number for pipe flow

$$\mathrm{Nu_D} = \frac{hD}{k}, \tag{8}$$

where D is the (inner or outer) diameter and k is the thermal conductivity of the fluid (the gas or the ambient fluid).

The *inner* film heat transfer coefficient can be determined from the Dittus-Boelter relation [2, 3], which is valid for forced convection in turbulent pipe flow with Reynolds numbers larger than 10^4 [17]. The Dittus-Boelter relation is

$$\mathrm{Nu_D} = 0.023 \cdot \mathrm{Re}^{0.8}\,\mathrm{Pr}^{0.4}, \tag{9}$$

where Re and Pr is respectively the Reynolds number and the Prandtl number of the gas.

The outer film heat transfer coefficient can be determined from a similar equation, valid for circular cylinders in cross flow with Reynolds numbers between 10^3 and $2 \cdot 10^5$ [17]

$$\mathrm{Nu_D} = 0.26 \cdot \mathrm{Re}^{0.6}\,\mathrm{Pr}^{0.3}, \tag{10}$$

where Re and Pr is respectively the Reynolds number and the Prandtl number of the ambient medium.

2.2.2 Equation of state

For high pressures, such as in the Norwegian export network, the selection of equation of state can have a significant impact on the simulation results [13, 18]. In this study the BWRS (Benedict–Webb–Rubin-Starling) equation of state [19] is used, to determine the gas density, and the compressibility factor Z and its derivatives. The BWRS equation is the following function of molar density ρ_m and temperature

$$\begin{aligned} P = \rho_m RT &+ \left(B_0 RT - A_0 - \frac{C_0}{T^2} + \frac{D_0}{T^3} - \frac{E_0}{T^4}\right)\rho_m^2 + \left(bRT - a - \frac{d}{T}\right)\rho_m^3 \\ &+ \alpha\left(a + \frac{d}{T}\right)\rho_m^6 + \frac{c\rho_m^3}{T^2}\left(1 + \gamma\rho_m^2\right)\exp\left(-\gamma\rho_m^2\right). \end{aligned} \tag{11}$$

The parameters A_0, B_0, etc. are 11 mixture parameters specific to BWRS, and are calculated using mixing rules and pure component properties given in [19], and a set of parameters A_i and B_i. The set of parameters A_i and B_i used in this study has been especially tuned for the Norwegian gas transport network [20].

2.2.3 Friction factor and viscosity

The Colebrook-White equation [1] is a classical semi-empirical relation used to calculate the friction factor f

$$\frac{1}{\sqrt{f}} = -2\log\left(\frac{\epsilon}{3.7D} + \frac{2.51}{\mathrm{Re}\sqrt{f}}\right), \tag{12}$$

where ϵ is the sand grain equivalent roughness of the inner pipeline wall. Here a value of 3 micrometer was used for the roughness. The Colebrook-White equation is an implicit equation, which is solved using the Newton-Rhapson method.

The Lee-Gonzales-Eakin correlation [21] is used to calculate the viscosity of the gas μ

$$\mu = K\exp\left(X\rho^Y\right), \tag{13}$$

where

$$K = \frac{(9.4 + 0.02M)\,T^{1.5}}{209 + 19M + T}, \tag{14}$$

$$X = 3.5 + \frac{986}{T} + 0.01M, \tag{15}$$

$$Y = 2.4 - 0.2X, \tag{16}$$

and M is the molecular weight of the gas.

3 NUMERICAL SCHEME

3.1 Governing equations

To solve the non-linear partial differential equations for the three *state variables* mass flow $\dot{m}$, pressure p, and temperature T, eqs. (5) to (7) are first discretized using a scheme similar to the BTCS (backward time, centered space) finite difference scheme, using cell averages [9, 10]. The pipeline is divided into N grid points, and the different variables are approximated at each section between the grid points by

$$y \approx \frac{y_{i+1}^{n+1} + y_i^{n+1}}{2}, \tag{17}$$

where y represents a general variable, superscripts n and $n+1$ denote time level, and subscripts i and $i+1$ denote grid points. Time derivatives are approximated by

$$\frac{\partial y}{\partial t} \approx \frac{y_{i+1}^{n+1} + y_i^{n+1} - \left(y_{i+1}^{n} + y_i^{n}\right)}{2\Delta t}, \tag{18}$$

and spatial derivatives by

$$\frac{\partial y}{\partial x} \approx \frac{y_{i+1}^{n+1} - y_i^{n+1}}{\Delta x}. \tag{19}$$

This scheme is first order accurate in time, and second order accurate in space, and have been shown to give accurate results for pipelines and boundary conditions comparable to the ones used in the present study [13, 22]. Central difference schemes are known to be very prone to oscillations, but this problem is avoided by choosing an appropriate time step and grid spacing, and by using smooth transients, avoiding discontinous changes in boundary conditions [22]. A different approach could be using an upwind (backward difference) scheme for the spatial derivatives, but upwind schemes do not take into account acoustic information traveling from points which are downstream [23], so central differences are preferred.

When replacing eqs. (17) to (19) in eqs. (5) to (7) non-linear equations in $\dot{m}$, p and T are aquired. These equations are linearized by "lagging" behind parts of the non-linear terms [24]

$$y^{n+1} \to y^n. \tag{20}$$

The result is a set of linear equations, with three equations for each pipe section, and $N-1$ total pipe sections, giving a total of $3(N-1)$ equations. The number of unknowns at time level $n+1$ is $3N$ (N for each state variable), so three boundary conditions are needed. Here the inlet mass flow $\dot{m}_1$, outlet pressure p_N, and inlet temperature T_1 are chosen. The linear equations with boundary conditions are written on matrix form

$$\boldsymbol{A}\boldsymbol{x} = \boldsymbol{b}, \tag{21}$$

where the vector $\boldsymbol{x}$ has length $3(N-1)$ and contains the unknowns

$$\boldsymbol{x} = \left[\dot{m}_2^{n+1}, \ldots, \dot{m}_N^{n+1}, p_1^{n+1}, \ldots, p_{N-1}^{n+1}, T_2^{n+1}, \ldots, T_N^{n+1}\right]^{-1}, \tag{22}$$

the matrix $\boldsymbol{A}$ has shape $3(N-1) \times 3(N-1)$ and contains the coefficients in front of the unknowns, and the vector $\boldsymbol{b}$ contains the known terms including the boundary conditions. Equation (21) is solved using matrix inversion and the Jacobi iterative method [11]. This entails finding $\boldsymbol{x}$ using matrix inversion

$$\boldsymbol{x} = \boldsymbol{A}^{-1}\boldsymbol{b}, \tag{23}$$

where the inverse $\boldsymbol{A}^{-1}$ is found using a linear algebra library. In the Jacobi iterative method the unknows at time level $n+1$ are given the values from $\boldsymbol{x}$, and terms like the friction factor, compressibility factor etc., are updated using the new mass flow, pressure and temperature. This gives a new set of coefficients $\boldsymbol{A}$ and known terms $\boldsymbol{b}$, and the procedure is repeated until the unknowns converge.

4 SIMULATIONS

4.1 Pipeline description

A simplified pipeline was modelled, based on typical off-shore pipelines that transport gas from Norway to Europe. The simplified pipeline profile is illustrated in fig. 1, and the pipe wall composition in fig. 2.

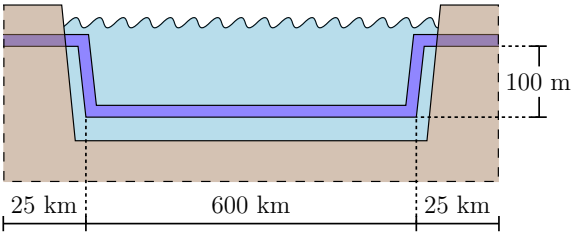

Figure 1: Illustration of the simplified pipeline. The pipe is on-shore and buried 2 m underground for the first and last 25 km, and 100 m below sea level and exposed to sea water for 600 km between the on-shore sections. Figure created freely after figure in [5].

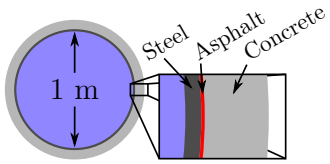

Figure 2: Illustration of pipe and pipe wall materials. The model pipeline has an inner diameter of 1 m, and the pipe wall consists of 24 mm of steel, coated with 7 mm of a protective asphalt coating, and finally 80 mm of concrete.

The pipeline has an inner diameter of 1 m, and consists of a steel pipeline, coated with a protective asphalt coating, and an outer concrete shell. The pipeline is on-shore and buried underground for the first 25 km. It is then 100 m below sea level and exposed to sea water for 600 km, before it is on-shore and buried for the final 25 km.

4.1.1 Boundary conditions

The boundary conditions for the pipeline was constant inlet temperature of 33 °C, constant outlet pressure of 10 MPa, and constant air and sea water temperatures of respectively 6 °C and 4 °C. The system was thermalized with constant inlet mass flow of 600 kg/s, and then the mass flow rate was gradually decreased from 600 kg/s to 200 kg/s in a span of 4 minutes to emulate a transient. The mass flow transient is shown in fig. 3. These conditions correspond to a Reynolds number of 40 to 50 million.

The gas composition was kept fixed at the values shown in table 1.

4.2 Sensitivity study

Which parameters to include in the sensitivity study were determined by looking at which variables appear in the governing equations (eqs. (5) to (7)), in addition to other correlations that are used in the simulations. The focus was on simplifications and empirical correlations in the models, not on input parameters like pipe diameter, ambient temperature, etc. The following nine parameters are included in the study:

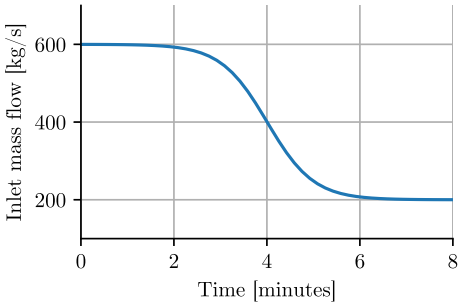

Figure 3: Plot of the inlet mass flow boundary condition, which simulates a transient occuring in a time span of approx 4 minutes.

- the Colebrook-White correlation for the friction factor f, eq. (12)
- the compressibility factor Z and three derivatives: $\frac{\partial Z}{\partial T}\Big|_p$, $\frac{\partial Z}{\partial p}\Big|_T$ and $\frac{\partial Z}{\partial T}\Big|_\rho$, which are all calculated from the equation of state
- Nusselt number relations (the Dittus-Boelter equation and eq. (10)) for inner and outer film heat transfer coefficients, which go into the calculation of the heat transfer between the gas and the surroundings Ω
- the correlation for heat capacity of the gas at constant volume c_v
- the Lee-Gonzales-Eakin correlation for the viscosity of the gas μ, eq. (13), which mainly enters the simulations via the Reynolds number, $\mathrm{Re} = \frac{\rho u D}{\mu}$

To investigate the sensitivity of the model a *base case* was first established using standard model parameters and the boundary conditions described in section 4.1. The inlet

Table 1: The gas. composition used for the simulations.

Component	Mole fraction
CH_4	0.8916
C_2H_6	0.073513
C_3H_8	0.005104
iC_4H_{10}	0.000251
nC_4H_{10}	0.000311
iC_5H_{12}	0.000009
nC_5H_{12}	0.000024
N_2	0.006980
CO_2	0.022208

flow rate transient was initiated at around 2 hours, and the pipeline was simulated for 104 hours after the transient. The simulation was then repeated several times, with a different parameter modified by a constant factor of 1.2 each time. The corresponding response in the modelled flow, pressure, and temperature were recorded for each case.

5 RESULTS AND DISCUSSION

5.1 Simulation results

In fig. 4 is a plot of the boundary conditions for the base case, and the results from a simulation where the compressibility factor Z was increased by 20 %. From the figure

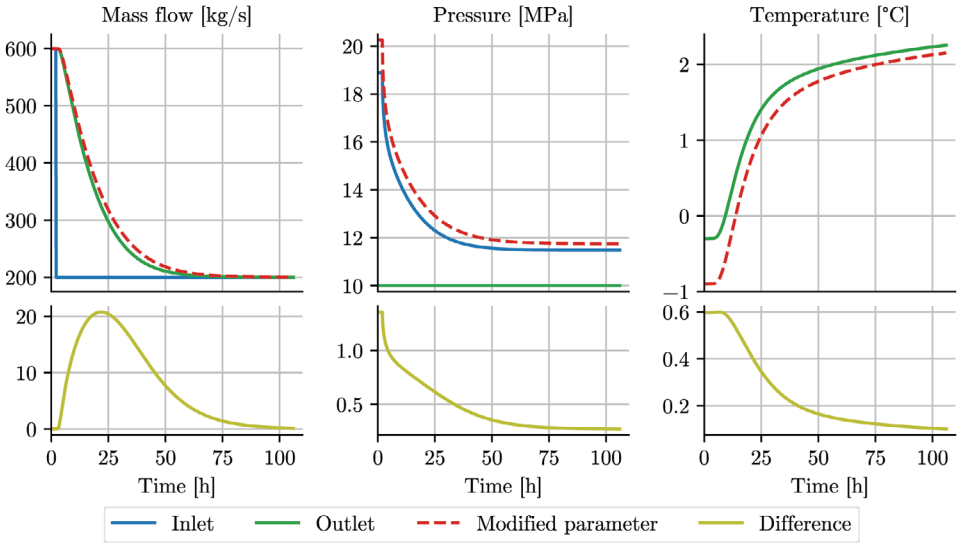

Figure 4: A plot of the results from the base case, and from a simulation with a modified parameter (the compressibility factor Z). The inlet flow rate transient occurs at 2 hours, and the boundary conditions are then kept constant for 104 hours. The three bottom plots show the difference between the base case and the modified parameter simulation, at respectively the outlet, the inlet and the outlet. The constant inlet temperature of 33 °C is not shown.

it is clear that the difference between the base case (y^0) and the cases with a modified parameter (y) vary with time during the transient, so to more easily analyze the results, both the time average relative difference

$$\overline{\Delta y_{\text{rel}}} = \frac{1}{n}\sum_{i=1}^{n} \Delta y_{\text{rel},i} = \frac{1}{n}\sum_{i=1}^{n} \frac{y_i - y_i^0}{y_i^0}, \qquad \text{where } n \text{ is the number of time steps,} \tag{24}$$

and the maximum relative difference

$$\max\left(\Delta y_{\text{rel}}\right) = \max\left(\frac{y_i - y_i^0}{y_i^0}\right) \tag{25}$$

was calculated for mass flow, pressure and temperature. This was calculated for each parameter in the sensitivity study, at every grid point in the simulations. Since a transient case is simulated, and both the temperature and the pressure vary between the inlet and the outlet, relative differences are used. A plot of the maximum and average differences as function of position, for all parameters in the study, are shown in fig. 5.

From fig. 5 a) and b) it can be seen that the parameters with the highest impact on both mass flow and pressure are the friction factor f and the compressibility factor Z. For the mass flow the greatest impact is at the outlet, with a gradual decrease from the inlet to the outlet. For the pressure the situation is reversed. This behaviour is caused by how the simulations are set up, with the mass flow as boundary condition at the inlet and the pressure as boundary condition at the outlet.

The average impact for the whole pipeline was calculated by averaging over the time averaged difference for each grid point. A list of the average impact of all parameters is listed in table 2. The average impact on mass flow is found to be 1.43 % for the friction factor and 0.90 % for the compressibility factor, which is respectively 6.6 and 4.1 times higher than the third most important factor, $\partial Z/\partial p|_T$, which has an average impact of 0.22 %. The average impact on pressure is 3.09 % for the friction factor and 2.07 % for the compressibility factor, which is respectively 14.3 and 9.6 times higher than the third most important factor, the viscosity μ, which has an average impact of 0.22 %.

Table 2: Table of the average relative difference in mass flow, pressure and temperature, for all parameters in the sensitivity study.

	Average relative difference		
Parameter	Mass flow [%]	Pressure [%]	Temperature [%]
Z	0.90	2.1	0.029
$\partial Z/\partial p\vert_T$	0.22	0.053	0.0084
$\partial Z/\partial T\vert_p$	0.19	0.061	0.016
$\partial Z/\partial T\vert_\rho$	0.10	0.057	0.045
h_{outer}	0.017	0.0073	0.0061
h_{inner}	0.0033	0.0015	0.0015
c_v (gas)	0.088	0.023	0.032
μ (gas)	0.078	0.22	0.0027
f	1.4	3.1	0.031

For the temperature it is seen from fig. 5 c) that the situation is less clear-cut. From table 2 it is seen that the parameter which gives the highest average difference along the

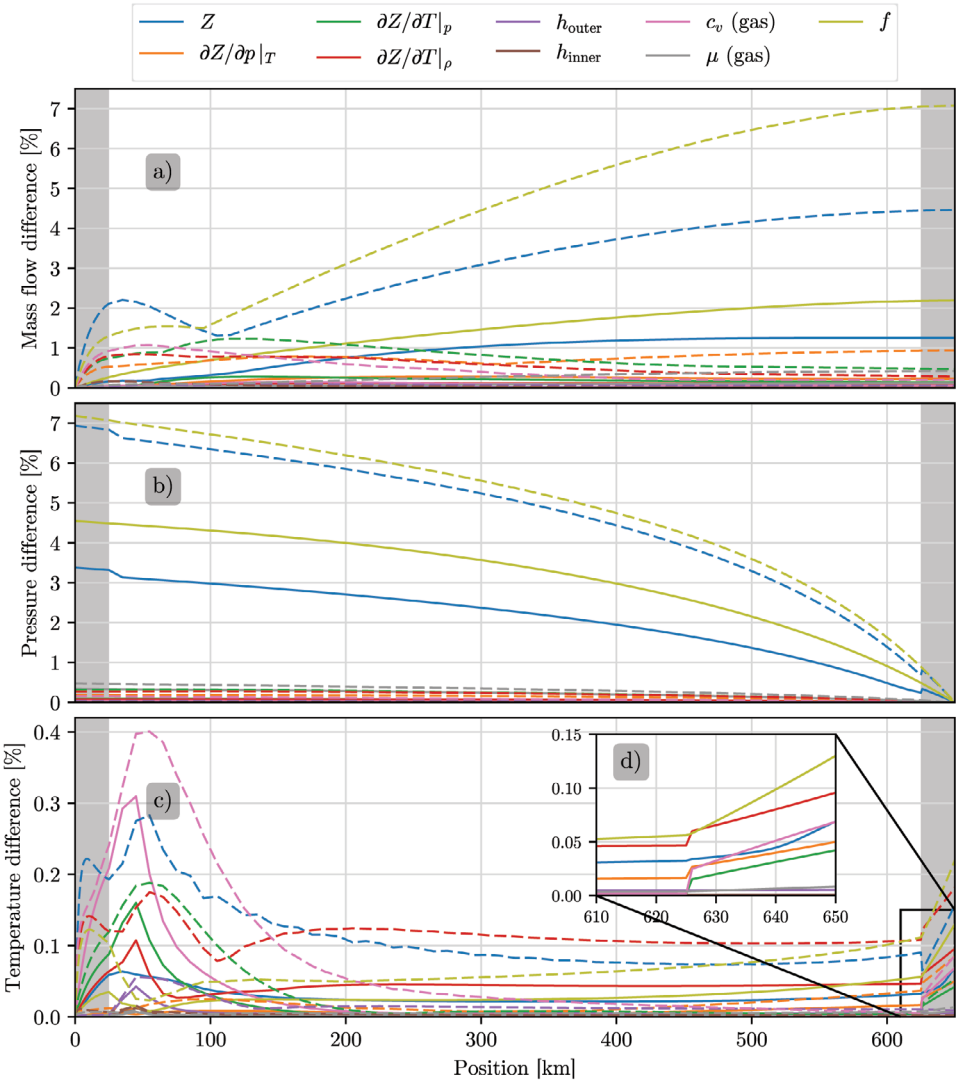

Figure 5: Plots of the maximum (dashed lines) and time average (solid lines) difference between the base case and the cases with a parameter increased by 20 %, for each grid point used in the simulations. The gray shaded areas on the left and right side illustrate the on-shore parts of the pipeline.

whole pipeline is the derivative of the compressibility factor $\partial Z/\partial T|_\rho$, with an average difference of 0.045 %, 1.41 times the impact of the next parameter (c_v) and 1.48 times the impact of the third parameter (f). The effects on temperature are in general seen to be much smaller than for mass flow and pressure, and there are no parameters that stand out in the same way they for mass flow and pressure

In fig. 5 c), peaks in the temperature responses of up to 0.31 % are observed around 20 km off-shore, before the impact of all parameters steadily decrease until they stabilize around 100 km to 200 km off-shore. Also, between 125 km (100 km off-shore) and landfall at 625 km, all parameters have much lower impact than closer to the start of the pipeline; no parameter have a higher maximum impact than 0.15 % or an average impact of more than 0.06 %. The stable behaviour in this area is caused by the fixed sea temperature, which acts as a thermal reservoir, so after a long off-shore section the gas comes to a thermal equilibrium with the sea water, and the gas temperature is governed by the ambient temperature.

Finally, there is a steady increase in the impact on temperature between landfall and the outlet for most parameters. This is because the boundary condition for the thermal exchange between the gas and the ambient changes at landfall (the pipeline goes from being exposed to sea water to buried under ground), and the thermal equilibrium between the gas and the ambient is disturbed. Some details on the temperature response near the outlet can be seen in the inset in fig. 5 d). It is clear that some of the parameters that have very little effect on the temperature while off-shore, like the heat capacity c_v and the derivative of the compressibility factor $\partial Z/\partial T|_p$, have a much higher effect after going on-shore, and on the final outlet temperature, even though the final effect is still small. The impact of the derivative of the compressibility increases from 0.0012 % at 625 km to 0.042 % at the outlet, a factor of 12.9, and the impact of the heat capacity c_v increases from 0.0018 % at 625 km to 0.069 % at the outlet, a factor of 13.8. The trend in the plot indicates that the impact would be even bigger with a longer on-shore section. In general it is observed that the exposure to the sea seem to reduce the impact of changes in the model parameters on the temperature.

To further analyze the temperature responses, the maximum and average temperature differences at certain points of interest along the pipeline are shown in a bar chart in fig. 6. It is seen that the heat capacity c_v is the parameter with the highest impact between all the selected points on the pipeline, with the two highest *average* temperature differences (respectively at 20 km off-shore, and at the end of the on-shore section), and the highest and third highest *maximum* differences (respectively at 20 km off-shore and at the end of the on-shore section). The parameter with the highest impact at 300 km off-shore is the derivative of the compressibility factor $\partial Z/\partial T|_\rho$, while at the end of the off-shore section and at the outlet it is the friction factor f.

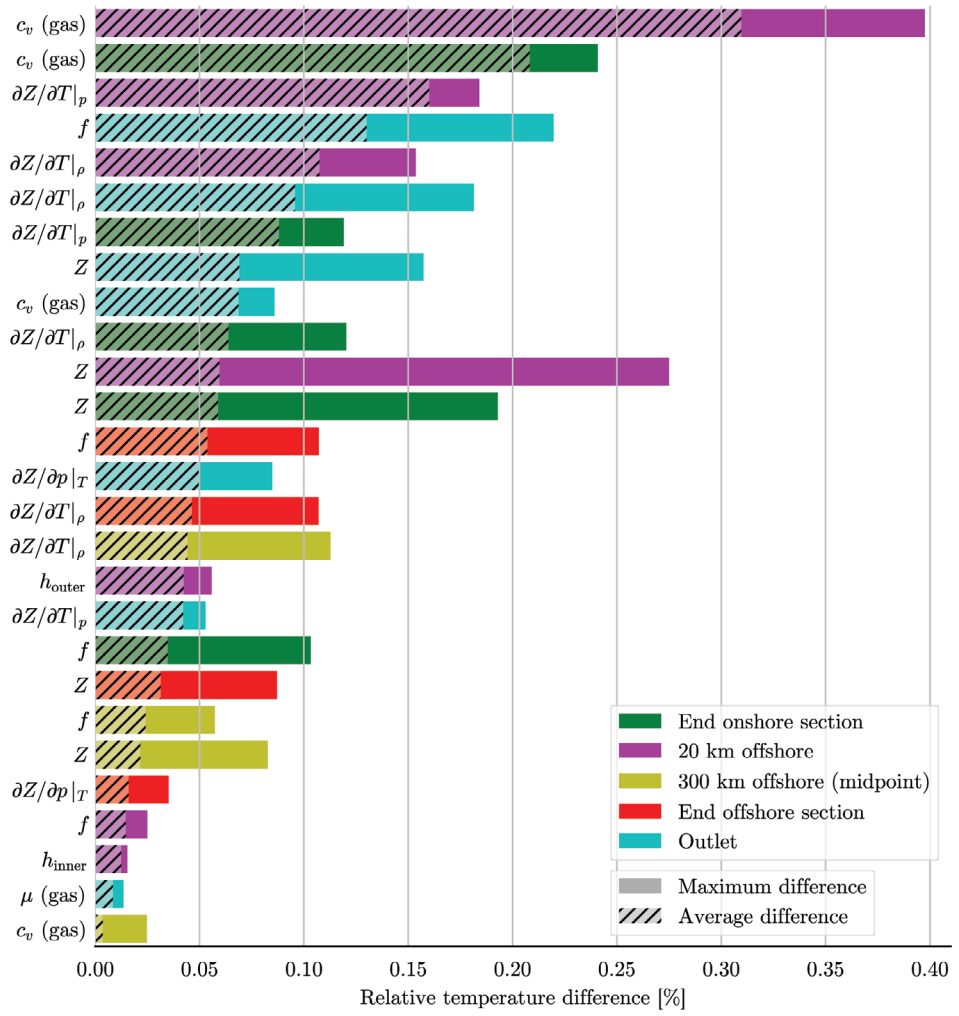

Figure 6: Chart of the average relative difference (the hatched bars) and maximum relative difference (the solid bars) in temperature between the base case and the cases with modified parameters, for 5 different points on the pipeline (the end of the on-shore section, 20 km off shore, 300 km off shore, and the end of the off-shore section). The bars are sorted by descending average error. Only parameters/points with average relative difference above 0.0036 % are shown.

5.2 Comparisons with literature

The sensitivity study by Langelandsvik [4] was performed using steady state models, and most of the parameters are hard to relate to the present study. One parameter that is common for both studies is the viscosity. The viscosity was increased by 1 % by Langelandsvik, which lead to a change in volume flow of 0.03 % to 0.05 % and no observable change in outlet temperature (less than 0.01 °C or 0.004 %). Further, the density was modified by 1 %, which is equivalent to changing the compressibility factor by 1 %, since these values are linked via the equation of state

$$\frac{p}{\rho} = ZRT. \tag{4}$$

The modified density lead to a change in volume flow of 0.50 % and a change in the outlet temperature of around 0.01 °C (0.004 %).

These results does not agree that well with the present results. Here a change in the viscosity of 20 % leads to an average change in mass flow of 0.078 % and an average change in the outlet temperature of 0.84 %. Further, a change in the compressibility factor of 20 % leads to an average change in mass flow of 0.90 % and an average change in the outlet temperature of 0.84 %. The effects on temperature are somewhat in agreement, but the effect on the flow rates are not proportional to the changes in the two parameters. This is most likely caused by how the simulations performed by Langelandsvik are set up: the boundary conditions are inlet temperature, inlet pressure and outlet pressure. This means that the pressure drop is fixed, and any impact on pressure observed in the present work would appear as impacts on flow rate in the work by Langelandsvik.

The sensitivity study by Helgaker [5] used a similar simplified pipeline as in the present study, but a different methodology, so the results are not directly comparable. Helgaker used real boundary conditions based on measurement data, but with flow rates, pressures and temperatures in the same range as synthetic transient used in the present study. In the present study, different correlations were modified directly by a constant factor, while Helgaker modified the friction factor by changing the equivalent sand grain pipeline roughness; tested different equations of state; and modified different parameters used by the heat transfer model, like the thermal conductivity and heat capacity of the pipe wall and burial medium, the burial depth, the length of the buried sections, and the ambient temperature.

Helgaker used sand grain equivalent roughnesses (ϵ in eq. (12)) of 2 µm, 3 µm and 4 µm, and found no observable difference in outlet mass flow or outlet temperature between the three roughnesses, but a difference in inlet pressure of 0.15 MPa (approximately 0.8 % to 1.0 %). This contradicts the results from the present study, which shows that the friction factor is important for both mass flow, pressure and temperature. A rough estimate using the Colebrook-White equation shows that a change in the roughness of 1 µm leads to a change in the friction factor in the order of 2 %, compared to a change in the friction factor of 20 % used in the present study. This relatively small change in the friction

factor used by Helgaker might explain why no difference was observed in the mass flow or temperature. This estimate also shows that the relative effect on pressure when changing the friction factor seems to agree between the two studies, with a change in the friction factor of 0.8 % to 1.0 % leading to a change in the inlet pressure of approximately 1 % in the work by Helgaker, and a change in the friction factor of 20 % leading to a change in the inlet pressure of approximately 4.5 % to 7.2 % in the present work (see fig. 5).

The results of Helgaker for the heat transfer model are hard to compare to the present results, since the physical properties of the pipeline and surroundings were modified, while in the present study the correlations for the inner and outer heat transfer coefficients are modified. This is by design, since the present study sets out to determine where to apply effort when trying to improve the models themselves, not to determine which input to the models that are most important.

Helgaker also looked at the effect of the partial derivatives of Z, by setting them all to zero. He found that this had a small impact on the mass flow, but a considerable effect on the pressure during transients. It also had a large impact on the temperature, since setting $\frac{\partial Z}{\partial T}|_p$ to zero effectively removes the Joule-Thompson effect of cooling upon expansion. It is hard to compare these results to the present study, since setting the derivatives to zero is very different from modifying them by a constant factor of 20 %. But the maximum difference caused by modifying the different derivatives observed in fig. 5 indicate that these parameters are important during transients, which agree with the results of Helgaker.

6 CONCLUSIONS

To determine where to apply effort when trying to improve compressible gas flow models for long off-shore pipelines, the relative importance of a selection of model parameters were determined, by modifying nine different model parameters by 20 % one at the time, and investigating the response in mass flow, pressure and temperature.

It was found that, for the mass flow and pressure, the most important parameters by a factor of between 4 and 14 are the friction factor f and the compressibility factor Z, with an average impact on the modelled mass flow of 1.43 % for the friction factor and 0.90 % for the compressibility factor, and an average impact on the modelled pressure of 3.09 % for the friction factor and 2.07 % for the compressibility factor.

For the temperature, none of the parameters stood out like they did for mass flow and pressure, but it was found that the parameter with the highest average impact on the modelled temperature is the derivative of the compressibility factor with respect to temperature (at constant density) $\partial Z/\partial T|_\rho$, with an average difference of 0.045 %, 1.4 times the impact of the next parameter (the gas heat capacity c_v) and 1.5 times the impact of the third parameter (the friction factor f). Further, a peak in the temperature response for most of the parameters was observed around 20 km after going off-shore, with the highest peak attributed to the gas heat capacity c_v. The response of all parameters are greatly diminished after a long off-shore section, and the highest impact at 300 km

off-shore is attributed to $\partial Z/\partial T\big|_\rho$. Finally, at the end of the off-shore section, and at the outlet, the most important parameter is the friction factor f.

Acknowledgements

This work has been funded by the Norwegian gas operating company Gassco as part of a project to improve flow modeling of off-shore natural gas transmission pipelines. The author would like to thank his advisors Professor Maria Fernandino, Professor Emeritus Tor Ytrehus and Dr. Sigmund Mongstad Hope for helpful advice and fruitful discussions.

References

[1] C. F. Colebrook. "Turbulent flow in pipes, with particular reference to the transition region between the smooth and rough pipe laws". In: *Journal of the Institution of Civil Engineers* 11.4 (1939).

[2] R. Winterton. "Where did the Dittus and Boelter equation come from?" In: *International Journal of Heat and Mass Transfer* 41.4-5 (1998).

[3] F. W. Dittus and L. M. K. Boelter. "Heat transfer in automobile radiators of the tubular type". In: *International Communications in Heat and Mass Transfer* 12 (1985).

[4] L. I. Langelandsvik. "Modeling of natural gas transport and friction factor for large-scale pipelines: Laboratory experiments and analysis of operational data". PhD thesis. Norwegian University of Science and Technology, 2008.

[5] J. F. Helgaker. "Modeling Transient Flow in Long Distance Offshore Natural Gas Pipelines". PhD thesis. 2013.

[6] M. Chaczykowski, F. Sund, P. Zarodkiewicz, and S. M. Hope. "Gas composition tracking under transient conditions for pipeline transport systems". Preprint.

[7] H. Daneshyar. *One-Dimensional Compressible Flow*. Pergamon Press, 1976.

[8] F. M. White. *Viscous Fluid Flow*. Third Edit. McGraw-Hill Education, 2006.

[9] T. Kiuchi. "An Implicit Method for Transient Flow in Pipe Networks." In: *Transactions of the Japan Society of Mechanical Engineers Series B* 59.558 (1993).

[10] M. Abbaspour, K. S. Chapman, and A. Keshavarz. "Dynamic modelling of non-isothermal gas pipeline systems". In: *International Pipeline Conference*. 2004.

[11] J. H. Ferziger and M. Peric. *Computational Methods for Fluid Dynamics*. 3rd. Springer, 2002.

[12] M. Chaczykowski. "Transient flow in natural gas pipeline - The effect of pipeline thermal model". In: *Applied Mathematical Modelling* 34.4 (2010).

[13] J. F. Helgaker, A. Oosterkamp, L. I. Langelandsvik, and T. Ytrehus. "Validation of 1D flow model for high pressure offshore natural gas pipelines". In: *Journal of Natural Gas Science and Engineering* 16 (2014).

[14] A. Oosterkamp, J. F. Helgaker, and T. Ytrehus. “Modelling of natural gas pipe flow with rapid transients - case study of effect of ambient model”. In: *Energy Procedia* 64.C (2015).

[15] A. Oosterkamp. “Heat transfer modelling of natural gas pipe flow - effect of yearly ambient temperature cycles”. In: *The Twenty-sixth (2016) International Ocean and Polar Engineering Conference*. 2016.

[16] F. Sund, A. Oosterkamp, and S. M. Hope. “Pipeline Modeling - Impact of Ambient Temperature and Heat Transfer Modeling”. In: *Proceedings of the Twenty-fifth (2015) International Ocean and Polar Engineering Conference*. 2015.

[17] T. L. Bergman, A. S. Lavine, F. P. Incropera, and D. P. DeWitt. *Fundamentals of heat and mass transfer*. Seventh Ed. John Wiley & Sons Inc., 2011, p. 1076.

[18] M. Chaczykowski. “Sensitivity of pipeline gas flow model to the selection of the equation of state”. In: *Chemical Engineering Research and Design* 87.12 (2009).

[19] K. E. Starling. *Fluid Thermodynamic Properties for Light Petroleum Systems*. Gulf Publishing Company, 1973.

[20] J. Munch. *Tuning af parametre i BWRS-tilstandsligningen til brug i STATPIPES termodynamiske programpakke* [Tuning of parameters in the BWRS equation of state for use in STATPIPE’s thermodynamic software suite]. Tech. rep. Calsep ApS, 1985.

[21] A. L. Lee, M. H. Gonzalez, and B. E. Eakin. “The Viscosity of Natural Gases”. In: *Journal of Petroleum Technology* 18.8 (1966).

[22] M. Abbaspour and K. S. Chapman. “Nonisothermal Transient Flow in Natural Gas Pipeline”. In: *Journal of Applied Mechanics* 75.3 (2008).

[23] J. F. Helgaker, B. Müller, and T. Ytrehus. “Transient Flow in Natural Gas Pipelines Using Implicit Finite Difference Schemes”. In: *Journal of Offshore Mechanics and Arctic Engineering* 136.3 (2014).

[24] J. Thomas. *Numerical Partial Differential Equations: Finite Difference Methods*. Springer New York, 1998.

National Conference on Computational Mechanics
MekIT'17
B. Skallerud and H I Andersson (Eds)

NUMERICAL INVESTIGATION OF FLOW AROUND A STEP CYLINDER

Cai Tian*[1], Fengjian Jiang[1], Bjørnar Pettersen[1] and Helge I. Andersson[2]

[1]Department of Marine Technology, Norwegian University of Science and Technology (NTNU)

[2] Department of Energy and Process Engineering, Norwegian University of Science and Technology (NTNU)
e-mail: cai.tian@ntnu.no

Key words: Direct Numerical Simulation (DNS), Step cylinder, Vortex shedding

Abstract. Flow past a step cylinder with diameter ratio $D/d = 2$ at Reynolds number $Re_D = 150$ was simulated by directly solving the three-dimensional unsteady Navier-Stokes equations. The vortical structures and shedding frequencies of the wake flow were studied in details. One kind of streamwise vortices, i.e. the 'edge vortex' was observed. Three main vortex cells (S-cell vortex behind the small cylinder, L-cell vortex behind the large cylinder and N-cell vortex in between) and the beat frequency which were reported by previous papers were also precisely captured in the present simulation. Additionally, half-loop connection between two L-cell vortices and loop connection between two N-cell vortices were captured. Specially, we noticed antisymmetric topology between two adjacent N-cell cycle periods.

1 INTRODUCTION

In recent years, interfering effects in the wake of a step cylinder Fig 1 a) have received a lot of attention. Structures with similar shape of a step cylinder are used in many industrial applications, for example, the hull of a SPAR-platform, the outer wall of TV-towers, the supporting structures for offshore wind turbines (fixed and floating), and so on.

There are two important variables when considering flow past a step cylinder, i.e. the Reynolds number Re_D and the ratio between diameters of large cylinder and small cylinder (diameter ratio D/d). Many experimental and numerical investigations have been out based on these two parameters. Lewis and Gharib [1] reported two vortex interaction modes in the wake, direct and indirect modes. The direct mode happens when the diameter ratio is smaller than 1.25 ($D/d < 1.25$). In this mode, vortices shed from the large cylinder and the small cylinder have direct connections, and the vortex

interaction between them takes place in a very narrow region around the step. Only two dominating vortex shedding frequencies could be detected. When the diameter ratio becomes larger than 1.55 ($D/d > 1.55$), the indirect mode takes place. Except for the two dominated vortex shedding frequencies of the large and the small cylinder, another low vortex shedding frequency could be captured in the wake region downstream of the step. The vortex cell corresponding to this frequency was defined as N-cell by Dunn and Tavoularis [2]. In paper [2], three types of spanwise vortices were identified based on the shedding frequency: 1) S-cell vortex shedding from the small cylinder with the highest vortex shedding frequency; 2) N-cell vortex shedding in the interaction region [1] with the lowest vortex shedding frequency; 3) L-cell vortex shedding from the large cylinder. Moreover, Dunn and Tavoularis [2] also defined two kinds of streamwise vortices; the edge vortex and the junction vortex. The junction vortex was caused by the recirculation in the step region. The downwash of incoming fluid at the step region induced the edge vortex. They used hydrogen bubbles to visualize these two vortices by doing experiments with a step cylinder (D/d=2) for $Re_D = 1230$. Similar vortices were also observed by Morton and Yarusevych [3]. However, they did not show them directly by numerical simulations.

All of the papers [1, 2, 3] mentioned that the N-cell is a cyclic phenomenon (N-cell cycle). In [3], a detailed description and explanation were given. Morton and Yarusevych [3] suggested that it is the dislocation [4] in N-L cell boundary that causes the N-cell cycle. In their report, during this dislocation, a half-loop connection between two L-cell vortices was captured, but the repetition of L-cell half-loop connection was not shown. Weak cross-boundary or half-loop connections between N-cell vortices were assumed to exist, but they did not observe it.

The primary aim of the present work is to show the structure of streamwise vortices and to investigate the dislocation process in the N-L cell boundary. In order to achieve this, the flow past a step cylinder (D/d=2) at Reynolds number 150 has been studied by means of solving the full three-dimensional unsteady Navier-Stokes equations. The isosurface of λ_2 [5] and velocity spectra were plotted for detailed discussions.

2 FLOW CONFIGURATION AND COMPUTATIONAL METHOD

2.1 Introduction to MGLET

All simulations in this study were conducted by directly solving the full three-dimensional unsteady Navier-Stokes equations for an incompressible fluid. This is achieved with the code MGLET [6, 7]. In this second-order finite-volume solver, the governing equations are in integral form:

$$\int_A \mathbf{u} \cdot \mathbf{n} \; dA = 0 \tag{1}$$

$$\frac{\partial}{\partial t} \iiint_\Omega u_i \; d\Omega + \oint_A u_i \; \mathbf{u}\cdot\mathbf{n} \; dA = -\frac{1}{\rho} \oint_A p \; \mathbf{i_i} \cdot \mathbf{n} \; dA + \nu \oint_A grad \; u_i \cdot \mathbf{n} \; dA \tag{2}$$

where Ω is the control volume and A is the control surface, n is the unit vector on dA pointing out of Ω, and i_i is the Cartesian unit vector in x_i direction. The governing equations (1) and (2) are solved on a staggered Cartesian grid. By discretizing equation (2), the following format could be obtained:

$$\frac{\partial u}{\partial t} = D(u) + C(u) + G(p) = f(u, p) \tag{3}$$

In equation (3), D(u) represents the discretized diffusive term, C(u) represents the discretized convective term, and G(p) represents the discretized pressure term. The surface integral is approximated by the midpoint rule which is of second-order accuracy. The derivative in the integrand of the diffusive term is approximated by a central-difference formulation, which preserves the second-order accuracy. The volume integral in equation (2) is simply approximated by the product of the value of the integrand in the grid center and the control volume of the grid cell. The time integration of equation (3) is done by an explicit low-storage third-order Runge-Kutta scheme [8] (details can be found in [9]). The general idea is to use an explicit time advancement scheme and correct the pressure through solving a Poisson equation to fulfill a divergence-free velocity field:

$$div[(G(\delta p))]\Delta t = div(u^*) \tag{4}$$

Equation (4) is referred to as the discrete analog of the Poisson equation, in which δp is the pressure correction, and u^* is an intermediate velocity field calculated by omitting the pressure term in equation (3). This discretized Poisson equation is represented by a linear equation system at every time marching step. This linear equation system is solved iteratively by Stone's Strongly Implicit Procedure (SIP) [10].

The use of a staggered Cartesian grid brings the problem of interpreting the solid boundaries of the step cylinder in the computational domain. This problem is solved in MGLET by introducing a direct-forcing Immersed Boundary Method (IBM). In MGLET, the surface of the geometry is represented by an unstructured triangular mesh and read directly to IBM to block grid cells bounded by this surface. Then the cells at the fluid-solid interface will be transformed into internal boundary conditions by interpolation [11] from the fluid cells in the vicinity of the bluff body geometry. A more detailed description of the IBM used in MGLET can be found in [11].

2.2 Flow configuration and coordinate system

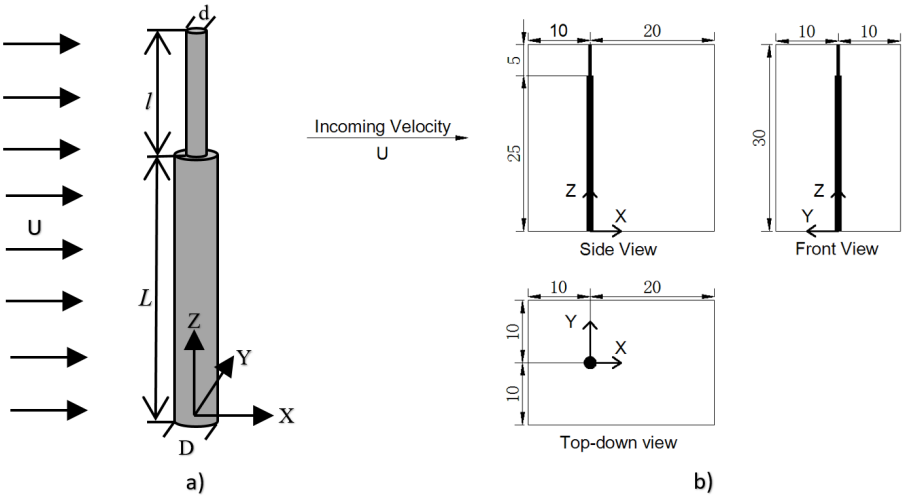

Figure 1: a) The stepped cylinder geometry considered in the present study; b) Domain size illustrated from different viewpoints (Diameter of large cylinder D is the length unit).

Figure 1 a) shows the shape of the step cylinder, in which $D = 1m$ represents the diameter of the large circular cylinder and $d = 0.5D$ represents the diameter of the small circular cylinder. l and L represent the length of the small and large cylinder, respectively. The computational domain is depicted in Figure 1 b). The step cylinder was placed in a continuous uniform flow, $U = 1m/s$, flowing in the X-direction. The inlet plane is placed 10D upstream from center of the cylinder, while the outlet plane is placed 20D downstream. The width of the domain in y-z plane is 20D. The height of the domian is 30D, with the small and the large cylinders occupying 5D and 25D, respectively. Morton and Yarusevych [3] used the same domain size and cylinder length to model flow over a stepped cylinder with the same Reynold number [3]. The following boundary conditions are used in all simulations:

- The inflow boundary: uniform velocity profile u=U, v=0, w=0;
- The outlet boundary: Neumann boundary condition ($\frac{\partial u}{\partial x} = \frac{\partial v}{\partial x} = \frac{\partial w}{\partial x} = 0$) and constant zero pressure condition;
- The body surfaces: no-slip and impermeable wall;
- The other four surfaces: free-slip boundary condition;

3 CASE SUMMARY AND GRID STUDY

3.1 Case overview

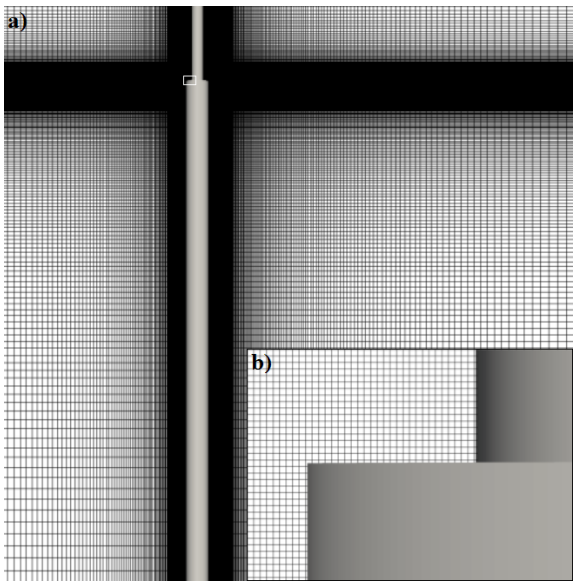

Figure 2: a) Mesh structures in x-z plane at y=0; b) A zoom-in plot of mesh in the step region (white rectangle)

Table 1: Case information of all simulations

Case	Re_D	Min Grid Spacing $\frac{\Delta}{D}$	Grid cells $N_x \times N_y \times N_z$	Total grid number	$\overline{C_D}$
1	150	0.01	414×356×384	56.59 million	0.645
2	150	0.02	264×204×356	19.17 million	0.641
3	150	0.05	244×184×336	15.09 million	0.636
4	150	0.08	196×140×324	8.89 million	0.632
5	150	0.1	174×124×304	6.56 million	0.628

Specific details of all cases are summarised in Table 1. The Reynolds number (Re_D) in this study is defined based on the diameter of large cylinder D and free-stream velocity U, i.e. $Re_D = \frac{UD}{\nu}$ where ν is the kinematic viscosity of the fluid. For all five cases, $Re_D = 150$. The size of the computational domain for all cases is $30D \times 20D \times 30D$. All

cases are simulated on a staggered Cartesian grid. In Fig 2 a), x-z plane view of the mesh structure at y=0 is presented. It is clear that there are two black bands. The quality of the grid in these two bands are better than the rest of the domain. These two bands make sure that the grid resolution near the step cylinder is good enough to resolve the flow phenomenon properly. Because of the abrupt change of cylinder diameter, the flow around the step is expected to be very complicated. A $2D \times 2D \times 2D$ "central block" wrapping the step area was built up. Uniform grid spacing (given in Table 1 as "Min Grid Spacing") is used in the "central block". A part of the uniform grid in the "central block" is plotted in the zoom-in plot, as shown in Fig 2 b). The approximate position of this grid is indicated by a white rectangle in Fig 2 a). The grid is gradually stretched outside of the central block to the far field and the max expansion rate is lower than 1.04. An immersed boundary method (IBM) [9, 11] is used to deal with the intersection between the Cartesian grid and the curved surface of the step cylinder. The same numerical method was used recently by Jiang *et al.* [12] to simulate the wake behind a prolate spheroid. In Fig 3, the drag coefficient $C_D = F_X^{tot}/\rho u^2(dl+DL)$ and the lift coefficient $C_L = F_Y^{tot}/\rho u^2(dl+DL)$ of the step cylinder for case 1 are plotted. It can be observed that fully developed flow was obtained after 250 time units(D/U). All cases have been running for at least 600 time units in parallel on a $SGI\ Altix\ ICE\ X\ SLES-11sp3$ cluster system. The time-step was set to guarantee the maximal CFL number lower than 0.6.

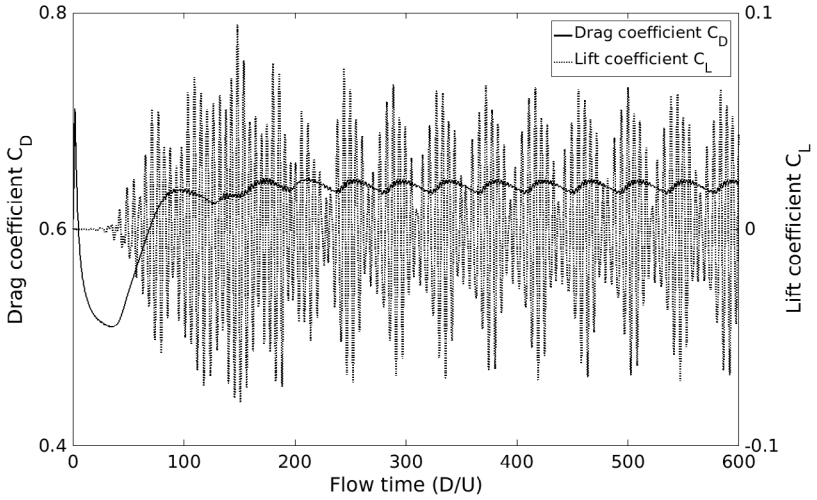

Figure 3: Drag coefficient and lift coefficient of step cylinder for *Case* 1.

3.2 Grid independence study

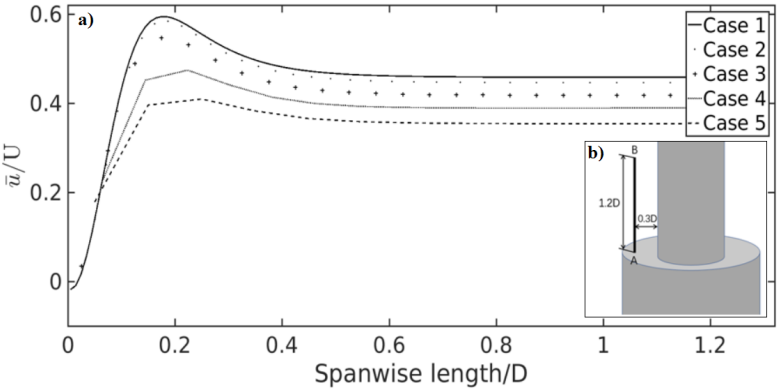

Figure 4: a) Mean streamwise velocity $\frac{\bar{u}}{U}$ distribution along line AB shown in Fig (b); b) Coordinates and length of line AB (in x-z plane with y=0).

In order to ensure that the grid resolution is good enough to capture all important fluid phenomena, especially the complicated flow close to the step, five grids were generated for grid study, as shown in Table 1. First, a rough check was done. Based on the data of mean total drag coefficients $\overline{C_D} = \overline{F_X^{tot}}/\rho U^2(dl + DL)$ in Table 1, an convergence tendency can be found. Additionally, the difference between $Case$ 1 and $Case$ 2 is smaller than 0.6% Then, mean streamwise velocity distributions along line AB (as indicated in the subplot of Fig 4 b)) are calculated to illustrate the flow field near the step. The distribution curves of $\frac{\bar{u}}{U}$ are shown in Figure 4 a). It can be observed that the finer the grid is, the more smoothly the curve becomes ($Case$ 1 and $Case$ 2). The convergence tendency is clear by comparing the discrepancy between adjacent curves. Moreover, the difference between $Case$ 1 and $Case$ 2 is almost negligible. It is therefore safe to conclude that the $Case$ 1 has a fine enough grid resolution. All results presented in the following discussions are therefore based on resolution $Case$ 1.

4 RESULTS

4.1 Overview of flow development

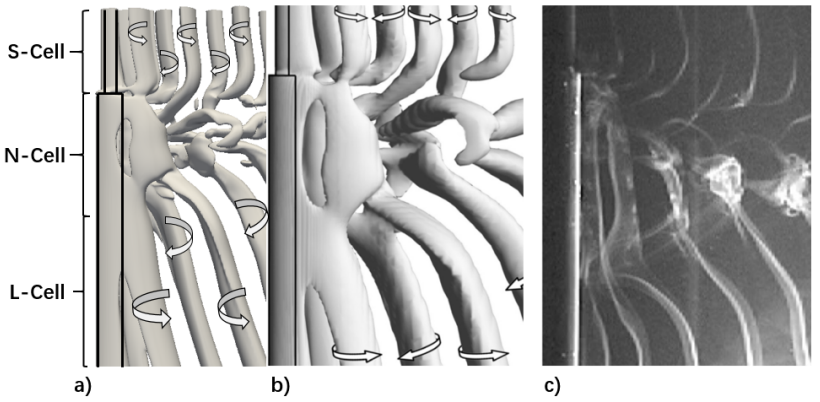

Figure 5: Vortex shedding in the wake of a step cylinder: a) Isosurfaces $\lambda_2 = -0.1$ for $Re_D = 150$ and D/d=2; b) Isosurfaces by Morton and Yarusevych [3] of $Q \approx 2 \times 10^{-3}$ c) Flow visualization image by Dunn and Tavoularis [2] for $Re_D = 150$ and D/d=1.98.

Overview of the vortical structures in the wake for $Re_D = 150$ is illustrated in Fig 5 a) by using isosurface of $\lambda_2 = -0.1$. Similar to the results of Morton and Yarusevych [3] and Dunn and Tavoularis [2], the vortex structures can be mainly divided into three types, namely, the S-cell, the N-cell and the L-cell. Comparing Fig 5 a), b) and c), we observed that the overall wake structures obtained by the present numerical simulation agrees well with previous numerical simulation [3] and experimental results[2]. Although the streamwise vortices is not detectable in Fig 5, the edge vortex was observed in the vicinity of the step. The junction vortex which was observed in [2, 3] was not captured by the present study. As can be observed in Fig 5, vortex structures in the N-cell area are far more complicated than those in the S-cell and L-cell areas. Moreover, it seems like all N-cell structures appear in the wake behind the large cylinder. Detailed discussions are presented in section 4.3.

4.2 Streamwise vortices

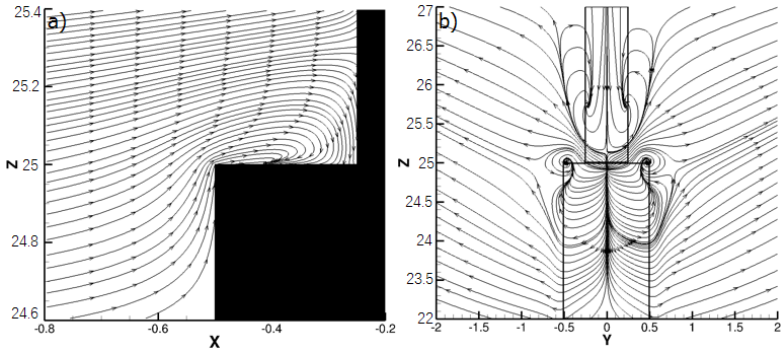

Figure 6: a) Streamline near the step area at x-z plane with y=0; b) Streamline of projected velocity vector in the y-z plane at a downstream position of x=0.6 (i.e. Plane 2 shown in Fig 7 a))

As the flow reaches the region near the step, the streamlines at the symmetry plane tend to separate at the leading edge of the small cylinder and produce a recirculation at the step surface of the large cylinder, which is shown in Fig 6 a). Due to this recirculation, a peak value of vorticity ω_y at the corresponding position was found in Fig 7 b). Based on the vortex structure in Fig 7 a), the concentrated high vorticity region at the shoulder in Fig 7 c) d) and the streamlines in Fig 6 b), it is clear that there is a streamwise vortex pair near the step. As discussed in [2], there might exist two different kinds of streamwise vortices in the step cylinder flow, i.e. the 'junction vortex' and the 'edge vortex', respectively. The 'junction vortex' is caused by recirculation, when viewing upstream, the left-hand vortex tube should rotate clockwise while the right-hand vortex should rotate counterclockwise. The 'edge vortex' has a different topology than the 'junction vortex'. Since the 'edge vortex' is essentially generated by downwash at the edge of the step, it has an opposite rotating direction compared to the 'junction vortex' on each side shoulder of the step [2]. In this way, we may identify the streamwise vortex in the present study. In Fig 6 b), by plotting streamlines in y-z plane just behind the step cylinder, it is easy to find that when viewing upstream from behind the step cylinder, the left-hand vortex rotates counterclockwise and the right-hand vortex rotates clockwise. It means that the streamwise vortex structure marked by a white circle in Fig 7 a) is not the branch of a 'junction vortex', but the 'edge vortex'. Furthermore, the contours of ω_x in y-z plane at different x positions were presented in Fig 7 c) and d).

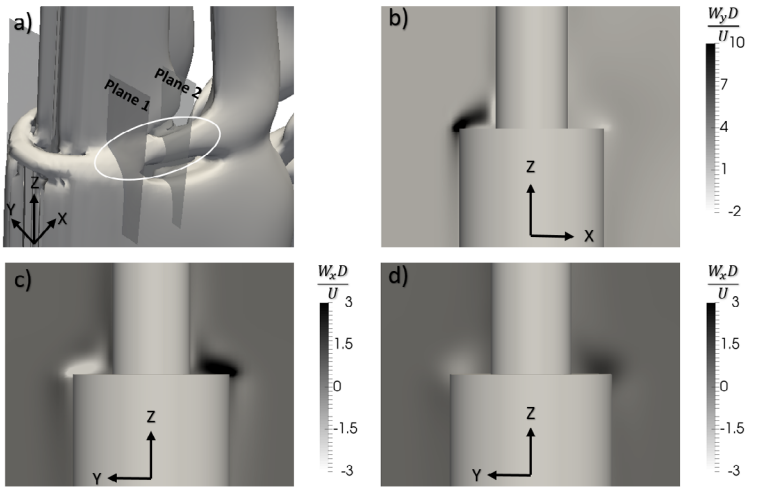

Figure 7: a) Isosurface $\lambda_2 = -0.1$ showing vortex structure near the step; b) Vorticity contour of ω_y at x-z plane of y=0 ; c) Vorticity contour of ω_x at y-z plane of x=0 (i.e. Plane 1 in a)); d) Vorticity contour of ω_x at y-z plane of x=0.6D (i.e. Plane 2 in a))

4.3 Spanwise vortex

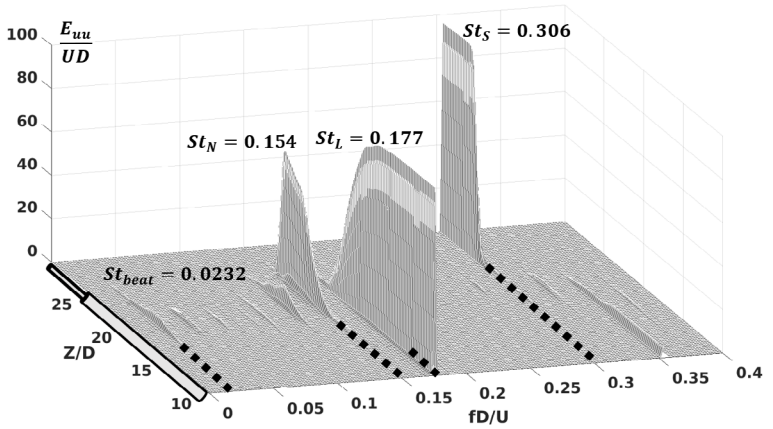

Figure 8: Streamwise velocity spectra for x/D=2.5 and y/D=0.75

Figure 8 shows the streamwise velocity spectra obtained to analyze the frequency and compositions of spanwise vortices. Also, by plotting the λ_2 isosurfaces in Fig 9, the

spanwise vortex structures in the wake can be clearly observed. In order to analyze the generation of N-cell cycle (definition of N, S, L cell can be seen in Fig 5), we present consecutive images through a N-cell cycle in Fig 9. Moreover, the features and repetitions of N-cell cycle are shown in Fig 10. It is worthy to mention that the N-cell cycle refers to the cyclic changes in the N-cell instead of the N-cell vortex shedding, the differences will be explained in the following discussions.

- *Spanwise vortex shedding frequency*

  The streamwise velocity data is sampled at discrete points along a line parallel to z-axis at x/D=2.5 and y/D=0.75. By Fast Fourier Transform of the time-series of u, streamwise velocity (E_{uu}) spectra are presented in Fig 8. From this figure, three dominating peaks can be observed, corresponding to S-cell $St_S = f_S D/U = 0.306$, N-cell $St_N = f_N D/U = 0.154$ and L-cell vortices $St_L = f_L D/U = 0.177$. Additionally a smaller peak at the beat frequency $St_{beat} = f_{beat} D/U = 0.0232$ is also captured. The beat frequency is caused by linear combinations and harmonics of the shedding frequencies of the adjacent vortices, which is commonly observed in quasiperiodic spectra associated with spanwise vortex cells [4, 13]. In comparision, [3] reported $St_S = 0.320$, $St_N = f_N D/U = 0.157$, $St_L = f_L D/U = 0.179$ and $St_{beat} = 0.022$. The maximum discrepancy is smaller than 6%, which is totally acceptable.

- *Main spanwise vortex structures*

  $S - cell\ vortex$: In Fig 9, first, behind the top half of the small cylinder, the S-cell vortex structures are shed, one by one, regularly and parallel to each other. This is similar to the wake structure behind a circular cylinder without a step. Secondly, behind the lower part of the small cylinder, due to the influence of the step, the complex connection between the N and S cell vortex appears. The connection can be mainly divided into two types: some of the S-cell vortices connected to the N-cell vortices, some of the S-cell vortices connected to the other side S-cell vortices forming a half-loop connection. For example, in Fig 9 a), the connection between vortex S2 and N1 belongs to the first type; while the connection between vortex S1 and S0 belongs to the second type.

  $L - cell\ vortex$: Similar to the S-cell vortex, behind the lower part of the large cylinder, L-cell vortex structures are parallel to each other regularly. When we come closer to the step, we observed complex connections between the N-cell and L-cell vortices. In Fig 9, there are mainly two types of connections. The first one is characterized by a L-cell vortex connects to a corresponding N-cell vortex, like N5 to L5, N7 to L7 and so on. The other type is characterized by one L-cell vortex connects to the subsequent L-cell vortex forming a half-loop connection, like L1' to L0' and L2' to L3' in Fig 10.

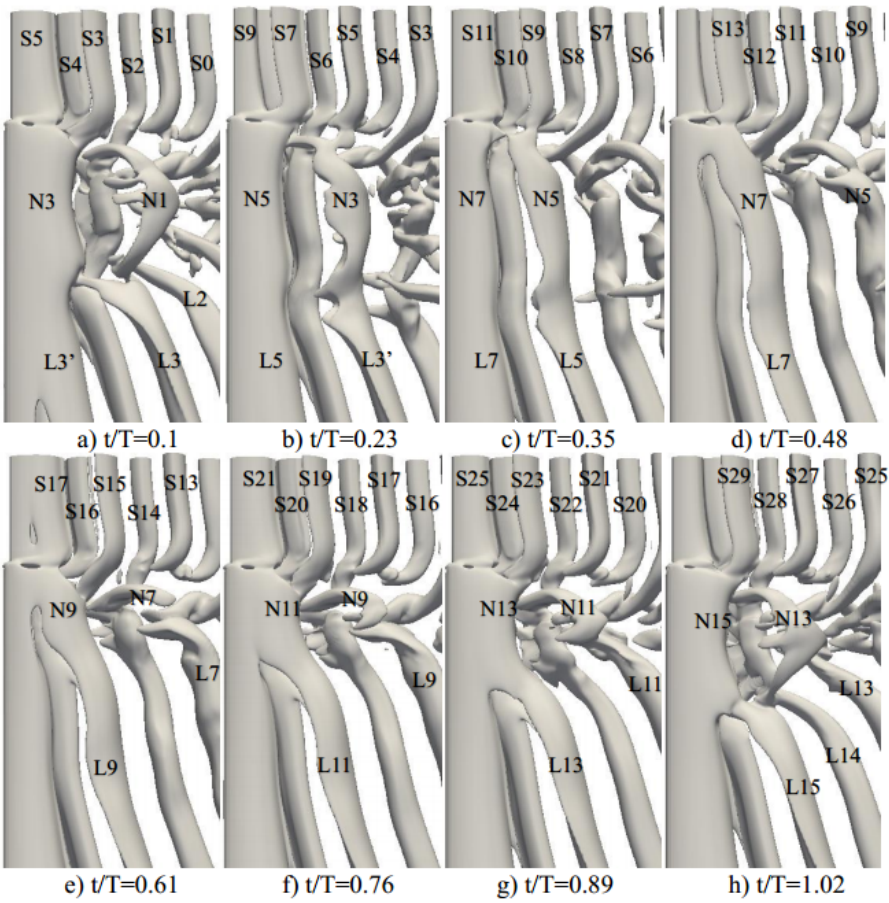

Figure 9: Isosurface of $\lambda_2 = -0.1$ showing N-cell development. T is the period of one N-cell cycle defined by the beat frequency.

$N-cell\ vortex$: There are two kinds of N-cell shedding: N-cell vortex shedding defined by St_N and N-cell cycle shedding defined by St_{beat}. The time sequences in Fig 9 show the whole process of an N-cell cycle development. It is clear that the vortex structures in a) and h) are very similar, representing the same phase in two adjacent periods. From Fig 9, it can be found that around 14 N-cell vortices are shed during one N-cell cycle. This estimation agrees well with those reported in [2, 3].

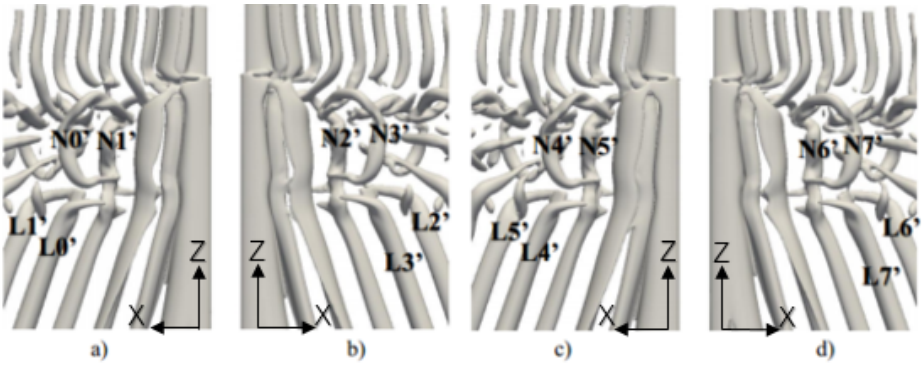

Figure 10: Isosurface of $\lambda_2 = -0.2$ showing features and repetitions of N-cell cycle a) t=659; b) t=701; c) t=743; d) t=785 ('D/U' is the time unit).

The features and repetition of $N-$cell cycle: The N-cell cycle is caused by the dislocation between N-L boundary [3]. It means the period of the N-cell cycle is long, compared to the three main vortex cells. Moreover, during a N-cell cycle, the interactions and variations of three vortex cells are very complicated. It is necessary to find clear features that may help to identify the different cycles. Through long time observation (more than 200D/U), two distinct characteristics were captured, as shown in Fig 10. The first one is a half-loop connection generated between two L-cells, like L1' and L0' in Fig 10 a). The other is that a N-cell vortex on one side connected to the subsequent N-cell vortex on the other side, forming a loop connection, like N0' and N1' in Fig 10 a). These two features always appear together and only once during every N-cell cycle. The half-loop connection was also captured by Morton and Yarusevych [3], but they did not show the repetition of this feature. Meanwhile, they speculated that the weak cross-boundary or half-loop N-cell vortex connections may persist but they couldn't observed it. The N-cell loop in Fig 10 nicely proves this speculation. To the authors' knowledge, this is the first time that the beat frequency is clearly identified and shown by the L-cell half-loop and N-cell loop.

5 CONCLUSION

The study shows good agreement with previous researches [2, 3]. For streamwise vortices, the 'jucntion vortex' which was captured in [2] was not observed in the present study. This may be explained by a Reynolds number effect. Dunn and Tavoularis [2] observed the 'junction vortex' for $Re_D = 1230$ which is much higher than in the present study. However, the 'edge vortex' mentioned in [2] is captured in the present case and clearly shown in Fig 7 a). By calculating the streamwise velocity spectra, shedding frequencies of

three main vortex cells together with the beat frequency were captured. The discrepancy is smaller than 6% compared to previous study [3]. The repetition of N-cell cycle was shown clearly in Fig 10. This phenomenon was speculated to exist in [3], but haven't been presented by any results. Another interesting observation is that the vortex structure is antisymmetric. Finally, different from the speculation about half-loop connection in [3], a full-loop connection between two N-cell vortices was observed.

In the future, higher Reynolds numbers (e.g. extending to 10^4) and higher diameter ratios between large cylinder and small cylinder will be investigated to explore when a 'junction vortex' can be observed. Additionally, a study about how the loop connection for N-cell vortices is generated and why the vortex structure become anti-symmetric would be of interest.

6 ACKNOWLEDGEMENTS

Computing time on Vilje was granted by the Norwegian Research Council (Program for Supercomputing). The first author would like to thank China Scholarship Council (CSC) for financial support.

REFERENCES

[1] C.G. Lewis and M. Gharib, *An exploration of the wake three dimensionalities caused by a local discontinuity in cylinder diameter*. Physics of Fluids A: Fluid Dynamics 4.1 (1992): 104-117.

[2] W. Dunn and S. Tavoularis *Experimental studies of vortices shed from cylinders with a step-change in diameter*. Journal of Fluid Mechanics 555 (2006): 409-437.

[3] C. Morton and S. Yarusevych *Vortex shedding in the wake of a step cylinder*. Physics of Fluids 22 (2010): 083602.

[4] C.H.K. Williamson, *Oblique and parallel modes of vortex shedding in the wake of a circular cylinder at low Reynolds numbers*. Journal of Fluid Mechanics 206 (1989): 579-627.

[5] J. Jeong and F. Hussain *On the identification of a vortex*. Journal of Fluid Mechanics 285 (1995): 69-94.

[6] M. Manhart, *A zonal grid algorithm for DNS of turbulent boundary layers*. Computers & Fluids 33.3 (2004): 435-461.

[7] M. Manhart and R. Friedrich *DNS of a turbulent boundary layer with separation*. International Journal of Heat and Fluid Flow 23.5 (2002): 572-581.

[8] J.H. Williamson, *Low-storage runge-kutta schemes*. Journal of Computational Physics 35.1 (1980): 48-56.

[9] N. Peller, *Numerische simulation turbulenter Strmungen mit immersed boundaries*. Diss. Universitt Mnchen (2010).

[10] H.L. Stone, *Iterative solution of implicit approximations of multidimensional partial differential equations*. SIAM Journal on Numerical Analysis 5.3 (1968): 530-558.

[11] N. Peller, et al. *Highorder stable interpolations for immersed boundary methods*. International Journal for Numerical Methods in Fluids 52.11 (2006): 1175-1193.

[12] F. Jiang, J.P. Gallardo and H.I. Andersson, *The laminar wake behind a 6: 1 prolate spheroid at 45 incidence angle*. Physics of Fluids 26 (2014): 113602.

[13] D. Gerich and H. Eckelmann *Influence of end plates and free ends on the shedding frequency of circular cylinders*. Journal of Fluid Mechanics 122 (1982): 109-121.

9th National Conference on Computational Mechanics
MekIT'17
B. Skallerud and H I Andersson (Eds)

NUMERICAL SIMULATION OF CAVITATING MARINE PROPELLER FLOWS

VILLE M. VIITANEN[1] AND TIMO SIIKONEN[2]

[1]VTT Technical Research Centre of Finland Ltd.
PO Box 1000, FI-02044 VTT, Finland
e-mail: ville.viitanen@vtt.fi - Web page: http://www.vtt.fi

[2]Aalto University
Department of Mechanical Engineering
PO Box 11000, 00076 Aalto, Finland
e-mail: timo.siikonen@aalto.fi - Web page: http://www.aalto.fi

Key words: Two-phase Flow, Cavitation, Turbulence Modelling, Marine Propellers, CFD

Abstract. A compressible homogeneous flow model is applied for the solution of two-phase flow around marine propellers. A novel method to solve phase volume fractions is proposed. The numerical method is applied for a model-size marine propeller in cavitating conditions, and the computed results are validated against experimental data in terms of global performance characteristics, local flow phenomena and cavitation prediction.

1 INTRODUCTION

Cavitation, when it occurs, is a dominant cause of many detrimental impacts faced by a marine propeller. Cavitation may trigger erosion, cause vibration problems, or result in high intensity underwater noise emission. Depending on the propeller operating conditions, many different forms of cavitation can be identified such as a steady attached sheet cavitation on the blade surface, a bubble or cloud cavitation on the blade or in the wake, and vortex cavitation where the propeller tip and hub vortices cavitate. Specifically, marine propellers are an important source of noise emitted from ships to the underwater environment and to the interior of the vessel. In the case of phase changes, the underwater noise from cavitation dominates other propeller-induced noise, excluding singing, and all other underwater noise from a ship [1]. For these reasons, an accurate prediction of the two-phase flow phenomena is important in the design of ship propellers.

In recent years, computational fluid dynamics (CFD) has been actively utilized to study the propeller performance in wetted and cavitating conditions [2–6]. Flow structures in the wake and tip vortex of a propeller employing different RANS (Reynolds-averaged

Navier-Stokes) or scale-resolving turbulence closures have been studied by [7] and [8]. Additionally, higher fidelity turbulence closures, such as the large eddy simulation (LES) or detached eddy simulation (DES) approaches have been used to compute the flow past marine propellers [4–6]. Specific attention towards propeller-induced noise has been given, *e.g.,* in Ref. [9]. Budich et al. [10] studied a propeller in cavitating conditions, where the authors focused on the shock wave dynamics including an erosion assessment.

In this paper, a numerical method for a solution to homogeneous two-phase flow is presented. In the solution, the phases share the same velocity but have different temperatures. Both phases are assumed to be compressible. A pressure-based algorithm similar to a single-phase solution [11] is used for the pressure-velocity coupling, and a finite-volume discretization is employed. For the void fraction equation, two different TVD flux limiters are applied, whereas for the other variables a MUSCL-interpolation [12] is utilized.

Previously, the present method has been applied for propeller flows in Refs. [7,13] . The computational case used in this paper is the Potsdam Propeller Test Case (PPTC) [14]. The results are compared to experimental data in terms of global propeller forces, cavitation observation and local flow phenomena. Multiple different turbulence closures are utilized: linear and non-linear two-equation models, as well as a hybrid RANS/LES model. The two-equation models used are Chien's low-Reynolds-number $k-\varepsilon$ model [15], Menter's SST $k-\omega$ [16], and the SST model with an Explicit Algebraic Reynolds Stress Model (EARSM) [17]. Beyond the traditional RANS approach, a DDES (delayed detached eddy simulation) approach based on the SST $k-\omega$ is used [18].

In the next section, the hydrodynamic modelling is described, followed by a description of the essential features of the solution methods. Next, the test case is introduced, followed by an assessment and validation of the numerical results. Finally, conclusions are drawn from the presented results.

2 FLOW MODEL

2.1 Governing equations

The flow model applied is based on a homogeneous flow assumption, which is a common assumption as far as cavitation is concerned [19]. The governing equations for the cavitation model are

$$\begin{aligned} \frac{\partial \alpha_k \rho_k}{\partial t} + \nabla \cdot \alpha_k \rho_k \mathbf{V} &= \Gamma_k \\ \frac{\partial \rho \mathbf{V}}{\partial t} + \nabla \cdot \rho \mathbf{V}\mathbf{V} + \nabla p &= \nabla \cdot \boldsymbol{\tau}_{ij} + \rho \mathbf{g}, \end{aligned} \tag{1}$$

where p is the pressure, $\mathbf{V}$ the velocity and $\boldsymbol{\tau}_{ij}$ the stress tensor, α_k is a void (volume) fraction of phase k, ρ_k the density, t the time, Γ_k the mass transfer term and $\mathbf{g}$ the gravity vector. For the mass transfer $\sum_k \Gamma_k = 0$ holds, and consequently only a single mass transfer term is needed. In the following, we define $\Gamma = \Gamma_g$.

Although the phase temperatures do not play a significant role in cavitation, the energy equations are always solved in the present method. The aim is to apply a compressible form of the equations. In order to predict the correct acoustic signal speeds, a complete model is needed. The phase temperatures T_g and T_l also have some influence on the solution via the material properties that are calculated as functions of the pressure and phase temperatures.

The energy equations for phase $k = g$ or l are written as

$$\frac{\partial \alpha_k \rho_k (e_k + \frac{V^2}{2})}{\partial t} + \nabla \cdot \alpha_k \rho_k (e_k + \frac{V^2}{2}) \mathbf{V} = \\ -\nabla \cdot \alpha_k \mathbf{q}_k + \nabla \cdot \alpha_k \boldsymbol{\tau}_{ij} \cdot \mathbf{V} + q_{ik} + \Gamma_k (h_{k\mathrm{sat}} + \frac{V^2}{2}) + \alpha_k \rho_k \mathbf{g} \cdot \mathbf{V}. \tag{2}$$

Here e_k is the specific internal energy, $\mathbf{q}_k$ the heat flux, q_{ik} interfacial heat transfer from the interface to phase k and $h_{k\mathrm{sat}}$ saturation enthalpy. Since $\sum_k \Gamma_k = 0$, by adding the energy equations together the following relationship is obtained between the interfacial heat and mass transfer

$$\Gamma_g = -\frac{q_{ig} + q_{il}}{h_{g\mathrm{sat}} - h_{l\mathrm{sat}}} \quad \text{and} \quad q_{ik} = h'_{ik}(T_{\mathrm{sat}} - T_k). \tag{3}$$

Above h'_{ik} is a heat transfer coefficient between the phase k and the interface. The interfacial heat-transfer coefficients are based on the mass transfer, as is shown in Section 2.3.

The momentum and total continuity equations in the homogeneous model do not change, except the material properties like density and viscosity are calculated as

$$\rho = \sum_k \alpha_k \rho_k \quad \text{and} \quad \mu = \sum_k \alpha_k \mu_k, \tag{4}$$

where μ is the dynamic viscosity. The turbulence effects are currently handled using single-phase eddy-viscosity models for the mixture.

2.2 Turbulence modelling

Nominally a Reynolds-averaged form of Eqs. (1-2) is used, but a detached eddy simulation (DES) that combines RANS and LES is also applied in the same form. Usually, in the cavitation modelling turbulence is taken into account using single-phase closures. Also in this study, the turbulence modelling is applied for the homogeneous mixture. The choice of turbulence closure plays an essential role in the numerical prediction of the performance of a marine propeller. While the global forces or steady cavitation patterns near the blades generally might not considerably differ between the turbulence closures, the utilized model can have a significant influence on unsteady flow structures, or on the flow in the wake of the propeller. In the case of unsteady propeller cavitation, the capturing of the cavitation dynamics is crucial in order to assess not only the performance but also the

erosive tendency of collapsing cavities, as well as the induced underwater noise. Moreover, accurate prediction of the wake flow is important when considering the propeller-rudder, propeller-pod or multi-propeller interactions, or the noise emitted by the propeller.

The RANS models applied in the present calculations are Chien's low-Reynolds-number $k-\varepsilon$ turbulence model [15], and Menter's SST $k-\omega$ model [16]. The latter formulation is used in connection with an Explicit Algebraic Reynolds Stress Model (EARSM) [17]. The applied hybrid RANS/LES approach called delayed detached eddy simulation (DDES) is also based on the SST-model [20]. With all models the calculations are performed up to the wall. The non-dimensional wall distance is adjusted such that the non-dimensional wall distance $d^+ \lesssim 1$ for the first cell.

The SST $k-\omega$ is a zonal model, referring to the formulation where the $k-\omega$ equations are solved only inside the boundary layer, and the standard $k-\varepsilon$ equations, transformed to the ω-formulation, are solved away from the walls. The models are coupled using a blending function F_1 [16]. Both the $k-\varepsilon$ and the $k-\omega$ turbulence models are isotropic, *i.e.*, and they predict the Reynolds stress tensor according to the Boussinesq approximation

$$-\rho\overline{u_i'u_j'} = 2\mu_T S_{ij} - \frac{2}{3}\delta_{ij}\rho k. \tag{5}$$

where μ_T is the eddy viscosity, S_{ij} the strain-rate tensor and k the turbulence kinetic energy. To account for turbulent anisotropy, an explicit algebraic Reynolds stress model (EARSM) is utilized [17]. The EARSM applied relies on the SST formulation, but with the Reynolds stress anisotropy tensor, defined as

$$a_{ij} = \frac{\overline{u_i'u_j'}}{k} - \frac{2}{3}\delta_{ij}, \tag{6}$$

evaluated from a linear pressure-strain model. The traditional Boussinesq approximation is replaced with the EARSM approach by modifying the Reynolds stress tensor as

$$-\rho\overline{u_i'u_j'} = 2\mu_T S_{ij} - \frac{2}{3}\rho k\delta_{ij} - \rho k a_{ij}^{(ex)}, \tag{7}$$

where the last term is the corrective extra-anisotropy tensor. When the EARSM is active, only the first three terms are kept in the implicit stage of solution.

Detached eddy simulation (DES) is a hybrid RANS/LES model, and functions as an LES subgrid model in regions where the local turbulent phenomena are of greater size than the local grid spacing [21]. A time-accurate solution is made to resolve the turbulent fluctuations. In the present cases, a second-order three-level fully implicit method is used. The DES model reduces to a RANS model in regions where the largest turbulent fluctuations are of a smaller size than the local grid spacing. In the present study, DES is based on the modification of the SST $k-\omega$ model [18]. In DES, the equation for the turbulent kinetic energy can be written with a modified dissipation term as

$$\rho\frac{Dk}{Dt} = P - \frac{\rho k^{3/2}}{l_{DES}} + D, \tag{8}$$

where l_{DES} is the length scale and D is the diffusion term. The DES length scale is computed as the minimum of the RANS length scale, $l_{RANS} = \sqrt{k}/\beta^*\omega$, and the local resolution Δ. Here $\beta^* = 0.09$ is a model constant. Parameter Δ is evaluated as the minimum of the local wall distance, and the grid resolution $\max(\Delta x_i)$, where Δx_i denotes the thickness of the cell in different index directions. The DES length scale is then

$$l_{DES} = \min(C_{DES}\Delta, l_{RANS}), \tag{9}$$

and the coefficient C_{DES} is computed from

$$C_{DES} = (1 - F_1)C^{k-\varepsilon}_{DES} + F_1 C^{k-\omega}_{DES}, \tag{10}$$

where the constants are $C^{k-\varepsilon}_{DES} = 0.61$, $C^{k-\omega}_{DES} = 0.78$, and F_1 is Menter's blending function. Furthermore, when utilizing the delayed DES (DDES), the length scale is replaced by the expression [20]

$$l_{DDES} = l_{RANS} - F_1 \max(0, l_{RANS} - C_{DES}\Delta). \tag{11}$$

Here $F_1 \to 1$ outside the boundary layer, and the length scale becomes $l_{DDES} = C_{DES}\Delta$ if the grid spacing permits. The DDES variant of DES aims to improve the accuracy compared to Eq. (9), which has in some instances been observed to cause grid-induced separation. It should be noted that the standard model constants (*e.g.,* 0.09, 0.61, 0.78) applied have not been validated in a full scale situation. Also in the following the effect of turbulence modelling will be studied by varying the turbulence closure, not the model parameters.

2.3 Mass and energy transfer

A number of mass transfer models has been suggested for cavitation [22]. Usually the mass transfer rate is proportional to a pressure difference from a saturated state or to a square root of that. In this study the mass transfer model is similar to that of Merkle et al. [19]

$$\Gamma_l = \frac{\rho_l \alpha_l \min\left[0, p - p_{\text{sat}}\right]}{\frac{1}{2}\rho_\infty V_\infty^2 (L_{\text{cav}}/V_{\text{cav}})\tau_l} + \frac{\rho_g \alpha_g \max\left[0, p - p_{\text{sat}}\right]}{\frac{1}{2}\rho_\infty V_\infty^2 (L_{\text{cav}}/V_{\text{cav}})\tau_g}, \tag{12}$$

where p_{sat} is the saturation pressure, ρ_∞ the reference (inlet) density, V_∞ the corresponding velocity. The evaporation time constants are made non-dimensional using the reference length L_{cav} and the velocity related to cavitation (V_{cav}). In some cases, such as on a propeller blade, the cavitation length and velocity differ from the reference length L_{ref} and the reference velocity (V_∞). The time constants correspond to the parameters of the original model as $\tau_l = 1/C_{\text{dest}}$ and $\tau_g = 1/C_{\text{prod}}$. There are several suggestions for the parameters C_{dest} and C_{prod}. A common choice is $C_{\text{dest}} = C_{\text{prod}} = 100$.

In the present method, the saturation pressure is based on the free-stream temperature, and the gas phase is assumed to be saturated, *i.e.* $T_g = T_{\text{sat}}$. Liquid temperature varies less because of the mass and energy transfer. Since the gas temperature is forced to be

$T_g = T_{\mathrm{sat}}$, $q_{ig} = 0$. From Eq. (3) the interfacial heat transfer can be solved for the liquid phase

$$q_{il} = -(h_{g\mathrm{sat}} - h_{l\mathrm{sat}})\Gamma_g - q_{ig} = (h_{g\mathrm{sat}} - h_{l\mathrm{sat}})\Gamma_l. \tag{13}$$

Using Eqs. (12) and (13), the interfacial transfer terms in the continuity and energy equations can be solved.

In order to decrease the oscillations in the solution owing to the rapid changes in the mass transfer, the mass transfer rate is under-relaxed between the iteration cycles as $\Gamma_l^{n+1} = \alpha_\Gamma \Gamma_l^* + (1 - \alpha_\Gamma)\Gamma_l^n$, where $\alpha_\Gamma = 0.5$ is an under-relaxation factor, n refers to the iteration cycle and Γ_l^* is calculated from Eq. (12). For small values $|\Gamma_l^n| < 0.1\,\mathrm{kg/m^3s}$ under-relaxation is not applied. The under-relaxation factor and the limit are quite arbitrary, although tested by numerous simulations.

3 Solution methods

3.1 Finite-volume Form

Eqs. (1) can be written in a general finite-volume form for a cell $\mathscr{V}_i$ as

$$\begin{aligned} \mathscr{V}_i \frac{d(\alpha_k \rho_k)_i}{dt} + \sum_j (S \alpha_k \rho_k \bar{u})_j &= \mathscr{V}_i \Gamma_{k,i}, \\ \mathscr{V}_i \frac{d(\rho \mathbf{V})_i}{dt} + \sum_j \dot{m}_j \mathbf{V}_j + \sum_j S_j n_j p_j &= \sum_j S_j (\boldsymbol{\tau}_{ij} \cdot \mathbf{n})_j + \mathscr{V}_i (\rho_i - \rho_0)\mathbf{g} \end{aligned} \tag{14}$$

where the sum is taken over all cell surfaces j, $\mathbf{n}_j$ is a surface normal on a cell face and S_j the cell face area. The mass flux $d\dot{m} = \rho \mathbf{V} \cdot \mathbf{n} dS = \rho \bar{u} dS$ can be identified in all field equations. In Eqs. (14) a Rhie-Chow type damping term is added via the convective velocity $\bar{u}$. Instead of the commonly used scaling, the term is scaled using an artificial sound speed [11]. Pressure differences are applied and the flux terms are written in terms of the void fraction. However, the implicit solution is based on mass fractions:

$$\mathscr{V}_i \frac{d(\rho x)_i}{dt} + \sum_j \dot{m}_j x_j = \mathscr{V}_i \Gamma_i. \tag{15}$$

This form in the implicit stage is convenient, since the same mass flows can be used in the Jacobian matrices.

Eqs. (14) can be applied for arbitrary cell shapes, although in the present solution a structured grid is applied. The viscous fluxes as well as the pressure terms are centrally differenced. For the convective part the variables on the cell surfaces are evaluated using a third-order upwind-biased MUSCL interpolation [12]. A flux limiter can be applied, but in this study this is done only for the void fraction. The application of a limiter function (ϕ) to the convective fluxes of the void fraction may be necessary, since it is essentially a discontinuous quantity through the phase boundary. This may lead to problems in a

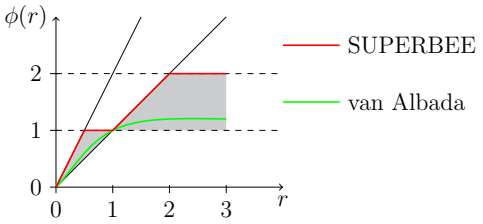

Figure 1: Van Albada and superbee limiters in the Sweby diagram.

numerical solution, and the void fraction could locally obtain non-physical values amidst an iterative solver. Additionally, cavitation volumes can exhibit rapid temporal and spatial variation when, for instance, bursts of cloud cavities or fine cavitating vortices are present. In this study, two different TVD limiters are utilized: the limiter of Van Albada [23], and the 'superbee' limiter of Roe [24]. The Van Albada limiter is a more diffusive one, whereas Roe's superbee is a compressive limiter. The behaviour of the limiters is depicted in Fig. 1. A review of the high-resolution limiters for two-phase flows is given, *e.g.,* in [25].

3.2 Solution algorithm

Two different solution strategies are utilized for the simulations of the flow around the rotating propeller. The first one is to rotate the computational domain with the propeller rate of revolution, and integrate the governing equations in the physical time. The three-level fully implicit scheme is applied with all turbulence closures. Consequently, results which are obtained from this strategy are referred to as transient. In this approach, a steady-state solution is sought within each physical time-step by iterating until the L_2 norms of the main variables have decreased by a sufficient amount, *i.e.*, at least 2-3 orders of magnitude. One hundred inner iterations are usually required within each physical time-step for non-cavitating simulations. In the present study, between 150-200 inner iterations were made for the cavitating simulations, depending upon the utilized turbulence model.

The second approach exploits the fact that the governing equations can yield a steady-state solution, when the equations are expressed in the coordinate system that is rotating with the propeller. Consequently, this solution method is referred to as quasi-steady. Absolute velocities are used in the solution, and the rotational movement of the propeller is accounted for in the convection velocity and as source terms in the y and z-momentum equations as the propeller is rotating around the x-axis. The equations are iterated until the global force coefficients and the L_2 norms of the main variables have obtained a sufficiently steady level, with the L_2 norms having decreased to $10^{-5} \ldots 10^{-7}$.

We note here that the transient simulation of the performance characteristics of an

open-water propeller is not usually necessary. In many cases, a quasi-steady RANS analysis provides excellent agreement in terms of the global propeller performance characteristics and steady cavitation patterns, which usually are the primary quantities and phenomena in which a propeller designer is often interested. However, in the future our aim is to predict propeller-induced underwater noise utilizing a computational hydroacoustic methodology, which in turn solely relies on transient CFD data as input [13].

The solution method is a segregated pressure-based algorithm where the momentum equations are solved first and then a coupled pressure-velocity correction is made. A pressure correction equation is derived from the continuity equations linked with the linearized momentum equation. The method is based on the corresponding algorithm for a single-phase flow [11]. The solution of the momentum and turbulence equations is straightforward and is not described here. The basic idea in the solution of all equations is that the mass balance is not forced at every iteration cycle, but rather the effect of the mass error is subtracted from the linearized equations. An example of this treatment is seen in Section 3.4.

3.3 Pressure-correction method

A derivation of a pressure correction equation is started by establishing a relationship between the pressure and velocity corrections on a cell face. Ignoring the off-diagonal terms (SIMPLE approximation), the following relationship is obtained between the velocity and pressure corrections:

$$\mathbf{V}'_{i+1/2} = -\frac{\mathscr{V}_{i+1/2}}{\bar{a}^u_{P,i+1/2}} \left(\nabla p'\right)_{i+1/2}, \tag{16}$$

where $\mathscr{V}_{i+1/2}$ is a volume of an auxiliary cell located at the face and the multiplier is obtained from the two diagonal elements of the Jacobian matrix for the momentum equations [11]

$$\frac{1}{\bar{a}^u_{P,i+1/2}} = \frac{1}{2}\left(\frac{1}{a^u_{P,i+1}} + \frac{1}{a^u_{P,i}}\right). \tag{17}$$

The two-phase solution is based on approximating the gradients of the pressure correction on the basis of an orthogonal grid assumption. Thus, for the SIMPLE method

$$\bar{u}'_{i+1/2} = -\frac{S_{i+1/2}}{\bar{a}^u_{P,i+1/2}}(p'_{i+1} - p'_i). \tag{18}$$

Next, the continuity equations are linearized as

$$\left[\frac{\mathscr{V}_i\rho_{k,i}}{\Delta t} + \sum_{out} S_j\rho_{k,i}\bar{u}_j\right]\delta\alpha_{k,i} + \left[\frac{\mathscr{V}_i\alpha_{k,i}}{\Delta t} + \sum_{out} S_j\alpha_{k,i}\bar{u}_j\right]\frac{\partial\rho_{k,i}}{\partial p}p'_i$$
$$+\left[\frac{\mathscr{V}_i\alpha_{k,i}}{\Delta t} + \sum_{out} S_j\alpha_{k,i}\bar{u}_j\right]\frac{\partial\rho_{k,i}}{\partial h_k}\delta h_{k,i} + \sum_j S_j\alpha_{k,j}\rho_{k,j}\bar{u}'_j = \Delta\dot{m}_{k,i}. \tag{19}$$

Here Δt is a local time-step based on a Courant number and $\Delta\dot{m}_{k,i}$ a mass balance error for phase k. The time-derivative terms are used for an inertial under-relaxation in all equations. In the transient case, a true time derivative is also linearized and added together with the inertial relaxation term. The true time-step size is defined via input. A simplification is obtained by dropping the $\sum_{out}$ -sums out from the multipliers of the first two terms. The change in void fraction can be eliminated on the basis of $\delta\alpha_g = -\delta\alpha_l$ and using $\delta h_k \approx p'/\rho_k$ results in the following equation

$$\frac{\mathscr{V}_i}{\rho_i c_i^2 \Delta t} p'_i + \sum_{k,j} \frac{1}{\rho_{k,i}} S_j \alpha_{k,j} \rho_{k,j} \bar{u}'_j = \sum_k \frac{\Delta\dot{m}_{k,i}}{\rho_{k,i}}, \tag{20}$$

where $\Delta\dot{m}_{k,j} = -\sum_j \dot{m}_{k,j} + \mathscr{V}_i \Gamma_{k,i}$ is the error in mass balance and the sound speed for a two-phase mixture is defined as

$$\frac{1}{\rho c^2} = \frac{\alpha}{\rho_g c_g^2} + \frac{1-\alpha}{\rho_l c_l^2} \quad \text{and} \quad \frac{1}{\rho_k c_k^2} = \frac{\partial \rho_k}{\partial p} + \frac{1}{\rho_k} \frac{\partial \rho_k}{\partial h_k}. \tag{21}$$

By making approximations in the densities ($\rho_{k,i} \approx \rho_{k,j}$) and using Eq. (18) the final pressure correction equation is obtained

$$\left[\frac{0.01 \mathscr{V}_i}{\rho_i c_i^2 \Delta t} + \frac{\mathscr{V}_i |\Gamma_i|}{\Delta p_{\max}} \left(\frac{1}{\rho_{g,i}} - \frac{1}{\rho_{l,i}} \right) \right] p'_i - \sum_j \frac{S_j^2}{\bar{a}^u_{P,j}} (p'_{j+} - p'_i) = \sum_k \frac{\Delta\dot{m}_{k,i}}{\rho_{k,i}}, \tag{22}$$

where p'_{j+} is the pressure change in the cell on the other side of face j. An extra multiplier of 0.01 has been added on the basis of test calculations. This is because the method is not time-accurate in this form and it was found that the convergence slows down in steady cases if the first term is too large. In the transient case, the true time-derivative terms are added on the RHS of the equations and the corresponding inertial term on the left-hand side.

Although the mass transfer term (12) depends on pressure in Eq. (22) a more general pseudo-linearization is applied in Eq. (22). The change in pressure caused by Γ is limited to

$$\Delta p_{\max} = C_p |p - p_{\text{sat}}| + \epsilon_p, \tag{23}$$

where $C_p = 1$ and $\epsilon_p = 0.01\,\text{Pa}$ have been used. Furthermore, an under-relaxation factor α_p has to be used for the pressure as with pressure correction methods in general.

It should be noted that eliminating the mass fractions from the continuity equations on the basis of $\delta x_g = -\delta x_l$ would lead to the same pressure correction equation as in the case of the single-phase flow [11]. However, the resulting method can only be used if $\Gamma = 0$, otherwise the mass will not be conserved.

3.4 Void fraction

As was mentioned above, in the solution of continuity equations mass fractions, (qualities) are applied, since this is convenient at the implicit stage. A drawback is caused by the small values of mass fraction, since the accuracy may be threatened with small voids. Because of this the explicit stage, *i.e.* the RHS of the continuity equations is expressed in terms of the void fraction.

If the diagonal element is not concerned, the coefficients in the linearized form of Eq. (15) are the same as the inviscid part of the momentum equations [11]. At the implicit stage, a residual concept is utilized and corrections to the existing values are solved. A residual is defined as the right-hand sides of Eqs. (14) as all $\sum_j$ terms are moved on that side. The residuals are evaluated using the values from the previous iteration cycle. By defining a change between the iteration cycles as $x^{n+1} = x^n + \delta x$, the time derivative term of Eq. (14) can be approximated as

$$\mathscr{V}_i \frac{\delta(\rho x)_i}{dt} \approx \mathscr{V}_i \frac{\rho_i^{n+1} x_i^{n+1} - \rho_i^n x_i^n}{\Delta t} = \mathscr{V}_i \frac{\rho_i^n \delta x_i + x_i^n \delta\rho_i + \delta\rho_i \delta x_i}{\Delta t}. \tag{24}$$

Here term $\mathscr{V}_i \delta\rho_i / \Delta t$ is the same as the total continuity residual, that is the total mass balance error $R_i^c = \Delta\dot{m}_{g,i} + \Delta\dot{m}_{l,i}$. From the total continuity equation we obtain

$$\mathscr{V}_i \frac{\delta\rho_i}{\Delta t} = -\sum_j \dot{m}_j^n - \sum_j \delta\dot{m}_j = R_i^c - \sum_j \delta\dot{m}_j. \tag{25}$$

By combining Eqs. (24) and (25)

$$\begin{gathered} \mathscr{V}_i \frac{\delta(\rho x)_i}{dt} = \mathscr{V}_i \frac{\rho_i^n \delta x_i + \delta\rho_i \delta x_i}{\Delta t} + x_i^n R_i^c - x_i^n \sum_j \delta\dot{m}_j = \\ \left(\mathscr{V}_i \frac{\rho_i^n}{\Delta t} - \sum_j \dot{m}_j^n - \sum_j \delta\dot{m}_j \right) \delta x_i + x_i^n R_i^c - x_i^n \sum_j \delta\dot{m}_j. \end{gathered} \tag{26}$$

Similarly, the flux terms at time level $n+1$ are linearized as

$$\sum_j (\dot{m}_j + \delta\dot{m}_j)(x_j + \delta x_j) = \sum_j \dot{m}_j x_j + \sum_j \dot{m}_j \delta x_j + \sum_j x_j \delta\dot{m}_j + \sum_j \delta\dot{m}_j \delta x_j. \tag{27}$$

The second-last term is combined with the last term arising from the linearization of the time derivative Eq. (26) as $\sum_j (x_j - x_i)\delta\dot{m}_j \approx 0$. The first term is a part of the residual $R_i^x \equiv \Delta\dot{m}_{g,i} = -\sum_j \dot{m}_j x_j + \mathscr{V}_i \Gamma_i$. By applying a first-order upwind discretization for the mass fractions, the two remaining terms can be divided into mass flows in and out of the computational cell as

$$\sum_j \dot{m}_j \delta x_j + \sum_j \delta\dot{m}_j \delta x_j = \sum_{in} \dot{m}_j \delta x_j + \sum_{in} \delta\dot{m}_j \delta x_j + \sum_{out} \dot{m}_j \delta x_i + \sum_{out} \delta\dot{m}_j \delta x_i. \tag{28}$$

By combining Eqs. (26–28)

$$\left(\mathscr{V}_i \frac{\rho_i^n}{\Delta t} - \sum_{in} \dot{m}_j^n - \sum_{in} \delta \dot{m}_j \right) \delta x_i - \sum_{in} \dot{m}_j \delta x_j^n + \sum_{out} \delta \dot{m}_j \delta x_i = R_i^x - x_i^n R_i^c. \tag{29}$$

The second term on the right-hand side of this equation removes the effect of the mass imbalance. Similar terms exist in the momentum and energy equations [11]. The double δ-terms are ignored, which results in

$$\left(\mathscr{V}_i \frac{\rho_i^n}{\Delta t} - \sum_{in} \dot{m}_j^n \right) \delta x_i - \sum_{in} \dot{m}_j \delta x_j^n = R_i^x - x_i^n R_i^c. \tag{30}$$

A corresponding equation is obtained from the liquid continuity equation. Since $x_g + x_l = 1$ only one equation can be solved. In the case of the homogeneous flow assumption, the two continuity equations can be merged by multiplying the gas continuity equation by $1 - x$ and the liquid continuity equation by x. The left-hand side of Eq. (30) remains unchanged, but on the right-hand side we have a new residual combined from the individual phase residuals weighted by the mass fractions. The advantage of this is that with small voids the gas continuity equation dominates and as $x \to 1$ it is in an opposite way. This treatment increases the accuracy near the phase boundaries.

A computation of a mass transfer term itself is under-relaxed with the previous value using the under-relaxation factor of $\alpha_\Gamma = 0.5$. For Eq. (30) the mass transfer term could not be linearized with respect to x. Instead, the following under-relaxation term is added on the diagonal of Eq. (30)

$$\frac{\mathscr{V}_i |\Gamma_i|}{\Delta x_{\max}}, \tag{31}$$

where the maximum change of quality is obtained from

$$\Delta x_{\max} = C_x \min(x, 1 - x) + \epsilon_x. \tag{32}$$

After the test calculations, $C_x = 0.05$ and $\epsilon_x = 1 \cdot 10^{-6}$ have been used. A size of ϵ_x will affect the formation of void at low values of x. The effect of the leading term in Eq. (32) is that the mass transfer term can change the quality x (or $1 - x$) by five per cent per iteration cycle except when $x_k = \mathcal{O}(10^{-6})$.

In addition to under-relaxation of Eq. (32) the mass fraction is updated from $x^{n+1} = 0.1x^n + 0.9x^*$, where the intermediate value $x^* = x^n + \delta x$ is restricted in the range of [0,1]. It should also be noted here that ad hoc parameters have been applied in the under-relaxation process and further tuning of the solution method should require more test calculations. According to the npresent computational experience, however, the constants seem to have very little influence on the speed of convergence, but their motivation is to increase the robustness of the method. Thus the algorithm can be efficiently applied in the present form for new designs.

3.5 Energy equations

The energy equations (2) are linearized with respect to enthalpy changes δh_k. Couplings between the liquid and gas energy equations as well as with the pressure correction equation are ignored for the moment. The linearization follows the guidelines for the single-phase flow [11] resulting in a complex treatment of energy, mass and momentum residuals on the right-hand side of the linearized equations. The interfacial heat transfer term (3) can be directly linearized with respect to the phase enthalpies, but in the case of the mass transfer term, a similar trick as in the solution of the mass fractions is applied. Thus, the following term is added on the diagonal of both energy equations

$$\mathscr{V}_i \left[\frac{|\Gamma_i|(h_{k\mathrm{sat}} + \frac{V^2}{2})}{\Delta h_{k\max}} + \frac{h'_{ik}}{c_{pk}} \right], \tag{33}$$

where c_{pk} is a specific heat capacity and $\Delta h_{k\max}$ governs the amount of under-relaxation [26]. In the case of cavitation, a large value of $\Delta h_{k\max} = h_{k\mathrm{sat}} + \frac{V^2}{2}$ can be used. The first term is more important in heat transfer calculations [26], where smaller values should be given for $\Delta h_{k\max}$.

After solving the enthalpy changes, the phase temperatures are updated as $T_k^{n+1} = T_k^n + \delta h_k / c_{pk}$. The iteration cycle is terminated by a solution of the turbulence equations, and after the iteration cycle the material properties are updated as functions of the pressure and the temperature.

4 TEST CASE

4.1 PPTC propeller

The investigated case is a model-size propeller with a diameter of 0.250 m. The five-bladed propeller has a right-handed direction of rotation. The skew of the propeller is moderate. Table 1 summarizes the main geometrical parameters of the PPTC propeller. A photograph of the propeller is shown in Fig. 2. In this study, the propeller operates in push configuration. A large database of experimental results has been made available by SVA Potsdam. The simulations were performed using a constant rate of revolutions, $n = 20\,1/\mathrm{s}$. The advance coefficient, the pressure coefficient and the cavitation number are defined as

$$J = \frac{V_A}{nD}\ , \quad C_p = \frac{p - p_\infty}{\frac{1}{2}\rho(nD)^2} \quad \text{and} \quad \sigma_n = \frac{p - p_{\mathrm{sat}}}{\frac{1}{2}\rho(nD)^2}, \tag{34}$$

respectively, where V_A is the propeller speed of advance, n the propeller rate of revolutions, D the propeller diameter, and p_{sat} the saturation pressure. In this paper, a single cavitating propeller operating condition is investigated with $J = 1.019$ and $\sigma_n = 2.024$. Additionally, one non-cavitating operating condition is considered at $J = 1.253$. In the time-accurate simulations, a physical time-step of $\Delta t = 0.139\,\mathrm{ms}$ is used, corresponding to 1° of propeller rotation. The thrust, torque and the efficiency of the propeller are

non-dimensionalized as

$$K_T = \frac{T}{\rho n^2 D^4}\ , \quad K_Q = \frac{Q}{\rho n^2 D^5} \quad \text{and} \quad \eta_0 = \frac{J}{2\pi}\frac{K_T}{K_Q}, \tag{35}$$

where T denotes the thrust, Q the torque and η_0 the efficiency, respectively.

Table 1: Main geometric parameters of the PPTC propeller [14].

Diameter [m]	0.250
Pitch ratio at $r/R = 0.7$	1.635
Chord at $r/R = 0.7$	0.417
EAR	0.779
Skew [°]	18.837
Hub ratio	0.300
Number of blades	5
Rotation	Right handed

Figure 2: Photograph of the PPTC propeller [14].

4.2 Grid and boundary conditions

The propeller is operated in push configuration, *i.e.*, the shaft is located in front of the propeller. The computational grid used consists of roughly 5.5 million cells in 28 grid blocks. The computational domain is shown in Fig. 3. Due to the symmetric nature of the problem of a propeller operating in uniform inflow, only one blade is modelled. The blades, hub and shaft are modelled as no-slip rotational surfaces coloured black in Fig. 3. A velocity boundary condition is applied at the inlet, denoted as the red face, and a pressure boundary condition is applied at the outlet. A slip boundary condition is applied at the simplified tunnel walls, which are coloured green in Fig. 3. Cyclic boundaries are

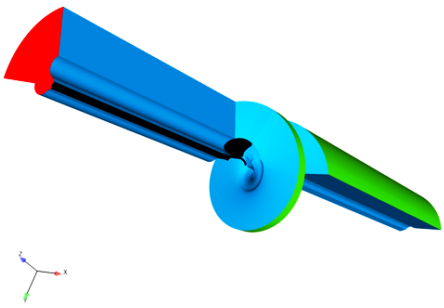

Figure 3: Grid topology used in the open-water computations.

denoted as the blue faces, and the whole computational domain is considered as rotating

with the given rate of rotation. The inflow velocity is set based on the advance numbers of the propeller, and the background pressure level is set based on the cavitation number. The inlet is located five propeller diameters upstream of the propeller, and the outlet is located ten diameters downstream of the propeller. The rectangular cavitation tunnel of SVA Potsdam was here modelled as a circular duct of the same cross-sectional area, thus enabling the quasi-steady computation of the problem. The radius of the computational domain is then 0.3385 m.

The surface grid on the suction side of the blade is shown in Fig. 4(a). The surface grid on the pressure side of the blade is similar. The grid has an O-O topology around the propeller blades. The grid resolution around the leading edge is fine, as shown in Fig. 4(b), and there are about 30 cells around the leading-edge radius. Due to the O-O topology, the same resolution is applied around the blade tip and the trailing edge as well. The grid is refined normal to the viscous surfaces such that $d^+ \approx 1$.

The grid points in the helical blocks located downstream of the propeller were concentrated in the region of the tip vortex. Figure 5 depicts the concentration of the grid points near the tip vortex induced by the rotating blades. In the figure, $|\Omega_i|$ denotes the absolute value of vorticity, and the propeller blades, hub and shaft are coloured dark red. The figure shows exemplary views of the resolution on the finest grid, demonstrating that the tip vortex is excellently maintained even beyond $x/D \approx 1$. There are roughly 18×14 grid points in the cross-section of the tip vortex on the finest grid on the plane $x/D = 1$. The helical blocks in the slipstream of the propeller are extended to a pitch corresponding to approximately 450° of rotation from the propeller plane.

The calculations were performed on three grid levels. On the coarse grid level, every second point in all directions is removed compared to the finer level grid. A solution on the coarse grid is used as an initial guess for the computations performed on the next finer grid level. In this paper, we present the results that were obtained on the finest grid.

5 RESULTS

In this section we present the numerical results of the PPTC test case in the investigated operating conditions. Unless otherwise stated, all cavitating results are obtained using the transient approach and with the superbee limiter for the void fraction. In all transient results depicting the propeller, a snapshot is shown with the propeller blade at the top-dead centre. Experimental results are given in Refs. [14, 27].

5.1 Propeller global forces

A comparison of the simulated results with the model tests (EFD) in the cavitating conditions in terms of the non-dimensional thrust and torque coefficients is given in Table 2. It can be seen that the propeller performance in terms of the global forces is captured relatively well utilizing any of the turbulence models. In this case, the best agreement with the experiments is obtained with the $k - \varepsilon$ turbulence model.

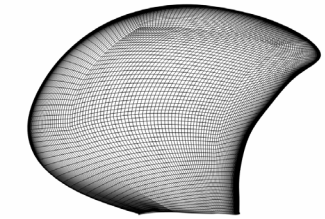

(a) Grid resolution on the suction side

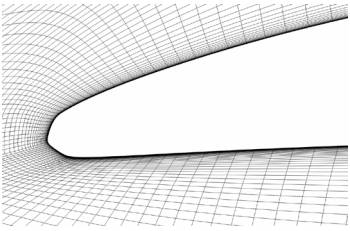

(b) Grid resolution near the LE

Figure 4: Grid resolution on the suction side and near the leading edge of the blade.

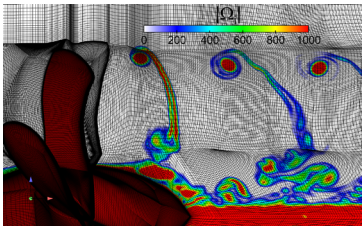

(a) Cut plane $y = 0$

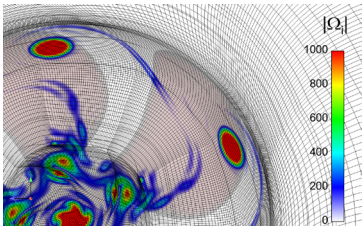

(b) Cut plane $x/D = 1$

Figure 5: Views of grid resolution on cut planes $y = 0$ and $x/D = 1$.

Table 2: Global performance characteristics of the propeller in cavitating conditions utilizing different turbulence closures.

Quantity	$k-\varepsilon$	SST $k-\omega$	SST $k-\omega$ EARSM	DDES with $k-\omega$
K_T (EFD)	0.374	0.374	0.374	0.374
K_T (CFD)	0.368	0.362	0.358	0.358
ΔK_T	-1.6%	-3.3%	-4.4%	-4.4%
$10 \times K_Q$ (EFD)	0.970	0.970	0.970	0.970
$10 \times K_Q$ (CFD)	0.947	0.934	0.930	0.923
ΔK_Q	-2.4 %	-3.8%	-4.3%	-5.1%
η_0 (EFD)	0.625	0.625	0.625	0.625
η_0 (CFD)	0.634	0.632	0.628	0.633
$\Delta\eta_0$	1.4%	1.1%	0.5%	1.2%

5.2 Comparison with LDV measurements

Circumferential distributions of velocity components in the wake of the propeller are compared to the LDV measurements conducted in a cavitation tunnel [14]. The LDV measurements were conducted at $J = 1.253$ in wetted conditions. Quasi-steady CFD computation utilizing the $k-\varepsilon$ turbulence model was conducted at $J = 1.269$ with the deviation[1] of $\Delta J = 1.3\%$ for the advance coefficient, $\Delta K_T = 2.6\%$ for the thrust

[1] $J = 1.269$ corresponds to the operation point of Case 2.3.2. of smp'11, to be assessed in a future work

coefficient, and $\Delta K_Q = 0.6\%$ for the torque coefficient. Comparison of the axial, radial and tangential velocity components is made on the cut-plane $x/D = 0.2$ at two radii. The first radius, shown in Fig. 6(a), corresponds to the location of maximum observed axial wake, which was $r/R = 0.966$ in the measurements, whereas the maximum wake occurred at $r/R = 0.920$ in the simulations. The second comparison is made at the radius $r/R = 0.7$, which is shown in Fig. 6(b).

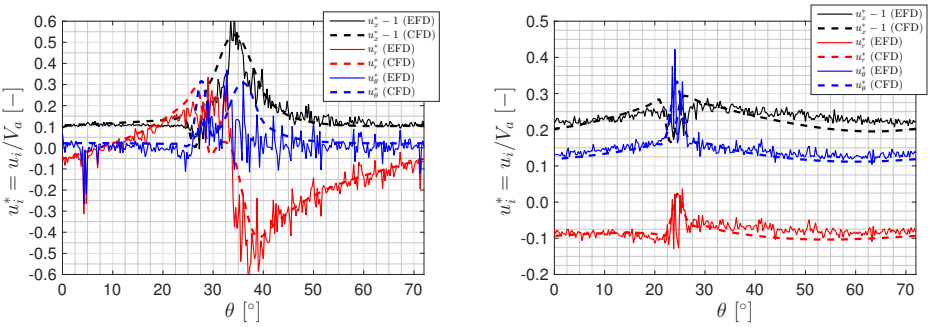

(a) Radii of maximum wake

(b) $r/R = 0.7$

Figure 6: Comparison of velocity components on the cut-plane $x/D = 0.2$ on constant radii. Experiments are described in [14].

Overall, good qualitative agreement is achieved between the experiments and the simulations. It is observed that the shape of the tip vortex and the propeller wake are well captured. The tip vortex strength or the wake created by the propeller is not observably dissipated at this x station. However, there is a difference of 5% between the EFD and CFD in the values of the radii in Fig. 6 at which the maximum wake is observed. A reason for the higher streamtube contraction might be the difference in the propeller loadings.

5.3 Cavitation observation

The cavitation patterns on the suction side of the propeller blades and in the wake of the propeller are compared with the observations made in the cavitation tunnel tests in Figs. 7 and 8. In the simulated results, the grey transparent surface denotes the iso-surface of $\alpha = 0.1$. The results are obtained with DDES. The experimental results are reported in [27]. The propeller has strong tip vortex and hub vortex cavitations, which are visible in the experiments and in the simulations. The shape and extent of the root cavitation, as well as the tip and hub vortex cavitations, are captured well. The tip and hub vortex cavitations extending far behind the propeller are captured exceptionally well, as shown in Fig. 8. Comparing the EFD and CFD results in Fig. 8, also the modal shapes of the cavitating tip vortex are qualitatively well captured. The simulation predicts

attached sheet cavitation at the leading edge, which is not observed in the experiments. We, however, note that the cavitation inception at the leading edge (LE) is sensitive to the manufacturing accuracy of the model propeller, and small inaccuracies especially concerning the sharp LE shape can alter the observed cavitation extent [13].

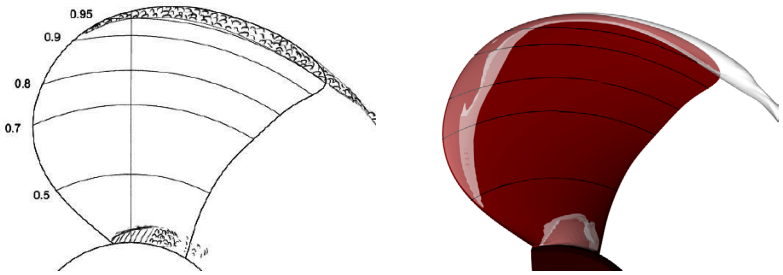

(a) EFD (b) CFD

Figure 7: Comparison of the cavitation patterns near the blade surfaces with the cavitation sketches according to observations made in the experiments. DDES using the superbee limiter. Experiments are described in [27].

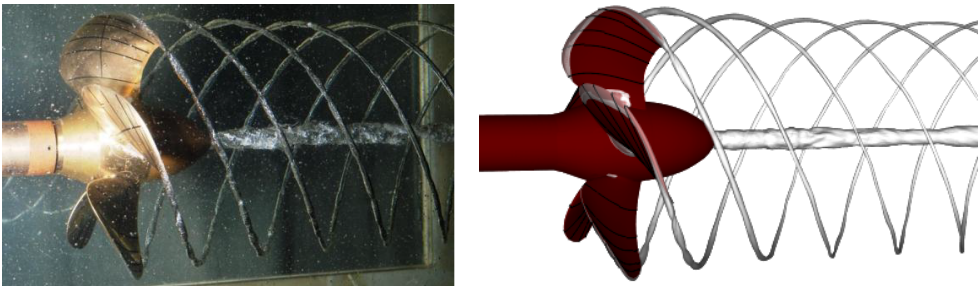

(a) EFD (b) CFD

Figure 8: Comparison of the tip and hub vortex cavitation extents behind the propeller. DDES using the superbee limiter. Experiments are described in [27].

Surface-restricted streamlines and non-dimensional pressure coefficients on the blade surface, predicted by the different turbulence models, are shown in Fig. 9. It can be seen that the surface pressure distributions are similar between the two turbulence models. The streamlines are mostly radially directed in a major part of the blade, without considerable difference between the turbulence models. The $k-\varepsilon$ model, however, apparently predicts a more laminar region close to the LE at smaller radii than the other choices. The effect of cavitation on the surface-restricted streamlines is significant. The re-entrant jets are

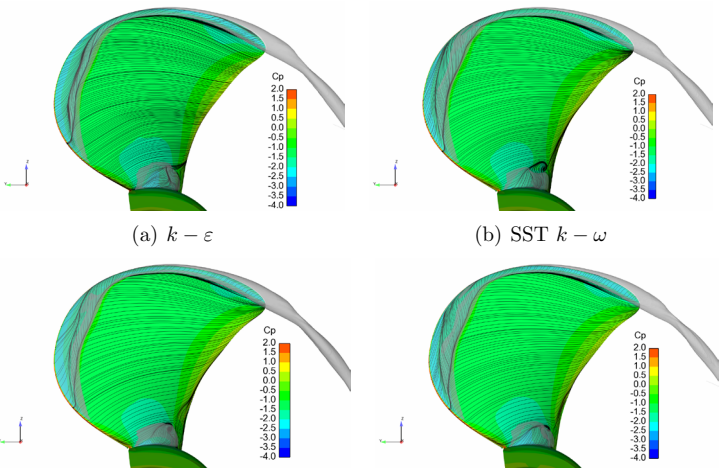

(a) $k-\varepsilon$ (b) SST $k-\omega$

(c) SST $k-\omega$ EARSM (d) DDES with SST $k-\omega$

Figure 9: Surface-restricted streamlines and non-dimensional pressure coefficients on the blade surface. Cavitating conditions utilizing different turbulence models. The grey transparent surface denotes the iso-surface of $\alpha = 0.1$.

directed towards the cavitating tip vortex at the closure line of the sheet cavitation. A similar phenomenon was observed by [28], see also Fig. 12. This behaviour appears as practically identical for all of the utilized turbulence closures. There is no considerable difference in the location of the cavity closure line between any of the utilized turbulence models. In addition, apparent flow separation is seen in the blade root region. With any of the $k-\omega$ based models or the SST-based DDES, the region of separating flow extends to a slightly higher radii near the trailing edge than for the $k-\varepsilon$ model.

5.4 Comparison of different flux limiters for the void fraction equation

A comparison of the Van Albada and superbee flux limiters for the void fraction is carried out utilizing the SST $k-\omega$ turbulence model and a quasi-steady solution. Integrating the total volume of vapour in the computational domain gives 20.15 mm^3 vapour with the Van Albada limiter, and 23.32 mm^3 with the superbee limiter, respectively. Fig. 10 shows a comparison of the cavitation extent in the wake of the propeller as predicted by the two limiters. Albeit not shown, the limiter applied had little influence on the cavitation patterns near the blade surface in this operating condition. In Fig. 10 results of the two computations are compared in a single picture, the figure being halved at the centre of the propeller hub in the vertical direction. In the top half we show results obtained with the Van Albada limiter, while in the bottom half those obtained with the superbee limiter. Overall, the predicted cavitation patterns near the blades and, to an extent also

in the wake, are relatively close to the cavitation observations made in the experiments regardless of the utilized limiter. The two flux limiters employed bear little difference to the prediction of the hub vortex cavitation. However, a notable difference is seen in the prediction of the tip vortex cavitation. The tip vortex cavitation as predicted with the Van Albada limiter narrows from $x/D \approx 1$ downstream, while similar dissipation is not observed in the cavitating tip vortex predicted by the superbee limiter, nor in the experiments. Furthermore, the modal shapes of the tip vortex cavitation seem slightly clearer as predicted with the superbee limiter. Lastly, we note that the tip vortex cavitation diminishes roughly 72° earlier in the simulations with the Van Albada limiter than with the superbee limiter.

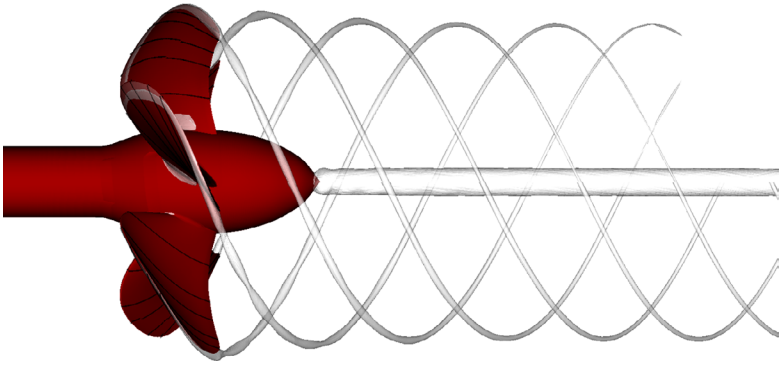

Figure 10: Comparison of computed cavitation extents with the different flux limiters. Top half: Van Albada limiter, bottom half: superbee limiter.

5.5 Flow structures behind the propeller

The vorticity magnitude and the pressure coefficient behind the propeller are shown in Fig. 11 in cavitating conditions. The figure shows a snapshot of the simulations with the propeller blade at the top-dead centre. The results utilizing the four different turbulence closures are visualized. As can be seen, a strong tip vortex is preserved well in the slipstream. Utilizing all but the $k-\varepsilon$ turbulence model, the high vorticity region together with the cavitating tip vortex is preserved close to the extent of the helical grid. The pressure in the tip vortex region predicted by the $k-\varepsilon$ model decreases in magnitude at around the extent of the propeller hub, halting the mass transfer and causing the vapour to vanish far sooner than with any of the other employed turbulence models. It can be observed that the overall flow field in the wake appears as rather smooth with the $k-\varepsilon$ model. Conversely, the disturbance at the tip vortex region is convected nearly unaffected by the distance it has travelled when utilizing the linear and non-linear SST $k-\omega$, or with DDES. Furthermore, with DDES, formation of auxiliary and unsteady vorticity appears

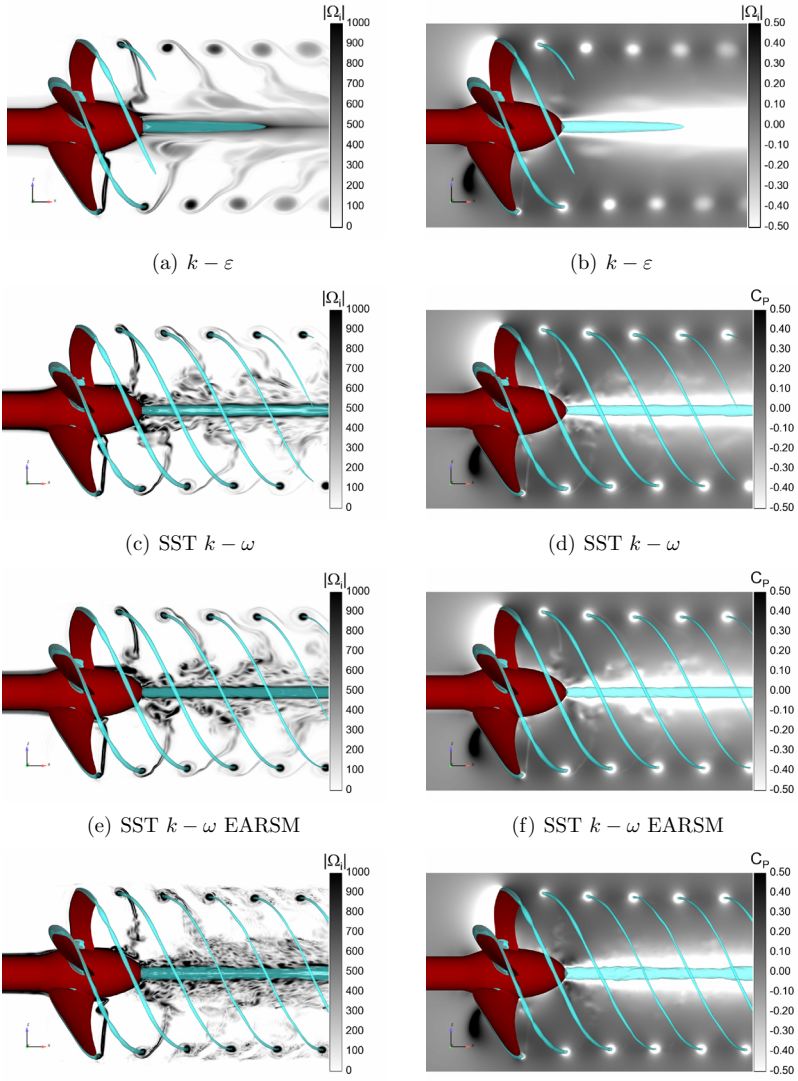

(a) $k-\varepsilon$ (b) $k-\varepsilon$

(c) SST $k-\omega$ (d) SST $k-\omega$

(e) SST $k-\omega$ EARSM (f) SST $k-\omega$ EARSM

(g) DDES with SST $k-\omega$ (h) DDES with SST $k-\omega$

Figure 11: Magnitude of the vorticity vector and the pressure coefficient on the cut plane $y = 0$ in cavitating conditions utilizing different turbulence models. The transparent iso-surface of the void fraction $\alpha = 0.1$ is coloured by blue.

around the strong tip vortices as we move downstream from the propeller. The apparent flow separation near the propeller root causes visible disturbances in the wake, which are significantly more pronounced in the results obtained with the linear and non-linear SST $k-\omega$ than with the $k-\varepsilon$ model, and differences between the linear and non-linear $k-\omega$ models seem mostly qualitative. DDES then again predicts more detailed vortical structures than the two-equation models.

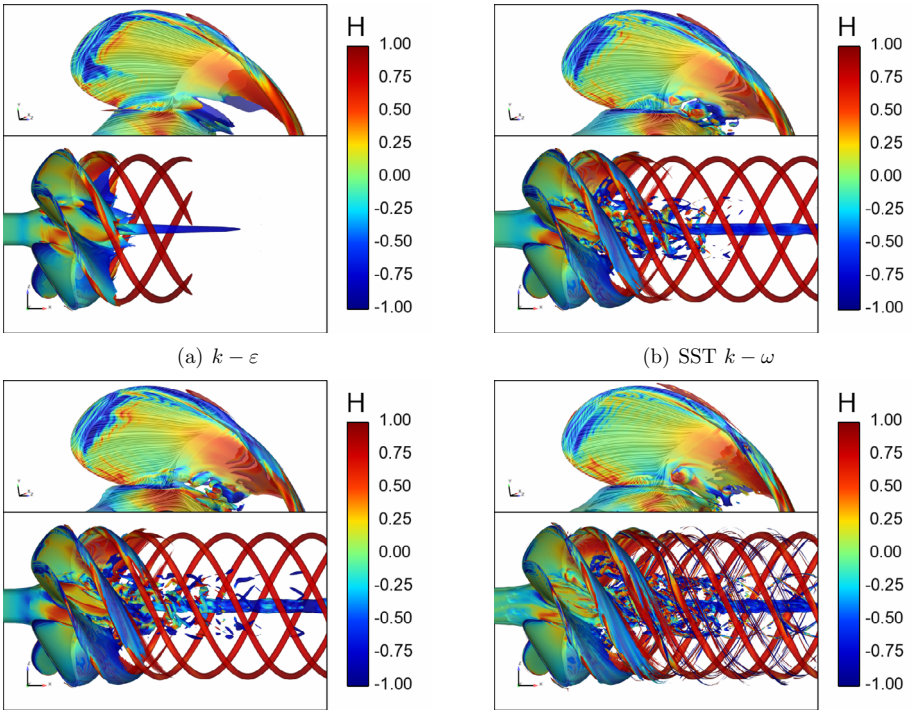

(a) $k-\varepsilon$ (b) SST $k-\omega$

(c) SST $k-\omega$ EARSM (d) DDES with SST $k-\omega$

Figure 12: Iso-surface of the magnitude of the vorticity vector $|\Omega_i| = 750$ 1/s near the suction side with blade surface restricted streamlines (top), near the propeller and in the wake (bottom). The iso-surface is coloured by helicity. Cavitating conditions utilizing different turbulence models.

The flow field is visualized at the suction side of the blade and in the wake by the iso-surface of the magnitude of the vorticity vector $|\mathbf{\Omega}| = 750\ 1/\mathrm{s}$. in Fig. 12 in cavitating conditions. The iso-surface is coloured by helicity $\mathsf{H} = \mathbf{V}_r \cdot \mathbf{\Omega}/(|\mathbf{V}_r||\mathbf{\Omega}|)$, where $\mathbf{V}_r$ is the relative velocity vector in the rotating reference frame. The helicity denotes the cosine of the angle between the relative velocity and the absolute vorticity vectors, and tends to ± 1 in the vortex cores, the sign indicating the direction of swirl. We observe strong tip and

hub vortices extending far in the wake. Minor instabilities are seen in the vorticity field near the sheet cavitation at the leading edge, but the re-entrant jet of the sheet cavitation near the LE is directed up towards the cavitating tip vortex. As we observed in Fig. 9, the vapour in the sheet cavity is convected toward the cavitating tip vortex, and the sheet cavitation itself is stable. The root region sheds unsteady vortical flow structures in the wake. The rather stable root cavitation in Fig. 7 causes apparent changes to the flow geometry which leads to separation. Observing the results obtained with the linear and non-linear SST $k-\omega$ model or with DDES, the flow departing the trailing edge exhibits unsteadiness up to approximately $r/R = 0.5$. The helical vortex track originating from the root region is clearer with DDES than with any of the two-equation models. Separate vortex filaments form close to the surface of the hub shortly after the trailing edge of the blade with the linear and non-linear SST $k-\omega$ model and with DDES. Utilizing the non-linear model, the vortical flow structures shed from the root region convect longer and more detailed in the propeller wake than with the other two-equation models. A similar phenomenon is observable for the cavitating hub vortex. Overall, DDES predicts considerably more detailed vortical flow shapes and structures in the wake of the propeller than any of the two-equation models. If we inspect Fig. 12(d) carefully, we notice a vortex pairing phenomenon taking place, where the strong tip vortex (with $\mathsf{H} \approx 1$) has a smaller and weaker vortex tube (with $\mathsf{H} \approx -1$) coiling around it. We do not observe similar phenomenon with the two-equation models. Dissipation is low in the tip vortex in the helical grid region with the linear and non-linear SST $k-\omega$ model and with DDES. Overall flow details in the wake obtained with $k-\varepsilon$ turbulence model are severely damped due to excess turbulent viscosity produced by the model [13].

6 CONCLUSIONS

A numerical method for a solution of cavitating propeller flows was described. In the solution method, a compressible homogeneous flow model is applied. The finite-volume based algorithm utilizes a pressure correction equation derived from the phase continuity and the mixture momentum equations. Several turbulence closures are used to describe turbulence in the mixture. Mass transfer between the phases is evaluated from the commonly used Merkle model.

The numerical method was applied for the PPTC propeller in wetted and cavitating conditions. The computed results were compared with experimental data. The predicted global propeller performance characteristics were in good agreement with the experiments. Differences between the utilized turbulence closures were not considerable, although the best correspondence was obtained with the $k-\varepsilon$ model. Cavitation patterns with all the utilized turbulence closures were also well predicted, especially near the blades. The cavitating tip and hub vortices were excellently captured with the linear and non-linear SST $k-\omega$ -models, as well as with DDES, and little difference was observed in the predicted steady cavities between these approaches. In the wake, more detailed vortical flow structures can be seen, as the complexity of the turbulence closure is increased.

Different flux limiters were applied for the convection term in the void-fraction equation: Van Albada's limiter and Roe's superbee limiter. With all other numerical settings kept untouched, the results demonstrate a significant difference in the predicted tip vortex cavitation extent between the different limiters. Using the more compressive limiter, better agreement was achieved with the experiments in terms of the cavitation prediction. The numerical results indicate, however, that the steady cavitation patterns in the vicinity of the blades did not considerably depend on the utilized limiter at the investigated operating condition.

In this study, our goal was to validate the present two-phase flow model and to compare turbulence modelling approaches for a model-scale propeller. The interaction between a full-scale marine propeller and a ship is very complex. The propeller usually operates in the vicinity of the hull in the three-dimensional wake of the ship, where the flow is mostly time-dependent, highly turbulent and, in adverse conditions, even separated. Additional complexity can follow from the interaction between the propeller and the ship wave system, or with rudders or other propellers in a multi-propulsor configuration. From a numerical point of view, the computational burden imposed by the propeller operating in behind ship conditions mainly results from the highly time-dependent nature of the problem, with the ship motions and the generated wave system following a time scale very different to that of the rotating propeller. Using a typical number of $\mathcal{O}(30)$ cores, usual computational times for a transient open-water calculation are of the order of days for a single propeller revolution. Conversely, a CFD simulation of a full-scale ship with an operating propeller could consume up to a month in order to achieve a reliable result.

In the future, the aim is to predict propeller-induced underwater noise. For this purpose the CFD solution will be linked with an acoustic solver. The flow solution will be developed by assuming unequal velocities for the phases [26]. This creates new challenges for modelling of turbulence and interfacial transfer, which will be important research topics in the future.

REFERENCES

[1] Lightelijn J. Advantages of different propellers for minimising noise generation. *Proceedings of the 3rd International Ship Noise and Vibration Conference*, Adler HE (ed.), London, UK, 2007.

[2] Sánchez-Caja A, Rautaheimo P, Salminen E, Siikonen T. Computation of the incompressible viscous flow around a tractor thruster using a sliding-mesh technique. *Seventh International Conference on Numerical Ship Hydrodynamics*, 1999.

[3] Sánchez-Caja A, Ory E, Salminen E, Pylkkanen J, Siikonen T. Simulation of incompressible viscous flow around a tractor thruster in model and full scale. *The 8th International Conference on Numerical Ship Hydrodynamics*, 2003; 22–25.

[4] Lu Nx, Bensow RE, Bark G. LES of unsteady cavitation on the Delft twisted foil. *Journal of Hydrodynamics, Ser. B* 2010; **22**(5):784–791.

[5] Muscari R, Di Mascio A, Verzicco R. Modeling of vortex dynamics in the wake of a marine propeller. *Computers & Fluids* 2013; **73**:65–79.

[6] Balaras E, Schroeder S, Posa A. Large-eddy simulations of submarine propellers. *Journal of Ship Research* 2015; **59**(4):227–237.

[7] Sipilä T, Sánchez-Caja A, Siikonen T. Eddy vorticity in cavitating tip vortices modelled by different turbulence models using the RANS approach. *6th European Conference on Computational Fluid Dynamics, (ECFD VI)*, Barcelona, Spain, 2014.

[8] Guilmineau E, Deng G, Leroyer A, Queutey P, Visonneau M, Wackers J. Influence of the turbulence closures for the wake prediction of a marine propeller. *Fourth International Symposium on Marine Propulsors (smp'15)*, Austin, Texas, USA, 2015.

[9] Ianniello S, Muscari R, Di Mascio A. Ship underwater noise assessment by the acoustic analogy. Part I: Nonlinear analysis of a marine propeller in a uniform flow. *Journal of Marine Science and Technology* 2013; **18**(4):547–570.

[10] Budich B, Schmidt SJ, Adams NA. Numerical investigation of a cavitating model propeller including compressible shock wave dynamics. *Fourth International Symposium on Marine Propulsors (smp'15)*, Austin, Texas, USA, 2015.

[11] Miettinen A, Siikonen T. Application of pressure- and density-based methods for different flow speeds. *International Journal for Numerical Methods in Fluids* 2015; **79**(5):243–267, doi:10.1002/fld.4051. URL `http://dx.doi.org/10.1002/fld.4051`, fld.4051.

[12] Van Leer B. Flux-vector splitting for the Euler equations. *Proceedings of the* 8^{th} *International Conference on Numerical Methods in Fluid Dynamics*, Aachen, 1982. (also Lecture Notes in Physics, Vol. 170, 1982).

[13] Viitanen V, Hynninen A, Lübke L, Klose R, Tanttari J, Sipilä T, Siikonen T. CFD and CHA simulation of underwater noise induced by a marine propeller in two-phase flows. *Fifth International Symposium on Marine Propulsors (smp'17)*, Espoo, Finland, 2017.

[14] Mach KP. Potsdam propeller test case (PPTC). LDV velocity measurements with the model propeller VP1304, SVA Potsdam Model Basin. *Report 3754*, SVA Potsdam 2011.

[15] Chien KY. Predictions of channel and boundary-layer flows with a low-Reynolds-number turbulence model. *AIAA Journal* 1982; **20**(1):33–38.

[16] Menter F. Influence of freestream values on $k-\omega$ turbulence model predictions. *AIAA Journal* 1992; **30**(6):1657–1659.

[17] Wallin S, Johansson A. A complete explicit algebraic Reynolds stress model for incompressible and compressible turbulent flows. *Journal of Fluid Mechanics* 2000; **403**:89–132.

[18] Strelets M. Detached eddy simulation of massively separated flows. *39th AIAA Aerospace Sciences Meeting and Exhibit*, Reno, NV, 2001. AIAA-2001-0879.

[19] Choi YH, Merkle CL. The application of preconditioning in viscous flows. *Journal of Computational Physics* 1993; **105**:207–230.

[20] Spalart PR, Deck S, Shur M, Squires K, Strelets MK, Travin A. A new version of detached-eddy simulation, resistant to ambiguous grid densities. *Theoretical and computational fluid dynamics* 2006; **20**(3):181–195.

[21] Shur M, Spalart P, Strelets M, Travin A. Detached-eddy simulation of an airfoil at high angle of attack. *Engineering Turbulence Modelling and Experiments 4*, 1999; 669–678.

[22] Frikha S, Coutier-Delgosha O, Astolfi JA. Influence of the cavitation model on the simulation of cloud cavitation on 2D foil section. *International Journal of Rotating Machinery* 2009; **2008**(Article ID 146234).

[23] Van Albada G, Van Leer B, Roberts W. A comparative study of computational methods in cosmic gas dynamics. *Astronomy and Astrophysics* 1982; **108**(76):76–84.

[24] Roe PL. Some contributions to the modelling of discontinuous flows. *Large-scale computations in fluid mechanics*, 1985; 163–193.

[25] Viitanen V. Verification of a homogeneous mixture model for the free surface problem. Master's thesis, Aalto University, School of Engineering. February, 2015. URL `http://urn.fi/URN:NBN:fi:aalto-201501301816`.

[26] Siikonen T. Numerical method for one-dimensional two-phase flow. *Numerical Heat Transfer, Part A: Applications* 1987; **12**(1):1–18.

[27] Heinke HJ. Potsdam propeller test case (PPTC). Cavitation tests with the model propeller VP1304, SVA Potsdam Model Basin. *Report 3753*, SVA Potsdam 2011.

[28] Sipilä T. RANS analyses of cavitating propeller flows. Licentiate thesis, Aalto University September 2012.

9. National Conference on Computational Mechanics
MekIT'17
B. Skallerud and H I Andersson (Eds)

LARGE SCALE CFD MODELLING OF WAVE PROPAGATION IN SULAFJORD FOR THE E39 PROJECT

W. WANG[1], H. BIHS[2], A. KAMATH[2] AND Ø. ARNTSEN[2]

[1]Department of Civil and Environmental Engineering
Norwegian University of Science and Technology
Trondheim 7491, Norway
e-mail: weizhi.wang@ntnu.no, web page: https://reef3d.com/

[2] Department of Civil and Environmental Engineering
Norwegian University of Science and Technology
Trondheim 7491, Norway

Key words: Large scale, CFD, Two phase flow, Level-set method, REEF3D, SWAN

Abstract. The coastal high way project E39 aims at building a continuous ferry-free road connection along the west coast of Norway. One of the major challenges in the project is to replace ferries with new fjord-crossing methods such as floating bridges and floating tunnels. The unique topographies of the Norwegian fjords pose deep water conditions and large scale wave transformations. This makes it more complicated to analyse the wave loads on the floating structures. In order to have a better knowledge of the wave height distribution, wave direction and wave transformation details, accurate simulations of wave propagations with good representations of the free surfaces are demanded. CFD (Computational Fluid Dynamics) is able to capture most complexities of the wave physics with few assumptions and has been widely and successfully applied on hydrodynamics. With increasing computational capacities, it is possible to use CFD on large scale simulations. Therefore, large scale three dimensional simulations of wave propagations into Sulafjord are performed in this paper with the CFD model REEF3D. The spectra wave model SWAN is used to obtain the wave data from offshore data and give inputs for the CFD simulation. The CFD simulations are performed with both regular and irregular waves and give the details of the free surfaces and wave transformations in the fjord, the results of which are also compared with the wave model SWAN. REEF3D solves the incompressible Navier-Stokes equations with finite difference method and uses level-set method to capture the free surface under the two phase flow approximation. Together with the implements of high order schemes, REEF3D demonstrates high performance on wave hydrodynamics. The large scale Sulafjord simulation shows high resolution results and the details of wave transformations are well visualised. The results at wave probes are also compared between REEF3D and SWAN.

1 INTRODUCTION

The coastal highway project E39 is a major marine civil engineering project in Norway. As part of the National Transport Plan (NTP) for 2014-2023, it is aimed to build a continuous ferry-free road connection between Kristiansand and Trondheim along the west coast of Norway, which covers around 1100 km in distance with seven major fjord crossings [6]. Three major bridge designs are proposed for fjord crossings, a single span suspension bridge, a floating bridge and a submerged tunnel [6]. The floating structure designs put new demands for accurate wave propagation simulation into the fjords. The Norwegian fjords are very unique as most of them have very steep slopes with rather deep water conditions. For example, the research object Sulafjord is 3200m to 5000m wide and up to 450m deep [11]. Though it is not the widest or deepest fjord, it has been chosen as the study case in this paper due to its representative features and reasonable domain size with respect to computation load. Besides, the study will make the numerical simulation keep pace with the ongoing field measurements in Sulafjord.

The numerical models for coastal simulation were initially developed with a statistical method based on significant wave height. But the requirement of a fine mesh in the coastal region due to the complex bathymetry demands the third generation wave models, such as MIKE 21 SW [23]. Another third generation model is the spectral wave model Simulating Waves Near shore (SWAN) developed by Delft University of Technology [23]. Both MIKE 21 SW and SWAN give good results in terms of predicting energy spectrum and significant wave height. However, as they are phase-averaged wave models, some phenomena like wave diffraction can not be represented well [23]. Therefore, a high resolution phase-resolved numerical model is needed to reflect detailed wave phenomena in the fjords.

Another application in coastal and harbour engineering is a Boussinesq equation based wave model. Boussinesq type equations have been used successfully for shallow water simulations. Improved versions of the Boussinesq equations further reduce the limitation of its application due to water depth (d) and wave length (L), which makes it possible to simulate waves with d/L ratio of 0.6 [15]. But in Sulafjord, the d/L ratio can be greater than 1 which corresponds to deep water conditions, where Boussinesq equations are not applicable.

As Computational Fluid Dynamics (CFD) is able to capture most of the complexity in the flow field with few assumptions, it is becoming the new alternative for modelling in coastal engineering. However, the limitation of CFD application to coastal engineering is the high demand on the computational resources. In recent years, super computer infrastructure and parallel computation technology have been improved at a fast pace. With increasing computational resources and improved CFD tools, large domain simulations of wave propagation for Sulajord is possible with CFD. To meet this challenge, REEF3D has

been developed at NTNU as a CFD code with focus on wave hydrodynamics by solving the incompressible Navier-Stokes equations [4] and has been applied to a wide range of marine applications, such as breaking wave kinematics [1], breaking wave-structure interaction [14] or floating body dynamics in waves [3]. This paper presents the large scale CFD wave modelling at Sulafjord using REEF3D.

A simulation is firstly performed with the spectral wave model SWAN to approximate the wave properties at the fjord entrance from the offshore wave data. Three wave height probes are used in the SWAN model which correspond to the three locations of the field measurements. The resulting wave height and period at the probe at the fjord entrance are then used as inputs in the CFD simulation. A CFD simulation with a unidirectional regular wave and a CFD simulation with a unidirectional irregular wave are conducted using REEF3D. Wave height probes corresponding to the same locations as those in SWAN are also used in the CFD simulations. The resulting wave properties from all three numerical simulations are compared at wave probes and the phase-resolved results from the CFD simulations are visualised and analysed against the wave transformation physics.

2 NUMERICAL MODEL

2.1 Governing Equations

Water wave hydrodynamics comply with the mass conservation and momentum conservation, which are represented by the incompressible Navier-Stokes equations, as shown in Eqn. (1) and Eqn. (2). For large scale water waves, the turbulence effect is ignored, and thus the turbulence terms in the equations are excluded.

$$\frac{\partial u_i}{\partial x_i} = 0 \tag{1}$$

$$\frac{\partial u_i}{\partial t} + u_j \frac{\partial u_i}{\partial x_j} = -\frac{1}{\rho}\frac{\partial p}{\partial x_i} + \frac{\partial}{\partial x_j}\left[\nu\left(\frac{\partial u_i}{\partial x_j} + \frac{\partial u_j}{\partial x_i}\right)\right] + g_i \tag{2}$$

where u is the velocity, ρ is the fluid density, p is the pressure, ν is the kinematic viscosity and g the acceleration due to gravity.

REEF3D solves the governing equations on a structured Cartesian grid and is able to implement high-order schemes with finite difference method .

For the convection terms in the Navier-Stokes equations, the conservative fifth-order weighted essentially non-oscillatory (WENO) scheme is applied. By using a convex combination of all stencils with each of them assigned with a weight, WENO is less sensitive

to round-off errors and also has better smoothness of the flux [10].

The third-order Total-Variation-Diminishing (TVD) Runge-Kutta scheme [5] is employed for time treatment in the momentum equations and the level set equations. The adaptive time step is also adopted in order to fulfil the Courant-Friedrichs-Lewy(CFL) criterion [9].

The Poisson equation for pressure is solved using the HYPRE library [12]. The HYPRE library provides high performance solvers that make large and detailed simulations possible and solve the problems faster at large scales. With the HYPRE library, REEF3D is able to use BiCGStab [24] as the iterative solver and geometric multi-grid PFMG [7] as the pre-conditioner for the Poisson equations. As a result, the solver scales very well.

2.2 Numerical Wave Tank

The level set method is adopted to capture the free surface. The level set function $\phi(\vec{x},t)$ is a signed distance function which is designed so that it equals to zero at the interface and shows opposite signs in the two different phases, as shown in Eqn. (3) [19].

$$\phi(\vec{x},t)\begin{cases} > 0 \; if \; \vec{x} \in phase \; 1 \\ = 0 \; if \; \vec{x} \in \Gamma \\ < 0 \; if \; \vec{x} \in phase \; 2 \end{cases} \tag{3}$$

REEF3D is able to apply various wave theories, such as linear wave theory, $2nd$-order and $5th$-order Stokes waves and irregular wave theories. The equations to describe the waves include the velocities in the horizontal and vertical direction u and w and the level set function ϕ for the surface elevation. As an example, the equations for deep water linear wave theory are represented in Eqn. (4).

$$\begin{aligned} u(x,z,t)_{analytical} &= \frac{\pi H}{T}\frac{cosh\left[k\left(z+d\right)\right]}{sinh\left(kd\right)}cos\theta \\ w(x,z,t)_{analytical} &= \frac{\pi H}{T}\frac{sinh\left[k\left(z+d\right)\right]}{sinh\left(kd\right)}sin\theta \\ \phi(x,z,t)_{analytical} &= \frac{H}{2}cos\theta - z + d \end{aligned} \tag{4}$$

The wave phase θ and the wave number k are described in Eqn. (5):

$$\begin{aligned} k &= \frac{2\pi}{L} \\ \theta &= kx - \omega t \end{aligned} \tag{5}$$

where H is the wave height, L is the wavelength, T is the wave period, ω is the angular wave frequency and z is the vertical coordinate measured from the still water level $z = 0$.

The wave is generated and absorbed using relaxation method [16]. The relaxation function formulated by Jacobsen [13] is implemented as shown in Eqn. (6).

$$\Gamma(\widetilde{x}) = 1 - \frac{e^{(\widetilde{x}^{3.5})} - 1}{e - 1} \; for \; \widetilde{x} \in [0; 1] \tag{6}$$

where $\widetilde{x}$ is scaled to the length of the relaxation zone.

The velocities and the free surface level defined in Eqn. (4) together with the pressure are ramped up in the wave generation zone to the analytical values from the desired wave theory and the waves are released into the working zone in the tank. In the numerical beach, the velocities are reduced smoothly to zero, free surface is damped to still water level and the pressure is relaxed to hydrostatic pressure. The process is shown in Eqn. (7)

$$\begin{aligned} u(\widetilde{x})_{relaxed} &= \Gamma(\widetilde{x})u_{analytical} + (1 - \Gamma(\widetilde{x}))u_{computational} \\ w(\widetilde{x})_{relaxed} &= \Gamma(\widetilde{x})w_{analytical} + (1 - \Gamma(\widetilde{x}))w_{computational} \\ p(\widetilde{x})_{relaxed} &= \Gamma(\widetilde{x})p_{analytical} + (1 - \Gamma(\widetilde{x}))p_{computational} \\ \phi(\widetilde{x})_{relaxed} &= \Gamma(\widetilde{x})\phi_{analytical} + (1 - \Gamma(\widetilde{x}))\phi_{computational} \end{aligned} \tag{7}$$

The complicated bathymetry of coastal region consisting of a set of scattered points is implemented using the inverse distance weighting method. This method obtains the values at the unknown points by interpolating the weighted average of the values at the known scattered points [20]. Additionally, an improved level set method is used for the geometric representation of the irregular solid boundary. As a result, the water surface is better captured near the irregular shoreline with very shallow water condition.

The irregular solid geometry at the seabed also poses a challenge to the boundary conditions. This challenge is solved by the ghost cell immersed boundary method (GCIBM) [2]. GCIBM makes the solution across the boundaries continuous by extrapolating data into the fictitious ghost cell. And therefore, the numerical discretisation deals with boundary conditions implicitly. The algorithm is originally based on the local directional approach in two dimensions [2].

3 SULAFJORD SIMULATION

3.1 Sulafjord description

The bathymetry for Sulafjord is obtained from the Norwegian Mapping Authority Kartverket. Fig. 1 (a) [8] shows the geographical domain of the entire Sulafjord region. The preliminary designs of the fjord crossing and the crossing locations are shown in Fig.1(b) [21]. Therefore, the main focus of the simulation is shown as a black box in Fig. 1. The most dangerous wave direction for the fjord is shown in Fig. 2 [17]. In this paper, only unidirectional waves are simulated with the direction of the most dangerous waves. The ongoing field measurements are conducted at location D, A and B, as shown

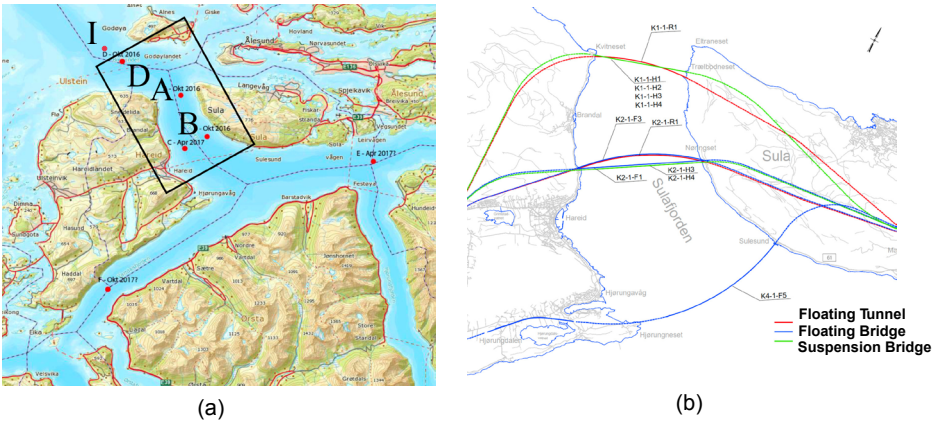

(a) (b)

Figure 1: (a)Locations of the wave height probes in the Sulafjord measurements and the domain of focus shown as the black box, (b)possible fjord crossing locations

in Fig.1(a), the coordinates of the three probes in UTM 33 coordinate system are listed in Table 1. Values at probe I from SWAN are used as inputs in REEF3D, the coordinate of which is also shown in Table 1.

Table 1: The wave height probes at Sulafjord

Probe denotation	x coordinate	y coordinate
I	31600.00	6957000.00
D	33109.42	6956082.14
A	38596.05	6953729.83
B	40026.88	6950883.83

3.2 Swan simulation of Sulafjord and corresponding offshore area

Before the waves reach Sulafjord, large scale wave shoaling occurs, which have significant effect on wave properties. Therefore, in order to have reasonable wave inputs in the fjord simulation, a spectral wave model simulation is used to get the wave properties from the offshore wave data. The initial wave properties are taken from offshore data according to the suggestion of the NORSOK Standard [18]. The selected significant wave height is 16m, the period is 18s. The directional width of the directional spreading function is chosen to be 2. The bottom geometry is obtained from the Norwegian Mapping Authority Kartverket. To optimise the computational resources and accuracy, a nesting

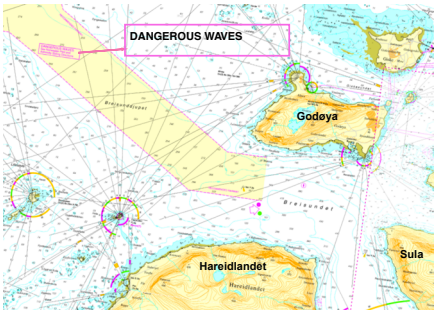

Figure 2: Dangerous wave direction for Sulafjord

technic is applied. By nesting, the overall region is simulated with a coarse resolution; this simulation provides boundary values to a finer grid of smaller area, which again provides boundary input values to an even finer grid at an even smaller domain. Generally it is advised to reduce step size from one nesting level to the next by a factor of 2 or 3 [22]. The mean wave direction is chosen to be 315° so the waves in general agree with the most dangerous wave direction. The mesh convergence study is shown in Fig.4. Therefore, four nesting layers are used with the mesh size of 200m, 100m, 50m and 25m. The bottom geometry and the layers of nesting are demonstrated in Fig. 3, the resulting significant wave height distribution is shown in Fig. 5. The significant wave height at inlet probe I is 5.34m and the peak period is 16.86s, which is later used as input in the CFD simulations.

3.3 Wave tank set up of the CFD simulations

In order to focus on the fjord crossing region and align the numerical wave propagation direction with the most dangerous wave direction, the sub-sea topography is further extracted for a smaller domain, shown as a black box in Fig. 1. The geometry is then rotated anti-clockwise of 55° so that the wave can propagate from the left side of the wave tank. The final geometry used in the simulation is shown in Fig. 6. The corresponding numerical tank is 10000 m long and 9000 m wide and the maximum water depth is 447 m. The wave generation zone is shown as a black box and the numerical beaches are shown as yellow boxes in Fig. 6. Considering the computational resources, the mesh size is chosen to be 20 m. As the main focus is to demonstrate the feasibility of large scale simulation, and the large scale simulation is very time consuming, no further mesh convergence study is conducted at the current stage.

The results at probe I from the SWAN simulation are used directly in the CFD simulations. The irregular wave consists of 700 wave components and the standard JONSWAP wave spectrum is used. The regular wave is a Stokes 5^th wave of 5.34m wave height and

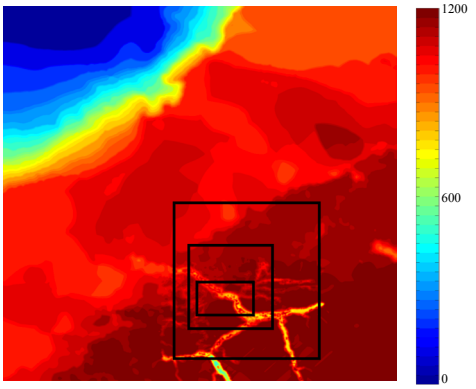

Figure 3: The bottom geometry of the SWAN simulation and the nesting layers in the simulation, the three black boxes represent the three nesting layers, smaller box has finer mesh

16.86s wave period.

3.4 CFD simulation results

The simulation results for both regular waves and irregular waves are shown in Fig. 7. Refraction can be observed along the fjord, where the wave propagation direction tends to be perpendicular to the bank at the near-shore area. The overlapping patterns of the refracted waves, diffracted waves and reflected waves can be seen around the tip of Sula island. The wave propagation is rather steady inside the fjord, with minor reflection from the banks. The different wave transformation phenomena are well presented in the simulation result. This gives CFD simulation a prominent advantage in comparison to the phase-averaged models where only the significant wave height contours are presented. From the fjord crossing infrastructure design point of view, the simulation is not only able to give the magnitudes of wave heights, but also the direction of the waves at specific locations and the interaction of different waves, which facilitate the analysis of wave loads.

The significant wave heights obtained from the SWAN simulation and the irregular wave simulation are compared with the mean wave heights from the regular wave simulation in Table 2. The mean wave periods are also compared. As can be seen, the regular wave simulation gives much higher wave height, indicating that the regular wave simulation with one propagation direction is too conservative from engineering point of view. The irregular wave CFD simulation also gives higher H_s than SWAN, but it is not easy to make a judgement of the accuracies. As SWAN is not performing well with the diffraction phenomenon [23], the results at the probes inside the fjord are not considered to be very convincing. Meanwhile, the irregular wave CFD simulation does not account for the

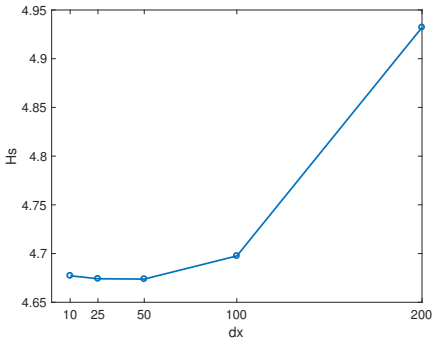

Figure 4: The mesh convergence study of the swan simulation

directional spreading function, which also leads to more conservative results. The data from the field measurements is only available for two months [8], which is not suitable for validation purpose. An observation of longer time is needed.

Table 2: The comparison of the wave properties at probes from the SWAN simulation, the regular wave CFD simulation and the irregular wave CFD simulation

Probes	SWAN		Regular wave CFD		Irregular wave CFD	
	H_s	T_m	H_m	T_m	H_s	T_m
D	4.67	9.95	5.33	16.86	6.91	8.38
A	2.57	9.71	7.31	16.92	5.11	7.53
B	2.28	9.37	7.41	16.97	5.12	8.68

4 CONCLUSIONS

The CFD simulation of the Sulafjord presents a good wave transformation process with reasonable computational resources. This gives confidence to large scale CFD simulations. As a first large scale CFD wave application on record for Norwegian fjords with deep water conditions, the detailed simulation results show the great potential of CFD capacity and introduce many promising topics for further development. The combination of SWAN and REEF3D reduces the cost on time and computational resources tremendously. The practice lays the foundation for the future development of an integrated numerical model consisting of CFD, Boussinesq model and fully non-linear potential flow model.

The uncertainties in the simulations and comparisons provoke the topic of developing

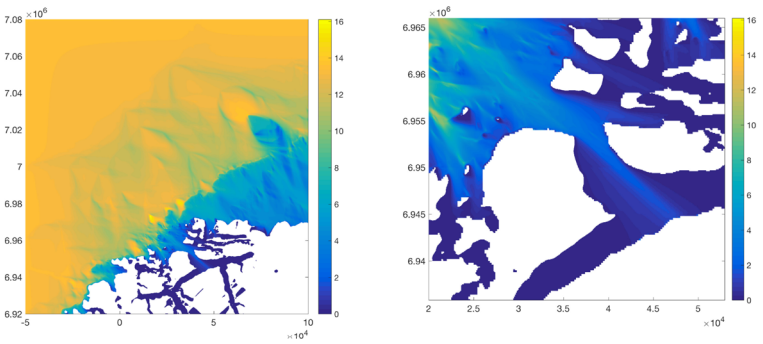

Figure 5: Significant wave height distribution of Sulafjord from swan simulation, to the left: the whole domain Hs distribution, to the right: Hs distribution at Sulasjord

a CFD simulation with a directional wave spectrum. Multi-chromatic waves and wave directional spreading functions are to be implemented in the future study. The field measurements for the duration of one whole year is needed to compare with the simulations. In conclusion, CFD models can be effectively applied on large scale wave simulation in Norwegian fjords and REEF3D shows satisfying capacity of carrying out such simulations. The attempt to optimise the advantages of each existing wave model and combine different models also shows promising potential.

Acknowledgement

This study has been carried out under the E39 fjord crossing project (No. 304624) and the authors are grateful to the grants provided by the Norwegian Public Roads Administration. This study was supported in part with computational resources at the Norwegian University of Science and Technology (NTNU) provided by NOTUR, http://www.notur.no.

REFERENCES

[1] M. Alagan Chella, H. Bihs, D. Myrhaug, and M. Muskulus. Breaking solitary waves and breaking wave forces on a vertically mounted slender cylinder over an impermeable sloping seabed. *Journal of Ocean Engineering and Marine Energy*, 3(1):1–19, 2017.

[2] P. A. Berthelsen and O. M. Faltinsen. A local directional ghost cell approach for incompressible viscous flow problems with irregular boundaries. *Journal of Computational Physics*, 227(9):4354 – 4397, 2008.

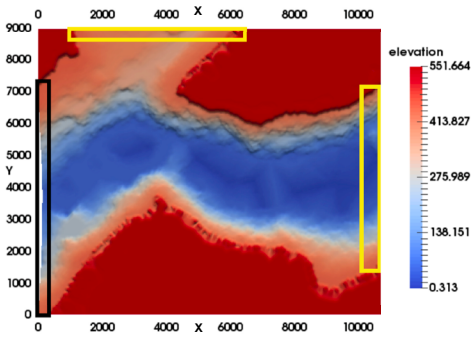

Figure 6: The bathymetry and numerical tank set up of Sulafjord CFD simulation

[3] H. Bihs and A. Kamath. A combined level set/ghost cell immersed boundary representation for floating body simulations. *International Journal for Numerical Methods in Fluids*, pages n/a–n/a, 2016. fld.4333.

[4] H. Bihs, A. Kamath, M. A. Chella, A. Aggarwal, and ivind A. Arntsen. A new level set numerical wave tank with improved density interpolation for complex wave hydrodynamics. *Computers Fluids*, 140:191 – 208, 2016.

[5] S. Chi-Wang and O. Stanley. Efficient implementation of essentially non-oscillatory shock-capturing schemes. *Journal of Computational Physics*, 77(2):439–471, August 1988.

[6] O. Ellevset. Project overview coastal highway route E39. www.vegvesen.no/attachment/300340/binary/527486, January.

[7] R. D. Falgout, J. E. Jones, and U. M. Yang. Conceptual interfaces in hypre. *Future Gener. Comput. Syst.*, 22(1-2):239–251, Jan. 2006.

[8] Fugro. Miljømålinger fjordkrysning e39 - presentasjon av andre måneds målinger. Technical Report $C75365_DPR_2$, Fugro Norway AS, February 2017.

[9] M. Griebel, T. Dornseifer, and T. Neunhoeffer. *Numerical Simulation in Fluid Dynamics: A Practical Introduction*. Society for Industrial and Applied Mathematics, Philadelphia, PA, USA, 1998.

[10] J. Guang-Shan and S. Chi-Wang. Efficient implementation of weighted eno schemes. *Journal of Computational Physics*, 126(1):202–228, 1996.

[11] J. A. Hasselø. Prosjektutviklingsmodell-teknologi. http://www.vegvesen.no/Europaveg/E39sulafjorden/dokumenter, December 2015.

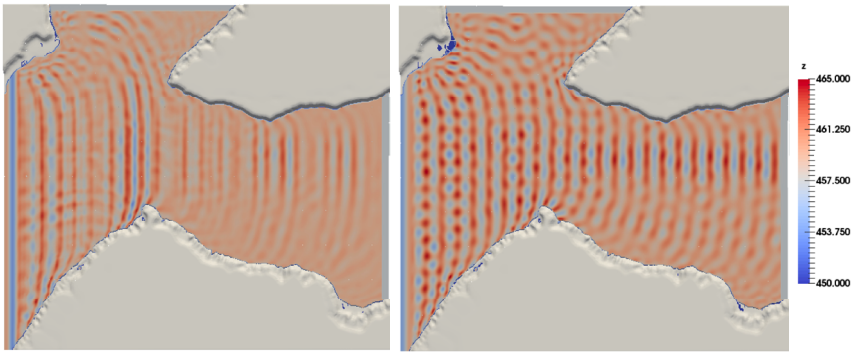

Figure 7: Wave pattern and free-surface of the regular wave CFD simulation at Sulafjord, to the left: irregular wave simulation; to the right regular wave simulation

[12] Hypre. Hypre: Scalable linear solvers and multigrid methods. https://computation.llnl.gov/projects/hypre-scalable-linear-solvers-multigrid-methods, January 2016.

[13] N. Jacobsen, D. Fuhrman, and J. Fredse. A wave generation toolbox for the open-source cfd library: Openfoam. *International Journal for Numerical Methods in Fluids*, 70(9):1073–1088, 2012.

[14] A. Kamath, M. A. Chella, H. Bihs, and Ø. A. Arntsen. Breaking wave interaction with a vertical cylinder and the effect of breaker location. *Ocean Engineering*, 128:105 – 115, 2016.

[15] P. A. Madsen and O. R. Srensen. A new form of the boussinesq equations with improved linear dispersion characteristics. part 2. a slowly-varying bathymetry. *Coastal Engineering*, 18(3):183 – 204, 1992.

[16] S. Mayer, A. Garapon, and L. S. Srensen. A fractional step method for unsteady free-surface flow with applications to non-linear wave dynamics. *International Journal for Numerical Methods in Fluids*, 28(2):293–315, 1998.

[17] Norgeskart. Sulafjord. http://www.norgeskart.no/?ga=1.148519543.1531380854.1484589939/26136/6963625/-land/+sjo.

[18] NORSOK. Actions and action effect. Standard N-003, Norwegian Oil Industry Association and the Federation of Norwegian Industry, Strandveien 18, Lysaker, Norway, September 2007.

[19] S. Osher and J. A. Sethian. Fronts propagating with curvature-dependent speed: Algorithms based on hamilton-jacobi formulations. *Journal of Computational Physics*, 79(1):12 – 49, 1988.

[20] D. Shepard. A two-dimensional interpolation function for irregularly-spaced data. In *Proceedings of the 1968 23rd ACM National Conference*, ACM '68, pages 517–524, New York, NY, USA, 1968.

[21] Statensvegvesen. Illustrasjonskart E39 sulafjorden. https://www.vegvesen.no/Europaveg/e39sulafjorden, 2015.

[22] SWAN. User manual swan cycle iii version 41.10a. Technical report, Delft University of Technology, 2017.

[23] T. J. Thomas and G. Dwarakish. Numerical wave modelling a review. *Aquatic Procedia*, 4:443 – 448, 2015.

[24] Van Der Vorst. Bi-cgstab: A fast and smoothly converging variant of bi-cg for the solution of nonsymmetric linear systems. *SIAM Journal on Scientific and Statistical Computing*, 13(2):631–644, 1992.

9. National Conference on Computational Mechanics
MekIT'17
B. Skallerud and H I Andersson (Eds)

GRAVITY EFFECTS ON THE WALL-NORMAL MOTION OF INERTIAL DISK-LIKE PARTICLES IN TURBULENT VERTICAL CHANNEL FLOW

WENJUN YUAN[1, 2], LIHAO ZHAO[3, 2], NIRANJAN REDDY CHALLABOTLA[2] AND HELGE I. ANDERSSON[2]

[1] Department of Process Equipment and Control Engineering
Xi'an Jiaotong University, 710049 Xi'an, China
e-mail: wenjun.yuan@ntnu.no

[2] Department of Energy and Process Engineering
Norwegian University of Science and Technology, 7491 Trondheim, Norway

[3] Department of Engineering Mechanics
Tsinghua University, 10084 Beijing, China

Key words: Disk-like Particles, Turbulent Flow, Gravity, Wall-normal Motion, Eulerian-Lagrangian Approach

Abstract. In this work, the dynamics of inertial disk-like particles in a turbulent vertical channel flow has been investigated. Direct numerical simulations are performed to obtain the turbulent flow field, and the disks are modeled as oblate spheroids with inertia and shape parameterized by means of Stokes number and aspect ratio. For each of the four disk classes, three different gravity configurations are considered: upward flow with gravity opposing, downward flow with aiding gravity, and channel flow in the absence of gravity. Results of the translation, rotation and orientation of disks with inward and outward motion judging from the particle wall-normal velocity have been reported. Though the gravity force is observed to alter the particle position and the tendency of moving towards or away from the nearest wall, the presence of gravity always inhibits the wall-normal motion of disks in the central region. Moreover, disk-like particles spin faster for inward motion in the near-wall region and for outward motion in the central region. It is found that disks are more likely to orient in the spanwise direction as moving towards the wall. The gravity force however has a negligible impact on the rotation and orientation of particles, except that heavy disks in the channel center have less tendency to orient randomly when the flow is upward or downward.

1 INTRODUCTION

Suspensions of tiny rigid non-spherical particles are commonly encountered in many industrial, environmental and biological applications. Due to the widespread practical importance, dynamics of non-spherical particle-laden suspensions has been a topic of research

in both homogenous isotropic turbulence [1,2] and wall-bounded turbulence [3-8] by means of advanced experimental and numerical approaches. The readers can refer to [9-11] for an overview of different types of experimental and numerical methodologies available for the investigation of non-spherical particles.

Among the previous work, the dynamics of non-spherical particles has been commonly studied by assuming regular axisymmetric shapes, i.e. either prolate (rod-like) or oblate (disk-like) spheroids. Zhang *et al.* [3] were the first to investigate prolate spheroidal particle transport and deposition in fully developed turbulent channel flow using direct numerical simulations (DNSs) along with a point-particle approach. Later, Mortensen *et al.* [4,5] and Marchioli *et al.* [6,7] adopted this method and studied the dynamics of a wide range of prolate spheroidal particles in wall turbulence. They pointed out that inertial rods, similar to spheres [12,13], tend to accumulate in the viscous sublayer and preferentially concentrate in the low-speed streaks. In addition, the orientation and rotation of rods in the near-wall region are strongly dependent on its elongation and this effect reduces with the increase of inertia [4,6]. Prolate spheroids orient randomly in the central region where the fluid vorticity is almost isotropic, and exhibit preferential alignment with the local fluid vorticity in the near-wall region where strong velocity gradients exist [14,15]. However, only a few studies have focused on suspensions of disk-like particles in turbulent flows compared with those of rod-like particles. Njobuenwu and Fairweather [16] investigated the dynamics of spheroidal particles using large-eddy simulation (LES) and a Lagrangian particle tracking technique, and noted that oblate spheroids segregate in the low-speed streaks in the same manner as spheres and prolate spheroids. Challabotla *et al.* [17] explored the dynamics of inertia-free spheroids in wall turbulence by means of DNS, and observed that the shape-dependence of the particle orientation carries over to the particle rotation, and the mean spin is reduced with increasing departure from sphericity. They further concluded that near-wall spheroids with large inertia tend to orient their long axis in the mean-shear plane, though inertial oblate spheroids prefer to align their symmetry axes normal to the local fluid vorticity [18].

Moreover, the gravity force has a significant effect on particle dispersion and deposition in a vertical pipe flow via the crossing trajectory mechanism [19]. Marchioli *et al.* [20] and Nilsen *et al.* [21] studied the concentration of spheres with different gravity configurations, and observed that spherical particles have a tendency to gather in the channel center in the downward flow. Challabotla *et al.* [22,23] further explored the dynamics of rods in a turbulent vertical channel flow. They reported that the upward flow suppresses the drift velocity of particles, eventually giving rise to a more uniform rod distribution throughout the channel as compared to the distinct near-wall accumulation in the downward flow and in the absence of gravity. However, according to our recent study, disk-like particles behave quite differently from rod-like particles in turbulent vertical channels [24]. A common feature is that the role of gravity on the spheroid concentration diminishes with higher inertia and the spheroid shape has only a modest influence. The wall-normal motion of spheroids plays an important role on the final distribution, and deserves further investigations for channel flow with different gravity configurations.

The present paper focuses on the wall-normal motion of disk-like particles in turbulent vertical channel flow, and is an extension of our earlier study [24] on the statistical

performance of disk-like particles modeled as oblate spheroids. In order to understand how gravity affects the dynamics of particles with different shape and inertia, we now judge from the particle drift velocity in the channel, and distinguish particles with inward (towards the nearest wall) and outward (away from the nearest wall) motions. The results from simulations of upward flow (GU), and downward flow (GD) in a vertical channel will be compared with results from channel flow simulations in which gravity is neglected (G0).

2 METHODOLOGY

The dynamics of rigid disk-like particles suspended in channel flow turbulence is modeled in an Eulerian-Lagrangian approach. The continuous Newtonian fluid phase, in which disks are suspended, is governed by continuity and Navier–Stokes equations,

$$\frac{\partial u_i}{\partial x_i} = 0, \tag{1}$$

$$\rho_f \left(\frac{\partial u_i}{\partial t} + u_j \frac{\partial u_i}{\partial x_j} \right) = -\frac{\partial p}{\partial x_i} + \mu \frac{\partial^2 u_i}{\partial x_j \partial x_j} + \underbrace{\left(-\frac{\partial P}{\partial x} \pm \rho_f g \right)}_{2\tau_w / h} \delta_{x,i}, \tag{2}$$

where u_i is the component of the fluid velocity vector in the x_i direction, and ρ_f, p and μ denote the fluid density, fluctuating pressure and dynamic viscosity, respectively. The fluid flow is driven through the vertical plane channel by means of a constant body force, which includes the negative mean pressure gradient $\partial P/\partial x$ and a negative or a positive gravity force $\rho_f g$, i.e. the last term to the right in Eq. (2).

In addition, a general spheroidal particle is characterized by three semiaxes $a = b \neq c$. The rigid disk-like particles in our simulations are modeled as oblate spheroidal point-particles with aspect ratio $\lambda = c/a < 1$. Two different Cartesian frames of reference are used to study the dynamics of oblate spheroidal point particles in channel flow turbulence. The translational motion of a disk-like spheroid is governed by Newton's second law of motion, expressed in the inertial reference frame $x_i = (x, y, z)$, in which the turbulent flow field is obtained; while the rotational motion is governed by Euler's equation, which is formulated in a particle frame $x_i' = (x', y', z')$ with its origin in the mass centre and the coordinate axes aligned with the principal directions of inertia of the spheroid,

$$m \frac{dv_i}{dt} = F_i, \tag{3}$$

$$I'_{ij} \frac{d\omega'_j}{dt} + \varepsilon_{ijk} \omega'_j I'_{kl} \omega'_l = N'_i. \tag{4}$$

Here, m is the particle mass and ε_{ijk} denotes the Levi-Civita alternating or permutation tensor. $v_i = dx_i/dt$ is the translational particle velocity in the inertial frame, whereas ω' and I'_{ij} denote the angular velocity and the moment of inertia tensor of the oblate spheroid in the particle frame, respectively.

The spheroidal particles are sufficiently small, so that the neighboring flow can be

considered as Stokesian. Thus, the drag force F_i acting on a spheroid from the surrounding fluid can be expressed as,

$$F_i = \pi\mu a K_{ij}\Delta u_j \pm \left(1-\frac{1}{D}\right)mg\delta_{x,i}, \tag{5}$$

where $D=\rho_p/\rho_f$ is the ratio between the particle density and fluid density. Δu_j is the slip velocity vector defined as $\Delta u_j = u_{p,j} - v_j$, with $u_{p,j}$ and v_j are the fluid velocity at the particle location and the particle translational velocity in the x_j direction, respectively.

The resistance tensor K_{ij} is represented in the inertial frame and related to the resistance tensor K'_{ij} in the particle reference frame as $K_{ij} = A^t_{ik}K'_{kl}A_{lj}$, where A_{ij} denotes the orthogonal transformation matrix which relates the same vector in the two different frames through the linear transformation $x'_i = A_{ij}x_j$. Just as in Eq. (2), the positive and negative signs apply for downward and upward flow, respectively. The first term on the right-hand side of Eq. (5) represents the hydrodynamic drag force from the surrounding fluid on a non-spherical particle, while the second term represents the gravity and buoyancy forces. The resistance tensor K'_{ij} obtained by Challabotla *et al.* [18] for oblate spheroids is a diagonal matrix with elements,

$$K'_{xx} = K'_{yy} = \frac{32\left(1-\lambda^2\right)^{3/2}}{\left(3-2\lambda^2\right)C - 2\lambda\left(1-\lambda^2\right)^{1/2}},\ K'_{zz} = \frac{16\left(1-\lambda^2\right)^{3/2}}{\left(1-2\lambda^2\right)C + 2\lambda\left(1-\lambda^2\right)^{1/2}}, \tag{6}$$

where $C = \pi - 2\tan^{-1}(\lambda(1-\lambda^2)^{-1/2})$.

The torque components N_i' for a three-axial ellipsoidal particle in creeping shear flow originally derived by Jeffery [25] are simplified for a spheroid to,

$$\begin{bmatrix} N'_x \\ N'_y \\ N'_z \end{bmatrix} = \begin{bmatrix} \dfrac{16\pi\mu a^3\lambda}{3\left(\beta_0+\lambda^2\gamma_0\right)}\left[\left(1-\lambda^2\right)S'_{yz} + \left(1+\lambda^2\right)\left(\Omega'_x-\omega'_x\right)\right] \\ \dfrac{16\pi\mu a^3\lambda}{3\left(\alpha_0+\lambda^2\gamma_0\right)}\left[\left(\lambda^2-1\right)S'_{xz} + \left(1+\lambda^2\right)\left(\Omega'_y-\omega'_y\right)\right] \\ \dfrac{32\pi\mu a^3\lambda}{3\left(\alpha_0+\beta_0\right)}\left(\Omega'_z-\omega'_z\right) \end{bmatrix}. \tag{7}$$

Here, S'_{ij} and Ω'_i denote the fluid rate-of-strain tensor and the rate-of-rotation vector, respectively. The analytical expressions for the shape factors (α_0, β_0, γ_0) for oblate spheroids have been derived by Siewert *et al.* [26],

$$\alpha_0 = \beta_0 = \frac{-\lambda^2}{1-\lambda^2} + \frac{\lambda C}{2\left(1-\lambda^2\right)^{3/2}},\ \gamma_0 = \frac{2}{1-\lambda^2} - \frac{\lambda C}{\left(1-\lambda^2\right)^{3/2}}. \tag{8}$$

The ability of a disk-like particle to adjust to the ambient flow field can be estimated by the particle response time τ_p. Shapiro and Goldenberg [27] introduced a translational relaxation time based on the orientation-averaged resistance tensor $\bar{K} = 3(K'^{-1}_{xx} + K'^{-1}_{yy} + K'^{-1}_{zz})^{-1}$. This is a relevant time scale for isotropically oriented particles and has been widely used for prolate spheroids [4,5]. The same definition of an equivalent response time has also been adopted by

Challabotla *et al.* [18] for the oblate spheroids,

$$\tau_p = \frac{4Da^2}{3\upsilon}\frac{\lambda}{\bar{K}} = \frac{\lambda C}{2\left(1-\lambda^2\right)^{\frac{1}{2}}}\frac{2Da^2}{9\upsilon}, \tag{9}$$

where υ is the kinematic fluid viscosity. The Stokes number St is defined as the ratio between the response time τ_p and the viscous time scale υ/u_τ^2 based on the wall-friction velocity u_τ,

$$\mathrm{St} = \frac{\tau_p}{\upsilon/u_\tau^2}. \tag{10}$$

We use DNS to simulate a turbulent channel flow at Reynolds number $Re_\tau = 180$ based on u_τ and the channel half-height h. The variables are be normalized by the viscous scales for velocity u_τ, length (υ/u_τ) and time (υ/u_τ^2). The computational set-up and the flow solver are essentially the same as in the preceding simulation studies of dilute suspensions of spheroids in turbulent channel flow reported by Mortensen *et al*. [4,5] and Challabotla *et al.* [22,23]. In the present work, it is assumed that the solid suspension is sufficiently dilute so that the one-way coupled Eulerian-Lagrangian approach can be justified, i.e. the feedback from the disks onto the fluid is ignored. The size of disk-like particles does not exceed the Kolmogorov length scale.

3 RESULTS AND DISCUSSIONS

Simulations are performed for oblate spheroids with aspect ratios $\lambda = 0.33$, 0.1 and Stokes numbers St = 1, 30. Combined with the three different gravity configurations: no gravity (G0), downward flow (GD), and upward flow (GU), a total of 12 different cases have been considered. In each case, 2×10^5 disk-like particles with the same normalized semi major-axis $a^+ = 0.36$ are tracked in the turbulent field. In order to obtain reliable particle statistics, the results are computed by averaging instantaneous data in the time window from $t^+ = 5{,}400$ to 10,800 (viscous time units) and also in both the homogeneous streamwise and spanwise directions.

The statistically averaged percentage of disk-like particles with inward and outward motions are shown in Fig. 1 as a function of the normalized wall-normal coordinate z^+. It is clear that there is a greater proportion of particles moving towards the nearest wall in the central region, and the effect of gravity on this phenomenon is nearly unaffected by the particle shape but depends on the particle inertia. For particles with modest inertia (St = 1), the gravity force has little impact on the tendency of particles to move towards or away from the nearest wall. While for large inertia (St = 30), disk-like particles in the channel center are more likely to move towards the nearest wall in the downward flow, whereas the upward flow weakens this tendency.

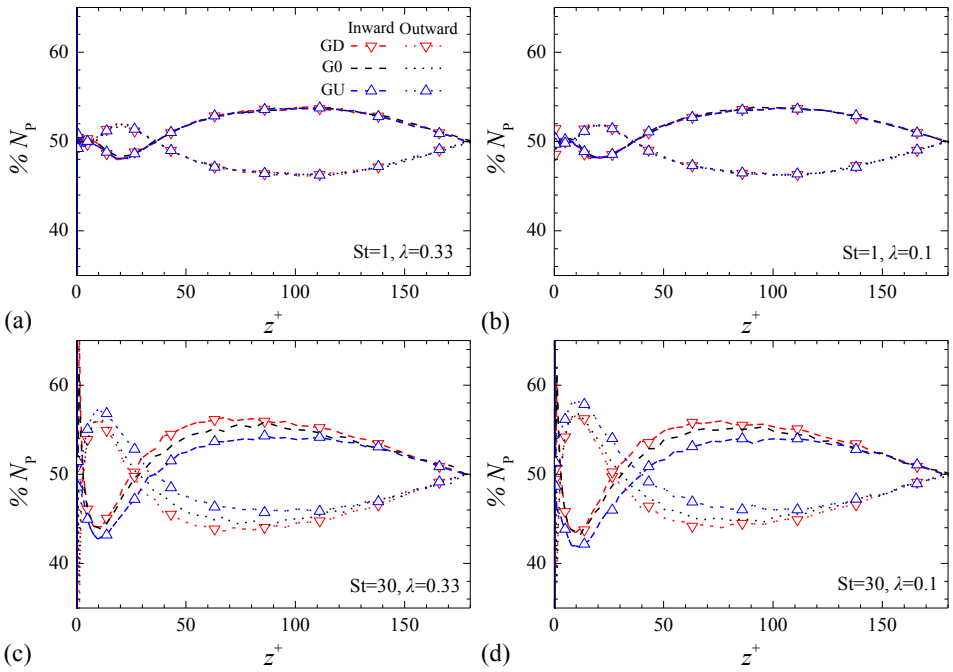

Figure 1: Statistically-averaged percentage of disk-like particles with inward or outward motions in the wall-normal direction. (a) St = 1, λ = 0.33; (b) St = 1, λ = 0.1; (c) St = 30, λ = 0.33; (d) St = 30, λ = 0.1.

Nevertheless, by virtue of inward turbulent fluid motions in the buffer region, most of inertial particles also move toward the nearest channel wall in the viscous sublayer, and the increased inertia enlarges the percentage of this kind inward motion. Though this average-percentage analysis does not present the final distribution of particles, it is suggested that the downward flow promotes a larger majority of particles to move towards the nearest channel wall in the central region, while the upward flow drives particles in the buffer layer to move outward to the central region. Thus, it can be inferred that the particle distribution may be more evenly across the channel in the upward flow in this large inertia case. This is consistent with the final distribution observed in our previous work [24].

Fig. 2 shows the mean wall-normal fluid velocity $<u_{p,z}>$ conditionally sampled at particle locations. The angle bracket notation < > presents statistically-averaged value. Simlarly, the gravity effect on the statistical fluid velocity sampled at particle locations has nothing to do with the spheroid shape but is closely associated with the inertia. As particles are drifted by the fluid flow, it is noted that inward particles are likely to locate in inward fluid excursions, and outward particles are likely to locate in outward fluid excursions. The wall-normal fluid velocity sampled at particle locations decreases with the rising inertia, in spite of the fact that the overall $<u_{p,z}>$ is increasing.

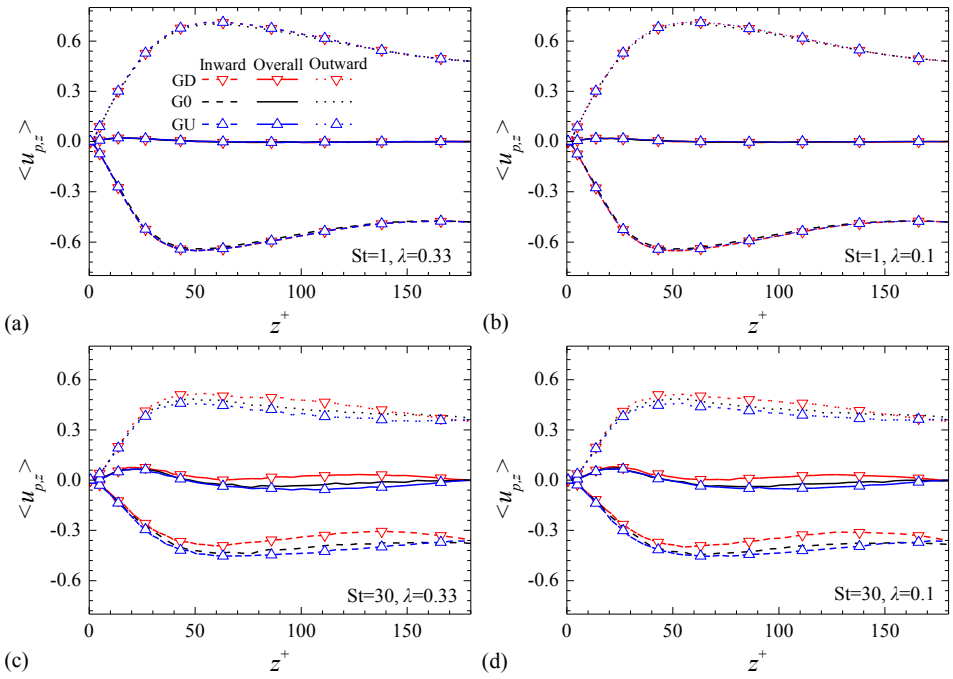

Figure 2: Mean wall-normal fluid velocity sampled at particle locations. (a) St = 1, λ = 0.33; (b) St = 1, λ = 0.1; (c) St = 30, λ = 0.33; (d) St = 30, λ = 0.1.

For modest inertia, the local fluid velocity statistics are nearly unaffected by the gravity force. This is similar as the statistically-averaged percentage of particles with inward and outward motions shown in Fig. 1. The overall $<u_{p,z}>$ is nearly zero for low-Stokes-number particles, which is different from the cases with large inertia in which the overall $<u_{p,z}>$ slightly increases in a limited range and drops to zero at $z^+ \approx 50$. The $<u_{p,z}>$ sampled for inward and outward particles always has the same changing trend as that of large inertia particles. The absolute local wall-normal fluid velocity always increases in the viscous sublayer and the buffer layer, and almost keeps constant in the central region.

However, for large inertia, the gravity force is observed to play an important role on the local wall-normal fluid velocity. In the presence of gravity, the upward flow slightly induces inward particles to the regions with higher wall-normal fluid velocity in the whole channel, and the downward flow obviously promotes outward particles to regions with higher wall-normal fluid velocity in the inner wall layer. In general, the overall performance is that particles always locate in outward fluid excursions in the near-wall region. In the central region, however, inertia disk-like particles are more likely to locate in inward fluid excursions in the upward flow and in outward fluid excursions in the downward flow. Interestingly,

though the overall $<u_{p,z}>$ in the no-gravity flow is between the two cases with gravity force, both inward and outward $<u_{p,z}>$ are not always between them. The no-gravity $<u_{p,z}>$ for inward and outward particles is the highest once the corresponding particles move into the outer layer.

The mean wall-normal slip velocity $<\Delta u_z>$ is then presented in Fig. 3. The particle shape has no impact while the inertia plays an important role on the mean wall-normal slip velocity. For modest inertia, though the gravity force has a negligible effect on $<\Delta u_z>$, wall-normal slip velocities for particles with inward and outward motions are quite different. $<\Delta u_z>$ rises with increasing distance from the wall, and changes more rapidly for particles moving towards the channel wall. The mean wall-normal slip velocity peaks for inward particles before for outward particles with a larger maximum value, and then drops to zero at a position closer to the wall. In addition, the mean wall-normal slip velocity is negative when particles are further from the nearest wall, and the overall $<\Delta u_z>$ between that of particles with separate inward and outward motions eventually returns to zero in the channel center. This observation indicates that particles with inward motions experience drift force towards the channel center, whereas particles with ouward motion experience drift force towards the channel wall in the central region.

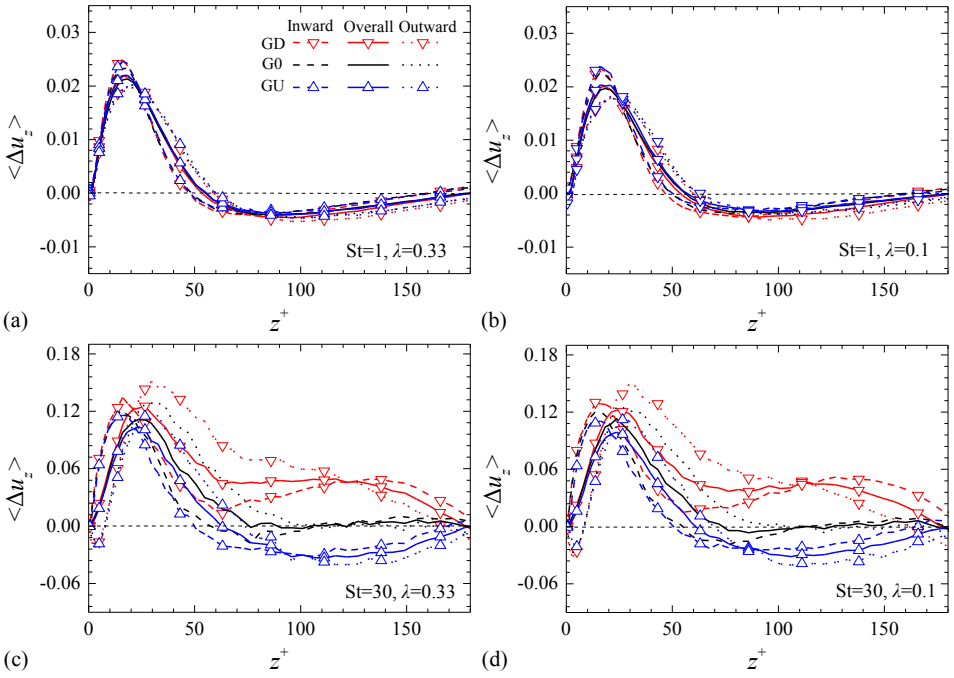

Figure 3: Mean wall-normal slip velocity of disk-like particles. (a) St = 1, λ = 0.33; (b) St = 1, λ = 0.1; (c) St = 30, λ = 0.33; (d) St = 30, λ = 0.1.

On the other hand, the maximum $<\Delta u_z>$ markedly rises with the growing inertia, which is opposite to $<u_{p,z}>$ presented in Fig. 2. Based on the definition of slip velocity, we can obtain that, $<v_z>$ drops for the large inertia. Furthermore, the gravity force is also observed to have a siginficant influence on the mean wall-normal slip velocity at St = 30. In the near-wall region, the downward flow leads outward particles to larger positive slip velocity, whereas the upward flow affects inward particles. However, the overall $<\Delta u_z>$ always experience the same changes with the overall $<u_{p,z}>$. In particular, $<\Delta u_z>$ for outward particles is negative in the visous sublayer, which implies the deceleration process due to turbulence sweep events. The inward and outward particles experience the same $<\Delta u_z>$ at somewhere in the channel. The upward flow promotes this place closer to the channel wall, suggesting that inward particles are more likely to experience drift force toward the channel wall in the upward flow. Ultimately, in the presence of gravity, $<\Delta u_z>$ is inevitably negative for outward particles and positive for inward particles in the central region, which further indicates that the gravity inhibits the wall-normal motion of particles near the channel center.

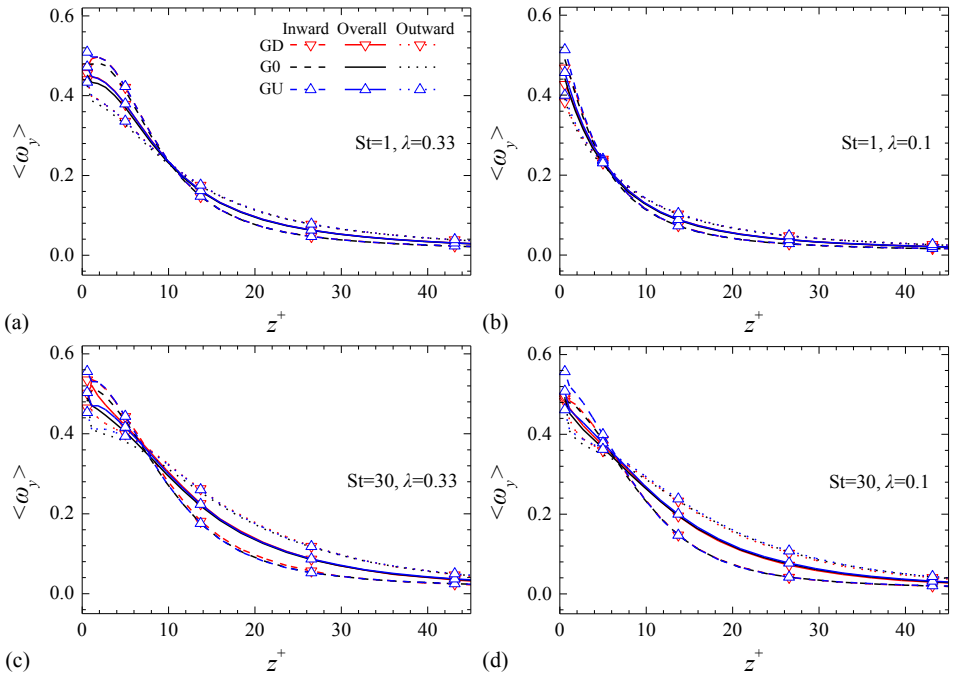

Figure 4: Mean spanwise angular velocity in the near wall region of disk-like particles. (a) St = 1, λ = 0.33; (b) St = 1, λ = 0.1; (c) St = 30, λ = 0.33; (d) St = 30, λ = 0.1.

Figure 4 shows the mean spanwise angular velocity $<\omega_y>$ for $z^+ \leq 50$. Clearly, both the particle shape and inertia affect the mean spanwise angular velocity. The presence of gravity,

however, has a negligible influence on this rotational behavior. Disk-like particles are inclined to rotate in the near-wall region, and $<\omega_y>$ decreases as particles move away from the nearest wall, and eventually become close to zero near the channel center. Especially, disks with a higher aspect ratio λ always have a larger angular velocity near the channel wall. This agrees with the conclusion of Challabotla *et al.* [17] that the mean spin is reduced with increasing departure from sphericity. Still, inward particles are observed to rotate faster in the near-wall region, whereas outward particles have a larger angular velocity in the central region. The large-Stokes-number particles are more likely to have a mean rotation that is almost equal to the mean fluid rotation, and the large inertia results in the position that inward and outward particles have the same angular velocity much closer to the channel wall.

Root-mean-square (rms) values of the three angular velocity components near the wall are shown in Fig. 5 for St = 1 (left column) and St = 30 (right column). It is noted that disk-like particles possess fairly strong angular velocity fluctuations in the streamwise and wall-normal directions, in spite of the fact that the mean rotation components about the streamwise and wall-normal axes are zero. Similarly to $<\omega_y>$ in Fig. 4, the gravity effect is modest and almost confined to a region very close to the channel wall, whereas the particle shape shows significant impact on the angular velocity fluctuations.

The angular velocity fluctuations next to the channel wall are larger for St = 1 than for St = 30. The anisotropic rms-values always have the highest level in the spanwise direction and the lowest level in the streamwise direction. This reflects the prevailing anisotropic vorticity fluctuations in the buffer region. In addition, in the near-wall region ($z^+ > 15$), $\mathrm{rms}(\omega_y')$ and $\mathrm{rms}(\omega_z')$ are further seen to slightly increase with increasing λ, while $\mathrm{rms}(\omega_x')$ is observed to decrease as disks are closer spheres. This is because of the different moment of inertia for disk-like particles with different λ [18], and this aspect ratio effect vanishes almost completely for the most inertial particles. The intensity of the spin fluctuations reduces with the distance from the wall and also tends towards isotropy in the central region. In contrast, the wall-normal spin fluctuation is stronger for spheroids with smaller λ. As the mean spin $<\omega_z> = 0$, it can be inferred that the high level of $\mathrm{rms}(\omega_z')$ represents a vigorous flipping behavior superimposed onto the disk-like particle's primary rotation about its symmetry axis.

Moreover, inward particles experience stronger angular velocity fluctuations in the central region, whereas outward particles have larger rms-values in near-wall region. This observation is opposite to $<\omega_y>$ for inward and outward particles. By revisiting Eq. (7), the observed particle spin is accordingly a signature of the local flow field and, in particular, of the fluid rotation in the vicinity of the particles. Though the gravity force influences the distribution of particles through altering the preferential location of particles (Fig. 2), the spin associated with the mechanism of particle-turbulence interaction is not changed. Therefore, from a statistical viewpoint, particles just adjust their angular velocity to the local fluid field according to distance from the wall. However, inward and outward particles prefer to locate at different positions in the wall-normal direction, so that they have different rotational features.

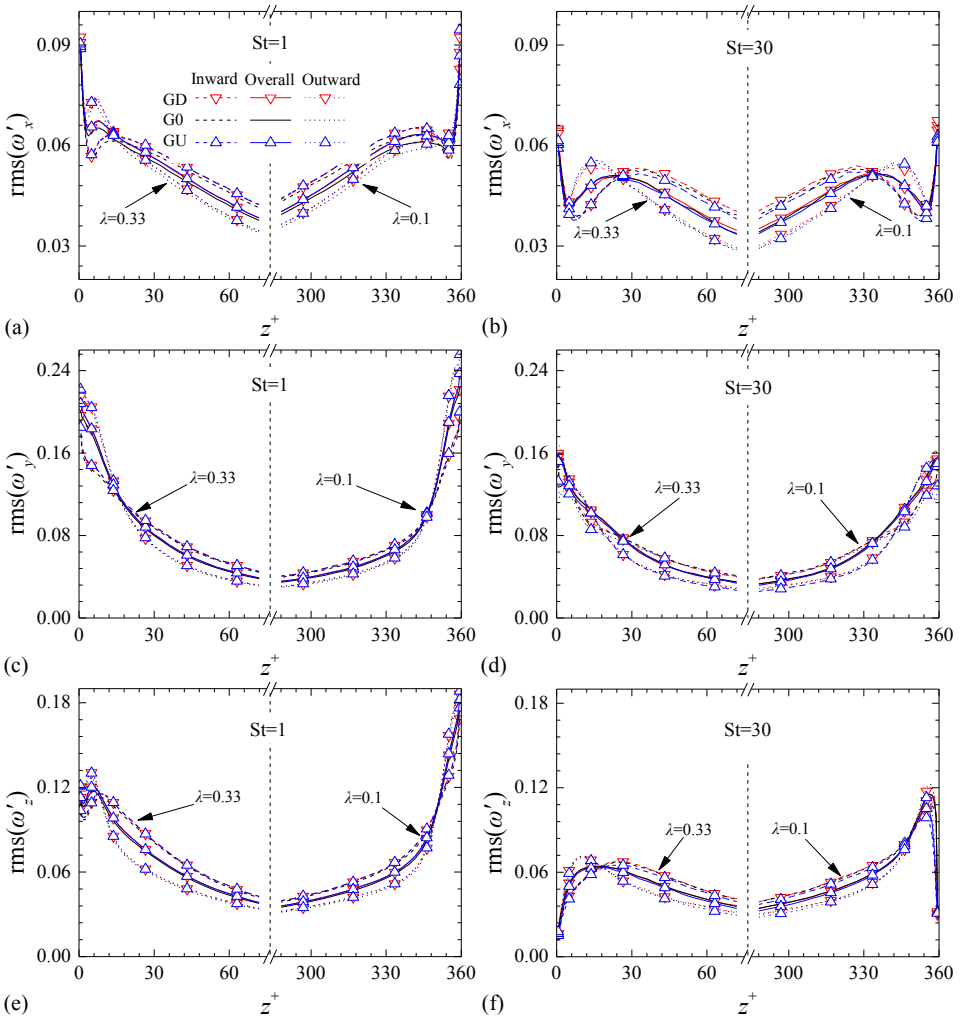

Figure 5: rms-values of the particle angular velocity fluctuations in different directions for St = 1 (left column) and St = 30 (right column). (a, b) streamwise direction; (c, d) spanwise direction; (e, f) wall-normal direction.

Figure 6 presents the mean absolute direction cosines for St = 1 (left column) and St = 30 (right column). Here, the orientation of an oblate spheroidal particle is measured as $<|\cos\theta_i|>$, referred to as the direction cosine, and defined in terms of the angle θ_i between the symmetry axis of the spheroid and the x_i-axis of the inertial frame. It is quite clear that the orientation for inward disk-like particles is different from for outward disk-like particles.

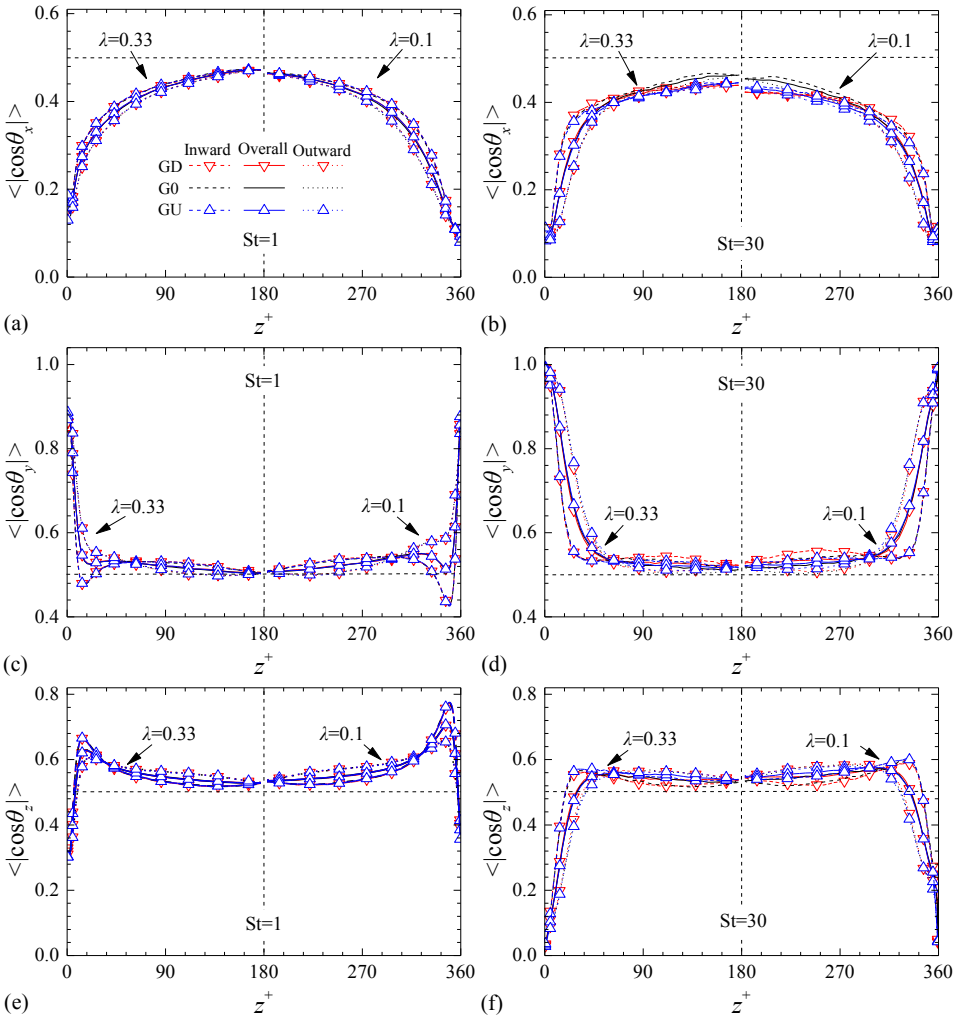

Figure 6: Mean absolute direction cosines of disk-like particles relative to (a, b) streamwise direction; (c, d) spanwise direction; (e, f) wall-normal direction for St = 1 (left column) and St = 30 (right column).

In the near-wall region, all disk-like particles tend to orient in the spanwise y-direction, i.e. $<|\cos\theta_y|> \approx 1$. This preferential orientation is shape-dependent in the vicinity of the wall, and disk-like particles with aspect ratio $\lambda = 0.1$ also have a tendency to orient in the wall-normal direction. In addition, the preferential orientation in the spanwise y-direction is more pronounced for outward particles than for inward particles. The inward particles, especially

for modest inertia, are also likely to orient in the wall-normal direction at $z^+ \approx 20$. In general, the overall performance of disk-like particles is at variance with the observation of rods near the wall [4,6], and a common feature of prolate and oblate spheroids in the near-wall region is that both tend to align their long axis in the mean-shear plane.

Besides, in the channel center, the mean absolute direction cosines in the three directions are about 0.5 with no impact from the anisotropy of particles, reflecting a nearly random orientation of disk-like particles. However, for large inertia, the preferential orientation of disk-like particles, especially in the streamwise direction, is moreover observed to be influenced by the presence of gravity. For instance, the upward flow causes the orientation angle of particles with outward motion to be more random for $z^+ \geq 55$. In particular, the mean absolute direction cosines slightly departure from 0.5 in the channel center with the presence of gravity. This indicates that disk-like particles are less likely to orient randomly in the central region when the flow is either upward or downward.

4 CONCLUSIONS

The influence of the gravity force on the wall-normal motion of disk-like particles has been studied in a turbulent vertical channel flow. The turbulent flow field is obtained by means of a direct numerical simulation, and non-spherical particles modeled as oblate spheroids are tracked as Lagrangian point-particles subjected to Stokes drag, gravity and buoyancy forces and Jeffery torques. Altogether 4 different particle classes have been studied, with inertia and shape parameterized by means of Stokes number and aspect ratio. The inward and outward particle motions judging from its wall-normal velocity have been analysed in upward flow, downward flow, and channel flow in the absence of gravity.

The results show that the translational motion of disk-like particles is controlled by the inertia, whereas the particle shape mainly influences on the rotation and orientation. The presence of gravity alters the wall-normal motion of particles, not only the tendency of moving inward or outward, but also the position of particles. The gravity force is further observed to inhibit the wall-normal motion of particles in the central region. In addition, disk-like particles with inward motions rotate faster in the near-wall region, whereas outward moving particles rotate faster in the central region. However, disks moving towards the channel wall are more likely to orient in the spanwise direction in the near-wall region. The presence of gravity has a negligible influence on the rotation and orientation of particles, except for the striking effect on the orientation of large inertia particles in the central region. In the channel center, heavy disks always have less tendency to orient randomly when the flow is either upward or downward.

Acknowledgements

Computing time on Notur was granted by Research Council of Norway (Programme for Supercomputing, Grant no. NN2649K). W. Y. would also like to acknowledge the financial support from China Scholarship Council and the encouragement from Prof. Jianqiang Deng.

REFERENCES

[1] M. Byron, J. Einarsson, K. Gustavsson, G. Voth, B. Mehlig, E. Variano. Shape-dependence of particle rotation in isotropic turbulence. *Phys. Fluids* (2015) **27**: 035101.

[2] S. Parsa, E. Calzavarini, F. Toschi, G. A. Voth. Rotation rate of rods in turbulent fluid flow. *Phys. Rev. Lett.* (2012) **109**: 134501.

[3] H. Zhang, G. Ahmadi, F. G. Fan, J. B. McLaughlin. Ellipsoidal particles transport and deposition in turbulent channel flows. *Int. J. Multiph. Flow* (2001) **27**: 971-1009.

[4] P. H. Mortensen, H. I. Andersson, J. J. J. Gillissen, B. J. Boersma. On the orientation of ellipsoidal particles in a turbulent shear flow. *Int. J. Multiph. Flow* (2008) **34**: 678-683.

[5] P. H. Mortensen, H. I. Andersson, J. J. J. Gillissen, B. J. Boersma. Dynamics of prolate ellipsoidal particles in a turbulent channel flow. *Phys. Fluids* (2008) **20**: 093302.

[6] C. Marchioli, M. Fantoni, A. Soldati. Orientation, distribution, and deposition of elongated, inertial fibers in turbulent channel flow. *Phys. Fluids* (2010) **22**: 033301.

[7] C. Marchioli, A. Soldati. Rotation statistics of fibers in wall shear turbulence. *Acta Mech.* (2013) **224**: 2311-2329.

[8] F. Zhao, W. K. George, B. G. M. van Wachem. Four-way coupled simulations of small particles in turbulent channel flow: The effects of particle shape and Stokes number. *Phys. Fluids* (2015) **27**: 083301.

[9] G. A. Voth, A. Soldati. Anisotropic particles in turbulence. *Annu. Rev. Fluid Mech.* (2017) **49**: 249–276.

[10] C. Kleinstreuer, Y. Feng. Computational analysis of non-spherical particle transport and deposition in shear flow with application to lung aerosol dynamics--a review. *J. Biomech. Eng* (2013) **135**: 021008.

[11] M. Mandø, L. Rosendahl. On the motion of non-spherical particles at high Reynolds number. *Powder Technol.* (2010) **202**: 1-13.

[12] C. Marchioli, A. Soldati. Mechanisms for particle transfer and segregation in a turbulent boundary layer. *J. Fluid Mech.* (2002) **468**: 283-315.

[13] A. Soldati, C. Marchioli. Physics and modelling of turbulent particle deposition and entrainment: Review of a systematic study. *Int. J. Multiph. Flow* (2009) **35**: 827-839.

[14] L. Zhao, N. R. Challabotla, H. I. Andersson, E. A. Variano. Rotation of nonspherical particles in turbulent channel flow. *Phys. Rev. Lett.* (2015) **115**: 244501.

[15] D. O. Njobuenwu, M. Fairweather. Simulation of inertial fibre orientation in turbulent

flow. *Phys. Fluids* (2016) **28**: 063307.

[16] D. O. Njobuenwu, M. Fairweather. Effect of shape on inertial particle dynamics in a channel flow. *Flow Turbul. Combust.* (2014) **92**: 83-101.

[17] N. R. Challabotla, L. Zhao, H. I. Andersson. Shape effects on dynamics of inertia-free spheroids in wall turbulence. *Phys. Fluids* (2015) **27**: 061703.

[18] N. R. Challabotla, L. Zhao, H. I. Andersson. Orientation and rotation of inertial disk particles in wall turbulence. *J. Fluid Mech.* (2015) **766**: R2.

[19] W. S. J. Uijttewaal, R. V. A. Oliemans. Particle dispersion and deposition in direct numerical and large eddy simulations of vertical pipe flows. *Phys. Fluids* (1996) **8**: 2590-2604.

[20] C. Marchioli, M. Picciotto, A. Soldati. Influence of gravity and lift on particle velocity statistics and transfer rates in turbulent vertical channel flow. *Int. J. Multiph. Flow* (2007) **33**: 227-251.

[21] C. Nilsen, H. I. Andersson, L. H. Zhao. A Voronoi analysis of preferential concentration in a vertical channel flow. *Phys. Fluids* (2013) **25**: 115108.

[22] N. R. Challabotla, L. Zhao, H. I. Andersson. Gravity effects on fiber dynamics in wall turbulence. *Flow Turbul. Combust.* (2016) **97**: 1095-1110.

[23] N. R. Challabotla, L. Zhao, H. I. Andersson. On fiber behavior in turbulent vertical channel flow. *Chem. Eng. Sci.* (2016) **153**: 75-86.

[24] W. Yuan, H. I. Andersson, L. Zhao, N. R. Challabotla, J. Deng. Dynamics of disk-like particles in turbulent vertical channel flow. *Int. J. Multiph. Flow* (2017) **96**: 86-100.

[25] G. B. Jeffery. The motion of ellipsoidal particles immersed in a viscous fluid. *Proc. R. Soc. Lond. Ser. A* (1922) **102**: 161-179.

[26] C. Siewert, R. P. J. Kunnen, M. Meinke, W. Schröder. Orientation statistics and settling velocity of ellipsoids in decaying turbulence. *Atmos. Res.* (2014) **142**: 45-56.

[27] M. Shapiro, M. Goldenberg. Deposition of glass-fiber particles from turbulent air-flow in a pipe. *J. Aerosol Sci.* (1993) **24**: 65-87.

9. National Conference on Computational Mechanics
MekIT'17
B. Skallerud and H I Andersson (Eds)

SCALES OF A TURBULENT COUETTE-POISEUILLE FLOW WITH VANISHING MEAN WALL SHEAR

KUN YANG[1], LIHAO ZHAO[2] AND HELGE I. ANDERSSON[1]

[1]Department of Energy and Process Engineering
Norwegian University of Science and Technology
7491 Trondheim, Norway
e-mail: tiffany.kun.yang@ntnu.no

[2] Department of Engineering Mechanics
Tsinghua University
10084 Beijing, China
e-mail: zhaolihao@tsinghua.edu.cn

Key words: Wall-bounded Turbulent Flows; Coherent Near-wall Turbulent Structures; Large-scale Structures

Abstract. This study is focused on a turbulent Couette-Poiseuille flow which is driven by a streamwise pressure gradient and relative wall motion. The parameters were carefully prescribed to yield a specific flow with vanishing mean shear at one wall. The distinct shear conditions at the opposite walls result in asymmetry of wall-normal distributions of statistical flow properties such as mean and rms velocity/vorticity and shear stresses with respect to the channel center. The mean streamwise velocity profile demonstrates a longer log-scale region than a conventional Poiseuille flow. In addition, the commonly observed coherent near-wall turbulent structures in the form of streamwise streaks only occur near the fixed wall. Using a spanwise two-point correlation coefficient of the streamwise velocity fluctuation, a growth of the spanwise length associated with the large-scale structures is observed throughout the whole channel. The small-scale streaky structures are only confined near the fixed wall (local) but are strong, while the large-scale structures occupy the whole channel height (global) but are weak. The dominating role switches from the small-scales to the large-scales in the buffer layer next to the fixed wall.

1 INTRODUCTION

Wall-bounded flows are commonly encountered in many natural processes and engineering applications. In particular, turbulent flows between two parallel walls have been widely applied and extensively studied. A flow driven by a streamwise pressure gradient between two solid walls is often referred to as a Poiseuille flow (hereby 'P flow' for brevity).

For a fully-developed turbulent P flow, the wall-normal distribution of the statistical flow quantities is symmetric with respect to the channel center. It is well documented that the near-wall region of a conventional P flow is characterized by coherent streamwise streaky structures, which play an important role in turbulence regeneration cycles [1, 2, 3]. These streamwise streaks are flanked by alternating streamwise vortices, which associate with strong sweep and ejection events of locally high and low velocity. The origin of the streamwise streaks has been explored in various studies [4, 5, 6], some of which argue that the local high mean shear rate is crucial in the formation of such coherent streaky structures [7].

Another commonly encountered wall-bounded turbulent flow is the turbulent Couette flow ('C flow'), for which the flow is driven by the relative motion of the two boundary walls. One important difference of a C flow from a P flow is the formation of large-scale structures which occupy almost the whole domain [8]. Direct numerical studies (DNS) studies on C flows usually require a much larger domain size than that of P flows, since it has been argued that those large-scale structures may be induced by the periodic boundary conditions applied in the numerical model [9, 10]. Near the walls of a C flow, coherent streaky structures similar to those in a P flow are also observed. A detailed examination of the characteristic spanwise spacing of the near-wall streaks in a C flow reveals that they bear two distinct length scales, one with a similar value to that of a P flow and one with a larger value [11]. The multiple length scales are caused by the imprinting of the large-scale structures into the near-wall regions.

Both the P flow and the C flow have a statistical flow field that is symmetric with respect to the channel center. This symmetry is broken by imposing both a streamwise pressure gradient and a relative wall motion to the wall-bounded flow, which leads to a so-called turbulent Couette-Poiseuille flow ('CP flow'). This study concerns the flow scales formed in the asymmetric flow field of a CP flow. In order to evaluate the role of mean shear rate in the formation of coherent near-wall streaky structures and of the flow structures in the whole domain, the relative wall motion was carefully chosen to yield a vanishing mean shear rate at the moving wall. For the current flow Re_τ equals 180, defined by half channel height and the friction velocity u_τ at the non-zero-shear wall. In our recent paper [12], we have presented statistics, scales of flow structures and energy conversion for this particular CP flow. The current paper will provide more details of the mean velocity profile and explore the competition between different scales.

2 METHODOLOGY

We conducted a direct numerical simulation on a turbulent CP flow, with the special consideration of obtaining zero mean shear at one wall by setting it to move relative to the other wall (fixed wall). The computational domain is demonstrated in Figure 1. To accommodate the large-scale structures presumed to form in such a flow, we applied a domain size of $L_x \times L_y \times L_z = 36h \times 10h \times 2h$, which is almost 3 times longer in streamwise and 1.6 times wider in the spanwise direction than the P flow case at the same Re_τ

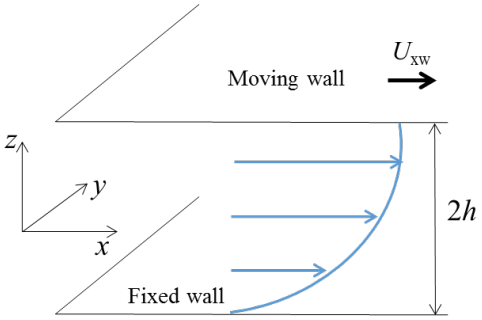

Figure 1: Sketch of the computational domain.

[1]. The fluid in-between the two solid walls is driven by a pressure gradient in the x-direction and the relative wall velocity U_{xw}. The flow is governed by the incompressible Navier-Stokes equations and the continuity equation, which are given in Equations 1 (in which the quantities are normalized by u_τ and h and this normalization is denoted by the prime), where $\tilde{u}_i$ denotes the instantaneous velocity in three (x_i) directions at time t and $\tilde{p}$ is the instantaneous pressure.

$$\begin{aligned} \frac{\partial \tilde{u'}_i}{\partial t'} + \tilde{u'}_j \frac{\partial \tilde{u'}_i}{\partial x'_j} &= -\frac{\partial \tilde{p'}}{\partial x'_i} + \frac{1}{Re_\tau} \frac{\partial^2 \tilde{u'}_i}{\partial x'_j \partial x'_j} \\ \frac{\partial \tilde{u'}_i}{\partial x'_i} &= 0 \end{aligned} \tag{1}$$

The flow field was calculated using a pseudo-spectral method in the homogeneous streamwise (x-) and spanwise (y-) directions, and a second-order central finite difference method in the wall-normal (z-) direction. The validity of this DNS code has been well established [13, 14, 15, 12]. During the simulation, the computational domain was discretised into $576 \times 260 \times 192$ grid points in the streamwise (x-), spanwise (y-) and wall-normal (z-) directions, respectively. We applied a uniform grid spacing in the homogeneous planes, with $\Delta x^+ = 11.25$ and $\Delta y^+ = 6.93$. In the wall-normal (z-) direction, finer grid spacing is applied closer to the walls, and the first wall-normal grid spacing is $\Delta z^+ = 0.88$ next to the wall and the largest wall-normal grid spacing $\Delta z^+ = 2.86$ is found at the channel center.

Unless otherwise specified, all quantities are normalised using the viscous units at the fixed wall and the '+' sign is used to indicate non-dimensionality. Correspondingly, $u_i^+ = \tilde{u}_i/u_\tau, x_i^+ = x_i/(\nu/u_\tau) = t/(\nu/u_\tau^2)$, where ν is the fluid kinematic viscosity. By means of Reynolds averaging, the instantaneous flow velocities can be decomposed into a mean and a fluctuation component as $\tilde{u}_i = U_{im} + u_i$ in x-, y- and z- directions, respectively, where U_{im} is the mean velocity and u_i is the fluctuation component.

3 RESULTS

The calculation was conducted up to $t = 65.2h/u_\tau$ (or $t^+ = 11,736$) to allow a random flow field to develop into a fully statistically steady turbulent flow and to store enough samples for statistical analysis, with a time step of $\Delta t = 0.0002h/u_\tau$ (or $\Delta t^+ = 0.036$). In total 122 samples were taken to study the statical properties of the flow field. Mean streamwise velocity and shear stresses are presented and compared with the conventional Poiseuille flow field (P flow) [1] at the same Re_τ in Figure 2.

3.1 Statistics of the CP flow

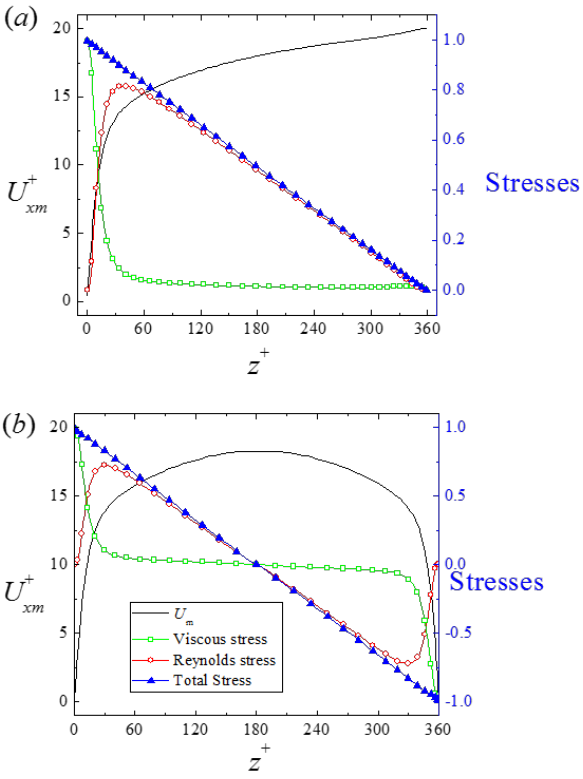

Figure 2: Wall-normal distribution of statistical flow properties at $Re_\tau = 180$ for (a) the current CP flow and (b) a reference P flow [1].

Figure 2 demonstrates the key properties of the current CP flow. As can be seen, while the distribution of mean streamwise velocity and shear stresses is either symmetric or anti-symmetric with respect to the channel center for the P flow, the variations are asymmetric for the CP flow. For the latter, the mean streamwise velocity is zero at the fixed wall and increases to the maximum value at the moving wall, giving a vanishing total (i.e. viscous plus Reynolds) mean shear stress at the moving wall. The maximum total shear stress is found only at the fixed wall for the CP flow and decreases towards the moving wall.

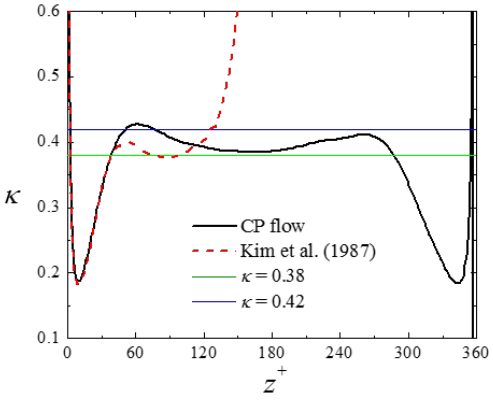

Figure 3: Measure of the von Karman constant κ across the channel height.

An important feature of the mean streamwise velocity distribution in a conventional P flow is the log-scale approximation, always formulated as $U^+_{xm} = \kappa^{-1}\ln z^+ + B$. At $Re_\tau = 180$, the von Karman constant κ is around 0.4 and the additive constant B is about 5.5 [1]. The application range of the log-scale approximation for the current CP flow is evaluated in Figure 3, in which the wall-normal distribution of the κ constant (obtained from $\kappa = \mathrm{d}(\ln z^+)/\mathrm{d}U^+_{xm}$) is shown. It is seen that the distribution of U^+_{xm} for the CP flow results in a much elongated log-scale region compared to that of the P flow case. While the log-scale range of the P flow spans from $z^+ \approx 60$ to 120 (roughly 1/3 of the half channel height below the channel center, that of the CP flow spans all across the channel core up to near the moving wall from $z^+ \approx 60$ to 300 (ca. 2/3 of the whole channel height). The averaged von Karman constant for the CP flow has a value of about 0.397 [12], which is similar but slightly smaller than that of the P flow.

3.2 Scales of the flow structures

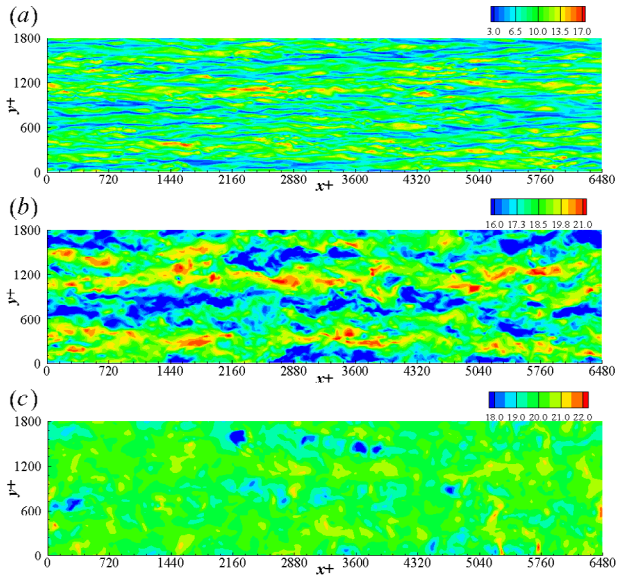

Figure 4: Contours of instantaneous streamwise velocity $\tilde{u}_x^+$ at various wall-normal locations: (a) Near the fixed wall at $z^+ \approx 10$, (b) at the channel center of $z^+ = 180$ and (c) near the moving wall at $z^+ \approx 350$.

As mentioned in the Introduction, it has been argued that the mean shear rate plays an important role in inducing the coherent near-wall turbulent structures in the form of streamwise oriented streaks in low-speed regions [7]. The current CP flow serves as a good candidate to evaluate this issue, by providing distinguishing wall conditions with maximum mean shear rate at the fixed wall and zero mean shear rate at the moving wall. To demonstrate the local flow structures, Figure 4 shows contours of the streamwise velocity fluctuations at three representative wall-normal locations, i.e. near the fixed wall, in the channel center and near the moving wall, respectively. Near the fixed wall, the streamwise oriented low-speed streaks are clearly observed (Figure 4(a)). As we move away from the fixed wall to the center region, streamwise oriented streaks with clearly wider spanwise spacing are still visible, but the number of streaks is clearly reduced. Further away from the fixed wall and much closer to the moving wall, the streaks are no longer observed, and the velocity contours are in the form of 'patch-like' structures. Comparing between the three plots, an enlarging trend of the fluid structures as the mean shear rate reduces is clearly observed. The outer-layer large scales distinguished from the inner-layer small scales have also been observed in P flow at high Re [16] and in C flows [10].

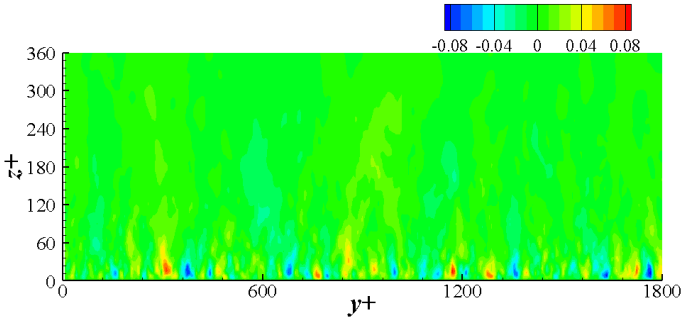

Figure 5: Cross-flow plane of the contour of $\tilde{\omega}_x^+$, averaged along the streamwise direction. Relative strong streamwise vorticity is only observed near the fixed wall.

Since the strong near-wall coherent structures are accompanied by streamwise vorticity ($\tilde{\omega}_x$), disappearing of those small-scale structures can be visualized by the distribution of $\tilde{\omega}_x^+$ along the channel height. Figure 5 shows the contours in the cross-flow plane of $\tilde{\omega}_x^+$ (averaged along the streamwise direction). As shown in Figure 5, strong $\tilde{\omega}_x^+$ distributes only close to the fixed wall. At larger z^+, the streamwise vortices reduce strength while become slightly stretched. They finally become too weak to be seen far enough away from the wall (z^+ large enough).

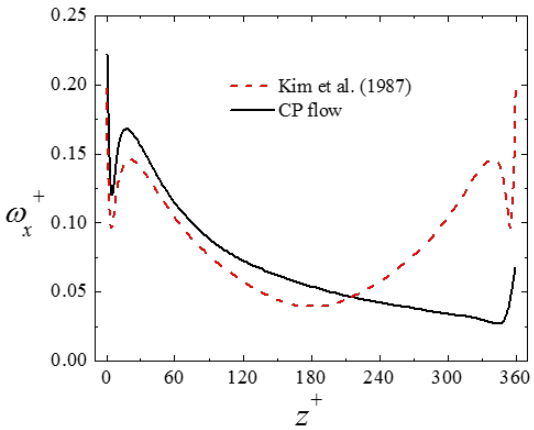

Figure 6: Wall-normal distribution of ω_x^+ (normalized streamwise vorticity). Results for a P flow [1] are also included for comparison.

The fluctuation of the streamwise vorticity is compared with the P flow [1] in Figure 6. The high peak of ω_x^+ close to the fixed wall represents the strong intensity of the streamwise vorticity associated with the near-wall coherent turbulent structures. Once leaving the high peak near the fixed wall, ω_x^+ decreases until very close to the moving wall. Unlike the symmetric flow field of a P flow, there is no high peak near the opposing moving wall in the current CP flow. This observation confirms that the strong near-wall coherent structures are only confined close to the fixed wall, and can not form near the moving wall where the mean shear rate approaches zero. The maximum values at the two walls are caused by the wall-induced streamwise vorticity [1]. The modest maximum value at the moving wall indicates the presence of the large-scale structures. The value of ω_x^+ at the fixed wall is higher than at the moving wall, because the streamwise vortices associated with the near-wall streaks are much stronger than the large-scale structures.

It has been previously shown that the average spanwise spacing between the near-wall streaks is approximately 100 wall units (ν/u_τ^2) for a P flow at $Re_\tau = 180$ [1]. The spanwise spacing can be evaluated by a spanwise two-point correlation coefficient of the streamwise velocity fluctuation, $R_{u_x u_x}(\delta y)$, which is defined as:

$$R_{u_x u_x}(\delta y) = \frac{\overline{u_x(x,y,z,t)u_x(x,y+\delta y,z,t)}}{u_{xrms}(z,t)u_{xrms}(z,t)}, \tag{2}$$

in which δy is the spanwise distance between two sampling grid points.

To quantify the enlarging scales, the calculated $R_{u_x u_x}(\delta y)$ at three selected wall-normal locations featuring near the fixed wall ($z^+ \approx 10$), in the channel center ($z^+ = 180$) and near the moving wall ($z^+ \approx 350$) is given in Figure 7(a). The distance between the minimum point of the $R_{u_x u_x}(\delta y)$ curve and the origin is used to represent half the average spanwise spacing between the streaks [1, 11], which is represented by $\lambda^+/2$. Near the fixed wall, the curve bears a sharp minimum point at $\delta y \approx 0.3h$, yielding a δy^+ of about 55 ($\lambda^+ \approx 110$), similar to that reported previously for a P flow[1]. The negative peak becomes less abrupt and moves to larger $\delta y/h$ as one leaves the fixed wall region and approaches the moving wall. As can be observed in Figure 7(a), a minimum value can be identified at $\delta y/h \approx 1.7$ for the wall-parallel plane at the channel center, and an even more blunt negative peak is found at $\delta y/h \approx 2$ for the wall-parallel plane close to the moving wall. This trend of less prominent negative peaks of $R_{u_x u_x}(\delta y)$ at larger $\delta y/h$ values is consistent with the previously observed enlarging scales of the flow structures in Figure 4.

The conversion from the inner-layer small scales to the out-layer large scales happens in the buffer layer, and is reflected by the relative magnitude of the different negative peaks (or minimum values) of $R_{u_x u_x}(\delta y)$, shown in Figure 7(b). As seen, within a thin layer between $z^+ = 26$ to 30, all curves have two minimum values, one closer to the fixed wall at $\delta y/h \approx 0.3$ and the other at $\delta y/h \approx 0.6$. The two negative peaks indicate the coexistence of the two different scales. Within this coexistence-region, the strengths (reflected by the relative magnitudes) of these two scales compete and switch their roles

at a certain z^+. It is observed that the negative peak with the largest magnitude switches from the one at smaller $\delta y/h$ to the one at larger $\delta y/h$ as one moves away from the fixed wall. This indicates that the dominant role is switched from the small-scale structures (associated with peak at smaller $\delta y/h$) to the large-scale structures at a certain distance away from the fixed wall.

The average spanwise spacing (λ^+) along the wall-normal direction is plotted in Figure 8. In previous studies, λ^+ is always determined by the lowest min (i.e. the minimum value with the largest magnitude), which is shown by the green triangles in Figure 8. As a result, for a flow with large-scale structures like the current CP flow, there is a jump of λ^+ as the flow scales switch from being dominated by the small ones to by the large ones. To clearly show the coexistence of the two scales and their competing strengths, the λ^+ value obtained from the two peaks observed in Figure 7(b) is included in Figure 8. From Figure 8 an overall increase of λ^+ is observed as the moving wall is approached or as the mean shear rate is reduced. For $z^+ < 40$, the 1$^{\text{st}}$-found peak (the peak found at the smaller $\delta y/h$) represents the small scales, while the 2$^{\text{nd}}$-found peak represents the large scales. The small scales slowly increase while the large scales remain constant. The 2$^{\text{nd}}$-found min becomes more prominent (now the 1$^{\text{st}}$ lowset) than the 1$^{\text{st}}$-found min (now the 2$^{\text{nd}}$-lowest) at around $z^+ \approx 30$, when the large scales take over the small scales. It is worthwhile noting that, there are more negatives peaks (the several top points in the figure) found at even larger $\delta y/h$, but our focus here is the first two peaks which stand for the near-wall small scales and the large-scale structures. Above $z^+ \approx 35$, the small scales are no longer detected, and both negative peaks are associated with the large scales. The 1$^{\text{st}}$ found peak now represents the 1$^{\text{st}}$ length scale while the 2$^{\text{nd}}$ found peak represents the 2$^{\text{nd}}$ length scale of the large scales. This means the large scales now dominate the flow field. The average spanwise spacing of the large-scale structures continues to grow further away from the fixed wall.

Both Figure 7 and 8 show that the small scales are only confined near the fixed wall and are local, but they are more intensive. On the contrary, the large scales are global over the whole channel, but are relatively weak.

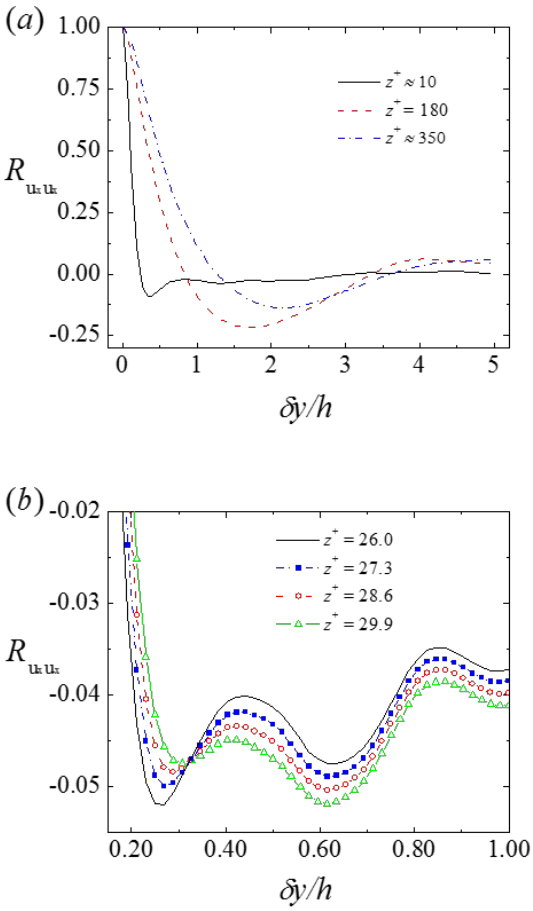

Figure 7: Spanwise two-point correlation coefficient of streamwise velocity fluctuation calculated at various wall-parallel planes. (*a*) At selected z^+ planes spanning across the channel and (*b*) at z^+ planes in the buffer layer.

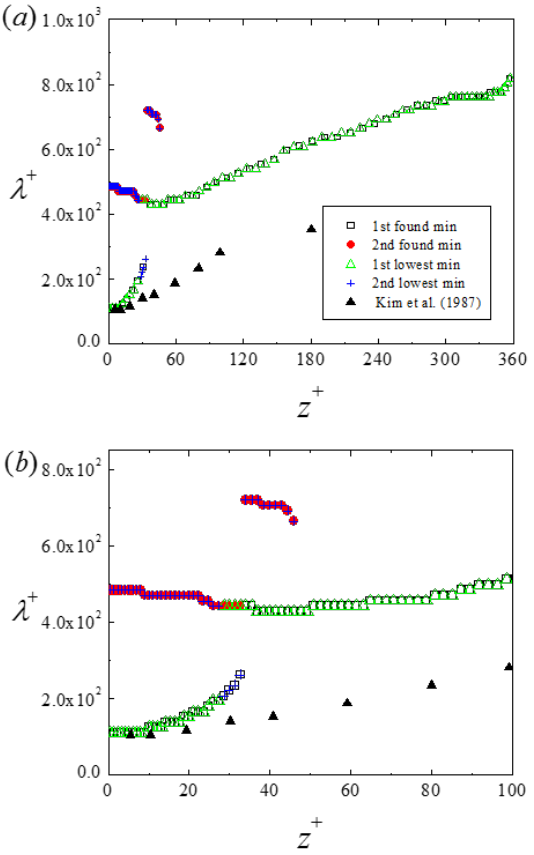

Figure 8: Variation of λ^+ obtained from evaluating the $R_{u_x u_x}(\delta y)$ curves. (a) Along the whole channel height and (b) zoom-in near the fixed wall. Results from P flow [1] are included for comparison. The 1st found min is the negative peak found at the smaller $\delta y/h$ and the 2nd min at the larger $\delta y/h$. The 1st found min is associated with the near-wall small scales while the 2nd found min is with the large scales. The 1st lowest min is the negative peak with the largest magnitude and the 2nd lowest min with the 2nd largest magnitude.

4 CONCLUSIONS

We present selected results from a DNS study of a specific turbulent Couette-Poiseuille flow (CP flow) driven by a streamwise pressure gradient and two relative moving walls at $Re_\tau = 180$ based on the friction velocity at the reference (fixed) wall and half channel height. The driving pressure gradient and the relative velocity of the walls were chosen so that the mean shear rate at the moving wall vanished. This enables us to evaluate the effects of zero mean shear rate on the overall flow structures, in particular the coherent near-wall turbulent streaky structures and the global large-scale structures.

Unlike a turbulent Poiseuille flow (P flow) at the same Re_τ, the wall-normal distribution of the statistical flow properties (i.e. mean and rms velocity, shear stresses and vorticity) is asymmetric with respect to the channel center. The maximum shear stresses occur near the fixed wall, while they reduce to zero at the moving wall where the mean streamwise velocity is the highest. The log-scale approximation applies over a much larger wall-normal region for the CP flow than for the P flow, with a similar (although slightly lower) von Karman constant.

The total mean shear rate reduces linearly from the fixed wall to the moving wall. The coherent near-wall streaky structures can be observed near the fixed wall in the CP flow. Nearby the moving wall, streaks cease to form, and the flow structures appear to be 'patch-like'. As a result, the strong streamwise vorticity which accompanies the low-speed streaks can only be observed near the fixed wall. However, the wall values of ω_x^+ indicate the presence of the weak large-scale vortical structures.

Underlying characteristic spanwise length scales of the flow structures can be quantitatively examined by a spanwise two-point correlation coefficient of the streamwise velocity fluctuation. The spanwise spacing of the streaks near the fixed wall is identified by the negative peak found at the smallest $\delta y/h$ for $z^+ \approx 10$, and has a similar value to that in the P flow. Away from the fixed wall, the spanwise spacing increases, indicating an increase of the flow scales. The switch of the dominating role between the small-scale near-wall streaks and the large-scale structures is observed within the buffer layer between $z^+ \approx 25$ to 30 for the present flow. The results show that the near-wall streaks are strong but local, while the large-scale-structures are weak but global.

5 ACKNOWLEDGEMENT

The authors would like to thank the Research Council of Norway (NFR) for the grants (Project No. 250744) and the support from Sigma2 for the computational resources (NN2649K).

REFERENCES

[1] Kim, J., Moin, P. and Moser, R. Turbulence statistics in fully developed channel flow at low Reynolds number. *J. Fluids Mech.* (1987) **177**:133-166.

[2] Wallace, J.M., Eckelmann, H. and Brodkey, R.S. The wall region in turbulent shear flow. *J. Fluids Mech.* (1972) **54**:39-48.

[3] Robinson, S.K. Coherent motions in the turbulent boundary layer. *Annu. Rev. Fluid Mech.* (1991) **23**:601-639.

[4] Jeong, J., Hussain, F., Schoppa, W. and Kim, J. Coherent structures near the wall in a turbulent channel flow. *J. Fluids Mech.* (1997) **332**:185-214.

[5] Waleffe, F. Exact coherent structures in channel flow. *J. Fluids Mech.* (2011) **435**:93-102.

[6] Schoppa, W. and Hussain, F. Coherent structure generation in near-wall turbulence. *J. Fluids Mech.* (2002) **453**:57-108.

[7] Rogers, M. and Moin, P. The structure of the vorticity field in homogeneous turbulent flows. *J. Fluids Mech.* (1987) **176**:33-66.

[8] Komminaho, J., Lundbladh, A. and Johansson, A.V. Very large structures in plane turbulent Couette flow. *J. Fluids Mech.* (1996) **320**:259-285.

[9] Bech, K.H., Tillmark, N., Alfredsson, P.H. and Andersson, H.I. An investigation of turbulent plane Couette flow. *J. Fluids Mech.* (1995) **286**:291-325.

[10] Tsukahara, T., Kawamura, H. and Shingai K. DNS of turbulent Couette flow with emphasis on the large-scale structure in the core region. *J. Turbul.* (2006) **7**:N19.

[11] Pirozzoli, S., Bernardini, M. and Orlandi, P. Large-scale motions and inner/outer layer interactions in turbulent Couette-Poiseuille flows. *J. Fluids Mech.* (2011) **680**:534-563.

[12] Yang, K., Zhao, L. and Andersson, H.I. Turbulent Couette-Poiseuille flow with zero wall shear. *Int. J. Heat Fluid Flow* (2017) **63**:14-27.

[13] Gillissen, J.J.J., Boersma, B.J., Mortensen, P.H., and Andersson, H.I. On the performance of the moment approximation for the numerical computation of fiber stress in turbulent channel flow. *Phys. Fluids* (2007) **19**:035102.

[14] Zhao, L., Andersson, H.I. and Gillissen, J.J.J. Interphasial energy transfer and particle dissipation in particle-laden wall turbulence. *J. Fluids Mech.* (2013) **715**:32-59.

[15] Mortensen, P.H., Andersson, H.I., Gillissen, J.J.J. and Boersma, B.J. Dynamics of prolate ellipsoidal particles in a turbulent channel flow. *Phys. Fluids* (2008) **20**:933102.

[16] Balakumar, B.J. and Adrian, R.J. Large- and very-large-scale motions in channel and boundary-layer flows. *Phil. Trans. R. Soc. A* (2007) **365**:665-681.

Authors Index

Aggarwal, A. 25

Ahmad, N. 311

Alendal, G. 57

Andersson, H. I. 111, 337, 369, 425, 441

Arntsen, Ø. A 85

Arntsen, Ø. A. 25, 85, 311, 411

Arslan, T. 327

Aursand, E. 35

Avlesen, H. 57

Ayder, E. 327

Bazilevs, Y. 169, 245

Berntsen, J. 57

Bihs, H. 25, 71, 85, 137, 231, 311, 411

Challabotla, N. R. 425

Chella, M. A. 25, 71, 85

Dadmarzi, F. H 111

Eidnes, S. 121

Fornes, P. 137

Friedemann, C. J. 151

Groen, J. 21

Hans Petter Langtangen..... 1

Haugen, B. 245

Helgedagsrud, T. A. 169, 245

Holzapfel, G. A. 3

Ilseng, A. 215

Jiang, F. 337, 369

Kamath, A. 71, 231, 311, 411

Korobenko, A. 169

Kvamsdal, T. 245

Larsen, S. D. 21

Liestyarini, U. C. 299

Liu, H. 191

Liu, S. 299

Lorentzon, J. 7

Lu, J. Z. 231

Mathisen, K. M. 169, 245

Mortensen, M. 151, 273

Narasimhamamurthy, V. D. 111
Nilsen, C. 103
Nocente, A. 327
Nordal, S. 137
Nossen, J. 151
Ogden, R. W. 3
Øiseth, O. A. 169
Okstad, K. M. 245
Ong, M. C. 299
Pakzodi, C. 25, 71
Pettersen, B. 111, 337, 369
Prot, V..... 215
Prot, V. E. 191
Raknes, S. B. 245
Revstedt, J. 7
Ringholm, T. 121
Sigmund, O. 21
Siikonen, T. 385
Skallerud, B. 191, 215
Stokke, B. T. 215
Strandenes, H. 337
Sund, F. 351
Thiem, Ø. 57
Tian, C. 369
Vitanen, V. M. 385
Wang, W. 411
Xing, Y. 299
Yang, K. 441
Yuan, W. 425
Zhao, L. 425, 441

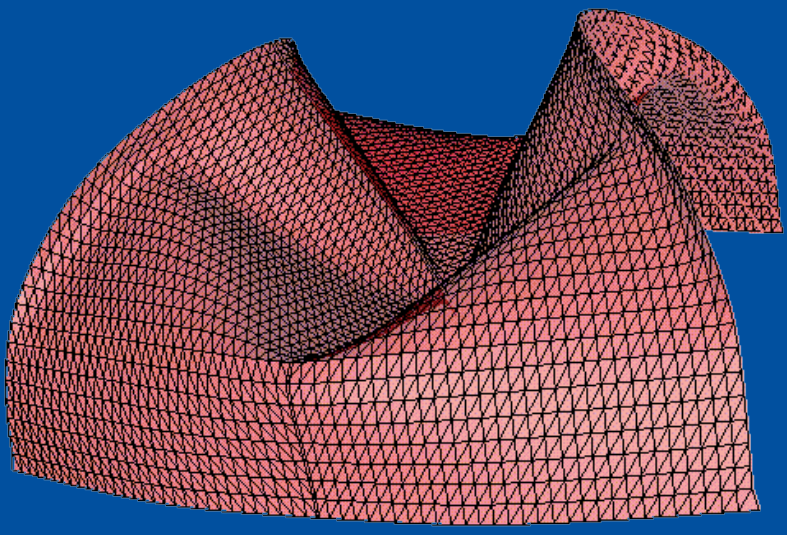

NTNU
Norwegian University of
Science and Technology

CIMNE
International Center
for Numerical Methods in Engineering